Supramolecular Materials for Opto-Electronics

RSC Smart Materials

Series Editors:
Hans-Jörg Schneider, *Saarland University, Germany*
Mohsen Shahinpoor, *University of Maine, USA*

Titles in this Series:
1: Janus Particle Synthesis, Self-Assembly and Applications
2: Smart Materials for Drug Delivery: Volume 1
3: Smart Materials for Drug Delivery: Volume 2
4: Materials Design Inspired by Nature
5: Responsive Photonic Nanostructures: Smart Nanoscale Optical Materials
6: Magnetorheology: Advances and Applications
7: Functional Nanometer-Sized Clusters of Transition Metals: Synthesis, Properties and Applications
8: Mechanochromic Fluorescent Materials: Phenomena, Materials and Applications
9: Cell Surface Engineering: Fabrication of Functional Nanoshells
10: Biointerfaces: Where Material Meets Biology
11: Semiconductor Nanowires: From Next-Generation Electronics to Sustainable Energy
12: Supramolecular Materials for Opto-Electronics

How to obtain future titles on publication:
A standing order plan is available for this series. A standing order will bring delivery of each new volume immediately on publication.

For further information please contact:
Book Sales Department, Royal Society of Chemistry, Thomas Graham House, Science Park, Milton Road, Cambridge, CB4 0WF, UK
Telephone: +44 (0)1223 420066, Fax: +44 (0)1223 420247
Email: booksales@rsc.org
Visit our website at www.rsc.org/books

Supramolecular Materials for Opto-Electronics

Edited by

Norbert Koch
Humboldt University of Berlin, Berlin, Germany
E-mail: norbert.koch@physik.hu-berlin.de

RSC Smart Materials No. 12

Print ISBN: 978-1-84973-826-2
PDF eISBN: 978-1-78262-694-7
ISSN: 2046-0066

A catalogue record for this book is available from the British Library

Published by The Royal Society of Chemistry,
Thomas Graham House, Science Park, Milton Road,
Cambridge CB4 0WF, UK

Registered Charity Number 207890

For further information see our web site at www.rsc.org

Preface

The power of supramolecular assembly strategies, where mostly non-covalent interactions between individual building blocks are exploited, to form well-defined two- and three-dimensional architectures is impressive. Careful design of molecules to facilitate directed hydrogen-bonding, π–π, and electrostatic interactions can lead to hierarchically ordered structures spanning the nano- to the macroscale. In addition, covalent bonds between molecules are used to form supramolecular assemblies, and the properties of the subunits can be largely retained by keeping their direct electronic coupling strength low. In an overarching scheme, complex multi-component structures are assembled first and subsequently locked into position by initiating covalent bonds. Achieving an appropriate balance of all intermolecular forces to reach the desired bulk structures is challenging.

When aiming to use supramolecular systems in electronic and opto-electronic devices, such as transistors, light emitting diodes, photovoltaic cells, and memory elements, the challenges increase rapidly. Key for device functionality is the proper combination of conducting, semiconducting, and insulating materials, some or even all of which may be provided for by supramolecular assemblies and on various length scales. Furthermore, typical device structures are composed of numerous layers of materials and it has transpired that the interfaces between layers are of paramount importance for device performance.

Consequently, the interaction between a substrate – often an electrode – and the assembly building blocks introduces another degree of freedom for steering structure formation, which thus differs from the bulk. The same holds when considering the formation of heterojunctions of different supramolecular materials, where adverse side effects such as intermixing and induced orientations may occur. In addition, since opto-electronic components are two- or multi-terminal devices, the question of how

RSC Smart Materials No. 12
Supramolecular Materials for Opto-Electronics
Edited by Norbert Koch

Published by the Royal Society of Chemistry, www.rsc.org

electronic equilibrium across the entire layer stack is established must be addressed. We can think of the stack as a sequence of materials with varying energy gaps (*i.e.*, semiconductors), where the alignment of energy levels to a common Fermi-level may introduce space charges, mostly close to the interfaces. This induced charge density represents yet another source of interaction that influences the supramolecular structure formation.

For opto-electronic functionality, the requirements regarding structural perfection are tremendous. Every defect will widen the energy spread of the density of states where charge carrier transport takes place, thus reducing carrier mobility. Furthermore, radiative exciton recombination, *e.g.*, in a light emitting diode, can be tremendously reduced by defects, particularly trapped charges. Therefore, the envisioned devices require either extreme structure control or, at least, fault-tolerant architectures must be implemented.

To comprehensively understand supramolecular materials for opto-electronic applications and to derive reliable material design guidelines, experiment and theory must go hand in hand. True multiscale modeling must be applied, starting from an *ab initio* approach for the building blocks or moderately large assemblies to unravel fundamental electronic and optical properties, and continuing to larger length- and time-scales through parameterization of electrons and eventually atoms to predict structure formation up to device-relevant scales.

All these topics and challenges are discussed in the chapters of this book. Experts, who define the frontiers of the respective fields, present state-of-the-art understanding of supramolecular assemblies consisting of conjugated molecular moieties to achieve opto-electronic functionality, and show how these formidable challenges are presently tackled. Research towards supramolecular systems for opto-electronics remains vivid and will benefit from increasingly tight interactions of chemistry, physics, material science, and electrical engineering.

Norbert Koch
Berlin

Contents

Chapter 1 Self-assembled Supramolecular Materials in Organic Electronics **1**
Emilie Moulin, Eric Busseron and Nicolas Giuseppone

1.1 Introduction 1
1.2 Conducting Supramolecular Materials 2
1.2.1 Thiophene Derivatives 2
1.2.2 Tetrathiafulvalene Derivatives 6
1.2.3 Porphyrins and Pyrroles Derivatives 7
1.2.4 Polyaromatic Derivatives 10
1.2.5 Perylene Derivatives 11
1.2.6 Triarylamine Derivatives 14
1.2.7 Other Aromatic Molecules 15
1.3 Organic Field Effect Transistors 18
1.3.1 Thiophene Derivatives 19
1.3.2 Tetrathiafulvalene Derivatives 20
1.3.3 Phthalocyanine Derivatives 21
1.3.4 Perylene Derivatives 21
1.3.5 Other Aromatic Molecules 24
1.4 Organic Light-Emitting Devices 26
1.4.1 Oligo(phenylenevinylene) Derivatives 26
1.4.2 Fluorene Derivatives 27
1.4.3 Polyaromatic Molecules 27
1.4.4 Metallic and Inclusion Complexes 29
1.4.5 H-bond and Metallo-supramolecular Polymers 30
1.5 Organic Photovoltaic Devices 32
1.5.1 Thiophene Derivatives 32
1.5.2 Porphyrin and Phthalocyanine Derivatives 36

RSC Smart Materials No. 12
Supramolecular Materials for Opto-Electronics
Edited by Norbert Koch

Published by the Royal Society of Chemistry, www.rsc.org

1.5.3 Diketopyrrolopyrrole Derivatives 37
1.5.4 Hexabenzocoronene Derivatives 38
1.5.5 Rylene Derivatives 39
1.5.6 Triarylamines Molecules 40
1.5.7 Other Aromatic Molecules 40
1.6 Conclusion 41
Acknowledgements 42
References 42

Chapter 2 Multicomponent Assembly Strategies for Supramolecular Systems 53
Dimas G. de Oteyza

2.1 Introduction 53
2.2 Taming the Driving Forces behind Multicomponent Self-Assembly 55
2.2.1 Molecule–Substrate Interactions 57
2.2.2 Intermolecular Interactions 63
2.3 Electronic Considerations in Multicomponent Molecular Assemblies 80
2.3.1 Standard Interfacial Models 80
2.3.2 Supramolecular Environment-Dependent Electronic Properties 84
2.4 Concluding Remarks 88
References 89

Chapter 3 Low-Dimensional Supramolecular Assemblies on Surfaces 98
Tianchao Niu, Jia Lin Zhang and Wei Chen

3.1 Introduction 98
3.2 1D Molecular Chains 99
3.2.1 Substrate Template Directed Self-Assembly of 1D Molecular Chains 100
3.2.2 1D Molecular Chains Assembled through Hydrogen Bonding 101
3.2.3 Metal–Organic Coordination Bonds Assisted Assembly of 1D Molecular Chains 103
3.2.4 On-Surface Synthesis towards Covalently Bonded 1D Molecular Chains 104
3.3 2D Molecular Networks 106
3.3.1 Single-Component Supramolecular Structures on Surfaces 107
3.3.2 Binary Molecular Networks 109
3.3.3 On-Surface Covalent-Bonded Molecular Networks 112

3.4 Conclusion 115
Acknowledgement 116
References 116

Chapter 4 Self-Assembled Mono- and Multilayers for Functional Opto-Electronic Devices 119
Antonio Facchetti, Rocio Ponce Ortiz and Tobin J. Marks

4.1 Introduction 119
4.2 Concepts of Molecular Self-Assembly for Mono- and Multilayer Fabrication and Function 120
4.3 Applications of SAM and SAMT to Organic Opto-Electronic Devices 125
4.3.1 Organic Field-Effect Transistors 128
4.3.2 Bulk-Heterojunction Solar Cells 144
4.3.3 Organic Light-Emitting Diodes 152
4.3.4 Electro-Optic Devices 154
4.4 Conclusions 158
Acknowledgments 159
References 159

Chapter 5 Amphiphilic Design for Supramolecular Materials with Opto-Electronic Functions 173
Subi J. George, Ankit Jain and K. Venkata Rao

5.1 Introduction 173
5.2 Electronic Functionality 176
5.2.1 p-Type Semiconducting Amphiphiles 176
5.2.2 n-Type Semiconducting Amphiphiles 181
5.2.3 Miscellaneous π-Conjugated Amphiphiles 183
5.2.4 Multi-chromophoric p-n Amphiphiles 186
5.2.5 Supramolecular Amphiphiles 190
5.3 Optical Functionality 191
5.4 Conclusion 198
References 198

Chapter 6 Chiral Supramolecular Structures as Spin Filters 203
Ron Naaman and David H. Waldeck

6.1 Introduction 203
6.2 Theory 205
6.2.1 Spin–Orbit Coupling Magnitude 207
6.2.2 Resonances 207
6.3 Experimental Results 208
6.3.1 Spin-Dependent Photoelectron Transmission 208
6.3.2 Spin-Dependent Conductivity 211

6.4 Applications and Implications 218
6.4.1 Memory Device 218
6.5 Conclusions 222
Acknowledgements 223
References 223

Chapter 7 Solution Processed Multilayer Organic Light Emitting Diodes 226
Manuel Auer, Leonid Pevzner, Stefan Sax and Emil J. W. List-Kratochvil

7.1 Introduction 226
7.2 Multilayer Structures from the same Solvent by Diverse Fabrication Strategies 229
7.2.1 Blade Coating 230
7.2.2 Liquid Buffer Layer 231
7.2.3 Electrospray Deposition 232
7.2.4 Transfer Printing 233
7.2.5 Lamination 234
7.3 Multilayer Structures from the same Solvent by Chemical Reaction 235
7.3.1 Cross-Linking by the Addition of Reactive Groups 236
7.3.2 Thermal Stabilization 246
7.3.3 The Precursor Route 247
7.3.4 Universal Cross-Linking 248
7.4 Multilayer Structures from Orthogonal Solvents 250
7.4.1 Polar Solvents 252
7.4.2 Fluorinated Solvents 257
7.4.3 Hybrid Approaches 259
7.5 Conclusion and Outlook 265
Acknowledgements 266
References 266

Chapter 8 Concepts and Modeling for Charge Transport in Organic Electronic Materials 273
K. Sebastian Radke, F. Ortmann and G. Cuniberti

8.1 Introduction 273
8.2 Kubo Formalism 275
8.3 *Ab Initio* Material Parameters and Disorder Models 277
8.3.1 Hamiltonian for Coupled Electrons and Phonons 277
8.3.2 *Ab Initio* Material Parameters 279
8.3.3 Disorder Models 282

8.4 Polaron Transport Approaches 282
8.4.1 Three-Dimensional Anisotropic Mobility 283
8.4.2 Limiting Cases 286
8.5 Quantum Dynamic Charge Propagation Techniques 289
8.5.1 Introduction 289
8.5.2 Polaron Theory Based Charge Propagation 291
8.5.3 Mixed Quantum–Classical Propagation 292
8.6 Résumé 304
Acknowledgements 305
References 305

Chapter 9 Simulations of Morphology and Charge Transport in Supramolecular Organic Materials 309
Denis Andrienko

9.1 Introduction 309
9.2 Morphology Simulations 314
9.2.1 First-Principles Calculations 315
9.2.2 Atomistic Models 316
9.2.3 Coarse-Grained Models 318
9.3 Charge Transport 320
9.3.1 Diabatic States 321
9.3.2 Charge Transfer Rates 324
9.3.3 Electronic Coupling Elements 325
9.3.4 Reorganization Energies 328
9.3.5 Driving Forces 328
9.3.6 Charge Mobility 335
9.4 Finite-Size Effects 337
9.5 Stochastic Models 338
9.6 Interfaces and Long-Range Interactions 339
9.7 Excited States 341
9.8 Software 342
9.9 Outlook 344
Acknowledgements 344
References 345

Subject Index 363

CHAPTER 1

Self-assembled Supramolecular Materials in Organic Electronics

EMILIE MOULIN, ERIC BUSSERON AND NICOLAS GIUSEPPONE*

SAMS Research Group – University of Strasbourg – Institut Charles Sadron, CNRS, 23 rue du Loess, BP 84087, 67034 Strasbourg Cedex 2, France
*Email: giuseppone@unistra.fr

1.1 Introduction

Organic electronics[1] is of great fundamental interest in materials science and is also recognized as one of the most promising and competitive markets for industry. In particular, its expansion will be supported by the development of active components being easily processable, flexible, energy friendly, cheap, and compatible with their downscaling towards nano-devices. In this research field, high-molecular-weight conjugated polymers in the form of thin plastic films are easy to synthesize and to process for incorporation in devices.[2] However, these materials show limitations in the precise ordering of their crystalline layers in the bulk, thus impacting the mobilities of charge-carriers required for enhanced performances. Conversely, recrystallization or vapor-phase deposition of low-molecular-weight π-conjugated organic molecules leads to 100% crystalline orientation, but single crystals are impractical to process.[3] At the smallest scales, the very intriguing electronic properties of single molecules have also been

RSC Smart Materials No. 12
Supramolecular Materials for Opto-Electronics
Edited by Norbert Koch

Published by the Royal Society of Chemistry, www.rsc.org

demonstrated, but problems arise from contacts with the electrodes and from thermal noise producing undesired orientation and conformational motions.[4]

Quite recently, so-called supramolecular electronics[5] has been proposed as a promising intermediary-scale approach that rests on the design of electronic components at a length of 5–100 nm, that is, between plastic electronics (μm) and molecular electronics (Å). Supramolecular engineering, which programs self-assembly processes under thermodynamic control,[6,7] represents a key bottom-up strategy to build and process relatively soft functional objects while introducing ''pseudo-crystalline'' electroactive domains corresponding to this typical intermediate length scale. In the past ten years, since the seminal works of several groups who demonstrated the potential of this approach with supramolecular assemblies such as gels and liquid crystals, several soft nanoribbons, nanotubes, nanorods, and nanowires of low dimensionality have been designed and incorporated into organic electronic devices.[8,9] In the following sections, we discuss some recent examples of supramolecular electroactive nanostructures displaying various electronic properties such as conducting materials, field-effect transistors, light-emitting diodes, and photovoltaic devices. Within each of these sections, electroactive self-assemblies are classified along with the molecular structure of their components.

1.2 Conducting Supramolecular Materials

This section specifically focuses on soft self-assemblies made of small organic molecules, or of short monodisperse oligomers, and yielding to π-stacked one-dimensional (1D) conducting nano-objects with high aspect ratio, a geometry attracting much attention for its crucial impact on advanced nanosciences.[10] These supramolecular structures are classified according to their chemical composition, such as for instance: (i) thiol-based heterocycles such as thiophenes and tetrathiafulvalenes (TTFs); (ii) nitrogen-containing heterocyclic molecules; (iii) aromatic molecules including perylene-tetracarboxylic diimides (PTCDIs), fluorenes, anthracenes, and hexabenzocoronenes (HBCs); derivatives; and (iv) triarylamines. For each category, we shall emphasize the most remarkable advances achieved in the recent literature regarding three interlinked aspects of crucial importance for further developments in organic electronics: structure, conductivity properties, and processability.

1.2.1 Thiophene Derivatives

Conjugated polymers of thiophenes are among the best candidates for thin film (opto)electronic devices because of their small band gap, their relatively high charge carrier mobility, and their high quantum yield for fluorescence. Feringa and van Esch first described an alternative supramolecular approach in which bis-urea derivatives incorporating mono- or bis-thiophene spacers

can self-assemble by hydrogen bonds into ribbons that enforce the π-stacking of the central heterocycles.[11] Lamellar fibers with lengths of 20–100 μm and breadths of 2–10 μm were imaged by electronic microscopy and molecular modeling studies of the closely packed layers were also found to be coherent with X-ray powder diffraction analyses. The charge mobility properties of these materials were determined by a pulse radiolysis time-resolved microwave conductivity technique (PR-TRMC) technique, which minimizes effects of domain boundaries and impurities. The authors measured values up to 5×10^{-3} cm^2 V^{-1} s^{-1}, thus showing that supramolecular cofacial ordering provided by the bis-urea interactions can improve the through-space mobility of charge carriers close to that measured in covalent conjugated polythiophenes (7×10^{-3} cm^2 V^{-1} s^{-1}). Along the same lines, other groups developed symmetric oligothiophene[12] and oligo(thienylene-vinylene)[13] derivatives with lateral hydrogen bond forming segments, yielding conducting gels with values reaching 4×8 10^2 S m^{-1} upon I_2 doping and by solvent evaporation casting in a four-probe configuration. In these cases, non-linear *I/V* curves indicate contact resistance due to a charge injection barrier. All the aforementioned examples highlight the role of the self-assembly and of the gelation process to achieve electronic properties that can rival covalent conducting molecules.

Recently, the group of Barbarella described the synthesis of octa- and tetrathioether-substituted octathiophenes and studied the morphology and conductivity of the corresponding self-assemblies.[14] Scanning electron microscopy (SEM) and atomic force microscopy (AFM) imaging revealed that the sulfur-overrich molecule formed superhelices and even double helices of superhelices with lengths ranging from 100 nm up to 5 μm whereas the core tetra-substituted molecule formed tape-like fibrils of similar lengths. Both types of fibers grown on ITO (indium tin oxide) were then analyzed by tunneling atomic force microscopy in torsion mode (Tr-TUNA), which allows simultaneous surface topography and nanoscale conductivity measurement. Finally, charge carrier mobilities of both octathiophenes were determined using conductive-AFM (C-AFM) (9.8×10^{-7} cm^2 V^{-1} s^{-1} for the octa-substituted system *versus* 5 10^{-6} cm^2 V^{-1} s^{-1} for the tetra-substituted one) and could be rationalized based on X-ray diffraction of the fibers films, which shows that the presence of substituents on the outermost rings induces disorder and therefore influences the distance between parallel octathiophene rows.

In another approach, Stupp and co-workers[15] achieved the self-assembly of short oligothiophene rod-coils by conjugation to a dendron capable of self-associating by hydrogen bonding. These molecules can be dissolved at high temperature in toluene/THF mixtures and form birefringent gels (1 wt%) after cooling at room temperature. These gels present blue-shifted absorbance and red-shifted fluorescence compared to solutions, in agreement with the formation of H-aggregates. A TEM (transmission electron microscopy) micrograph illustrates the formation of ribbons with a width of a single dendron dimer (9.7 ± 0.3 nm), while AFM revealed a thickness of

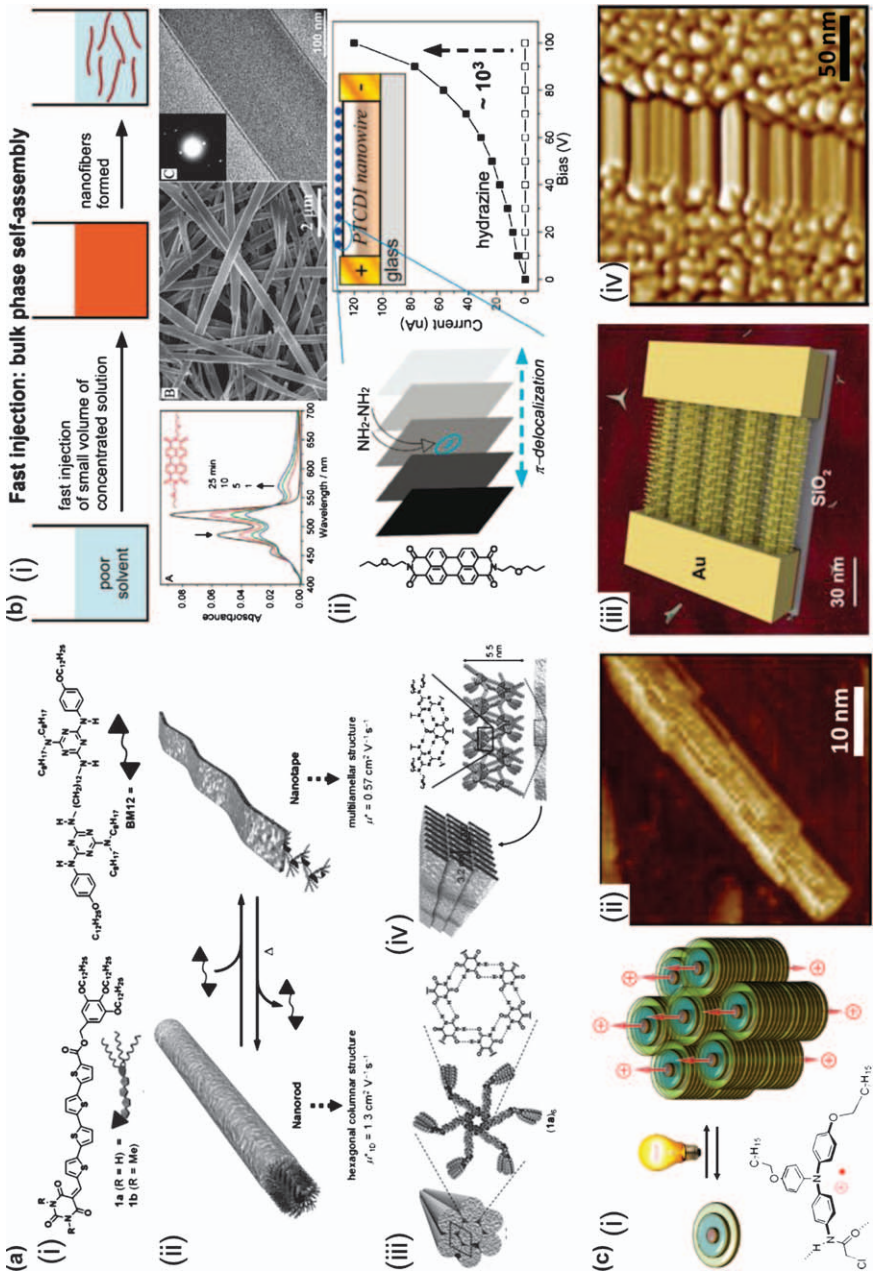

6–8 nm, and small-angle X-ray scattering confirmed their expected internal solid-state packing. Films obtained from the self-assembled state were cast on a four-probe electrode, indicating a conductivity of 7.9×10^{-3} S m^{-1}, which is three orders of magnitude higher than those cast from the solution in THF, outlining the major role played by the π–π stacking. Further alignment of the ribbons was obtained using an alternating current electric field, resulting in a collective orientation parallel to the electric field over the 100 μm gap as illustrated by AFM imaging.

Using a supramolecular dynamic exchange, interconvertible oligothiophene nanorods and nanotapes were reported with high charge carrier mobilities by Yagai.[16] Here, the association of a barbituric acid to a quaterthiophene leads to hydrogen bonded hexameric rosettes (7.3 ± 0.3 nm diameter), which then hierarchically stack on top of each other up to the formation of hexagonally packed one-dimensional nanorods (Figure 1.1a). The addition of 1 equivalent of bis-melamine derivative **BM12** induces a slow exchange process leading to a supramolecular copolymer by preferential melamine/barbituric acid mixed binding, which results in the formation of tape-like multilamellar nanostructures 1.7 nm thick and 5.5 nm wide as determined by AFM. Interestingly, the reverse formation of nanorods from nanotapes was then possible by heating at 80 °C, a behavior apparently related to an entropy-driven process associated to the release of **BM12**.

Figure 1.1 (a) (i) Chemical structure of oligothiophene–barbituric acid **1a**, **b** and bis-melamine **BM12** derivatives; (ii) schematic representation of interconversion between nanorod and nanotape; (iii) proposed packing motif of **1a** to form hexagonally-ordered nanorods; (iv) proposed packing motif of **1a**·**BM12** to form a lamellar structure. (b) (i) Top panel, a scheme showing the self-assembly process *via* rapid dispersion. Bottom panel: (A) absorption spectra showing the formation of crystalline phase (nanobelts) of propoxyethyl-PTCDI when dispersed in methanol, (B) SEM image of the nanobelts (gold stained) cast on glass, and (C) TEM image of a single nanobelt cast on SiO_2 film. Inset: electron diffraction over a nanobelt cast on carbon film. (ii) Enhancing 1D electrical conductivity (left) through cofacial π-electronic delocalization of doped charges and *I–V* curves (right) measured on a single nanobelt fabricated from the PTCDI as shown: (□) in air and (■) in saturated hydrazine vapor. Inset shows a schematic illustration of the two-electrode device fabricated on glass with a single nanofiber deposited across the gap (80 μm); (c) Light-triggered self-construction of supramolecular organic nanowires as metallic interconnects. (i) Nucleation of the fibers by supramolecular associations of a modified triarylamine upon light irradiation; (ii) AFM image of the self-assembled fiber; (iii) directed growth and insertion of the 100 nm fibers addressed by the electric field within electrodes; and (iv) corresponding AFM image of the nanowires displaying high conductivity characteristics.
(a) Reproduced with permissions from ref. 16; (b) reproduced with permission from ref. 56; (c): (i) and (ii) reproduced with permission from ref. 69, (iii) graphic by Mathieu Lejeune, (iv) reproduced with permission from ref. 70.

Extremely high intrinsic hole mobilities were measured by using flash photolysis time-resolved microwave conductivity (FP-TRMC), with values of 1.3 $cm^2 V^{-1} s^{-1}$ for the nanorods and of 0.57 $cm^2 V^{-1} s^{-1}$ for the nanotapes, a lower value for the later probably indicating interchain transportation.

1.2.2 Tetrathiafulvalene Derivatives

Tetrathiafulvalene with its 14 π-electrons is categorized as non-aromatic, in contrast to its radical counterpart ($TTF^{\bullet+}$) involving 6π-electrons of the 1,3-dithiolium ring. Remarkably, the charge transfer complex $TTF/TTF^{\bullet+}$ is strongly stabilized in this mixed valence form, and therefore allows electric conductivity. In general, however, such conductive molecular complexes are obtained in a single crystal state, which makes them problematic for materials applications, but supramolecular chemistry has recently brought new developments to produce soft assemblies of TTF with fibrous structures.[17] For instance, Chujo used organic anions such as heptafluorobutyrate, propanesulfonate, and undecanesulfonate to grow self-assembled nanofibers of mixed valence TTF with controlled anisotropy/morphology and resulting in semiconducting films.[18] SEM observations revealed the formation of fibers with diameters in the 100 nm range, whose semiconducting properties were influenced by the nature of the organic anions, with values up to 1 S m^{-1}. Recently, Iyoda and co-workers reported a series of star-shaped pyrrole-fused tetrathiafulvalenes that display good conductivities (1.2–2.4 S m^{-1}) upon doping with iodine in compressed pellets or in single crystals.[19] However, these values could not be retained in spin-coated films (one order of magnitude lower). Starting from a similar molecule, they could nevertheless form amorphous spin-coated films with good conductivities (up to 440 S m^{-1}) owing to the multidimensional π–π stacking between TTF units.[20] Interestingly, doping and undoping processes could be repeated up to six times on a 140 nm thick film with very limited loss in conductivity in the doped state and more than three orders of magnitude lower conductivity in the undoped one. Going to smaller and softer monodimensional materials, the same group also synthesized hexakis(tetrathiafulvalenylethynyl)benzene (**2**) which, after oxidation to its monocationic form $\mathbf{2}^{\bullet+} \cdot ClO_{4-}$ in chloroform, readily form deep green fibrous material by self-assembly upon addition of hexane.[21] The fibers, 50 nm in diameter and several μm long, revealed a hexagonally ordered lamellar structure with a π–π stacking distance of 3.51 Å and a conductivity of 0.11 S m^{-1}, *i.e.* two orders of magnitude higher for this 1D morphology compared to the film made of the same molecule.

To further improve the softness of these materials, several groups have synthesized TTF-based mesophases and gelators thanks to their substitutions with hydrophilic poly(ethylene glycol) tails,[22] peptides,[23] or amides,[24] displaying moderate conductivities (10^{-3}–10^{-1} S m^{-1}). For instance, Tatewaki and Kimura described enantiopure (*S*)-TTF and (*R*)-TTF having four chiral amide end groups and which can self-assemble in the presence of 2,3,5,6-tetrafluoro-7,7′,8,8′-tetracyano-*p*-quinodimethane (F_4TCNQ).[25] When

(*S*)-TTF was dissolved in hot toluene with a stoichiometric amount of F_4TCNQ and then cooled to room temperature, gelation occurred with the formation of left-handed twisted fibers having a diameter of 50 nm and a length above 10 μm as illustrated by TEM images. The assembly, resulting from a combination of 1D charge-transfer stacks and hydrogen bonding among chiral amide groups, hierarchically organizes in lamellar structures with an interlayer distance of 3.3 nm and with partial cross-linking producing gelation. By drop casting on evaporated gold electrodes with a gap distance of 500 μm, a conductivity of 10^{-2} S m^{-1} was measured for (*S*)-TTF-F_4TCNQ at room temperature. This gel presents a semiconducting behavior as illustrated by the measurement of the temperature dependence of the electrical conductivity (σ_{RT}). In addition, point-contact current imaging atomic force microscopy (PCI-AFM) measurements were performed to determine the conductivity of a single fiber, and the non-linear *I/V* curve revealed a maximum conductivity of 10^{-1} S m^{-1}. Recently, the group of Kanbara reported the formation of cast and self-supported films from guanosine molecules decorated with two TTF moieties.[26] Upon oxidation with TCNQ, moderate conductivities were observed (0.07–3.66 S m^{-1}) for the casted films. Interestingly, the self-supported films were shown to be very flexible before oxidation and became brittle upon oxidation. Both the conductivities and stiffness of the films can be attributed to the π–π stacking interactions of the TTF moieties in the oxidized state. Finally, tetrabenzoate-TTF ligands have been incorporated into a metal–organic framework (MOF), in which they form infinite 1D channels with distances between intermolecular sulfur of 3.8 Å that correspond to distances in TTF-containing charge transfer salts.[27] Using a combination of FP-TRMC and time-of-flight (TOF)[28] current transient measurements, the intrinsic charge mobility of this MOF was determined to be 0.2 cm^2 V^{-1} s^{-1}, which is two orders of magnitude higher than the charge mobility observed for the ligand itself and rivals the best common organic conductors.

1.2.3 Porphyrins and Pyrroles Derivatives

Porphyrins and phthalocyanines are 18 π-electron aromatic macrocycles that consist of four isoindole units linked together through their 1,3-positions by either methine or aza bridges, respectively. Porphyrins are ubiquitous in nature as they are involved in numerous photosynthetic processes, whereas phthalocyanines are purely synthetic molecules that are particularly used as dyes or pigments. Owing to the original functions of porphyrin derivatives, this family of molecules has been particularly studied for applications in organic electronics such as organic field effect transistors (OFETs) and organic photovoltaic devices (OPVs).[29] Semisynthetic bacteriochlorophyll derivatives, so-called zinc chlorins, have recently been considered as new charge carriers for supramolecular electronics based on naturally occurring systems.[30] For instance, amphiphilic zinc chlorins have been shown to form well-defined nanotubes in water, with a diameter of 6 nm, along with

interesting electronic properties such as conductivities up to 0.48 S m^{-1} and charge-carrier mobilities of 0.03 cm^2 V^{-1} s^{-1}. Improved charge-carrier mobilities in the solid state have even been observed by PR-TRMC for other zinc chlorin derivatives, differing only by a free or a protected alcohol. In that particular example, both derivatives lead either to 2D stack aggregates or to 1D tubular assemblies, which display charge transport mobilities of 0.28 and 0.07 cm^2 V^{-1} s^{-1}, respectively. The group of Aida also reported the first example of an amphiphilic liquid crystalline (LC) triply fused metalloporphyrin, which displays an efficient 1D electron mobility of 0.27 cm^2 V^{-1} s^{-1} at room temperature.[31] Interestingly, the amphiphilic design of the molecule was essential for both LC and conducting properties of this *n*-type organic semiconductor as mixing the hydrophobic molecule with the hydrophilic one led to a macroscopic phase separation. In a more recent work, they have also demonstrated that the nature of the peripheral side chains on each rings of a fused metalloporphyrin can strongly influence the electronic properties of the self-assembly.[32] Indeed, whereas homotropic molecules formed orthorhombic LC phases associated to a twisted geometry of the fused porphyrin dimer, heterotropic molecules displayed rectangular columnar LC mesophases due to a slipped geometry of the fused dimer. Interestingly, TOF experiments revealed that both phases present similar π-electronic properties but show opposite types of semiconductivity, the homotropic one being *p*-type and the heterotropic one being *n*-type. This example clearly highlights how the design of the molecule influences the electronic properties of the self-assembled system. In the 1980s, fluoroaluminium phthalocyanines (PcAlF) without peripheral groups were shown to display conductivities in the solid state of up to $\sim$5 S m^{-1} upon iodine doping.[33] However, one main problem associated with phthalocyanines is their low solubility in organic solvents and, therefore, they are hardly solution-processable. Recently, well-designed fluoroaluminium phthalocyanines incorporating tetra-*tert*-butyl side chains have been reported to form two-dimensional arrays, using a casting solution method, and to retain efficient hole mobilities ($\sim$0.3 cm^2 V^{-1} s^{-1}) at room temperature, which rival values observed for PcAlF, along with fairly high dark dc-conductivities ($\sim$0.1 S m^{-1}).[34] Owing to their large, planar π-electronic macrocycles, phthalocyanines and porphyrins have been lately incorporated in porous materials such as covalent organic frameworks (COF). For instance, the group of Yaghi reported the solvothermal synthesis of such COFs incorporating porphyrin units, which were shown to arrange in stacked layers by powder X-ray diffraction (XRD).[35] FP-TRMC measurements on a drop-casted film of these COFs reveal very high one-dimensional hole mobilities of 8.1 and 3.0 cm^2 V^{-1} s^{-1}, which could be ascribed to the eclipsed arrangements and π-conjugated intralayer structures of the COFs and exceed conductivities of inorganic amorphous silicon and most common conjugated polymers. Based on a very similar framework, Jiang and co-workers demonstrated that the presence of metal ions within the porphyrin macrocycle can precisely affect the conducting nature of the material.[36] Indeed,

whereas the metal-free COF displays hole-transport properties with a minimum mobility of $\sim$3.5 $cm^2\ V^{-1}\ s^{-1}$, the corresponding CuP-COF demonstrates electron-transport abilities (0.19 $cm^2\ V^{-1}\ s^{-1}$) whereas the ZnP-COF displays an ambipolar character (0.016 and 0.032 $cm^2\ V^{-1}\ s^{-1}$ for electron and hole mobilities, respectively). This influence of central metal ions on electronic properties of COFs was also recently demonstrated for phthalocyanine derivatives.[37] In that case, the presence of the metal ions was essential for the photoconductive properties of the material. Finally, notably, the electronic properties of COFs can be finely tuned by chemically modifying the nature of their edges.[38] Indeed, when benzotriazole was used as the connecting unit with the phthalocyanine, an *n*-type semiconductor with electron mobilities of 0.6 $cm^2\ V^{-1}\ s^{-1}$ was observed. However, when a benzene unit was incorporated instead of the benzotriazole, the COF displayed p-type semiconducting properties with a minimum hole mobility of 1.3 $cm^2\ V^{-1}\ s^{-1}$.

Polypyrrole is a well-known conjugated polymer that displays metallic or semiconducting properties while retaining the mechanical and processability properties of conventional polymers.[39] Very high conductivities (up to 2×10^4 S m^{-1} for a film made from acetonitrile) have been measured for this covalent polymer upon doping with various electrolytes or anions. Over the last few years, ion-based materials made of dipyrrolyl-diketone boron complexes coordinated to anions (so-called receptor modules) have been considered as a new kind of soft materials such as gels or liquid crystals potentially displaying interesting electrical properties.[40] The conductivities of such small molecules were first investigated by FP-TRMC in the crystal state.[41] Very high hole mobilities (up to 1 $cm^2\ V^{-1}\ s^{-1}$) along with anisotropic properties were recorded for various crystals and attributed to the slipped parallel stacking of π-planes as revealed by XRD. Interestingly, subtle modifications of the core structure without affecting π–π stacking interactions led to the formation of soft materials that were shown to retain the electrical conductivities observed in the crystal state.[42] In these cases, additional N–H$\cdots$F–B hydrogen-bonding and dipole–dipole interactions were also responsible for stacking into columnar structures, which present thermotropic liquid crystal properties. When gallic carboxylate ions were used instead of halide anions to form the receptor module, the presence of supplementary van der Waals interactions induces the formation of various mesophases with several transition temperatures, as determined by differential scanning calorimetry (DSC) and XRD.[43] Interestingly, both charge mobilities and electrical conductivities were shown to vary depending on the temperature at which the measurements were recorded, demonstrating the importance of the structures of the mesophases for such physical properties. Furthermore, when the receptor module was made with the halide anion, gallic-trialkylammonium cations could also induce the formation of columnar mesophases either by charge-by-charge or by charge-segregated arrangements as revealed by XRD.[44] This molecular arrangement had a great influence on the charge-carrier mobility of the assembly as a difference by

one order of magnitude was observed between both materials in favor of the charge-segregated one. These receptor modules have also lately been combined with phenylene- or pyrimidine-bridged bis(imidazolium) dicationic anion receptors.[45] The obtained mesophases correspond to charge-by-charge columnar self-assemblies, which display intrinsic charge-carrier mobility up to 0.5 $cm^2\ V^{-1}\ s^{-1}$. Interestingly, tuning the dicationic anion receptor induces changes in the conductivity values. All these examples clearly highlight the potential of ion-based materials for conducting devices with highly tunable charge-carrier mobilities.

1.2.4 Polyaromatic Derivatives

Müllen and co-workers pioneered the self-assembly of hexa-*peri*-hexabenzocoronenes, consisting of 13 fused benzene rings symmetrically substituted by paraffinic side chains, which form discotic liquid-crystalline materials over a wide temperature range and display interesting electrical properties such as high charge-carrier mobility.[46] First, one-dimensional intracolumnar charge mobilities up to $0.5\times10^{-4}\ cm^2\ V^{-1}\ s^{-1}$ were measured in the liquid crystal phase of **C14BC** by PR-TRMC which does not require the need of electrode contacts.[47] This value can be compared to highly oriented pyrolytic graphite (HOPG), whose mobility is 1 $cm^2\ V^{-1}\ s^{-1}$ in the plane of the covalent carbon sheet and $3\times10^{-4}\ cm^2\ V^{-1}\ s^{-1}$ in the direction perpendicular to the sheets. This drop of one order of magnitude can be explained by a greater π–π overlap in graphene (a cofacial distance of 3.35 Å compared to 3.6 Å for **C14BC**), as well as a higher disorder in the mesomorphic material. However, the one-dimensional nature of charge transport in **C14BC**, in addition to its easy processability, remains of particular interest for applications in materials science. HBCs have also been used for the formation of conducting nanotubes.

The discovery of multi- and single-walled carbon nanotubes (MWCNTs and SWCNTs) has triggered remarkable scientific and technological advances in nanosciences. They are formed by the rolling up of graphene sheets and display extraordinary electronic properties.[48] In particular, MWCNTs, in which curved graphene sheets are stacked perpendicularly to the longer axis of the tubes, are characteristic of a graphite structure. Using a supramolecular approach, Fukushima and Aida reported in 2004 that amphiphilic Gemini-shaped HBCs **Amp-HBC** were able to self-assemble from a cooling solution of THF into a new kind of graphitic nanotubes.[49] These, in sharp contrast to MWCNTs, consist of walls formed from numerous molecular graphene sheets stacked parallel to the longer axis of the tube. SEM and TEM imaging revealed their uniform diameter of 20 nm, with a wall thickness estimated around 3 nm and resulting in an internal tube diameter of 14 nm. The electron diffraction pattern with a scattering at 3.6 Å is compatible with the plane-to-plane separation of the π-stacked HBC units and comparable to the diffraction of graphite at 3.35 Å. By adding 20% v/v of water in THF, both coiled and tubular objects can be observed, highlighting

the nature of the tape precursor, which consists of a bilayer held by the interdigitation of the long alkyl chains. For conductivity measurements, a single piece of the nanotube was randomly positioned across a 180 nm platinum nanogap on a SiO_2 substrate. Upon addition of an equimolar amount of a one-electron oxidant ($NOBF_4$), the nanotube revealed a conducting *I/V* profile with an ohmic behavior, in contrast with the insulating behavior of the non-oxidized structure. In addition, the conductivity decreased as the temperature was lowered to 150 K, demonstrating the semiconducting character of the nanotube and, with a value of 2.5 MW at 285 K, this conductivity is comparable to that of inorganic semiconductor nanotubes composed of gallium nitride.[50] In a similar kind of self-assembly involving chiral amphiphilic HBCs, which enforce one-handed helical chirality of micrometric nanotubes, it was found that, by exposure to I_2 vapors, one charge carrier was generated for 10–11 HBC molecules.[51] This doping resulted in the transition from insulator to semiconducting behavior with strong anisotropic conductions along ($\rho_{\parallel} = 5$ S m^{-1}) and across ($\rho_{\perp} = 0.35$ S m^{-1}) the fiber axis, highlighting again the importance of the 1D structure for efficient conduction.

Recently, the group of Müllen reported the synthesis of a new class of coronenes, namely, so-called hexathienocoronenes (HTCs), which were expected to exhibit physical properties from both HBCs and thiophene derivatives.[52] However, when these molecules were incorporated in thin-films transistors obtained by vacuum deposition, only moderate field-effect mobilities could be recorded (0.002 cm^2 V^{-1} s^{-1}) although a columnar packing with interlayer distances of 3.37 Å in the dimer stack and 3.5 Å between the dimers was observed by XRD.

Finally, π-bowl molecules such as sumanene or trifluoromethylated corannulene, have been reported recently as very efficient charge-conducting molecules in the crystal or in a polycrystalline film, respectively.[53,54] Using TRMC experiments, the needle-like sumanene crystal, made of 1D columnar stacks, was shown to display an intracolumnar electron mobility of 0.75 cm^2 V^{-1} s^{-1} along the π-bowl stacking axis, which is very close to that of a single crystal of C_{60}.[53] Although corannulenes have been known for several decades, an efficient charge-carrier mobility of 0.9 cm^2 V^{-1} s^{-1} was reported only quite recently owing to a well-defined intermolecular π-stacking arrangement, which creates a highly conductive pathway.[54]

1.2.5 Perylene Derivatives

Planar π-conjugated perylene-tetracarboxylic diimides (PTCDIs) are blue fluorescent dyes with high thermal and photo-stability (molar extinction coefficients up to 40 000 M^{-1} cm^{-1} around 450 nm and quantum yields of more than 0.9).[55] They have been employed to explore 1D self-assemblies as photon- and electron-carriers (n-type) in opto-electronic nanodevices.[56] The chemical modification of PTCDIs side chains strongly affects the strength and conformation of their molecular stacking when self-assembled into

crystal lattice, thus providing numerous options to achieve shape-defined 1D assemblies. Because in solution the thermodynamics favor π–π stacking between the molecular skeletons over the lateral associations afforded by the van der Waals interactions among the side chains, monodimensional growth can be achieved. For instance, nanobelts were obtained by the rapid solution dispersion of dipropoxyethyl PTCDI from a good solvent (*e.g.* chloroform) into a poor solvent (*e.g.* methanol). This readily promotes the crystalline phase as illustrated by the bathochromic shift and the isosbestic characteristic point in UV absorption spectrometry, by the electronic micrographs, and by the electronic diffraction pattern showing the molecule plane perpendicular to the π–π stacking direction (Figure 1.1b (i)). When precipitation proceeds too fast for some molecular systems, and in particular when interactions are stronger between side chains, other techniques can be employed such as (i) slow diffusion methods (by phase transfer or vapor diffusion), (ii) seeded growth, (iii) sol–gel processing, and (iv) surface-supported annealing in a closed chamber saturated with an appropriate solvent vapor or by direct vaporization. In a theoretical study on the influence of side chains on charge mobilities in perylene-diimide derivatives, it was demonstrated that, to maximize charge-carrier mobilities, side-chains should not only be considered in the self-assembly process as soft entropic interactions but also as stronger specific interactions, such as hydrogen bonds.[57] Recently, perylene bis-imide incorporating hydrogen-bonding motifs has been co-polymerized with ditopic building blocks into millimetre-long fibers.[58] Interestingly, the stacking of perylene units was not the driving force of the polymerization along the long axis of the fibers, but accounted for the height of the nanostructure. Nevertheless, the intrinsic 1D electron mobility observed for these nanofibers (0.6 $cm^2\ V^{-1}\ s^{-1}$) rivals the highest mobilities of columnar stacks of PTCDIs derivatives. In a more recent, work, the same group has shown that hydrogen-bonded networks incorporating perylene units can be structurally rearranged from fibrillar assemblies to lamellar structures in the bulk upon heating.[59] This structural transition, which arises from a molecular rearrangement from rosette to linear type, is associated with a remarkable increase in transient photoconductivity, resulting from a higher probability of charge carrier generation in the lamellar structure as demonstrated by transient absorption spectroscopy.

PTCDI nanobelts can be reversibly n-doped by reducing agents such as hydrazine, producing stable anionic radicals delocalized along the intermolecular π–π stacking (Figure 1.1b (ii)).[60] This efficient charge separation followed by transport of the charge carrier toward the supramolecular structure enables electrical conductivity enhancement when the nanobelt is submitted to hydrazine vapors. Measurements were performed by depositing a single nanobelt on gold electrodes separated by a distance of 50–100 μm, thanks to their deposition by drop-casting from a diluted solution. Current–voltage (*I*/*V*) data revealed, for the quasi-linear region at low bias (up to 50 V), a conductivity of 10^{-3} S m^{-1} – a good value reflecting the

ordered 1D cofacial electronic delocalization. The *I/V* curve measured with the PTCDI nanobelt becomes non-linear at higher voltage bias, implying an injection-limited charge transport, as previously observed for conducting polymer nanowires.[61] In addition, when the nanobelt was immersed in saturated hydrazine vapors, the conductivity was dramatically increased to the 0.5–1.0 S m^{-1} range (which is two orders of magnitude higher than that of undoped silicon). Moreover, this high modulation ratio implies potential application of these self-assemblies in electrical sensing of various gaseous reducing species including organic amines, CO, and NO.

Amphiphilic PTCDIs were also demonstrated to give various self-assembled morphologies depending on the solvent used for their solution-phase processing.[62] For instance, PTCDI (**1**) was shown to form either well-defined 1D nanobelts or 2D nanoleaves when processed from methanol or *n*-hexane, respectively, as demonstrated by scanning electron microscopy (SEM) images. X-Ray diffraction patterns of the aggregates revealed a π–π interaction between perylene rings and longer range periodicity when self-assembled from methanol, because of a higher interpenetration of the imide hexyl chains compared to hexane. The measurements of *I/V* data were determined by drop casting and evaporation of either methanol or *n*-hexane on an interdigitated ITO electrode with a 75 μm spacing. The much higher conductivity observed when the self-assembly was prepared from methanol (3.3×10^{-1} S m^{-1}) compared to *n*-hexane (1.2×10^{-2} S m^{-1}) is attributed to the higher one-dimensional stack order, leading to a higher mobility of charge carriers. This very high conductivity in the nanobelts exceeds by about three orders of magnitude that measured for polymer nanowires such as polythiophene.[63] The group of Li also demonstrated that lysine-substituted 1,6,7,12-tetrachloroperylene bis-imide readily form various nanostructures ranging from nanowire to nanobelt or nanosheet and nanotube, depending on the solvent used and the sample concentration.[64] *I–V* measurements on the different self-assemblies confirmed the influence of the molecular ordering on the conductivity as average conductivities of 1 and 10^{-4} S m^{-1} were obtained for nanosheets and nanotubes, respectively. Chen and co-workers also highlighted recently that not only solvents but also the presence of an external stimulus, such as metal ions, could lead to various morphologies with different physical properties.[65] In this work, crown ether-functionalized PTCDIs were shown to dimerize into rope-like or belt-like nanostructures in chloroform in the presence of K^+ or in methanol, respectively. This morphological change was associated with a drop in conductivity of more than one order of magnitude for the belt-like structure. It has also been noted lately that subtle changes in molecular structures can strongly impact the morphologies along with the physical and electronic properties.[66] For instance, a dimer of perylene bis-imide with an odd number of methylene units between the PTCDIs will display gel-like properties with a charge carrier mobility of 0.57 cm^2 V^{-1} s^{-1}, whereas the same dimer with an even number of methylene units will form lamellar architectures without viscosity and a charge mobility of 1.8 cm^2 V^{-1} s^{-1}.

Finally, PTCDIs have been recently co-assembled with oligo(phenylenevinylene) (OPPV) *via* charge-transfer interactions, using a non-covalent amphiphilic design.[67] The resulting gels, made of interconnected networks of fibers 30–40 nm high, were shown to exhibit high conductivity (2 S m^{-1}) by conductive AFM, which represents one of the highest conductivities obtained so far for self-assembled systems without external doping.

1.2.6 Triarylamine Derivatives

Triarylamine (TAA)-based molecules have been used as active materials for decades in opto-electronic devices such as organic light-emitting diodes, organic solar cells, organic field-effect transistors, or in the Xerox process, because they display interesting photoconductivity properties and high hole-transport mobilities.[68] Recently, our own group discovered that properly modified TAA molecules were able to produce self-assemblies thanks to their stacking in columnar fibrils.[69] We demonstrated that a simple irradiation by visible light of a solution of these molecules in chloroform can generate a non-covalent polymerization leading to supramolecular triarylamine nanowires (STANWs) (Figure 1.1c (i)). This process occurs thanks to a highly synergistic phenomenon that starts with the formation of a catalytic quantity of triarylammonium radicals ($TAA^{\bullet+}$) when excited by light, the chlorinated solvent being the electronic acceptor. This radical can in turn form a charge transfer complex with its neutral counterpart, and subsequently continue the elongation by combining charge transfer, hydrogen bonding, and π–π stacking for the primary growth, as well as hydrogen bonding and van der Waals interactions for the secondary growth leading to the aggregation of several columnar fibrils in larger and stiffer fibers (typically 10–50 nm wide and 50–1000 nm long). The internal packing of the nanostructure was determined by combining high resolution AFM imaging together with *ab initio* calculations showing that columns are formed of stacks of TAA with an alternative handedness and a twist of 60° from one stack to the other (''snowflake'' packing), the hydrogen bonding being a source of lateral attraction between columns (Figure 1.1c (ii)). It was also demonstrated that STANWs can protect holes from quenching by the environment as stabilized in the 1D stack, possibly indicating interesting conducting properties.

We then demonstrated the possibility to take advantage of this triggering capability for probing the conduction properties of the supramolecular assemblies when trapped between pre-patterned metallic electrodes (Figure 1.1c (iii)).[70] We used a lateral device geometry with an inter-electrode distance matching the observed delocalization length of STANWs, that is in the 50–100 nm range, and drop cast a solution of TAA on the circuit. Subsequent sample irradiation using white light resulted in a rise of the current by six orders of magnitude, with corresponding conductance values reaching several tens of millisiemens. AFM imaging of the device revealed the presence of wires oriented along the electric field with homogeneous diameters of 12 ± 2 nm and with length and positioning matching exactly the electrode

gap (Figure 1.1c (iv)). The combination of light-triggering and voltage-casting processes therefore results in an organic conductor geometry that fills the void between metallic contacts. We also found that applying an initial voltage threshold through the gap – concomitantly to the light irradiation – was a necessary condition for the efficient and stable formation of STANWs. This suggests that the optimal formation scenario leading to localized assembly starts with one electrode attracting a positively charged radical, which shares its electronic wave function with the metallic substrate, and then primes the next molecules stacking over it. The elongation process is polarized along the electric field and is self-limiting: when the other electrode is reached, its electron reservoir provides the neutralization path for stopping growth of the STANWs. This self-construction[71] scenario is also supported by the fact that a shorter exposure time to white light is able to prime the interconnect formation, with a resistance closure occurring afterwards in the dark. These two-terminal devices, with channel and interface contacts in series, exhibit an ohmic resistive nature related to high conductivity values, as shown by *I/V* measurements. We estimated a channel conductivity exceeding 5×10^{3} S m^{-1}, and an interface resistance per unit length below 2×10^{-4} Ω m. Only sorted single-walled metallic carbon nanotubes with ballistic charge transport (*i.e.*, exempt of charge scattering) can demonstrate better values. Temperature-dependent studies revealed resistivity values systematically and reliably diminishing with decreasing temperatures, down to 1.5 K, showing for the first time an ohmic contact resistance with an intrinsic metallic character[72] for STANWs. This interface resistance value was determined to be six orders of magnitude smaller than that measured for the best conducting polymers, and four orders of magnitude lower than those of the best contacts on organic semiconductor single crystals. The corresponding current density was thus estimated to be about 2×10^{6} A cm^{-2}, which is remarkably high for organic films and corresponds to the current density value encountered in copper wires.

In contrast to previous triarylamine derivatives, STANWs thus take advantage of a self-organization process to create metallic interconnects with exceptional conductivity properties in two-point geometry. One may suggest that the estimated large density of charge carriers, the delocalization of radicals throughout the triarylamine stacks, and the sharing of their electronic wave functions with the metallic substrate might be the reasons for such low resistance both in the bulk and at the metal interface. The solution processing, the light-triggered self-assembly, and the directional supramolecular growth enabled, for the first time, the insertion of organic interconnects in pre-determined positions by means of a bottom-up approach, making possible the addressed control of nanoscale organic circuits.

1.2.7 Other Aromatic Molecules

Conjugated polymers based on aromatic molecules such as carbazole, aniline, *etc.* are well-known for their electrical properties but are hardly

processable, which renders their large-scale applications difficult. In the last few years, supramolecular self-assemblies based on these monomeric units have emerged as softer materials. For instance, organic nanowires based on 9,9′-dimethyl-3,3′carbazyl stacks in a mixed valence state could be easily synthesized by oxidation of 9-methylcarbazole by iron(II) perchlorate and displayed an electric conductivity of 3×10^{-3} S m^{-1}, which is lower than that of a polycarbazole film prepared by electropolymerization.[73] In another example, nanofibers made of two or three low-molecular-weight amphiphilic salts, such as aniline hydrochloride, were easily synthesized from a THF solution due to $\pi-\pi$ stacking and ionic interactions and presented conductivities in films up to 7.7×10^{-3} S m^{-1}, which were attributed to the presence of freely movable ions.[74]

Percec *et al.* have demonstrated that self-assemblies of π-stacks of donors, acceptors, and donor–acceptors can drive the formation of liquid crystals with promising opto-electronic properties.[75] For that, the authors elaborated a library based on a semi-fluorinated tapered dendron[76] that was substituted at its extremity with various electroactive aromatic donors (naphthalene, pyrene, carbazole) or with an acceptor (nitrofluorenone). The (co)-self-assembly of these aromatic wedges in a mixed donor–acceptor stacking drives the formation of high-density columnar liquid crystalline phases (10^{12} columns per cm^2) with the fluorinated periphery of the dendron shielding the core from moisture. Time-of-flight methods were used to determine very good charge carrier mobilities (10^{-4}–10^{-3} cm^2 V^{-1} s^{-1}), which are two to five orders of magnitude higher than those of the related donor and acceptor compounds in the amorphous state, thus reflecting the one-dimensional structuring of the stacks. X-Ray and double-quantum NMR spectroscopy studies provided information about the typical distances and the ''sandwich'' stacking within the columns, and also demonstrated that these orientate perpendicular to the surface. The processability of this system is also closely related to its structure, in which a good organization occurs between the electroactive aromatic centre, the dendron phenyl (inner ring), and the alkyl chains (outer ring). This clear separation is not totally achieved when the material is precipitated from the solution, as it indeed necessitates slow cooling from the melt into the liquid crystals, which allows self-repairing of the defects. Recently, liquid crystalline phases presenting a transition from a columnar rectangular phase to an isotropic one at around 60 °C were observed for verdazyl radical derivatives.[77] Interestingly, this change in mesophase was associated with a drop in conductivity by a factor of 10 upon increasing the temperature above the phase transition one. The group of Aida also recently reported on a conducting hexagonal columnar liquid crystalline phase based on triphenylene hexacarboxylic esters.[78] Owing to strong intercolumnar dipole–dipole interactions, LC films were homotropically aligned on up to 12 different substrates and displayed hole mobilities at zero *E*-field of 0.5×10^{-2} cm^2 V^{-1} s^{-1}, which is one order of magnitude higher than the mobility observed for the corresponding hexaalkoxytriphenylene derivative.

Conducting gels based on π-conjugated molecules have been widely studied, but there are only few reports on such stimuli-responsive gels. Recently, the group of Miyata studied such a material made of a dehydrobenzoannulene derivative.[79] This molecule was shown to form a gel made of 30 nm-width fibers upon a heating/cooling process. After ultrasonic treatment, a suspension of 100 nm-wide fibers was observed and the cycle could be repeated several times. Interestingly, this nanofiber-to-nanofiber transformation was associated with a drop in charge-carrier mobility from 0.61 $cm^2\ V^{-1}\ s^{-1}$ for the gel to 0.23×10^{-4} $cm^2\ V^{-1}\ s^{-1}$ for the suspension, which represents the first example of an ultrasound-controlled conducting wire. The group of Yagai also reported on a vesicle to ribbon rearrangement of a dipolar dye self-assembly upon addition of a complementary hydrogen-bond receptor.[80] In this example, although the morphological and optical changes were really striking, changes in isotropic charge-carrier mobilities were only limited (same order of magnitude, 10^{-3} $cm^2\ V^{-1}\ s^{-1}$), but the slightly higher mobility observed for the ribbon could be attributed to a more efficient overlap of the π-conjugated chromophores.

In 2008, the first example of semiconducting COFs incorporating small aromatic molecules such as pyrene and triphenylene was reported.[81] Owing to the eclipsed arrangements of the aromatic units, this organic framework displays p-type semiconducting properties, which was confirmed upon doping of the drop-casted film with iodine. Recently, the pyrene units were replaced by benzothiadiazole units, therefore leading to a 2D donor–acceptor COF, in which donors and acceptors form well-defined conducting channels.[82] FP-TRMC measurements reveal the ambipolar nature of the material with hole and electron mobilities of 0.01 and 0.04 $cm^2\ V^{-1}\ s^{-1}$, respectively. This strategy to form segregated donor–acceptor systems could be generalized to any donor/acceptor redox couple and is very attractive for opto-electronic applications. Lately, metal–organic frameworks incorporating disulfhydrylbenzene moieties have been synthesized and present interesting electronic properties.[83] Indeed, films made of PMMA (poly(methyl methacrylate)) and MOF in a 1 : 1 ratio exhibit intrinsic charge carriers mobilities of 0.01–0.02 $cm^2\ V^{-1}\ s^{-1}$, which are comparable to those found in common organic semiconductors such as polythiophenes or rubrene.

One-dimensional self-assemblies of biocompatible nanostructures are also envisaged in the literature for the design of biosensors, of biologically inspired photovoltaic devices, or of electronically active matrices for cell differentiation. In this direction, fluorenylmethoxycarbonyl-tri-leucine (Fmoc-L_3) was demonstrated to form a hydrogel upon enzyme-triggered self-assembly, thanks to a subtilisin-catalyzed hydrolysis of its methyl ether precursor (Fmoc-L_3-OMe).[84] This gel, originating from the wrapping of the π-β structure involving stacking of the fluorene protecting group and hydrogen bonding of the leucine residues, was deposited onto a glass substrate and dried to leave a xerogel consisting of a network of entangled fibers. Morphological studies of the xerogel revealed the fibers being established, as expected, on straight peptide nanotubes with an external

diameter of 16 nm and an inner one of 7 nm. Wide-angle X-ray scattering (WAXS) also suggested π–π stacking of the Fmoc residues at around 3.6 Å and of β-sheets at 4.7 Å. The complex impedance plot data for the dried network consisted of both electronic and ionic conductivity when impedance measurements were made in air, the later being caused by the presence of ion-containing water absorbed onto the hydrophilic nanostructure. In vacuum, restriction to a purely electronic transport led to an increase of the measured resistance from 0.1 to 500 MΩ per sq.

Another oligopeptide (LLKK) linked by its N-terminus to an anthracene segment was also shown to combine β-sheet formation together with π–π stacking of anthracene units in a head-to-tail arrangement (or J-aggregate) with efficient electronic communication.[85] The supramolecular assembly was prepared by a casting method bringing a benzene saturated solution of peptide onto silicon substrates. One-dimensional fiber-like nanostructures were obtained with lengths varying from 60 to 100 μm, widths from 0.1 to 1 μm, and heights from 40 to 120 nm. By using the same deposition on gold microelectrodes (separated by a gap of 3 μm), current–voltage measurements were performed revealing significantly non-linear *I/V* curves, changing from 8×10^{-2} S m^{-1} at −1.5 V, to 1.1 S m^{-1} at 3 V. With the best preparations, the measured current could reach values of up to 10 S m^{-1}, which can be compared to that obtained with reference anthracene bulk material of 10^{-8} S m^{-1}. To explain such enhancements, the authors suggested the presence of remaining benzene (solvent) as doping agent in the nanofibers, as well as the reduced diameter of the nanostructures enforcing a communication between the anthracenes along the longitudinal axis of the piling. Conducting self-assembled cyclic peptide nanotubes vertically oriented on gold substrates have also been studied.[86] An efficient charge transfer, determined to be mainly dominated by hopping, was recorded through these molecular junctions by C-AFM. The structure of the nanotube, particularly its length, was also shown to affect the electronic properties of the self-assembly.

1.3 Organic Field Effect Transistors

The field-effect transistor is one of the most basic building blocks in electronics and nanoelectronics. In particular, organic field-effect transistors (OFETs)[87] are three-terminal components in which the current flow, through the active organic layer and between two of the terminals (known as the source and drain), is controlled by the bias applied to the third terminal (known as the gate). In addition, OFETs have an insulating layer between the semiconductor layer and the gate. The expected intrinsic properties of OFETs for practical use include high charge-carrier mobilities, large on/off current ratios ($I_{on/off}$), and threshold voltages (V_{th}) close to zero, while keeping good processability and low cost of the organic material. A lot of progress has been made in this field and several reviews have been recently

published regarding the implementation of functional supramolecular structures in these devices.[88]

1.3.1 Thiophene Derivatives

Thiophene derivatives, in particular in their oligomer/polymer form, have also been inserted in OFET devices.[89] For instance, tetra- and hexathiophene modified at their extremities by peptidic residues have been shown to form entangled β-sheet networks of fibers by TEM imaging.[90] When a solution of the hexathiophene derivative was drop-casted in an OFET device, hole mobilities up to 3.8×10^{-5} cm^2 V^{-1} s^{-1} were observed. However, if fibers made of the tetrathiophene molecules were precisely aligned within the device using a noodle preparation technique, a hole mobility of 0.03 ± 0.005 cm^2 V^{-1} s^{-1} was obtained for the parallel direction whereas one-order-of-magnitude lower mobilities were observed in the perpendicular direction. Recently, the group of Barbarella combined a wet lithographic technique with the non-solvent vapor-induced crystallization of octathiophene derivatives to form aligned fibers with precise control over density and size in OFET devices.[91] Devices made of all aligned fibers showed saturated charge mobilities increased by about three orders of magnitude compared to the randomly distributed fibers, a strong decrease of the threshold voltages, and an increase by one order of magnitude of on/off current ratios. These results show that alignment of fibers through confinement effects is a really attractive technique for OFET device fabrication and should be applicable for many other known supramolecular fibers.

A novel donor–acceptor semiconducting co-oligomer was reported to self-assemble in fibers by Melucci and co-workers.[92] This co-oligomer is constituted of benzothiadiazole and thiophene units and showed a liquid crystalline behavior in the range 185–347 °C. As-prepared OFET devices made from chloroform solution gave hole mobilities (μ_{h+}) in the 10^{-5} cm^2 V^{-1} s^{-1} range, which could be improved by two orders of magnitude (2.5×10^{-3} cm^2 V^{-1} s^{-1}) after annealing at 200 °C. When a toluene solution of the co-oligomer was cast on SiO_2 substrate, the formation of bundles of fibers several hundreds of micrometers wide and about a micrometer long were noticed. New OFET devices made out of these fibers displayed an average mobility of $8.3\times10^{-4} \pm 2.4$ 10^{-4} cm^2 V^{-1} s^{-1} with a maximum value of 1.3×10^{-3} cm^2 V^{-1} s^{-1}, which is two orders of magnitude higher than the value observed for the drop-casted film and could reflect the improved packing within the fibers. Another donor–acceptor semiconducting copolymer poly(didodecylquaterthiophene-*alt*-didodecylbithiazole), which forms highly crystalline thin films after thermal annealing was reported by Lee *et al.*[93] Field-effect mobilities of 0.04 cm^2 V^{-1} s^{-1} were obtained for samples without annealing, whereas with an annealing at 180 °C (mesophase) excellent field-effect mobilities of 0.33 cm^2 V^{-1} s^{-1} were reached. Additional interesting characteristics of these OFETs are their good environmental stability and their bias-stress stability, which are comparable

to those of amorphous silicon. Perepichka and co-workers studied the self-assembly of three thiophene derivatives (anthraxtetrathiophenes and benzotrithiophene) at the liquid–solid interface.[94] Trichlorobenzene solutions of these compounds were deposited on HOPG crystal (highly oriented pyrolytic graphite) and studied by scanning tunneling microscopy, which showed that all molecules self-assemble readily into ordered patterns. Two derivatives give a crystalline layer with an oblique unit cell, whereas the last one shows a hexagonal structure. Thin-film OFET devices built from these thiophene derivatives displayed hole mobilities in the range 10^{-4}–10^{-3} cm^2 V^{-1} s^{-1} with on-off ratios of $\sim 10^3$ and threshold voltages between -15 and -10 V. Self-assembled oligoarene nanoribbons made of fused benzene and thiophene units were first studied in single-wire OFETs, presenting mobilities up to 0.01 cm^2 V^{-1} s^{-1}, an on/off ratio of 10^3, and threshold voltages between -31 and -18 V.[95] In an improved version of these OFETs, a slow crystallization process *via* mixed solvents allowed a better contact between the dielectric and the single crystals, resulting in a mobility as high as 2.1 cm^2 V^{-1} s^{-1}, an on/off ratio of 2×10^5, and a threshold of -7 V.[96] Co-crystals of a sulfur-bridge annulene with fullerenes C_{60} and C_{70} resulted in an alternating donor–acceptor layer structure as proved by X-ray experiments.[97] OFET devices built from these two co-crystals with a bottom-gate top-contact architecture led in both cases to an ambipolar behavior with electron and hole mobilities of $\mu^{e}_{sat} = 0.01$ cm^2 V^{-1} s^{-1} and $\mu^{h}_{sat} = 0.3$ cm^2 V^{-1} s^{-1}, respectively, for the C_{60} co-crystal and of $\mu^{e}_{sat} = 0.05$ cm^2 V^{-1} s^{-1} and $\mu^{h}_{sat} = 0.07$ cm^2 V^{-1} s^{-1} for the C_{70} co-crystal.

1.3.2 Tetrathiafulvalene Derivatives

Klinke and co-workers have reported the complexation of a TTF derivative bearing two pyrene moeities with single-walled carbon nanotubes (SWCNTs) in OFET devices.[98] The complexation of both components induced first a shift of the threshold voltage to more positive values, indicating a transfer of electron density from SWCNT to the TTF derivative. Then, field-effect hole mobilities showed an increased value from 9 to 11 cm^2 V^{-1} s^{-1} thanks to the adsorption of the TTF compound. Upon oxidation with iodine vapors, hole mobilities (μ_{h+}) were increased up to 13 cm^2 V^{-1} s^{-1}. TTF moieties have also been recently fused with naphthalene diimides (NDIs) to produce new conjugated electron donor–acceptor molecules.[99] When thin films were incorporated into OFET devices, compounds containing one NDI and one TTF moieties displayed an ambipolar semiconducting behavior, whereas molecules made of one NDI and two TTF moieties behaved as p-type semiconductors. Annealing procedures at 140–160 °C were mandatory for both classes of compounds to reach efficient hole and/or electron mobilities in devices ($\mu_{h+} = 0.31$ cm^2 V^{-1} s^{-1}, V_{th}: -5 to 6 V, $I_{on/off} = 10^4$ for the best OFET device). This fact was supported by AFM imaging and XRD experiments, which clearly correlated the increased performances after annealing with a morphological evolution of the films.

1.3.3 Phthalocyanine Derivatives

A tetraoctyl-substituted vanadyl phthalocyanine, which forms a discotic liquid crytalline phase, has been quite recently synthesized and further incorporated in OFET devices.[100] After annealing at 120 °C, highly ordered thin-films with edge-on alignement as shown by XRD experiments were obtained and a mobility up to 0.017 $cm^2 V^{-1} s^{-1}$ could be recorded in the device, along with a low threshold voltage and an on/off current ratio of 4×10^3. Other phthalocyanine derivatives such as two supramolecular triple decker complexes composed of tris(phthalocyanato)europium with crown ether heads and hydrophobic tails were synthesized and inserted in OFET devices.[101] Both complexes showed good carrier mobilities (0.28–0.33 $cm^2 V^{-1} s^{-1}$), with, however, a noticeable difference regarding the direction of the current. In one case, the current was shown to flow parallel to the aromatic phthalocyanine due to a J-aggregate arrangement whereas, in the second case, it flowed parallel to the long axis of the complexes due to H-aggregate arrangements. However, the molecular structure is not the only parameter that affects the electronic properties of OFET devices. In a recent work, the group of Chaure studied the influence of the annealing temperature on OFET devices based on a liquid crystalline compound.[102] For copper octakis(hexyl)phthalocyanine, a temperature dependent growth of crystallites was observed, resulting in different shapes, sizes and orientations. Annealing at 100 °C proved to be the best temperature to achieve high performance thanks to a highly packed rod-like crystallite morphology with a good grain interconnectivity. Under these conditions, a field-effect mobility (μ_{sat}) of 0.7 $cm^2 V^{-1} s^{-1}$, threshold voltage of −1 V, and on/off ratio of 8.4×10^7 could be measured. Zinc phthalocyanine (ZnPc) has also been incorporated in covalent donor–acceptor dyads with fullerene and showed to self-assemble in columnar liquid crystals (Figure 1.2d).[103] A discotic rectangular columnar mesophase was observed at 160 °C by XRD measurements, which suggests that fullerene moieties form an helical alignment along the ZnPc columnar structures. TOF was then used to determine efficient ambipolar charge-transport properties, with an electron mobility of 0.26 $cm^2 V^{-1} s^{-1}$ and an hole mobility of 0.11 $cm^2 V^{-1} s^{-1}$.

1.3.4 Perylene Derivatives

Perylene has been extensively studied in OFET devices.[104] Recently, Samori and co-workers have demonstrated the influence of both processing techniques and side-chains on the morphology of perylene tetracarboxydiimide (PDI) nanofibers.[105] Two types of processing techniques were used: a solvent vapor annealing (SVA) and a solvent induced precipitation (SIP). Although both techniques led to fibers several hundred micrometres long and up to tens of micrometres wide, SIP gave bundles of fibers whereas SVA provided isolated fibers. Consequently, strong variations were observed in the characteristic parameters of field-effect transistors built with these nanofibers.

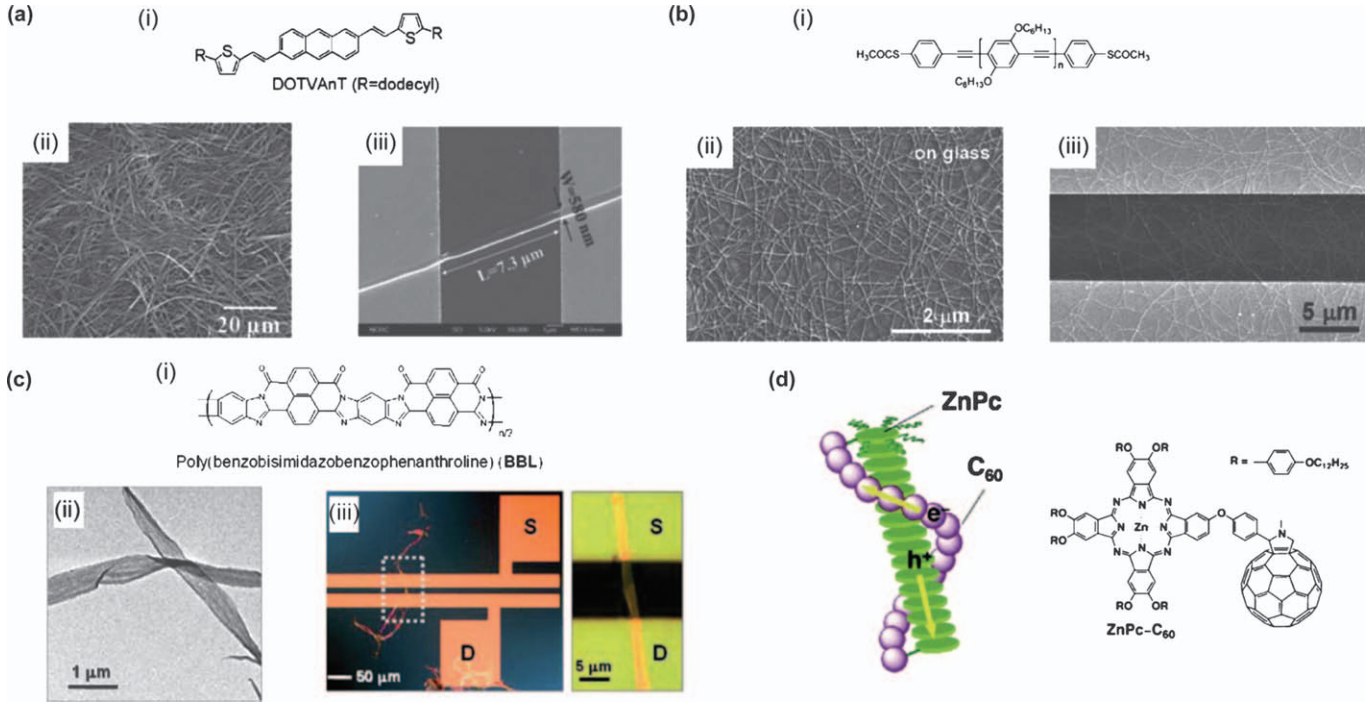

Figure 1.2 (a) (i) Structure of 2,6-bis(2-thienylvinyl)anthracene derivative and SEM images of (ii) its xerogel and of (iii) the bottom-contact single-nanofiber transistor of the considered molecule. (b) (i) Structure of the poly(*para*-phenylene-ethynylene) polymers with thioacetate end groups; (ii) SEM image of the self-assembled nanowires on glass substrates from THF solution and (iii) SEM image of the transistor device with nanowires between the source and drain electrodes. (c) (i) Structure of poly(benzobisimidazo-benzophenanthroline); (ii) TEM image of the self-assembled nanoribbons; (iii) typical single nanoribbon transistor and a close-up showing the nanoribbon bridging the source–drain electrodes. (d) Structure and proposed schematic model of the liquid crystal arrangement of the considered phthalocyanine–fullerene dyad.
(a) Reproduced with permission from ref. 115; (b) reproduced with permission from ref. 119; (c) reproduced with permission from ref. 120; (d) reproduced with permission from ref. 103.

In a latter example, a perylene-hexabenzocoronene conjugate linked by an ethynylene bridge was integrated in OFET devices.[106] By SIP, bundles of fibers could be obtained up to 50 μm long and less than 1 μm wide. In comparing devices made from cast fiber networks and spin-coated thin-film upon light illumination, clear changes in current at all gate voltages were measured, with at least one order of magnitude lower performance observed for the spin-coated thin-film. This example also shows how OFET from fiber networks can be used as a double gating transistor modulated either optically (by photoexcitation) or electrically (by gate control). Schenning and co-workers took advantage of the self-complementarity of hydrogen-bonded oligo(*p*-phenylenevinylene) and perylene tetracarboxydiimide molecules to produce thin-films with an internal rod-like morphology.[107] Bundles of rods longer than 500 nm and with a diameter of 80–100 nm were obtained. Although OFET devices displayed ambipolar transport, both electron and hole mobilities (10^{-7} cm^2 V^{-1} s^{-1}) and on/off ratio (10^2) were low. Recently, Yagai and co-workers followed a similar supramolecular approach to produce a lamellar morphology from a melamine derivative bearing two perylene bis-imides after annealing in OFET devices.[108] An improved solubility of the latter was clearly observed when mixed with mono-dodecylated cyanurate or barbiturate as a result of the complementary recognition. However, no improvement in terms of electron mobility was observed between the melamine derivative alone and its complexes. One main problem occurring in OFET is the precise positioning of organic wires within the devices. Using a known perylene tetracarboxylic-diimide derivative, Bao and co-workers described the fabrication of high performance single-crystalline microwire OFETs.[109] In this study, the average diameters and lengths of nanowires were 519 nm and 340 μm, respectively, with mobilities as high as 1.4 cm^2 V^{-1} s^{-1} for the single microwire deposited in thin film. Using of a filtration-and-transfer method, wires could be efficiently aligned leading to a maximum mobility of 0.24 cm^2 V^{-1} s^{-1} for multiple wire OFETs (V_{th}: −13 to +24 V, $I_{on/off} > 10^5$). Slight modifications of the chemical structure such as dithioperylenes were reported to form self-assembled nanoribbons with interesting electronic properties.[110] Single-crystalline nanoribbons OFETs showed an average hole mobility of 0.45 cm^2 V^{-1} s^{-1} with a maximum as high as 2.13 cm^2 V^{-1} s^{-1} with a current on/off ratio of 10^6 and an average threshold voltage of −14 V. This excellent hole mobility can be attributed to the compressed highly ordered packing mode directed by S$\cdots$S interactions. Supramolecular charge transfer nanofibers made of bundles of cylindrical micelles have also been recently used in OFET devices.[111] Charge-transfer amphiphiles made of coronene tetracarboxylate and viologen derivatives were shown to arrange radially along the width of the cylindrical micelles, whereas the donor–acceptor parts are stacked face-to-face along the length of the fibers. Field-effect mobilities (μ_{sat}) from 4.4 to 0.14 cm^2 V^{-1} s^{-1} were measured when increasing the channel width from 1 to 6 μm. Although the OFET device was sensitive to air (drop in charge carrier mobility after 7 days in air), the authors demonstrated that the electrical characteristics of

the device can be recovered by simply placing a drop of deionized water on top of the circuit. This self-repairing property is quite unique as most OFET devices can barely recover after degradation by atmospheric humidity.

1.3.5 Other Aromatic Molecules

It has also been shown that the conducting properties of discotic HBCs should be improved for incorporation in devices and in particular for deposition between electrodes. Indeed, the development of appropriate techniques has become an essential challenge for the fabrication of unperturbed long-range-oriented organic semiconductors. The zone-casting of dodecyl-substituted HBC from solution directly onto a desired substrate provides columnar structures uniaxially aligned in the casting direction.[112] High-resolution transmission electron microscopy (HRTEM) images illustrate the homogeneous morphology of the cast film down to the nanometer scale, while the electron-diffraction pattern confirmed the 4.9 Å intracolumnar period associated to a 3.5 Å cofacial distance between HBCs tilted at an angle of 45° along the stacking direction. An OFET device was constructed by using this zone casting technique on a SiO_2/silicon substrate, and subsequent shadow-mask evaporation of gold electrodes separated by a gap of 25 μm. The measured characteristic of the OFET – parallel to the columnar alignment – revealed a very good on/off ratio of 10^4 for a turn on voltage of −15 V, as well as mobilities up to 10^{-6} cm^2 V^{-1} s^{-1} in the saturation regime. This value remains two orders of magnitude lower than the intrinsic values obtained by PR-TRMC, probably because of the presence of local intracolumnar packing defects, which can constitute localized barriers for charge carrier movement along the stacks. This example sheds light on the remaining challenges facing chemists in order to implement their functional structures in efficient nanoelectronic devices.

Discotic quaterrylene tetracarboxylic diimide was studied by Müllen and co-workers in OFET devices, which showed an ambipolar behavior associated to electron and hole mobilities of 1.5×10^{-3} and 1×10^{-3} cm^2 V^{-1} s^{-1}, respectively.[113] After annealing at 100 °C for 1 h, the hole transport property surprisingly vanished but the electron transport ability remained albeit with a lower mobility value of 2×10^{-4} cm^2 V^{-1} s^{-1}. A tetracene core substituted with an aryl and a perfluoaryl groups was shown to self-assemble by a face-to-face stacking between aryl and perfluoaryl substituents and C–H···F interactions between fluorine atoms and hydrogens of the tetracene core as proved by single-crystal X-ray experiments.[114] Organic thin film transistors devices built from this molecule showed an average hole mobility of 4.2×10^{-2} cm^2 V^{-1} s^{-1} with an on/off ratio greater than 10^5 and a threshold voltage of -12.8 ± 6.4 V. Replacement of all fluorines in the structure by hydrogen atoms led to a decrease of this hole mobility by two orders of magnitude (3.1×10^{-4} cm^2 V^{-1} s^{-1}, V_{th}: -28.0 ± 9.5 V, $I_{on/off}>10^4$), demonstrating the influence of these interactions on the molecular packing and its arising properties. Organogels based on thienylvinylene anthracene have

been reported for the fabrication of film-type and single-nanofiber OFETs (Figure 1.2a).[115] The supramolecular organization in fibers clearly leads to higher performance compared to the film-casting versions, with a field-effect mobility of 0.48 $cm^2\ V^{-1}\ s^{-1}$, a threshold voltage ranging from −4.1 to −9.8 V and an on/off current ratio of 10^5. Isomeric carbozolocarbazole derivatives, made of two fused carbazole units, have lately been reported as promising organic molecules for semiconducting materials.[116] In this structure/activity study, the different isomers were shown to display electrochemical and optical properties and also different morphologies as revealed by AFM imaging of thin films produced by vapor deposition. For the most promising isomer, a p-type semiconducting behavior was observed with a field effect mobility of 0.02 $cm^2\ V^{-1}\ s^{-1}$, a threshold voltage of −64 V and an on/off ratio of 10^6 in air. Interestingly, for this isomer, substitution of the nitrogen atoms with alkyl or aryl group was shown to greatly affect its electronic performance, with a drop in conductivities by more than two orders of magnitude.

Amphiphilic oligo(*p*-phenylenevinylenes) derivatives with both hydrophobic and hydrophilic chains were recently synthesized by George and coworkers.[117] In a mixture of 25% THF in water, thanks to the amphiphilic nature of the derivatives, self-assembled 2D sheets were obtained with widths of 5–50 μm. An increase in THF percentage to 20% in water revealed the formation of rolled-tubes with lengths up to several micrometers and average diameters of 300 nm. Comparison of both sheets and rolled tubes in OFET devices revealed the higher field-effect mobility of the sheet ($8\times10^{-3}\ cm^2\ V^{-1}\ s^{-1}$ and an on/off current ratio of 10^3) compared to the tubes ($1.03\times10^{-4}\ cm^2\ V^{-1}\ s^{-1}$). Recently, a donor–acceptor charge transfer system made of a distyrylbenzene and a dicyanodistyrylbenzene have been inserted into single crystalline OFET devices using a solvent vapor annealing process.[118] Both anisotropic and ambipolar charge carrier transport properties were observed for this charge transfer co-crystal with hole and electron mobilities up to 6.7×10^{-3} and 6.7 $cm^2\ V^{-1}\ s^{-1}$, respectively. XRD and AFM experiments along with polarized photoluminescence studies further confirmed that efficient charge transport is occurring effectively along the long crystal axis, which corresponds to the molecular stack direction.

Finally, poly(*p*-phenylene-ethynylene) derivatives with thioacetate end groups have been reported to self-assemble into crystalline nanowires with diameters ranging from 5 to 15 nm and lengths up to hundreds of micrometers (Figure 1.2b).[119] Mobilities of these objects in OFET devices have shown values up to 0.1 $cm^2\ V^{-1}\ s^{-1}$, which is several orders of magnitude higher than thin-film devices of the same polymer. Nanobelt architectures up to 1 μm wide and up to 150 μm long prepared from poly(benzobisimidazobenzophenanthroline) polymers have also been inserted in OFET devices, which were shown to present long-term stability (Figure 1.2c).[120] Electron mobilities were measured for both single and networks of nanobelts with respective values of $7\times10^{-3}\ cm^2\ V^{-1}\ s^{-1}$ (V_{th}: 11.2 V, $I_{on/off} \approx 10^4$) and 4×10^{-3} $cm^2\ V^{-1}\ s^{-1}$ (V_{th}: 11.9 V, $I_{on/off} \approx 10^4$).

1.4 Organic Light-Emitting Devices

Organic light-emitting devices are promising candidates for next-generation display technology and solid-state lighting applications and are currently divided into two classes.[121] The first one is composed of organic light-emitting diodes (OLEDs), which are constituted of several semiconducting organic layers sandwiched between two electrodes, one of them being transparent to light. The second class makes use of light-emitting electrochemical cells (LECs) that consist of a single-layer of ionic luminescent materials inserted between an ITO electrode and a metallic one. Recently, self-assembled supramolecular materials for the construction of OLEDs and LECs have attracted a lot of attention and have been extensively reviewed.[122]

1.4.1 Oligo(phenylenevinylene) Derivatives

Oligo(*p*-phenylenevinylene) (OPPV) moieties are well-studied synthons in supramolecular chemistry, as they can be easily modified to reach various morphologies and they present interesting optical properties. In 2009, the group of Ajayaghosh reported the optical properties of a supramolecular organogel composed of intertwined twisted helical fibrillar assemblies made of OPPV decorated with cholesterol units.[123] In combination with a small percentage of a red-light-emitting acceptor, this resulting gel was shown to emit white light upon excitation at 380 nm with a very good purity (CIE (Commission internationale de l'éclairage) coordinates: 0.31, 0.35), which results from a partial energy transfer occurring simultaneously between the blue emission of the donor monomers, the green emission of the donor aggregates, and the red emission from the acceptor. Moreau and co-workers later studied the light emitting properties of an oligo(phenylenevinylene) imide derivative that can be capped with 2,4-diamino-1,3,5-triazine derivatives by hydrogen bond interactions.[124] Interestingly, whereas the OPPV derivative alone poorly emits light due to its aggregation, the resulting heterotrimers further self-assemble into J-aggregates, due to the bulkiness of the triazine moieties, with good opto-electronic properties. Indeed, OLED devices made of these co-self-assemblies display a luminance of 190 cd m^{-2} at 14.5 V, which corresponds to an increase by two orders of magnitude compared to the single OPPV aggregates. Recently, solvent-free liquid OPPVs blended with tris(8-hydroxyquinolinato)aluminium (Alq3) and rubrene were reported to emit white light with CIE coordinates that vary depending on the concentration of each organic molecule.[125] However, although this blend could be used as white-emitting ink, paint, or coating for a UV-LED (ultraviolet-light emitting diode), no molecular ordering was observed by XRD of the OPPV liquids. Finally, an orange dye derived from a phenylenevinylene was combined with a blue-emitting diphenylpyrroline to form rod-like segregated triblock micelles when mixed with cetyltrimethylammonium bromide, as demonstrated by fluorescence microscopy imaging.[126] Upon excitation at 365 nm, a colloidal suspension of these triblock micro-rods

displays white-light-emitting properties with high quality, and photoluminescence properties as high as $36 \pm 5\%$.

1.4.2 Fluorene Derivatives

Polyfluorene is a well-known class of π-conjugated polymer, whose emission properties can be easily tuned by introducing proper co-monomers.[127] Based on this observation, the group of Schenning reported a series of five molecules made of dialkylfluorene units linked with five different aromatic moieties in order to cover the whole visible range for light emission.[128] Upon dissolution in methylcyclohexane, two compounds were shown to form fibrillar morphologies and could produce organogels at precise concentrations. Interestingly, when these two compounds were mixed with two other derivatives in order to cover the whole visible range, a white-light-emitting gel was reached and presented a similar appearance to the two individual gels. Using a combination of WAXS, AFM, optical spectroscopy, and molecular modeling, a mechanism based on the entanglement of individual 1D fibers was proposed to explain the lyotropic behavior of this organogel. Recently, three π-conjugated molecules decorated at their extremities with self-complementary hydrogen bonding groups were shown to self-assemble into vesicle-like aggregates in THF solution with their emission spectra corresponding to the blue, yellow-green, and red colors of the CIE plot.[129] Further co-self-assembly of very precise proportions of these three molecules led to vesicles that emit white light such as the D65 standard (0.313, 0.331 CIE coordinates), the D50 or even warm light. However, although these self-assemblies seem very promising as white-light-emitting supramolecular systems, so far they have not been inserted in OLED devices.

1.4.3 Polyaromatic Molecules

Polyaromatic molecules such as acene or perylene are very promising candidates for light-emitting devices as they can be easily tailored, present very high quantum yields, and are well-known as charge carriers. For instance, Del Guerzo *et al*. have described the self-assembly of blends of tetracene derivatives leading to color-tunable organogels constituted of fluorescent nanofibers (Figure 1.3a).[130] Under near-UV light excitation, both organogels and dry films of nanofibers emit white light, which is polarized in the blue spectral region. Additional confocal fluorescence microspectroscopy experiments demonstrated that each individual nanofiber emits white light. Perylenes decorated with peptidic units have also been reported to self-assemble into long fibers of 70–80 nm width upon mixing with stilbenes incorporating a tris-amino acid moiety.[131] In a *o*-dichlorobenzene solution and after excitation at 365 nm, thanks to FRET (Förster resonance energy transfer), white light emission with CIE coordinates very close to pure white light (0.33, 0.33 CIE coordinates) was observed with an energy transfer efficiency from the donor to the acceptor of 43% (although individual molecules

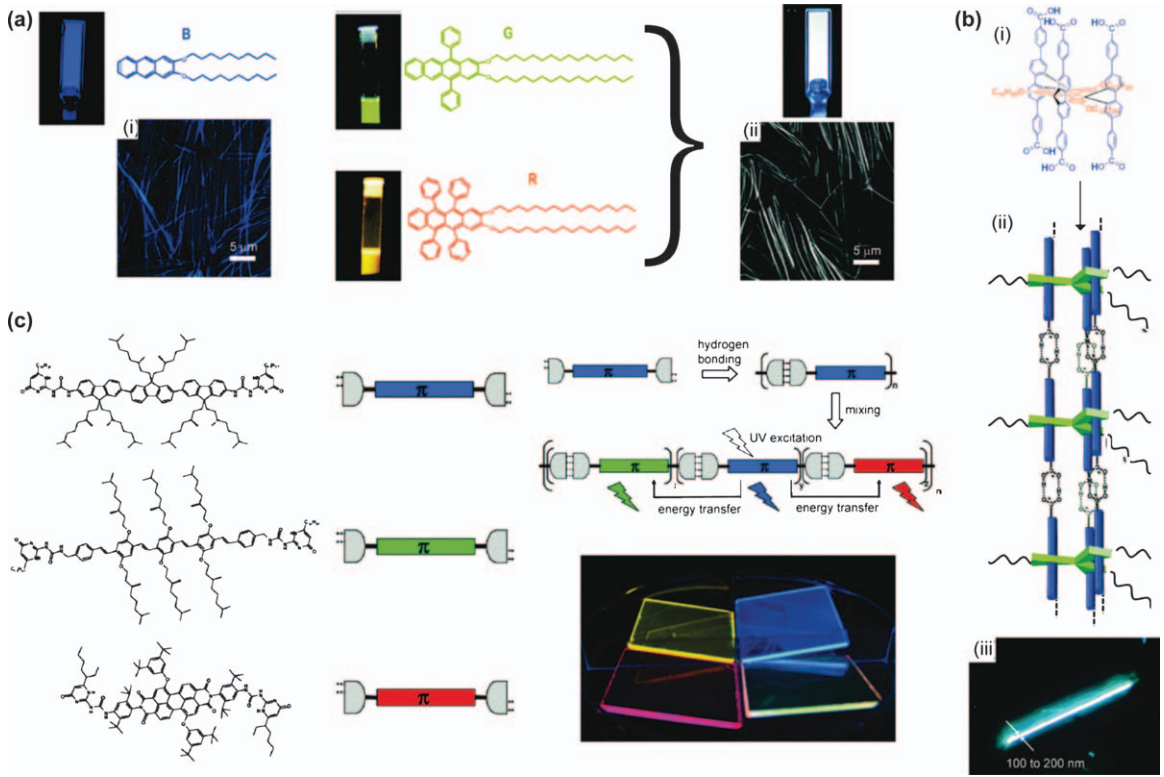

Figure 1.3 (a) Molecular structures and images of a 2 mM **B**-gel in DMSO, a 10 μM **G** solution in THF, and a 10 μM **R** solution in THF under UV light (λ_{ex} 365 nm). Fluorescence intensity obtained by confocal microscopy of (i) a gel made of **B** and (ii) a gel made of the three components **R**, **G**, **B** in DMSO at 22 °C. (b) (i) and (ii) Structure of an hexa-acid compound forming self-assembled polymeric nanowires and (iii) associated fluorescence micrograph. (c) Chemical structures of di-ureidopyrimidinones and schematic illustration of their use for the creation of white photoluminescence.
(a) Reproduced with permission from ref. 130; (b) adapted with permission from ref. 146; (c) reproduced with permission from ref. 144.

emit either in the blue or the orange). Even if this solution was not directly processed in OLED devices, it was successfully used to coat a glass plate or a UV-LED, which both presented white light emission properties. In a similar approach based on FRET, nanometric micelles made of amphiphilic perylene derivatives as energy acceptors have been successfully loaded with bis-carbazoles molecules as energy donors.[132] In aqueous solution under a UV lamp, these nanosized objects displayed white fluorescence, due to a partial energy transfer between the bis-carbazole donor and the perylene acceptor within the micelles. This example represents the smallest white-light emitting system based on only two fluorescence color components. Using several supramolecular interactions, such as π–π stacking and hydrogen bonding, naphthalene diimides were recently self-assembled as J-aggregates in interconnected lamellar structures in mixtures of methylcyclohexane and chloroform.[133] Whereas blue emission corresponding to the monomeric chromophore was observed in chloroform, white-light emission occurred in the non-polar mixture of solvents with CIE coordinates approaching the pure white light. The impressive fluorescence quantum efficiency observed for this single-component system can be attributed to the J-type π-stacking but also relies on the presence of hydrogen bonding as no self-assembly, and therefore property, is observed in the absence of this supramolecular interaction. In a recent example, electrostatic interactions were used to form soft hybrids made of an amino-clay, a coronene tetracarboxylate as the donor, and sulforhodamine G as the acceptor.[134] Depending on the amount of acceptor, emitting hydrogels or films of various colors were obtained as well as a highly pure white-light-emitting film (0.33, 0.32). The good processability and high transmittance of these chromophoric-clay assemblies was demonstrated by writing and coating on glass substrates and flexible plastic surfaces.

1.4.4 Metallic and Inclusion Complexes

The harvesting of triplet energy using metal-containing compounds has proven to be a successful means of making efficient OLEDs. Therefore, iridium and platinum complexes have been particularly studied as OLED materials and have been recently reviewed.[135] Thus, only a few examples of state-of-the-art iridium- or platinum-based devices will be mentioned. Using an iridium complex as a mixture in an ionic liquid, the group of Bolink reported a LEC device showing an extrapolated lifetime to half the initial luminance ($t_{1/2}$) of 4000 h (initial luminance 670 Cd m^{-2}), and sub-second turn-on times in applying a pulsed current driving method.[136] Using a combination of two or three iridium complexes that emit at different wavelengths, Su and co-workers described one of the only white LEC devices, showing the best performance to date with an external quantum efficiency (EQE) of 7.4% and a power efficiency of 15 lm W^{-1}.[137] De Cola and co-workers designed a platinum(II) complex incorporating terpyridine-like ligands which self-assembles in a 3D network of bright gelating nanofibers.[138]

This gel could be easily processed to form luminescent films with a luminescent quantum yield up to 87%. When processed as dopant in OLED devices, a maximum current efficiency of 15.6 cd A^{-1} at a brightness of 203 cd m^{-2} was observed. One of the main problems observed in phosphorescent OLEDs with both iridium and platinum complexes is a decrease of their emitting efficiency due to aggregation of the emitter at high concentration, the concentration quenching and/or triplet–triplet annihilation. One strategy to circumvent this problem is to use cyclometalated ligands and therefore create a supramolecular steric hindrance. For instance, a novel spiro[fluorene-9,9′-xanthene]-functionalized platinum(II) complex was recently synthesized and inserted in OLED devices.[139] Orange electrophosphorescence was observed for the most efficient device, exhibiting a maximum luminance of 3335 cd m^{-2} and a maximum external quantum efficiency of 5.2%.

Owing to the potential luminescent properties of both the metal centers and the organic linkers, metal–organic frameworks have been widely studied as promising candidates for light emitting devices. This field was recently reviewed[140] and, therefore, only one recent example will be presented here. From many examples in the literature, white-light-emitting materials have been mainly produced from dichromatic and trichromatic approaches. Such approaches are, however, scarce for white-light-emitting MOFs. In recent work, a 2D lanthanum/pyridine-2,6-dicarboxylate MOF doped with small amounts of both terbium and europium ions was reported as an almost pure white-light-emitting material (0.33, 0.31).[141] Interestingly, although this MOF displays blue light emission without doping, it presents an emission spectra ranging either from blue to blue-green or form blue-red to red when it is doped either with Tb^{3+} or with Eu^{3+}, respectively. Thus, this white-light-emitting MOF can be considered as a trichromatic material, which could find potential applications in lighting or imaging, for instance.

To control the intermolecular aggregation between polymer chains, which can affect the luminescent efficiency and color purity of OLED, inclusion complexes such as the rotaxination of conjugated polymers are a promising approach. For instance, the group of Cacialli has reported that energy transfer, from a blue emitting cyclodextrin threaded polymer to a green emitting poly(9,9-dioctylfluorene-*alt*-benzothiadiazole), is strongly reduced by controlling the minimum intermolecular distance between emitting moieties through non-covalent encapsulation of the blue component in the cyclodextrin macrocycles.[142] In OLED devices, the contribution of both polymers was observed with the emission of warm light at 0.282 and 0.336 CIE coordinates and the power efficiency reached an encouraging value of 0.39 cd A^{-1}.

1.4.5 H-bond and Metallo-supramolecular Polymers

Supramolecular polymerization by H-bonds or by metal–ligand coordination is an efficient way to form soft materials that present properties that cannot be observed in the individual monomers. This approach has been widely

used in various fields ranging from biomedicine up to organic electronics.[7] Concerning our present purpose, supramolecular Zn(II) metallo-polymers of π-conjugated bis(terpyridine) macroligands with poly(ε-caprolactone) on their side chains were studied for their opto-electronic properties and shown to demonstrate blue photoluminescence with high quantum yields both in diluted solution and in the solid state.[143] This property was attributed to the suppression of the aggregation that usually occurs with metallo-polymers. Using complementary quadruple hydrogen bonding ureidopyrimidone units, the group of Meijer also described a supramolecular copolymer resulting from the self-assembly in films of blue, green, and red π-conjugated oligomers (Figure 1.3c).[144] White electroluminescence was achieved with −0.31 and 0.45 CIE coordinates by using an appropriate ratio of the different oligomers. Other examples of supramolecular polymers using hydrogen-bond interactions were also described for the fabrication of OLED devices. For instance, Chang and co-workers have reported the synthesis of π-conjugated poly(triphenylamine-carbazole), which exhibits an amorphous nature, high thermal stability, good hole injection, and electron-blocking ability in the solid state owing to the supramolecular cross-linking of uracil units between polymer chains.[145] Trilayer OLED devices based on this polymer as a hole injection/transport layer and tris(8-hydroxyquinolinato)aluminium (Alq3) have shown improved performances compared to PEDOT-PSS-based devices. A rigid hexa-acid compound was also reported to form supramolecular polymeric nanowires by hydrogen bonding (Figure 1.3b).[146] Diameters between 100 and 200 nm and lengths up to hundreds of micrometers were observed for this self-assembled system, which presents a solid-state absolute photoluminescence (PL) efficiency of 22%, representing only a loss of 10% against their solvent efficiency. Recently, the group of Huang developed new supramolecular polymers produced using host–guest interactions and studied their photophysical and electroluminescent properties in OLED devices.[147] For instance, such a supramolecular polymer incorporating fluorene moieties was used as a host material for yellow emission phosphorescent complexes.[148] In solution-processed phosphorescent organic light-emitting diode (PhOLED) devices, a very high maximum luminance efficiency (LE_{max}) of 18.2 cd A^{-1} was observed along with a maximum brightness (L_{max}) of 731 cd m^{-2}. Using the same methodology, the same group also reported the formation of supramolecular phosphorescent polymers incorporating an iridium complex within a fluorene-based monomer.[149] These polymers displayed an intrinsic glass transition at 72.5–81.5 °C which is not present in the monomers and presented interesting electroluminescent properties in solution-processed PhOLED devices (LE_{max} 14.6 cd A^{-1} at a luminance of 450 cd m^{-2} and L_{max} 2863 cd m^{-2}). Interestingly, when iridium complexes were inserted as side chains in such a supramolecular polymer (in this case, without electroactive groups in the main backbone), a luminous efficiency of 2.19 cd A^{-1} at a current density of 2.1 mA cm^{-1} was observed, which arises only from the iridium complex.[150]

1.5 Organic Photovoltaic Devices

Intensive research is currently carried out in the field of organic photovoltaic devices, because of their lower cost compared to silicon-based materials and the easy processing of the active layer.[151,152] Two main approaches have been considered to produce efficient devices with small molecules. The first one, the so-called dye-sensitized solar cells (DSCs),[152] rests on the absorption of light by an organic dye anchored on a TiO_2 surface. The electrons are then injected from the excited dye into the conduction band of TiO_2, leading to the generation of an electric current. The other approach, termed bulk heterojunction (BHJ) solar cells, rests on a network of donor–acceptor heterojunctions.[151] For these later devices, the morphology of the active layer plays a critical role in the device's performances and particular attention was devoted to its ordering. One way to achieve this organization is to use supramolecular materials capable of self-assembling in well-defined nanostructures.[7]

1.5.1 Thiophene Derivatives

Poly(3-hexylthiophene) (P3HT) in combination with PCBM ([6,6]-phenyl-C_{61}-butyric acid methyl ester) is one of the most studied polymers for solar cells devices built on a bulk heterojunction, which reach power conversion efficiencies of around 5%.[153] One way to improve these performances is to optimize the molecular design of the donor molecules. For instance, the group of Barbarella has described the influence of the side chains on the photovoltaic performance of a regioregular head-to-head thiophene hexadecamer.[154] To reduce backbone distortion, which decreases delocalization, thioalkyl chains have been introduced instead of alkyl groups on the hexadecathiophene, leading to p-type semiconductors with a FET charge mobility of up to 9.5×10^{-4} cm^2 V^{-1} s^{-1} (no charge mobility detectable for the alkyl-substituted molecule). AFM images of blends of the thioalkyl derivative with PCBM reveal a good phase separation between the donor and the acceptor molecules and, indeed, performances in non-optimized BHJ devices are very promising for further applications (current density (J_{SC}) 5.13 mA cm^{-2}; open circuit voltage (V_{OC}) 0.64 V; power conversion efficiency (PCE) 1.49%). In another example, bithienyl-substituted benzodithiophene was used as the donor unit in acceptor–donor–acceptor small molecules with indenedione as the acceptor.[155] In combination with $PC_{70}BM$, films of these molecules display an interconnected network morphology, which could explain their high performance as photoactive layer in BHJ solar cells (J_{SC} 11.05 mA cm^{-2}; V_{OC} 0.92 V; PCE 6.75%). The high fill factor observed for these small molecules (up to 66.4%) confirms the potential of small molecules for further applications in commercial devices.

Another way to improve the performance of OPV devices is to achieve a better structuring of the active layer. The use of supramolecular interactions

such as hydrogen-bonding and/or π–π stacking seems particularly promising for reaching this goal. For instance, a hairpin-shaped oligothiophene in combination with $PC_{60}BM$ was used by Stupp and co-workers to build bulk heterojunction solar cells.[156] Fluorescence experiments in solution have shown that charge transfer occurs between this hairpin donor molecule and the fullerene acceptor. As-prepared photovoltaic devices made of this mixture showed a current density of 0.72 mA cm^{-2}, an open circuit voltage of 0.53 V, and a power conversion efficiency of 0.14%. Interestingly, upon annealing at different temperatures, in particular at 80°C, a PCE of 0.22%, due to both higher J_{SC} and V_{OC}, was observed, which represents an increase of 57% compared to the non-annealed device. When $PC_{70}BM$ was used instead of $PC_{60}BM$, a similar trend with annealing was observed although a slightly higher temperature (90 °C) gave the best performance (J_{SC} 1.79 mA cm^{-2}; V_{OC} 0.62 V; PCE 0.48%). Using a slightly modified hairpin-shaped molecule presenting diketopyrrolopyrrole arms instead of oligothiophene, the same group studied the influence of the preparation pathway used for OPV devices on their efficiencies.[157] Two approaches were studied: (i) the one-step mixing of both the donor and acceptor ($PC_{71}BM$) moieties and (ii) a stepwise pathway, *i.e.* after self-assembly of the donor molecule into a network of long supramolecular nanowires, the acceptor is added. Interestingly, devices made from pathway (i) were reported as non-functional, whereas devices obtained after stepwise pathway (ii) led to very efficient devices (J_{SC} 2.98 mA cm^{-2}; V_{OC} 0.66 V; PCE 0.53% for a 1 : 1 mixture of donor and acceptor in chlorobenzene). This difference in efficiencies can be attributed to a possible disruption of the formation of the self-assembling nanowires by the acceptor in the one-pot process. In the absence of the self-assembling hairpin core on the donor molecule, devices were 54% less efficient. In another example, the group of Kimura reported the formation of ordered structures using disk-shaped molecules incorporating a pyrene unit as structuring motif decorated with four tri- or tetrathiophenes presenting peripheral alkyl chains.[158] Films obtained from blends with $PC_{70}BM$ present a bicontinuous network structure arising from a phase-segregation process, which retains the ordered structure of the pyrene-cored compound. Evaluation of the photovoltaic performances of these self-assembled structures in BHJ solar cells devices revealed a PCE of 2.6%, which is comparable to the one observed for a P3HT/PCBM blend in the same device (2.8%). However, a 40% drop of the fill factor (FF = 0.36) compared to the reference (0.62) indicated the poor balance of charge carrier mobilities in the active layer. Peptidic units are known to form secondary structures such as α-helices or β-sheet structures. Recently, a polylysine was decorated with hexathiophene derivatives and TEM imaging of this polymer revealed the formation of branched networks in organic solvents such as cyclohexane or chlorobenzene.[159] In solar cell devices, blends of this polypeptide with PCBM showed an improvement of PCE compared to reference compounds that do not produce any helical arrangement of chromophores, highlighting once again the importance of the morphology of the active layer in OPV devices. Supramolecular

interactions have recently been used to structure an active layer made of P3HT capped with a fullerene moieties.[160] In particular, the solvent used for film formation was crucial to reach high photocurrent generation. Indeed, whereas THF-cast films presented nanospherical morphologies, films made from dichlorobenzene solutions displayed interconnected fibrous networks. Conductive and photoconductive AFM imaging of these films revealed the influence of the morphology on the photoconducting properties of the polymer as low dark current and photocurrent were observed for the nanospheres, whereas high performances were observed for the fibrous network.

Another way to control the morphology of the active layer in small molecule BHJ solar cells relies on the processing within the OPV devices. Recently, the groups of Bazan and Heeger described a donor–acceptor–donor molecule that presents a PCE as high as 6.7% in blends with $PC_{70}BM$.[161] Such a high PCE was observed when a small percentage of 1,8-iodooctane was used to control the nanomorphology of the blends, as demonstrated by TEM. Indeed, this additive was shown to reduce the domain sizes from 20–30 nm to 15–20 nm, which resulted in an increase in the PCE from 4.52% to 6.70%. This example highlights the influence of a chemical additive during the processing; alternative processing methods such as annealing can also be used to improve the performance of BHJ solar cells.[162]

Organogels based on thiophene derivatives have also been used as active layers in BHJ devices. For example, an electron-rich tetra- or hexathiophene was co-self-assembled with an electron-poor perylene bis-imide to obtain n/p heterojunction nodes (Figure 1.4a).[163] Interestingly, sorted elongation of pure oligothiophene nanofibers and of pure perylene bis-imide nanofibers was observed from a 1 : 1 mixture of both compounds and resulted in the formation of organogels with large interface areas between the p-type and n-type conductors, as demonstrated by SEM. Bulk heterojunction devices made out of these organogels resulted in an efficient photoresponse, but no performance regarding these devices was reported.

Among others, it should be mentioned that self-assembling nanostructures can also be detrimental to OPV performances. Indeed, a donor–acceptor–donor molecule incorporating a barbiturate derivative as hydrogen bonding recognition unit was shown to form well-ordered nanoribbons both in the presence and in the absence of $PC_{61}BM$.[164] When the hydrogen bond motifs were capped with methyl groups, no more ribbons were formed and a bicontinuous network was observed for blends with fullerenes, resulting in an increase of the PCE by one order of magnitude compared to the self-assembling supramolecular synthon.

Finally, although tetrathiafulvalenes are very promising candidates for conducting materials, examples of incorporation of a TTF in photovoltaic devices are rare and have been reviewed recently.[165] They have been incorporated in both dye-sensitized and BHJ solar cells without controlling precisely the morphology. A TTF derivative modified with a L-glutamide-derived lipid unit was reported as an organogelator in various

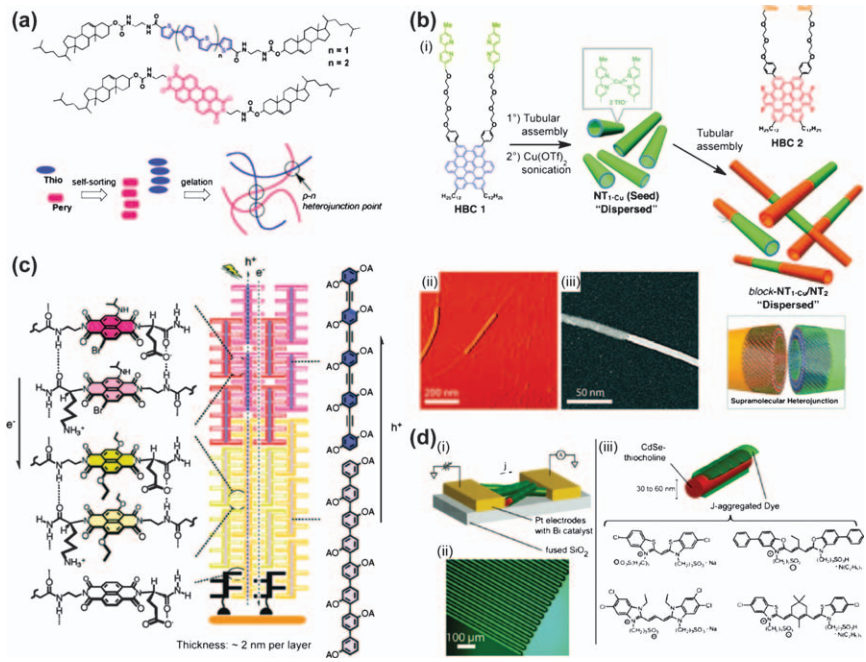

Figure 1.4 (a) Chemical structures of the oligothiophene and perylene organogelators with schematic representation of their self-sorting organogel formation yielding p-n heterojunction points. (b) (i) Molecular structures of two HBCs and schematic illustrations of the preparation of a supramolecular heterojunction made of semiconducting nanotubular segments; (ii) tapping-mode AFM and (iii) scanning TEM micrograph of the nanotubular segments. (c) Molecular structures of *p*-oligophenyl, *p*-oligophenylethynyl chromophores, and naphthalene-diimides, together with their corresponding supramolecular heterojunction architectures resulting in oriented multicolored antiparallel redox gradients (OMARG). (d) Overview of a J-aggregate/CdSe nanowire color-selective photodetector; (i) schematic of J-aggregate-coated nanowires contacted between electrodes; (ii) optical micrograph, showing interdigitated electrodes used to grow and test devices; faint brown shading between electrodes is the sparse network of CdSe nanowires; (iii) detail of J-aggregate-templated CdSe nanowires with the structure of J-aggregating dyes. (a) Reproduced with permission from ref. 163; (b) adapted with permission from ref. 183; (c) reproduced with permission from ref. 190a; (d) reproduced with permission from ref. 199.

organic solvents.[166] Upon addition of C_{60}, the gelation ability of the small molecule was enhanced and SEM imaging of both xerogels indeed showed networks of fibers in both cases, with a ten-fold increase in widths for the doped one. Interestingly, the doped xerogel deposited on an ITO electrode presents a stable, rapid, and reproducible photocurrent upon exposure to light. However, their incorporation in OPV devices has not been reported yet.

1.5.2 Porphyrin and Phthalocyanine Derivatives

Owing to their well-known light harvesting properties, porphyrins have been particularly developed for dye-sensitized solar cells.[167] For instance, a zinc porphyrin/squaraine dyad sensitizer was decorated with a light-harvesting antenna by metal–ligand interaction to increase its absorption in the 450–550 nm range.[168] DSC devices made of this supramolecular complex and incorporating antennas in the electrolyte displayed a 30% increase in efficiency compared to the device made of the porphyrin sensitizer with the antenna that could not form a supramolecular complex. This increase in efficiency can be attributed to a FRET from the antenna to the dyad.

Recently, the porphyrin synthon was also considered for use in BHJ devices. For example, Aida and co-workers have reported that enantiopure and racemate forms of porphyrin-fullerene dyads self-assemble into various structures.[169] In particular, racemate generates nanometric spheres with a mean diameter of 300 nm, whereas enantiopure compound gives nanofibers up to 10 μm long. Casted film of the spherical assemblies show only a small hole mobility of 1.5×10^{-4} cm^2 V^{-1} s^{-1} and no electron mobility by the TOF method. Meanwhile, nanofibers exhibit an ambipolar charge-transporting character with hole and electron mobilities of 0.10 and 0.14 cm^2 V^{-1} s^{-1}, respectively. As a consequence, upon photoirradiation, only the nanofibers displayed a detectable photocurrent on micrometer-gap electrodes. By slightly modulating the linker and its rigidity between the porphyrin and the fullerene, the same group demonstrated that bilayer or monolayer nanotubes could be produced.[170] The bilayer nanotube, which presented a diameter of 32 nm, consisted of a coaxially segregated donor–acceptor heterojunction, whereas the monolayer one, with a smaller diameter (7.5 nm), was composed by alternating donor/acceptor stacking. Although both nanostructures were photoactive, these differences in molecular arrangement had an impact on the photoconductivities of both nanostructures, with the bilayer nanotube presenting an ambipolar charge-transporting character and being much more photoconductive than the monolayer nanotube. This observation was confirmed when measuring the V_{OC} and the J_{SC} of both nanostructures inserted in devices. Recently, a properly designed prophyrin-C_{60} dyad was shown to self-assemble into a supramolecular ''double-cable'' structure with the core channel made of the p-type porphyrins and the n-type C_{60} standing as three helices at the periphery of the cable.[171] Using both wide-angle X-ray diffraction and electron diffraction experiments, the precise structure of this self-assembly was determined with columns packed into a hexagonal lattice and a full helical turn observed for a stack of 129 molecules rotated for 44 turns. In BHJ devices, a blend of this nanostructure with a low band-gap conjugated polymer resulted in a phase-separated columnar morphology that presented high photovoltaic performances (J_{SC} 13.5 mA cm^{-2}, V_{OC} 0.66 V, PCE 3.36%, and FF 0.38). Porphyrin and fullerene derivatives have also been combined in non-covalent dyad systems in OPV devices. For instance, Hasobe and co-workers have reported the hierarchical

self-assembly of a zinc meso-tetra(4-pyridyl)porphyrin into flakes in the absence of fullerene derivatives and into hexagonal or distorted polygonal hollow nanotubes depending on the size of the fullerene particles.[172] Regenerative I^-/I^{3-} photoelectrochemical cells made with these nanotubes showed, at an input power of 20 mW cm^{-2}, a PCE of 0.63% when the nanotube is filled with a C_{60} derivative, whereas a PCE of 0.03% was observed for the zinc porphyrin alone. PCBM has also been incorporated in liquid crystalline porphyrins which form columnar aggregates with a hexagonal lattice in homeotropically aligned thin films, as determined by XRD.[173] The resulting doped blends kept the liquid crystal phase of the porphyrin derivative, allowing the formation of highly ordered nanostructured thin films that are promising for use in OPV devices (PCE 0.71% after annealing). Phthalocyanines decorated with amide and carboxylic acid functions have been self-assembled vertically in nanorods on ITO surfaces, forming large and ultra-dense arrays.[174] The conductivity measured by a conducting AFM tip was shown to be 20–100 times greater than an amorphous film of zinc phthalocyanines. When this nanorod-arrayed film was used as a hole-transporting layer in an organic solar cell device, high photovoltaic performances (J_{SC} 7.50 mA cm^{-2}, V_{OC} 0.56 V, PCE 2.31%, and FF 0.55) were reached although they were not as high as the one observed for a classical PEDOT : PSS active layer. Nonetheless, precise structuring of the surface using oriented π–π stacks showed great improvement compared to the same device made with an amorphous film (J_{SC} 1.71 mA cm^{-2}, V_{OC} 0.41 V, PCE 0.14%, and FF 0.20).

1.5.3 Diketopyrrolopyrrole Derivatives

Diketopyrrolopyrrole (DPP) is a chromophoric unit that has been widely used in industrial applications as high-performance pigments. Recently, this synthon, which can be involved in both hydrogen-bonding and π–π stacking interactions, has been connected with thiophene units and inserted in small molecules for solution-processed small-molecule BHJ solar cells. The group of Nguyen has been particularly active in developing such new small molecules. For instance, in their seminal work, a DPP fragment, which presents an electron accepting ability, was coupled with two electron donating terthiophene units at their 2 and 5 positions.[175] One advantage of the thiophene units is their ability to induce an intramolecular charge transfer with the DPP core, which leads to a broadening of the absorption of these molecules. When they are blended with PCBM and used as active layer in a BHJ device, high photovoltaic performances can be reached (J_{SC} 8.42 mA cm^{-2}, V_{OC} 0.67 V, PCE 2.33%, and FF 0.45). Interestingly, the morphology of the active layer as fiber-like structures was not affected during blending and a continuous film without phase segregation was observed, which probably accounts for the device performance. By finely tuning the substitution of the nitrogen atoms of the DPP fragments and the possible functional groups connected to the thiophene units, improved performances in BHJ devices

were observed leading to a PCE of 4.8%, the highest reported so far for DPP-containing small molecules.[176] A good nanostructuring of the blend along with a good match between the molecular orbital levels of both the donor and the acceptor can be ascribed for the observed photovoltaic properties. To further improve the supramolecular arrangement of these molecules, electron-rich π-stacking units such as triphenylamine or pyrene units have also been connected to the dithienyl-DPP core.[177] For the molecule substituted with pyrene at its C2 position, a very efficient thin film BHJ device was produced (J_{SC} −8.3 mA cm^{-2}, V_{OC} 0.76 V, PCE 4.1%, and FF 0.58). Using a combination of AFM, XRD, and grazing-incidence X-ray scattering, thin films of both the single molecule and its blend with $PC_{71}BM$ showed a closely-packed, highly crystalline network, which arises from the strong π–π interactions between the pyrene units. By fine tuning the dithienyl-DPP core, new donor materials with liquid crystalline properties induced by the formation of H-aggregates have been synthesized recently.[178] The liquid crystalline mesophase was only observed upon heating above 117 °C and, indeed, BHJ devices obtained after annealing at 140 °C displayed increased performances (J_{SC} 8.27 mA cm^{-2}, V_{OC} 0.93 V, PCE 4.2%, and FF 0.54) compared to the as-cast device (PCE 2.6%). AFM imaging of thin films confirmed the re-organization of blend films into large and homogeneous interpenetrating networks upon thermal annealing.

1.5.4 Hexabenzocoronene Derivatives

Based on both their self-assembling and electronic properties, hexabenzocoronene derivatives have also been considered for BHJ solar cells.[179] For instance, HBC discotic liquid crystals were combined with a perylene dye to produce thin films with vertically segregated perylene and HBC having a large interfacial surface area.[180] When incorporated into a diode geometry by solution casting, these films show a photovoltaic response (J_{SC} −33.4 μA cm^{-2}, V_{OC} 0.69 V, PCE 1.95%, and FF 0.40) initiated by a photoinduced charge transfer and an effective transport in the two π-systems. The group of Aida has synthesized photoconductive nanotubes by a controlled self-assembly of the HBC–trinitrofluorenone (TNF) covalent D–A dyad.[181] Such nanotubes have a coaxial configuration in which a molecular layer of electron-accepting TNF laminates an electron-donating graphitic bilayer of π-stacked HBC. Such a structure creates an extremely wide interface for the spatially segregated redox couple, providing an on/off ratio greater than 10^4 upon photo-irradiation. Such building of a heterojunction within the nanotube configuration and using fullerene as an electron accepting layer was successfully used in photovoltaic devices.[182] The same group has also reported a supramolecular linear p–n junction composed of two different graphitic nanotubes by a stepwise self-assembly of two kinds of HBCs having different electronic structures (Figure 1.4b).[183] The lifetime of the charge carriers generated in the heterojunction nanotubes is five times longer than those measured for the nanotubes composed of a single component,

demonstrating that the probability of the charge recombination is reduced. Modifying the substitution of the HBC core with difluorenyl moieties leads to a self-assembly into columnar discotic liquid crystals.[184] Solar cell devices based on the blend of these compounds with $PC_{60}BM$ (1 : 2) generated, after thermal annealing at 150 °C, a short circuit current (J_{SC}) of 2.68 mA cm^{-2} and a PCE of 1.46%. Modifications of bifluorenyl-HBCs by oligothiophenes dendrons led to an organization in discotic columnar array, without any phase transition between −100 and 250 °C.[185] BHJ devices based on a blend of these compounds and $PC_{70}BM$ (1 : 2) showed a J_{SC} of 5.71 mA cm^{-2} along with a PCE of 2.64% for the best one. More recently, diketopyrrolopyrrole units were appended to the same bifluorenyl-HBC core and a discotic liquid crystalline phase was observed over a large range of temperatures.[186] Blends with $PC_{71}BM$ in BHJ solar cells showed a J_{SC} of 3.96 mA cm^{-2}, a V_{OC} of 0.86 V, and PCE of 1.59%. All these examples highlight the influence of small molecular changes on morphologies and thereby on device performances.

Dibenzotetrathienocoronene (6-DBTTC) was shown to self-assemble into a network of cables only after thermal treatment above 100 °C.[187] Devices made of a spin-cast donor layer annealed at 150 °C followed by an acceptor layer of fullerene deposited by thermal evaporation showed a power conversion efficiency of 1.9% (J_{SC} 6.7 mA cm^{-2} and V_{OC} 0.6 V). The importance of the structure of the donor layer was demonstrated with non-annealed devices, which displayed a PCE of 0.6% and a J_{SC} of 1.8 mA cm^{-2}. These molecules have also been used in blended films with $PC_{70}BM$.[188] In this case, grazing incidence wide-angle X-ray scattering (GIWAXS) demonstrated the formation of supramolecular complexes in the bulk, owing particularly to the concave shape of 6-DBTTC, which is able to coordinate the ball shape of $PC_{70}BM$. Devices made of a 1 : 2 ratio of 6-DBTTC : $PC_{70}BM$ as the active layer demonstrated an enhanced PCE of 2.7% and the presence of these supramolecular complexes was shown to positively affect charge separation in the active layer.

1.5.5 Rylene Derivatives

The group of Matile has proposed a new supramolecular n/p-heterojunction (SHJ) approach with oriented multicolored antiparallel redox gradients (OMARGs) to build well-defined surface architectures for BHJ solar cells.[189] In particular, they have introduced the programmed assembly of interdigitating intra- and interlayer recognition motifs on conducting surfaces (Figure 1.4c).[190] These self-assembled zippers allow the access to supramolecular coaxial n/p-heterojunctions with good photocurrents and high fill factors (0.50–0.60). To reach a well-defined n/p-heterojunction at the nanoscale, Würthner and co-workers have described the synthesis of a tryad composed of two triaminotriazine-substituted oligo(phenylenevinylenes) connected to a perylene bis-imide by hydrogen bonding.[191] The trimer was shown to self-assemble into right-handed supercoils. However, OPV devices show only poor diode behavior due to the lateral organization of the

supercoils at the surface. Increasing the absorption spectra of small molecules is a strategy commonly used to achieve better efficiencies. Using a non-covalent metal–ligand interaction, a zinc porphyrin was coupled with and *N*-pyridyl-perylene-imide anchored on a TiO_2 surface, leading to a supramolecular dyad with an increased absorption between 450 and 650 nm.[192] Using cyclic voltammetry measurements on the supramolecular complex, the porphyrin was shown to be a better electron donor whereas the electron density of the perylene unit was reduced. When this dyad was introduced in dye-sensitized solar-cell devices, a larger efficiency than those observed for the individual dyes was recorded (PCE 1.1%, 0.72% and 0.09% for the dyad, the perylene and the porphyrin units, respectively). This supramolecular approach can be seen as a new strategy to construct multichromophoric dye-sensitized solar cells.

1.5.6 Triarylamines Molecules

As mentioned earlier, triarylamine molecules have been widely used as donor motifs in opto-electronic devices, particularly in dye-sensitized organic solar cells, without controlling precisely their nanostructures.[193] The group of Kumar recently introduced two strategies to control the nanostructuring of triarylamine moieties, which results in improved device efficiencies. As a first approach, they decorated a triarylamine molecule with a self-complementary hydrogen bond motif.[194] AFM imaging of films revealed the formation of interconnected fibrous nanostructures 85–110 nm wide, following a hierarchical self-assembly process based on 1D hydrogen-bonded chains and further interchain H-aggregation. Evaluation of the photovoltaic performances of both non-self-assembling and self-assembling molecules demonstrated higher fill factor (49% *versus* 38%) and higher device energy conversion efficiency (2.4% *versus* 2.25%) for the self-organizing system. In a second approach, they took advantage of the light-triggered self-assembling properties of properly designed triarylamine, that we reported on conducting materials,[69,70] to enhance the efficiencies of OPV devices.[195] Therefore, new strongly dipolar ''push–pull'' bis-acetamido-functionalized triarylamines were synthesized and shown to self-assemble upon light irradiation in chloroform, even in the presence of $PC_{61}BM$. Such molecules were then further incorporated in OPV devices and photovoltaic performances of the irradiated molecules exceeded those of the non-irradiated ones, demonstrating the importance of the morphology to achieve highly efficient devices.

1.5.7 Other Aromatic Molecules

Dyads and triads made of donor (D) and acceptor (A) units are a well-known strategy by which to obtain low-bandgap organic materials for use in BHJ solar cells. Recently, the efficiencies of two triads (ADA and DAD) based on dithieno(dialkyl)fluorene units as donors and benzothiadiazole units as

acceptors have been compared in such devices.[196] Whereas the DAD molecule presented a crystalline state, the ADA molecule displayed nematic liquid crystalline behavior and both molecules presented similar HOMO and LUMO levels. When blended with $PC_{61}BM$ in BHJ devices, the liquid crystalline molecule surprisingly displayed much lower photovoltaic performances than the crystalline DAD molecule. This example highlights the importance of the morphology (the high fluidity of the nematic phase being detrimental to the performances) over the molecular orbital energy levels. Fluorene units decorated on both sides by thiophene groups have also been used to produce a cross-linked polymer network that presents nematic liquid-crystalline gelating behavior.[197] A film of this gel was then covered with an electron-acceptor molecule layer deposited to form a vertically separated distributed interface between donors and acceptors. Incorporation of such an architecture in a photovoltaic device led to performances such as a V_{OC} of 1.1 V and a PCE of 0.6% for a monochromatic irradiance of 45 mW cm^{-2}. A low band-gap conjugated main-chain polymer containing melanin side chains was cross-linked with complementary uracil-based electroactive fragments, which induced a lowering of both the HOMO and LUMO levels of the supramolecular network, compared to the polymer itself.[198] When blended with $PC_{70}BM$, smooth films with no apparent aggregation except a nanoscale phase separation could be observed by AFM. This nanostructuration along with a better match between the molecular orbital levels of the donor and the acceptor led to improved photovoltaic properties for the polymer networks (PCE and J_{SC} respectively 3 and 2.6 times greater than the ones of the polymer alone).

In addition to their interest for energy purposes, OPV devices could also be used as photodetectors by converting a light signal into an electrical one. Bawendi and co-workers reported the conception of photodetector devices based on the self-assembly of J-aggregates dyes onto crystalline inorganic nanowires, allowing the distribution of both light harvesting and charge transport functions between two materials optimized for each role (Figure 1.4d).[199] The deposition of strongly-negative cyanine dyes by spin coating onto thiocholine-treated CdSe nanowires resulted in formation of J-aggregates at the nanowires' surface. This process was shown to be reversible using exclusively solution phase processing and, thus, a switchable color sensitization of the device from blue to red to green was explored. These color-sensitized devices demonstrated three specific and narrow absorption bands with a resulting photocurrent enhancement of up to 2.8-fold greater than the bare CdSe nanowire device.

1.6 Conclusion

Supramolecular electronics is a recent subdomain of organic electronics that targets a length scale between single molecules and organic thin films. It aims to take advantage of self-assembly strategies to construct monodimensional conducting channels and to integrate them in electronic

devices. After a decade of experimental developments, these concepts have already been shown to be of great interest for further implementations in nanotechnologies. Here we have illustrated that various families of molecules have particular potential in this field, and that important challenges have now been addressed to improve the conductivity properties of these π-conjugated systems either as semiconductors or organic metals. In addition, by using several processing, casting, and aligning strategies, these soft materials have already been engineered and integrated in (opto)electronic devices such as field effect transistors, light emitting diodes, and organic solar cells. These materials open new doors for further fundamental investigations on charge transport phenomena and for technological applications in which bottom-up fabrication processes can overlap with pre-patterned top-down circuitries for improved miniaturization and efficiency.

Acknowledgements

We thank the European Research Council under the European Community's Seventh Framework Program (FP7/2007-2013)/ERC Starting Grant agreement n°257099. We wish to thank the Centre National de la Recherche Scientifique (CNRS), the international center for Frontier Research in Chemistry (icFRC), the Laboratory of Excellence for Complex System Chemistry (LabEx CSC), the University of Strasbourg (UdS), and the Institut Universitaire de France (IUF).

References

1. (a) P. Samorì, F. Cacialli, H. L. Anderson and A. E. Rowan, *Adv. Mater.*, 2006, **18**, 1235; (b) R. D. Miller and E. A. Chandross, *Chem. Rev.*, 2010, **110**, 1.
2. S. R. Forrest, *Nature*, 2004, **428**, 911.
3. F.-J. Meyer zu Heringdorf, M. C. Reuter and R. M. Tromp, *Nature*, 2001, **412**, 517.
4. (a) M. A. Reed, C. Zhou, C. J. Muller, T. P. Burgin and J. M. Tour, *Science*, 1997, **278**, 252; (b) A. Nitzan and M. A. Ratner, *Science*, 2003, **300**, 1384.
5. E. W. Meijer and A. P. H. J. Schenning, *Nature*, 2002, **419**, 353.
6. (a) J.-M. Lehn, *Science*, 2002, **295**, 2400; (b) G. M. Whitesides and B. Grzybowski, *Science*, 2002, **295**, 2418; (c) T. Aida, E. W. Meijer and S. I. Stupp, *Science*, 2012, **335**, 813.
7. (a) E. Moulin, G. Cormos and N. Giuseppone, *Chem. Soc. Rev.*, 2012, **41**, 1031; (b) E. Busseron, Y. Ruff, E. Moulin and N. Giuseppone, *Nanoscale*, 2013, **5**, 7098.
8. (a) A. P. H. J. Schenning and E. W. Meijer, *Chem. Comm.*, 2005, 3245; (b) M. Hasegawa and M. Iyoda, *Chem. Soc. Rev.*, 2010, **39**, 2420; (c) F. S. Kim, G. Ren and S. A. Jenekhe, *Chem. Mater.*, 2011, **23**, 682; (d) S. S. Babu, S. Prasanthkumar and A. Ajayaghosh, *Angew. Chem. Int. Ed.*, 2012, **51**, 1766.

9. E. Moulin, J.-J. Cid and N. Giuseppone, *Adv. Mater.*, 2013, **25**, 477.
10. (a) E. Gomar-Nadal, J. Puigmartí-Luis and D. B. Amabilino, *Chem. Soc. Rev.*, 2008, **37**, 490; (b) C. Li, H. Bai and G. Shi, *Chem. Soc. Rev.*, 2009, **38**, 2397.
11. F. S. Schoonbeek, J. H. van Esch, B. Wegewijs, D. B. A. Rep, M. P. de Haas, T. M. Klapwijk, R. M. Kellogg and B. L. Feringa, *Angew. Chem. Int. Ed.*, 1999, **38**, 1393.
12. D. A. Stone, A. S. Tayi, J. E. Goldberger, L. C. Palmer and S. I. Stupp, *Chem. Commun.*, 2011, 5702.
13. (a) S. Prasanthkumar, A. Saeki, S. Seki and A. Ajayaghosh, *J. Am. Chem. Soc.*, 2010, **132**, 8866; (b) S. Prasanthkumar, A. Gopal and A. Ajayaghosh, *J. Am. Chem. Soc.*, 2010, **132**, 13206.
14. F. Di Maria, P. Olivelli, M. Gazzano, A. Zanelli, M. Biasiucci, G. Gigli, D. Gentili, P. D'Angelo, M. Cavallini and G. Barbarella, *J. Am. Chem. Soc.*, 2011, **133**, 8654.
15. B. W. Messmore, J. F. Hulvat, E. D. Sone and S. I. Stupp, *J. Am. Chem. Soc.*, 2004, **126**, 14452.
16. S. Yagai, T. Kinoshita, Y. Kikkawa, T. Karatsu, A. Kitamura, Y. Honsho and S. Seki, *Chem. Eur. J.*, 2009, **15**, 9320.
17. (a) J. L. Segura and N. Martín, *Angew. Chem. Int. Ed.*, 2001, **40**, 1372; (b) D. Canevet, M. Sallé, G. Zhang, D. Zhang and D. Zhu, *Chem. Commun.*, 2009, 2245.
18. K. Tanaka, T. Kunita, F. Ishiguro, K. Naka and Y. Chujo, *Langmuir*, 2009, **25**, 6929.
19. M. Takase, N. Yoshida, T. Nishinaga and M. Iyoda, *Org. Lett.*, 2011, **13**, 3896.
20. M. Takase, N. Yoshida, T. Narita, T. Fujio, T. Nishinaga and M. Iyoda, *RSC Advances*, 2012, **2**, 3221.
21. M. Hasegawa, H. Enozawa, Y. Kawabata and M. Iyoda, *J. Am. Chem. Soc.*, 2007, **129**, 3072.
22. A. Jain, K. V. Rao, U. Mogera, A. A. Sagade and S. J. George, *Chem. Eur. J.*, 2011, **17**, 12355.
23. T. Kitamura, S. Nakaso, N. Mizoshita, Y. Tochigi, T. Shimomura, M. Moriyama, K. Ito and T. Kato, *J. Am. Chem. Soc.*, 2005, **127**, 14769.
24. (a) J. Puigmartí-Luis, V. Laukhin, Á. Pérez del Pino, J. Vidal-Gancedo, C. Rovira, E. Laukhina and D. B. Amabilino, *Angew. Chem. Int. Ed.*, 2007, **46**, 238; (b) X.-J. Wang, L.-B. Xing, W.-N. Cao, X.-B. Li, B. Chen, C.-H. Tung and L.-Z. Wu, *Langmuir*, 2011, **27**, 774.
25. Y. Tatewaki, T. Hatanaka, R. Tsunashima, T. Nakamura, M. Kimura and H. Shirai, *Chem. Asian J.*, 2009, **4**, 1474.
26. S. J. Choi, J. Kuwabara and T. Kanbara, *Chem. Asian J.*, 2010, **5**, 2154.
27. T. C. Narayan, T. Miyakai, S. Seki and M. Dincă, *J. Am. Chem. Soc.*, 2012, **134**, 12932.
28. S. Tiwari and N. C. Greenham, *Optical and Quantum Electronics*, 2009, **41**, 69.

29. H. Imahori, T. Umeyama, K. Kurotobia and Y. Takano, *Chem. Commun.*, 2012, 4032.
30. (a) S. Sengupta, D. Ebeling, S. Patwardhan, X. Zhang, H. von Berlepsch, C. Böttcher, V. Stepanenko, S. Uemura, C. Hentschel, H. Fuchs, F. C. Grozema, L. D. A. Siebbeles, A. R. Holzwarth, L. Chi and F. Würthner, *Angew. Chem. Int. Ed.*, 2012, **51**, 6378; (b) S. Patwardhan, S. Sengupta, L. D. A. Siebbeles, F. Würthner and F. C. Grozema, *J. Am. Chem. Soc.*, 2012, **134**, 16147.
31. T. Sakurai, K. Shi, H. Sato, K. Tashiro, A. Osuka, A. Saeki, S. Seki, S. Tagawa, S. Sasaki, H. Masunaga, K. Osaka, M. Takata and T. Aida, *J. Am. Chem. Soc.*, 2008, **130**, 13812.
32. T. Sakurai, K. Tashiro, Y. Honsho, A. Saeki, S. Seki, A. Osuka, A. Muranaka, M. Uchiyama, J. Kim, S. Ha, K. Kato, M. Takata and T. Aida, *J. Am. Chem. Soc.*, 2011, **133**, 6537.
33. R. S. Nohr, P. M. Kuznesof, K. J. Wynne, M. E. Kenney and P. G. Siebenman, *J. Am. Chem. Soc.*, 1981, **103**, 4371.
34. W. Zhang, K. Ochi, M. Fujiki, M. Naito, M. Ishikawa, K. Kaneto, W. Takashima, A. Saeki and S. Seki, *Adv. Funct. Mater.*, 2010, **20**, 3941.
35. S. Wan, F. Gándara, A. Asano, H. Furukawa, A. Saeki, S. K. Dey, L. Liao, M. W. Ambrogio, Y. Y. Botros, X. Duan, S. Seki, J. F. Stoddart and O. M. Yaghi, *Chem. Mater.*, 2011, **23**, 4094.
36. X. Feng, L. Liu, Y. Honsho, A. Saeki, S. Seki, S. Irle, Y. Dong, A. Nagai and D. Jiang, *Angew. Chem. Int. Ed.*, 2012, **51**, 2618.
37. X. Ding, X. Feng, A. Saeki, S. Seki, A. Nagai and D. Jiang, *Chem. Commun.*, 2012, 8952.
38. (a) X. Ding, J. Guo, X. Feng, Y. Honsho, J. Guo, S. Seki, P. Maitarad, A. Saeki, S. Nagase and D. Jiang, *Angew. Chem. Int. Ed.*, 2011, **50**, 1289; (b) X. Ding, L. Chen, Y. Honsho, X. Feng, O. Saengsawang, J. Guo, A. Saeki, S. Seki, S. Irle, S. Nagase, V. Parasuk and D. Jiang, *J. Am. Chem. Soc.*, 2011, **133**, 14510.
39. T. V. Vernitskaya and O. N. Efimov, *Russ. Chem. Rev.*, 1997, **66**, 443.
40. B. Dong and H. Maeda, *Chem. Commun.*, 2013, 4085.
41. H. Maeda, Y. Bando, Y. Haketa, Y. Honsho, S. Seki, H. Nakajima and N. Tohnai, *Chem. Eur. J.*, 2010, **16**, 10994.
42. H. Maeda, Y. Terashima, Y. Haketa, A. Asano, Y. Honsho, S. Seki, M. Shimizu, H. Mukai and K. Ohta, *Chem. Commun.*, 2010, 4559.
43. H. Maeda, K. Naritani, Y. Honsho and S. Seki, *J. Am. Chem. Soc.*, 2011, **133**, 8896.
44. B. Dong, T. Sakurai, Y. Honsho, S. Seki and H. Maeda, *J. Am. Chem. Soc.*, 2013, **135**, 1284.
45. B. Dong, T. Sakurai, Y. Bando, S. Seki, K. Takaishi, M. Uchiyama, A. Muranaka and H. Maeda, *J. Am. Chem. Soc.*, 2013, **135**, 14797.
46. A. M. Craats, J. M. Warman, K. Müllen, Y. Geerts and J. D. Brand, *Adv. Mater.*, 1998, **10**, 36.
47. A. M. Craats, J. M. Warman, A. Fechtenkötter, J. D. Brand, M. A. Harbison and K. Müllen, *Adv. Mater.*, 1999, **11**, 1469.

48. R. C. Haddon, *Acc. Chem. Res.*, 2002, **35**, 997.
49. (a) J. P. Hill, W. Jin, A. Kosaka, T. Fukushima, H. Ichihara, T. Shimomura, K. Ito, T. Hashizume, N. Ishii and T. Aida, *Science*, 2004, **304**, 1481; (b) Y. Yamamoto, *Bull. Chem. Soc. Jpn.*, 2011, **84**, 17.
50. J. Goldberger, R. He, Y. Zhang, S. Lee, H. Yan, H.-J. Choi and P. Yang, *Nature*, 2003, **422**, 599.
51. (a) Y. Yamamoto, T. Fukushima, W. Jin, A. Kosaka, T. Hara, T. Nakamura, A. Saeki, S. Seki, S. Tagawa and T. Aida, *Adv. Mater.*, 2006, **18**, 1297; (b) T. Yamamoto, T. Fukushima, A. Kosaka, W. Jin, Y. Yamamoto, N. Ishii and T. Aida, *Angew. Chem. Int. Ed.*, 2008, **47**, 1672.
52. L. Chen, S. R. Puniredd, Y.-Z. Tan, M. Baumgarten, U. Zschieschang, V. Enkelmann, W. Pisula, X. Feng, H. Klauk and K. Müllen, *J. Am. Chem. Soc.*, 2012, **134**, 17869.
53. T. Amaya, S. Seki, T. Moriuchi, K. Nakamoto, T. Nakata, H. Sakane, A. Saeki, S. Tagawa and T. Hirao, *J. Am. Chem. Soc.*, 2009, **131**, 408.
54. B. M. Schmidt, S. Seki, B. Topolinski, K. Ohkubo, S. Fukuzumi, H. Sakurai and D. Lentz, *Angew. Chem. Int. Ed.*, 2012, **51**, 11385.
55. A. J. Breeze, A. Salomon, D. S. Ginley, B. A. Gregg, H. Tillmann and H.-H. Hörnhold, *Appl. Phys. Lett.*, 2002, **81**, 3085.
56. L. Zang, Y. Che and J. S. Moore, *Acc. Chem. Res.*, 2008, **41**, 1596.
57. F. May, V. Marcon, M. R. Hansen, F. Grozema and D. Andrienko, *J. Mater. Chem.*, 2011, **21**, 9538.
58. S. Yagai, T. Seki, H. Murayama, Y. Wakikawa, T. Ikoma, Y. Kikkawa, T. Karatsu, A. Kitamura, Y. Honsho and S. Seki, *Small*, 2010, **6**, 2731.
59. S. Yagai, M. Usui, T. Seki, H. Murayama, Y. Kikkawa, S. Uemura, T. Karatsu, A. Kitamura, A. Asano and S. Seki, *J. Am. Chem. Soc.*, 2012, **134**, 7983.
60. Y. Che, A. Dakar, X. Yang, T. Naddo, J. Zhao and L. Zang, *J. Am. Chem. Soc.*, 2007, **129**, 6354; Y. Che, A. Dakar, K. Balakrishnan and L. Zang, *J. Am. Chem. Soc.*, 2007, **129**, 7234.
61. N. Stutzmann, R. H. Friend and H. Sirringhaus, *Science*, 2003, **299**, 1881.
62. Y. Chen, Y. Feng, J. Gao and M. Bouvet, *J. Coll. Int. Sci.*, 2012, **368**, 387.
63. G. A. O'Brien, A. J. Quinn, D. A. Tanner and G. Redmond, *Adv. Mater.*, 2006, **18**, 2379.
64. Y. Sun, C. He, K. Sun, Y. Li, H. Dong, Z. Wang and Z. Li, *Langmuir*, 2011, **27**, 11364.
65. A. You, J. Gao, D. Li, M. Bouvet and Y. Chen, *Supramol. Chem.*, 2012, **24**, 851.
66. X. Lin, M. Hirono, T. Seki, H. Kurata, T. Karatsu, A. Kitamura, D. Kuzuhara, H. Yamada, T. Ohba, A. Saeki, S. Seki and S. Yagai, *Chem. Eur. J.*, 2013, **19**, 6561.
67. K. V. Rao and S. J. George, *Chem. Eur. J.*, 2012, **18**, 14286.
68. Z. Ning and H. Tian, *Chem. Commun.*, 2009, 5483.
69. E. Moulin, F. Niess, M. Maaloum, E. Buhler, I. Nyrkova and N. Giuseppone, *Angew. Chem. Int. Ed.*, 2010, **49**, 6974.

70. (a) V. Faramarzi, F. Niess, E. Moulin, M. Maaloum, J.-F. Dayen, J.-B. Beaufrand, S. Zanettini, B. Doudin and N. Giuseppone, *Nature Chem.*, 2012, **4**, 485; (b) J. J. Armao, M. Maaloum, T. Ellis, G. Fuks, M. Rawiso, E. Moulin and N. Giuseppone, *J. Am. Chem. Soc.*, 2014, **136**(32), 11382–11388.
71. N. Giuseppone, *Acc. Chem. Res.*, 2012, **45**, 2178.
72. J. S. Brooks, *Chem. Soc. Rev.*, 2010, **39**, 2667.
73. T. Tokuda, K. Murashiro, M. Kubo, H. Masu, M. Imanari, H. Seki, N. Aoki, Y. Ochiai, H. Kanoh and K. Hoshino, *Langmuir*, 2012, **28**, 16430.
74. W. Zhou and H. Yu, *ACS App. Mater. Interfaces*, 2012, **4**, 2154.
75. V. Percec, M. Glodde, T. K. Berra, Y. Miura, I. Shiyanovskaya, K. D. Singer, V. S. K. Balagurusamy, P. A. Heiney, I. Schnell, A. Rapp, H.-W. Spiess, S. D. Hudson and H. Duan, *Nature*, 2002, **419**, 384.
76. S. D. Hudson, H.-T. Jung, V. Percec, W.-D. Cho, G. Johansson, G. Ungar and V. S. K. Balagurusamy, *Science*, 1997, **278**, 449.
77. A. Jankowiak, D. Pociecha, J. Szczytko, H. Monobe and P. Kaszyński, *J. Am. Chem. Soc.*, 2012, **134**, 2465.
78. T. Osawa, T. Kajitani, D. Hashizume, H. Ohsumi, S. Sasaki, M. Takata, Y. Koizumi, A. Saeki, S. Seki, T. Fukushima and T. Aida, *Angew. Chem. Int. Ed.*, 2012, **51**, 7990.
79. H. Shigemitsu, I. Hisaki, H. Senga, D. Yasumiya, T. S. Thakur, A. Saeki, S. Seki, N. Tohnai and M. Miyata, *Chem. Asian J.*, 2013, **7**, 1372.
80. S. Yagai, Y. Nakano, S. Seki, A. Asano, T. Okubo, T. Isoshima, T. Karatsu, A. Kitamura and Y. Kikkawa, *Angew. Chem. Int. Ed.*, 2010, **49**, 9990.
81. S. Wan, J. Guo, J. Kim, H. Ihee and D. Jiang, *Angew. Chem. Int. Ed.*, 2008, **47**, 8826.
82. X. Feng, L. Chen, Y. Honsho, O. Saengsawang, L. Liu, L. Wang, A. Saeki, S. Irle, S. Seki, Y. Dong and D. Jiang, *Adv. Mater.*, 2012, **24**, 3026.
83. L. Sun, T. Miyakai, S. Seki and M. Dincă, *J. Am. Chem. Soc.*, 2013, **135**, 8185.
84. H. Xu, A. K. Das, M. Horie, M. S. Shaik, A. M. Smith, Y. Luo, X. Lu, R. Collins, S. Y. Liem, A. Song, P. L. A. Popelier, M. L. Turner, P. Xiao, I. A. Kinloch and R. V. Ulijn, *Nanoscale*, 2010, **2**, 960.
85. Y. Sun, L. Jiang, K. C. Schuermann, W. Adriaens, L. Zhang, F. Y. C. Boey, L. De Cola, L. Brunsveld and X. Chen, *Chem. Eur. J.*, 2011, **17**, 4746.
86. M. Mizrahi, A. Zakrassov, J. Lerner-Yardeni and N. Ashkenasy, *Nanoscale*, 2012, **4**, 518.
87. (a) C. Wang, H. Dong, W. Hu, Y. Liu and D. Zhu, *Chem. Rev.*, 2012, **112**, 2208; (b) M. Mas-Torrent and C. Rovira, *Chem. Rev.*, 2011, **111**, 4833; (c) A. Facchetti, *Mater. Today*, 2007, **10**, 28; (d) J. Mei, Y. Diao, A. L. Appleton, L. Fang and Z. Bao, *J. Am. Chem. Soc.*, 2013, **135**, 6724.
88. (a) Y. Yamamoto, *Sci. Tech. Adv. Mater.*, 2012, **13**, 33001; (b) S. S. Babu, S. Prasanthkumar and A. Ajayaghosh, *Angew. Chem. Int. Ed.*, 2012, **51**, 1766; (c) D. M. Bassani, L. Jonusauskaite, A. Lavie-Cambot, N. D. McClenaghan, J.-L. Pozzo, D. Ray and G. Vives, *Coord. Chem. Rev.*,

2010, **254**, 2429; (d) H. Imahori, T. Umeyama, K. Kurotobi and Y. Takano, *Chem. Commun.*, 2012, 4032; (e) B. R. Kaafarani, *Chem. Mater.*, 2011, **23**, 378; (f) F. S. Kim, G. Ren and S. A. Jenekhe, *Chem. Mater.*, 2011, **23**, 682.

89. I. F. Perepichka and D. F. Perepichka, eds., *Handbook of Thiophene-Based Materials: Applications in Organic Electronics and Photonics*, John Wiley & Sons, Chichester, 2009.
90. (a) B. D. Wall, S. R. Diegelmann, S. Zhang, T. J. Dawidczyk, W. L. Wilson, H. E. Katz, H.-Q. Mao and J. D. Tovar, *Adv. Mater.*, 2011, **23**, 5009; (b) A. M. Sanders, T. J. Dawidczyk, H. E. Katz and J. D. Tovar, *ACS Macro Lett.*, 2012, **1**, 1326.
91. D. Gentili, F. Di Maria, F. Liscio, L. Ferlauto, F. Leonardi, L. Maini, M. Gazzano, S. Milita, G. Barbarella and M. Cavallini, *J. Mater. Chem.*, 2012, **22**, 20852.
92. N. Crivillers, L. Favaretto, A. Zanelli, I. Manet, M. Treier, V. Morandi, M. Gazzano, P. Samorì and M. Melucci, *Chem. Commun.*, 2012, 12162.
93. D. H. Kim, B.-L. Lee, H. Moon, H. M. Kang, E. J. Jeong, J.-I. Park, K.-M. Han, S. Lee, B. W. Yoo, B. W. Koo, J. Y. Kim, W. H. Lee, K. Cho, H. A. Becerril and Z. Bao, *J. Am. Chem. Soc.*, 2009, **131**, 6124.
94. R. Gutzler, C. Fu, A. Dadvand, Y. Hua, J. M. MacLeod, F. Rosei and D. F. Perepichka, *Nanoscale*, 2012, **4**, 5965.
95. Y. Zhou, W.-J. Liu, Y. Ma, H. Wang, L. Qi, Y. Cao, J. Wang and J. Pei, *J. Am. Chem. Soc.*, 2007, **129**, 12386.
96. Y. Zhou, T. Lei, L. Wang, J. Pei, Y. Cao and J. Wang, *Adv. Mater.*, 2010, **22**, 1484.
97. J. Zhang, J. Tan, Z. Ma, W. Xu, G. Zhao, H. Geng, C. A. Di, W. Hu, Z. Shuai, K. Singh and D. Zhu, *J. Am. Chem. Soc.*, 2013, **135**, 558.
98. A. Wurl, S. Goossen, D. Canevet, M. Sallé, E. M. Pérez, N. Martín and C. Klinke, *J. Phys. Chem. C*, 2012, **116**, 20062.
99. L. Tan, Y. Guo, Y. Yang, G. Zhang, D. Zhang, G. Yu, W. Xua and Y. Liu, *Chem. Sci.*, 2012, **3**, 2530.
100. S. Dong, H. Tian, D. Song, Z. Yang, D. Yan, Y. Geng and F. Wang, *Chem. Commun.*, 2009, 3086.
101. Y. Gao, P. Ma, Y. Chen, Y. Zhang, Y. Bian, X. Li, J. Jiang and C. Ma, *Inorg. Chem.*, 2009, **48**, 45.
102. N. B. Chaure, C. Pal, S. Barard, T. Kreouzis, A. K. Ray, A. N. Cammidge, I. Chambrier, M. J. Cook, C. E. Murphy and M. G. Cain, *J. Mater. Chem.*, 2012, **22**, 19179.
103. H. Hayashi, W. Nihashi, T. Umeyama, Y. Matano, S. Seki, Y. Shimizu and H. Imahori, *J. Am. Chem. Soc.*, 2011, **133**, 10736.
104. B. A. Jones, A. Facchetti, M. R. Wasielewski and T. J. Marks, *J. Am. Chem. Soc.*, 2007, **129**, 15259.
105. R. C. Savage, E. Orgiu, J. M. Mativetsky, W. Pisula, T. Schnitzler, C. L. Eversloh, C. Li, K. Müllen and P. Samorì, *Nanoscale*, 2012, **4**, 2387.
106. M. Treier, A. Liscio, J. M. Mativetsky, M. Kastler, K. Müllen, V. Palermo and P. Samorì, *Nanoscale*, 2012, **4**, 1677.

107. P. Jonkheijm, N. Stutzmann, Z. Chen, D. M. de Leeuw, E. W. Meijer, A. P. H. J. Schenning and F. Würthner, *J. Am. Chem. Soc.*, 2006, **128**, 9535.
108. T. Seki, Y. Maruya, K.-I. Nakayama, T. Karatsu, A. Kitamura and S. Yagai, *Chem. Commun.*, 2011, 12447.
109. J. H. Oh, H. W. Lee, S. Mannsfeld, R. M. Stoltenberg, E. Jung, Y. W. Jin, J. M. Kim, J.-b. Yoo and Z. Bao, *Proc. Natl. Acad. Sci. USA*, 2009, **106**, 6065.
110. W. Jiang, Y. Zhou, H. Geng, S. Jiang, S. Yan, W. Hu, Z. Wang, Z. Shuai and J. Pei, *J. Am. Chem. Soc.*, 2011, **133**, 1.
111. A. A. Sagade, K. V. Rao, U. Mogera, S. J. George, A. Datta and G. U. Kulkarni, *Adv. Mater.*, 2013, **25**, 559.
112. W. Pisula, A. Menon, M. Stepputat, I. Lieberwirth, U. Kolb, A. Tracz, H. Sirringhaus, T. Pakula and K. Müllen, *Adv. Mater.*, 2005, **17**, 684.
113. H. N. Tsao, W. Pisula, Z. Liu, W. Osikowicz, W. R. Salaneck and K. Müllen, *Adv. Mater.*, 2008, **20**, 2715.
114. T. Okamoto, K. Nakahara, A. Saeki, S. Seki, J. H. Oh, H. B. Akkerman, Z. Bao and Y. Matsuo, *Chem. Mater.*, 2011, **23**, 1646.
115. J.-P. Hong, M.-C. Um, S.-R. Nam, J.-I. Hong and S. Lee, *Chem. Commun.*, 2009, 310.
116. M. Más-Montoya, R. Ponce Ortiz, D. Curiel, A. Espinosa, M. Allain, A. Facchetti and T. J. Marks, *J. Mater. Chem. C*, 2013, **1**, 1959.
117. B. Narayan, S. P. Senanayak, A. Jain, K. S. Narayan and S. J. George, *Adv. Funct. Mater.*, 2013, **23**, 3053.
118. S. K. Park, S. Varghese, J. H. Kim, S.-J. Yoon, O. K. Kwon, B.-K. An, J. Gierschner and S. Y. Park, *J. Am. Chem. Soc.*, 2013, **135**, 4757.
119. H. Dong, S. Jiang, L. Jiang, Y. Liu, H. Li, W. Hu, E. Wang, S. Yan, Z. Wei, W. Xu and X. Gong, *J. Am. Chem. Soc.*, 2009, **131**, 17315.
120. A. L. Briseno, S. C. B. Mannsfeld, P. J. Shamberger, F. S. Ohuchi, Z. Bao, S. A. Jenekhe and Y. Xia, *Chem. Mater.*, 2008, **20**, 4712.
121. (a) B. Geffroy, P. le Roy and C. Prat, *Polym. Int.*, 2006, **55**, 572; (b) K. T. Kamtekar, A. P. Monkman and M. R. Bryce, *Adv. Mater.*, 2010, **22**, 572; (c) L. Xiao, Z. Chen, B. Qu, J. Luo, S. Kong, Q. Gong and J. Kido, *Adv. Mater.*, 2011, **23**, 926; (d) M. C. Gather, A. Köhnen and K. Meerholz, *Adv. Mater.*, 2011, **23**, 233; (e) S. Chen, L. Deng, J. Xie, L. Peng, L. Xie, Q. Fan and W. Huang, *Adv. Mater.*, 2010, **22**, 5227.
122. (a) D. Ray, C.-K. Liang, N. D. McClenaghan and D. M. Bassani, *Curr. Phys. Chem.*, 2011, **1**, 169; (b) R. D. Costa, E. Ortí, H. J. Bolink, F. Monti, G. Accorsi and N. Armaroli, *Angew. Chem. Int. Ed.*, 2012, **51**, 8178; (c) G. M. Farinola and R. Ragni, *Chem. Soc. Rev.*, 2011, **40**, 3467; (d) T. Hu, L. He, L. Duan and Y. Qiu, *J. Mater. Chem.*, 2012, **22**, 4206; (e) C. Ulbricht, B. Beyer, C. Friebe, A. Winter and U. S. Schubert, *Adv. Mater.*, 2009, **21**, 4418.
123. C. Vijayakumar, V. K. Praveen and A. Ajayaghosh, *Adv. Mater.*, 2009, **21**, 2059.
124. N. Delbosc, M. Reynes, O. J. Dautel, G. Wantz, J.-P. Lère-Porte and J. E. Moreau, *Chem. Mater.*, 2010, **22**, 5258.

125. S. Santhosh Babu, J. Aimi, H. Ozawa, N. Shirahata, A. Saeki, S. Seki, A. Ajayaghosh, H. Möhwald and T. Nakanishi, *Angew. Chem. Int. Ed.*, 2012, **51**, 3391.
126. Y. Lei, Q. Liao, H. Fu and J. Yao, *J. Am. Chem. Soc.*, 2010, **132**, 1742.
127. W.-Y. Lee, K.-F. Cheng, T.-F. Wang, C.-C. Chueh, W.-C. Chen, C.-S. Tuan and J.-L. Lin, *Macromol. Chem. Phys.*, 2007, **208**, 1919.
128. R. Abbel, R. van der Weegen, W. Pisula, M. Surin, P. Leclère, R. Lazzaroni, E. W. Meijer and A. P. H. J. Schenning, *Chem. Eur. J.*, 2009, **15**, 9737.
129. K.-P. Tseng, F.-C. Fang, J.-J. Shyue, K.-T. Wong, G. Raffy, A. Del Guerzo and D. M. Bassani, *Angew. Chem. Int. Ed.*, 2011, **50**, 7032.
130. C. Giansante, G. Raffy, C. Schäfer, H. Rahma, M.-T. Kao, A. G. L. Olive and A. Del Guerzo, *J. Am. Chem. Soc.*, 2011, **133**, 316.
131. D. K. Maiti and A. Banerjee, *Chem. Commun.*, 2013, 6909.
132. X. Zhang, D. Görl and F. Würthner, *Chem. Commun.*, 2013, 8178.
133. M. R. Molla and S. Ghosh, *Chem. Eur. J.*, 2012, **18**, 1290.
134. K. V. Rao, K. K. R. Datta, M. Eswaramoorthy and S. J. George, *Adv. Mater.*, 2013, **25**, 1713.
135. (a) C.-L. Ho and W.-Y. Wong, *Coord. Chem. Rev.*, 2013, **257**, 1614; (b) W.-Y. Wong and C.-L. Ho, *J. Mater. Chem.*, 2009, **19**, 4457.
136. D. Tordera, S. Meier, M. Lenes, R. D. Costa, E. Ortí, W. Sarfert and H. J. Bolink, *Adv. Mater.*, 2012, **24**, 897.
137. H.-C. Su, H.-F. Chen, Y.-C. Shen, C.-T. Liao and K.-T. Wong, *J. Mater. Chem.*, 2011, **21**, 9653.
138. C. A. Strassert, C.-H. Chien, M. D. Galvez Lopez, D. Kourkoulos, D. Hertel, K. Meerholz and L. De Cola, *Angew. Chem. Int. Ed.*, 2011, **50**, 946.
139. X.-H. Zhao, G.-H. Xie, Z.-D. Liu, W.-J. Li, M.-D. Yi, L.-H. Xie, C.-P. Hu, R. Zhu, Q. Zhao, Y. Zhao, J.-F. Zhao, Y. Qian and W. Huang, *Chem. Commun.*, 2012, 3854.
140. Y. Cui, Y. Yue, G. Qian and B. Chen, *Chem. Rev.*, 2012, **112**, 1126.
141. X. Rao, Q. Huang, X. Yang, Y. Cui, Y. Yang, C. Wu, B. Chen and G. Qian, *J. Mater. Chem.*, 2012, **22**, 3210.
142. S. Brovelli, F. Meinardi, G. Winroth, O. Fenwick, G. Sforazzini, M. J. Frampton, L. Zalewski, J. A. Levitt, F. Marinello, P. Schiavuta, K. Suhling, H. L. Anderson and F. Cacialli, *Adv. Funct. Mater.*, 2010, **20**, 272.
143. A. Winter, C. Friebe, M. D. Hager and U. S. Schubert, *Macromol. Rapid Commun.*, 2008, **29**, 1679.
144. R. Abbel, C. Grenier, M. J. Pouderoijen, J. W. Stouwdam, P. E. L. G. Leclère, R. P. Sijbesma, E. W. Meijer and A. P. H. J. Schenning, *J. Am. Chem. Soc.*, 2009, **131**, 833.
145. Y.-L. Chu, C.-C. Cheng, Y.-C. Yen and F.-C. Chang, *Adv. Mater.*, 2012, **24**, 1894.
146. J. Luo, T. Lei, L. Wang, Y. Ma, Y. Cao, J. Wang and J. Pei, *J. Am. Chem. Soc.*, 2009, **131**, 2076.

147. J. Zhang, K. Zhang, X. Huang, W. Cai, C. Zhou, S. Liu, F. Huang and Y. Cao, *J. Mater. Chem.*, 2012, **22**, 12759.
148. J. Zhang, K. Zhang, S. Liu, A. Liang, X. Huang, F. Huang, J. Peng and Y. Cao, *RSC Advances*, 2013, **3**, 3829.
149. A.-H. Liang, K. Zhang, J. Zhang, F. Huang, X.-H. Zhu and Y. Cao, *Chem. Mater.*, 2013, **25**, 1013.
150. A.-H. Liang, S. Dong, K. Zhang, X. Xiao, F. Huang, X.-H. Zhu and Y. Cao, *Macromol. Rapid Commun.*, 2013, **34**, 1301.
151. M. Wang and F. Wudl, *J. Mater. Chem.*, 2012, **22**, 24297 and references therein.
152. S. Zhang, X. Yang, Y. Numata and L. Han, *Energy Environ. Sci.*, 2013, **6**, 1443.
153. M. T. Dang, L. Hirsch and G. Wantz, *Adv. Mater.*, 2011, **23**, 3597.
154. F. Di Maria, M. Gazzano, A. Zanelli, G. Gigli, A. Loiudice, A. Rizzo, M. Biasiucci, E. Salatelli, P. D'Angelo and G. Barbarella, *Macromolecules*, 2012, **45**, 8284.
155. S. Shen, P. Jiang, C. He, J. Zhang, P. Shen, Y. Zhang, Y. Yi, Z. Zhang, Z. Li and Y. Li, *Chem. Mater.*, 2013, **25**, 2274.
156. I. D. Tevis, W.-W. Tsai, L. C. Palmer, T. Aytun and S. I. Stupp, *ACS Nano*, 2012, **6**, 2032.
157. A. Ruiz-Carretero, T. Aytun, C. J. Bruns, C. J. Newcomb, W.-W. Tsai and S. I. Stupp, *J. Mater. Chem. A*, 2013, **1**, 11674.
158. K. Takemoto, M. Karasawa and M. Kimura, *ACS Appl. Mater. Interfaces*, 2012, **4**, 6289.
159. R. J. Kumar, J. M. MacDonald, T. B. Singh, L. J. Waddington and A. B. Holmes, *J. Am. Chem. Soc.*, 2011, **133**, 8564.
160. D. A. Kamkar, M. Wang, F. Wudl and T.-Q. Nguyen, *ACS Nano*, 2012, **6**, 1149.
161. Y. Sun, G. C. Welch, W. L. Leong, C. J. Takacs, G. C. Bazan and A. J. Heeger, *Nat. Mater.*, 2012, **11**, 44.
162. J. A. Love, C. M. Proctor, J. Liu, C. J. Takacs, A. Sharenko, T. S. van der Poll, A. J. Heeger, G. C. Bazan and T.-Q. Nguyen, *Adv. Funct. Mater.*, 2013, DOI: 10.1002/adfm.201300099.
163. K. Sugiyasu, S.-I. Kawano, N. Fujita and S. Shinkai, *Chem. Mater.*, 2008, **20**, 2863.
164. R. B. Kanth Siram, M. Stephen, F. Ali and S. Patil, *J. Phys. Chem. C*, 2013, **117**, 9129.
165. F. G. Brunetti, J. L. Lopez, C. Atienza and N. Martin, *J. Mater. Chem.*, 2012, **22**, 4188.
166. X. Yang, G. Zhang, D. Zhang and D. Zhu, *Langmuir*, 2010, **26**, 11720.
167. L.-L. Li and E. W.-G. Diau, *Chem. Soc. Rev.*, 2013, **42**, 291.
168. J. Warnan, Y. Pellegrin, E. Blart and F. Odobel, *Chem. Comm.*, 2012, **48**, 675.
169. Y. Hizume, K. Tashiro, R. Charvet, Y. Yamamoto, A. Saeki, S. Seki and T. Aida, *J. Am. Chem. Soc.*, 2010, **132**, 6628.
170. R. Charvet, Y. Yamamoto, T. Sasaki, J. Kim, K. Kato, M. Takata, A. Saeki, S. Seki and T. Aida, *J. Am. Chem. Soc.*, 2012, **134**, 2524.

171. C.-L. Wang, W.-B. Zhang, H.-J. Sun, R. M. Van Horn, R. R. Kulkarni, C.-C. Tsai, C.-S. Hsu, B. Lotz, X. Gong and S. Z. D. Cheng, *Adv. Energy Mater.*, 2012, **2**, 1375.
172. A. S. D. Sandanayaka, T. Murakami and T. Hasobe, *J. Phys. Chem. C*, 2009, **113**, 18369.
173. (a) X. Zhou, S.-W. Kang, S. Kumar, R. R. Kulkarni, S. Z. D. Cheng and Q. Li, *Chem. Mater.*, 2008, **20**, 3551; (b) L. Li, S. W. Kang, J. Harden, Q. Sun, X. Zhou, L. Dai, A. Jakli, S. Kumar and Q. Li, *Liq. Cryst.*, 2008, **35**, 233.
174. Z. Lu, C. Zhan, X. Yu, W. He, H. Jia, L. Chen, A. Tang, J. Huang and J. Yao, *J. Mater. Chem.*, 2012, **22**, 23492.
175. A. B. Tamayo, B. Walker and T.-Q. Nguyen, *J. Phys. Chem. C*, 2008, **112**, 11545.
176. J. Liu, B. Walker, A. Tamayo, Y. Zhang and T.-Q. Nguyen, *Adv. Funct. Mater.*, 2013, **23**, 47.
177. O. P. Lee, A. T. Yiu, P. M. Beaujuge, C. H. Woo, T. W. Holcombe, J. E. Millstone, J. D. Douglas, M. S. Chen and J. M. J. Fréchet, *Adv. Mater.*, 2011, **23**, 5359.
178. W. Shin, T. Yasuda, G. Watanabe, Y. Seok Yang and C. Adachi, *Chem. Mater.*, 2013, **25**, 2549.
179. H. Seyler, B. Purushothaman, D. J. Jones, A. B. Holmes and W. W. H. Wong, *Pure Appl. Chem.*, 2012, **84**, 1047.
180. L. Schmidt-Mende, A. Fechtenkötter, K. Müllen, E. Moons, R. H. Friend and J. D. MacKenzie, *Science*, 2001, **293**, 1119.
181. Y. Yamamoto, T. Fukushima, Y. Suna, N. Ishii, A. Saeki, S. Seki, S. Tagawa, M. Taniguchi, T. Kawai and T. Aida, *Science*, 2006, **314**, 1761.
182. Y. Yamamoto, G. Zhang, W. Jin, T. Fukushima, N. Ishii, A. Saeki, S. Seki, S. Tagawa, T. Minari, K. Tsukagoshi and T. Aida, *Proc. Nat. Acad. Sci. USA*, 2009, **106**, 21051.
183. W. Zhang, W. Jin, T. Fukushima, A. Saeki, S. Seki and T. Aida, *Science*, 2011, **334**, 340.
184. W. W. H. Wong, T. B. Singh, D. Vak, W. Pisula, C. Yan, X. Feng, E. L. Williams, K. L. Chan, Q. Mao, D. J. Jones, C.-Q. Ma, K. Müllen, P. Bäuerle and A. B. Holmes, *Adv. Funct. Mater.*, 2010, **20**, 927.
185. W. W. H. Wong, C.-Q. Ma, W. Pisula, A. Mavrinskiy, X. Feng, H. Seyler, D. J. Jones, K. Müllen, P. Bäuerle and A. B. Holmes, *Chem. Eur. J.*, 2011, **17**, 5549.
186. W. W. H. Wong, J. Subbiah, S. R. Puniredd, B. Purushothaman, W. Pisula, N. Kirby, K. Müllen, D. J. Jones and A. B. Holmes, *J. Mater. Chem.*, 2012, **22**, 21131.
187. A. A. Gorodetsky, C.-Y. Chiu, T. Schiros, M. Palma, M. Cox, Z. Jia, W. Sattler, I. Kymissis, M. Steigerwald and C. Nuckolls, *Angew. Chem. Int. Ed.*, 2010, **49**, 7909.
188. S. J. Kang, J. B. Kim, C.-Y. Chiu, S. Ahn, T. Schiros, S. S. Lee, K. G. Yager, M. F. Toney, Y.-L. Loo and C. Nuckolls, *Angew. Chem. Int. Ed.*, 2012, **51**, 8594.

189. R. Bhosale, J. Míšek, N. Sakai and S. Matile, *Chem. Soc. Rev.*, 2010, **39**, 138.
190. (a) N. Sakai, R. Bhosale, D. Emery, J. Mareda and S. Matile, *J. Am. Chem. Soc.*, 2010, **132**, 6923; (b) R. Bhosale, A. Perez-Velasco, V. Ravikumar, R. S. K. Kishore, O. Kel, A. Gomez-Casado, P. Jonkheijm, J. Huskens, P. Maroni, M. Borkovec, T. Sawada, E. Vauthey, N. Sakai and S. Matile, *Angew. Chem. Int. Ed.*, 2009, **48**, 6461.
191. F. Würthner, Z. Chen, F. J. M. Hoeben, P. Osswald, C.-C. You, P. Jonkheijm, J. V. Herrikhuyzen, A. P. H. J. Schenning, P. P. A. M. van der Schoot, E. W. Meijer, E. H. A. Beckers, S. C. J. Meskers and R. A. J. Janssen, *J. Am. Chem. Soc.*, 2004, **126**, 10611.
192. D. K. Panda, F. S. Goodson, S. Ray, R. Lowell and S. Saha, *Chem. Commun.*, 2012, **48**, 8775.
193. M. Liang and J. Chen, *Chem. Soc. Rev.*, 2013, **42**, 3453.
194. R. J. Kumar, J. Subbiah and A. B. Holmes, *Beilstein J. Org. Chem.*, 2013, **9**, 1102.
195. R. J. Kumar, Q. I. Churches, J. Subbiah, A. Gupta, A. Ali, R. A. Evans and A. B. Holmes, *Chem. Commun.*, 2013, **49**, 6552.
196. P.-O. Schwartz, E. Zaborova, R. Bechara, P. Lévêque, T. Heiser, S. Méry and N. Leclerc, *New J. Chem.*, 2013, **37**, 2317.
197. M. Carrasco-Orozco, W. C. Tsoi, M. O'Neill, M. P. Aldred, P. Vlachos and S. M. Kelly, *Adv. Mater.*, 2006, **18**, 1754.
198. D. Patra, M. Ramesh, D. Sahu, H. Padhy, C.-W. Chu, K.-H. Wei and H.-C. Lin, *Polymer*, 2012, **53**, 1219.
199. B. J. Walker, A. Dorn, V. Bulović and M. G. Bawendi, *Nano Lett.*, 2011, **11**, 2655.

CHAPTER 2

Multicomponent Assembly Strategies for Supramolecular Systems

DIMAS G. DE OTEYZA

Centro de Física de Materiales (CSIC-UPV/EHU) - Materials Physics Center (MPC), Paseo Manuel Lardizabal 5, 20018 San Sebastián, Spain
Email: d_g_oteyza@ehu.es

2.1 Introduction

Organic-based opto-electronic devices have long penetrated the market, keep increasing their share at high growth rates, and are foreseen to maintain this trend over the coming years. This development goes hand in hand with research efforts devoted to advance the functionality and efficiency of organic materials. In this frame, an important role is played by molecular engineering as a tool to tune and improve their electronic, optic or magnetic properties.[1–3] The possibility to do so by synthetic design is among the most compelling aspects of organic semiconductors, which are generally classified into two main groups: polymers and oligomers or small molecules. The physics underlying the functionality of each of them is similar, and the main difference relates to their processing methods.[4]

Polymers require deposition from solution, while oligomers offer a wider range of processing possibilities. Among them, organic molecular beam deposition (OMBD) is most common. In OMBD the molecules are sublimated under vacuum and a substrate of choice is placed in front of the associated molecular beam, resulting in adsorption and self-assembled growth

RSC Smart Materials No. 12
Supramolecular Materials for Opto-Electronics
Edited by Norbert Koch

Published by the Royal Society of Chemistry, www.rsc.org

of molecular films. However, alternatives include organic vapor phase deposition, a method by which the molecules are evaporated in the presence of an inert carrier gas that flows through heated tubes transporting the molecules toward a cooled substrate on which condensation sets in – or even deposition from solution as in the case of polymers, since many oligomers are also soluble or can be made soluble by synthetic addition of side chains. A second essential difference between polymers and oligomers is the degree of order they can achieve in condensed films, which is significantly lower in the polymer case. In this context, it is important to stress that in addition to the intrinsic molecular properties, other factors like the molecular arrangement in the actual devices are similarly important for the final device performance. This includes the crystalline structure (or the absence thereof) and the morphology of the deposited material, whose control and optimization is therefore as desirable as that of the molecular properties.[5–7]

Many essential processes involved in device operation occur at the multiple interfaces within the devices.[8] Focusing by way of example on donor–acceptor heterojunction-based organic photovoltaic cells, the general working mechanism is commonly pictured as consisting of five separate processes: (1) photon absorption and exciton formation, (2) exciton diffusion towards the donor–acceptor interface, (3) free charge carrier generation by exciton dissociation, (4) charge transport towards the electrodes, and (5) charge collection at the metal–organic interface.[6–8] Of these processes, at least the exciton dissociation and the charge collection take place directly at organic–organic or metal–organic interfaces. In addition, the interfaces can also have an indirect impact on the other processes by influencing the film structure if they act as substrates and templates for the growth of molecular layers atop.[9] As a consequence, well engineered interfaces in terms of both crystalline and electronic properties are of paramount importance for further development of organic electronics. A requisite along these lines is sufficient understanding of the underlying physical and chemical processes determining such interfacial properties, which has been the goal of countless investigations over recent decades.

Among the numerous kinds of interfaces involving organic materials, the best defined are those in which high-purity molecules are deposited by OMBD onto inorganic substrates. This is ideally done under ultra-high vacuum (UHV), allowing for the use of substrates with atomically controlled structure and cleanliness. As opposed to other deposition methods affected by the presence of liquid solvents or contaminants, OMBD provides interfaces in a perfectly controlled environment, greatly simplifying the analysis and understanding of subsequent interface characterizations. This chapter describes organic layers prepared mostly by these means, and the strategies followed to control their crystalline and electronic properties.

Most of the related work to date has been performed on single-component molecular layers. Such studies have greatly helped to improve our current knowledge of organic self-assembly. However, in this chapter special emphasis is put on self-assembly of multicomponent supramolecular systems.

On the one hand, multicomponent systems can be highly relevant for potential applications requiring materials with distinct functionalities. A common example is that of combinations of p- and n-type semiconductors, as needed, for example, in solar cells or organic light-emitting diodes. On the other hand, they provide an even greater flexibility in the design strategies of their properties.

In the following, the interactions driving molecular self-assembly are numbered and described, together with examples of their use for the growth of multicomponent supramolecular layers with tailored structures. Subsequently, considerations about the effect of different components in molecular layers on the electronic properties are outlined, as well as potential ways to leverage that knowledge for the rational design of the interface.

2.2 Taming the Driving Forces behind Multicomponent Self-Assembly

The growth of molecular thin films is an intricate process in which the resulting molecular arrangements depend on the delicate balance of many disparate interactions. Focusing on two-dimensional systems, intermolecular and molecule–substrate interactions come into play and each of them includes many variations, often present simultaneously. The complexity of the scenario is such that even slight changes in one of the system parameters, as for example the sample temperature[10] or molecular surface coverage,[11] may sway the balance toward different dominating interactions and cause significant changes in the final interface structure. Besides, since growth processes are inherently away from equilibrium, not only thermodynamics but also kinetics have to be considered. That is to say, incoming molecular flux, adsorption, desorption or surface diffusion, in combination with growth temperature, are additional factors that can influence the formation of metastable molecular structures and film morphologies.[12,13]

All these interactions and processes governing organic thin film growth differ significantly from those studied for many decades in inorganic materials.[14,15] Here, the interactions are typically much weaker and non-covalent (van der Waals, hydrogen bonds, electrostatic interactions, *etc.*), with shallower interaction potentials. In addition, organic molecules are large and generally anisotropic. This provides them with additional orientational and vibrational degrees of freedom that are not included in conventional growth models based on inorganic materials and that greatly affect fundamental processes. Representative examples of this include configuration-dependent diffusion coefficients[16–18] or varying Ehrlich–Schöbel barriers in interlayer molecular transport.[19,20] An overview of the typical energies (or barriers, for kinetic processes) and length scales involved in the most relevant interactions and processes for two-dimensional (2D) organic thin-film growth is given in Table 2.1[21] and discussed in more detail in the sections below.

Table 2.1 Typical values of the associated energies and length scales of the most common interactions and processes involved in the self-assembly of supramolecular layers. Republished with permission of Annual Reviews, Inc, from ref. 21; permission conveyed through Copyright Clearance Center, Inc.

	Energy range (eV)	Distance	Character
Adsorption[a]	$E_{ad} \approx 0.5–10$	≈1.5–3 Å	Directional, site selective
Surface migration[a]	$E_m \approx 0.05–3$	≈2.5–4 Å	1D/2D
Rotational motion[a]	$E_{rot} \sim E_m$	Short	2D
Indirect substrate mediated[a]	$E_s \approx 0.001–0.1$	Å to nm range	Oscillatory
Reconstruction mediated[a]	$E_s \sim 1$	Short	Covalent
Van der Waals[b]	$E_m \approx 0.02–0.1$	<1 nm	Nonselective
Hydrogen bonding[b]	$E_{as} \approx 0.05–0.7$	≈1.5–3.5 Å	Selective, directional
Electrostatic ionic[b]	$E_{as} \approx 0.05–2.5$	Long range	Nonselective
Metal–ligand interactions[b]	$E_{as} \approx 0.5–2$	≈1.5–2.5 Å	Selective, directional

[a]Surface-specific aspects. Provided values are representative for metal–organic interfaces.
[b]Characteristics of direct intermolecular non-covalent interactions are representative for 3D compounds.

It is important to keep in mind that the interactions responsible for the formation of specific supramolecular structures do not necessarily have to be those contributing the largest amount to the formation energy. As mentioned above, several distinct interactions contribute simultaneously and, considering them to be independent, the overall formation energy is the sum of all contributions. A simplified example is shown in Figure 2.1, which represents the bottom of two different potential wells associated with arbitrary interactions, each with a different equilibrium distance and distance dependence. As observed from the total formation energy curve, the total equilibrium distance is mainly determined by the steeper interaction potential, rather than the deeper one.

All the above is valid for the growth of single-component and multicomponent layers alike. The latter, however, provide a much larger flexibility to use the distinct interactions for the design of supramolecular layers. On the one hand, the combination of different molecular species allows a more modular approach, in which different functional groups required for specific interactions (*e.g.* proton-donors and proton-acceptors necessary for H-bond formation) are introduced into each of the different organic species to optimize certain interactions among them. On the other hand, a larger number of parameters are available that increase the possibilities (and at the same time the complexity) of multicomponent supramolecular assembly, such as,

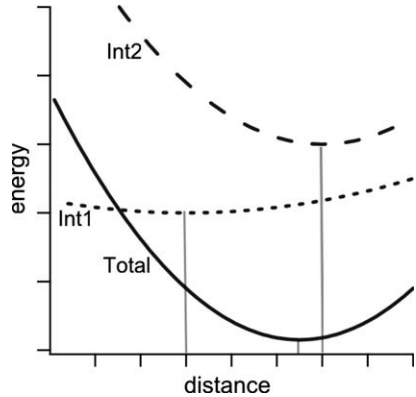

Figure 2.1 Schematic representation of the bottom of two potential wells associated with arbitrary interactions Int1 (short dash) and Int2 (long dash) that contribute to a total potential (continuous line). The minimum energy equilibrium distances are marked with gray lines for each of the potential curves, evidencing how the final equilibrium distance of the total potential is mainly determined by the steeper, rather than by the deeper potential well.

for example, their relative molecular ratios, deposition order, or the different kinetic responses of each species.

2.2.1 Molecule–Substrate Interactions

Adsorption is the first step in the growth of molecular films and is typically classified into physisorption or chemisorption depending on the molecule–substrate interactions. The former is characterized by weak, long-range van der Waals interactions that are hardly directional along the substrate surface, while the latter involves a strong, local chemical bond formation by electron exchange, and therefore presents a larger surface corrugation potential. Nevertheless, because a continuous spectrum of interaction strengths exists between both extremes, classification is often difficult. As an adsorbate approaches the substrate, their respective electronic states interact, broadening and shifting the energy of the molecular orbitals.[22,23] However, little interaction occurs if the substrate has no states at the energy of the molecular orbitals, leaving the latter largely unperturbed. This is important for molecular deposition on insulators and semiconductors. In such cases the frontier molecular orbitals (highest occupied molecular orbital, HOMO, and lowest unoccupied molecular orbital, LUMO), which typically dominate the adsorbate/substrate chemistry,[24,25] may fall in a band gap, with a consequent absence of chemical interactions and therefore representing a pure physisorption scenario. Under these circumstances, molecule–substrate van der Waals interactions are often surpassed by intermolecular interactions and the molecules arrange in a way optimizing the latter. Organic semiconductors owe their semiconducting properties to

the presence of conjugated double bonds, which require a sp^2 hybridization of the C atoms along their molecular backbone and generally lead to planar structures (although deviations from planarity can arise from additional side groups, sp^3 hybridized heteroatoms, twisted molecular structures caused, for example, by steric hindrance at the expense of a reduced conjugation, *etc*.). Optimized intermolecular interactions on weakly interacting substrates are commonly obtained for such molecules by arranging in a standing-up configuration to maximize intermolecular contact.

When deposited on metals, which lack band gaps around the Fermi level, the molecular orbitals hybridize with the substrate states. The low energy molecular orbitals in organic semiconductors, whether occupied or unoccupied (including HOMO and LUMO), normally have π character and are oriented perpendicular to the plane of the conjugated backbone. Particularly important are their interactions with the metal d-band, which to a large extent determine the adsorbate–substrate interaction strength or adsorption energy.[22,26,27] These interactions generally exceed those between molecules (Table 1), and unless strong chemisorption takes place through specific heteroatoms, potentially causing the molecules to tilt,[28,29] π–d interactions generally drive organic semiconductors to lie with their main conjugated backbone parallel to the substrate surface. On metals, as a result of the local hybridizations, the interaction potential is more corrugated than for pure physisorption on insulators and related to the substrate crystal structure. An example is given in Figure 2.2, which depicts the adsorption energy of perfluoropentacene (PFP) on a Ag(111) surface as a function of its position on the substrate.[10]

The first remarkable observation in Figure 2.2 is the anisotropy in the interaction potential. The Ag(111) surface is characterized by a sixfold symmetry (threefold if underlying Ag layers are also considered), but because of the molecular anisotropy the symmetry in the interaction potential is reduced. While a significant corrugation is indeed evident in the adsorption energy map, it is dramatically smoothed out in the direction along the long molecular axis, which can be understood as follows. If the molecular dimensions greatly exceed the substrate lattice, the molecule–substrate interaction potential is averaged over the whole molecule and therefore smoothed out as compared to that of atomic adsorbates or smaller molecules. For an elongated molecule like PFP this effect is strongest along its long axis. As a result, the corrugation in the adsorption energy is very smooth along this direction, but much less along the short axis. This characteristic effect of extended molecules has important consequences on kinetic parameters affecting their self-assembly, like for example diffusion. While for atomic adsorbates or smaller molecules diffusion typically takes place by movements between adjacent substrate-lattice sites, such a shallow interaction potential can make long jumps, spanning multiple lattice spacings, the dominating scenario in molecular diffusion.[30,31]

Diffusion during film growth is highly convolved with other kinetic processes like adsorption, desorption, and nucleation, which in addition to molecule–substrate interactions also involves intermolecular interactions.

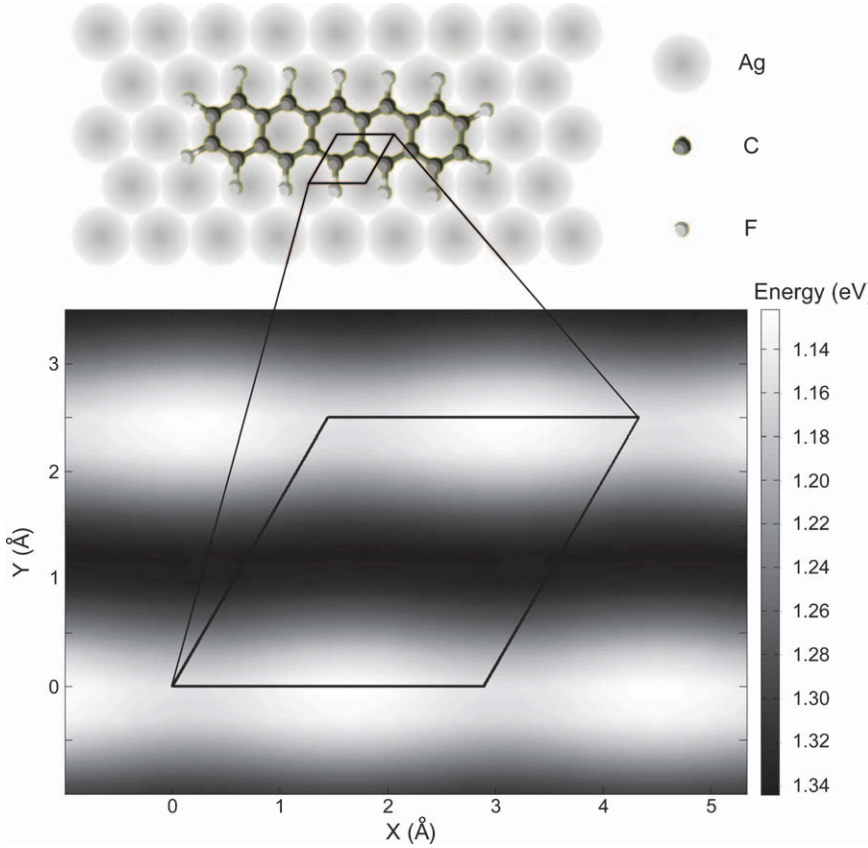

Figure 2.2 Adsorption energy of perfluoropentacene on a Ag(111) surface as a function of its position on the surface. Calculations are performed for the molecule in the experimentally found orientation and maintained fixed. Molecular structure, substrate structure and relative orientation are schematically shown on top. Below, a color-coded adsorption energy map is given in reference to the molecular displacement. The origin corresponds to the molecular center located on a top-site, and the Ag structure is marked in relation to the scheme above.
Adapted with permission from ref. 10. Copyright 2012 American Chemical Society.

The influence of kinetic parameters on the resulting growth structures is therefore difficult to predict and as a result scarcely used in the rational design of 2D multicomponent assemblies. However, their important role in film growth is well known. By way of example, kinetic limitations have been shown to hamper the formation of thermodynamically favored molecular blends of two differently functionalized Zn(II) porphyrin derivatives on a Cu(111) surface.[32] For an appropriate molar ratio a thermodynamically favored crystalline blend can form. However, this only occurs for coverage well under a full monolayer, whereas for high surface coverage a retarded

diffusion and mass transport hinder the formation of the ordered multicomponent layer.[32]

To avoid this undesirable scenario, a sweet spot in the balance among all involved interactions is required. An example of this might be a system with a well-defined thermodynamic-equilibrium blend structure to aim for, but with smooth potentials that allow reaching it by effective molecular diffusion. In fact this scenario is not uncommon: in many systems different molecular species form thermodynamically stable ordered molecular blends regardless of growth parameters such as their co-deposition or sequential deposition order, total coverage, or deposition rate.[33–35] Besides, kinetic hurdles can often be overcome thermally. This has been shown for sequentially deposited multicomponent layers in which the first deposited species forms a relatively stable structure. Then, annealing might be necessary but sufficient to overcome the barrier to break that single-component structure and form the thermodynamically favored crystalline molecular blend.[36,37]

Nevertheless, the slow dynamics associated with kinetic barriers can also be exploited to control the structure of multicomponent assemblies. Self-assembly of octachloro zinc phthalocyanines ($ZnPcCl_8$) on Ag(111) has been shown to evolve at room temperature within tens of hours (the transformation can be accelerated by gentle annealing) from a low density to a compact packing structure through two phase transitions (Figure 2.3a–d).[38,39] Except

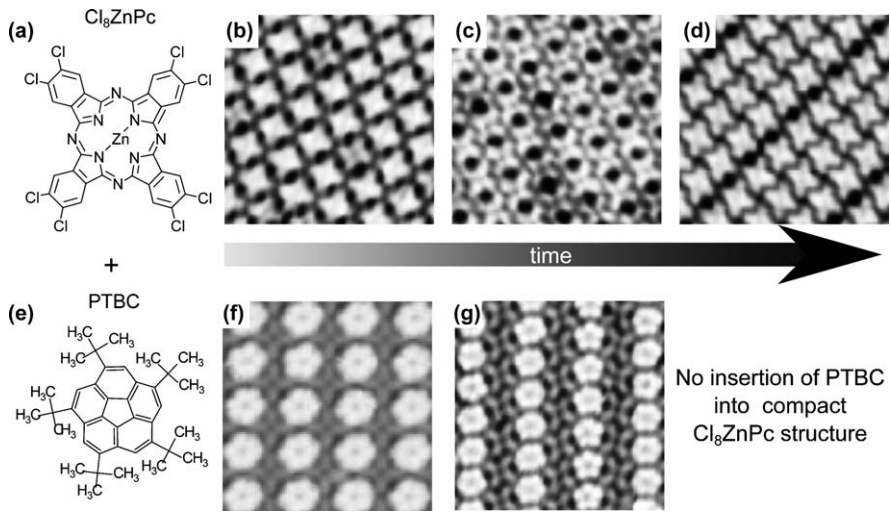

Figure 2.3 Chemical structure of Cl_8ZnPc (a) and 10×10 nm^2 STM images of the self-assembled structures on Ag(111) as a function of time (b–d). Chemical structure of PTBC (e) and 9×9 nm^2 STM images of the multicomponent layer structures formed upon deposition of PTBC on (f) the Cl_8ZnPc structure shown in (b) and (g) the Cl_8ZnPc structure shown in (c).
(b)–(d) Adapted with permission from ref. 38. Copyright 2006 American Chemical Society. (f) and (g) Adapted with permission from ref. 40. Copyright © 2008 Wiley-VCH Verlag GmbH, Weinheim.

in the last, most compact and stable $ZnPcCl_8$ structure, deposition of penta-*tert*-butyl-corannulene (PTBC) on top renders ordered $ZnPcCl_8$-PTCB blends in which PTCB inserts itself into the pores of the $ZnPcCl_8$ films, pushing the surrounding molecules apart. Most importantly, depending on the initial $ZnPcCl_8$ structure, which can be selectively prepared, the resulting blend displays well differentiated multicomponent assemblies (Figure 2.3e–g).[40]

Even if the interaction potential is smeared out for extended molecules, the remaining corrugation is still often a key parameter determining molecular self-assembly. Its azimuthal anisotropy is mirrored not only in favored diffusion directions,[16–18,31] often requiring additional molecular rotations (with their associated kinetic barriers,[41] see Table 1) for a true two-dimensional diffusion, but even more importantly in favored molecular adsorption sites and orientations. Proof of it is the enormous number of molecular layers on crystalline surfaces that exhibit an epitaxial relation, *i.e*. a well-defined geometric relation, between the substrate and overlayer structures.[42,43] However, excessively strong corrugation in the molecule–substrate interactions can also pose serious limitations to molecular self-assembly by forcing the molecules into positions and orientations solely determined by the substrate. Under these circumstances, while certain molecular blends fulfilling the conditions imposed by the surface might still allow arrangements with sufficient intermolecular interactions,[44,45] many other blends do not. In addition, because intermolecular interactions are a *sine qua non* requisite for the growth of ordered structures, formation of ordered multicomponent assemblies is often prevented for this reason. Evident examples are displayed in Figure 2.4.

In the figure we find two different molecular blends [cobalt phthalocyanine (CoPc) with copper tetraphenyl-porphine (CuTTP) in a 1:1 ratio on the one hand,[46] and copper phthalocyanine (CuPc) with perfluoropentacene (PFP) in a 1:1 ratio on the other hand] deposited on two different Au surfaces at room temperature (RT), namely, the reconstructed Au(111) and the reconstructed Au(100). RT scanning tunneling microscopy (STM) measurements show CoPc and CuTTP blends in a 1:1 ratio to phase-segregate into ordered regions of only CuTTP (lower part of Figure 2.4b) and disordered blend regions (upper part of Figure 2.4b) when deposited on Au(111). In contrast, using the Au(100) surface as substrate, highly ordered blend structures form with alternating rows of CoPc and CuTTP molecules oriented along the (110) substrate directions (Figure 2.4c).[46] The capability to arrange into a long-ranged ordered structure on Au(100) but not Au(111) highlights the limiting role of the substrate towards the self-assembly of ordered molecular layers as described above.

In this respect there is a pronounced system specificity, as it depends on the particular interaction potential landscape of each molecule–substrate combination. That interaction potential defines the favored molecule adsorption sites and orientations, but also the resilience associated with deviations from the equilibrium positions. Such deviations occur to optimize the required intermolecular interactions, which on the other hand depend

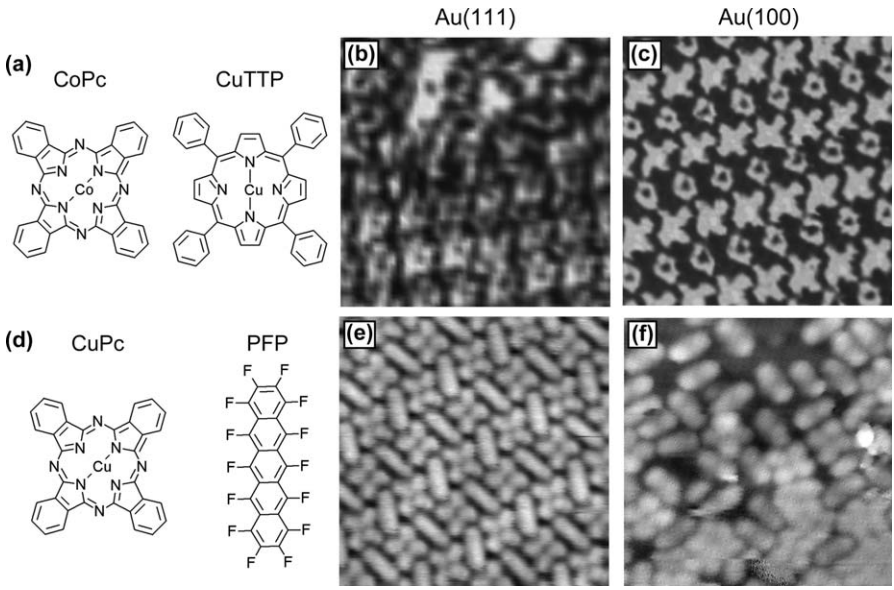

Figure 2.4 Chemical structures of two different pairs of molecules [CoPc and CuTTP in (a); CuPc and PFP in (d)], each used for deposition in a 1 : 1 ratio on two different substrates. (b) and (c) 10×10 nm^2 Constant current STM images of the CoPc : CuTTP blend on reconstructed Au(111) and reconstructed Au(100), respectively. (e) and (f) 10×10 nm^2 Constant current STM images of the CoPc : CuTTP blend on the same reconstructed Au(111) and reconstructed Au(100), respectively. Each molecular blend self-assembles into a crystalline multicomponent layer only on one of both surfaces, which changes from one blend to the other.
(b) and (c) Adapted with permission from ref. 46. Copyright 2003 American Chemical Society.

on the particular molecular structures to be combined. For example, Figures 2.4(d)–(f) show complementary measurements on CuPc and PFP blends on the same two substrates. Submonolayer coverage forms islands of highly ordered mixed layers on Au(111) (Figure 2.4e), while a disordered blend, with PFP anchored holding two discrete orientations and CuPc diffusing around in the spaces in between, is found on Au(100) (Figure 2.4f). The results are therefore similar to the CoPc and CuTTP blends (Figures 2.4b and 2.4c) in terms of an ordered and a disordered blend structure, but on opposite surfaces. That is, it confirms the crucial role of the substrate structure, and also the specificity of its effect on each molecular blend.

Being so system-specific, molecule–substrate interactions are generally difficult to exploit for rational design of multicomponent molecular assemblies. However, one way to use them in a controlled manner is if the substrate properties present a modulation beyond the crystalline periodicity. The particular patterns of that modulation can later act as growth templates. Examples thereof include surface reconstructions, dislocation networks, or

vicinal surfaces. This idea was initially developed with inorganic materials,[47,48] and has been extended later on to organic molecules.[49–51] Focusing on the particular case of multicomponent molecular structures, this approach has been applied with the periodically spaced steps of vicinal surfaces.[33,52] Step edges present different electronic properties than other surface sites due to the lower coordination of edge atoms, charge redistribution (resulting in an electron-deficient region above and an electron-rich region below the steps) and the associated edge dipoles.[53] As a result, they act as the preferential adsorption sites of many organic species (schematically shown in Figure 2.5a), and well-defined linear arrays of steps have been used to align and distribute multicomponent supramolecular linear chains. An example is depicted in Figure 2.5(b–c) with blends of 1,4-bis(2,4-diamino-1,3,5,-triazine)benzene (BDATB) and 3,4,9,10-perylenetetracarboxylic diimide (PTCDI) on Au(11,12,12).[33]

Alternatively, previous growth of single- or multi-component molecular networks can also act as substrate template for subsequent deposition of different molecular species. This greatly increases the possibilities, given the enormous variety of molecular networks in terms of structure symmetry and dimensions as compared to inorganic crystals. Despite the relatively smooth interaction potential associated with non-covalent intermolecular interactions, its modulation along many molecular assemblies has been demonstrated to be sufficient to act effectively as growth template.[54–56] In addition, such modulation can be further enhanced by the use of molecular arrays consisting of blends of different molecules,[57] molecular dislocation networks,[10,58] or porous structures on which additionally deposited molecules adsorb at the pre-defined pores in a host–guest scenario.[37,59–62] A beautiful example is shown in Figures 2.5(d)–(f).[63] Figure 2.5(d) depicts the commensurate structure formed upon deposition of 1,3,5-tri(4′-bromo-4,4′-biphenyl)benzene (BPB) on a Si(111)-B $\sqrt{3}\times\sqrt{3}$R30° surface, which includes two differently sized pores as marked in the image. Subsequent deposition of C_{60} leads to its adsorption on either kind of pore and to the formation of a disordered blend structure. As opposed to C_{60}, the larger molecule 1,3,5-tri(4-bromophenyl)benzene (TBB, Figure 2.5e) is unable to fit in the smaller pores in the BPB network. However, it perfectly matches in size and shape the largest of the nanopores. Deposition of TBB onto the porous BPB layer therefore leads to a long-range ordered structure with TBB adsorbing only onto the larger pores (Figure 2.5e), a structure that is further stabilized by π–π interactions between the tilted phenyl rings of TBB and BPB. Now the crystalline molecular layer features only one type of pores, and can serve as a template for C_{60}, the deposition of which now results in a well-ordered three-component molecular blend (Figure 2.5f).

2.2.2 Intermolecular Interactions

Among the multiple classification schemes applicable to intermolecular interactions, probably the most relevant for the design of supramolecular

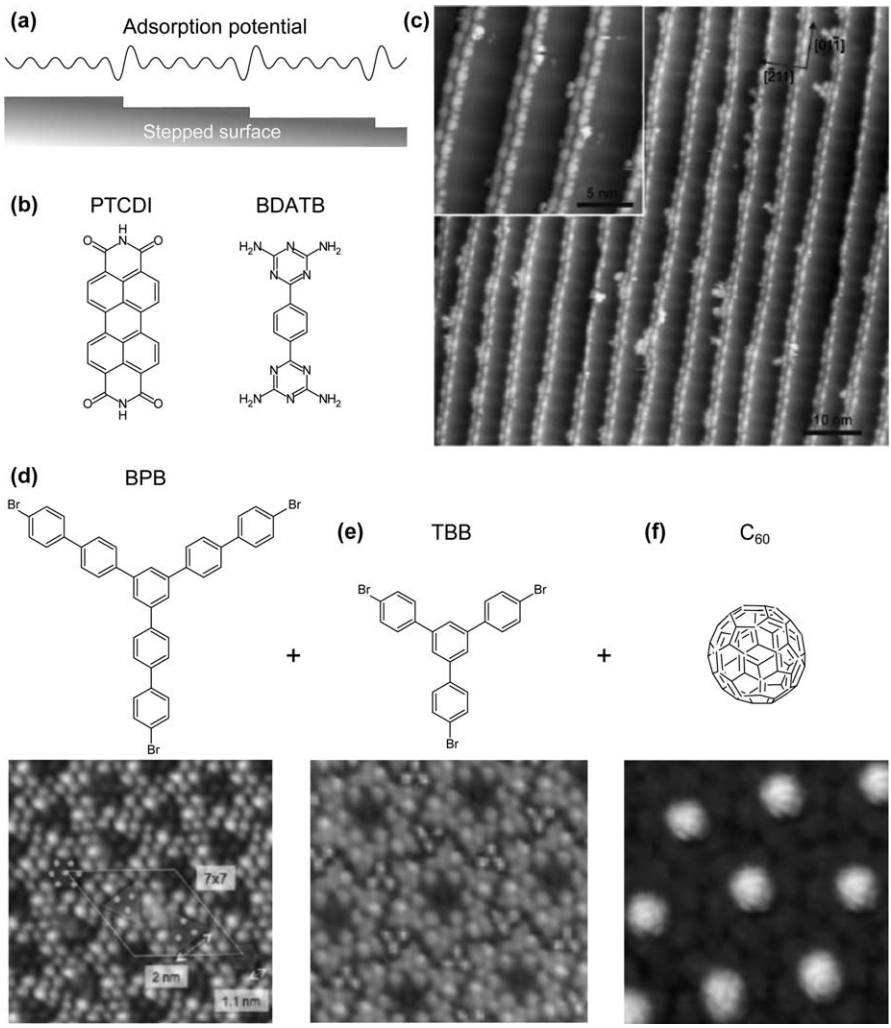

Figure 2.5 (a) Schematic representation of the adsorption potential on a periodically stepped surface, with a small period corrugation related to the substrate crystalline structure and a longer period corrugation arising from the surface steps that can be leveraged for designed molecular adsorption patterns. (b) Molecular structures of PTCDI and BDATB. (c) STM image of PTCDI and BDATB heteromolecular wires grown along the steps of a Au(11,12,12) surface. (d) Chemical structure of BPB and 14×14 nm^2 STM image of its resulting self-assembled layer structure on a Si(111)-B $\sqrt{3}\times\sqrt{3}$R30° surface. The 7×7 overlayer structure is marked on the image, as well as the two different pores and their sizes. (e) Chemical structure of TBB and 14×14 nm^2 STM image of the molecular blend after its deposition on a BPB network as in (d), selectively filling the larger pores. (f) Chemical structure of C_{60} and 14×14 nm^2 STM image of the molecular blend after its deposition on a BPB-TBB network as in (e), selectively filling the remaining, smaller pores.
(c) Adapted with permission from ref. 33. Copyright © 2007 Wiley-VCH Verlag GmbH, Weinheim. (d), (e) and (f) Adapted with permission from ref. 63. Copyright 2012 American Chemical Society.

systems is their directionality. The effect of directional interactions (H-bonds, metal coordination, or covalent bonding) on supramolecular layers is easier to rationalize and predict than that of their non-directional counterparts, and therefore most commonly used in the rational design of multicomponent films. Nevertheless, non-directional interactions (van der Waals, dipole–dipole) have been shown to be equally relevant and, even if associated with additional comprehension complexity, usable in a comparable way. Examples for each are provided in the following sections.

2.2.2.1 Hydrogen Bonding

Hydrogen bonds are probably the most important of non-covalent intermolecular interactions due to their great relevance in many disparate fields, ranging from biochemistry to inorganic chemistry, supramolecular chemistry or materials science. They arise from the electrostatic attraction between the partial positive charge in H atoms covalently bonded to more electronegative elements (X–H, both atoms together commonly termed as proton donor) and a partial negative charge on another atom (A, proton acceptor).[64,65] In addition to the atomic species involved (X and A), the H-bond is also characterized by the bond length (distance from H to A) and the angle spanned in X–H$\cdots$A. The bond strength correlates inversely with the bond length and increases as the angle approaches 180°, therefore favoring linear geometries (geometries with bond lengths above 3.5 Å and/or angles below 90° are generally no longer considered H-bonds).[64,65] The dependence on the geometry, involved atomic species, and even on the neighboring supramolecular environment causes the energies associated with H-bonds to span over more than two orders of magnitude (Table 1).[21,64,65]

Hydrogen bonding has been demonstrated to drive the self-assembly of molecules into all kinds of ordered arrangements, ranging from extended 2D layers[66] to nanoporous[67] or linear structures.[68] While all these kinds of structures have been successfully grown from single molecular species, the use of multiple different molecules facilitates the molecular design aiming for a directed growth of tailored supramolecular structures. The known preference for linear alignment of the H-bonds, in combination with complementary located proton donors and proton acceptors on different molecular species, allows intuitive predictions of the supramolecular arrangements. A breakthrough in this approach was the successful synthesis of porous honeycomb networks by co-deposition of melamine and PTCDI on Ag/Si(111) (Figure 2.6a),[37] in which the melamine acts as the linker between PTCDI molecules and imposes its threefold symmetry on the supramolecular structure. Elegant variations of the supramolecular structures by appropriate molecular design include the use of a different linker of only twofold symmetry as BDATB to achieve linear supramolecular arrangements (Figure 2.6b),[33] or substitution of PTCDI by cyanuric acid to obtain smaller pores in the supramolecular network.[69] Each molecular junction in the

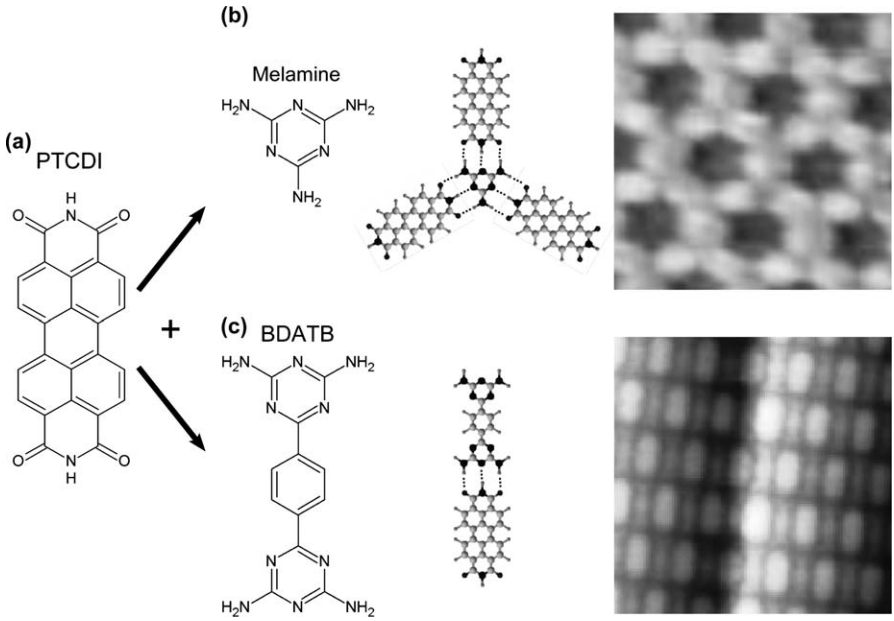

Figure 2.6 (a) Chemical structure of PTCDI. (b) Chemical structure of melamine, together with a scheme of its complementarity with PTCDI to form H-bonded supramolecular structures with threefold symmetry, and a 15×15 nm^2 STM image of the resulting blend structure on a Ag/Si(111) surface. (c) Chemical structure of BDATB, together with a scheme of its complementarity with PTCDI to form linear H-bonded supramolecular structures, and a 15×15 nm^2 STM image of the resulting blend structure on Au(11,12,12).
(b) Reprinted by permission from Macmillan Publishers Ltd: Nature (ref. 37), copyright 2003. (c) Adapted with permission from ref. 33 (Copyright © 2007 Wiley-VCH Verlag GmbH, Weinheim).

aforementioned molecular combinations involves three H-bonds that give the supramolecular structures excellent stability. As a consequence of the strong intermolecular interactions, the same supramolecular structures can be grown on different substrates.[70–72] Quantitative energies have been obtained from DFT calculations for PTCDI-BDATB networks and for melamine–cyanuric acid dimers. Formation energies associated with each frontal triple H-bond were 0.92 eV for the former[73] and 0.65 eV for the latter.[74] Taking into account the formation of nine H-bonds per melamine molecule in the 2D network, intermolecular interactions significantly exceed the molecule–substrate adsorption energy, calculated to be 0.2 eV for melamine and 0.22 eV for cyanuric acid on Au(111).[74] Nevertheless, the interaction potential associated with the H-bonds was found to be smoother than that of the molecule–substrate interactions. The substrate, therefore, still played an important role in the assembly geometry, since the equilibrium structure was slightly extended with respect to that calculated for a free standing layer, in order to satisfy optimum molecule–substrate coupling.[74]

In addition to the symmetry and dimensions of multicomponent H-bonded supramolecular structures, a certain degree of control can also be obtained over the extension of the structures, not only by limiting the molecular coverage but by addition of ''terminal molecules'' as opposed to ''linkers''.[75] This has been demonstrated with combinations of three molecules. Two of the molecules are designed following a similar principle as for the PTCDA-BDATB blend above, with complementary functional groups at both ends of mirror-symmetric molecules. However, addition of a molecule with functional groups available for H-bonds only on one side terminates the supramolecular structure. The concentration of such terminal molecules is proposed as a handle on the average supramolecular structure length.[75]

A widely studied family of H-bonded, multicomponent molecular blends are layers formed from combinations of fluorinated and non-fluorinated molecules.[44,76–81] Fluorination of molecules increases their ionization potential and electron affinity.[82,83] In fact, it represents one of the most popular routes to synthesize n-type organic semiconductors. Many of these molecular mixtures can therefore be seen as nanostructured donor–acceptor blends, which are inherently relevant in opto-electronic applications. As both molecules are surrounded all over by proton acceptors and proton donors, these blends lack an intuitive predictability of their supramolecular arrangements. The wide availability of proton donors and acceptors facilitates the formation of a large number of H-bonds with many different molecular arrangements. The lack of predictability of the resulting structures is made up for by the easy growth of varied crystalline blends, since most molecular combinations present stable mixed structures. This is exemplified in Figure 2.7(a), where PFP is combined in different molecular ratios with CuPc on a Ag(111) surface. For each of the molecular ratios the molecules find crystalline arrangements allowing the formation of enough H-bonds to confer the structure remarkable stability; and this occurs despite the molecule–surface interaction constrain that locks the molecules in all structures to the same, optimum azimuthal orientations, which in turn coincide with that of the molecules in their respective single component layers (only half of the PFP molecules in the 1:2 blend deviate from those preferred orientations and their crystallographic equivalents). A similar scenario is shown in Figure 2.7(b), which displays the structures of molecular blends in a 1:1 ratio, all on graphite, of perfluorinated copper-phthalocyanines (F_{16}CuPc) in combination with various differently shaped and sized molecules, namely, sexiphenyl (6P), pentacene (PEN), diindenoperylene (DIP), and chloroaluminium-phthalocyanine (AlClPc).[77,78] All structures differ significantly from each other, and yet in each of them each F_{16}CuPc molecule is involved in 6 to 12 H-bonds.[77,78] C–H$\cdots$F are among the weakest possible H-bonds because of the hardness or lack of polarizability of organic fluorine.[64,65] DFT calculations of molecular blends of F_{16}CuPc with DIP and with PEN yielded binding energies per C–H$\cdots$F bond between 57 and 77 meV,[81,84–86] well within the typical energy range reported for such interactions.[64,65,87,88] However, due to the large number of bonds that can be

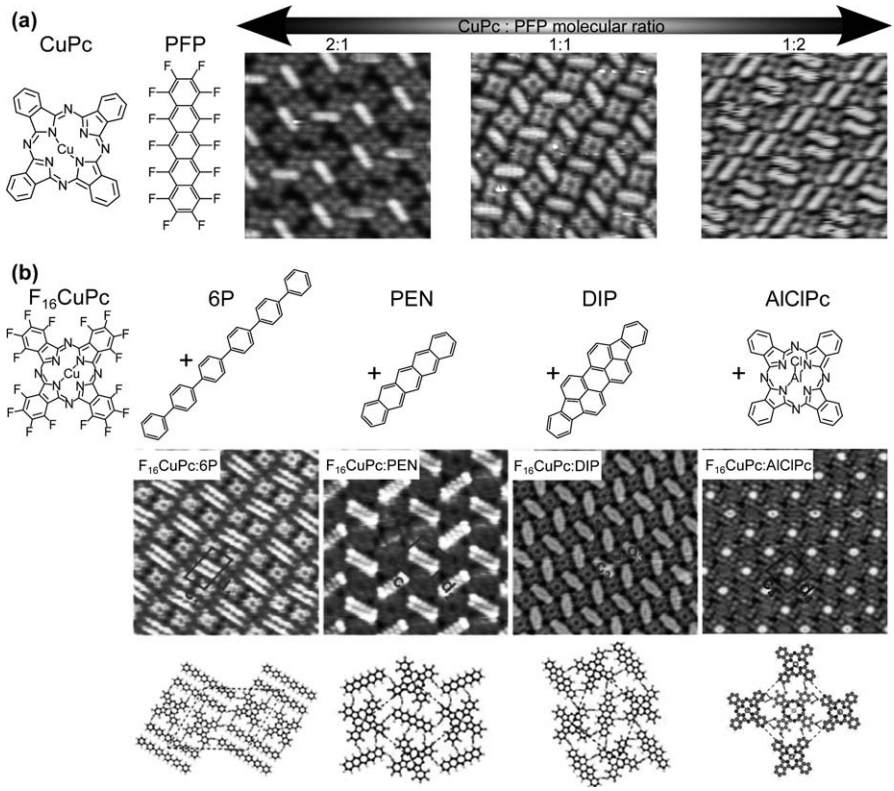

Figure 2.7 (a) Chemical structures of CuPc and PFP, and 9.5×9.5 nm^2 STM images of the crystalline blend structures of varying molecular ratio. (b) Chemical structures of F_{16}CuPc and various molecules with which it is combined in a 1:1 ratio, namely, 6P, PEN, DIP and AlClPc. Below the structures are STM images (15×15 nm^2, 10×10 nm^2, 15×15 nm^2 and 15×15 nm^2, respectively) of the resulting blend structures. Model representation of the structures are shown at the bottom, with estimated C–H · · · F bonds marked as intermolecular lines.
(a) Adapted with permission from ref. 79. Copyright 2013 American Chemical Society. (b) Adapted with permission from ref. 77. (Copyright © 2010 Wiley-VCH Verlag GmbH & Co. KGaA, Weinheim.) and from ref. 78. (Copyright 2011, AIP Publishing LLC).

formed, the stabilization energy per unit cell becomes significant and amounts to over 1 eV.

2.2.2.2 Metal Coordination

Metal-coordination has many attributes in common with H-bonding, including specificity, directionality and, despite its larger associated binding energies (Table 1), also the reversibility of binding that allows formation of structures with a high degree of perfection. Intensive research on

metal–organic coordination networks in solution has provided important and still growing know-how for the synthesis of porous structures with tailored sizes, shapes and functionalities, aiming for potential uses in industrial applications like separation, heterogeneous catalysis or gas storage.[89] Unfortunately, design rules and all the wealth of knowledge of these systems in solution have been found not to apply to surface-supported metal–organic frameworks under UHV. The reasons behind this are the new 2D confinement and also the electronic effect of the metal substrate, which affects the oxidation states of the linker metal-centers. Nevertheless, their synthesis on surfaces and under UHV has not only been demonstrated but has readily shown a great degree of control over the resulting structures. The tunability of the metal-coordinated structures profits from the wide range of functional groups on the organic ligands that can act as binding groups (carboxyl, pyridine, hydroxyl or cyano groups),[90,91] and that can be combined with varied metal centers such as iron, cobalt, copper and nickel.[92]

The metal–organic coordination geometry often mirrors the symmetry of the underlying substrate, evidencing its important role in the self-assembly. A good example is trimesic acid on Cu(110) surfaces.[93] Despite the threefold symmetry of the molecule, on the twofold symmetric Cu(110) surface it forms linear metal-coordinated polymers both with Cu coordination adatoms, as well as and with additionally co-deposited Fe atoms as metal centers. Nevertheless, a series of metal–ligand combinations has strongly favored intrinsic coordination symmetries.[90,94] Proof of this is the growth of similar self-assembled structures on substrates of different symmetries and materials, as occurs with the threefold symmetry of Fe centers combined with biphenol ligands both on Ag(111) and Cu(100)[90] (Figure 2.8a).

Therefore, appropriate choice of substrate and coordination motifs offers significant freedom in the design of metal–organic structures. The structure periodicities and pore sizes can be further controlled by molecular design of the ligand length.[95] As for other intermolecular interactions, a new range of possibilities is opened up if different molecules are combined. Figure 2.8(b) shows six different metal–organic networks combining two bipyridine with three bis-carboxylic acid ligands *via* Fe metal centers on Cu(100). The pyridine-carboxyl-Fe combination leads to a strongly favored coordination motif that renders rectangular networks with the carboxylic acids along one direction and the pyridines along the perpendicular direction. Varying the ligand dimensions directly changes each associated side length of the rectangular pores independently, which, for example, can in turn be used to influence the network's response in host–guest interactions with subsequently deposited molecular species.[96]

2.2.2.3 Covalent Bonding

The strongest and most directional interaction in multicomponent assembly processes is the generation of covalent bonds between initially independent oligomers. This approach holds a special appeal due to its profound

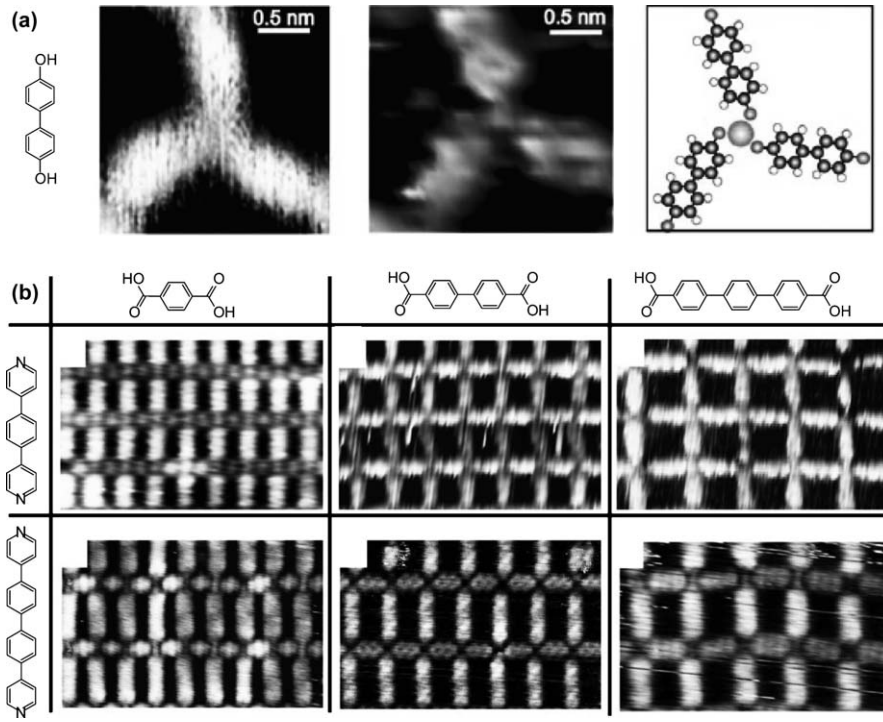

Figure 2.8 (a) STM topographs of the threefold Fe(biphenolate)$_3$ network node on an Ag(111) surface (left) and a Cu(100) surface (middle), together with a model of the threefold binding of the nodal Fe(biphenolate)$_3$ motif (right). (b) STM images of six binary metal–organic networks resulting from combinations of two different bipyridine ligands with three different bis-carboxylic acid ligands. The images demonstrate the tunability of the periodicities of the rectangular porous networks. All images are 9.4×6.0 nm^2.
(a) Reprinted with permission from ref. 90. Copyright © 2007 Wiley-VCH Verlag GmbH, Weinheim. (b) Reprinted with permission from ref. 91. Copyright (2007) National Academy of Sciences, U.S.A.

implications on the structural and electronic properties of the resulting products. From the structural point of view, covalent linkage greatly outperforms all other interactions in terms of stability, which is often a critical issue for non-covalently bonded supramolecular structures. From the electronic point of view, on the one hand the charge transfer integral, which is a measure of the intermolecular electronic coupling, is greatly enhanced and therefore allows better charge transport performance.[97] On the other hand, the whole electronic structure can change dramatically (compare for example the electronic structures of sp^2 bonded hydrocarbon oligomers with the fascinating band structure of many of them connected into an extended layer of sp^2 bonded carbon, graphene). In general, the HOMO–LUMO gap of semiconducting oligomers is known to depend on the extent of the

conjugation backbone, and on linear structures it often follows a simple phenomenological model given by:

$$E_g(N_c) \approx E_g^{\infty} + A/N_c \quad (2.1)$$

where N_c is the number of carbon atoms along the conjugated chain, E_g^{∞} the gap of an infinite polymer and A a fitting parameter.[98] Therefore, by covalently linking conjugated oligomers, the extent of the conjugation can be enhanced and the overall semiconducting band gap reduced. Lastly, surface-supported covalent linkage under UHV also offers appealing aspects from a technical point of view. It allows the synthesis of molecular structures not attainable by other means due to, for example, lack of solubility hampering synthesis in solution. It also allows the synthesis of functional molecular structures directly at the surface of interest, avoiding potential problems in their processing and deposition, which could arise, for example, from lack of solubility or because of thermal fragmentation of excessively large structures during sublimation.

Pioneering works in the surface-supported synthesis of supramolecular structures include the Ullmann coupling of two iodobenzene molecules at the steps of a Cu(111) surface under UHV,[99] and the polymerization of self-assembled diacetylene compounds into extended polydiacetylene wires.[100] However, both of these experiments made use of an STM tip to guide or trigger the reactions. Several years later, a seminal work reported the thermally activated synthesis of covalently bonded porphyrins by Ullmann coupling.[101] The reactants formed covalently bonded structures tailored by careful molecular design to yield dimers, linear chains or 2D networks (Figure 2.9a). Ever since, a rapidly increasing number of different surface-supported chemical reactions under UHV are being demonstrated. Among them we find azide-alkyne click-chemistry,[102] enediyne cyclizations,[103,104] synthesis of polymeric Fe-phthalocyanines from Fe and 1,2,4,5-tetracyanobenzene (TCNB),[105] tautomerization of N-heterocycles into carbene intermediates followed by oligomerization,[106] desulfurization,[107] aldehyde–amine coupling,[108,109] alkyne homo-coupling,[110,111] cyclodehydrogenation,[112,113] dehydrogenative C–C coupling,[114] amine–isocyanate coupling,[115] boronic acid self-condensation and esterification with diol groups,[116] imidization between anhydrides and amines,[117,118] or linear coupling of alkanes.[119] Unlike Ullman coupling, in which the heterolytic cleavage leaves behind halogen atoms, which normally remain on the surface,[120] most other reactions present either no side products,[102–106] or only byproducts like H_2O or H_2 that easily desorb into the vacuum.[108–119] All these reactions together form an ever growing chemical toolbox to be used and combined for the synthesis of covalently bonded structures of growing complexity and/or functionality. By way of example, Ullman coupling has been combined with subsequent dehydrogenation to yield atomically precise graphene nanoribbons of great interest for potential electronic applications.[121,122]

Covalent linkage offers a higher specificity and directionality than other non-covalent interactions, which should in principle facilitate the design

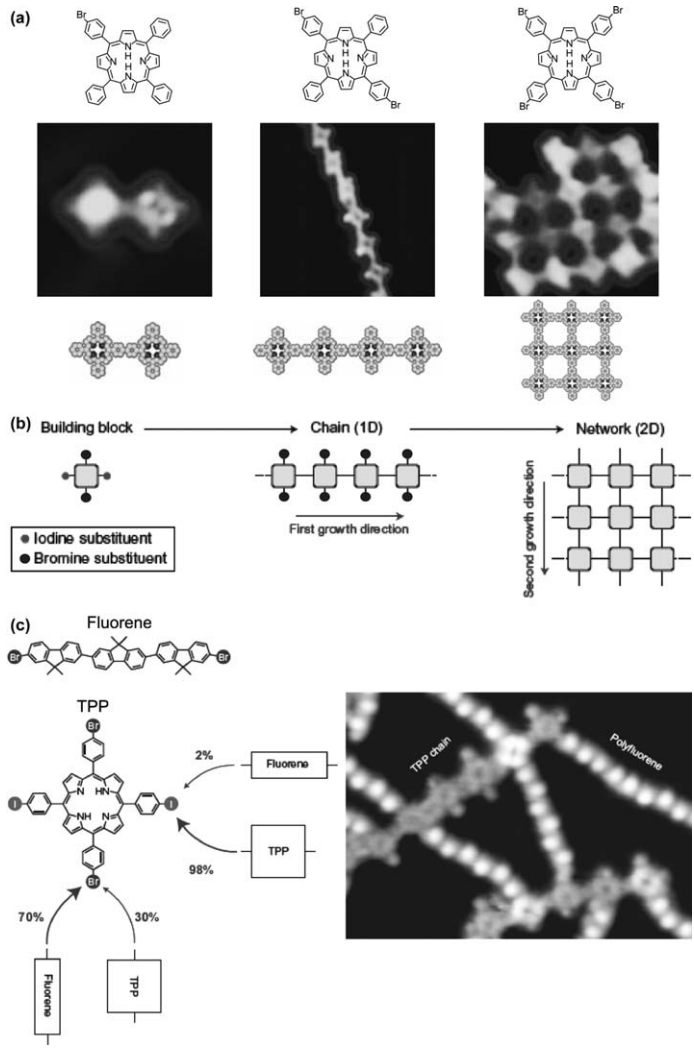

Figure 2.9 (a) Chemical structures of the different precursor molecules designed to render dimers, linear polymers or 2D polymeric networks, together with STM images (5×5 nm^2, 10×10 nm^2, 8.5×8.5 nm^2, respectively) of the resulting structures on Au(111) and the associated models. (b) Scheme of the hierarchic approach towards improved 2D polymeric networks. By an appropriate choice of halogen atoms with different activation energies, first linear polymers can be formed that are then covalently linked into a 2D network in well differentiated steps. (c) Scheme of the hierarchic approach to form linear polymeric structures interconnected covalently by different molecular species and 13×18 nm^2 STM image of the resulting structure on Au(111).
(a) Reprinted by permission from Macmillan Publishers Ltd: Nature Nanotechnology (ref. 101), copyright 2007. (b) and (c) Reprinted by permission from Macmillan Publishers Ltd: Nature Chemistry (ref. 126), copyright 2012.

and directed growth of supramolecular structures. Making use of appropriate molecular combinations, analogous approaches to those previously described for H-bonded structures have been followed for covalent bonding. That is, the symmetry of linker molecules has been changed from two- to threefold to create linear structures or 2D networks, respectively,[117,118] and one of the two molecules used to form a porous network has been exchanged by a larger one to increase the pore sizes.[116] However, although experiments have been reasonably successful, the degree of order and control over the resulting polymeric structures is still far from that found in non-covalently stabilized structures. The reason behind this is the irreversibility of the described reactions, which hampers self-healing and kinetically impedes reaching the thermodynamic equilibrium structure. Taking the boronic acid coupling for porous network formation as an example, this reaction yields H_2O as a side product. Under UHV and at the reaction temperatures, H_2O readily desorbs from the surface. If H_2O remains available, the dehydrogenative covalent bonding is a reversible reaction. As a consequence, the same reaction run in solution[123] or on surfaces under a regulated water presence[124] produces the same porous networks but with greatly enhanced crystallinity. Reversible covalent bonding therefore represents a significant advantage for the tailored design of supramolecular structures, and while it has been demonstrated in solution or under ambient pressure conditions with controlled atmospheres it remains to be studied whether reversibility could also be attainable by some means under UHV, as, for example, under controlled H_2O addition in low partial pressures.

The use of conventional non-covalent self-assembly can also help in the synthesis of controlled polymeric supramolecular structures. For example, the self-assembled arrangement of the first deposited reactant can determine the structure of the products after addition and reaction with a second reactant.[109] Diverse deposition parameters of the reactants affect the resulting structures after their covalent linkage, which in turn also differ from the self-assembled arrangements of *ex situ* synthesized products. These differences can be traced back to kinetic hurdles, which therefore can be used to choose and synthesize the desired structures.[109] The molecule–substrate interactions can also be used to provide appropriate templates for the alignment of polymeric structures,[125,126] or to provide the confinement required for otherwise unfeasible reaction selectivity, as shown by the striking linear coupling of inert alkanes along the 1D grooves of a reconstructed Au(110)-(1×3) surface.[119] Beyond the templating or confinement effect, it is important to remember that the substrate often also acts as a conventional catalyst and plays a major role in many of the reactions.[127] This has, for example, been studied for alkyne Glaser coupling. The selectivity with respect to other undesired side reactions increases dramatically from Au(111) or Cu(111) to Ag(111).[110] This also provides added difficulties to reactions performed on insulators, on which the catalytic activity is much lower and the adsorption energy greatly reduced (facing problems of potential desorption), while being technologically necessary substrates for

many applications. Although some of the reactions previously numbered are also expected to run on insulators, few such examples have been reported to date.[105,128,129]

An elegant approach towards controlled synthesis of polymeric structures is hierarchic assembly. It has been recently exemplified with several systems,[126,129–131] demonstrating a successful increase in the degree of order in the polymeric structures. In two of the systems, linear porphyrin arrays were first obtained and subsequently covalently linked into a 2D porphyrin network. In one case the first linear arrays were formed by metal-coordination and then covalently bonded by Ullmann coupling.[130] Other work used covalent bonding by Ullmann coupling in both assembly steps (schematically explained in Figure 2.9b), triggered independently by a clever choice of different halogens with disparate activation energies.[126] Taking one step further, this hierarchic assembly process allows the use of different linker molecules between the initial linear polymers. Although the structures obtained by combining linear porphyrin polymers with brominated fluorene derivatives show limited order (Figure 2.9c), it is a proof of principle of the enormous potential of this approach, which could possibly be further improved by more selective reactions (as opposed to radical-mediated mechanisms) and orthogonal chemistry combinations.

2.2.2.4 *Van der Waals Interactions*

Van der Waals interactions are ubiquitous in any supramolecular assembly, both between molecules and between molecule and substrate. They therefore determine many supramolecular structures short of other competing interactions. Despite their omnipresence, their weakness, lack of significant selectivity and of directionality complicate the characterization of their impact on supramolecular structures, and significant efforts are being made to improve quantitative descriptions from theoretical methods.[132,133]

Nevertheless, ways to make use of van der Waals interactions for directed supramolecular self-assembly have been successfully developed. In this respect, it is the 2D confinement imposed by the substrate that allows the probably most common strategy: the interdigitation of alkyl chains. Besides, on graphite, alkyl chains present a pronounced preference for adsorption along the main symmetry directions due to their excellent lattice match. This confers some kind of directionality to the collective interactions and provides an important handle for the design of supramolecular structures. Together with the appropriate choice of the molecular core and the functionalization sites, semiconducting molecules have been self-assembled, driven mainly by van der Waals interactions, into porous networks,[134,135] crystalline 2D arrays (Figure 2.10a),[136] or 1D arrays (Figure 2.10b).[137] In addition, because the alkyl chains effectively act as spacers, the periodicity of the structures is easily tuned by variation of the chain lengths. This is shown for the case of the tetraphenylporphyrin derivatives in Figure 2.10(b),[137] where the distance between molecular rows is plotted as a function of the

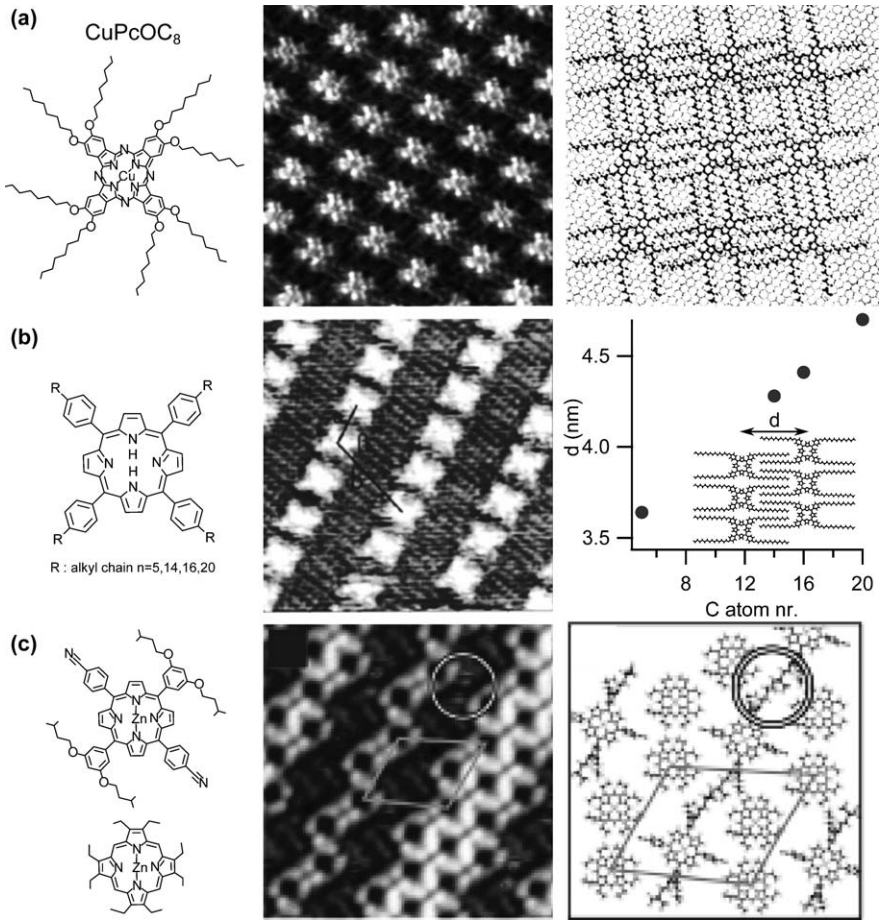

Figure 2.10 (a) Chemical structure, 14.6×14.6 nm^2 STM image and model of the van der Waals stabilized self-assembled layer of $CuPcOC_8$ on graphite. (b) Chemical structure and 15×15 nm^2 STM image of the linear arrangement of alkyl chain-functionalized porphyrin derivatives on graphite. The dependence of the lateral periodicity of the structure on chain length is depicted on the right. (c) Chemical structure, 10×10 nm^2 STM image and model of van der Waals stabilized molecular blends prepared under vacuum on Cu(111).
(a) Adapted with permission from ref. 136. Copyright 2000 American Chemical Society. (b) Adapted with permission from ref. 137. Copyright © 2001 John Wiley & Sons, Ltd. (c) Adapted with permission from ref. 32. Copyright 2010 American Chemical Society.

number of C atoms along the alkyl chain. The spacing varies from 3.64 nm for $n = 5$ to 4.7 nm for $n = 20$ in a perfectly linear dependence, evidencing its easy control by molecular design.

In addition to the pattern periodicity, the stability of the supramolecular patterns also increases together with the chain length.[137] Rough estimations

of the van der Waals stabilization energy between interdigitated alkyl chains amount to 49.2 meV per CH_2 if flanked by alkyl chains on both sides, and 22 meV per CH_2 if flanked only on one side. The interaction with the graphite substrate is estimated to be 64.2 meV per CH_2, which is comparable to the 65 meV estimated per sp^2 carbon atom in aromatic units.[135] Regardless of the estimation accuracy, for long and multiple chains the van der Waals-related stabilization energy adds up to significant amounts that easily compete with otherwise stronger interactions like H-bonds.[138]

However, most reported cases of tailored van der Waals-driven supramolecular assembly have been performed in solution, where alkyl chain functionalization is a common route to provide solubility to the materials. Within the main focus of this chapter, that is, UHV deposited multicomponent systems, few examples have been reported. One of them is shown in Figure 2.10(c), in which the van der Waals interactions from the alkoxy chains are considered among the main stabilization contributions to the supramolecular arrangement of this molecular blend on Cu(111).[32]

2.2.2.5 *Dipole–Dipole Interactions*

Another source of intermolecular interactions in 2D systems is that between permanent molecular dipoles, or even higher order multipoles. Dipole–dipole interactions are relevant for the supramolecular ordering of molecules with dipole moments as small as 0.1 D, as is the case of styrene.[139] Depositing 0.5–0.9 ML on Au(111), styrene adsorbs on the fcc and hcp regions of the herringbone reconstruction and orders ferroelectrically. Furthermore, fcc and hcp domains, separated by the mostly uncovered reconstruction soliton walls (which are energetically unfavored adsorption sites for many molecules), align antiferroelectrically. However, besides in-plane electric dipoles, often absent in organic semiconducting molecules, out-of-plane dipoles also play an important role in supramolecular assembly. This has been shown with molecules with intrinsic permanent dipoles on metal surfaces, where the electrostatic intermolecular interactions are further enhanced by the metallic surface.[140] But even more importantly, interface dipoles resulting solely from molecular adsorption have the same effect.[141] As discussed in more detail in Section 2.3.1, a series of physicochemical processes occur as a molecule adsorbs on a metallic surface. These result in a net interface dipole that accounts for various contributions, strongly depends on the particular molecule–substrate combination, and gives rise to changes in the system's work function. As a consequence, dipole–dipole interactions from out-of-plane oriented interface dipoles can be considered an additional general contribution to the intermolecular interactions driving self-assembly processes.

Several theoretical works have modeled the pattern formation driven by these interactions between two phases with different work-functions.[142–144] The calculations yield droplet domains as the most stable pattern for very disparate coverage ratios, and periodically striped phases for more similar

relative coverages (the calculated thresholds are 0.28 : 0.72). Based on these results, dipole–dipole interactions have provided satisfactory explanations for several experimental results, from the pattern formation upon O adsorption on Cu(110)[145] to that of large dendrimer molecules on mica.[146] However, it must be said that interactions arising from potential adsorbate-caused strain fields follow the same $1/r^3$ scaling as dipole–dipole interactions, making the two interaction types difficult to distinguish.[142,143] In the context of multicomponent assembly of organic semiconductors under UHV, dipole–dipole interactions have been used to explain the supramolecular arrangement found in one of the seminal works on supramolecular self-assembly of molecular blends. The work describes blends of chloro[subphthalocyaninato]boron(III) (SubPc) and fullerenes (C_{60}), and the electrostatic interactions between the intrinsic dipole of the SubPc and the interface-dipole from the C_{60}–Ag(111) interface are claimed to be among the main stabilizing interactions of their long-range ordered mixed structures (Figure 2.11a).[147]

Figure 2.11(b) depicts an example of molecular blends on Au(111), in which the crystalline structure of two molecular combinations with homeomorphic species can be tuned by molecular design to change from a H-bond directed 2D network to a dipole–dipole interaction directed 1D striped structure. In particular, the combinations involve DIP with fluorinated (F_{16}CuPc) and non-fluorinated copper-phthalocyanines (CuPc), respectively.[148] For the former, 16 C–H $\cdots$ F bonds per unit cell provide the blend structure with excellent stability.[76,84] However, on exchanging the

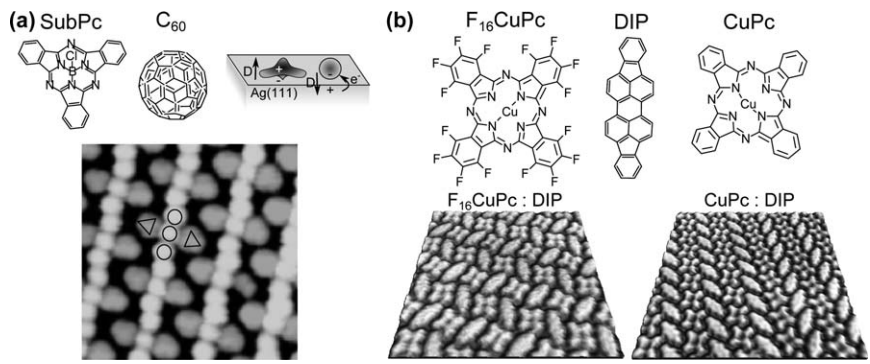

Figure 2.11 (a) Molecular structure and 12×12 nm^2 STM image of SubPc and C_{60} molecular blends on Ag(111). Triangles and circles are overlaid on some of the molecules in the STM image to mark SubPc and C_{60}, respectively. A model representing the intrinsic electric dipole of the SubPc and the interface charge transfer-associated dipole is shown in the upper scheme. (b) Molecular structures of F_{16}CuPc, DIP and CuPc, and 12×12 nm^2 STM images of the H-bond stabilized F_{16}CuPc : DIP 1 : 1 molecular blend and the dipole–dipole directed CuPc : DIP 1 : 1 molecular blend.
(a) Adapted with permission from ref. 147. Copyright © 2002 Wiley-VCH Verlag GmbH, Weinheim. (b) Reproduced from ref. 148.

fluorines in F_{16}CuPc by H atoms the C–H$\cdots$F bonds are eliminated, allowing the interplay of weaker, long-range electrostatic interactions. CuPc monolayers on Au(111) are reported to lower the work function by 1.2 eV,[149] and DIP monolayers by 1.05 eV.[150] From the Helmholtz equation:

$$\Delta\phi = \frac{ne\mu}{\varepsilon_0\varepsilon} \tag{2.2}$$

where n is the dipole density, e is the electron charge, μ the dipole moment, ε_0 the vacuum permittivity and ε the relative dielectric constant, those work function shifts can easily be related to effective interface dipoles of 6.15 D per CuPc and 5 D per DIP (assuming $\varepsilon = 1$ and the reported unit cells for CuPc and DIP monolayers on Au(111)[151,152]). The interactions arising from that difference in work function and associated interface dipoles favor a supramolecular arrangement with striped linear patterns, which is additionally stabilized by favorable epitaxial relations with the substrate, as reported on Au(111) and Cu(111).[148] The pattern width can be additionally modified by the molecular ratio.

2.2.2.6 *Substrate-Mediated Interactions*

Substrate-mediated intermolecular interactions are understood as those arising from the effects caused by molecular adsorption on surfaces, which would therefore not be present in imaginary free-standing structures. The previous subsection has already described interactions arising from the adsorption-induced interface dipoles (or the formally analogous interactions from adsorption-induced elastic strain fields on the substrate), which were grouped together with the dipole–dipole interactions arising from intrinsic electric dipoles. But in addition to those, other possible substrate-mediated interactions exist.

Adsorbates or surface defects impose their potential on the substrate's electrons. As a consequence they act as scattering centers for the electron wavefunctions and thereby create Friedel oscillations in the surface charge density.[153,154] Because adsorbates' binding energies depend on the substrate electron density, two and more adsorbates can show preferred adsorption sites at specific relative distances interacting *via* their respective Friedel oscillations. Confined to the 2D electron system of a metallic surface, theoretical models of those interactions show a distance dependence as $\cos(2k_F r)/r^2$, that is, they show an oscillatory behavior with period of half the Fermi wavelength ($\lambda_F/2$) and $1/r^2$ decay for large distances.[154] Such behavior has been confirmed experimentally on various different metal surfaces with inorganic adatoms and with small molecules.[155–158] Typical extension and stabilization energies are a few nanometers and from a few meV to a few tens of meV, respectively (Table 1). With larger molecules like pentacene, the same concept has been proposed to be the driving mechanism of the long-range ordered structure with equidistant unidirectional molecular rows on

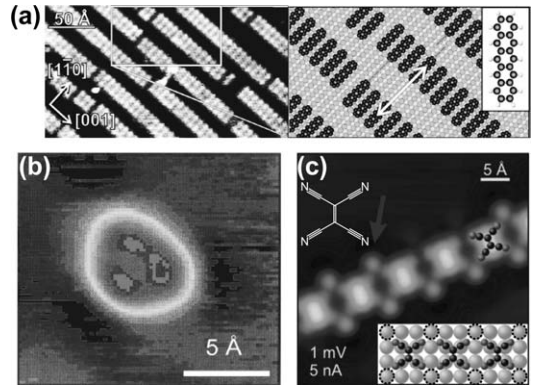

Figure 2.12 (a) STM image and the associated structure model of the equidistant unidirectional pentacene rows on Cu(110). (b) STM image of benzene on Pt(111), evidencing the perturbation of the electronic structure of the substrate surrounding the molecule. (c) Chemical structure of TCNE and STM image of the supramolecular structure resulting from its self-assembly on Cu(100). A molecule is superimposed on the image as a guide to the eye. The arrow marks one of the buckled Cu atoms. Inset: a model of the self-assembled structure; the dotted line circles mark the lifted Cu atoms participating in the substrate-mediated interactions.
(a) Reprinted with permission from ref. 159. Copyright (2002) by the American Physical Society. (b) Reprinted with permission from ref. 160. Copyright (1993) by the American Physical Society. (c) Adapted with permission from ref. 164. Copyright 2008 American Chemical Society.

Cu(110) (Figure 2.12a), which could be imaged by STM at room temperature and was unaffected by annealing processes up to 450 K.[159]

Besides scattering electrons, adsorbates hybridize with the underlying substrate and thereby perturb the substrate's electronic structure in their immediate vicinity. An example is shown in Figure 2.12(b), which corresponds to an STM image of a benzene molecule on Pt(111) and shows a clear threefold symmetric anisotropy in the STM contrast of the substrate around the molecule. Being directly related to the substrate's local density of states,[160] these electronic perturbations might translate into favored (or disfavored) adsorption sites for neighboring molecules.[161,162] Few attempts have been made to quantify this kind of substrate-mediated interactions. From the experimental side, an example is the benzene/Au(111) system, for which a binding energy of 5 meV was estimated, compared with an adsorption energy of 0.64 eV.[163] In turn, according to DFT calculations the substrate-mediated contribution to the binding energy between perfluoropentacene molecules on Ag(111) amounts to 30 meV, in a reasonably comparable ratio to its adsorption energy of 1.2 eV.[10]

In addition to the electronic perturbations, adsorbates can also perturb the crystalline structure of the underlying substrates. Beyond a simple elastic strain field, a significant lattice rearrangement can also be induced. This,

however, involves considerable energies and only occurs for strong chemisorptive molecule–substrate interactions. Then, in a similar scenario as the electronic perturbations, the new crystalline arrangement of the substrate may favor the adsorption of other adsorbates next to it. Such is the case of TCNE molecules on Cu(100) depicted in Figure 2.12(c).[164] The cyano groups interact so strongly with the Cu atoms that these are pulled out, forming a buckled surface structure. These ''outer'' Cu atoms set up optimum binding sites for the cyano groups of the next molecules in a scenario reminiscent of metal-coordination. As a result, such surface-mediated intermolecular interactions are relatively directional, and have been shown to drive the anisotropic growth of various molecule–substrate systems.[165,166]

2.3 Electronic Considerations in Multicomponent Molecular Assemblies

Most important for the functionality of organic supramolecular structures in opto-electronic applications are their electronic properties, although in this respect a differentiation from the crystalline structure is somewhat meaningless because of their intimate interrelation. In the following, the standard models used to describe the electronic structure of metal–organic interfaces are outlined. Subsequently, the way in which molecular blends affect the interface electronic structure is explained and potential strategies that allow for supramolecular layers with rationally designed electronic energy level alignment are introduced.

2.3.1 Standard Interfacial Models

A simple schematic representation of the electronic structure of a metal substrate and an organic semiconductor far from each other and at a metal–organic interface are depicted in Figure 2.13(a) and (b), respectively. Important quantities for our discussion are the metal work function (ϕ_m), ionization energy (IE), and electron affinity (EA). EA is defined as the energy gained by an initially neutral molecule upon addition of an electron to its LUMO level, while the IE corresponds to the energy required to excite an electron from the HOMO of a neutral molecule to the vacuum level. Unlike in inorganic semiconductors with highly delocalized electrons and holes, addition or removal of an electron in small molecules involves substantial electronic and even atomic relaxations. This is important to keep in mind, since the experimentally accessed HOMO and LUMO levels involve charged molecules and may therefore differ significantly not only from the levels of a neutral molecule, but also from the levels obtained with different spectroscopic techniques.[167] Regardless of these details, which are beyond the scope of this chapter, important changes in the electronic levels occur when the molecules approach the surface and form a metal–organic interface.

As described in Section 2.2.1, as a molecule approaches a clean metallic substrate, the respective electronic states hybridize, broadening and modifying the molecular orbitals.[22,23,27] In addition, screening from surrounding molecules and from the substrate also alter the molecular orbital energies, lowering the HOMO–LUMO gap and shifting their energies.[168–171] The scenario is further complicated by the interface dipole σ that generally appears upon molecular adsorption. The origin of σ can be traced back to several different contributions.[172] One is the so-called ''pillow-effect'' related to Pauli repulsion. The metal work function consists of two contributions, the bulk chemical potential and the surface dipole. The latter arises from the decay of the electron wavefunctions from the metal surface into the vacuum.[53] The negative charge of the electron density beyond the metal surface leaves a positive charge density on the inner side of the surface, and thereby an electronic dipole (surface dipole) with its associated electrostatic potential. When a molecule adsorbs on the surface, the Pauli repulsion exerted by the molecule's electrons pushes the substrate's electron wavefunctions back toward the surface.[172,173] This cushion-effect charge redistribution lowers the surface dipole and thereby the work function. Other potential contributions to σ might be the dipoles associated with charge transferred between molecule and substrate, intrinsic permanent dipoles of the adsorbates, or other charge redistributions arising for example from strong chemical bonds. All occurring contributions may add up or also cancel each other and are accounted for by the effective interface dipole σ, which commonly scales proportionally with the metal work function,[172,174] and the surface dipole component of the metal work function.[175]

Key to the functionality of the metal–organic interfaces are the electron injection barrier (EIB) and hole injection barrier (HIB), which correspond to the energy offset between the Fermi level and the HOMO or LUMO, respectively. In a simple Schottky–Mott model, assuming vacuum level alignment throughout the metal–semiconducting interface, the HIB and EIB should vary predictably with a slope $S = 1$ as a function of the metal work function (Figure 2.13c). This is often the case for organic layers on passivated or contaminated metal surfaces such as those arising, for example, from spin-coating polymer deposition or oligomer sublimation onto ambient-exposed substrates.[175–177] Under these circumstances the passivation layer (e.g. residual hydrocarbon contaminants) on the substrate surface acts as a spacer between the metal and the organic semiconductor. As a consequence, molecular adsorption does not cause any cushion effect on the already contaminant-modified metal surface. Substrate and molecular orbitals are largely decoupled and hardly hybridize, hampering partial charge transfer. However, charge transfer can still occur *via* tunneling of integer electrons if the metal Fermi level aligns with electronic states on the molecule. At this point, further work function variations will be compensated by the interface dipoles associated with the transferred charge, pinning the charge injection barriers to the Fermi level. This is mirrored in a slope $S = 0$ in a plot of charge carrier injection barrier *versus* metal work function

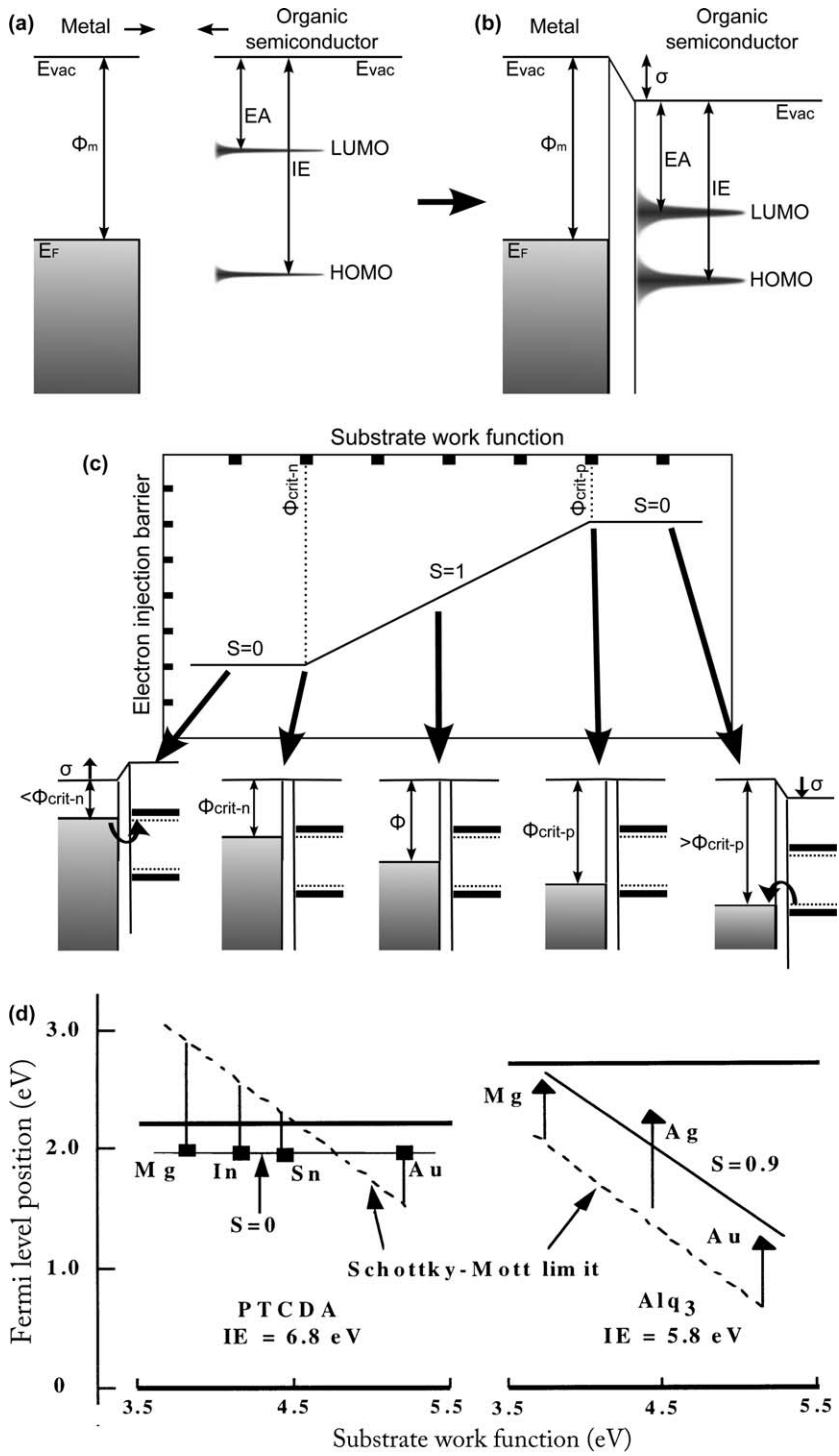

(Figure 2.13c).[175,176] Such a plot therefore features three well-differentiated regions. For work functions between two critical values $\phi_{\text{crit-p}}$ and $\phi_{\text{crit-n}}$ the charge injection barriers vary with a slope $S = 1$, implying that the Fermi level moves freely within the semiconducting gap as the work function is changed. However, for work functions above and below $\phi_{\text{crit-p}}$ and $\phi_{\text{crit-n}}$, respectively, interface charge transfer sets in. This generates an associated interface dipole σ opposing the Fermi level migration within the gap and turns S to 0. Interestingly, $\phi_{\text{crit-p}}$ and $\phi_{\text{crit-n}}$ differ from the HOMO and LUMO resonances measured by photoemission and inverse photoemission (Figure 2.13c), which has been explained by charge transfer to polaronic states not accessed by those experimental techniques,[175] or also by an onset of gap states.[176]

For metal–organic interfaces formed by OMBD on atomically clean metal surfaces the scenario is more complex and the Schottky–Mott model no longer applies. In addition to the interface dipole, the hybridization of substrate and molecular orbitals generates a density of states within the HOMO–LUMO gap that affects how the charge injection barriers depend on the metal work function. The induced density of interface states (IDIS)

Figure 2.13 Schematic representation of the electronic structure of an organic semiconductor and a metallic substrate far from each other (a) and at a metal–organic interface (b). The interface dipole resulting in a shift of the vacuum level (E_{vac}) upon molecular adsorption is represented as σ. The clean metal work function (prior to molecular adsorption) is represented as ϕ_{m}. Electron affinity (EA) and ionization potential (ionization energy, IE) mark the energy positions of the LUMO and HOMO, respectively, with respect to the thin film vacuum level. The offset between Fermi level (E_{F}) and HOMO or LUMO corresponds to the hole injection barrier (HIB) and electron injection barrier (EIB), respectively. (c) Dependence of the charge carrier injection barriers on the substrate work function (top), together with schematic pictures of the interface energy level alignment (bottom) at representative work functions. Dotted lines within the HOMO–LUMO gap mark the positions at which Fermi level pinning sets in. (d) Measured Fermi level positions at interfaces between various metals and two organic semiconductors, PTCDA and Alq3. The top of their HOMO is plotted at the zero of the vertical energy scale. The LUMO energy is plotted assuming a HOMO–LUMO separation equal to the photon energy at the onset of optical absorption. The measured position of the Fermi level within the gap is plotted for metals of different work functions (horizontal axis), as well as the expected position predicted in the Schottky–Mott limit vacuum level alignment (dashed lines). The vertical lines drawn from each experimental data point represent the magnitude of the measured interface dipole. In principle, the magnitude of the interface dipole should be equal to the vertical distance between the experimental Fermi level position and the Schottky–Mott limit. A best-fit line, and its associated slope, is also drawn to the experimental points for each molecular material.
(d) Reprinted from ref. 180, Copyright 2000, with permission from Elsevier.

model, formerly applied to inorganic metal–semiconductor interfaces,[178] has also been successfully applied to the description of this kind of metal–organic interface.[23,179] The presence of gap states results in partial charge transfer upon work function variations, which in turn lead to the formation of an interface dipole that opposes, to a certain extent, the Fermi level migration. The density of gap states, associated with the adsorption height and the degree of molecule–substrate interactions, dictates the level to which the Fermi level is free to move within the semiconductor gap upon work function variations, or is pinned to the adsorbate states.[23,179] These two extremes lead to slopes of 1 and 0, respectively, in plots such as that shown in Figure 2.13(c), but a continuum of intermediate values is possible as well. Figure 2.13(d) shows the interface energy level alignment dependence on substrate work function for two molecules, 3,4,9,10-perylenetetracarboxydianhydride (PTCDA, $S = 0$) and tris(8-hydroxyquinoline)aluminium (Alq3, $S = 0.9$), as representative examples of the two extremes.[180]

2.3.2 Supramolecular Environment-Dependent Electronic Properties

As described in the sections above, a rapidly increasing number of investigations are being focused on the tailored growth of multicomponent supramolecular structures. However, the design has been mainly applied to the structural properties, rather than the electronic ones. In fact, detailed studies on how the new supramolecular environment in multicomponent structures affects the interface electronic properties are to date relatively scarce, despite the fact that it has been repeatedly shown that a naïve extrapolation of the single-component interfacial properties to the molecules in a blend is often erroneous.[73,79,84,85,181,182] A visual example is given in Figure 2.14, which displays an STM image of a self-assembled molecular blend of copper phthalocyanine (CuPc) and perfluoropentacene (PFP) with segregated domains of pure CuPc and of a crystalline mixed structure with a 1 : 1 molecular ratio. The CuPc in each of the domains shows different contrast (brighter in the mixed structure). A height profile shows that it corresponds to a difference of ~ 0.4 Å. Because in STM the contrast does not only depend on the topography but also the system's local density of states, the reason behind the measured height difference could be structural, electronic, or a combination of both. It has been reported that adsorption heights can change for varying intermolecular interactions,[13,84,182,183] a condition that definitely applies if we compare single-component CuPc and mixed structures. Here, however, a strong electronic contribution to the contrast difference is made clear by STM images at different biases in which CuPc looks, as naïvely expected, similar in both kinds of domains (see the respective image and profile insets in Figure 2.14). Spectroscopy measurements discussed below confirm the different electronic properties.

Possible reasons behind the supramolecular-environment dependence of the electronic properties are manifold. Most obvious are those associated with chemical changes in a molecular blend, as could be any intermolecular

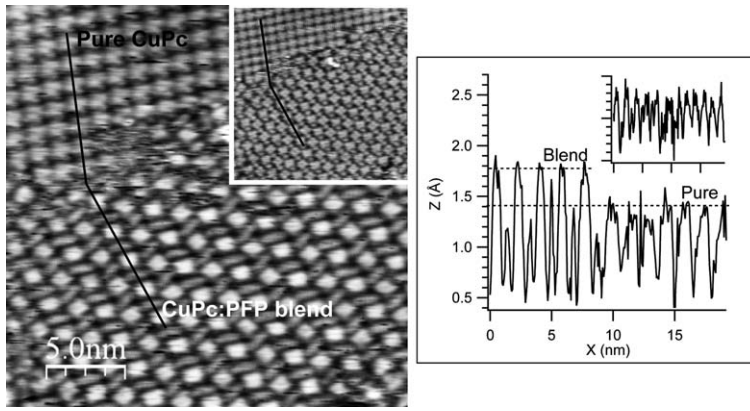

Figure 2.14 STM image (–0.43 V, 34 pA, 25×25 nm^2) of a CuPc : PFP mixed layer on Cu(111) showing phase segregation of a pure CuPc domain and a crystalline CuPc : PFP 1 : 1 blend domain. The STM contrast of the same CuPc molecules is clearly different depending on its supramolecular environment. This is confirmed with a topographic profile along the line marked in the image, showing an apparent height difference of ~0.4 Å. Horizontal dotted lines in the profile mark the average height for CuPc in single-component and blend domains. The electronic origin of the contrast is evidenced in the bias dependence, since the height difference disappears for different scanning parameters as shown in the respective image and profile insets (imaging parameters: –0.86 V, 9 pA, profile graph ticks are spaced as in main graph).

charge transfer between the different molecular species, or significantly changed hybridization with the substrate in the new chemisorbed supramolecular arrangements. However, beyond these more obvious strong chemical effects, a series of finer physicochemical phenomena also play important roles. By way of example, the formation of H-bonds, while not involving intermolecular charge transfer, still causes important rearrangements in the intramolecular charge density. This charge redistribution has a significant impact on the laterally inhomogeneous electrostatic potential on the supramolecular structure, which in turn affects the energy of the electronic states. This effect has been described in detail for strongly H-bonded PTCDI : BDATB blends, for which DFT calculations and scanning tunneling spectroscopy (STS) measurements show in good qualitative agreement an upward shift (referred to the single-component layer spectra) of the BDATB molecular levels and a downward shift of the PTCDI ones on the order of few tenths of eV.[73]

In addition, the energies of processes associated with addition or extraction of electrons from molecules are greatly affected by screening effects of the surrounding material. Such processes may occur during operation of organic-based electronic devices, but also in electron spectroscopies like photoemission, inverse photoemission, or STS, commonly used to characterize metal–organic interfaces and their associated energy levels.[168] The

strongest screening comes from the metallic substrate, which hardly changes when going from a single-component layer to a molecular blend if the adsorption heights remain unaltered. In contrast, the additional screening contribution of the surrounding molecules can easily change in the new supramolecular environments, thereby modifying their electronic properties. A beautiful demonstration thereof is provided in a thorough study of the screening effect of molecular materials on STS spectra. It compares STS spectra of C_{60}, on metal surfaces, in many systematically varied supramolecular environments, from single molecules to 2D layers, and various other structures involving additional molecular species.[168] A simple model accounting for screening from molecular materials predicts a charging energy reduction of:[184]

$$N \times f(\alpha) = \frac{Ne^2\alpha}{2R^4} \tag{2.3}$$

where N is the coordination number, α the molecular polarizability,[185] and R the intermolecular distance. This simple model provides excellent quantitative agreement with the STS measurements on C_{60}, which show shifts of $\sim$400 meV in their LUMO energy on comparing isolated molecules with 2D close-packed structures.[168]

Spectroscopic studies on methodically varied donor–acceptor molecular blends on metal surfaces have revealed characteristic, general shifts of donor- and acceptor-related electronic states in opposite directions, namely, upward in energy for donors and downward for acceptors.[79] An example is depicted in Figure 2.15(a), which shows the core level photoemission spectra of F_{16}CuPc (acceptor), pentacene (donor), and of the various blend ratios that render crystalline supramolecular networks as displayed in the associated STM images, all grown and measured on Au(111). A rightwards (to lower binding energy [BE]) shift is clearly observed in all core-levels as the concentration of donor molecules decreases from pure donor layers (top), through donor–acceptor blends, to pure acceptor layers (bottom). The same trend is detected for the valence band peaks, particularly HOMO levels in the valence band photoemission spectra displayed in Figure 2.15(b), and the same is also inferred for LUMO levels from complementary near-edge X-ray absorption spectroscopy (NEXAFS) analysis of the same system. These results suggest rigid shifts in the donor and acceptor band structure as a function of the blend stoichiometry, which has been further confirmed with DFT calculations.

The excellent match of the additionally measured work function changes for each layer with the core level shifts (whether calculated or measured) and HOMO level shifts supports the ideal interfacial vacuum-level alignment scenario depicted in Figure 2.16, in which changes in the vacuum level rigidly shift all molecular levels by the same amount. Under these circumstances, those shifts are directly associated with variations in the charge carrier injection barriers. A simple model assuming a linear

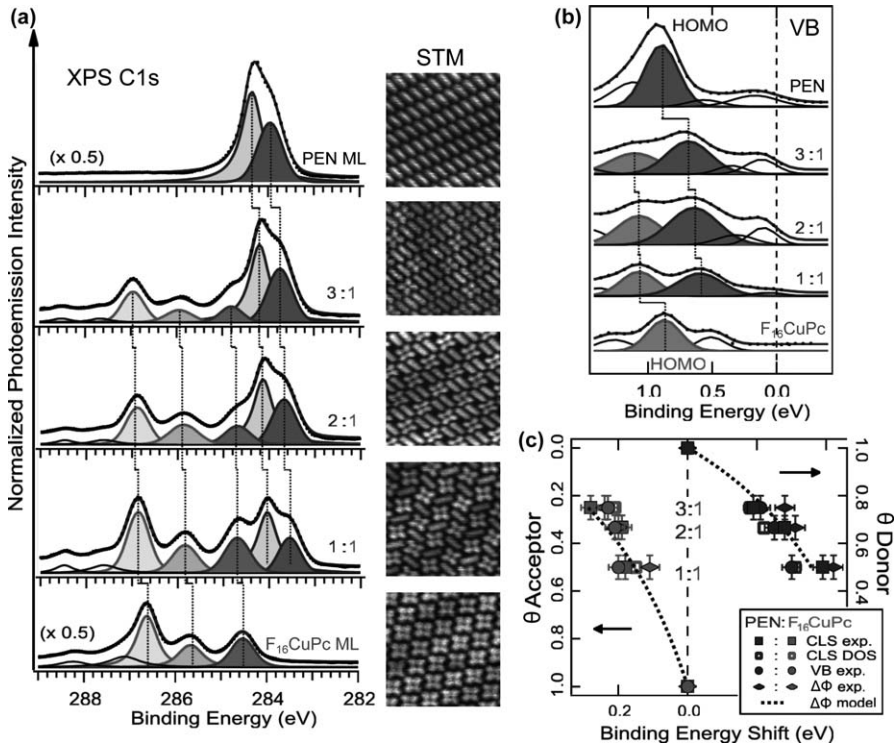

Figure 2.15 (a) C 1s core-level spectra from donor-rich (top) to acceptor-rich (bottom) monolayer blends, measured by photoemission on the F_{16}CuPc-PEN/Au(111) system at molecular ratios exhibiting long-range crystalline order as previously determined by STM (associated 9.5×9.5 nm^2 images on the right). (b) Valence band spectra of the structures shown in (a). (c) Superposition of experimentally measured core-level shifts (filled squares), calculated core-level shifts (empty squares), measured HOMO shifts (filled circles), measured vacuum level shifts (filled diamonds) and vacuum level shifts estimated from single-component data (dotted line), all referred to single component layer values.
Adapted with permission from ref. 79. Copyright 2013 American Chemical Society.

dependence of the interface dipole with the partial coverage of each molecule yields:

$$\Delta\phi_{\mathrm{acc}} = \frac{S_{\mathrm{don}}}{S_{\mathrm{don}} + S_{\mathrm{acc}}} (\sigma_{\mathrm{don}} - \sigma_{\mathrm{acc}}) \tag{2.4}$$

$$\Delta\phi_{\mathrm{don}} = \frac{S_{\mathrm{acc}}}{S_{\mathrm{don}} + S_{\mathrm{acc}}} (\sigma_{\mathrm{acc}} - \sigma_{\mathrm{don}}) \tag{2.5}$$

where S_{don} and S_{acc} are the surface areas covered by the different molecules, and σ_{don} and σ_{acc} are the interface dipoles associated with pure donor and acceptor monolayers, respectively. The model shows good agreement with

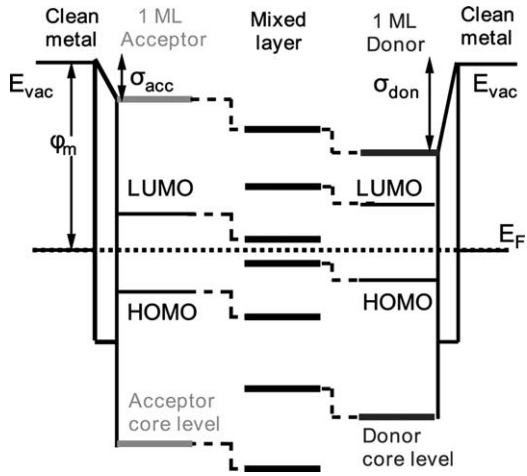

Figure 2.16 Schematic diagram of the energy level alignment of single-component layers and molecular blends on metal surfaces, where the varying vacuum level and the associated shifts of molecular states upon blending in a vacuum level pinning scenario are highlighted by dotted lines. Reproduced with permission from ref. 79. Copyright 2013 American Chemical Society.

the experimental curves (Figure 2.15c) and therefore allows prediction of the vacuum level shifts, and in turn changes in charge carrier injection barriers, from available single-component layer data.

Complementary measurements on other metal substrates and blends with exchanged fluorination (combining perfluoropentacene and CuPc) render similar results and confirm the generality of these donor and acceptor shifts. The reason for this is that, regardless of the substrate, acceptors typically present lower or even oppositely directed interface dipoles than donors. This is on the one hand due to the opposite charge transfer contribution. On the other hand, fluorinated acceptors typically lie farther from the substrate than their corresponding non-fluorinated donors, thereby reducing the Pauli repulsion contribution to the interface dipole.[79,186] Deviations from the vacuum level pinning scenario increase for interfaces on which molecule–substrate interactions are stronger. This is most common for donor molecules, whose closer proximity to the substrate surface favors higher induced densities of interface states.[23,79] Nevertheless, regardless of certain system-dependent deviations in the total extent of the energy shifts, the general scenario represents a potential route to tune the interface energetics and the associated charge carrier injection barriers by choosing molecules with appropriately different interface dipoles and blending them in adequate ratios.

2.4 Concluding Remarks

Organic-based devices are already a reality, but are still believed to offer great margins for improvement and expansion. Particularly promising is the

potential departure from the established top-down fabrication methods through an increasingly important role of molecular self-assembly in device fabrication. In addition to the associated cost reduction, self-assembly offers control over the resulting structures at greatly reduced length scales. Progress along these lines, however, requires the design and growth of increasingly complex and efficient supramolecular structures. Detailed knowledge of the opto-electronic properties of molecular systems is needed for their design to provide them with optimized functionality. Their growth in turn requires a thorough understanding of the processes involved in self-assembly. The possibilities of supramolecular assemblies offered in terms of both crystalline and electronic structures, which ultimately define their functionality, is significantly increased in multicomponent molecular blends. Therefore, this chapter reviews, with special emphasis placed on 2D multicomponent supramolecular systems, our increasing knowledge on the multiple interrelated processes and interactions that play a part in molecular self-assembly. In addition to their description, examples are provided of routes to leverage each of those processes and interactions for the tailored growth of supramolecular structures. The dependence of the structure's electronic properties on their supramolecular arrangements is additionally addressed as a key factor of nonnegotiable consideration along the roadmap towards rationally designed functionalities.

References

1. H. Usta, A. Facchetti and T. J. Marks, *Acc. Chem. Res.*, 2011, **44**, 501.
2. A. Pron and P. Rannou, *Prog. Polym. Sci.*, 2002, **27**, 135.
3. X. Y. Wang, C. Avendano and K. R. Dunbar, *Chem. Soc. Rev.*, 2011, **40**, 3213.
4. *Physics of Organic Semiconductors*, ed. W. Brütting and C. Adachi, Wiley-VCH Verlag GmbH, Weinheim (Germany), 2nd edition, 2012.
5. C. R. Newman, C. D. Frisbie, D. A. da Silva Filho, J.-L Bredas, P. C. Ewbank and K. R. Mann, *Chem. Mater.*, 2004, **16**, 4436.
6. H. Hoppe and N. S. Sariciftci, *J. Mater. Res.*, 2004, **19**, 1924.
7. J. Roncali, *Acc. Chem. Res.*, 2009, **42**, 1719.
8. N. Koch, *ChemPhysChem*, 2007, **8**, 1438.
9. W. Chen, D.-C. Qi, H. Huang, X. Gao and A. T. S. Wee, *Adv. Funct. Mater.*, 2011, **21**, 410.
10. E. Goiri, J. M. Garcia-Lastra, M. Corso, Z. M. Abd El-Fattach, J. E. Ortega and D. G. de Oteyza, *J. Phys. Chem. Lett.*, 2012, **3**, 848.
11. D. Ecija, R. Otero, L. Sanchez, J. M. Gallego, Y. Wang, M. Alcami, F. Martin, N. Martin and R. Miranda, *Angew. Chem. Int. Ed.*, 2007, **46**, 7874.
12. R. Ruiz, D. Choudhary, B. Nickel, T. Toccoli, K.-C. Chang, A. C. Mayer, P. Clancy, J. M. Blakely, R. L. Headrick, S. Iannotta and G. G. Malliaras, *Chem. Mater.*, 2004, **16**, 4497.

13. L. Kilian, A. Hauschild, R. Temirov, S. Soubatch, A. Scholl, A. Bendounan, F. Reinert, T.-L. Lee, F. S. Tautz, M. Sokolowski and E. Umbach, *Phys. Rev. Lett.*, 2008, **100**, 136103.
14. H. Brune, *Surf. Sci. Rep.*, 1998, **31**, 121.
15. J. Stangl, V. Holy and G. Bauer, *Rev. Mod. Phys.*, 2004, **76**, 725.
16. R. Otero, F. Hummelink, F. Sato, S. B. Legoas, P. Thostrup, E. Laegsgaard, I. Stensgaard, D. S. galvao and F. Besenbaccher, *Nat. Mater.*, 2004, **3**, 779.
17. F. Sato, S. B. Legoas, R. Otero, F. Hümmelink, P. Thostrup, E. Lægsgaard, I. Stensgaard, F. Besenbacher and D. S. Galvão, *J. Chem. Phys.*, 2010, **133**, 224702.
18. J. A. Miwa, S. Weigelt, H. Gersen, F. Besenbacher, F. Rosei and T. R. Linderoth, *J. Am. Chem. Soc.*, 2006, **128**, 3164.
19. G. Hlawacek, P. Puschnig, P. Frank, A. Winkler, C. Ambrosch-Draxl and C. Teichert, *Science*, 2008, **321**, 108.
20. X. N. Zhang, E. Barrena, D. Goswami, D. G. de Oteyza, C. Weis and H. Dosch, *Phys. Rev. Lett.*, 2009, **103**, 136101.
21. J. V. Barth, *Annu. Rev. Phys. Chem.*, 2007, **58**, 375.
22. B. Hammer and J. K. Norskov, *Surf. Sci.*, 1995, **343**, 211.
23. H. Vazquez, F. Flores and A. Kahn, *Org. Electron.*, 2007, **8**, 241.
24. K. Fukui, *Science*, 1982, **218**, 747.
25. S. Wilke, M. H. Cohen and M. Scheffler, *Phys. Rev. Lett.*, 1996, **77**, 1560.
26. B. Hammer and J. K. Norskov, *Nature*, 1995, **376**, 238.
27. L. Triguero, A. Föhlisch, P. Väterlein, J. Hasselström, M. Weinelt, L. G. M. Pettersson, Y. Luo, H. Agren and A. Nilsson, *J. Am. Chem. Soc.*, 2000, **122**, 12310.
28. L. J. Lauhon and W. Ho, *J. Phys. Chem. A*, 2000, **104**, 2463.
29. P. K. Milligan, B. Murphy, D. Lennon, B. C. C. Cowie and M. Kadodwala, *J. Phys. Chem. B*, 2001, **105**, 140.
30. F. Rosei, M. Schunack, Y. Naitoh, P. Jiang, A. Gourdon, E. Laegsgaard, I. Stensgaard, C. Joachim and F. Besenbacher, *Prog. Surf. Sci.*, 2003, **71**, 97.
31. M. Schunack, T. R. Linderoth, F. Rosei, A. Laegsgaard, I. Stensgaard and F. Besenbacher, *Phys. Rev. Lett.*, 2002, **88**, 156102.
32. N. Wintjes, J. Lobo-Checa, J. Hornung, T. Samuely, F Diederich and T. A. Jung, *J. Am. Chem. Soc.*, 2010, **132**, 7306.
33. M. E. Cañas-Ventura, W. Xiao, D. Wasserfallen, K. Mullen, H. Brune, J. V. Barth and R. Fasel, *Angew. Chem. Int. Ed.*, 2007, **46**, 1814.
34. Y. L. Huang, R. Wang, T. C. Niu, S. Kera, N. Ueno, J. Pflaum, A. T. S. Wee and W. Chen, *Chem. Commun.*, 2010, 9040.
35. W. Jin, D. B. Dougherty, W. C. Cullen, S. Robey and J. E. Reutt-Robey, *Langmuir*, 2009, **25**, 9857.
36. C. Bobisch, Th. Wagner, A. Bannani and R. Moller, *J. Chem. Phys.*, 2003, **119**, 9804.
37. J. A. Theobald, N. S. Oxtoby, M. A. Phillips, N. R. Champness and P. H. Beton, *Nature*, 2003, **424**, 1029.

38. M. Koudia, M. Abel, C. Maurel, A. Blieck, D. Catalin, M. Mossoyan, J.-C. Mossoyan and L. Porte, *J. Phys. Chem. B*, 2006, **110**, 10058.
39. M. Abel, V. Oison, M. Koudia, C. Maurel, C. Katan and L. Porte, *ChemPhysChem*, 2006, **7**, 82.
40. B. Calmettes, S. Nagarajan, A. Gourdon, M. Abel, L. Porte and R. Coratger, *Angew. Chem. Int. Ed.*, 2008, **47**, 6994.
41. L. J. Lauhon and W. Ho, *J. Chem. Phys.*, 1999, **111**, 5633.
42. D. E. Hooks, T. Fritz and M. D. Ward, *Adv. Mater.*, 2001, **13**, 227.
43. S. R. Forrest, *Chem. Rev.*, 1997, **97**, 1793.
44. T. N. Krauss, E. Barrena, H. Dosch and Y. Wakayama, *ChemPhysChem*, 2009, **10**, 2445.
45. W. Chen, H. Li, H. Huang, Y. Fu, H. L. Zhang, J. Ma and A. T. S. Wee, *J. Am. Chem. Soc.*, 2008, **130**, 12285.
46. K. Suto, S. Yoshimoto and K. Itaya, *J. Am. Chem. Soc.*, 2003, **125**, 14976.
47. H. Brune, M. Giovannini, K. Bromann and K. Kern, *Nature*, 1998, **394**, 451.
48. D. D. Chambliss, R. J. Wilson and S. Chiang, *Phys. Rev. Lett.*, 1991, **66**, 1721.
49. R. Otero, Y. Naitoh, F. Rosei, P. Jiang, P. Thostrup, A. Gourdon, E. Lægsgaard, I. Stensgaard, C. Joachim and F. Besenbacher, *Angew. Chem., Int. Ed.*, 2004, **43**, 2092.
50. K. Ait-Mansour, M. Treier, P. Ruffieux, M. Bieri, R. Jaafar, P. Gorning, R. Fasel and O. Groning, *J. Phys. Chem. C*, 2009, **113**, 8407.
51. N. Néel, J. Kröger and R. Berndt, *Adv. Mater.*, 2006, **18**, 174.
52. M. Ruiz-Oses, N. Gonzalez-Lakunza, I. Silanes, A. Gourdon, A. Arnau and J. E. Ortega, *J. Phys. Chem. B*, 2006, **110**, 25573.
53. R. Smoluchowski, *Phys. Rev.*, 1941, **60**, 661.
54. B. Xu, C. Tao, W. G. Cullen, J. E. Reutt-Robey and E. D. Williams, *Nano Lett.*, 2005, **5**, 2207.
55. H. L. Zhang, W. Chen, L. Chen, H. Huang, X. S. Wang, J. Yuhara and A. T. S. Wee, *Small*, 2007, **3**, 2015.
56. W. Chen, H. L. Zhang, H. Huang, L. Chen and A. T. S. Wee, *Appl. Phys. Lett.*, 2008, **92**, 193301.
57. Y. L. Huang, W. Chen and A. T. S. Wee, *J. Am. Chem. Soc.*, 2011, **133**, 820.
58. Y. Wei, S. W. Robey and J. E. Reutt-Robey, *J. Am. Chem. Soc.*, 2009, **131**, 12026.
59. S. Stepanow, M. Lingenfelder, A. Dmitriev, H. Spillmann, E. Delvigne, N. Lin, X. Deng, C. Cai, J. V. Barth and K. Kern, *Nat. Mater.*, 2004, **3**, 229.
60. H. Spillmann, A. Kiebele, M. Stohr, T. A. Jung, D. Bonifazi, F. Cheng and F. Diederich, *Adv. Mater.*, 2006, **18**, 275.
61. M. Stöhr, M. Wahl, H. Spillmann, L. H. Gade and T. A. Jung, *Small*, 2007, **3**, 1336.
62. L. Piot, F. Silly, L. Tortech, Y. Nicolas, P. Blanchard, J. Roncali and D. Fichou, *J. Am. Chem. Soc.*, 2009, **131**, 12864.

63. B. Baris, J. Jeannoutot, V. Luzet, F. Palmino, A. Rochefort and F. Cherioux, *ACS Nano*, 2012, **6**, 6905.
64. T. Steiner, *Angew. Chem. Int. Ed.*, 2002, **41**, 48.
65. G. R. Desiraju, *Acc. Chem. Res.*, 2002, **35**, 565.
66. L. Kilian, A. Hauschild, R. Temirov, S. Soubatch, A. Scholl, A. Bendounan, F. Reinert, T.-L. Lee, F. S. Tautz, M. Sokolowski and E. Umbach, *Phys. Rev. Lett.*, 2008, **100**, 136103.
67. G. Pawin, K. L. Wong, K. Y. Kwon and L. Bartels, *Science*, 2006, **313**, 961.
68. A. Schiffrin, A. Riemann, W. Auwarter, Y. Pennec, A. Weber-Bargioni, D. Cvetko, A. Cossaro, A. Morgante and J. V. Barth, *Proc. Nat. Acad. Sci.*, 2007, **104**, 5279.
69. L. M. A. Perdigao, N. R. Champness and P. H. Beton, *Chem. Commun.*, 2006, 538.
70. L. M. A. Perdigao, E. W. Perkins, J. Ma, P. A. Staniec, B. L. Rogers, N. R. Champness and P. H. Beton, *J. Phys. Chem. B*, 2006, **110**, 12539.
71. F. Silly, A. Q. Shaw, G. A. D. Briggs and M. R. Castell, *Appl. Phys. Lett.*, 2008, **92**, 023102.
72. P. A. Staniec, L. M. A. Perdigao, B. L. Rogers, N. R. Champness and P. H. Beton, *J. Phys. Chem. C*, 2007, **111**, 886.
73. N. Gonzalez-Lakunza, M. E. Canas-Ventura, P. Ruffieux, R. Rieger, K. Mullen, R. Fasel and A. Arnau, *ChemPhysChem*, 2009, **10**, 2943.
74. H.-M. Zhang, Z.-X. Xie, L.-S. Long, H.-P. Zhong, W. Zhao, B.-W Mao, X. Xu and L.-S. Zheng, *J. Phys. Chem. C*, 2008, **112**, 4209.
75. A. Llanes-Pallas, M. Matena, T. Jung, M. Prato, M. Stohr and D. Bonifazi, *Angew. Chem. Int. Ed.*, 2008, **47**, 7726.
76. E. Barrena, D. G. de Oteyza, H. Dosch and Y. Wakayama, *ChemPhysChem*, 2007, **8**, 1915.
77. Y. L. Huang, W. Chen, H. Li, J. Ma, J. Pflaum and A. T. S. Wee, *Small*, 2010, **6**, 70.
78. T. C. Niu, Y. L. Huang, J. T. Sun, S. Kera, N. Ueno, A. T. S. Wee and W. Chen, *Appl. Phys. Lett.*, 2011, **99**, 143114.
79. A. El-Sayed, P. Borghetti, E. Goiri, C. Rogero, L. Floreano, G. Lovat, D. J. Mowbray, J. L. Cabellos, Y. Wakayama, A. Rubio, J. E. Ortega and D. G. de Oteyza, *ACS Nano*, 2013, **7**, 6914.
80. K. W. Hipps, L. Scudiero, D. E. Barlow and M. P. Cooke Jr., *J. Am. Chem. Soc.*, 2002, **124**, 2126.
81. Y. Wakayama, D. G. de Oteyza, J. M. Garcia-Lastra and D. J. Mowbray, *ACS Nano*, 2011, **5**, 581.
82. F. Babudri, G. M. Farinola, F. Naso and R. Ragni, *Chem. Commun.*, 2007, 1003.
83. M. L. Tang and Z. Bao, *Chem. Mater.*, 2011, **23**, 446.
84. D. G. de Oteyza, I. Silanes, M. Ruiz-Oses, E. Barrena, B. P. Doyle, A. Arnau, H. Dosch, Y. Wakayama and J. E. Ortega, *Adv. Funct. Mater.*, 2009, **19**, 259.

85. D. G. de Oteyza, J. M. Garcia-Lastra, M. Corso, B. P. Doyle, L. Floreano, A. Morgante, Y. Wakayama, A. Rubio and J. E. Ortega, *Adv. Funct. Mater.*, 2009, **19**, 3567.
86. A. El-Sayed, D. J. Mowbray, J. M. García-Lastra, C. Rogero, E. Goiri, P. Borghetti, A. Turak, B. P. Doyle, M. Dell'Angela, L. Floreano, Y. Wakayama, A. Rubio, J. E. Ortega and D. G. de Oteyza, *J. Phys. Chem. C*, 2012, **116**, 4780.
87. D. G. Golovanov, K. A. Lyssenko, M. Yu. Antipin, Y. S. Vygodskii, E. I. Lozinskaya and A. S. Shaplov, *CrystEngComm*, 2005, **7**, 53.
88. A. DerHovanessian, J. B. Doyon, A. Jain, P. R. Rablen and A.-M. Sapse, *Org. Lett.*, 1999, **1**, 1359.
89. S. Kitagawa, R. Kitaura and S. Noro, *Angew. Chem. Int. Ed.*, 2004, **43**, 2334.
90. S. Stepanow, N. Lin, D. Payer, U. Schlickum, F. Klappenberger, G. Zoppellaro, M. Ruben, H. Brune, J. V. Barth and K. Kern, *Angew. Chem. Int. Ed.*, 2007, **46**, 710.
91. A. Langner, S. L. Tait, N. Lin, C. Rajadurai, M. Ruben and K. Kern, *Proc. Nat. Acad. Sci.*, 2007, **104**, 17927.
92. S. Clair, S. Pons, S. Fabris, S. Baroni, H. Brune, K. Kern and J. V. Barth, *J. Phys. Chem. B*, 2006, **110**, 5627.
93. T. Classen, G. Fratesi, G. Costantini, S. Fabris, F. L. Stadler, C. Kim, S. de Gironcoli, S. Baroni and K. Kern, *Angew. Chem. Int. Ed*, 2005, **44**, 6142.
94. S. L. Tait, A. Langner, N. Lin, R. Chandrasekar, O. Fuhr, M. Ruben and K. Kern, *Chem. Commun.*, 2009, 2502.
95. U. Schlickum, R. Decker, F. Klappenberger, G. Zoppellaro, S. Klyatskaya, M. Ruben, I. Silanes, A. Arnau, K. Kern, H. Brune and J. V. Barth, *Nano Lett.*, 2007, **7**, 3813.
96. S. Stepanow, M. Lingenfelder, A. Dmitriev, H. Spillmann, E. Delvigne, N. Lin, X. Deng, C. Cai, J. V. Barth and K. Kern, *Nat. Mater.*, 2004, **3**, 229.
97. C. R. Newman, C. D. Frisbie, D. A. da Silva Filho, J.-L. Bredas, P. C. Ewbank and K. R. Mann, *Chem. Mater.*, 2004, **16**, 4436.
98. S. Yang, P. Olishevski and M. Kertesz, *Synth. Met.*, 2004, **141**, 171.
99. S. W. Hla, L. Bartels, G. Meyer and K.-H. Rieder, *Phys. Rev. Lett.*, 2000, **85**, 2777.
100. Y. Okawa and M. Aono, *Nature*, 2001, **409**, 683.
101. L. Grill, M. Dyer, L. Lafferenz, M. Persson, M. V. Peters and S. Hecht, *Nat. Nanotech.*, 2007, **2**, 687.
102. F. Bebensee, C. Bombis, S.-R. Vadapoo, J. R. Cramer, F. Besenbacher, K. V. Gothelf and T. R. Linderoth, *J. Am. Chem. Soc.*, 2013, **135**, 2136.
103. D. G. de Oteyza, P. Gorman, Y.-C. Chen, S. Wickenburg, A. Riss, D. J. Mowbray, G. Etkin, Z. Pedramrazi, H.-Z. Tsai, A. Rubio, M. F. Crommie and F. R. Fischer, *Science*, 2013, **340**, 1434.
104. Q. Sun, C. Zhang, Z. Li, H. Kong, Q. Tan, A. Hu and W. Xu, *J. Am. Chem. Soc.*, 2013, **135**, 8448.

105. M. Abel, S. Clair, O. Ourdjini, M. Mossoyan and L. Porte, *J. Am. Chem. Soc.*, 2011, **133**, 1203.
106. M. Matena, T. Riehm, M Stohr, T. A. Jung and L. H. Gade, *Angew. Chem. Int. Ed.*, 2008, **47**, 2414.
107. L. E. Dinca, C. Fu, J. M. MacLeod, J. Lipton-Duffin, J. L. Brusso, C. E. Szakacs, D. Ma, D. F. Perepichka and F. Rosei, *ACS Nano*, 2013, **7**, 1652.
108. S. Weigelt, C. Busse, C. Bombis, M. M. Knudsen, K. V. Gothelf, T. Strunskus, C. Wöll, M. Dahlbom, B. Hammer, E. Lægsgaard, F. Besenbacher and T. R. Linderoth, *Angew. Chem. Int. Ed.*, 2007, **46**, 9227.
109. S. Weigelt, C. Bombis, C. Busse, M. M. Knudsen, K. V. Gothelf, E. Lægsgaard, F. Besenbacher and T. R. Linderoth, *ACS Nano*, 2008, **2**, 651.
110. H.-Y. Gao, H. Wagner, D. Zhong, J.-H. Franke, A. Studer and H. Fuchs, *Angew. Chem. Int. Ed.*, 2013, **52**, 4024.
111. Y.-Q. Zhang, N. Kepcija, M. Kleinschrodt, K. Diller, S. Fischer, A. C. Papageorgiou, F. Allegretti, J. Bjork, S. Klyatskaya, F. Klappenberger, M. Ruben and J. V. Barth, *Nat. Commun.*, 2012, **3**, 1286.
112. G. Otero, G. Biddau, C. Sánchez-Sánchez, R. Caillard, M. F. López, C. Rogero, F. J. Palomares, N. Cabello, M. A. Basanta, J. Ortega, J. Méndez, A. M. Echavarren, R. Pérez, B. Gómez-Lor and J. A. Martín-Gago, *Nature*, 2008, **454**, 865.
113. A. Lisa Pinardi, G. Otero-Irurueta, I. Palacio, J. I. Martinez, C. Sanchez-Sanchez, M. Tello, C. Rogero, A. Cossaro, A. Preobrajenski, B. Gomez-Lor, A. Jancarik, I. G. Stara, I. Stary, M. F Lopez, J Mendez and J. A. Martin-Gago, *ACS Nano*, 2013, **7**, 3676.
114. M. I. Veld, P. Iavicoli, S. Haq, D. B. Amabilino and R. Raval, *Chem. Commun.*, 2008, 1536.
115. J. Greenwood, H. A. Fruchtl and C. J. Baddeley, *J. Phys. Chem. C*, 2013, **117**, 4515.
116. N. A. A. Zwaneveld, R. Pawlak, M. Abel, D. Catalin, D Gigmes, D. Bertin and L. Porte, *J. Am. Chem. Soc.*, 2008, **130**, 6678.
117. M. Treier, N. V. Richardson and R. Fasel, *J. Am. Chem. Soc.*, 2008, **130**, 14054.
118. M. Treier, R. Fasel, N. R. Champness, S. Argent and N. V. Richardson, *Phys. Chem. Chem. Phys.*, 2009, **11**, 1209.
119. D. Zhong, J.-H. Franke, S. K. Podiyanachari, T. Blömker, H. Zhang, G. Kehr, G. Erker, H. Fuchs and L. Chi, *Science*, 2011, **334**, 213.
120. J. A. Lipton-Duffin, O. Ivasenko, D. F. Perepichka and F. Rosei, *Small*, 2009, **5**, 592.
121. J. Cai, P. Ruffieux, R. Jaafar, M. Bieri, T. Braun, S. Blankenburg, M. Muoth, A. P. Seitsonen, M. Saleh, X. Feng, K. Mullen and R. Fasel, *Nature*, 2010, **466**, 470.
122. Y. C. Chen, D. G. de Oteyza, Z. Pedramrazi, C. Chen, F. R. Fischer and M. F. Crommie, *ACS Nano*, 2013, **7**, 6123.

123. A. P. Cote, A. I. Benin, N. W. Ockwig, M. O'Keeffe, A. J. Matzger and O. M. Yaghi, *Science*, 2005, **310**, 1166.
124. C.-Z. Guan, D. Wang and L.-J. Wan, *Chem. Commun.*, 2012, 2943.
125. A. Saywell, J. Schwarz, S. Hecht and L. Grill, *Angew. Chem. Int. Ed.*, 2012, **51**, 5096.
126. L. Lafferentz, V. Eberhardt, C. Dri, C. Africh, G. Comelli, F. Esch, S. Hecht and L. Grill, *Nat. Chem.*, 2012, **4**, 215.
127. J. Mendez, M. F. Lopez and J. A. Martin-Gago, *Chem. Soc. Rev.*, 2011, **40**, 4578.
128. M. Kittelmann, P. Rahe, M. Nimmrich, C. M. Hauke, A. Gourdon and A. Kuhnle, *ACS Nano*, 2012, **5**, 8420.
129. M. Kittelmann, M. Nimmrich, R. Lindner, A. Gourdon and A. Kuhnle, *ACS Nano*, 2013, **7**, 5614.
130. T. Lin, X. S. Shang, J Adisoejoso, P. N. Liu and N. Lin, *J. Am. Chem. Soc.*, 2013, **135**, 3576.
131. T. Faury, S. Clair, M. Abel, F. Dumur, D. Gigmes and L. Porte, *J. Phys. Chem. C*, 2012, **116**, 4819.
132. G. Li, I. Tamblyn, V. R. Cooper, H.-J. Gao and J. B. Neaton, *Phys. Rev. B*, 2012, **85**, 121409.
133. G. Mercurio, E. R. McNellis, I. Martin, S. Hagen, F. Leyssner, S. Soubatch, J. Meyer, M. Wolf, P. Tegeder, F. S. Tautz and K. Reuter, *Phys. Rev. Lett.*, 2010, **104**, 036102.
134. G. Schull, L. Douillard, C. Fiorini-Debuisschert, F. Charra, F. Mathevet, D. Kreher and A. J. Attias, *Nano Lett.*, 2006, **6**, 1360.
135. S. Lei, K. Tahara, F. C. De Schryver, M. Van der Auweraer, Y. Tobe and S. De Feyter, *Angew. Chem. Int. Ed.*, 2008, **47**, 2964.
136. X. Qiu, C. Wang, S. Yin, Q. Zeng, B. Xu and C. Bai, *J. Phys. Chem B*, 2000, **104**, 3570.
137. H. Wang, C. Wang, Q. Zeng, S. Xu, S. Yin, B. Xu and C. Bai, *Surf. Interface Anal.*, 2001, **32**, 266.
138. K. S. Mali, K. Lava, K. Binnemans and S. De Feyter, *Chem. Eur. J.*, 2010, **16**, 14447.
139. A. E. Baber, S. C. Jensen and E. C. H. Sykes, *J. Am. Chem. Soc.*, 2007, **129**, 6368.
140. T. Yokoyama, T. Takahashi, K. Shinozaki and M. Okamoto, *Phys. Rev. Lett.*, 2007, **98**, 206102.
141. I. Fernandez-Torrente, S. Monturet, K. J. Franke, J. Fraxedas, N. Lorente and J. I. Pascual, *Phys. Rev. Lett.*, 2007, **99**, 176103.
142. D. Vanderbilt, *Surf. Sci. Lett.*, 1992, **268**, L300.
143. K.-O. Ng and D. Vanderbilt, *Phys. Rev. B*, 1995, **52**, 2177.
144. W. Lu and D. Salac, *Phys. Rev. Lett.*, 2005, **94**, 1461023.
145. K. Kern, H. Niehus, A. Schatz, P. Zeppenfeld, J. George and G. Comsa, *Phys. Rev. Lett.*, 1988, **67**, 855.
146. F. T. Xu, S. C. Street and J. A. Barnard, *J. Phys. Chem. B*, 2003, **107**, 12762.

147. M. de Wild, S. Berner, H. Suzuki, H. Yanagi, D. Schlettwein, S. Ivan, A. Baratoff, H.-J. Guentherodt and T. A. Jung, *ChemPhysChem*, 2002, **3**, 881.
148. D. G. de Oteyza, E. Barrena, H. Doch, J. E. Ortega and Y. Wakayama, *Phys. Chem. Chem. Phys.*, 2011, **13**, 4220.
149. H. Peisert, M. Knupfer, T. Schwieger, J. M. Auerhammer, M. S. Golden and J. Fink, *J. Appl. Phys.*, 2002, **91**, 4872.
150. A. C. Durr, N. Koch, M. Kelsch, A. Ruhm, J. Ghijsen, R. L. Johnson, J.-J. Pireaux, J. Schwartz, F. Schreiber, H. Dosch and A. Kahn, *Phys. Rev. B*, 2003, **68**, 115428.
151. D. G. de Oteyza, E. Barrena, M. Ruiz-Oses, I. Silanes, B. P. Doyle, J. E. Ortega, A. Arnau, H. Dosch and Y. Wakayama, *J. Phys. Chem. C*, 2008, **112**, 7168.
152. D. G. de Oteyza, A. El-Sayed, J. M. Garcia-Lastra, E. Goiri, T. N. Krauss, A. Turak, E. Barrena, H. Dosch, J. Zegenhagen, A. Rubio, Y. Wakayama and J. E. Ortega, *J. Chem. Phys.*, 2010, **133**, 214703.
153. M. F. Crommie, C. P. Lutz and D. M. Eigler, *Nature*, 1993, **363**, 524.
154. M. L. Merrick, W. Luo and K. A. Fichthorn, *Prog. Surf. Sci.*, 2003, **72**, 117.
155. J. Repp, F. Moresco, G. Meyer and K.-H. Rieder, *Phys. Rev. Lett.*, 2000, **85**, 2981.
156. J. V. Barth, T. Zambelli, J. Wintterlin, R. Schuster and G. Ertl, *Phys. Rev. B*, 1997, **55**, 12902.
157. N. Knorr, H. Brune, M. Epple, A. Hirstein, M. A. Schneider and K. Kern, *Phys. Rev. B*, 2002, **65**, 115420.
158. M. Mehlhorn, V. Simic-Milosevic, S. Jaksch, Paul Scheier and K. Morgenstern, *Surf. Sci.*, 2010, **604**, 1698.
159. S. Lukas, G. Witte and C. Woll, *Phys. Rev. Lett.*, 2002, **88**, 028301.
160. P. S. Weiss and D. M. Eigler, *Phys. Rev. Lett.*, 1993, **71**, 3139.
161. M. M. Kamma, S. J. Stranick and P. S. Weiss, *Science*, 1996, **274**, 118.
162. E. C. H. Sykes, P. Han, S. A. Kandel, K. F. Kelly, G. S. McCarty and P. S. Weiss, *Acc. Chem. Res.*, 2003, **36**, 945.
163. E. C. H. Sykes, B. A. Mantooth, P. Han, Z. J. Donhauser and P. S. Weiss, *J. Am. Chem. Soc.*, 2005, **127**, 7255.
164. D. Wegner, R. Yamachika, Y. Wang, V. W. Brar, B. M. Bartlett, J. R. Long and M. F. Crommie, *Nano Lett.*, 2008, **8**, 131.
165. A. Kuhnle, L. M. Molina, T. R. Linderoth, B. Hammer and F. Besenbacher, *Phys. Rev. Lett.*, 2004, **93**, 086101.
166. T.-C. Tseng, C. Urban, Y. Wang, R. Otero, S. L. Tait, M. Alcami, D. Ecija, M. Trelka, J. M. Gallego, N. Lin, M. Konuma, U. Starke, A. Nefedov, A. Langner, C. Woll, M. A. Herranz, F. Martin, N. Martin, K. Kern and R. Miranda, *Nat. Chem.*, 2010, **2**, 374.
167. D. Cahen and A. Kahn, *Adv. Mater.*, 2003, **15**, 271.
168. I. Fernandez-Torrente, K. J. Franke and J. I. Pascual, *J. Phys.: Cond. Mat.*, 2008, **20**, 184001.
169. J. B. Neaton, M. S. Hybertsen and S. G Louie, *Phys. Rev. Lett.*, 2006, **97**, 216405.

170. K. S. Thygesen and A. Rubio, *Phys. Rev. Lett.*, 2009, **102**, 046802.
171. J. L. Cabellos, D. J. Mowbray, E. Goiri, A. El-Sayed, L. Floreano, D. G. de Oteyza, C. Rogero, J. E. Ortega and A. Rubio, *J. Phys. Chem. C*, 2012, **116**, 17991.
172. H. Ishii, K. Sugiyama, E. Ito and K. Seki, *Adv. Mater.*, 1999, **11**, 605.
173. G. Witte, S. Lukas, P. S. Bagus and C. Wöll, *Appl. Phys. Lett.*, 2005, **87**, 263502.
174. L. Yan, N. J. Watkins, S. Zorba, Y. Gao and C. W. Tang, *Appl. Phys. Lett.*, 2002, **81**, 2752.
175. S. Braun, W. R. Salaneck and M. Fahlman, *Adv. Mater.*, 2009, **21**, 1.
176. J. Hwang, A. Wan and A. Kahn, *Mater. Sci. Engin. R*, 2009, **64**, 1.
177. A. S. Wan, J. Hwang, F. Amy and A. Kahn, *Org. Electron.*, 2005, **6**, 47.
178. W. Monch, *Rep. Prog. Phys.*, 1990, **53**, 221.
179. M. G. Betti, A. Kanjilal, C. Mariani, H. Vazquez, Y. J. Dappe, J. Ortega and F. Flores, *Phys. Rev. Lett.*, 2008, **100**, 027601.
180. I. G. Hill, D. Milliron, J. Schwartz and A. Kahn, *Appl. Surf. Sci.*, 2000, **166**, 354.
181. N. Gonzalez-Lakunza, I. Fernandez-Torrente, K. J. Franke, N. Lorente, A. Arnau and J. I. Pascual, *Phys. Rev. Lett.*, 2008, **100**, 156805.
182. K. J. Franke, G. Schulze, N. Henningsen, I. Fernandez-Torrente, J. I. Pascual, S. Zarwell, K. Ruck-Braun, M. Cobian and N. Lorente, *Phys. Rev. Lett.*, 2008, **100**, 036807.
183. C. Stadler, S. Hansen, I. Kröger, C. Kumpf and E. Umbach, *Nat. Phys.*, 2009, **5**, 153.
184. K. D. Bonin, V. V. Kresin, *Electric-Dipole Polarizabilities of Atoms, Molecules, and Clusters*, World Scientific, Singapore, 1997.
185. K. J. Miller and J. Savchik, *J. Am. Chem. Soc.*, 1979, **101**, 7206.
186. N. Koch, A. Gerlach, S. Duhm, H. Glowatzki, G. Heimel, A. Vollmer, Y. Sakamoto, T. Suzuki, J. Zegenhagen, J. P. Rabe and F. Schreiber, *J. Am. Chem. Soc.*, 2008, **130**, 7300.

CHAPTER 3

Low-Dimensional Supramolecular Assemblies on Surfaces

TIANCHAO NIU,[a] JIA LIN ZHANG[b] AND WEI CHEN*[a,b]

[a] Department of Chemistry, National University of Singapore, 3 Science Drive 3, 117543, Singapore; [b] Department of Physics, National University of Singapore, 2 Science Drive 3, 117542, Singapore
*Email: phycw@nus.edu.sg

3.1 Introduction

The realization of molecular electronic devices that use single or a few molecules as functioning component is one of the ultimate goals to meet the stringent requirements for electronic device miniaturization.[1] Over the past few decades, intensive research efforts have been devoted to the development of molecular electronics, including designing and synthesis of molecules with desired functionality, single molecule device fabrication and characterization, assembling functional molecules into long-range ordered nanostructure arrays, investigation and engineering of molecule/electrode interface properties, and theoretical understanding of the molecular electronic device working principle.[2] However, many challenges still exist, for example, the lack of precise control of the interfacial properties between the molecules and electrodes (*i.e.*, poor reproducibility and reliability), limited understanding of the charge transport mechanism at the single molecule level, how to engineer and position functional molecules into

RSC Smart Materials No. 12
Supramolecular Materials for Opto-Electronics
Edited by Norbert Koch

Published by the Royal Society of Chemistry, www.rsc.org

extended and well-ordered device arrays over macroscopic area, how to precisely integrate individual molecules with external electrical circuits, and so on.[3]

Low-dimensional supramolecular architectures with well-defined arrangement and desired functionalities are important building blocks for functional molecular nanodevices as well as ideal model systems to investigate the working mechanism of molecular electronics at the atomic scale. Molecular self-assembly on solid surfaces represents a promising bottom-up approach for the construction of these well-defined low-dimensional molecular architectures.[4] It involves the assembly and ordering of molecules and/or atoms on the substrates, to achieve precise control of the composition, dimension, distribution and the organization of the supramolecular architectures.[5] However, the underlying mechanisms governing the self-assembly process are still less understood.[6] Extensive efforts have been made to reveal the general rules in these self-ordering phenomena, including exploring the roles of different types of intermolecular interactions on the self-assembly process (such as van der Waals forces, dipole–dipole, hydrogen bonding, and metal–ligand coordination), as well as an understanding of the effects of substrates on the adsorption and aggregation of the molecular building blocks (such as molecule–substrate interfacial charge transfer, substrate-mediated intermolecular interactions, and surface-assisted polymerization).[4,7,8]

In this chapter, the construction of one-dimensional (1D) molecular chains and two-dimensional (2D) molecular networks involving single component or binary molecular building blocks based on the non-covalent interactions will be discussed, including hydrogen-bonding and metal–ligand coordination. We will also discuss on-surface polymerization induced covalently bonded 1D molecular chains and 2D molecular networks.

3.2 1D Molecular Chains

When the organic electronic devices reach the single molecule limit, interconnecting these functional units requires the molecular wires to enable the charges and excitons transport within the devices.[9] Knowing how to fabricate conducting molecular wires in a reproducible way is essential for molecular electronic devices.[10] In particular, covalently bonded single polymer chains represent promising candidates for molecular nanodevices due to the efficient charge transport along these molecular wires.[11] In the following sections, we will discuss various approaches to construct these 1D molecular chains, including (i) substrate template directed self-assembly of 1D molecular chains; (ii) 1D molecular chains assembled through hydrogen bonding; (iii) metal–organic coordination bonds assisted assembly of 1D molecular chains; and (iv) on-surface synthesis towards covalently bonded 1D molecular chains.

3.2.1 Substrate Template Directed Self-Assembly of 1D Molecular Chains

Various types of atomic-scale templates, such as reconstructed surfaces like the herringbone reconstructed Au(111),[12–14] regular step bunches,[15,16] and/or vicinal templates (*e.g.*, Au(788)[17]), have been utilized to constrain molecules into well-ordered structures. For example, the monatomic stepped edges of the Au(11,12,12) template surface as shown by the scanning tunneling microscopy (STM) image in Figure 3.1(A) can direct the formation of a double- and single-row of the molecular chains consisting of perylene-tetra-3,4,9,10-carboxylic acid diimide (PTCDI) molecules and

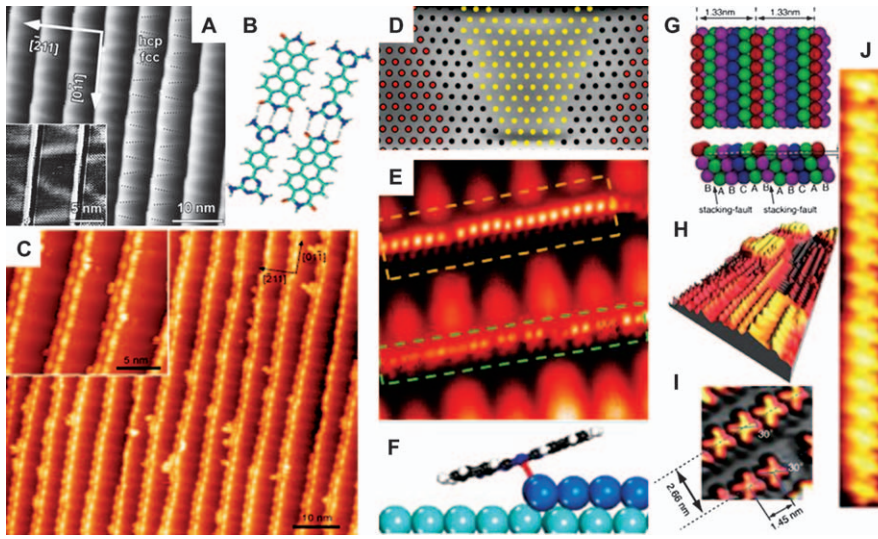

Figure 3.1 (A) STM image highlighting the 2D superlattice of steps and discommensuration lines separating FCC and HCP stacking areas on the Au(11,12,12) template surface. (B) Model of the threefold hydrogen-bonding pattern of PTCDI and BDATB. (C) STM image showing the double heteromolecular wires running along the lower step edges of the Au(11,12,12) template surface. (D) Top view of a stepped Au(677) surface. (E) 15×15 nm^2 STM image of FePc molecules decorating the step edges to form 1D molecular chains. (F) Optimized adsorption configuration of FePc molecules on Au(111) step edge. (G) Schematic illustration of a striped Ag surface on In/Si(111)-(4×1). (H) 30×60 nm^2 STM image showing the formation of CoPc molecular chains on the striped Ag surface. (I) 5×5 nm^2 STM image revealing the unique rotation angle of CoPc molecules within a chain. (J) A CoPc chain obtained on the striped surface.[20]

(A) Reproduced reprinted from ref. 12, with permission from the American Chemical Society, copyright 2006; (B) and (C) reprinted from ref. 15, with permission from John Wiley & Sons, copyright 2007; (D) reprinted from ref. 14, with permission from American Physical Society, copyright 2010; (E) and (F) reprinted from ref. 19, with permission from American Chemical Society, copyright 2011; (G) and (J) reprinted from ref. 20, with permission from American Chemical Society, copyright 2013.

1,4-bis(2,4-diamino-1,3,5-triazine)benzene (BDATB) at the coverage of 0.15 monolayer (ML) (Figure 3.1B and C). These 1D chains composed of alternating PTCDI and BDATB molecules are stabilized by the intermolecular N–H···O and N···H–N hydrogen bonding as schematically shown in Figure 3.1(B).

The molecular arrangement within the as-deposited molecular aggregates depends on the atomic structure of the substrate, molecular structure, and the interplay between the intermolecular and molecule–substrate interactions. For some particular functional-molecules such as large phthalocyanines or porphyrins and their derivatives, interaction with the step edges is complex due to the chemical bonding formation *via* multiple channels, such as the bonding between the central metal atom of the molecules and the substrate, and the coupling between the molecular peripheral ligands and the substrate.[18] As shown in Figure 3.1(D), the selective anchoring of iron phthalocyanine on the step edges of Au(111) arises from the different adsorption energy on the face-centered-cubic (FCC) and hexagonal-close-packed (HCP) regions.[19] One-dimensional molecular chains on the monatomic step edges can only be formed in the FCC surface reconstruction regions after increasing the coverage to 0.6 ML, with the FePc molecules preferring to reside onto the FCC-step-edges (Figure 3.1E and F). Therefore, the fabrication of artificial surface template is one of the efficient ways to realize the uniform and highly ordered 1D molecular chains. As shown in Figure 3.1(G), a surface with regular step arrays differing from the atomic steps has been constructed by rational decorating the Si(111) surface firstly with In and followed by Ag.[20] The fractional atomic steps can be formed due to the stacking-faults and the lattice matching between striped Ag and In/Si(111) surface. Highly ordered 1D cobalt-phthalocyanine molecular chains aligned along the striped Ag surface can be formed. The CoPc molecules within each single chain are uniformly orientated and densely packed. The maximum length of the CoPc molecular chains is about 25 nm, which is comparable with the domain size of the Ag striped structures.

3.2.2 1D Molecular Chains Assembled through Hydrogen Bonding

Various intermolecular non-covalent interactions, such as hydrogen bonding, metal–ligand coordination, and dipole–dipole interactions, and even covalent bonding have been exploited to construct long-range ordered molecular chain arrays. Owing to the directional and selective nature of hydrogen bonding with moderate strength, it is able to achieve controllable synthesis of desired functional molecular superstructures on surfaces.[21] Pioneering works are the construction of uniform long-range ordered 1D chains *via* benzoic acids on metal surfaces. For example, the well-known 4-[*trans*-2-(pyrid-4-yl-vinyl)]benzoic acid (PVBA) can form long-range ordered 1D chains on Ag (111) (Figure 3.2A and B) in a head-to-tail arrangement

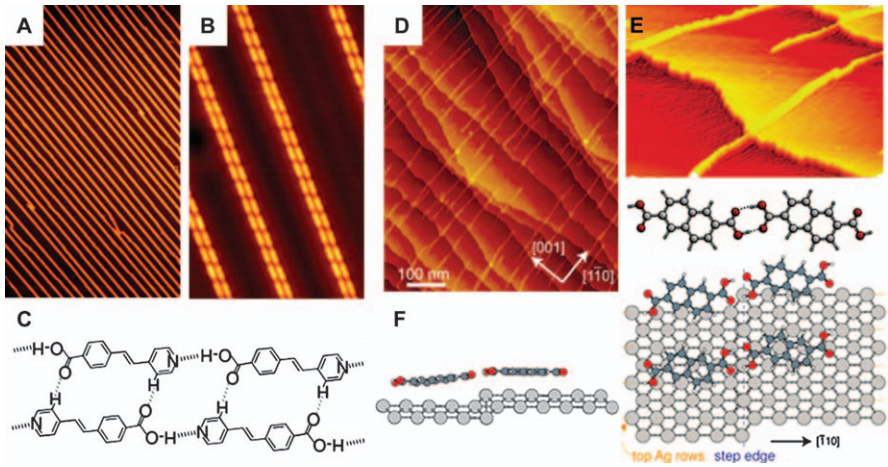

Figure 3.2 (A) 100×160 nm^2 and (B) 20×32 nm^2 STM images of PVBA doublet chains obtained after deposition and further annealing low concentrations of PVBA at 300 K on Ag(111). (C) Schematic representation of the double chains stabilized by intermolecular hydrogen bonding. (D) 600×800 nm^2 and (E) STM images showing the extended 1D supermolecular arrays crossing stepped surface *via* assembly of 2,6-naphthalenedicarboxylic acid (NDCA) on a Ag(111) surface. (F) DFT calculated structure of the NDCA dimers at a step edge, stabilized through the intermolecular hydrogen bonding.
(A)–(C) Reprinted from ref. 22, with permission from John Wiley & Sons, copyright 2000; (D) and (F) from ref. 23, with permission from American Physical Society, copyright 2008; (E) from ref. 58, with permission from Springer, copyright 2010.

stabilized through the O–H···N intermolecular hydrogen bonding[22] (Figure 3.2C). In some cases, the low-coordinated atoms at the step edges of metal surfaces provide special sites to accommodate molecules. As such, these molecular chains can cross over the step edges on the Ag(111) surface and possess long-range ordering and high stability by using 2,6-naphthalenedicarboxylic acid (NDCA) as the basic building block[23] (Figure 3.2D–F).

Rational selection of the organic building blocks and substrates can lead to the construction of various hydrogen-bonding stabilized functional molecular arrays. However, the relatively weak strength of the hydrogen bonding can induce multiple pathways and structural instability under certain conditions. Metal–ligand coordination bonding is highly directional and possesses intermediate strength, thereby representing one promising route towards the construction of molecular arrays. Moreover, various metals and ligands can be utilized to realize the fabrication of molecular nanostructure arrays with desired functionality and great diversity. As such, the coordination chemistry assisted formation of well-defined complex superstructures has been one of the widely used approaches,[24] which will be discussed in detail in the following section.

3.2.3 Metal–Organic Coordination Bonds Assisted Assembly of 1D Molecular Chains

Metal–organic coordination bonds formed between the organic ligands and the metallic atoms can be realized and manipulated by choosing suitable building blocks.[25] The peripheral sides of the suitable organic ligands can provide complementary bonding sites to interact with metal atoms. Therefore, geometrical control of the assembled superstructures can be realized by tuning the ligand geometry and choosing the right binding sites (*i.e.*, functional groups) to the metals.[25]

On metal surfaces, the step edges and surface defects can contribute adatoms for direct assembly of the organic molecules without further deposition of extra metal atoms. For example, it is known that the Cu adatom can exist on Cu surfaces even at moderate temperatures, enabling the stabilization of molecular aggregates *via* metal–ligand coordination bonding between the pyridyl groups and Cu adatoms.[26] As demonstrated in Figure 3.3(A), the bis(pyridyl)porphyrins can be aggregated into 1D molecular chain arrays *via* the N · · · Cu bond.[27] The one-dimensionally aligned pyridyl-Cu-pyridyl coordination motif indicates that the terminal pyridyl

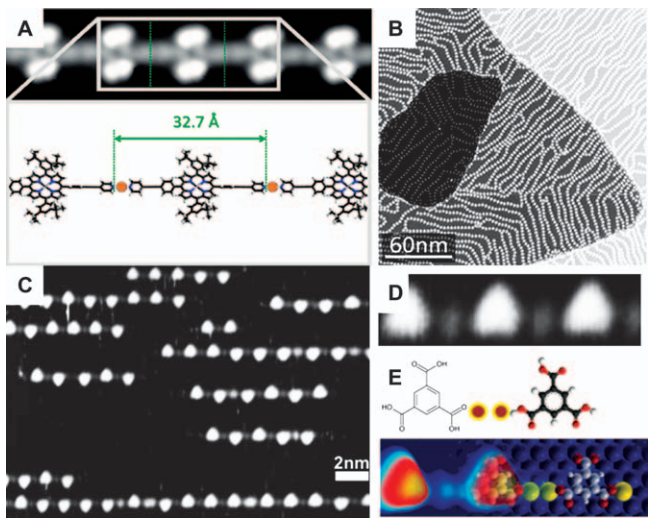

Figure 3.3 (A) 16×5 nm^2 STM image of the one-dimensional supramolecular assembly following deposition of bis(pyridyl)porphyrins on Cu(111); bottom: schematic model of the linear chain shown in (A) – the straight segments have a stride of about 32.7 Å. (B) Large scale STM image showing the chain on Cu(111) surface. (C) Representative STM images of [-Cu-TMA-Cu-]$_n$ chains on Cu (110) surface. (D) High-resolution STM image (4×0.8 nm^2) of the metal–organic molecular chain as shown in C. (E) Optimized model of the 1D chain.
(A) and (B) Reprinted from ref. 27, with permission from American Chemical Society, copyright 2010; (C)–(E) reprinted from ref. 28, with permission from John Wiley & Sons, copyright 2005.

rings are tilted instead of flat-lying on the surface (bottom of Figure 3.3A). As a consequence, the steric repulsions between H atoms of neighboring pyridyl rings prevent the formation of three-fold or four-fold symmetric coordination networks (Figure 3.3B). The formation of uniform 1D structures can also be delicately steered by using anisotropic surfaces such as Cu(110). This type of surface can act as the template to direct the formation of well-controlled molecular chains on it because of the preferential confinement within the troughs.[28] As illustrated in Figure 3.3(C), well-ordered 1D molecular chains can be formed after the deposition of trimesic acid (TMA) on Cu(110), which predominantly adsorbs along the ⟨1-10⟩ direction. The strong molecule–metal interfacial interactions enable the registry of TMA molecules with Cu(110). Upon deposition on Cu(110), TMA molecules undergo deprotonation, effectively couple with the Cu adatoms, and hence form the unidirectionally aligned 1D chains, in which individual TMA components interlink through Cu dimer centers *via* the formation of N · · · Cu coordination bonds.

3.2.4 On-Surface Synthesis towards Covalently Bonded 1D Molecular Chains

On-surface synthesis through covalent bonding of the organic molecules into rigid architectures is of great interest in the preparation of molecular nanostructures. Such processes are generally carried out after the deposition of molecules on metal surfaces under ultra-high vacuum conditions followed by thermal annealing at high temperatures to initiate the covalent coupling (schematic model in Figure 3.4F).[6] Grill *et al.* demonstrated that polymeric molecular chains can be formed on Au(111) through the covalent coupling of the *trans*-bromophenyl porphyrin[29] (Figure 3.4A–C). A single conjugated polymer chain has been successfully achieved by the same group through annealing the as-grown dibromoterfluorene (DBTF) monomers on an Au(111) surface at 520 K.[30] The terminated bromine atoms can be released after being activated at the first stage, followed by the diffusion and aggregation of the activated terfluorene radicals towards the formation of well-defined polymeric chains (Figure 3.4D–F).

As mentioned above, the synthesis of those 1D linear molecular chains is mostly carried out on the high-symmetric (111) surfaces, which lead to the preferential growth direction along the equivalent crystallographic axes. On the herringbone-reconstructed Au(111) surface, the linear structures can be perturbed by the elbow sites, such as the bended DBTF polymer chains on Au (111) (Figure 3.4E). The unidirectional growth of linear polymer chains can be realized by using inherent anisotropic surfaces as templates, such as (110) surfaces. For example, the Cu(110) surface can serve as both a template and a catalyst to promote polymerization through the classical Ullmann coupling. 2,5-Diiodo-3,4-ethylenedioxythiophene (DIEDOT) or 2,5-dibromo-3,4-ethylenedioxythiophene (DBEDOT) molecules are the monomers for the construction of poly(3,4-ethylenedioxythiophene) (PEDOT). By exploiting

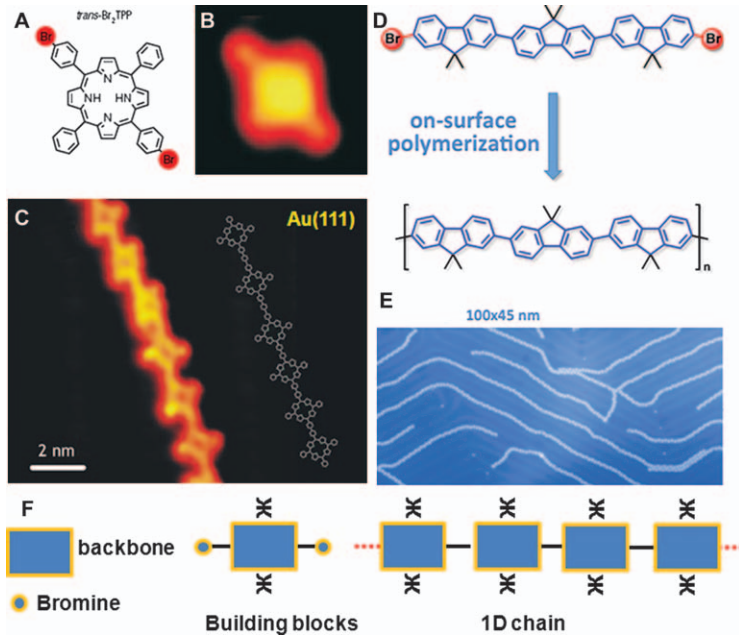

Figure 3.4 (A) Chemical structure of Br_4TPP molecule (substituent Br atoms are highlighted in red). (B) STM image of single Br_4TPP intact molecule (3.5×3.5 nm^2) where the brominated legs appear larger than the counter lobes. (C) 1D polymeric chain formed after activation and connection (10×10 nm^2); the schematic model is depicted inset.[29] (D) Molecular structure of DBTF monomer. (E) STM image of the long covalently bound molecular chain, following the herringbone reconstruction of the Au(111) (45×100 nm^2). (F) Scheme of sequential activation mechanism. (A)–(C) reprinted from ref. 29, with permission from Nature Publishing Group, copyright 2010; (D) and (E) reprinted with permission from Stefan Hecht.

Ullmann coupling (Figure 3.5A), epitaxially aligned PEDOT chains can be fabricated and tuned by varying the coverage of monomers, and hence the monomer chains, dimer chains, and trimer chains can be fabricated under different coverage (Figure 3.5B–D). To achieve all-*cis* conformation of the PEDOT chains, the upstanding configuration with the sulfur atom pointing towards the substrate is required to maximize the molecule–substrate interactions[31] (model in Figure 3.5D).

The covalent-bonded molecular chains with tunable functionality as described above are truly attractive for future molecular devices.[32] However, such on-surface polymerization usually involves the halogen-substituted molecular precursors, thereby introducing contamination of halogen atoms released during the covalent bonding processes. Therefore, the creation of molecular chains *via* a clean surface reaction without surface contamination from the byproducts (such as halogen atoms) would be highly desirable. One example is the polymerization of porphyrins by activation of the C–H bond,

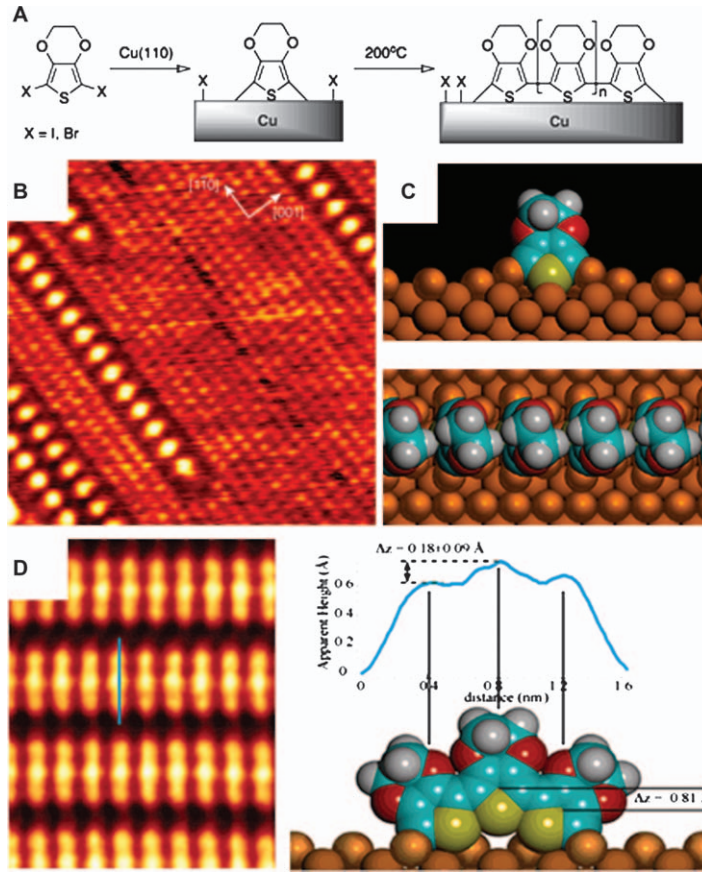

Figure 3.5 (A) Formation of epitaxially confined *cis*-PEDOT on Cu(110) *via* Ullmann coupling. (B) 8.9×8.9 nm^2 STM image showing the linearly stacked of EDOT molecules on Cu(110). (C) DFT calculated structures viewed from front (top) and top (bottom) respectively; Cu atoms are lifted out of the top substrate layer to participate in bonding to the EDOT. (D) 5×6 nm^2 STM image of the uniform trimer stripes on the Cu(110), the line profile demonstrated the stacking of the trimer structure shown on the right. (A)–(D) Reprinted from ref. 31, with permission from National Academy of Sciences of the United States of America, copyright 2010.

with the byproduct of hydrogen only, and hence the clean synthesis can be realized.[33]

3.3 2D Molecular Networks

The challenge in constructing well-defined 2D molecular networks is to achieve great structural controllability, tunability and stability, and to impose desired functionality into these molecular nanostructure arrays.[34] Elegant examples have been summarized in many review papers that discuss

the critical roles of various intermolecular interactions, including the hydrogen bonding, metal–ligand and dipole–dipole interaction, to steer the aggregation of the molecules into a well-ordered pattern.[35,36] Besides these intermolecular interactions, the substrates also play important roles in the self-assembly process. Generally, molecules tend to form densely packed uniform islands on chemically inert substrates like graphite; whereas on chemically active substrates, like Cu(111), both the molecule–substrate interfacial charge transfer and substrate-mediated intermolecular interactions would impact the supramolecular arrangement on it. Other elegant examples include the enhanced dipole–dipole repulsion induced periodic distribution of tetrathiafulvalene (TTF) on Au(111)[37] and the unidirectionally aligned molecular rows of pentacene on Cu(110) induced by substrate-mediated intermolecular repulsion.[38] Therefore, comprehensive understanding of the substrate effects on the ordering of molecules with specific functional groups would be of great interest.[39]

3.3.1 Single-Component Supramolecular Structures on Surfaces

The self-assembly of functional organic semiconductors, such as phthalocyanine,[18] 3,4,9,10-perylenetetracarboxy-dianhydride (PTCDA),[39] and tetracyanoquinodimethane (TCNQ),[40] on different types of substrates has been intensively studied. It is found that the substrates play a dominant role in determining the molecular arrangement. In particular, the functional units on the molecules, like the cyanide (-CN) and hydride (-OH), can strongly bond with the metal substrates, and hence dramatically influence the conformation of the adsorbed molecules. Other functional groups, like the carboxylic and the hydrogen-donor groups can result in the formation of intermolecular hydrogen bonding. The dipole moment of the molecules, which is either permanent or induced after the adsorption onto the substrates, can also significantly influence the molecular ordering/aggregation on the surfaces.

In this section, the self-assembly of functional phthalocyanine molecules on different substrates will be used as a model system to understand the substrate effect on the molecular ordering and arrangement, including hexadeca-fluoro copper phthalocyanine (F_{16}CuPc) on HOPG, Ag(111), $BiAg_2$ surface alloy on Ag(111), and Bi(110). It is generally accepted that metal phthalocyanine molecules tend to lie flat on graphite/metal surfaces with their molecular π-plane parallel to the surface, which is dominated by the interfacial π–π interaction or π–d interactions.[41,42] However, the detailed in-plane orientation and packing geometry of these molecules could be largely influenced by the interplay of the molecule–substrate interfacial interactions and the intermolecular interactions.[43]

As shown in Figure 3.6(A), long-range ordered supramolecular structures can be formed after the deposition of copper phthalocyanine (CuPc) on HOPG,[44] which exhibits a square unit cell of 1.52×1.52 nm^2. However, in the

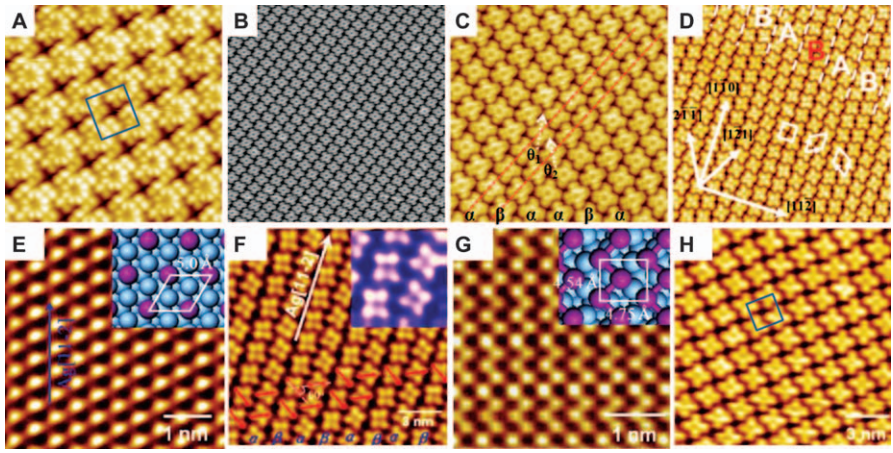

Figure 3.6 (A) 8×8 nm^2 High-resolution STM image of CuPc monolayer on HOPG. (B) 30×30 nm^2 STM image of the F_{16}CuPc monolayer on HOPG and (C) its corresponding high-resolution image (15×15 nm^2), where dashed lines indicate orientations of molecular rows and arrows indicate molecular axes.[41] (D) Molecularly resolved STM image of F_{16}CuPc on Ag(111). Three unit cells are highlighted by three white tetragons respectively. Different domains are separated by dashed lines and labelled "A" and "B". (E) $BiAg_2$ surface alloy with the $\sqrt{3}\times\sqrt{3}$ R30° structure. (F) The monolayer F_{16}CuPc on the $BiAg_2$ alloy surface. (G) STM image showing the structure of Bi(110) monolayer structure. (H) STM image of monolayer F_{16}CuPc on the Bi(110) surface.
(A) Reprinted from ref. 44, with permission from American Chemical Society, copyright 2010; (B) and (C) reprinted from ref. 41, with permission from Springer, copyright 2008; (D) reprinted from ref. 42, with permission from American Chemical Society, copyright 2008; (E)–(H) reprinted from ref. 43, with permission from American Chemical Society, copyright 2010.

case of F_{16}CuPc, in which the peripheral hydrogen atoms are substituted by fluorine atoms, alternating molecular stripes with two different in-plane molecular orientations can be formed. These stripes are denoted as α-orientation and β-orientation (Figure 3.6B and C). The nearly equivalent percentages of the two stripes indicate that molecules with both orientations are energetically favorable on HOPG. The striking differences of the in-plane orientation of CuPc and F_{16}CuPc monolayer on a graphite surface can be ascribed to the large repulsion between the negatively charged F atoms in F_{16}CuPc.

The Bi/Ag(111) system can be used as a model system to understand how the molecule–substrate interfacial interactions tailor the supramolecular packing and molecular orientation. Upon increasing the coverage of Bi on Ag(111), the surface phases can transform from Ag(111) into $BiAg_2$ surface alloy and Bi(110). The Ag(111) and $BiAg_2$ surface is metallic and possesses a relatively high density of states near the Fermi level, while the Bi(110) is

semi-metallic and exhibits a low density of states near the Fermi level. As the molecule–metal interfacial interaction is dominated by coupling between the molecular orbitals and substrate electronic states, F_{16}CuPc molecules can, hence, interact more strongly with the Ag(111) and $BiAg_2$ surface. Such strong interfacial interaction can lock F_{16}CuPc molecules to the specific adsorption sites on the substrate. In contrast, the relatively weak interfacial interaction between F_{16}CuPc and Bi(110) would result in a monolayer structure without any epitaxial relation with the substrate.

As shown in Figure 3.6(D), double-row molecular stripes are formed for F_{16}CuPc monolayer on Ag(111).[50] These long-range ordered stripes are strictly aligned along the [1–10] of Ag(111). One double-molecule-row (DMR) has an oblique unit cell with dimensions of 1.5 nm by 1.5 nm; while the neighboring DMR has a same size oblique unit with mirror symmetry. On the three-fold $BiAg_2$ surface alloy on Ag(111), F_{16}CuPc molecules possess a quasi-hexagonal unit cell with two types of in-plane orientations (Figure 3.6E and F). The molecules having the same in-plane orientation stack together to form molecular rows along the [-11-2] direction of Ag(111). Notably, the adsorption of F_{16}CuPc is in registry with the substrate lattice on both Ag(111) and the $BiAg_2$ surface alloy due to the strong interfacial interaction. Moreover, the formation of the alternating single-row and double-row molecular stripes can minimize the repulsive intermolecular interaction between neighboring F_{16}CuPc molecules.

In contrast, on Bi(110) (surface structure shown in Figure 3.6G), F_{16}CuPc molecules assemble into a highly ordered square lattice, which is not commensurate with the substrate. As shown in Figure 3.6(H), the intermolecular distance ($\sim$1.5 nm) within the densely packed F_{16}CuPc does not fit an integer multiple of any axis of the unit cell ($a = 0.454$ nm, $b = 0.475$ nm) of Bi(110). This indicates a relatively weak interfacial interaction between F_{16}CuPc and the semi-metallic Bi(110) and the intermolecular interactions (van der Waals forces) dominate the molecular packing under this condition.

Detailed analysis of these supramolecular networks shows that the controlled positioning and assembly of functional molecules depends on the interplay of multiple interactions on different strength and length scales. In general, relatively strong molecule–substrate interactions on metal substrates can constrain the molecules to adsorb in registry with the surface periodicity and lock them into specific adsorption sites, which may significantly reduce the structural tunability of the molecular nanostructures. Inert graphite has a smooth potential-energy surface as well as relatively weak interfacial interactions with adsorbed molecules, and is therefore an ideal substrate for constructing molecular nanostructures with a high degree of controllability and tunability.

3.3.2 Binary Molecular Networks

Beyond the single component molecular networks, binary/multi-component assemblies through the co-deposition of molecules can increase the

structural diversity and introduce novel functionalities. In particular, the periodicity or symmetry of these networks can be easily tuned by selecting suitable molecular building blocks and tuning the relative molecular ratios.[45] Various intermolecular interactions, including the non-covalent interactions such as hydrogen bonding, metal–ligand coordination, and donor–acceptor interactions, as well as the strong covalent bonding have been widely exploited for the construction of well-ordered molecular networks on surfaces.

3.3.2.1 *Tunable 2D Molecular Arrays on Graphite Stabilized* via *H-Bonding*

In this section, prototypical molecular systems consisting of F_{16}CuPc and *p*-sexiphenyl (6p) or pentacene or diindenoperylene (DIP) are used to demonstrate the tunability of 2D molecular networks on a graphite surface, which are stabilized *via* the formation of multiple intermolecular hydrogen bonds. By mixing F_{16}CuPc with 6p molecules, binary molecular networks with tunable intermolecular distances can be obtained by manipulating the relative ratio of the two molecules. As summarized in the top row of Figure 3.7, two F_{16}CuPc doublets can be interlinked by single or double 6p molecule at the 6p : F_{16}CuPc ratio of 1 : 2 and 1 : 1, respectively. On further increasing the 6p : F_{16}CuPc molecular ratio to 3 : 1, unidirectionally aligned F_{16}CuPc chain arrays separated by a 6p triplet are formed. By simply changing the relative ratio of the mixed components, molecular arrays with tunable intermolecular distances can be realized. On replacing the building blocks of 6p with pentacene or DIP, tunable molecular networks on HOPG can also be realized by manipulating the relative molecular ratios. It is found that the structural stability of these molecular networks is sustained by the multiple intermolecular C–F$\cdots$H–C hydrogen bonding between the electronegative periphery F atoms of F_{16}CuPc and the electropositive periphery H atoms of the 6p, pentacene and DIP. Notably, the desired functionality can be introduced into these supramolecular networks by using functional phthalocyanines such as polar phthalocyanines.[46]

3.3.2.2 *Metal–Organic Coordination Networks on Surfaces*

Metal coordination bonds have stronger bond strength than the hydrogen bonds. Two-dimensional nanoporous networks with designed size and chemical properties can be tailored by selecting suitable molecular building blocks and coordinated metal atoms.[47] K. Kern, J. V. Barth, N. Lin, and coworkers pioneered studies on metal–organic coordination networks (MOCNs). One example of MOCNs consisting of tailored pore sizes and chemical functionality is constructed by the modular assembly of polytopic

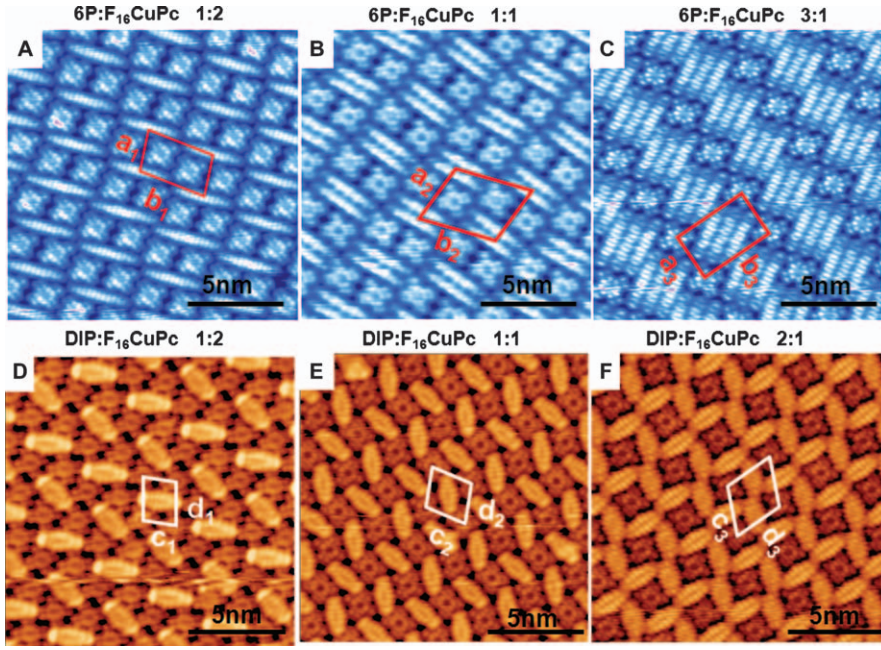

Figure 3.7 (A)–(C) Molecularly resolved 15×15 nm^2 STM images of F_{16}CuPc molecular dot arrays with tunable intermolecular distance controlled by the coverage of 6P, the relative ratio 6P : F_{16}CuPc is 1 : 2, 1 : 1 and 3 : 1 from left to right, respectively. (D)– (F) Molecularly resolved 15×15 nm^2 STM images of the F_{16}CuPc molecular dot arrays with tunable density controlled by the coverage of DIP. The ratio DIP : F_{16}CuPc is 1 : 2, 1 : 1 and 2 : 1 for (D), (E) and (F) respectively. The leaf-like bright feature represents a DIP molecule.
Figures reprinted from ref. 21, with permission from John Wiley & Sons, copyright 2010.

organic carboxylate linker molecules with iron atoms on Cu(100) under ultrahigh-vacuum conditions.[48] The linker molecules used are 1,4-dicarboxylic-benzoic acid (terephthalic acid, TPA), and 4,1,4′,1″-terphenyl-1,4″-dicarboxylic acid (TDA) (Figure 3.8). Both molecules strongly interact with Cu(100) and possess a different registry with Cu(100) substrate. This can also lead to the varied bonding configuration of the functional groups to Fe atoms, thereby resulting in the formation of 2D porous networks with distinct shapes and cavities sizes (Figure 3.8A–C). It is well known that carbonitrile groups can strongly coordinate to various transition metal atoms. They are promising candidates for the fabrication of MOCNs. As shown in Figure 3.8(D)–(F), ditopic molecules with same functional carbonitrile end group, but with different lengths varying from 1.66 to 2.09 to 2.53 nm, can be used to construct the 2D MOCNs networks with tunable honeycomb nanocavities on Ag(111).[47]

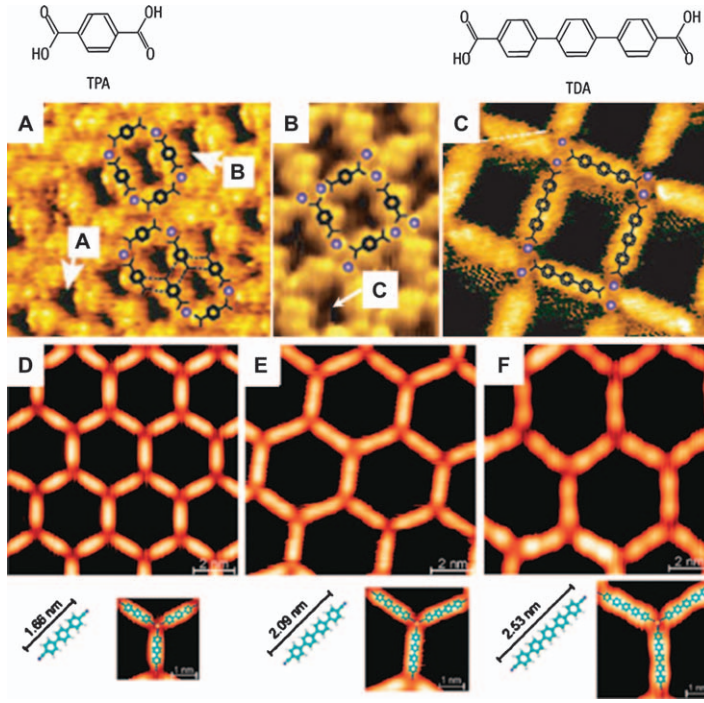

Figure 3.8 Top: molecular structure of terephthalic acid (TPA) and 4,1′,4′,1″-terphenyl-1,4″-dicarboxylic acid (TDA). STM images: (A) high-resolution image (6.5×7 nm^2) of ladder-type structures with two distinct types of nanocavities (marked by A and B). (B) STM image (4×7 nm^2) of fully interconnected network with complete 2D reticulation, giving rise to square cavities (marked by C). (C) High-resolution image (10×9 nm^2) of 2D reticulated Fe-TDA open network with rectangular nanocavities. Positioning of molecular backbone and ligands are marked; Fe atoms are shown as blue spheres.[48] (D)–(F) Tuning the cavity size of metal–organic honeycomb networks with designed linkers. STM images show the result of cobalt (Co)-directed assembly of (D) NC-Ph_3-CN, (E) NC-Ph_4-CN and (F) NC-Ph_5-CN on Ag(111). Bottom: structure of the molecules in (D)–(F) including their length and models of the threefold Co-carbonitrile coordination motif resolved.[47]
(A)–(C) Reprinted from ref. 48, with permission from Nature Publishing Group, copyright 2004; (D)–(F) reprinted from ref. 47, with permission from American Chemical Society, copyright 2007.

3.3.3 On-Surface Covalent-Bonded Molecular Networks

Recently, intensive research efforts have been focused on the rational fabrication of covalently interlinked molecular superstructures with good thermal and chemical stability and enhanced electrical conductivity.[6] Generally, on-surface polymerization can proceed based on several chemical reactions, including Ullmann coupling, alkyne homocoupling, imine coupling, dehydrogenation, and Bergman cyclization.[49–52] However, in many

cases, multiple bonding sites and energetically-equivalent bonding configurations always coexist and compete with each other, thereby leading to the formation of disordered molecular networks.[51] To fabricate highly ordered 2D covalently bonded molecular networks, molecular precursors or monomers must couple with each other through well-defined binding sites with high selectivity and arrange themselves in a highly ordered bonding configuration.

Two different approaches can be adopted to achieve controlled surface-assisted polymerization to form long-range ordered covalently bonded 2D networks:

1. error correction and surface-assisted crystallization after the covalent bond formation between monomers to achieve well-ordered 2D polymers, such as graphene growth on Cu(111) assisted by Ullmann coupling of hexabromobenzene (HBB);[53]
2. a stepwise process involving molecular building blocks pre-organizing into well-ordered 2D networks steered by non-covalent interactions, followed by polymerization within such 2D molecular networks initiated by heating or photo-irradiation, such as the surface-assisted cyclodehydrogenation of polyphenylene, which can provide tailored nanographene on Cu(111).[54]

In 2007, L. Grill and co-workers demonstrated the fabrication of 2D networks through covalent coupling of the bromine-terminated porphyrin molecules.[29] After that, on-surface polymerization has attracted increasing attention and is growing rapidly with the blooming of various reaction routes. Five years later, the same group presented the control of on-surface polymerization in a hierarchical manner by selective and sequential activation of specific sites under different substrate temperatures.[55] Furthermore, additional control of the preferred molecular orientation during the hierarchical growth can be achieved on an anisotropic template of Au(100). The molecular building block consists of a central porphyrin bonded with two bromine and two iodine substituents, *i.e.*, bis(4-bromophenyl) and bis(4-iodophenyl), in a linear *trans* configuration (Figure 3.9A). Notably, the bromine- and iodine-phenyl groups have different bond dissociation energies, thereby enabling stepwise dissociation of the two substituents under different substrate temperatures. Ideally, after deposition onto the surface, the molecules remain intact and leave the four halogen atoms arranged as shown in Figure 3.9(C). Heating the as-deposited molecules to 120 °C leads to the release of iodine atoms, and hence linear chains of the porphyrin molecules are created, leaving the bromine groups intact (Figure 3.9D). Further heating to at least 200 °C can result in the formation of networks, and hence the chains are connected into two-dimensional superstructures after the release of the bromine atoms (Figure 3.9E).

The as-constructed structures always exhibit disordering and broad size distribution on the surface.[55] So a template synthesis would be of great

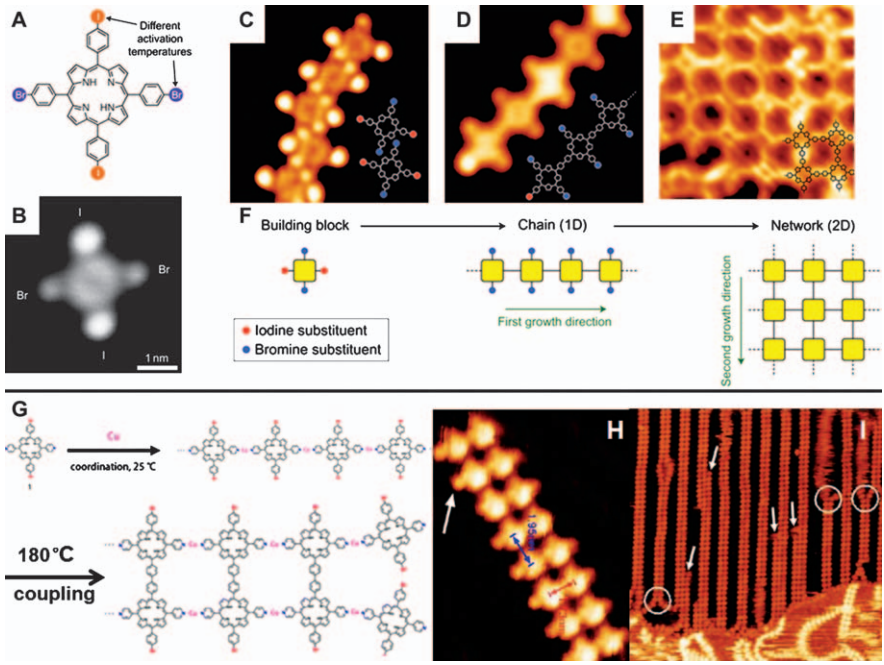

Figure 3.9 (A) Chemical structure of the *trans*-Br_2I_2TPP molecules; bromine (blue) and iodine (red) leaving groups have different activation temperatures. (B) STM image ($V = 0.5$ V, $I = 0.1$ nA) of a single *trans*-Br_2I_2TPP molecule on Au(111). (C)–(E) STM images of *trans*-Br_2I_2TPP molecules on Au(111): as deposited molecules at 80 K (8×8 nm^2, C), after heating the as-deposited molecules to 120 °C (8×8 nm^2, D, Step 1), and after further heating to 250 °C (10×10 nm^2, E, Step 2) (imaging at 180 °C). The corresponding chemical structures are indicated. (F) Scheme of the sequential activation mechanism. Green arrows indicate the different growth directions of the two sequential steps. (G) Schematic representation of Ullmann coupling of porphyrin derivate on Ag(111) assisted by the py–Cu–py coordination template. (H) High-resolution STM topograph (13×17n m^2) of a DR chain. (I) Uniformly distributed molecular chains on Ag(111) (100×100 nm^2).
(A)–(F) Reprinted from ref. 55, with permission from Nature Publishing Group, copyright 2012; (G)–(I) reprinted from ref. 56 with permission from American Chemical Society, copyright 2013.

interest to direct the ordering of the structures. In general, the template synthesis involves two steps: (i) the formation of non-covalently bonded molecular networks and (ii) activation and hence covalent bond formation under controlled conditions. Steering the on-surface polymerization has been achieved for the formation of porphyrin networks with a narrow size distribution based on a metal-directed template.[56] As reported by Lin and coworkers, the formation of Cu-pyridyl metal–ligand coordination networks can serve as template to steer the on-surface polymerization of porphyrin molecules on Au(111). The double row (DR) chain is developed from a

dimeric molecular seed step by step *via* the formation of py-Cu-py coordination. In an intermediate state, the Br groups of two anchored molecules are close enough to facilitate the Ullmann coupling. The deposited Cu atoms both serve as the catalysts in the Ullmann reaction and as the template to link the molecule together. Most of the products are DR chains with very smooth edges, which can be ascribed to preferable attachment of monomer at the end of an existing chain (Figure 3.9H and I).

It is worth mentioning that the structure of these 2D polymerized networks strongly depends on the coupling strength between the molecular precursors and the metal substrates, and the precursor mobility on different substrates.[57] For example, surface-assisted polymerization of the hexaiodo-substituted macrocycle cyclohexa-*m*-phenylene (CHP) on the Cu(111), Au(111) and Ag(111) surface has been systematically studied through the combination of STM, XPS measurements and DFT calculations.[57] It is found that on Cu(111) the molecular precursors of CHP strongly couple with the Cu substrate with very limited precursor mobility and hence ''open'' branched and disordered networks dominate; on Au(111), CHP weakly interacts with the Au substrate, thereby leading to the coexistence of the branched and small domains of compact networks; highly ordered and densely packed polyphenylene networks can only be formed on Ag(111). For a particular surface-assisted polymerization to form highly ordered 2D molecular networks, it is necessary to choose a suitable metal substrate that can effectively couple with the molecular precursor with an intermediate binding strength to initiate surface polymerization and covalent bond formation; meanwhile, the molecular precursors should have sufficient diffusion or mobility on the metal surface to couple with neighboring molecular precursors or networks in a highly ordered manner and with high selectivity.

3.4 Conclusion

In summary, molecular self-assembly on surfaces to form well-defined low-dimensional molecular superstructures is one of the promising approaches to construct molecular nanodevice arrays. These low-dimensional molecular nanostructure arrays can be fabricated by using well-defined 2D templates, or steered *via* various intermolecular non-covalent interactions (intermolecular hydrogen bonding, metal–ligand interaction) and even surface-assisted covalent bonding. It is found that the assembly of 1D molecular chains and 2D molecular networks with desired structures and functionalities strongly relies on the selected molecular building blocks, substrates and growth conditions. The realization of these well-defined molecular nanostructure arrays with desired functionalities over macroscopic area requires a comprehensive understanding of the underlying mechanisms governing the self-assembly processes.

One of the challenges to realize functional molecular electronics and organic nanodevices is how to integrate individual molecular nanostructures into extended circuits with high precision, great reproducibility, as well as

ease of device fabrication. Covalently bonded molecular nanostructures (*e.g.*, molecular wires) and carbon-based nano-architectures (*e.g.*, graphene nanoribbons) are promising candidates as electrical interconnecting wires to integrate functional molecules into extended device circuits over macroscopic area. It is highly desirable to have direct covalent bonding between the molecules, molecular wires and the electrodes, giving rise to efficient charge transport as well as good structural and chemical stability. By combing with graphene-based electrodes, it should be possible to construct all-carbon based devices in the near future.

Acknowledgement

The authors acknowledge the support by Singapore MOE grant R143-000-559-112.

References

1. E. Lortscher, *Nature Nanotechnol.*, 2013, **8**, 381.
2. S. V. Aradhya and L. Venkataraman, *Nature Nanotechnol.*, 2013, **8**, 399.
3. E. Lortscher, *Nature Nanotechnol.*, 2013, **8**, 381.
4. J. L. Zhang, T. C. Niu, A. T. S. Wee and W. Chen, *Phys. Chem. Chem. Phys.*, 2013, **15**, 12414.
5. J. C. Love, L. A. Estroff, J. K. Kriebel, R. G. Nuzzo and G. M. Whitesides, *Chem. Rev.*, 2005, **105**, 1103.
6. J. W. Colson and W. R. Dichtel, *Nature Chem.*, 2013, **5**, 453.
7. T. C. Tseng, C. Urban, Y. Wang, R. Otero, S. L. Tait, M. Alcami, D. Ecija, M. Trelka, J. M. Gallego, N. Lin, M. Konuma, U. Starke, A. Nefedov, A. Langner, C. Woll, M. A. Herranz, F. Martin, N. Martin, K. Kern and R. Miranda, *Nature Chem.*, 2010, **2**, 374.
8. P. Han and P. S. Weiss, *Surf. Sci. Rep.*, 2012, **67**, 19.
9. Y. F. Yao, H. L. Dong and W. P. Hu, *Polym. Chem.*, 2013, **4**, 5197.
10. A. Nitzan and M. A. Ratner, *Science*, 2003, **300**, 1384.
11. L. Lafferentz, F. Ample, H. Yu, S. Hecht, C. Joachim and L. Grill, *Science*, 2009, **323**, 1193.
12. W. D. Xiao, P. Ruffieux, K Aït-Mansour, O. Gröning, K. Palotas, W. A. Hofer, P. Gröning and R. Fasel, *J. Phys. Chem. B*, 2006, **110**, 21394.
13. H. Bulou and C. Goyhenex, *Phys. Rev. B*, 2002, **65**, 045407.
14. R. Gaspari, C. A. Pignedoli, R. Fasel, M. Treier and D. Passerone, *Phys. Rev. B*, 2010, **82**, 041408(R).
15. M. E. Canas-Ventura, W. Xiao, D. Wasserfallen, K. Mullen, H. Brune, J. V. Barth and R. Fasel, *Angew. Chem. Int. Ed.*, 2007, **46**, 1814.
16. M. E. Moyen, G. Agnus, A. Fleurence, T. Maroutian, F. Houze, A. Stupakiewicz, L. Masson, B. Bartenlian, W. Wulfhekel, P. Beayvillain and M. Hanbucken, *Appl. Phys. Lett.*, 2009, **94**, 233101.
17. V. Repain, G. Baudot, H. Ellmer and S. Rousset, *EPL (Europhys. Lett.)*, 2002, **58**, 730.

18. Y. Zhang, S. Du and H. J. Gao, *Phys. Rev. B*, 2011, **84**, 125446.
19. L. Z. Zhang, Z. H. Cheng, Q. Huan, X. B. He, X. Lin, L. Gao, Z. T. Deng, N. Jiang, Q. Liu, S. X. Du, H. M. Guo and H. J. Gao, *J. Phys. Chem. C*, 2011, **115**, 10791.
20. Y. Tanaka, P. Mishra, R. Tateishi, N. T. Cuong, H. Orita, M. Otani, T. Nakayama, T. Uchihashi and K. Sakamoto, *ACS Nano*, 2013, **7**, 1317.
21. Y. L. Huang, W. Chen, H. Li, J. Ma, J. Pflaum and A. T. S. Wee, *Small*, 2010, **6**, 70.
22. J. V. Barth, J. Weckesser, C. Cai, P. Günter, L. Bürgi, O. Jeandupeux and K. Kern, *Angew. Chem. Int. Ed.*, 2000, **39**, 1230.
23. J. Schnadt, E. Rauls, W. Xu, R. T. Vang, J. Knudsen, E. Laegsgaard, Z. Li, B. Hammer and F. Besenbacher, *Phys. Rev. Lett.*, 2008, **100**, 046103.
24. D. Kühne, F. Klappenberger, R. Decker, U. Schlickum, H. Brune, S. Klyatskaya, M. Ruben and J. V. Barth, *J. Am. Chem. Soc.*, 2009, **131**, 38813.
25. N. Lin, S. Stepanow, M. Ruben and J. V. Barth, *Top. Curr. Chem.*, 2009, **287**, 1.
26. S. L. Tait, A. Langner, N. Lin, S. Stepanow, C. Rajadurai, M. Ruben and K. Kern, *J. Phys. Chem. C.*, 2007, **111**, 10982.
27. D. Heim, K. Seufert, W. Auwarter, C. Aurisicchio, C. Fabbro, D. Bonifazi and J. V. Barth, *Nano Lett.*, 2010, **10**, 122.
28. T. Classen, G. Fratesi, G. Costantini, S. Fabris, F. L. Stadler, C. Kim, S. de Gironcoli, S. Baroni and K. Kern, *Angew. Chem. In. Ed.*, 2005, **44**, 6142.
29. L. Grill, M. Dyer, L. Lafferentz, M. Persson, M. V. Peters and S. Hecht, *Nature Nanotechnol.*, 2007, **2**, 687.
30. L. Lafferentz, F. Ample, H. Yu, S. Hecht, C. Joachim and L. Grill, *Science*, 2009, **323**, 1193.
31. J. A. Lipton-Duffin, J. A. Miwa, M. Kondratenko, F. Cicoira, B. G. Sumpter, V. Meunier, D. F. Perepichka and F. Rosei, *Proc. Natl. Acad. Sci. U.S.A.*, 2010, **107**, 11200.
32. A. Gourdon, *Angew. Chem. Int. Ed.*, 2008, **47**, 6950.
33. S. Haq, F. Hanke, M. S. Dyer, M. Persson, P. Iavicoli, D. B. Amabilino and R. Raval, *J. Am. Chem. Soc.*, 2011, **133**, 12031.
34. S. Mohnani and D. Bonifazi, *Coord. Chem. Rev.*, 2010, **254**, 2342.
35. D. M. Bassani, L. Jonusauskaite, A. Lavie-Cambot, N. D. McClenaghan, J. L. Pozzo, D. Ray and G. Vives, *Coord. Chem. Rev.*, 2010, **254**, 2429.
36. T. Kudernac, S. B. Lei, J. A. A. W. Elemans and S. De Feyter, *Chem. Soc. Rev.*, 2009, **38**, 402.
37. I. Fernandez-Torrente, S. Monturet, K. J. Franke, J. Fraxedas, N. Lorente and J. I. Pascual, *Phys. Rev. Lett.*, 2007, **99**, 176103.
38. S. Lukas, G. Witte and Ch. Wöll, *Phys. Rev. Lett.*, 2001, **88**, 028301.
39. F. S. Tautz, *Prog. Surf. Sci.*, 2007, **82**, 479.
40. A. T. S. Wee and W. Chen, *Phys. Scr.*, 2012, 014007.
41. Y. L. Huang, W. Chen, S. Chen and A. T. S. Wee, *Appl. Phys. A*, 2008, **95**, 107.
42. H. Huang, W. Chen and A. T. S. Wee, *J. Phys. Chem. C*, 2008, **112**, 14913.

43. K. H. L. Zhang, H. Li, H. Y. Mao, H. Huang, J. Ma, A. T. S. Wee and W. Chen, *J. Phys. Chem. C*, 2010, **114**, 11234.
44. Y. L. Huang, H. Li, J. Ma, H. Huang, W. Chen and A. T. S. Wee, *Langmuir*, 2010, **26**, 3329.
45. C. A. Palma, J. Bjork, M. Bonini, M. S. Dyer, A. Llanes-Pallas, D. Bonifazi, M. Persson and P. Samori, *J. Am. Chem. Soc.*, 2009, **131**, 13062.
46. Y. L. Huang, Y. Lu, T. C. Niu, H. Huang, S. Kera, N. Ueno, A. T. S. Wee and W. Chen, *Small*, 2012, **8**, 1423.
47. U. Schlickum, R. Decker, F. Klappenberger, G. Zoppellaro, S. Klyatskaya, M. Ruben, I. Silanes, A. Arnau, K. Kern, H. Brune and J. V. Barth, *Nano Lett.*, 2007, **7**, 3813.
48. S. Stepanow, M. Lingenfelder, A. Dmitriev, H. Spillmann, E. Delvigne, N. Lin, X. B. Deng, C. Z. Cai, J. V. Barth and K. Kern, *Nature Mater.*, 2004, **3**, 229.
49. G. Otero, G. Biddau, C. Sánchez-Sánchez, R. Caillard, M. F. López, C. Rogero, F. J. Palomares, M. A. Basanta, J. Ortega, J. Méndez, A. M. Echavarren, R. Pérez, B Gómez-Lor and J. A. Martín-Gago, *Nature*, 2008, **454**, 865.
50. J. Cai, P. Ruffieux, R. Jaafar, M. Bieri, T. Braun, S. Blankenburg, M. Muoth, A. P. Seitsonen, M. Saleh, X. Feng, K. Müllen and R. Fasel, *Nature*, 2010, **466**, 470.
51. Y. Q. Zhang, M. Kleinschrodt, K. Diller, S. Fischer, A. C. Parageorgiou, F. Allegretti, J. Bjork, S. Klyatskaya, F. Klappenberger, M. Ruben and J. V. Barth, *Nature Commun.*, 2012, **3**, 1286.
52. D. Y. Zhong, J. H. Franke, S. K. Podiyanachari, T. Blomker, H. M. Zhang, G. Kehr, G. Erker, H. Fuchs and L. F. Chi, *Science*, 2011, **334**, 213.
53. L. Jiang, T. C. Niu, X. Q. Lu, H. L. Dong, W. Chen, Y. Q. Liu, W. P. Hu and D. B. Zhu, *J. Am. Chem. Soc.*, 2013, **135**, 9050.
54. M. Treier, C. A. Pignedoli, T. Laino, R. Rieger, K. Müllen, D. Passerone and R Fasel, *Nature Chem.*, 2011, **3**, 61.
55. L. Lafferentz, V. Eberhardt, C. Dri, C. Africh, G. Comelli, F. Esch, S. Hecht and L. Grill, *Nature Chem.*, 2012, **4**, 215.
56. T. Lin, X. S. Shang, J. Adisoejoso, P. N. Liu and N. Lin, *J. Am. Chem. Soc.*, 2013, **135**, 3576.
57. N. M. Bieri, M. T. Nguyen, O. Groning, J. Cai, M. Treier, K. A. Mansour, P. Ruffieux, C. A. Pignedoli, D. Passerone, M. Kastler, K. Müllen and R. Fasel, *J. Am. Chem. Soc.*, 2010, **132**, 16669.
58. J. Schnadt, W. Xu, R. T. Vang, J. Knudsen, Z. Li, E. Lægsgaard and F. Besenbacher, *Nano Res.*, 2010, **3**, 459.

CHAPTER 4

Self-Assembled Mono- and Multilayers for Functional Opto-Electronic Devices

ANTONIO FACCHETTI,* ROCIO PONCE ORTIZ AND TOBIN J. MARKS

Polyera Corporation, Northwestern University and University of Malaga,
*Email: afacchetti@polyera.com

4.1 Introduction

Organic electronics envisions the fabrication of new opto-electronic devices using as a prime material an organic semiconductor to modulate charge transport or process light.[1] This approach may enable the fabrication of low cost, lightweight, mechanically flexible opto-electronic devices on plastic substrates and eventually using roll-to-roll printing methodologies. All of these devices have a primary materials set enabling specific functions. Furthermore, opto-electronic device performance and lifetime strongly depends on functional interfaces affecting charge exchange, controlling light confinement, enabling efficient adhesion among the different layers, as well as determining rheological parameters (viscosity, surface energy, wettability) for device fabrication if carried out from solution. In this chapter we will describe the utilization of self-assembled monolayers (SAMs) and multilayers (SAMTs) as key elements for the realization of opto-electronic devices such as organic field-effect transistors (OFETs), organic photovoltaic cells (OPVs), organic light-emitting diodes (OLEDs), and organic nonlinear

RSC Smart Materials No. 12
Supramolecular Materials for Opto-Electronics
Edited by Norbert Koch

Published by the Royal Society of Chemistry, www.rsc.org

optical devices such as electro-optic (EO) modulators.[2] First, we will describe the process of self-assembly and the most relevant families of self-assembly precursors (surfactants) for opto-electronics. Next, we focus on describing their utilization at important device interfaces such as cathode/photoactive layer and anode/photoactive layer for OPVs and OLEDs, source–drain/semiconductors and dielectric/semiconductors for OFETs, as well as acting as the major semiconductor/dielectric/NLO element for OFETs or NLO applications.

4.2 Concepts of Molecular Self-Assembly for Mono- and Multilayer Fabrication and Function

An example of the general phenomenon of self-assembly is the fabrication of monolayers (SAMs) and, upon consecutive processes, multilayers (SAMTs) by self-assembly of surfactant molecules on solid surfaces. Self-assembly in Nature occurs in supermolecular hierarchical organizations of interlocking components resulting in very complex systems.[3,4] These assemblies offer unique opportunities to increase fundamental understanding of self-organization, structure–property relationships, interfacial phenomena as well as implementation in new functional devices. Furthermore, SAMs and SAMTs are well-defined structures, which make them excellent models for interdisciplinary studies at the interface of chemistry with physics, biology, and engineering. In addition, the possibility of tailoring both head and tail groups of the constituent molecules makes SAMs excellent systems for fundamental studies of phenomena affected by competing intermolecular, molecular-substrates, and molecule–solvent interactions such as ordering and growth, wetting, adhesion, lubrication, and corrosion as well as how the electronic structure of molecules changes at the interface.

SAMs and SAMTs can be defined as ordered molecular assemblies enabled by the adsorption of an active surfactant on a solid surface (Figure 4.1). SAMT fabrication requires the presence of two functional end groups, typically with complementary chemistries, so that the layer-by-layer process can

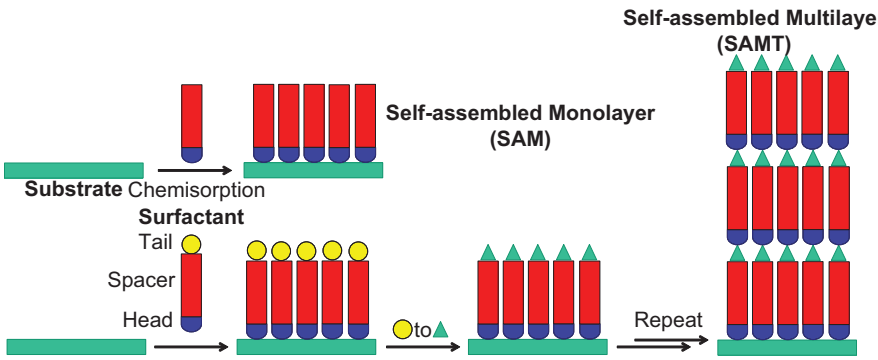

Figure 4.1 Schematic representation of the SAM and SAMT fabrication process.

be repeated consecutively. The order in these two-dimensional systems is produced by a spontaneous chemical synthesis at the interface, as the system approaches equilibrium. These simple processes make SAMs/SAMTs inherently manufacturable and thus technologically attractive for surface engineering in various modern devices. There are several classes of molecules able to self-assemble on metal and metal oxide surfaces but here we discuss selected studies related to chemistries relevant to opto-electronic devices described in the next section. Although the area is not limited to long-chain molecules,[5] SAMs of functionalized long-chain hydrocarbons have been most frequently used as building blocks of supermolecular structures.

Silane-derived SAMs are amongst the most used since they are physically and chemically robust and they self-assemble on common substrates, such as silicon and glass. The reactions of molecules functionalized with chlorosilanes, alkoxysilanes, and aminosilanes occur on hydroxylated surfaces as substrates (Figure 4.2). The driving force for this self-assembly is the *in situ* formation of polysiloxanes, which are connected to surface metal hydroxyl groups (-Met-OH) *via* Si-O-Met bonds. Examples of substrates on which these monolayers have been successfully prepared include silicon oxide,[6–11] aluminium oxide,[12,13] quartz,[14–16] glass,[17] mica,[18–20] zinc selenide,[21] and germanium oxide[22] as well as gold,[23–25] which can be activated by UV–ozone exposure.[26]

The most efficient way to fabricate SAMTs based on silanes is to create a monolayer surface terminated by hydroxyl groups. Once a subsequent monolayer is reacted on the ''activated'' monolayer, multilayer films may be built by repetition of this process (Figure 4.3). Such surfaces can be achieved in several ways such as reduction of a surface ester group with $LiAlH_4$,[27]

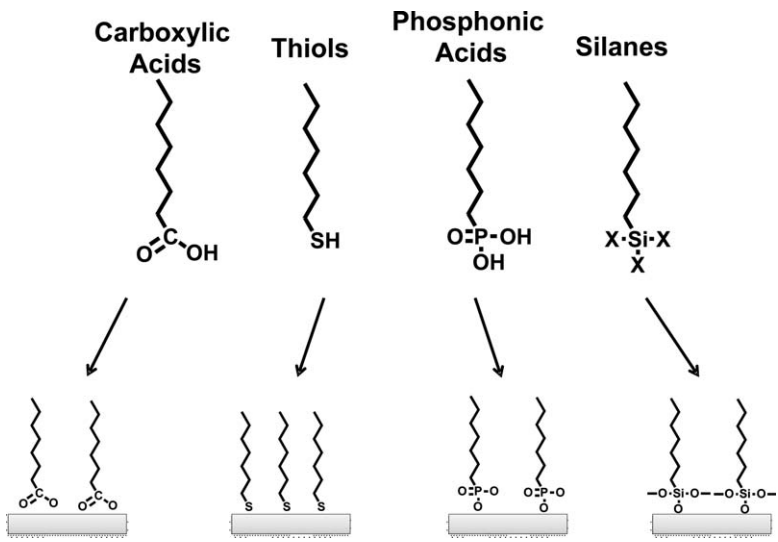

Figure 4.2 Chemical structure of alkyl chains functionalized with carboxylic, thiol, phosphonic acid and silane groups and representation of their self-assembly on substrate surfaces.

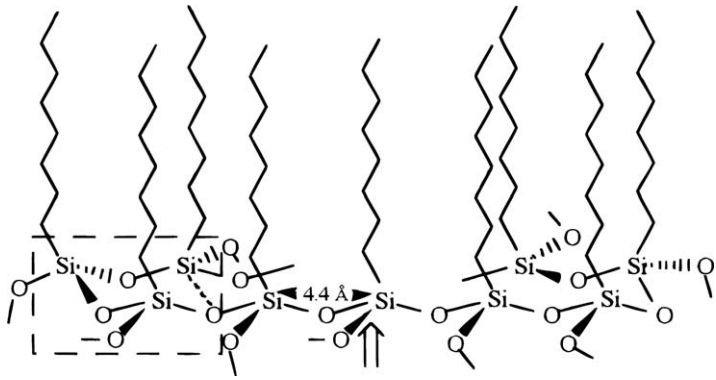

Figure 4.3 Schematic description of a polysiloxane at the monolayer–substrate surface. The arrow points to an equatorial Si–O bond that can be connected either to another polysiloxane chain or to the surface.

hydroboration–oxidation of a terminal vinyl group,[28,29] and reaction with alkyl bromides with silver chemistry.[30] Tillman *et al.* investigated the fabrication of multilayer films ~0.1 μm thick by self-assembly directly on silicon substrates.[31] A linear relationship between the film thickness and the layer number with a slope of 35 Å per layer was found. Ellipsometry data, optical absorbance intensities, and dichroic ratios for the multilayers all suggested that the samples were composed of distinct monolayers. However, IR data indicated that there may be more tilting or disordering of the alkyl chains in the seven-layer sample than for the monolayer samples. Marks *et al.* have demonstrated a SAMT strategy based on -$SiCl_3$-functionalized molecules and an S_N2 reaction for the preparation of SAMs with second harmonic nonlinear optical (NLO) properties.[32–36] The same group reported another major improvement as they found that spin coating of a dilute solution of [[4-[*N*,*N*-bis(3-hydroxypropyl)amino]phenyl]azo]-4-pyridine on a benzyl chloride SAM surface, followed by annealing at 110 °C, results in the facile formation of SAMs, with high order parameter. Using this process they could prepare a three-layer system in 1 h.[37] Finally, a major achievement from Sagiv *et al.* demonstrated hydrogen-bonded multilayers based on silane molecules.[38,39]

The initial studies involved aliphatic hydrocarbon silanes. However, the reproducibility of trichlorosilane-derived monolayers is a key issue since the quality of these films is very sensitive to the reaction conditions and solvent purity. For OTS (octadecyltrichlorosilane) the monolayer chemisorption formation time varied from 3 min [40] to 90 min[41] to over 24 h.[42] Studies affording different conclusions regarding film composition[43,44] and morphology[45–51] have been reported. Additional functionalities for the SAM as well as anchoring point for SAMT fabrication can be created using terminal-substituted alkyl silanes. Thus, SAMs terminated with halogens,[52–56] cyanide and thiocyanide,[57] methyl ether and acetate,[58] thioacetate,[59] vinyl,[60–69] (trimethylsilyl)-ethynyl,[70] methyl ester,[71,72] and *p*-chloromethylphenyl[73–77] have been

investigated. Monolayers with low surface free energies have also been prepared using partially fluorinated alkylsilanes.[78–81]

Another efficient way to fabricate SAMs and SAMTs is *via* precursors functionalized with groups forming insoluble salts on a given surface. Thus, phosphates react with tetravalent transition metal ions, affording very insoluble products.[82] Mallouk pioneered this area when discovering that self-assembled multilayers can be prepared simply by alternating adsorption of Zr^{4+} ions and α,ω-alkylidene diphosphate (1 in Figure 4.4) on a phosphorylated surface.[83] Other fundamental studies with these systems were carried out by Katz for NLO applications by using [[4-[bis(2-hydroxyethyl)amino]phenyl]azo]benzene phosphonate to form SAMs on zirconium-treated phosphorylated surfaces. Further reaction with $POCl_3$ and hydrolysis resulted in a new phosphorylated surface that could be treated with zirconium salt, and the process was repeated for SAMT fabrication.[84] The major advantage of the phosphate systems is in their high thermal stability, their simple preparation, the variety of substrates that can be used, and the stability of the precursor to water.

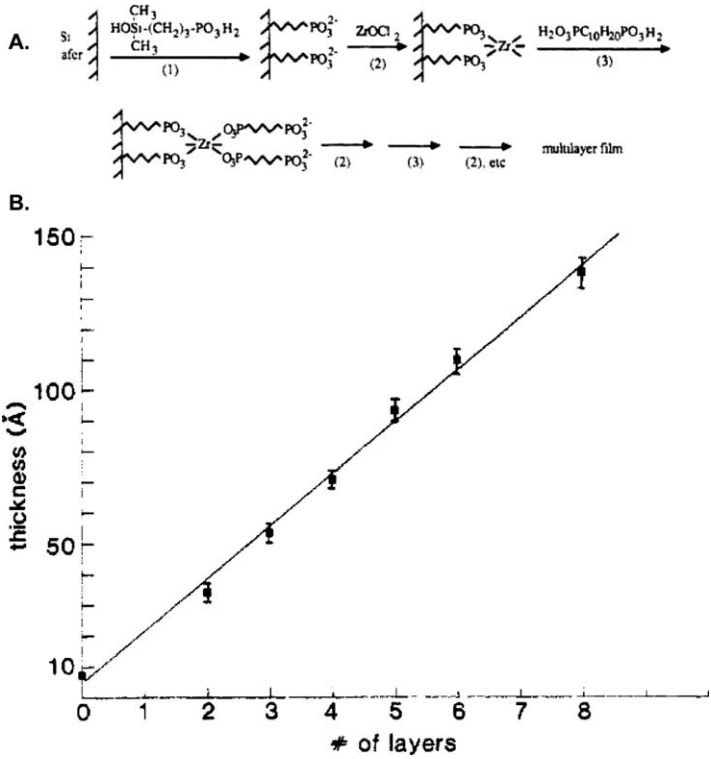

Figure 4.4 Different diphosphonic acids used in self-assembled multilayer preparation.
Reprinted with permission from ref. 83*a*. Copyright 1988 American Chemical Society.

Self-assembly chemistry based on sulfur compounds has been key to the development of this field of research and it is based on its strong affinity to late transition metal surfaces (Figure 4.5).[85–90] Several examples of functionalized molecules have been reported and include, among others, di-*n*-alkyl

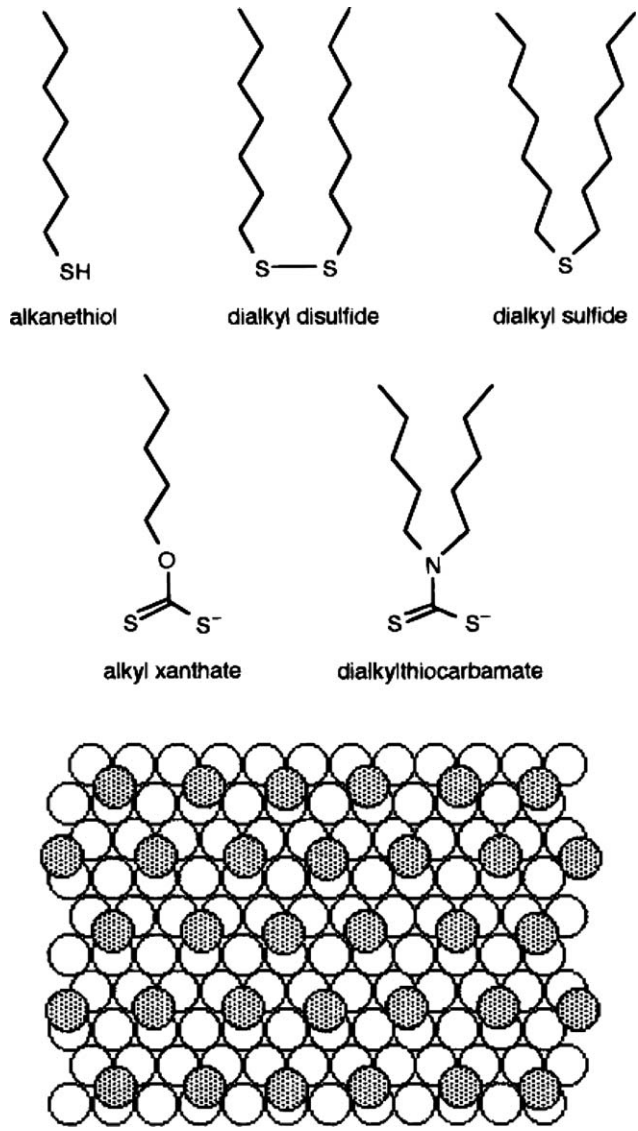

Figure 4.5 Top: chemical structure of organosulfur compounds that form monolayers on gold. Bottom: hexagonal coverage scheme for alkane thiolates on Au(111). The open circles are gold atoms and the shaded circles are sulfur atoms.
Adapted with permission from *Chemical Reviews* 1996, **96**, 1533. Copyright 1996 American Chemical Society.

sulfides,[91,92] di-*n*-alkyl disulfides,[93] thiophenols,[94,95] mercaptopyridines,[96] mercaptoanilines,[97] thiophenes,[98] cysteines,[99,100] xanthates,[101] thiocarbaminates,[102] thiocarbamates,[103] thioureas,[104] mercaptoimidazoles,[105–107] and alkaneselenols.[108] However, the most studied, and probably the best understood, SAM is that of alkane thiolates on Au(111) surfaces. Organosulfur compounds coordinate very strongly also to other relevant metals of the semiconductor industry including silver[109–113] and copper[114] as well as others such as platinum,[115] mercury,[116,117] iron,[118,119] colloidal gold particles,[120] GaAs,[121] and InP surfaces.[122] Important for charge injection, octadecanethiol monolayers provide excellent protection of the metal surface against oxidation.[123] For example, Ag coated with octadecane thiolate monolayers can be kept in ambient conditions without tarnishing for several months, and Cu coated with the same monolayer resists nitric acid.[124] Also important is the thermal stability of these functionalized metals. Thus, Hickman *et al.* have shown loss of sulfur from hexadecane thiolate monolayer on gold occurs over the range 170–230 °C.[125] They also investigated temperature-programmed desorption of methanethiolate SAMs on Au and reported a desorption maximum at ~220 °C,[126] which is similar to other studies.[127] However, loss can begin at as low as at ~100 °C.[128] Several studies also investigated the structure and stability of thiolate molecules on Ag(111).[129–131]

In another approach, Allara and Nuzzo[132] and Ogawa *et al.*[133] studied the adsorption of *n*-alkanoic acids on aluminium oxide, where the interactions are driven by an acid–base reaction. Schlotter *et al.* studied the spontaneous adsorption of such acids on silver.[134] Huang and Tao studied SAMs of long-chain diacetylene amphiphiles.[135] Finally, Linford and Chidsey demonstrated that robust monolayers can also be prepared where the alkyl chains are covalently bound to a silicon substrate mainly by C–Si bonds.[136] In the first experiments they used hydrogen-terminated silicon (H-Si(111) and H-Si(100)) and diacetyl peroxide.[144] Subsequent studies demonstrated various chemistries on hydrogen-terminated silicon surfaces (Figure 4.6).[137]

4.3 Applications of SAM and SAMT to Organic Opto-Electronic Devices

Electronic devices based on organic π-conjugated molecules and polymers, as well as other corollary materials, have been investigated to enable unique properties such as mechanical flexibility, light weight, new functionalities as well as reduce production costs. These devices include, but are not limited to, organic field-effect transistors (OFETs), organic light-emitting diodes (OLEDs), organic photovoltaics (OPVs), and organic electro-optic (EO) modulators.[138–148] OFETs will find applications in display backplanes and disposable electronics, such as sensors, smart cards (addressable identification (ID) and vending cards), and radio-frequency identification (RFID) tags. OLEDs are commercially available in flat/curved panel displays and will

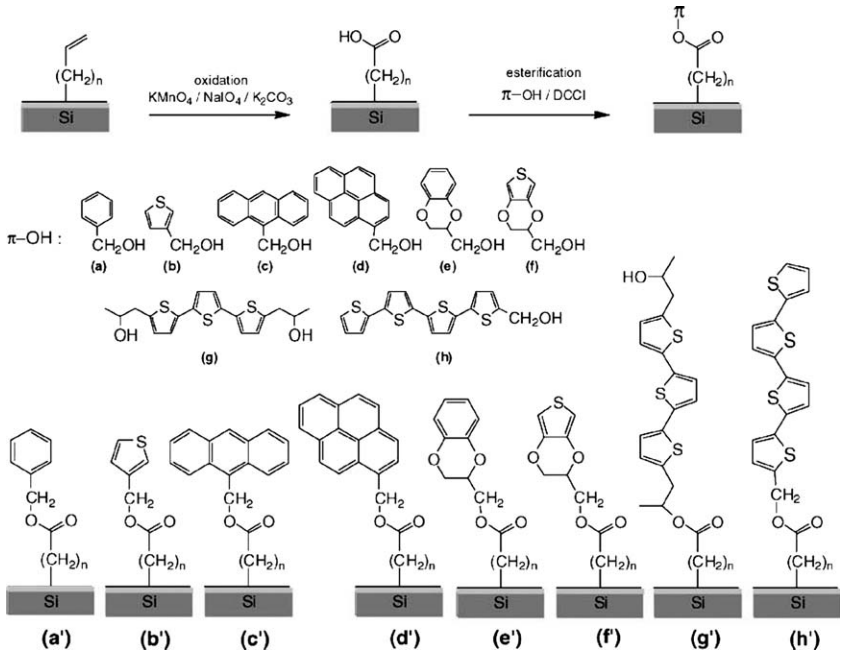

Figure 4.6 Synthesis of molecular diodes using sequential self-assembly along with the chemical structures of the alcohols used for SAM fabrication and schematic of the corresponding SAMs on silicon substrates.
Reprinted from ref. 137. Copyright 2006, with permission from Elsevier.

be used for solid-state lighting, 3D displays, and other appliances. Organic PV technologies will be part of the solution for the increased electrical energy demand as well as enable the fabrication of unique products by integrating energy production and electronics.

The performance and lifetime of every organic electronic device, which typically has a multilayer architecture, critically depend on both the photo-electro-active π-conjugated semiconductor, robustness of the other corollary materials, and quality of the interfaces. In these devices, metal electrodes are utilized to inject/extract charges into the organic semiconductor layer(s), polarize a dielectric, or apply an electric field (Figure 4.7). Particularly related to SAM functions, control over the interface properties between the π-conjugated organic semiconductor and the other materials is essential. This can vary from simple wettability or adhesion between different layers to tuning of the electronic structure of the material in the bulk or at the interfaces. For instance, factors such as the surface energy and work function greatly affect charge injection/extraction and transport in organic semiconductors.

Regarding field-effect transistors, interfaces (Figure 4.7A) play a crucial role in the overall device performance: the source/drain electrode/organic semiconductor interface influences charge carrier injection *via* modification of the semiconductor morphology on the electrode surface or *via* tuning of

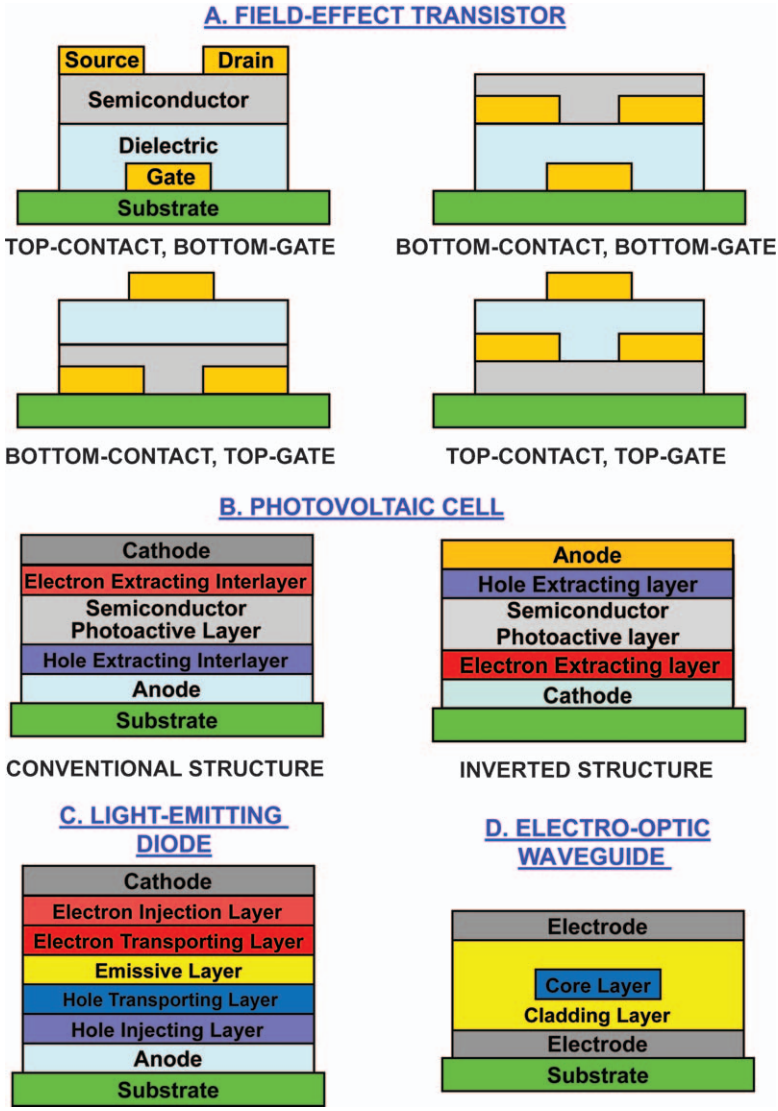

Figure 4.7 Structure of the indicated opto-electronic devices with indicated the most commonly used device architectures.

the electrode work function. The gate insulator/organic semiconductor interface is important for tuning the 2D charge transport *via* passivation of trap states, modification of the semiconductor morphology in the FET channel, as well as variation of the semiconductor electronic structure (density of states) *via* polarization effects. Several studies of dielectric interfacial effects focused on either chemically modifying the dielectric and source/drain electrode surfaces with self-assembled monolayers (SAMs) or

passivating the surface of the commonly used SiO_2 dielectric. Recently, gate dielectrics with excellent insulating and interfacial properties, such as organic/high-k metal oxide hybrid layers, SAM/SAMT, and ultrathin cross-linked polymers, have been used as alternatives to SiO_2 with great promise for low-voltage high performance OFETs.

Regarding bulk-heterojunction OPVs (Figure 4.7B), performance optimization requires control of charge transfer, charge transport, and carrier recombination in the photoactive semiconductor blend. The contact resistance between layers must be minimized to reduce the device series resistance, which is important in determining the fill factor and thus the power conversion efficiency. Furthermore, the effect of the electrode/organic interface on the film morphology and charge extraction/recombination is very important. Controlling the chemistry and physics of these interfaces can modulate the semiconductor/electrode energy level alignment, enhance charge extraction, tune light absorption, guide active layer morphology, tune charge trap states, tune the work functions of both anode and cathode to optimize the open circuit voltage, and ultimately allow the fabrication of high-efficiency OPV cells. Again, here SAMs/SAMTs have been fundamental for dramatic increases in performance.

To enable high-performance OLEDs a balanced hole/electron charge injection and transport must be achieved (Figure 4.7C). New materials can be developed to tune semiconductor electronic structure, charge transport, and emission color of the OLED; however, the interface modification between the organic semiconductors and the cathode/anode electrodes is critical to optimize charge-injection, -transport, and -recombination and to improve the OLED brightness and efficiency. A balanced charge injection requires the anode and cathode work functions to match the highest occupied molecular orbital (HOMO) and the lowest unoccupied molecular orbital (LUMO) levels of the hole transporting layer (HTL) and light-emitting layer (LEL), respectively. Finally, for electro-optic applications (Figure 4.6D), SAMs/SAMTs have been utilized as their fabrication enables the realization of intrinsically asymmetric layers – a prerequisite to EO activity.

In this section, we summarize the use of self-assembled mono- and multilayers as active materials and surface modifiers in various optoelectronic devices. We start with applications in organic FETs as semiconductors and dielectric materials as well as modifiers of the dielectric and the source/drain surfaces. Next, we move to applications in conventional and inverted OPV devices as charge extraction promoters. Finally, we briefly summarize their use in OLED interfaces and EO devices.

4.3.1 Organic Field-Effect Transistors

As discussed in the Introduction, OFETs will be used to fabricate new types of circuits, probably starting with flexible backplanes for electrophoretic displays. A typical thin-film transistor, which is the common OFET architecture, consists of three basic elements (Figure 4.7A): (1) an organic

semiconductor film, (2) an insulating/dielectric layer, and (3) three electrodes. Two electrodes, the source and the drain, are in direct contact with the semiconductor, whereas the third electrode, the gate, is separated from the semiconductor film by the dielectric layer. Figure 4.7(A) illustrates the typical OFET architectures. In this device the current flow between the drain and source electrodes (I_D) is modulated by the applied gate voltage (V_G). An ''off'' state of a transistor occurs when no gate voltage is applied between the gate and the source electrodes ($V_G = 0$ V). I_D is very low in the ''off'' state as long as the semiconducting material is not unintentionally doped. When a voltage is applied to the gate, charges are induced into the semiconducting layer at the interface between the semiconductor and dielectric layer. As a result of the increased number of charge carriers, the drain–source current increases, and this is called the ''on'' state of a transistor. Holes and electrons are the majority charge carriers for p-channel and n-channel transistors, respectively, whereas OFETs where both charges are mobiles are defined as ambipolar. The major performance parameters are the field-effect mobility (μ), the on/off ratio ($I_{on} : I_{off}$), and the threshold voltage (V_T). The field-effect mobility quantifies the average charge carrier drift velocity per unit electric field, the on/off ratio is defined as the drain–source current ratio between the ''on'' and the ''off'' states, whereas the V_T is the voltage after which the induced charges are mobile.[149–152]

Vuillaume and co-workers first investigated the use of SAMs as gate dielectric materials.[153] Octadecyltrichlorosilane (OTS) as well as olefin and carboxylate SAMs were then grafted onto the surfaces of p-doped Si substrates covered with a 1.0–1.5 nm-thick native oxide affording a $\sim$3 nm thick organic layer (Figure 4.8). This monolayer is as an excellent electrical insulator exhibiting a leakage current density of $\sim 10^{-8}$ A cm^{-2} at 5.8 MV cm^{-1}, which is $\sim$5 orders of magnitude lower than for bare substrates. Deep level transient spectroscopy (DLTS) was employed to estimate the SAM interface state density, which can be reduced by 10$\times$ (2×10^{11} cm^2 eV^{-1}) by annealing the film at 350 °C. Note that these films can be thermally stable up to 450 °C. The maximum measured film capacitance was

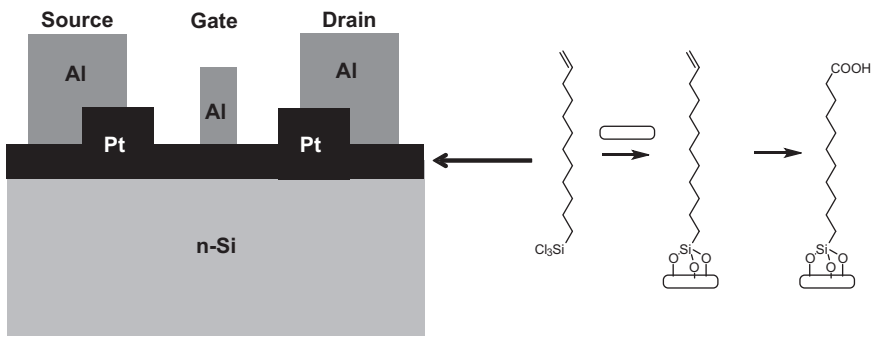

Figure 4.8 Schematic cross-section of the hybrid (organic SAM/silicon) nano-FET (not to scale) along with the chemistry for the grafting to the substrate.

found to be only $\sim$150 nF cm^{-2}, which is much lower than the theoretical capacitance value estimated by the OTS/native SiO_2 film thickness and the k values of an hydrocarbon (2.5) and SiO_x (3.9). Several reasons for the difference were offered by the authors (excessive leakage, series resistance, Fermi level pinning, maximum charge storage in ultra-thin films); however, none are sufficient to explain the difference. In a successive paper, the same group[154] investigated alkyl SAMs with various chain lengths (1.9–2.6 nm) and found that the conductivity ($\sim$ 4.6×10^{-15} S cm^{-1}) is independent of the film thickness and comparable to that of bulk polyethylene ($\sim2\times10^{-16}$ S cm^{-1}). This result differs from the tunneling-dominated thickness-dependence mechanism commonly observed in thiol-based ultra-thin organic films,[155] and it was explained by the independence of the tunneling barrier heights ($\Delta\approx4$ eV for both hole and electrons) from the film thickness.

The Vuillaume group also fabricated nm-scale (channel length = 30 nm) sexithiophene (**6T**)-based FETs using alkyl-carboxylate monolayers (2 nm thick) as gate insulators.[156] The FETs were fabricated with electron-beam lithography/lift-off techniques for the deposition of both metal electrodes and **6T**, whereas the gate insulator was deposited by dipping. These OFETs function at low voltages (<2 V) and exhibit $\mu\approx3.6\times10^{-4}$ cm^2 V^{-1} s^{-1}, $I_{on}:I_{off}$ ratio $\approx$ 10^4, and $V_T=-1.3$ V. The same group[157] also demonstrated that 1-octadecene monolayers deposited on hydrogenated n$^-$, p$^-$, and p$^+$-Si(111) substrates by a free radical reaction between the SAM precursor C = C bond and Si–H, activated by UV-illumination, are densely packed and can be good ultra-thin insulators. This approach allows characterization of a silicon/dielectric SAM layer without a native oxide layer. Although fluctuation of the leakage current from device to device was observed, the current densities were within 10^{-4}–10^{-7} A cm^{-2}. Note that the SAM on n$^+$-Si substrates was found to be more disordered and therefore exhibits larger leakage current densities in MIS capacitors. The inferior properties of the SAM on n$^+$-Si demonstrates the important role of the surface potential and of the Fermi level position of the surface during chemisorption of the alkyl monolayers.

Halik *et al*. studied SAM-based FETs using OTS molecules deposited on Si substrates from the vapor phase.[158] The FETs were fabricated using α,ω-dialkyl sexithiophenes with different chain lengths (alkyl = ethyl, hexyl, decyl, and H) as the organic semiconductor layer. The current densities in an MIS structure were found to be $\sim3\times10^{-5}$ A cm^{-2} at 1 V for the devices based on OTS + α,ω-didecylsexithiophene. FET devices based on these vapor-deposited SAMs function only when the **6T** alkyl chain is sufficiently long to increase the effective thickness of the dielectric. In the most successful case, a mobility of 0.05 cm^2 V^{-1} s^{-1} was measured. Thus, the authors concluded that these devices were limited by the large dielectric leakage, presumably because the vapor-deposited OTS SAM is more disordered than the film obtained by solution. A considerable improvement in performance was achieved when the SAM insulator contains an aromatic (phenoxy) group at the end of the alkyl chain (Figure 4.9).[159] This SAM was found to be tightly-packed due to intra-SAM π–π interactions among the phenyl end-

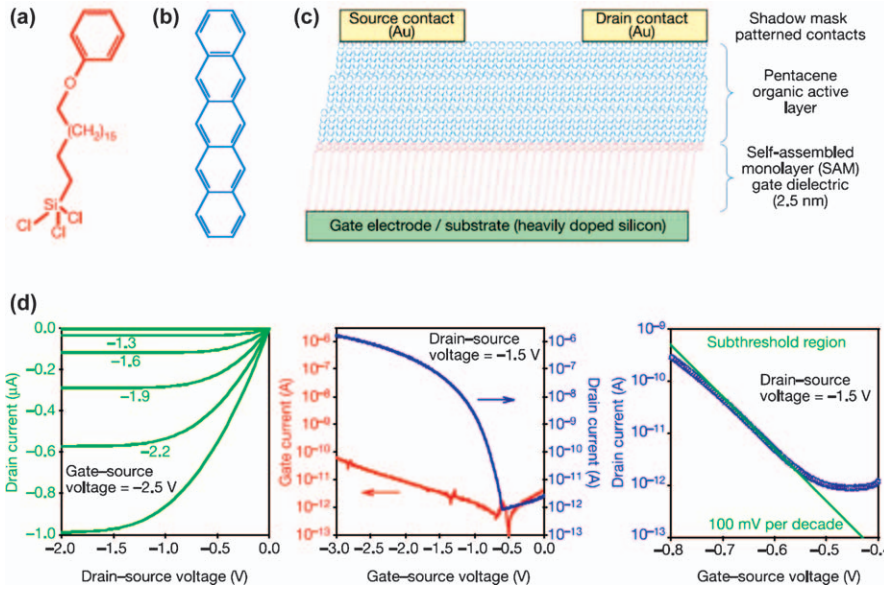

Figure 4.9 Chemical structures of the SAM precursor (a) and pentacene (b), and cross-section (c) and electrical characteristics (d) of a FET with molecular SAM gate dielectric.
Reprinted by permission from ref. 159. Macmillan Publishers Ltd: copyright 2004.

groups and exhibits very low leakage currents ($\sim 5\times10^{-7}$ A cm^{-2} at 1 V) and large breakdown fields ($\sim$14 MV cm^{-1}). A capacitance nearly 900 nF cm^{-2} was reported although it is not clear if this was a measured or an estimated value. Pentacene and diethyl-6T FETs (130 μm channel length, 170 μm channel width) were investigated and exhibit good response characteristics at low voltages (<2 V) with carrier mobilities as high as 1 and 0.2 cm^2 V^{-1} s^{-1}, respectively. The authors reported that attempts to fabricate pentacene FETs using simple alkyl SAMs failed, probably because of pentacene intercalation into the SAM layer.

Kobayashi *et al*. first investigated the use of organosilane self-assembled monolayers to control the charge density in the FET channel when using SiO_2 as the bulk gate insulator.[160] SAMs with fluorine and amino groups were found to accumulate holes and electrons in the transistor channel, respectively. These properties were explained in terms of the effect of the electric dipoles of the SAMs molecules, and weak charge transfer between organic films and SAMs. Three kinds of organosilane SAMs (Figure 4.10) were used. OFETs of n-channel C_{60} and p-channel pentacene were fabricated on top of the SAMs by molecular-beam deposition in a vacuum. The device properties were measured by three current/voltage probes *in situ* at 5×10^{-10} torr. The *I–V* characteristics clearly show that I_D and V_T strongly depend on the SAM type. For pentacene OFETs Figure 4.10 clearly shows that the $|I_D|$

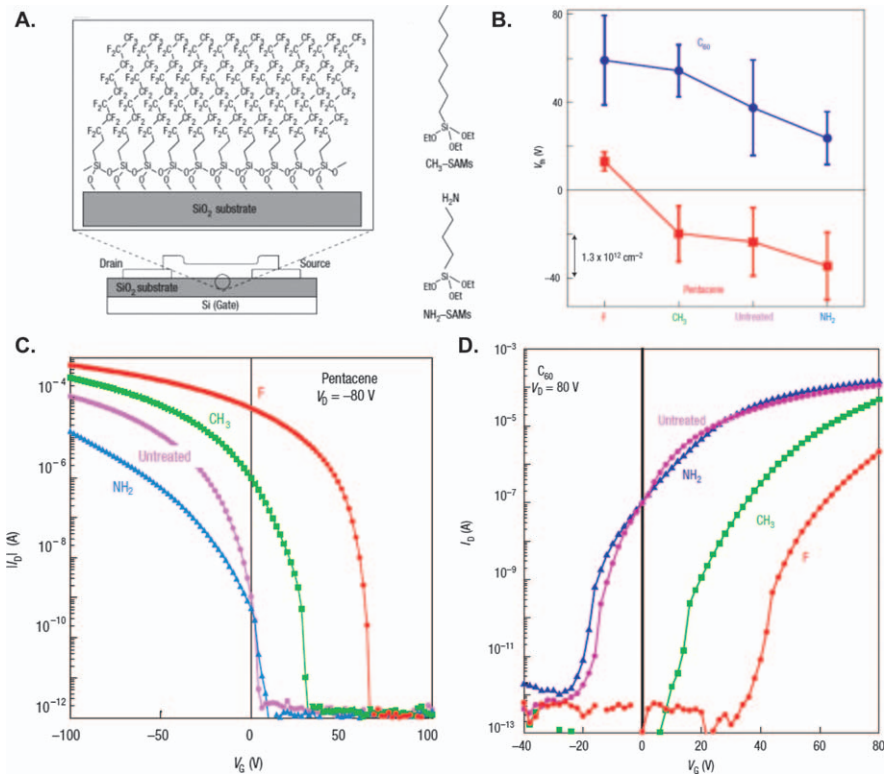

Figure 4.10 (A) FET structure and related SAMs molecules. (B) Summary of the threshold voltage V_T for the n-type C_{60} and p-type pentacene OFETs for different SiO_2 functionalizations. (C) and (D) Trans-conductance characteristics of pentacene and C_{60} devices grown on different SAMs. Reprinted from ref. 160 by permission from Macmillan Publishers Ltd.

values at $V_G = 0$ V are enhanced by six orders of magnitude in devices with F-SAMs compared with that of NH_2-SAMs, indicating that the surface carriers are significantly modulated by changing the SAMs molecules. Of particular interest is the change in V_T with the various SAM molecules shown in Figure 4.10. V_T shifts to positive values as the SAMs go from NH_2- through CH_3- to F-SAMs, associated with an increase in the mobility. The mobility of the device for the CH_3-SAMs is larger than that for the untreated device, in agreement with previous results for OTS treated pentacene FETs. Similar behavior was observed in the n-type C_{60} transistors. In this case, the drain current (I_D) for the NH_2-SAMs is the largest among SAMs-treated OFETs, in sharp contrast to the results of pentacene FETs (Figure 4.10), where F-SAMs showed the largest current. The V_Ts also change toward more negative values when going from F-SAM to NH_2 SAMs, tracking the I_D variations. The authors concluded that the ordering of SAMs molecules with molecular dipoles produces a built-in electric field across the OFET, which is

superimposed on the externally applied gate field. To rationalize the data the molecular dipoles of the SAMs orthogonal to the substrate surface were calculated by DFT and found as –2.202, +0.831, and –0.429 Debye, for fluoroalkyl-, alkyl- and aminoalkyl-silane molecules, respectively. This result indicates that F-SAMs, when molecules are uniformly aligned, generate the local electric field that accumulates holes in comparison to the CH_3-SAMs. This agrees fairly well with the experiments. On the other hand, the calculation of molecular dipoles has shown that the electron accumulation in NH_2-SAMs is not understood in terms of the dipole mechanism discussed above, as the calculated molecular dipole of NH_2-SAMs is rather small, and not pointing so as to accumulate electrons. Several explanations were offered for this inconsistency.

Our group first investigated self-assembled multilayers (SAMTs) as reliable dielectric materials for low-voltage OFETs.[161] These layers are now called self-assembled nanodielectrics (SANDs). This strategy utilizes 3D crosslinked SAMTs grown from solution *via* self-limiting sequential deposition of σ–π siloxane building blocks such as α,ω-difunctionalized hydrocarbon chains (Alk), and highly polarizable ''push–pull'' stilbazolium layers (Stb), and octachlorotrisiloxane capping layers (Cap; Figure 4.11). SAMTs having different architectures have been fabricated and are identified by the following

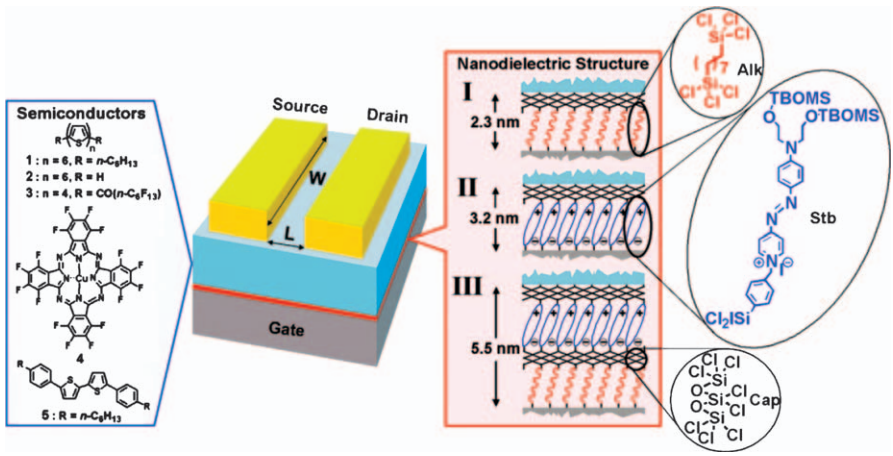

Figure 4.11 Schematic representation of the OFET components, showing the molecular structures of various organic semiconductors (left) and self-assembled nanodielectrics I–III (right). Highly n-type doped Si (100) wafers with a 1.5 nm native oxide or smooth ITO (a transparent conductor) are used as substrate gate electrodes. Nanodielectric layers are then sequentially deposited from solutions of silane precursors Alk, Stb, or Cap. The OFET device is completed by vacuum-deposition of 50 nm thick layers of p- or n-type organic semiconductors **1–4** or solution-deposition of semiconductor **5**, followed by source–drain gold electrode (100 nm) vacuum deposition.
Reprinted with permission from ref. 161. Copyright (2005) National Academy of Sciences, U.S.A.

nomenclature: **I** (layers: Alk + Cap), **II** (layers: Stb + Cap), and **III** (layers: Alk + Cap + Stb + Cap). The microstructures and electrical properties of **I–III** were characterized by X-ray reflectivity, optical absorption spectroscopy, non-linear optical second-harmonic generation measurements, AFM, and SEM. The excellent insulating properties of **I–III** were demonstrated by solution-phase cyclic voltammetry and quantitative solid-state MIS leakage current measurements, the latter being ~6 and ~9 orders of magnitude lower for **I/II** and **III**, respectively, than for Si/Si native oxide substrates (~ 0.1–1.0 A cm^{-2}). The measured breakdown fields for **I–III** were ~5–7 MV cm^{-1} over 200×200 μm^2. Capacitance–voltage (*C–V*) measurements on MIS structures (10^2–10^5 Hz) revealed maximum capacitances of $C_i = 400$ (**I**); 710 (**II**); 390 (**III**) nF cm^{-2} (±5%) at 10^2 Hz. The magnitudes of the effective dielectric constants of the Alk and Stb constituents of **I–III** were estimated from measuring SAMT C_i values in MIM structures. Importantly, the presence of the Si–SiO_2 interface strongly limits the maximum charge storage for MIS structures in the accumulation layer, resulting in underestimated C_i values. From the maximum MIM capacitance values [C_i ~ 1100 (**I**); 2500 (**II**); 760 (**III**) nF cm^{-2}], *k* of the Alk and Stb layers were found to be ~2.5 (close to that of bulk paraffins and alkyl SAMs) and ~16, respectively. This result illustrates the strategic importance of the highly π-polarizable dipolar layers in enhancing SAMT *k*, hence increasing C_i while preserving excellent insulator properties. OFETs (100 μm channel length and 5 mm channel width) were fabricated on the aforementioned SAMTs, with all devices exhibiting classical linear and saturation *I–V* responses at very low biases. Typical laboratory device yields are >95%. Similar transistor characteristics are obtained for a range of vapor/solution-deposited p- and n-type organic semiconductors, demonstrating broad generality. Note that these nanodielectrics can also be used to fabricate flexible FETs on commercially-available glass- and plastic (Mylar)-coated ITO substrates.

Hafnium oxide (HfO_2) has a large dielectric constant (16–29) and bandgap (5.8 eV) enabling its use a ultra-thin dielectric combining high capacitance and low leakage current.[162–164] Indeed, HfO_2 has emerged as a leading candidate to replace SiO_2 for downscaling below the 65 nm node in advanced metal oxide-semiconductor FET (MOSFET) applications. High-quality HfO_2 films are typically prepared by vapor phase methods such as atomic layer deposition, chemical vapor deposition, and physical vapor deposition. These methodologies are not compatible with inexpensive device fabrication. Thus, sol–gel processing has been utilized to fabricate high-quality metal oxide films, which could be compatible with the printed electronic platform. Jen and co-workers first reported on the use of phosphonate-based SAM/HfO_2 hybrid dielectrics for low-voltage OFET applications. The authors demonstrated that by using anthryl-terminated alkyl phosphonic acid (p-s-PA) SAMs, excellent dielectric films can be achieved, exhibiting a smooth surface, high capacitances (0.69 mF cm^{-2}), and low leakage current densities (down to ~10^{-9} A cm^{-2}). Pentacene-based OFETs operated at drain–source and gate–source voltages <1.5 V with high on–off current

ratios (10^5–10^6) and hole mobilities as high as 0.22 $cm^2\ V^{-1}\ s^{-1}$.[165] The charge carrier mobility improvement using the SAM-modified compared to the bare HfO_2 layer was explained by the lower SAM surface energy allowing better pentacene film morphology and the low-k monolayer surface physically buffering charge carriers from the underlying highly polar high-k surface, which is known to reduce charge carrier mobility in OFETs.[166] Jen and co-workers have also fabricated C_{60}-based OFETs using an ODPA SAM/sol–gel-processed hafnium oxide hybrid dielectric.[167] With the combination of high capacitance (580 nF cm^{-2}) and low leakage current density (8×10^{-9} A cm^{-2}), this hybrid dielectric yields C_{60}-based OFETs operating under 1.5 V with an average electron mobility of 0.28 $cm^2\ V^{-1}\ s^{-1}$, high on–off current ratio of 10^5, and low sub-threshold slope of 100 mV $decade^{-1}$. The low surface energy of ODPA allows C_{60} to form a thin film with large grains that provides an efficient charge carrier pathway for the low-voltage OFETs. Jen and co-workers also demonstrated a vacuum-free, low temperature solution-processed hybrid dielectric composed of a π–σ-PA SAM on amorphous sol–gel-processed HfO_2 for OFETs on plastic substrates. The π–σ-PA/HfO_x hybrid dielectric provides high capacitance (0.54 mF cm^{-2}), low-leakage current (2×10^{-8} A cm^{-2}), and has a chemically and electrically compatible dielectric interface for evaporated and solution-processed acene semiconductors. The utility of this dielectric was demonstrated by fabricating pentacene and TIPS-Pen-based OFETs with operating voltages <2 V and hole mobilities of 0.32 and 0.38 $cm^2\ V^{-1}\ s^{-1}$ for pentacene and TIPS-Pen, respectively.[168]

Our group has also utilized transition metal oxides, instead of SiO_2, for the fabrication of SAMT dielectrics. For this work, low-temperature solution-processed zirconia- (ZrO_2)[169] and hafnia- (HfO_2)[170] based self-assembled nanodielectrics consisted of alternating layers of a π-electron phosphonic acid and an ultrathin ZrO_2 (Zr-SAND) or HfO_2 layer (Hf-SAND). These SANDs present a great advantage compared to our previously described silane-based SAND, since they are processed under ambient conditions. Zr-SANDs exhibit large-area uniformity, well-defined nanostructure, very large electrical capacitance (up to 750 nF cm^{-2}), leakage currents as low as 10^{-7} A cm^{-2}, and excellent thermal stability. They are compatible with either organic (pentacene) and inorganic (zinc tin oxide; ZTO) semiconductors showing excellent electrical metrics. In fact, field effect mobilities of the order of ~0.3–0.4 and ~3.0–3.5 $cm^2\ V^{-1}\ s^{-1}$ have been achieved for pentacene and ZTO, respectively. However, we demonstrated that the addition of an additional self-assembled *n*-alkyl phosphonic acid monolayer on top of the multilayer is beneficial in the case of organic thin film transistors; pentacene OFETs exhibit mobilities up to 0.74 $cm^2\ V^{-1}\ s^{-1}$ for these alkyl-terminated SAMTs. Thus, insertion of this *n*-alkyl phosphonic acid layer allows the formation of an optimized interface between the dielectric film and semiconductor, which is a prerequisite for optimum OFET performance.

Substitution of ZrO_2 with HfO_2 in these nanodielectrics (with thicknesses as low as 3.1 nm) yields the largest SAND capacitance to date (1.1 μF cm^{-2})

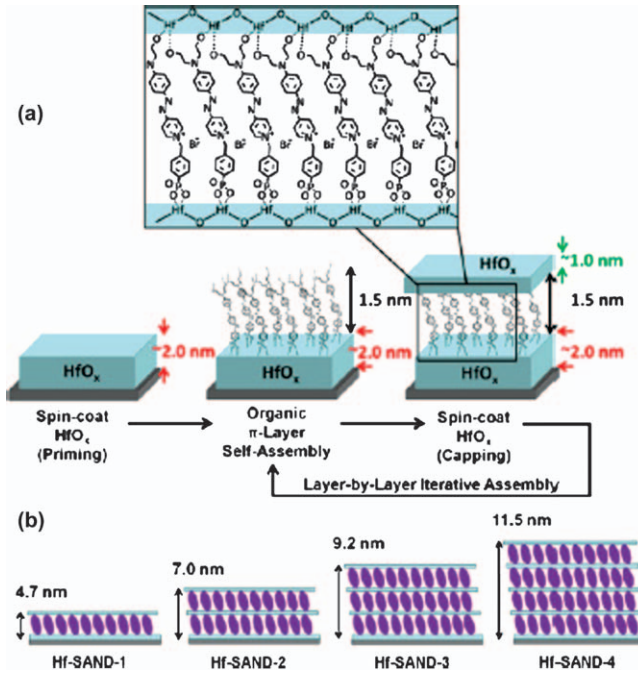

Figure 4.12 (a) Solution-based self-assembly procedure to fabricate Hf-SAND. (b) Schematic of various Hf-SAND multilayers including the estimated thicknesses.
Reprinted with permission from ref. 170. Copyright 2013 American Chemical Society.

for a solid-state solution-processed hybrid inorganic–organic gate dielectrics and affords gate leakages below 10^{-7} A cm^{-2} (Figure 4.12). This Hf-SAND was tested in semiconductor-enriched single-walled carbon nanotube-based transistors and afforded record on-state transconductances (5.5 mS) at large on : off current rations of $\sim 10^5$, with steep 150 mV dec^{-1} and intrinsic field-effect mobilities up to 137 cm^2 V^{-1} s^{-1}. Furthermore, we demonstrated excellent compatibility with device post-processing methodologies. In a following work,[171] we went a step further and used this Hf-SAND to fabricate a low-voltage, inkjet printed, low-temperature combustion-processed, amorphous indium gallium zinc oxide (a-IGZO) FET. We demonstrated a $>4\times$ enhancement in electron mobility for devices processed below 300 °C with respect to SiO_2 and ALD-HfO_2-based OFETs, while other electrical metrics were either unchanged or enhanced.

The nature of the end group of the SAM and its surface chemistry has been also investigated to understand how it affects OFET characteristics such as threshold voltage, device hysteresis, and/or electrical performance. Nouchi *et al*. found that modification of the OFET electrodes with SAM has a noticeable impact on the device metrics. In particular, an anomalous hysteresis

was reported in C_{60}-OFETs when the Au electrodes were modified with 1-alkane-thiole SAMs.[172] Nouchi *et al*. found that the output characteristics of a modified OFET displayed a reversed hysteresis where the forward sweep I_D values were smaller than the backward ones, and this effect was larger for lower density and longer chains of the SAM molecules. The authors determined that such hysteresis was caused by tunneling-barrier narrowing accompanied by the structural change of the SAMs, most probably due to an electrically-stimulated order–disorder transition of the SAM structure. They presumed that this anomalous hysteresis could cancel out the hysteresis caused the charge-trapping by tuning the density and length of SAM molecules on the electrodes.

Halik *et al*. also analyzed the effect of SAM functionalization on the hysteresis and threshold voltage of pentacene and dihexyl-sexithiophene-based OFETs.[173] However, in this contribution, they functionalized the semiconductor–dielectric interface instead of the electrodes and they used mixed self-assembled monolayers of molecules with dipolar and acceptor character (Figure 4.13). To this end, they used a pentadecafluorooctadecylphosphonic acid ($F_{15}C_{18}$-PA) and a C_{60}-terminated phosphonic acid (C_{60}-C_{18}-PA). They found that threshold voltages were determined by the dipole moment of the SAM. Interestingly, they also saw that the hysteresis strongly depended on the SAM composition, and increased from a clockwise hysteresis of –10 mV for pure $F_{15}C_{18}$-PA to an anticlockwise one of 400 mV for pure C_{60}-C_{18}-PA (Figure 4.13b). The authors ascribe this fact to the electron acceptor character of the C_{60} which allowed dielectric charging during operation.

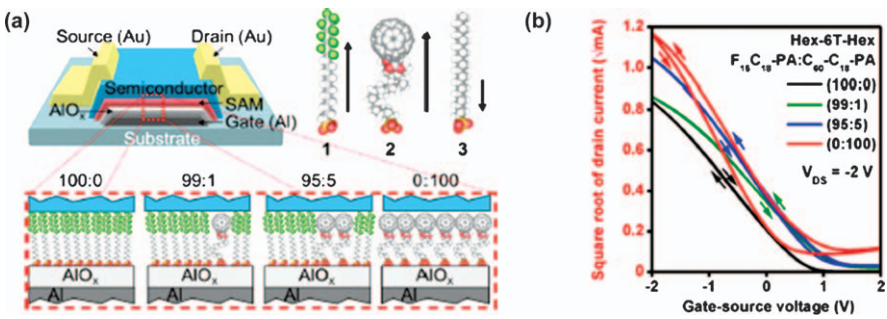

Figure 4.13 (a) (Top-left) Schematic cross section of a bottom-gate top-contact transistor with AlO_x/SAM hybrid dielectrics. (Top-right) Chemical structure of SAM precursors and direction of their molecular dipole moments (arrow heads show negative ends of the dipoles). (Bottom) Schematic representation of pure and mixed SAM hybrid dielectrics. (b) Transfer characteristics of devices with pure and mixed SAM hybrid dielectrics.
Reprinted with permission from ref. 173. Copyright 2012, AIP Publishing LLC.

The effect of the nature of the SAM end group on OFET device metrics has also been analyzed by Padma *et al.*[174] using trichlorosilane derived-SAMs and Jen *et al.*[175] using phosphonic-acid derived SAMs. Both contributions agree in that self-assembled monolayers promoting favorable semiconductor nucleation and growth (such as SAMs having phenyl end groups) diminishes grain boundaries and, therefore, increases field-effect mobilities, while also improving threshold voltages. In the study carried out by Jen, the effect of SAM surfaces energies was also analyzed and they found that surface energy tends to be a negligible factor in device performance provided that a homogeneous semiconductor surface is achieved.

The source–drain electrical contacts in OFETs significantly influence device operation due to mismatch of the work function between the electrode material and the semiconductor, interfacial dipole formation, and variation of the semiconductor morphology at the interface, as well as possible semiconductor degradation. Thus, although most of the SAM/SAMT work relates to functionalizing the organic semiconductor/dielectric interface,[176] contact modification is of prime interest. Staggered (top-contact) device architectures typically exhibit better performance than coplanar (bottom-contact) devices because of improved intimate adhesion of the metal to the semiconductor. However, the top-contact geometry is incompatible with photolithographic processes and large-scale integration, and does not allow one to produce sub-20 nm channel lengths, which may be necessary to enhance the driving currents. Therefore, it is desirable to use a bottom-contact configuration, which is compatible with fine lithograph processing, for device applications, such as flexible displays and circuits. Initial work on pentacene OFETs has shown that SAM functionalization of the Au contacts with thiolates changes the Au surface and hence the morphology of the pentacene film deposited on the electrodes. These bottom-contact/bottom-gate SAM modified transistors showed improved performance and are compatible with lithographic definition of the source and drain electrodes.[159,177] SAMs of alkanethiols with different chain length on Au electrodes evidenced the odd–even effect of different numbers of carbons due to the anisotropic coupling between the alkanethiol terminal bond and the HOMO level of ordered pentacene molecules. These results showed that charge injection occurs by through-bond tunneling of holes mediated by the alkanethiol layer and that for long-chains the charge injection across the alkanethiol monolayer completely governs the transistor behavior.[178] Several other aliphatic and aromatic SAM thiolates were used to modify the Au electrodes for pentacene FETs.[179] Using the SAM to modify the Au work function clearly affects charge injection in bottom-contact poly(3-hexylthiophene) FETs.[180] Furthermore, SAM-modification of the electrodes can improve electronic coupling between the contacts and the semiconductor and thereby dramatically decrease contact resistance in nanoscale OFETs.[181]

Gold was found to be the best contact materials for several p- and n-channel semiconductors. When moving to other metals such as Ag and Cu as bottom contact electrodes, the contact resistance and energetic mismatch

typically result in lower performance for pentacene OFETs, which again was addressed by using thiolate SAMs.[182] Tuning the Ag work function with aromatic thiol SAMs significantly reduces the hole injection barrier for solution processed (triisopropylsilylethynyl)pentacene (TIPS-Pen) OFETs as well as affording very stable electrical contacts.[183] Quite recently, it has been demonstrated that the interfacial morphology between SAM-modified contacts and the transistor channel dominates FET performance. Semiconductor film morphology can impact the overall performance even more than changing the Schottky barrier and charge injection using a bare silicon oxide dielectric and gold electrodes modified with SAMs of opposite dipole moments.[184] SAM-modified S–D contact properties (*e.g.*, surface energy and supramolecular interactions) can also be tuned to induce the growth of crystalline organic semiconductors on the contacts that can extend tens of micrometers into the transistor channel and significantly impact the OFET characteristics.[185]

Complementary thin-film transistor circuits composed of TIPS–Pen and a rylene carboxylic diimide derivative for p- and n-channel OFETs were fabricated on flexible foils.[186] The so-called staggered FET configuration was used, meaning that the semiconductors layers are deposited last. The work function of the injecting gold electrodes was modified using several SAMs (Figure 4.14). For optimized contacts the mobility of the n- and p-channel FETs was 0.5 and 0.2 $cm^2\ V^{-1}\ s^{-1}$, respectively. Strongly degraded performance is obtained when the n-channel material was printed on contacts optimized for the p-channel FET, and *vice versa*. This illustrates that for CMOS circuits careful work-function engineering is required to allow proper injection for both electrons and holes. Thus, the authors showed for the first time that by using a bimolecular mixture for the SAM they can systematically vary the work function, and demonstrated how this affects the performance of discrete n-type and p-type transistors, as well as CMOS inverters and ring oscillators. Under optimal processing conditions a 19-stage ring oscillator with 10 μs stage delay operating at 20 V was realized.

With the emergence of new solution processable organic semiconductors, more studies have focused on the top-gate bottom-contact (TGBC) architecture considering the advantages indicated above. TGBC FETs have been fabricated on plastic foils but greater performances are generally observed with glass or silicon substrates. A peculiarity of the TGBC architecture is that the semiconductor film is also in contact with the substrate. However, no studies have systematically addressed chemical modifications of the substrate/semiconductor interface and whether this chemistry plays an important role in the TGBC device performance. In a recent study Facchetti *et al.* fabricated TGBC FETs where the glass substrate surface was functionalized with various SAMs prior to the deposition of the organic semiconductor (Figure 4.15A). The SAMs were selected to provide a direct comparison with the abundant literature data available for SAM-functionalized BGTC FETs. The silane precursors were chosen because they contain alkyl/phenyl-amino (**1** and **2**), alkyl (**3** and **4**), and halo-alkyl (**5** and **6**) functionalities, resulting in

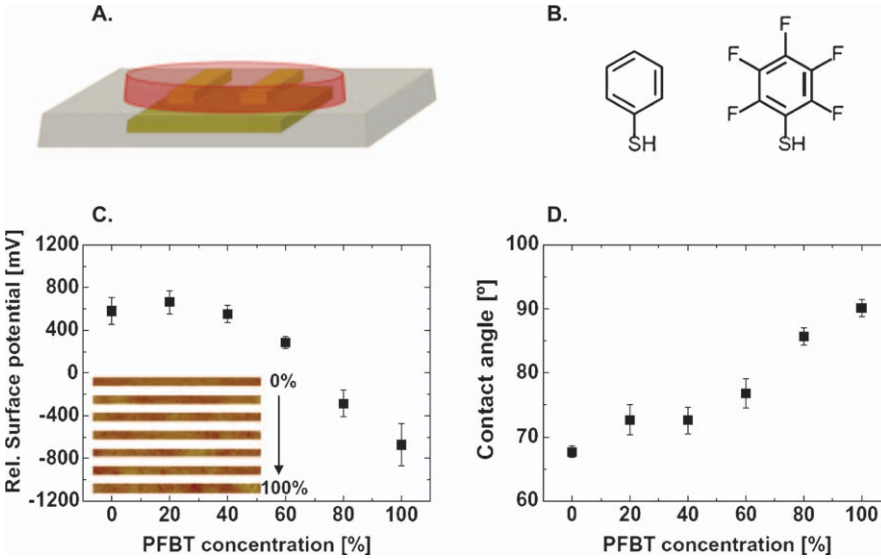

Figure 4.14 (a) Schematic representation of the transistor structure used in this study. (b) Chemical structure of the thiol molecules: left phenylthiol (PT) and right pentafluorobenzenethiol (PFBT). (c) Variation in surface potential of gold electrodes after modification with different concentrations (weight%) of thiols plotted *versus* the relative weight ratio of PFBT in the PFBT–PT solution. The surface potential was measured with respect to non-treated gold (0 V). Inset: scanning Kelvin probe microscopy images of Au modified with different PFBT–PT treatments. The color scale was 40 mV indicating that the work function is homogeneous over entire surface (voltage difference smaller than 40 mV). Scanned area was 2000×50 nm^2. (d) Contact angle of water on gold electrodes after modification with different concentrations of thiols *versus* the relative weight ratio of PFBT in the PFBT–PT solution. Reprinted from ref. 186. Copyright 2012, with permission from Elsevier.

SAMs with tuned chemical structure, dipole moments/electric fields, and charge transfer capabilities (Figure 4.15B). Indeed, several groups have shown that amino SAMs of type **1**/**2** favor electron accumulation resulting in strong V_T shifts to positive values for both n-channel and p-channel BGTC FETs *versus* electron-neutral alkyl (**3**/**4**) SAM-based FETs, whereas halo SAMs of type **5**/**6** preferentially accumulate holes leading to negative V_T shifts.[187] Two representative organic semiconductors were selected as channel materials: a core-cyanated perylene n-channel molecule (N1400) and a triarylamine p-channel polymer (PTAA) (Figure 4.15C). The results demonstrated that the electrical parameters of both n- and p-channel semiconductors strongly depend on the chemical characteristic of the SAM molecule, as in the case of conventional BGTC FETs (Figure 4.15D, E). Equally important, the electrical conductivity at $V_G = 0$ V, OFF current, and V_T variations *versus* SAM type exhibit opposite trends. Numerical simulation demonstrated that these effects originate from charge carrier density

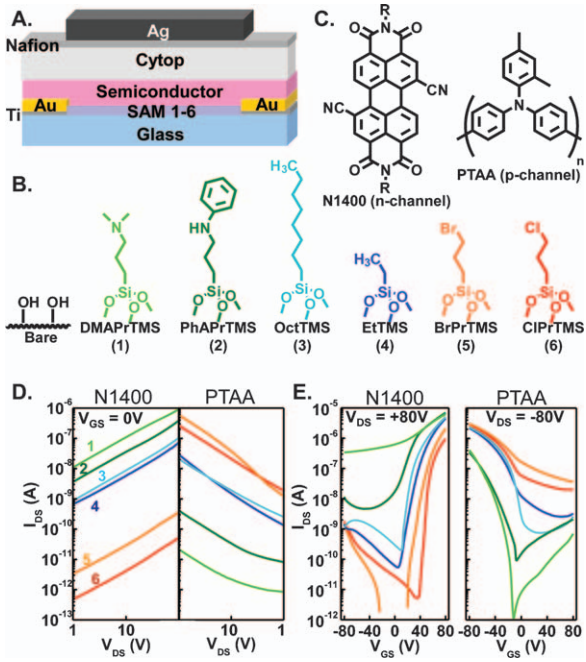

Figure 4.15 (A) Schematic representation of the TGBC FET structure used in this study. (B) Chemical structure of the SAM precursors **1**–**6**. *I*–*V* plots for FETs with different SAMs measured with (C) of the n-channel (N1400) and p-channel (PTAA) semiconductors and (D) a floating gate and (E) in the saturation regime at the indicated biases.
Adapted with permission from *J. Am. Chem. Soc*. 2011, **133**, 9968. Copyright 2011 American Chemical Society.

variations in the semiconductor film resulting from the combination of the SAM (E_{SAM}) and gate (E_G) electric fields.

Since SAM modification of both semiconductor–dielectric and semiconductor–electrodes interfaces[188] is desired to enhance the device electrical performance, the Jen group has developed a way to simultaneously modify the bottom-contact electrodes and dielectric surfaces of low-voltage C_{60} and pentacene OFETs by deposition of spin-cast monolayers.[189] To this end, they used different phosphonic acid-SAMs that can be easily deposited on both metal oxide dielectrics (HfO_2) and metal electrodes (Ag) (Figure 4.16). The authors found that rational selection of the alkyl chain length of the SAM led to optimized OFETs through a balance combination of low-contact resistance at the bottom-contact electrodes and excellent semiconductor–dielectric interface for compact semiconductor grain growth. For pentacene devices, mobilities of ~ 0.6 $cm^2V^{-1}s^{-1}$ with V_T of –0.6 and high on/off ratio of 10^7 were achieved, while C_{60}-devices showed the following electrical metrics: $\mu = 3.7$ cm^2 V^{-1} s^{-1}; $V_T = 1.6$ V and $I_{on} : I_{off} = 10^7$, using a SAM of n-octylphosphonic acid in both cases.

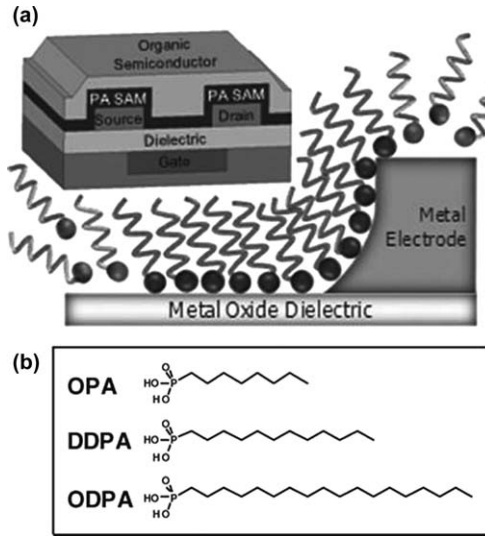

Figure 4.16 (a) Schematic of bottom-contact bottom-gate OFET using single-component spin-cast SAMs to simultaneously modify metal contact and dielectric surfaces. (b) Chemical structures used as SAMs. Reprinted with permission from ref. 189. Copyright 2011 Wiley-VCH Verlag GmbH.

More recently, OFETs where monolayers are used as the semiconductor channels (SAMFETs) have been investigated.[190] For these devices initial studies showed inverse scaling, that is, device mobility decreases dramatically with increasing channel length.[191] Only sub-micrometer channels have shown a gate-dependent source–drain current, with the mobility in longer channels being negligible. De Leew *et al.* have demonstrated SAMFETs in which the extracted device mobility is virtually independent of channel length (Figure 4.17).[192] Furthermore, to investigate this contradiction in the scaling of the mobility, they investigated SAMFETs with varying monolayer coverage and channel lengths.[193] By ensuring both proper charge carrier injection and an ordered SAM microstructure, they systematically probed charge transport in this two-dimensional percolating semiconductor network. For sub-monolayer coverage, the anomalous inverse scaling behavior reported previously for SAMFETs is reproduced and can be accounted for by numerical and analytical percolation models. In both papers, SAMFETs were prepared on heavily doped silicon wafers (acting as the common gate) covered with a 200 nm layer of thermally grown SiO_2. The gold source and drain contacts were defined by conventional photolithography and wet etchant chemistry. Titanium (10 nm) was used as an adhesion layer. A liquid-crystalline active molecule consisted of a mesogenic quinquethiophene core, end-capped with an ethyl group to enhance stability and solubility. To bind the molecule to the SiO_2 gate dielectric, a monochlorosilane anchoring group was attached *via* an undecane spacer. To induce self-assembly of the

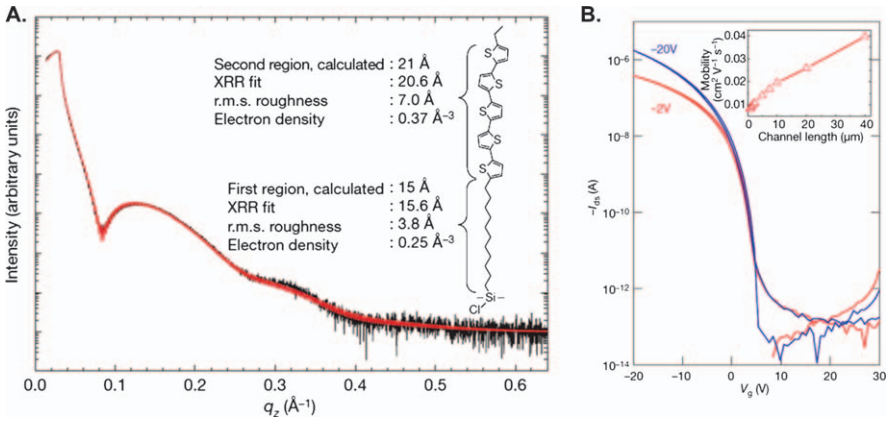

Figure 4.17 (A) X-Ray reflectivity (XRR) of the SAM on silicon dioxide. The solid red line is the fit to the experimental data. The measurements reveal a layer thickness equivalent to one monolayer. Inset: chemical structure of the semiconductor SAM precursor. (B) Linear and saturated transfer characteristics of a SAMFET using drain biases of –2 and –20 V, respectively; I_{ds}, drain–source current; V_g, gate voltage. Inset: linear mobility as a function of channel length.
Reprinted by permission from ref. 192. Macmillan Publishers Ltd: copyright 2008.

molecules, the SiO_2 gate dielectric was activated with an oxygen plasma treatment followed by acid hydrolysis. The SAM was then formed by submerging the substrate in a dry toluene solution of the semiconducting molecule. The coverage could be varied by changing the immersion time. A typical transfer characteristic for a SAMFET transistor with a channel length of 40 μm and a channel width of 1000 μm is presented in Figure 4.17(B). The p-type SAMFET shows almost no hysteresis and a linear and saturated mobility of $\sim$0.04 $cm^2\ V^{-1}\ s^{-1}$. The mobility was found to be thermally activated, with an activation energy of about 80 meV.

More recently Halik *et al*. fabricated SAMFETs on very rough flexible substrates.[194] To achieve these devices the challenge was to create a SAM as a 2D π-π-stacked system imaging a 3D-topography because the surface roughness exceeds the length of the molecule. The authors used [12-(benzo[*b*]benzo[4,5]thieno[2,3-*d*]thiophen-2-yl)dodecyl]phosphonic acid (BTBT-C12–PA) as an active monolayer on an Al-gate pattern placed on rigid SiO_2 as well as on flexible poly(ethylene naphthalate) (PEN) substrates. The p-type SAMFETs operate at the low supply voltage of 3 V due to a thin hybrid dielectric of 5.1 nm thickness with charge carrier mobility of 10^{-2} $cm^2\ V^{-1}\ s^{-1}$. These devices were found to withstand mechanical bending and operate in channel areas up to 20000 μm^2, demonstrating that the molecular approach is fully compatible with large area, flexible electronics applications. Finally, very recently a novel perylene-bis-imide with a phosphonic acid anchor group for n-channel SAMFETs was reported by Strohriegl *et al*.[195]

The molecule self-assembles covalently onto aluminium oxide dielectrics. A homogeneous and dense monolayer is spontaneously formed in which the molecules stand upright to the surface. Electron mobilities of $\sim 10^{-3}$ cm^2 V^{-1} s^{-1} were achieved on rigid as well on flexible substrates. To test the suitability of the perylene-bis-imide in more complex circuits, a flexible NMOS bias inverter based on SAMFETs was established, underpinning the capability of n-type SAMFETs for flexible organic electronics.

4.3.2 Bulk-Heterojunction Solar Cells

Organic photovoltaic (OPVs) cells are promising candidates for low-cost energy production.[196,197] The best OPV cells reported to date consist of a layer of a polymer donor and a fullerene acceptor forming a bulk heterojunction (BHJ) sandwiched between a transparent metal oxide conductor, such as ITO, and a metal electrode.[198,199] Upon illumination, the photogenerated excitons migrate to the donor–acceptor interface and dissociate into charge carriers due to the difference in energy levels between the two semiconductors. After separation, the charges then drift under the inherent electric field created by the work-function difference between the asymmetric electrodes and, ultimately, will be collected by the corresponding electrodes. Several strategies have been pursued to enhance OPV performance including the development of new donor semiconductors with enhanced carrier mobility and broader absorption of the solar radiation,[200,201] new methods to control film morphology for improving charge transport and reducing recombination mechanisms,[202] and novel device architectures for tandem[203,204] and inverted cells.[205] Furthermore, optimization of charge collection efficiency and interfacial stability at the organic active layer/inorganic electrode junction is considered to be of paramount importance. OPV cells are mostly fabricated using two device architectures (Figure 4.7B). In the conventional approach, the photoactive layer is sandwiched between an ITO anode and a low-work-function metal cathode, such as Ca/Al or LiF/Al. Electrode degradation is a major concern in this structure since the low work-function metal is vulnerable to air oxidation.[206,79] For inverted architectures, an electron transport/hole-blocking layer (such as titanium dioxide, TiO_2, or zinc oxide, ZnO) is inserted between ITO and the photoactive layer to selectively collect electrons, while a high-work-function metal is used as the top electrode for hole collection. This architecture is inherently more stable to ambient and more easily scalable in manufacture. In both types of structure, the electrical contact characteristics and quality between the photoactive organic layer and the electrodes are a critical factor that determines device characteristics, such as short-circuit current density (J_{sc}), open-circuit voltage (V_{oc}), and fill factor (FF). Another key OPV parameter, the series resistance (R_s), is attributed to the bulk conductivity of the photoactive and interfacial layers; thus, materials with high charge carrier mobility and ohmic contact at the interfaces are required to achieve high J_{sc}.[207] The V_{oc} can be increased by matching the Fermi levels of the anode and cathode to

the HOMO of the donor and the LUMO of the acceptor, respectively. Finally, the shunt resistance (R_{sh}) is a parameter related to the quality of the thin films and their interfaces and should be maximized for high-performance devices. Non-optimal R_{sh} originates from the loss of charge carriers through leakage paths including pinholes in the films and the recombination and trapping of the carriers during their transit through the cell leading to decreased device performance.

In conventional OPV architectures using ITO as the anode, PEDOT : PSS has often been used as an interlayer to planarize the ITO electrode and increase its work function for efficient hole collection.[208] Although PEDOT : PSS is widely used, its acidic nature produces chemical instability at the ITO/PEDOT : PSS interface and its electrical inhomogeneity[209] limits electron blocking capability.[210,211] Thus, several hole-extracting interlayers were developed including crosslinked PEDOT : PSS replacements[212] and sulfonated poly(diphenylamine) (SPDPA) derivatives.[213] Transition metal oxides such as vanadium oxide (V_2O_5),[214] molybdenum oxide (MoO_3),[215] nickel oxide (NiO),[216] and tungsten oxide (WO_3)[217] have also been employed as hole-transporting/electron-blocking buffers to improve the interfacial properties between ITO and active layer in the conventional PSCs.[218,219]

SAMs with a permanent dipole moment have been employed to tune the work function of ITO contacts (Figure 4.18).[220,221] Thus, P3HT : PCBM cells were fabricated using ITO functionalized with a series of silane-based SAMs with different terminal groups (CH_3, NH_2, CF_3).[222] The SAM with the electron-withdrawing CF_3 group was found to effectively increase the work function of ITO from 4.70 to 5.16 eV, providing a better match with the HOMO level of P3HT for efficient collection of holes. Furthermore, the CF_3 group enhances the surface energy of the ITO, improving the BHJ film morphology. As a result, the devices with the CF_3-terminated SAM exhibit PCEs >3%. Note that ITO surface coverage with a thin layer of polytetrafluoroethylene (PTFE) can also generate an interfacial dipole enhancing the ITO work function and improving device performance *versus* the unfunctionalized substrates.[223]

Interface engineering at the electron-collecting electrode is also very important for improvement of the performance of conventional architecture PSCs. A thermally deposited thin film of low-work-function metals, such as Al (4.3 eV) or Ca/Al (2.8 eV), is typically used for collecting electrons. A sub-monolayer of LiF between Al and the active organic layer improves device performance through the formation of a favorable dipole moment across the junction, which facilitates electron collection. Sol–gel deposited titanium oxide (TiO_2) has also been used as an interfacial layer between the photoactive layer and Al contact.[224–226] This solution-processed multifunctional buffer layer acts not only as an electron-transporting/hole-blocking layer, but also as an oxygen barrier and optical spacer leading to significantly improved device efficiency and stability.[227] Park *et al*. have doped Cs into the TiO_2 layer for even improved electron extraction in P3HT/PCBM OPV cells.[228] Jen *et al*. incorporated a solution-processed thin

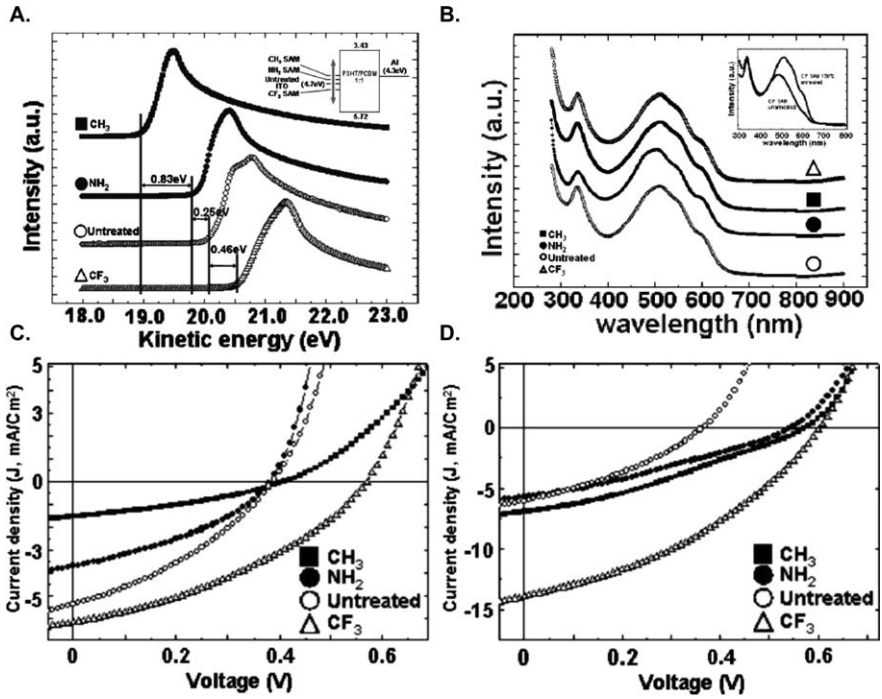

Figure 4.18 (A) Secondary electron emission spectra for the indicated SAMs on ITO substrates. Inset: schematic energy level diagram of the electron-donating and electron-withdrawing SAM treated ITOs. (B) UV absorption spectra of the P3HT/PCBM active layer for the various surface-treated ITOs; the intensity and peak shift do not vary for the various surface treatments. Inset: comparison of UV absorption spectra of the P3HT/PCBM active layer for the CF_3 SAM treated ITOs between unannealed and annealed samples. *J–V* characteristics of the OPV devices with the various SAM-treated ITO substrates for the as-prepared (C) and annealed (D) films.
Reprinted with permission from ref. 220. Copyright 2007, AIP Publishing LLC.

film of zinc oxide nanoparticles (ZnO NPs) as an electron-transporting buffer layer to improve the performance of PSCs. This layer combines excellent solution processability and good electron transport (electron mobility = 2.5 $cm^2\ V^{-1}\ s^{-1}$).[229,230] The Fermi level of ZnO (4.3 eV) matches well with the LUMO of PCBM (4.3 eV), which facilitates efficient electron transfer and extraction from the polymer : fullerene blend. In addition to the optical spacer effect,[231] the low-lying valence band of ZnO can also prevent hole carriers in the blend from reaching the cathode.

Jen *et al*. first demonstrated SAM-modified ZnO for the fabrication of OPV cells. It was known that ZnO electrical properties can be easily tuned by modifying the ZnO surface with a self-assembled functional molecular layer.[232,233] Thus P3HT-PCBM cells with a SAM modified ZnO layer were

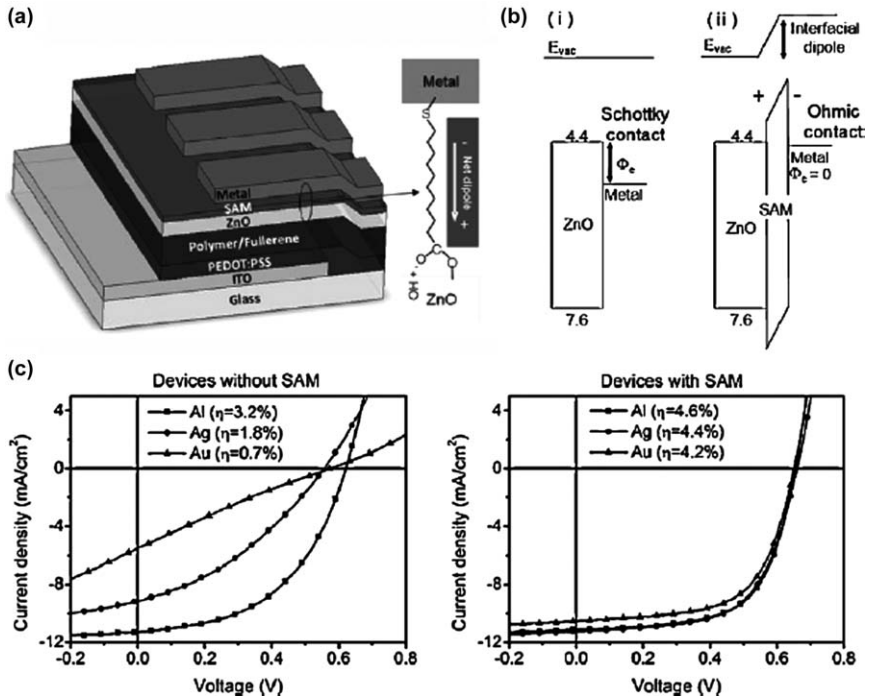

Figure 4.19 (a) Device architecture of the polymer solar cell with SAM-modified ZnO/metal bilayer cathodes. (b) Schematic illustration of the energy level diagram of the devices with (i) ZnO/metal cathode and (ii) ZnO/SAM/metal cathode. (c) The current density–voltage (*J*–*V*) characteristics and power conversion efficiencies of polymer solar cells with and without SAM-modified ZnO/metal cathodes measured under AM1.5 illumination with a light intensity of 100 mW cm.
Reprinted with permission from ref. 235. Copyright 2008, Wiley-VCH Verlag GmbH.

fabricated. The device performance varied significantly depending on the dipole direction and chemical bonding between the SAM and metal (Figure 4.19).[234,235] SAMs with an unfavorable dipole across the ZnO and metal thin film will result in a Schottky contact and poor device efficiencies. On the other hand, an appropriate dipole across the ZnO and the metal thin film generated Ohmic contact and dramatically improved device efficiencies *versus* the control. With this interfacial modification strategy, even high-work-function metals, such as Ag and Au, could be used as cathodes for polymer solar cells to reach high PCEs. These findings paved the way for using solution-processable metal electrodes such as Ag for OPV module fabrication.

Recently, other SAMs such as thiol and benzoic acid derivatives (Figure 4.20) have also been shown to affect the efficiency and the free carrier's photogeneration in photovoltaic cells.[236] In the case of benzoic acid

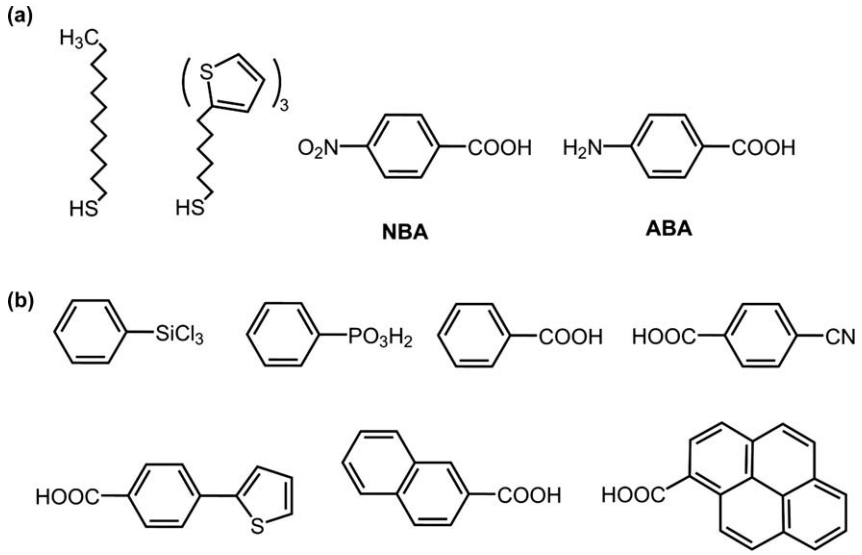

Figure 4.20 Chemical structures of thiol and benzoic-acid derived SAMs.

derivatives (*p*-nitro-benzoic acid, NBA, and *p*-amino-benzoic acid, ABA) it was found that grafted SAMs with permanent dipolar moment molecules on the ITO electrode enhance the creation of carriers at the interface, thus improving sexithiophene-based solar cells performances. However, the authors found that the contribution of photogenerated carriers to photocurrent was strongly dependent on dipole orientation; that is, the built-in potential would increase if the dipole layer field is in the same direction of the built-in electric field and *vice versa*. The effect of thiol SAMs, such as dodecanethiol or a terthiophene derived thiol (Figure 4.20a), was also found to enhance device performance, which can be related to a better degree of organization of the sexithiophene upper layer. Other benzoic acid-derived SAMs (Figure 4.20b) were used by Sagaw *et al.*[237] to functionalize the anodic ITO in P3HT/PCBM solar cells, and they obtained improvements of PCEs of 4.5–4.7 times with respect to unmodified ITO. They also found that the direction of the SAM dipolar moment with respect to the ITO surface has an impact on the V_{OC} of the devices.

The Northwestern University group has also modified ITO anodes with a series of interfacial layers based on robust silane-tethered bis(-fluoroaryl)amines (Figure 4.21).[238] That way, modified anode work functions ranging from 4.66 to 5.27 eV were achieved. The authors found significant performance enhancement on SAM-modified P3HT : $PC_{71}BM$ and PTB7 : $PC_{71}BM$ devices *versus* cells with unmodified glass/ITO anodes. Importantly, strong positive correlations between the electrochemically derived heterogeneous electron transport rate constants (k_s) and the solar cell performance metrics (V_{OC}, J_{SC}, and PCE) were found. Furthermore, it was experimentally found for the first time that k_s scales with the SAM out-of-plane dipole

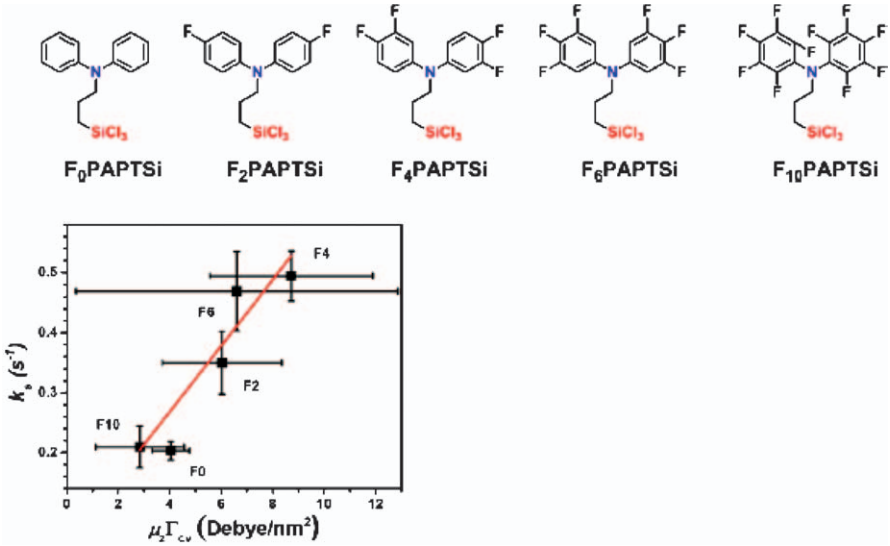

Figure 4.21 Molecular structures of silane-tethered bis(fluoroaryl)amines. Plot of k_s *versus* SAM out-of-plane dipole moment multiplied by the surface coverage.
Adapted with permission from ref. 238. Copyright 2013 American Chemical Society.

moment and surface coverage, to enhance hole extraction and suppress recombination processes. SAM-modification of ITO electrodes has also been attractive in bilayer (ZnO/P3HT) hybrid organic solar cells structures.[239] In these cells, it was demonstrated that ITO modification with *n*-propyltriethoxysilane affected not only the crystal growth of the ZnO layer but it also improved the crystallinity of the P3HT layer on top of the ZnO film. This was translated into enhanced electrical properties of both donor and acceptor layers, thus improving the PCE from 0.18% to 0.29%.

As far as inverted OPV cells are concerned, they have attracted great attention since their invention.[240–242] In these devices, the polarity of the ITO electrode is reversed *via* insertion of an electron-transporting/hole-blocking interlayer having a suitable work function for electron collection. A hole transporting/electron-blocking interlayer is inserted between the BHJ layer and a high-work-function metal electrode to enable hole collection. The performance of the inverted OPV structure critically depends on the choice of the buffer layers and their contact properties with the BHJ and the corresponding electrodes. Alkali metal salts such as Cs_2CO_3 have been found to be the most promising modifier to reduce the work function of ITO.[243–246] Recently, amorphous TiO_2 and ZnO thin films have also been explored as electron-selecting layers for inverted solar cells.[247,248] Since ZnO has a much higher electron mobility than TiO_2, ZnO is beneficial because it decreases the electrical resistance in OPV cells.[249] Thermally evaporated transition metal oxides such as WO_3[250] and MoO_3[251] have been employed

as the hole-extracting buffer to improve the interfacial properties between the BHJ layer and Ag top electrode.

Surface modification of the interface of hybrid inorganic/organic heterojunction devices with functional SAMs has also been shown to be an effective method to improve solar cell characteristics.[252] Thus, carboxylic acid-based SAMs with different dipole moments have been used to tune the interfacial properties of TiO_2/P3HT planar heterojunction cells and the results suggest that exciton dissociation efficiency and energy-level offset at the heterojunction can be tuned by the SAM chemical nature.[253] Jen *et al*. elaborated this approach in inverted P3HT : PCBM BHJ solar cells by using ITO modified with SAM-functionalized TiO_2 layers as an electron-collecting cathode and PEDOT : PSS/Ag as the hole-collecting anode. In general, charge recombination loss at the organic/inorganic interface significantly limits the performance of inverted-structure devices because of the unfavorable energetic and chemical interface. This loss was alleviated by using a C_{60}-based SAM. Such a functional monolayer served multiple purposes, including enhancement of interfacial exciton dissociation efficiency, passivation of inorganic-surface trap states, and optimization of upper organic layer morphology. As a result, the SAM-modified TiO_2 devices showed a PCE of 3.78%, which is a 35% improvement over the unmodified device.[254] Low-temperature processed ZnO NPs have also been used as the electron-selecting layer at the ITO/BHJ interface by Jen and co-workers to demonstrate environmentally stable and flexible inverted solar cells on plastic substrates.[255] To further improve the device performance, the surface of the ZnO-NP film was modified with a layer of C_{60}-SAM, resulting in very high PCEs (4.9%) for inverted PSCs.[256]

As previously seen in conventional solar cell architectures, Kim *et al*. modified the electron-selective ZnO interface in inverted polymer BHJ solar cells with benzoid acid-derivatives having different dipole orientations and magnitudes (4-fluorobenzoic acid (FBA), 4-*tert*-butylbenzoic acid (BBA), and 4-methoxybenzoic acid (MBA) in Figure 4.22).[257] The authors observed that using SAMs with the dipole moment directed toward the ZnO layer (FBA monolayer) greatly decreased the cell performances; while a SAM with the opposite dipole moment direction benefited the OPV metrics, by increasing the V_{OC} parameter with respect to cells with no SAM treatment. The authors also noted that the substituent of the 4-position of benzoic acid affected the active layer morphology, which can be related to J_{SC} and FF parameters. Thus, SAM based on BBA and MBA molecules improved all the solar cell parameters since they combine proper dipole moment direction and terminal substituent for improved active layer morphology.

More recently, fullerene-based SAMs have been implemented to modify the interface of the electron-selective ZnO layer, to decrease the electron charge traps, tune the energy level offset between semiconductors and organic layers, and improve the morphology of the upper active layer. Various C_{60}-substituted benzoic acid SAMs with different anchoring groups (catechol, carboxylic acid, and phosphonic acid) were tested (Figure 4.23).[258]

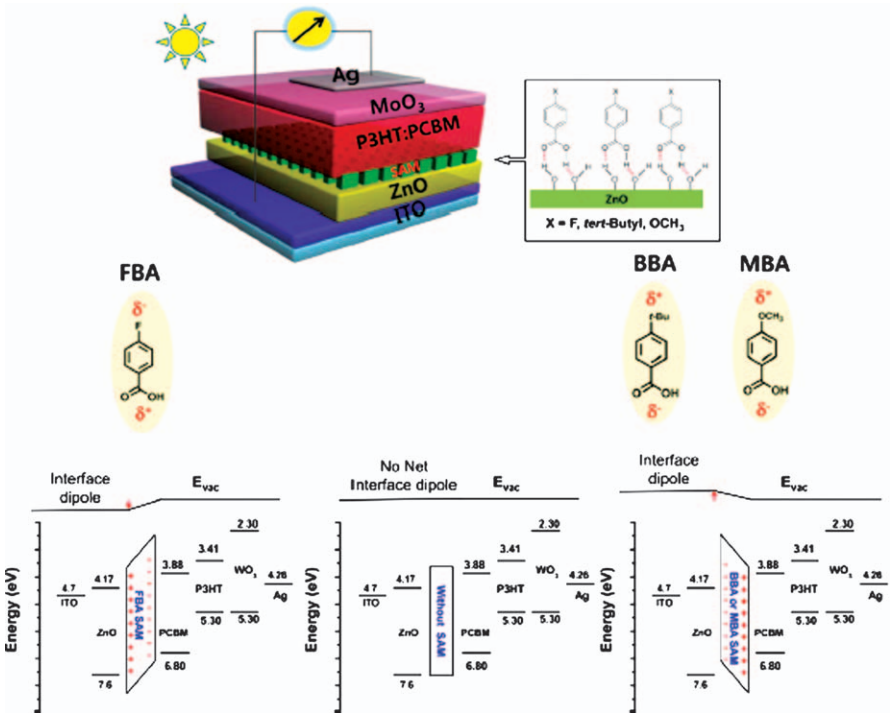

Figure 4.22 Schematic illustration of polymer solar cells with SAM modified ZnO. Schematic energy level diagram of the devices with SAM-modified ZnO. Reprinted with permission from ref. 257. Copyright 2013 American Chemical Society.

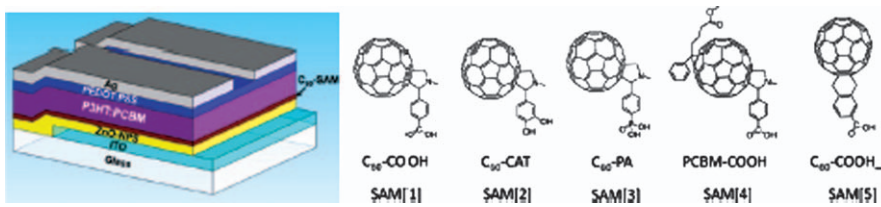

Figure 4.23 Device architecture of the inverted solar cell using different C_{60}-SAMs. Chemical structures of the C_{60}-SAMs.
Reprinted with permission from ref. 258. Copyright 2012 American Chemical Society.

The authors found that modification of the anchoring group and of the functionalization of the monolayer have an impact on the P3HT : PCBM device properties, with the efficiency being improved from 3.47% (without SAM modification) to 4.4% (using carboxylic acid C_{60}-SAMs), 4.19% (with the catechol C_{60}-SAMs), and 3.96% (with the phosphonic acid C_{60}-SAMs).

Other phosphonic acid-anchored C_{60} SAMs were used by Brabec *et al.*[259] to modify the electron extraction layer (Al-doped ZnO on ITO) of inverted P3HT

: PCBM solar cells. They found that while alkane monolayers (without C_{60}) deteriorate device performance, probably due to the formation of an insulating barrier, the use of a C_{60}-SAM modified cathode improves the PCE from 2.88% for unmodified devices to 3.32%. The authors ascribe this improvement mainly to increased fill factors, and to the fact that the fullerene at the end of the alkane chain mediates charge transfer from the active layer to the Al-doped ZnO film.

4.3.3 Organic Light-Emitting Diodes

OLEDs have become a significant industry for flat and curved panel displays because of improved efficiency, high brightness, and low drive voltages.[260–264] To enable highly efficient OLEDs, efficient and balanced electron- and hole-injection/transport from the cathodes and anodes is essential. To accomplish this goal, a multilayer device structure is commonly used for OLEDs, which typically includes a transparent and conductive indium tin oxide (ITO) anode, a hole transporting/injection layer (HTL), an emissive layer (EML), an electron transporting/injection layer (ETL) and a metallic cathode (Figure 4.7C).[265–268] OLED device performance is strongly dependent on the properties of the device interfaces, which dictate the charge-injection, -transporting, and -recombination properties. Consequently, significant efforts have been spent to modify these interfaces to maximize the performance of OLEDs using several approaches.[269–272]

Again, molecular self-assembly has emerged as an ideal pathway to reconcile inorganic and organic surfaces due to the versatility, processability, and high degree of order that can be achieved. Huang *et al*. first demonstrated the use of trichlorosilane-functionalized triarylamines-to modify ITO for enhanced hole-injection, thereby improving the turn-on voltage, brightness, and external quantum efficiency.[273–275] Liakos *et al*. compared phosphonic acid monolayers to various binding chemistries and found that phosphonic acid readily formed well-packed monolayers compared to the amine, trimethoxysilane, trichlorosilane, and epoxy binding groups. They also noted the difficulty in forming trichlorosilane monolayers due to self-polymerization.[276] In addition to hydrolytic stability and good surface loading, phosphonic acids couple with ITO through a condensation reaction in which a proton is transferred from the POH group to the ITO surface producing the metal–OP bond.[277] Since the surface hydroxyl content of ITO is relatively low,[278] the use of phosphonic acid may be advantegeous as it can protonate both bridging oxides and hydroxyl-groups on the ITO surface and so the number of molecules self-assembled on the ITO is less limited by the surface hydroxyl/H_2O content.[279] Nevertheless, phosphonic acid-derived SAMs are less hydrolytically and thermally stable than those prepared with silanes.

Phosphonic acid-functionalized triarylamines were first used by Jen and co-workers to form SAMs on ITO for OLED fabrication. Figure 4.24 shows the chemical structures of the molecules used for self-assembly. The device performance was consistent with the hole-transporting properties of

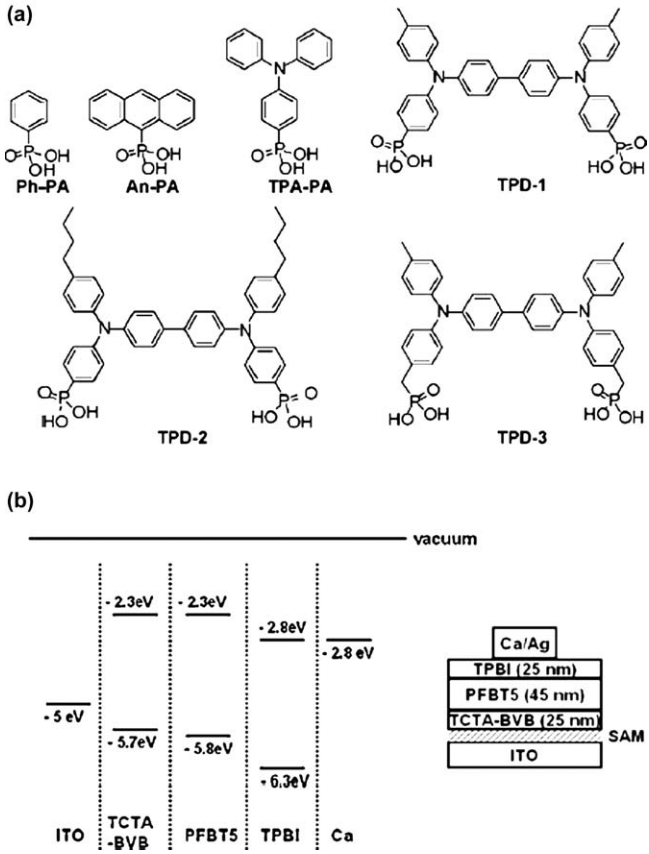

Figure 4.24 (a) Chemical structures of molecules used to form SAMs on ITO with improved hole injection. (b) Energy level diagram for LED structure. TCTABVB: tri(*N*-carbazolyl)triphenylamine-bis(vinylbenzyl); PFBT5: poly[2,7-(9,9-dihexylfluorene)-*co*-4,7-(2,1,3-benzothiadiazole)]. Reprinted with permission from ref. 280. Copyright 2008 Wiley-VCH Verlag GmbH.

triarylamine groups as measured by electrochemistry and improved surface energy matching with the hole-transporting layer. The turn-on voltage of these devices using SAM-modified anodes could be lowered by up to 3 V compared to bare ITO, yielding substantial current density and brightness increase. Variations in hole-injection and turn-on voltage between the different tetraphenyl-diamine (TPD)-based molecules were attributed to the position of alkyl-spacers within this series.[280]

More recently, also using phosphonic acid derivatives, Tao *et al*. analyzed the effect of self-assembled mixed monolayers from 1-butylphosphonic acid (BPA) and its trifluoromethyl-terminated analogue 4,4,4-trifluoro-1-butylphosphonic acid (FPA) in tuning the work function of the ITO anode electrode.[281] The authors demonstrated that the mixture of the two

molecules in different ratios allow continuous tuning of the ITO work function, from 5.0 to 5.75 eV. The authors also found that despite the current being higher with single-component FBA-modified ITO, due to it having the lowest hole-injection barrier, that did not necessarily yield higher luminescence efficiency because of unbalanced charge carriers. Therefore, they suggested that using different combinations of HTL and/or ETL materials, an electrode with a specific work function, would be needed to afford charge carrier balance and thus optimized luminance efficiency. The same authors also modified Au and Ag electrodes using a series of ω-trifluoromethylalkanethiols of different chain lengths[282] or mixed monolayers.[283] In the former work, they focused both on the effect of the dipole direction, due to odd–even chain length alternation, on the electrode work function and on the charge injection in a top emitting OLED device. It was demonstrated that both dipole moment and chain length could be used to modulate the charge injection, and their relative importance depended on the energy barrier at the interface. That is, if the energy gap between the metal and the organic layer was small, the current was influenced by the chain length of the SAM, or tunneling distance-dependent. Conversely, the current was injection barrier-dependent (dominated by the metal work function) when large energy gaps were present at the interface.

Finally, benzoid acid-derived SAMs have been also used to modify the ITO electrodes in order to facilitate hole-injection in OLEDs.[284] These layers were demonstrated to improve the interfacial organic–metal interface, thereby improving turn-on voltage, brightness, and external quantum efficiency. OLED devices fabricated with 4-[(3-methylphenyl)(phenyl)amino]benzoic acid-modified ITO showed enhanced hole injection current, increased electroluminescence emission, and improvement of turn-on voltage of around 1 V.

4.3.4 Electro-Optic Devices

The interest in nonlinear optics (NLO) is stimulated by applications in signal processing, communications, and data storage.[285,286] The study of NLO materials is concerned with the interaction of a physical medium with an electromagnetic field. As an electromagnetic field interacts with an NLO material, it is altered in various ways, including altering the frequency of the light, amplification of one light source by another, switching the light, or altering the transmission of the light through the medium.[287] These properties demonstrate the importance of NLO materials in various optical technologies that utilize light to acquire, store, transmit, and process information. Currently, considerable interest is being given to the development of materials that may be incorporated into electro-optic devices to create optical modulators.[288] These devices utilize the ability of NLO materials to alter the index of refraction of the material when a voltage is applied. By controlling the index of refraction, the phase of the polarized light propagating through nonlinear medium can be controlled to modulate

the light. Through the discovery of new materials processing light efficiently, there is the opportunity to greatly enhance optical network performance.

During the last decade, there has been great interest in developing organic-based NLO materials, offering substantial benefits over inorganic systems. Several advantages of molecule-based organic second-order NLO materials include low dielectric constants, high electro-optic coefficients, large hyperpolarizabilities, and intrinsic architectural tailorability as well as easy integration into optical waveguides, which is necessary for the fabrication of high bandwidth electro-optic devices.[289] To maximize the light field-induced polarization, several molecular and materials-related aspects must be taken into account. The individual π-conjugated molecular chromophores must possess high molecular hyperpolarizability (β) values. Furthermore, to preserve the molecular nonlinearities in the solid state (given by the $\chi^{(2)}$ coefficient or the electro-optic coefficient r_{33}), the organic chromophores should be organized in the solid state in the non-centrosymmetric environment. Given that molecular/multi-molecular chromophores are the active components in organic EO materials, the quest for EO devices with greater bandwidths and lower working voltages will require non-centrosymmetric chromophores having very large β values, thermal stability, and stable bulk macroscopic non-centrosymmetric alignment.

While SAM can afford NLO-active films (Figure 4.25),[290] practical applications (waveguide fabrication) require much thicker (microns) films. Therefore, several techniques have been developed to fabricate self-assembled

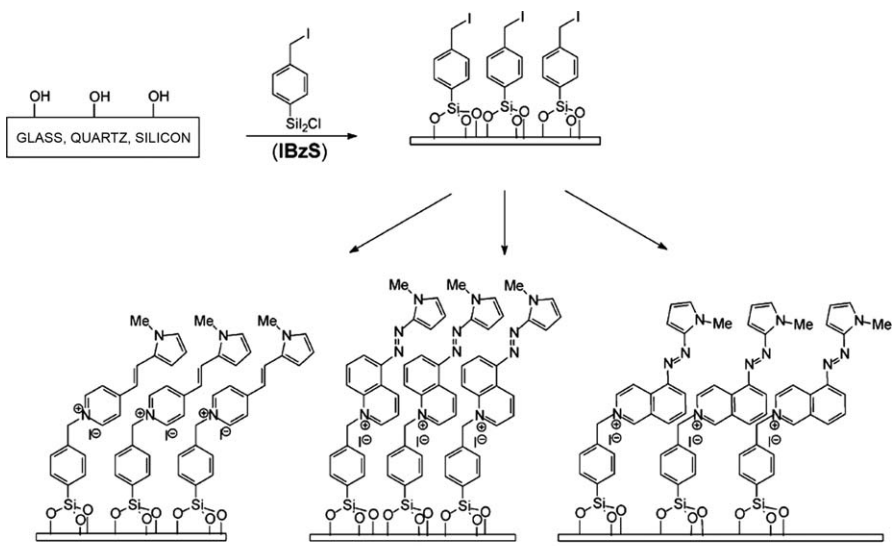

Figure 4.25 Fabrication of heterocycle-based SAMs exhibiting second-order NLO activity.
Reprinted with permission from ref. 290. Copyright 2002 American Chemical Society.

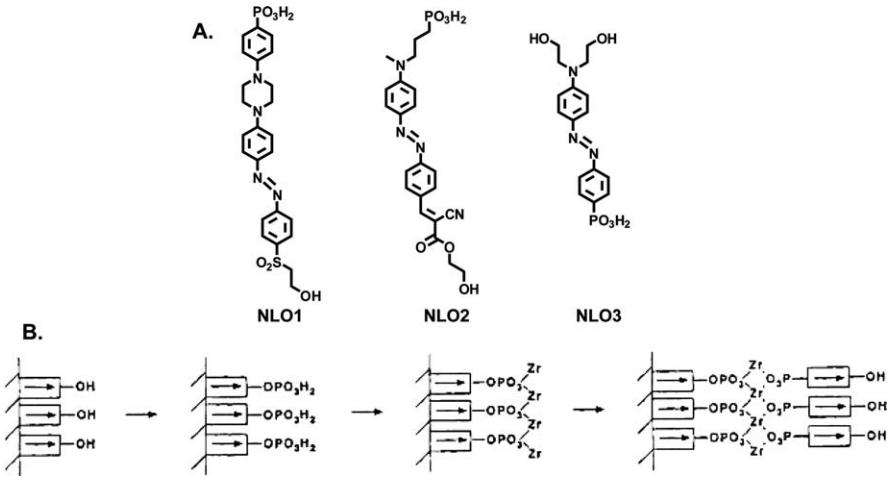

Figure 4.26 (A) Structure of representative phosphonic acid-functionalized NLO chromophores and (B) fabrication of the corresponding SAMTs. Adapted with permission from ref. 293. Copyright 1994 American Chemical Society.

multilayers that, in principle, can produce film of any desired thickness by repeating a sequence of chemisorption steps.[291] Katz first described a strategy for producing thermally stable second-order NLO films taking advantage of zirconium phosphonate/phosphate coordinative bonding to lock layers of a polar azo dye to each other, utilizing a three-step, polar deposition sequence of surface phosphorylation, zirconation, and dye adsorption.[292] The investigated structures are shown schematically in Figure 4.26. The film based on Katz's first chromophore generation (NLO3) showed relatively large second harmonic coefficients comparable in magnitude to that of $LiNbO_3$ (the benchmark material) and the films were stable to orientational randomization up to 150 °C. In a subsequent paper,[293] the same group reported the synthesis and polar film formation of several new nonlinear chromophores having optimized acceptors. For instance, the sulfone chromophore NLO1 was of interest because of its relative transparency in the visible region of the spectrum and its high thermal stability whereas NLO2 has an extended conjugation enabling improved response. Furthermore, NLO3 is somewhat basic, and the bulk nonlinearity may include contributions from its protonated form. Because NLO1 and NLO2 contain stronger electron-withdrawing substituents, they should be less susceptible to protonation.

The use of alkylsilane derivatives for NLO was pioneered by Marks and coworkers by utilizing a trichlorosilyl coupling agent, a NLO chromophore precursor, and a crosslinking "capping" molecule (Figure 4.27).[294] In the first generation procedure using key chromophore NLO4 (Figure 4.27), the coupling agent contains a trichlorosilyl head group that reacts with the hydroxylated surface, and a benzylic or alkyl halide surface group for further reaction. The

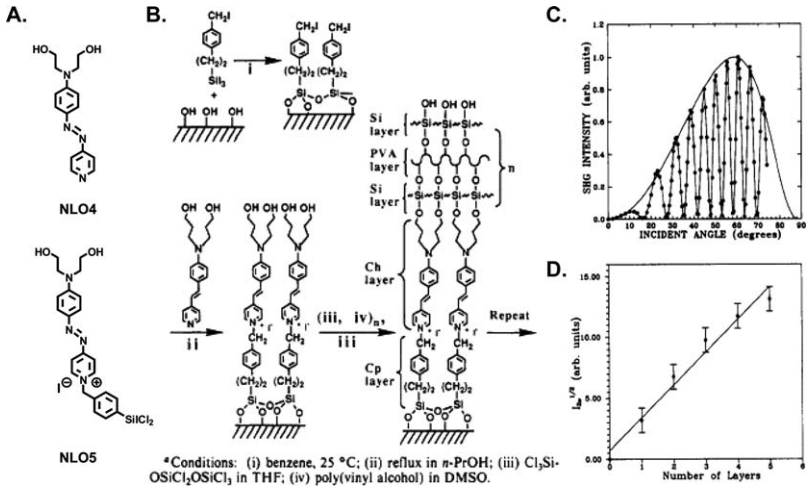

Figure 4.27 (A) Chromophores used for silane coupling chemistry; (B) corresponding fabrication scheme; (C) example of a SHG intensity–angle plot to measure the bulk hyperpolarizability; (D) intensity of the SHG signal *versus* number of chromophore layers.
Reprinted with permission from ref. 294*a*. Copyright 1990 American Chemical Society.

NLO chromophore precursor can undergo nucleophilic substitution with the surface group to form a quaternized pyridinium halide. The quaternization of the chromophore precursor not only attaches the chromophore to the surface but also activates the chromophore by forming a very strong electron-accepting pyridinium group. Each NLO chromophore used in this process also contains terminal hydroxy groups, which, following attachment of the chromophore to the surface, become available for reaction with an octachlorotrisiloxane "capping" agent. This capping agent reacts with the pendant hydroxyl groups, by the same reaction pathway as the trichlorosilyl coupling agent, to crosslink the chromophore layer and yield a hydroxy-terminated surface upon which the three-step process may be repeated. This type of self-assembled system allows for the layer-by-layer growth of NLO multilayer materials that, by the nature of their assembly, are inherently acentric and therefore do not require an external poling field to induce chromophore alignment. Self-assembled systems also form very robust and mechanically stable thin films as a consequence of the crosslinked siloxane network, which is formed during the deposition of the individual SAMs.[295] The multilayer structures were characterized by optical and XPS spectroscopy, advancing contact angle measurements, null ellipsometry, and NLO properties. The latter measurements revealed multilayer superlattices with good structural uniformity as demonstrated by the SHG intensity interference pattern (Figure 4.27C). A $\chi^{(2)}$ value of 2×10^{-7} esu at $\lambda = 1064$ nm for bulk samples was measured.[296]

The same group developed an efficient procedure to fabricate the same films using a protection–deprotection chemistry using chromophore

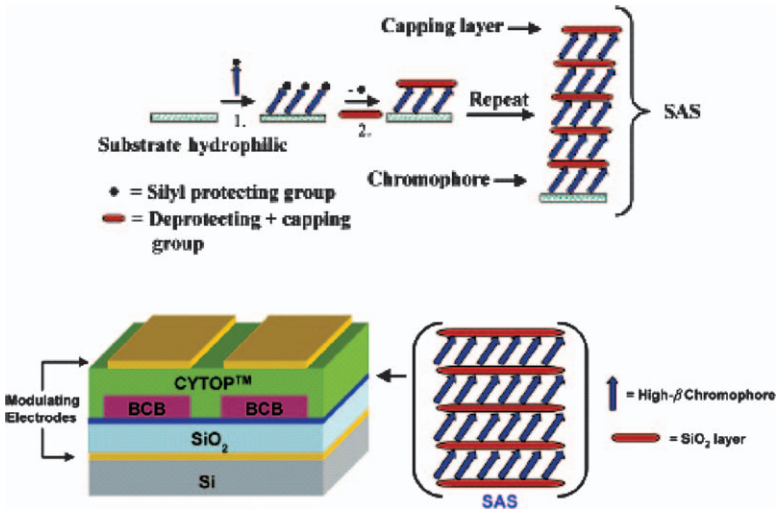

Figure 4.28 Synthetic route to the SAS layer and cross-section of a 'hybrid' Cyclotene™/SAS/Cyclotene™ based modulator.
Reprinted with permission from ref. 297. Copyright 2002 American Chemical Society.

NLO5 (Figure 4.27). The authors used highly reactive -$SiCl_2I$-functionalized, silyl-protected donor–acceptor azo-benzene chromophore derivatives and octachlorotrisiloxane as a deprotecting reagent/interlayer precursor without the need of a coupling reagent used in the first-generation films (Figure 4.27A). This process can be efficiently implemented in a vertical dipping procedure to yield polar films consisting of 40 alternating chromophore and capping layers. Each nanoscale bilayer (chromophore + polysiloxane layer 3.26 nm thick) can be grown in 40 min at least one order of magnitude more rapidly than previous siloxane-based solution deposition methodologies. Chromophore monolayer deposition from solution reaches completion in 15 min at 55 °C. The adherent, structurally regular assemblies exhibit appreciable electro-optic responses ($\chi(2) \sim 180$ pm V^{-1} and $r_{33} \sim 65$ pm V^{-1} by SHG measurements at 1064 nm) and high chromophore surface densities (40 $Å^2$ per chromophore).[297] Finally, the same group reported the fabrication of the first traveling-wave electro-optic modulators based on chromophoric SAMTs (termed SAS = self-assembled superlattices by these authors) possessing intrinsically polar microstructures (Figure 4.28). Although the thickness of the SAS layer was only ~150 nm, a π-phase shift is clearly observed. From the measured V_π value, the effective electro-optic coefficient of the SAS film is determined to be ~21.8 pm V^{-1} at an input wavelength of 1064 nm.[298,299]

4.4 Conclusions

New opto-electronic devices require a new set of materials for their optimal operation and unconventional fabrication. Self-assembly of organic molecules

represents a new pathway to fabricate the functional layers as well as to optimize critical device interfaces. Regarding the functional layers, SAMs but particularly SAMTs have been used as semiconductor, dielectric, and NLO component. Regarding device interfaces, as shown throughout this chapter, controlling interface quality is a common task for OFET, OLED, and OPV operations. For OFETs, source–drain contacts significantly influence device operation because of the contact resistance originating from work function mismatch and/or poor adhesion between the metal electrodes and the organic semiconductor or the semiconductor film morphology. The interface between the gate insulator and organic semiconductor critically affect major film-growth and electrical parameters starting from charge trapping, transport, and scattering. SAM/high-k metal oxide hybrid nanolayers with excellent dielectric and interfacial properties show good promise as an alternative to inorganic oxide-based gate dielectrics and have great potential for low-voltage high-performance OFETs. OLED device performance is significantly improved by the optimization of interfacial properties, which determine the efficient balance of charge-injection and thus exciton formation and light output efficiency. Interface engineering in OPV can reduce charge recombination sites, passivate charge trap states, control energy level alignment, tune photoactive layer morphology, improve materials compatibility, alter the work function of both anode and cathode for optimized open-circuit voltage, and ultimately allow the fabrication of high-efficiency OPV cells.

By developing the ability to fabricate photoactive films with a thickness controlled at the nano-scale, manipulate the nanoscale morphology of active materials, fabricate active and interfacial layers compatible with solution processing (spin-coating, dip-coating, drop-casting, stamping, and printing) on rigid and flexible substrates and control charge (hole/electron)-injection, -transport, -recombination (exciton formation), separation (exciton diffusion and dissociation), -selection, and -collection, organic electronics will evolve to fully realize its potential. In this context, the use of SAM and SAMT will be of prime importance.

Acknowledgments

Work at Northwestern was supported by the U.S. DOE Office of Basic Energy Sciences under Grant DE-FG02-08ER46536 (OPV), the NSF through the Northwestern U. MRSEC (Grant DMR-1121262) (Dielectrics), AFOSR (Grant FA9550-11-1-0142) (OFETs), and Polyera Corporation. R. P. O. thanks the MINECO of Spain for a ''Ramón y Cajal'' research contract.

References

1. OFET:(a) S. Holliday, J. E. Donaghey and I. McCulloch, *Chemistry of Materials*, 2014, **26**, 647; (b) W. Xie and C. D. Frisbie, *MRS Bulletin*, 2013, **38**, 43; (c) H. Klauk, *Organic Electronics II* 2012, 355, OLED:; (d) S. D. Dimitrov and J. R. Durrant, *Chemistry of Materials*, 2014,

26, 616; (e) H.-C. Liao, C.-C. Ho, C.-Y. Chang, M.-H. Jao, S. B. Darling and W.-F. Su, *Materials Today*, 2013, **16**, 326; (f) A. Facchetti, *Chem Mater.*, 2011, **23**, 733, OLED:; (g) D. Li, H. Zhang and Y. Wang, *Chemical Society Reviews*, 2013, **42**, 8416; (h) C. Groves, *Nature Materials*, 2013, **12**, 597; (i) S. Chen, Q. Wu, M. Kong, X. Zhao, Z. Yu, P. Jia and W. Huang, *Journal of Materials Chemistry C: Materials for Optical and Electronic Devices*, 2013, **1**, 3508, EO:; (j) W. Wu, J. Qin and Z. Li, *Polymer*, 2013, **54**, 4351; (k) S. Suresh, A. Ramanand, D. Jayaraman and P. Mani, *Reviews on Advanced Materials Science*, 2012, **30**, 175.

2. (a) R. E. Palmer, A. P. G. Robinson and Q. Guo, *ACS Nano*, 2013, **7**, 6416; (b) S. A. Claridge, W.-S. Liao, J. C. Thomas, Y. Zhao, H. H. Cao, S. Cheunkar, A. C. Serino, A. M. Andrews and P. S. Weiss, *Chemical Society Reviews*, 2013, **42**, 2725; (c) F. Zerbetto, *Advanced Materials*, 2013, **25**, 449.
3. (a) C. Nicosia and J. Huskens, *Materials Horizons*, 2014, **1**, 32; (b) A. Ulman, *An Introduction to Ultrathin Organic Films*; Academic Press: Boston, 1991.
4. (a) X. Ye and L. Qi, *Science China: Chemistry*, 2014, **57**, 58; (b) H. Kuhn and A. Ulman, in *Thin Films*, Ulman A., ed., Academic Press, New York, 1995, vol. 20.
5. D. A. Tirrell, *MRS Bull.*, 1991, July, 23.
6. J. Sagiv, *J. Am. Chem. Soc.*, 1980, **102**, 92.
7. P. Silberzan, L. Léger, D. Ausserré and J. J. Benattar, *Langmuir*, 1991, **7**, 1647.
8. S. R. Wasserman, Y.-T. Tao and J. M. Whitesides, *Langmuir*, 1989, **5**, 1074.
9. J. D. Le Grange, J. L. Markham and C. R. Kurjian, *Langmuir*, 1993, **9**, 1749.
10. R. Maoz and J. Sagiv, *J. Colloid Interface Sci.*, 1984, **100**, 465.
11. J. Gun and J. Sagiv, *J. Colloid Interface Sci.*, 1986, **112**, 457.
12. J. Gun, R. Iscovici and J. Sagiv, *J. Colloid Interface Sci.*, 1984, **101**, 201.
13. N. Tillman, A. Ulman, J. S. Schildkraut and T. L. Penner, *J. Am. Chem. Soc.*, 1988, **110**, 6136.
14. S. Brandriss and S. Margel, *Langmuir*, 1993, **9**, 1232.
15. K. Mathauser and C. W. Frank, *Langmuir*, 1993, **9**, 3002.
16. K. Mathauser and C. W. Frank, *Langmuir*, 1993, **9**, 3446.
17. J. Gun and J. Sagiv, *J. Colloid Interface Sci.*, 1986, **112**, 457.
18. G. Carson and S. Granick, *J. Appl. Polym. Sci.*, 1989, **37**, 2767.
19. C. R. Kessel and S. Granick, *Langmuir*, 1991, **7**, 532.
20. D. K. Schwartz, S. Steinberg, J. Israelachvili and Z. A. N. Zasadzinski, *Phys. Rev. Lett.*, 1992, **69**, 3354.
21. J. Gun, R. Iscovici and J. Sagiv, *J. Colloid Interface Sci.*, 1984, **101**, 201.
22. J. Gun and J. Sagiv, *J. Colloid Interface Sci.*, 1986, **112**, 457.
23. H. O. Finklea, L. R. Robinson, A. Blackburn, B. Richter, D. L. Allara and T. Bright, *Langmuir*, 1986, **2**, 239.
24. I. Rubinstein, E. Sabatani, R. Maoz and J. Sagiv, *Proc. Electrochem.Soc.*, 1986, **86**, 175.

25. I. Rubinstein, E. Sabatani, R. Maoz and J. Sagiv, *Electroanal. Chem.*, 1987, **219**, 365.
26. D. L. Allara, A. N. Parikh and F. Rondelez, *Langmuir*, 1995, **11**, 2357.
27. N. Tillman, A. Ulman and T. L. Penner, *Langmuir*, 1989, **5**, 101.
28. S. R. Wasserman, Y.-T. Tao and J. M. Whitesides, *Langmuir*, 1989, **5**, 1074.
29. L. Netzer, R. Iscovichi and J. Sagiv, *Thin Solid Films*, 1983, **100**, 67.
30. C. N. Sukenik, personal communication.
31. N. Tillman, A. Ulman and T. L. Penner, *Langmuir*, 1989, **5**, 101.
32. K. Ogawa, N. Mino, H. Tamura and M. Hatada, *Langmuir*, 1990, **6**, 1807.
33. D. Q. Li, M. A. Ratner, T. J. Marks, C. H. Zhang, J. Yang and G. K. Wong, *J. Am. Chem. Soc.*, 1990, **112**, 7389.
34. A. K. Kakkar, S. Yitzchaik, S. B. Roscoe, F. Kubota, D. S. Allan, T. J. Marks, Z. Xu, W. Lin and G. K. Wong, *Langmuir*, 1993, **9**, 388.
35. S. Yitzchaik, S. B. Roscoe, A. K. Kakkar, D. S. Allan, T. J. Marks, Z. Xu, T. Zhang, W. Lin and G. K. Wong, *J. Phys. Chem.*, 1993, **97**, 6958.
36. S. B. Roscoe, S. Yitzchaik, A. K. Kakkar, T. J. Marks, W. L. Lin and G. K. Wong, *Langmuir*, 1994, **10**, 1337.
37. W. Lin, S. Yitzchaik, W. Lin, A. Malik, M. K. Durbin, A. G. Richter, G. K. Wong, P. Dutta and T. Marks, *Angew. Chem., Int. Ed. Engl.*, 1995, **34**, 1497.
38. R. Maoz, R. Yam, G. Berkovic and J. Sagiv, in *Thin Films*, A. Ulman, ed., Academic Press, New York, 1995, vol. 20.
39. R. Maoz, J. Sagiv, D. Degenhardt, H. Möhwald and P. Quint, *Supramol. Sci.*, 1995, **2**, 9.
40. P. Silberzan, L. Léger, D. Ausserré and J. J. Benattar, *Langmuir*, 1991, **7**, 1647.
41. R. Banga, J. Yarwood, A. M. Morgan, B. Evans and J. Kells, *Langmuir*, 1995, **11**, 4393.
42. S. R. Wasserman, Y.-T. Tao and J. M. Whitesides, *Langmuir*, 1989, **5**, 1074.
43. R. Maoz and J. Sagiv, *J. Colloid Interface Sci.*, 1984, **100**, 465.
44. C. P. Tripp and M. L. Hair, *Langmuir*, 1992, **8**, 1120.
45. R. Maoz and J. Sagiv, *J. Colloid Interface Sci.*, 1984, **100**, 465.
46. S. R. Cohen, R. Naaman and J. Sagiv, *J. Chem. Phys.*, 1986, **90**, 3054.
47. T. Ohtake, N. Mino and K. Ogawa, *Langmuir*, 1992, **8**, 2081.
48. K. Mathauser and C. W. Frank, *Langmuir*, 1993, **9**, 3002.
49. K. Mathauser and C. W. Frank, *Langmuir*, 1993, **9**, 3446.
50. S. R. Wasserman, G. M. Whitesides, I. M. Tidswell, B. M Ocko, P. S. Pershan and J. D. Axe, *J. Am. Chem. Soc.*, 1989, **111**, 5852.
51. I. M. Tidswell, B. M. Ocko, P. S. Pershan, S. R. Wasserman, G. M. Whitesides and J. D. Axe, *Phys. Rev.*, 1990, **B 41**, 1111.
52. M. K. Chaudhury and G. M. Whitesides, *Science*, 1992, **255**, 1230.
53. N. Balachander and C. N. Sukenik, *Langmuir*, 1990, **6**, 1621.
54. Y. W. Lee, J. Reed-Mundell, C. N. Sukenik and J. E. Zull, *Langmuir*, 1993, **9**, 3009.

55. J. A. Chupa, S. Xu, R. F. Fishchetti, R. M. Strongin, J. P. McCauley, A. B. Smith and J. K. Blasie, *J. Am. Chem. Soc.*, 1993, **115**, 4383.
56. S. Paulson, K. Morris and B. P. Sullivan, *J. Chem. Soc., Chem. Commun.*, 1992, 1615.
57. N. Balachander and C. N. Sukenik, *Langmuir*, 1990, **6**, 1621.
58. M. K. Chaudhury and G. M. Whitesides, *Science*, 1992, **255**, 1230.
59. S. R. Wasserman, H. Biebuyck and G. M. Whitesides, *J. Mater.Res.*, 1989, **4**, 886.
60. P. Silberzan, L. Léger, D. Ausserré and J. J. Benattar, *Langmuir*, 1991, **7**, 1647.
61. S. R. Wasserman, Y.-T. Tao and J. M. Whitesides, *Langmuir*, 1989, **5**, 1074.
62. L. Netzer, R. Iscovichi and J. Sagiv, *Thin Solid Films*, 1983, **100**, 67.
63. M. Maoz and J. Sagiv, *Langmuir*, 1987, **3**, 1034.
64. M. Maoz and J. Sagiv, *Langmuir*, 1987, **3**, 1045.
65. R. Maoz, L. Netzer, J. Gun and J. Sagive, *J. Chim. Phys. (Paris)*, 1988, **85**, 1059.
66. L. Netzer, R. Iscovici and J. Sagiv, *Thin Solid Films*, 1983, **99**, 235.
67. R. Netzer and J. Sagiv, *J. Am. Chem. Soc.*, 1983, **105**, 674.
68. R. Maoz and J. Sagiv, *Thin Solid Films*, 1985, **132**, 135.
69. K. Ogawa, N. Mino, H. Tamura and M. Hatada, *Langmuir*, 1990, **6**, 851.
70. K. Ogawa, N. Mino, H. Tamura and M. Hatada, *Langmuir*, 1990, **6**, 1807.
71. M. Pomerantz, A. Segmüller, L. Netzer and J. Sagiv, *Thin Solid Films*, 1985, **132**, 153.
72. N. Tillman, A. Ulman and T. L. Penner, *Langmuir*, 1989, **5**, 101.
73. Y. W. Lee, J. Reed-Mundell, C. N. Sukenik and J. E. Zull, *Langmuir*, 1993, **9**, 3009.
74. D. Q. Li, M. A. Ratner, T. J. Marks, C. H. Zhang, J. Yang and G. K. Wong, *J. Am. Chem. Soc.*, 1990, **112**, 7389.
75. A. K. Kakkar, S. Yitzchaik, S. B. Roscoe, F. Kubota, D. S. Allan, T. J. Marks, Z. Xu, W. Lin and G. K. Wong, *Langmuir*, 1993, **9**, 388.
76. S. Yitzchaik, S. B. Roscoe, A. K. Kakkar, D. S. Allan, T. J. Marks, Z. Xu, T. Zhang, W. Lin and G. K. Wong, *J. Phys. Chem.*, 1993, **97**, 6958.
77. S. B. Roscoe, S. Yitzchaik, A. K. Kakkar, T. J. Marks, W. L. Lin and G. K. Wong, *Langmuir*, 1994, **10**, 1337.
78. I. M. Tidswell, B. M. Ocko, P. S. Pershan, S. R. Wasserman, G. M. Whitesides and J. D. Axe, *Phys. Rev.*, 1990, **B 41**, 1111.
79. M. K. Chaudhury and G. M. Whitesides, *Science*, 1992, **255**, 1230.
80. G. Wegner, *Thin Solid Films*, 1992, **216**, 105.
81. C. P. Tripp, R. P. N. Veregin and M. L. Hair, *Langmuir*, 1993, **9**, 3518.
82. G. Cao, H.-G. Hong and T. E. Mallouk, *Acc. Chem. Res.*, 1992, **25**, 420.
83. (a) H. Lee, L. J. Kepley, H.-G. Hong and T. E. Mallouk, *J. Am. Chem. Soc.*, 1988, **110**, 618; (b) H. Lee, L. J. Kepley, H.-G. Hong, S. Akhter and T. E. Mallouk, *J. Phys. Chem.*, 1988, **92**, 2597.
84. (a) H. E. Katz, M. L. Schilling, S. B. Ungahse, T. M. Putvinski and C. E. D. Chidsey, Supramolecular Architecture, in *ACS Symposium Series 499*, Bein, T., ed., American Chemical Society: Washington, DC, 1992, pp.

24–32; (b) H. E. Katz, M. L. Schilling, C. E. D. Chidsey, T. M. Putvinski and R. S. Hutton, *Chem. Mater.*, 1991, **3**, 699.
85. L. H. Dubois and R. G. Nuzzo, *Ann. Phys. Chem.*, 1992, **43**, 437.
86. C. D. Bain and G. M. Whitesides, *Adv. Mater.*, 1989, **1**, 506.
87. J. P. Folkers, J. A. Zerkowski, P. E. Laibinis, C. T. Seto and G. M. Whitesides, Supramolecular architecture, in *ACS Symposium Series 499*, Bein, T. ed., American Chemical Society: Washington, DC, 1992, pp. 10–23.
88. T. R. Lee, P. E. Laibinis, J. P. Folkers and G. M. Whitesides, *Pure Appl. Chem.*, 1991, **63**, 821.
89. G. M. Whitesides and G. S. Ferguson, *Chemtracts-Org. Chem.*, 1988, **1**, 171.
90. H. Sellers, A. Ulman, Y. Shnidman and J. E. Eilers, *J. Am. Chem. Soc.*, 1993, **115**, 9389.
91. E. B. Troughton, C. D. Bain, G. M. Whitesides, D. L. Allara and M. D. Porter, *Langmuir*, 1988, **4**, 365.
92. E. Katz, N. Itzhak and I. Willner, *J. Electroanal.Chem.*, 1992, **336**, 357.
93. R. G. Nuzzo and D. L. Allara, *J. Am. Chem. Soc.*, 1983, **105**, 4481.
94. E. Sabatani, J. Cohen-Boulakia, M. Bruening and I. Rubinstein, *Langmuir*, 1993, **9**, 2974.
95. M. A. Bryant, S. L. Joa and J. E. Pemberton, *Langmuir*, 1992, **9**, 753.
96. M. A. Bryant, S. L. Joa and J. E. Pemberton, *Langmuir*, 1992, **9**, 753.
97. W. Hill and B. Wehling, *J. Phys. Chem.*, 1993, **97**, 9451.
98. T. T.-T. Li, H. Y. Liu and M. J. Weaver, *J. Am. Chem. Soc.*, 1984, **106**, 1233.
99. J. M. Cooper, K. R. Greenough and C. J. McNeil, *J. Electroanal.Chem.*, 1993, **347**, 267.
100. K. Uvdal, P. Bodö and B. Liedberg, *J. Colloid Interf.Sci.*, 1992, **149**, 162.
101. A. Ihs, K. Uvdal and B. Liedberg, *Langmuir*, 1993, **9**, 733.
102. Th. Arndt, H. Schupp and W. Schepp, *Thin Solid Films*, 1989, **178**, 319.
103. J. A. Mielczarski and R. H. Yoon, *Langmuir*, 1991, **7**, 101.
104. T. R. G. Edwards, V. J. Cunnane, R. Parsons and D. Gani, *J. Chem. Soc., Chem. Commun.*, 1989, 1041.
105. A. J. Arduengo, J. R. Moran, J. Rodriguez-Paradu and M. D. Ward, *J. Am. Chem. Soc.*, 1990, **112**, 6153.
106. G. Xue, X.-Y. Huang, J. Dong and J. Zhang, *J. Electroanal.Chem.*, 1991, **310**, 139.
107. S. Bharathi, V. Yegnaraman and G. P. Rao, *Langmuir*, 1993, **9**, 1614.
108. M. G. Samanat, C. A. Broen and J. G. Gordon, *Langmuir*, 1992, **8**, 1615.
109. A. Ulman, *J. Mater. Educ.*, 1989, **11**, 205.
110. P. E. Laibinis, G. M. Whitesides, D. L. Allara, Y.-T. Tao, A. N. Parikh and R. G. Nuzzo, *J. Am. Chem. Soc.*, 1991, **113**, 7152.
111. M. W. Walczak, C. Chung, S. M. Stole, C. A. Widrig and M. D. Porter, *J. Am. Chem. Soc.*, 1991, **113**, 2370.
112. P. E. Laibinis and G. M. Whitesides, *J. Am. Chem. Soc.*, 1992, **112**, 1990.
113. A. Ihs and B. Liedberg, *Langmuir*, 1994, **10**, 734.

114. M. W. Walczak, C. Chung, S. M. Stole, C. A. Widrig and M. D. Porter, *J. Am. Chem. Soc.*, 1991, **113**, 2370.
115. K. Shimazu, Y. Sato, I. Yagi and K. Uosaki, *Bull.Chem. Soc. Jpn.*, 1994, **67**, 863.
116. A. Demoz and D. J. Harrison, *Langmuir*, 1993, **9**, 1046.
117. N. Muskal, I. Turyan, A. Shurky and D. Mandler, *J. Am. Chem. Soc.*, 1995, **117**, 1147.
118. M. Stratmann, *Adv. Mater.*, 1990, **2**, 191.
119. M. Volmer, M. Stratmann and H. Viefhaus, *Surf. Interface Anal.*, 1990, **16**, 278.
120. M. Brust, M. Walker, D. Bethell, D. J. Schiffrin and R. Whyman, *J. Chem. Soc., Chem. Commun.*, 1994, 801.
121. C. W. Sheen, J. X. Shi, J. Martensson, A. N. Parikh and D. L. Allara, *J. Am. Chem. Soc.*, 1992, **114**, 1514.
122. Y. Gu, B. Lin, V. S. Smentkowski and D. H. Waldeck, *Langmuir*, 1995, **11**, 1849.
123. P. E. Laibinis and G. M. Whitesides, *J. Am. Chem. Soc.*, 1992, **114**, 9022.
124. A. Ulman, unpublished results.
125. J. J. Hickman, D. Ofer, C. Zou, M. S. Wrighton, P. E. Laibinis and G. M. Whitesides, *J. Am. Chem. Soc.*, 1991, **113**, 1128.
126. R. G. Nuzzo, B. R. Zegarski and L. H. Dubois, *J. Am. Chem. Soc.*, 1987, **109**, 733.
127. D. M. Jaffey and R. J. Madix, *J. Am. Chem. Soc.*, 1994, **116**, 3012.
128. J. B. Schlenoff, M. Li and H. Ly, *J. Am. Chem. Soc.*, 1995, **117**, 12528.
129. A. Dhirani, M. A. Hines, A. J. Fisher, O. Ismail and P. Guyot-Sionnest, *Langmuir*, 1995, **11**, 2609.
130. J. Y. Gui, D. A. Stern, D. G. Frank, F. Lu, D. C. Zapien and A. T. Hubbard, *Langmuir*, 1991, **7**, 955.
131. J. Y. Gui, F. Lu, D. A. Stern and A. T. Hubbard, *J. Electroanal. Chem.*, 1990, **292**, 245.
132. D. L. Allara and R. G. Nuzzo, *Langmuir*, 1985, **1**, 45.
133. H. Ogawa, T. Chihera and K. Taya, *J. Am. Chem. Soc.*, 1985, **107**, 1365.
134. N. E. Schlotter, M. D. Porter, T. B. Bright and D. L. Allara, *Chem. Phys. Lett.*, 1986, **132**, 93.
135. D. Y. Huang and Y.-T. Tao, *Bull. Inst. Chem., Acad. Sin.*, 1986, **33**, 73.
136. M. R. Linford and C. E. D. Chidsey, *J. Am. Chem. Soc.*, 1993, **115**, 12631.
137. D. K. Aswal, S. Lenfant, D. Guerin, J. V. Yakhmi and D. Vuillaume, *Analytica Chimica Acta*, 2006, **568**, 84.
138. C. W. Tang and S. A. VanSlyke, *Appl. Phys. Lett.*, 1987, **51**, 913.
139. J. H. Burroughes, D. D. C. Bradley, A. R. Brown, R. N. Marks, K. Mackay, R. H. Friend, P. L. Burns and A. B. Holmes, *Nature*, 1990, **347**, 539.
140. R. H. Friend, R. W. Gymer, A. B. Holmes, J. H. Burroughes, R. N. Marks, C. Taliani, D. D. C. Bradley, D. A. dos Santos, J.-L. Bredas, M. Logdlund and W. R. Salaneck, *Nature*, 1999, **397**, 121.
141. C. W. Tang, *Appl. Phys. Lett.*, 1986, **48**, 183.

142. N. S. Sariciftci, L. Smilowitz, A. J. Heeger and F. Wudl, *Science*, 1992, **258**, 1474.
143. H. Hoppe and S. C. Sariciftci, *J. Mater. Res.*, 2004, **19**, 1924.
144. F. Garnier, R. Hajlaoui, A. Yassar and P. Srivastava, *Science*, 1994, **256**, 1684.
145. H. Sirringhaus, T. Kawase, R. H. Friend, T. Shimoda, M. Inbasekaran, W. Wu and E. P. Woo, *Science*, 2000, **290**, 2123.
146. G. Horowitz, *J. Mater. Res.*, 2004, **19**, 1946.
147. H. Sirringhaus, *Adv. Mater.*, 2005, **17**, 2411.
148. S. R. Forrest, *Nature*, 2004, **428**, 911.
149. R. A. Street, *Adv. Mater.*, 2009, **21**, 2007.
150. D. Braga and G. Horowitz, *Adv. Mater.*, 2009, **21**, 1473.
151. M. Burghard, H. Klauk and K. Kern, *Adv. Mater.*, 2009, **21**, 2586.
152. C. D. Dimitrakopoulos and P. R. L. Malenfant, *Adv. Mater.*, 2002, **14**, 99.
153. (a) P. Fontaine, D. Goguenheim, D. Deresmes, D. Vuillaume, M. Garet and F. Rondelez, *Appl. Phys. Lett.*, 1993, **62**, 2256; (b) J. Collet and D. Vuillaume, *Appl. Phys. Lett.*, 1998, **73**, 2681.
154. (a) D. Vuillaume, C. Boulas, J. Collet and J. V. Davidovits, *Appl. Phys. Lett.*, 1996, **69**, 1646; (b) C. Boulas, J. V. Davidovits, F. Rondelez and D. Vuillaume, *Phys. Rev. Lett.*, 1996, **76**, 4797.
155. (a) E. Tran, M. A. Rampi and G. M. Whitesides, *Angew. Chem. Int. Ed.*, 2004, **43**, 3835; (b) W. Wang, T. Lee and M. A. Reed, *Phys. Rev. B: Cond. Matt.*, 2003, **68**, 035416/1-035416/7; (c) D. J. Wold and C. D. Frisbie, *J. Am. Chem. Soc.*, 2001, **123**, 5549.
156. J. Collet, O. Tharaud, A. Chapoton and D. Vuillaume, *Appl. Phys. Lett.*, 2000, **76**, 1941.
157. (a) S. Kar, C. Miramond and D. Vuillaume, *Appl. Phys. Lett.*, 2001, **78**, 1288; (b) C. Miramond and D. Vuillaume, *J. Appl. Phys.*, 2004, **96**, 1529.
158. M. Halik, H. Klauk, U. Zschieschang, G. Schmid, S. Ponomarenko, S. Kirchmeyer and W. Weber, *Adv. Mater.*, 2003, **15**, 917.
159. M. Halik, H. Klauk, U. Zschieschang, G. Schmid, C. Dehm, M. Schuetz, S. Maisch, F. Effenberger, M. Brunnbauer and F. Stellacci, *Nature*, 2004, **431**, 963.
160. S. Kobayashi, T. Nishikawa, T. Takenobu, S. Mori, T. Shimoda, T. Mitani, H. Shimotani, N. Yoshimoto, S. Ogawa and Y. Iwasa, *Nature Mater.*, 2004, **3**, 317.
161. M.-H. Yoon, A. Facchetti and T. J. Marks, *Proc. Nat. Acad. Sci. USA*, 2005, **102**, 4678.
162. J. Robertson, *Rep. Prog. Phys.*, 2006, **69**, 327.
163. Y. Aoki, T. Kunitake and A. Nakao, *Chem. Mater.*, 2005, **17**, 450.
164. A. B. Mukhopadhyay, C. B. Musgrave and J. F. Sanz, *J. Am. Chem. Soc.*, 2008, **130**, 11996.
165. O. Acton, G. Ting, H. Ma, J. W. Ka, H. L. Yip, N. M. Tucker and A. K.-Y. Jen, *Adv. Mater.*, 2008, **20**, 3697.
166. I. N. Hulea, S. Fratini, H. Xie, C. L. Mulder, N. N. Iossad, G. Rastelli, S. Ciuchi and A. F. Morpurgo, *Nat. Mater.*, 2006, **5**, 982.

167. O. Acton, G. Ting, H. Ma and A. K.-Y. Jen, *Appl. Phys. Lett.*, 2008, **93**, 083302.
168. O. Acton, G. Ting, H. Ma, D. Hutchins, Y. Wang, B. Purushothaman, J. E. Anthony and A. K.-Y. Jen, *J. Mater. Chem.*, 2009, **19**, 7929.
169. Y.-G. Ha, J. D. Emery, M. J. Bedzyk, H. Usta, A. Facchetti and T. J. Marks, *J. Am. Chem. Soc.*, 2011, **133**, 10239.
170. K. Everaerts, J. D. Emery, D. Jariwala, H. J. Karmel, V. K. Sangwan, P. L. Prabhumirashi, M. L. Geier, J. J. McMorrow, M. J. Bedzyk, A. Facchetti, M. C. Hersam and T. J. Marks, *J. Am. Chem. Soc.*, 2013, **135**, 8926–8939.
171. K. Everaerts, L. Zeng, J. W. Hennek, D. I. Camacho, D. Jariwala, M. J. Bedzyk, M. C. Hersam and T. J. Marks, *ACS Appl. Mater. Interfaces*, 2013, **5**, 11884.
172. R. Nouchi and Y. Kubozono, *Org. Electron.*, 2010, **11**, 1025.
173. A. Jedaa, M. Salinas, C. M. Jäger, T. Clark, A. Ebel, A. Hirsch and M. Halik, *Appl. Phys. Lett.*, 2012, **100**, 063302.
174. N. Padma, S. Sen, S. N. Sawant and R. Tokas, *J. Phys. D: Appl. Phys.*, 2013, **46**, 325104.
175. D. O. Hutchins, T. Weidner, J. Baio, B. Polishak, O. Acton, N. Cernetic, H. Ma and A. K.-Y. Jen, *J. Mater. Chem. C*, 2013, **1**, 101.
176. (a) I. McCulloch, M. Heeney, M. L. Chabinyc, D. DeLongchamp, R. J. Kline, M. Colle, W. Duffy, D. Fischer, D. Gundlach, B. Hamadani, R. Hamilton, L. Richter, A. Salleo, M. Shkunov, D. Sparrowe, S. Tierney and W. Zhang, *Adv. Mater.*, 2009, **21**, 1091; (b) J. A. Lim, H. S. Lee, W. H. Lee and K. Cho, *Adv. Funct. Mater.*, 2009, **19**, 1515; (c) S. Liu, W. M. Wang, A. L. Briseno, S. C. B. Mannsfeld and Z. N. Bao, *Adv. Mater.*, 2009, **21**, 1217; (d) S. Allard, M. Forster, B. Souharce, H. Thiem and U. Scherf, *Angew. Chem. Int. Ed.*, 2008, **47**, 4070; (e) J. Zaumseil and H. Sirringhaus, *Chem. Rev.*, 2007, **107**, 1296; (f) V. Coropceanu, J. Cornil, D. A. da Silva Filho, Y. Olivier, R. Silbey and J. L. Bredas, *Chem. Rev.*, 2007, **107**, 926; (g) A. R. Murphy and J. M. J. Fréchet, *Chem. Rev.*, 2007, **107**, 1066; (h) J. E. Anthony, *Angew. Chem. Int. Ed.*, 2008, **47**, 452; (i) J. E. Anthony, *Chem. Rev.*, 2006, **106**, 5028; (j) C. R. Newman, C. D. Frisbie, D. A. da Silva Filho, J. L. Bredas, P. C. Ewbank and K. R. Mann, *Chem. Mater.*, 2004, **16**, 4436; (k) H. E. Katz, Z. N. Bao and S. L. Gilat, *Acc. Chem. Res.*, 2001, **34**, 359; (l) S. A. DiBenedetto, A. Facchetti, M. A. Ratner and T. J. Marks, *Adv. Mater.*, 2009, **21**, 1407; (m) A. Facchetti, M. H. Yoon and T. J. Marks, *Adv. Mater.*, 2005, **17**, 1705; (n) J. Veres, S. Ogier and G. Lloyd, *Chem. Mater.*, 2004, **16**, 4543.
177. D. J. Gundlach, L. L. Jia and T. N. Jackson, *IEEE Electron. Dev. Lett.*, 2001, **22**, 571.
178. P. Stoliar, R. Kshirsagar, M. Massi, P. Annibale, C. Albonetti, D. M. de Leeuw and F. Biscarini, *J. Am. Chem. Soc.*, 2007, **129**, 6477.
179. S. R. Saudari, P. R. Frail and C. R. Kagan, *Appl. Phys. Lett.*, 2009, **95**, 023301.

180. B. H. Hamadani, D. A. Corley, J. W. Ciszek, J. M. Tour and D. Natelson, *NanoLett.*, 2006, **6**, 1303.
181. G. S. Tulevski, Q. Miao, A. Afzali, T. O. Graham, C. R. Kagan and C. Nuckolls, *J. Am. Chem. Soc.*, 2006, **128**, 1788.
182. C. A. Di, G. Yu, Y. Q. Liu, X. Xu, D. Wei, Y. Song, Y. Sun, Y. Wang, D. Zhu, J. Liu, X. Liu and D. Wu, *J. Am. Chem. Soc.*, 2006, **128**, 16418.
183. J. P. Hong, A. Y. Park, S. Lee, J. Kang, N. Shin and D. Y. Yoon, *Appl. Phys. Lett.*, 2008, **92**, 143311.
184. K. Asadi, Y. Wu, F. Gholamrezaie, P. Rudolf and P. W. M. Blom, *Adv. Mater.*, 2009, **21**, 4109.
185. D. J. Gundlach, J. E. Royer, S. K. Park, S. Subramanian, O. D. Jurchescu, B. H. Hamadani, A. J. Moad, R. J. Kline, L. C. Teague, O. Kirillov, C. A. Richter, J. G. Kushmerick, L. J. Richter, S. R. Parkin, T. N. Jackson and J. E. Anthony, *Nat. Mater.*, 2008, **7**, 216.
186. W. Smaal, C. Kjellander, Y. Jeong, A. Tripathi, Bas van der Putten, A. Facchetti, H. Yan, J. Quinn, J. Anthony, K. Mynyd, W. Dehaened and G. Gelinck, *Organic Electronics*, 2012, **13**, 1686.
187. (a) S. Kobayashi, T. Nishikawa, T. Takenobu, S. Mori, T. Shimoda, T. Mitani, H. Shimotani, N. Yoshimoto, S. Ogawa and Y. Iwasa, *Nature Mater.*, 2004, **3**, 317; (b) K. P. Pernstich, S. Haas, D. Oberhoff, C. Goldmann, D. J. Gundlach, B. Batlogg, A. N. Rashid and G. J. Schitter, *J. Appl. Phys.*, 2004, **96**, 6431.
188. J. Youn, G. R. Dholakia, H. Huang, J. W. Hennek, A. Facchetti and T. J. Marks, *Adv. Funct. Mater.*, 2012, **22**, 1856.
189. O. Acton, M. Dubey, T. Weidner, K. M. ÓMalley, T.-W Kim, G. G. Ting, D. Hutchins, J. E. Baio, T. C. Lovejoy, A. H. Gage, D. G. Castner, H. Ma and A. K.-Y. Jen, *Adv. Funct. Mater.*, 2011, **21**, 1476.
190. (a) J. J. Brondijk, W. S. C. Roelofs, S. G. J. Mathijssen, A. Shehu, T. Cramer, F. Biscarini, P. W. M. Blom and D. M. De Leeuw, *Phys. Rev. Lett.*, 2012, 109; (b) A. Rumpel, M. Novak, J. Walter, B. Braunschweig, M. Halik and W. Peukert, *Langmuir*, 2011, **27**, 15016; (c) T. Stubhan, M. Salinas, A. Ebel, F. C. Krebs, A. Hirsch, M. Halik and C. J. Brabec, *Adv. Energy Mater.*, 2012, **2**, 532.
191. G. M. Whitesides and B. Grzybowski, *Science*, 2002, **295**, 2418.
192. E. C. P. Smits, *et al*., *Nature*, 2008, **455**, 956.
193. S. G. J. Mathijssen, E. C. P. Smits, P. A. van Hal, H. J. Wondergem, S. A. Ponomarenko, A. Moser, R. Resel, P. A. Bobbert, M. Kemerink, R. A. J. Janssen and D. M. de Leeuw, *Nat. Nanotechnol.*, 2009, **4**, 674.
194. T. Schmaltz, A. Y. Amin, A. Khassanov, T. Meyer-Friedrichsen, H.-G. Steinrueck, A. Magerl, J. J. Segura, K. Voitchovsky, F. Stellacci and M. Halik, *Advanced Materials*, 2013, **25**, 4511.
195. A. Ringk, W. S. Christian Roelofs, E. C. P. Smits, C. van der Marel, I. Salzmann, A. Neuhold, G. H. Gelinck, R. Resel, D. M. de Leeuw and P. Strohriegl, *Organic Electronics*, 2013, **14**, 1297–1304.
196. G. Dennler, M. C. Scharber and C. J. Brabec, *Adv. Mater.*, 2009, **21**, 1323.

197. F. C. Krebs, *Sol. Energy Mater. Sol. Cells*, 2009, **93**, 394.
198. G. Li, V. Shrotriya, J. S. Huang, Y. Yao, T. Moriarty, K. Emery and Y. Yang, *Nat. Mater.*, 2005, **4**, 864.
199. W. L. Ma, C. Y. Yang, X. Gong, K. Lee and A. J. Heeger, *Adv. Funct. Mater.*, 2005, **15**, 1617.
200. E. Bundgaard and F. C. Krebs, *Sol. Energy Mater. Sol. Cells*, 2007, **91**, 954.
201. R. Kroon, M. Lenes, J. C. Hummelen, P. W. M. Blom and B. De Boer, *Polym. Rev.*, 2008, **48**, 531.
202. J. Peet, M. L. Senatore, A. J. Heeger and G. C. Bazan, *Adv. Mater.*, 2009, **21**, 1521.
203. A. Hadipour, B. de Boer and P. W. M. Blom, *Adv. Funct. Mater.*, 2008, **18**, 169.
204. J. Y. Kim, K. Lee, N. E. Coates, D. Moses, T. Q. Nguyen, M. Dante and A. J. Heeger, *Science*, 2007, **317**, 222.
205. L. M. Chen, Z. R. Hong, G. Li and Y. Yang, *Adv. Mater.*, 2009, **21**, 1434.
206. M. Jorgensen, K. Norrman and F. C. Krebs, *Sol. Energy Mater. Sol. Cells*, 2008, **92**, 686.
207. P. W. M. Blom, V. D. Mihailetchi, L. J. A. Koster and D. E. Markov, *Adv. Mater.*, 2007, **19**, 1551.
208. F. L. Zhang, M. Johansson, M. R. Andersson, J. C. Hummelen and O. Inganas, *Adv. Mater.*, 2002, **14**, 662.
209. L. S. C. Pingree, B. A. MacLeod and D. S. Ginger, *J. Phys. Chem. C*, 2008, **112**, 7922.
210. H. Yan, P. Lee, N. R. Armstrong, A. Graham, G. A. Evmenenko, P. Dutta and T. J. Marks, *J. Am. Chem. Soc.*, 2005, **127**, 3172.
211. K. W. Wong, H. L. Yip, Y. Luo, K. Y. Wong, W. M. Lau, K. H. Low, H. F. Chow, Z. Q. Gao, W. L. Yeung and C. C. Chang, *Appl. Phys. Lett.*, 2002, **80**, 2788.
212. A. W. Hains and T. J. Marks, *Appl. Phys. Lett.*, 2008, **92**, 023504.
213. C. Y. Li, T. C. Wen and T. F. Guo, *J. Mater. Chem.*, 2008, **18**, 4478.
214. V. Shrotriya, G. Li, Y. Yao, C. W. Chu and Y. Yang, *Appl. Phys. Lett.*, 2006, **88**, 073508.
215. Y. H. Niu, H. Ma, Q. M. Xu and A. K.-Y. Jen, *Appl. Phys. Lett.*, 2005, **86**, 0835041.
216. M. D. Irwin, B. Buchholz, A. W. Hains, R. P. H. Chang and T. J. Marks, *Proc. Natl. Acad. Sci. USA*, 2008, **105**, 2783.
217. S. Han, W. S. Shin, M. Seo, D. Gupta, S. J. Moon and S. Yoo, *Org. Electron.*, 2009, **10**, 791.
218. M. D. Irwin, B. Buchholz, A. W. Hains, R. P. H. Chang and T. J. Marks, *Proc. Natl. Acad. Sci. USA*, 2008, **105**, 2783.
219. S. Han, W. S. Shin, M. Seo, D. Gupta, S. J. Moon and S. Yoo, *Org. Electron.*, 2009, **10**, 791.
220. J. S. Kim, J. H. Park, J. H. Lee, J. Jo, D. Y. Kim and K. Cho, *Appl. Phys. Lett.*, 2007, **91**, 112111.

221. S. Khodabakhsh, B. M. Sanderson, J. Nelson and T. S. Jones, *Adv. Funct. Mater.*, 2006, **16**, 95.
222. J. S. Kim, J. H. Park, J. H. Lee, J. Jo, D. Y. Kim and K. Cho, *Appl. Phys. Lett.*, 2007, **91**, 112111.
223. B. Kang, L. W. Tan and S. R. P. Silva, *Appl. Phys. Lett.*, 2008, **93**, 133302.
224. J. Y. Kim, S. H. Kim, H. H. Lee, K. Lee, W. L. Ma, X. Gong and A. J. Heeger, *Adv. Mater.*, 2006, **18**, 572.
225. J. K. Lee, N. E. Coates, S. Cho, N. S. Cho, D. Moses, G. C. Bazan, K. Lee and A. J. Heeger, *Appl. Phys. Lett.*, 2008, **92**, 243308.
226. A. Hayakawa, O. Yoshikawa, T. Fujieda, K. Uehara and S. Yoshikawaa, *Appl. Phys. Lett.*, 2007, **90**, 163517.
227. S. H. Park, A. Roy, S. Beaupre, S. Cho, N. Coates, J. S. Moon, D. Moses, M. Leclerc, K. Lee and A. J. Heeger, *Nat. Photonics*, 2009, **3**, 297.
228. M. H. Park, J. H. Li, A. Kumar, G. Li and Y. Yang, *Adv. Funct. Mater.*, 2009, **19**, 1241.
229. H. Faber, M. Burkhardt, A. Iedaa, D. Kalblein, H. Klauk and M. Halik, *Adv. Mater.*, 2009, **21**, 3099.
230. J. Gilot, M. M. Wienk and R. A. J. Janssen, *Appl. Phys. Lett.*, 2007, **90**, 143512.
231. J. Gilot, I. Barbu, M. M. Wienk and R. A. J. Janssen, *Appl. Phys. Lett.*, 2007, **91**, 113520.
232. A. Salomon, D. Berkovich and D. Cahen, *Appl. Phys. Lett.*, 2003, **82**, 1051.
233. T. C. Monson, M. T. Lloyd, D. C. Olson, Y. J. Lee and J. W. P. Hsu, *Adv. Mater.*, 2008, **20**, 4755.
234. H. L. Yip, S. K. Hau, N. S. Baek and A. K. Y. Jen, *Appl. Phys. Lett.*, 2008, **92**, 193313.
235. H. L. Yip, S. K. Hau, N. S. Baek, H. Ma and A. K. Y. Jen, *Adv. Mater.*, 2008, **20**, 2376.
236. H. Bedis, *J. Surf. Eng. Mater. Adv. Technol.*, 2011, **1**, 42.
237. L. Macaraig, T. Sagaw and S. Yoshikawa, *Energy Procedia*, 2011, **9**, 283.
238. C. K. Song, A. C. White, L. Zeng, B. J. Leever, M. D. Clark, J. D. Emery, S. J. Lou, A. Timalsina, L. X. Chen, M. J. Bedzyk and Tobin J. Marks, *ACS Appl. Mater. Interfaces*, 2013, **5**, 9924.
239. J.-M. Chiu and Y. Tai, *ACS Appl. Mater. Interfaces*, 2013, **5**, 6946.
240. G. Li, C. W. Chu, V. Shrotriya, J. Huang and Y. Yang, *Appl. Phys. Lett.*, 2006, **88**, 253503.
241. C. Waldauf, M. Morana, P. Denk, P. Schilinsky, K. Coakley, S. A. Choulis and C. J. Brabec, *Appl. Phys. Lett.*, 2006, **89**, 233517.
242. M. S. White, D. C. Olson, S. E. Shaheen, N. Kopidakis and D. S. Ginley, *Appl. Phys. Lett.*, 2006, **89**, 143517.
243. J. S. Huang, G. Li and Y. Yang, *Adv. Mater.*, 2008, **20**, 415.
244. H. H. Liao, L. M. Chen, Z. Xu, G. Li and Y. Yang, *Appl. Phys. Lett.*, 2008, **92**, 173303.

245. G. Li, C. W. Chu, V. Shrotriya, J. Huang and Y. Yang, *Appl. Phys. Lett.*, 2006, **88**, 253503.
246. H. H. Liao, L. M. Chen, Z. Xu, G. Li and Y. Yang, *Appl. Phys. Lett.*, 2008, **92**, 173303.
247. C. Waldauf, M. Morana, P. Denk, P. Schilinsky, K. Coakley, S. A. Choulis and C. J. Brabec, *Appl. Phys. Lett.*, 2006, **89**, 233517.
248. R. Steim, S. A. Choulis, P. Schilinsky and C. J. Brabec, *Appl. Phys. Lett.*, 2008, **92**, 093303.
249. M. S. White, D. C. Olson, S. E. Shaheen, N. Kopidakis and D. S. Ginley, *Appl. Phys. Lett.*, 2006, **89**, 143517.
250. C. Tao, S. P. Ruan, X. D. Zhang, G. H. Xie, L. Shen, X. Z. Kong, W. Dong, C. X. Liu and W. Y. Chen, *Appl. Phys. Lett.*, 2008, **93**, 193307.
251. C. Tao, S. P. Ruan, G. H. Xie, X. Z. Kong, L. Shen, F. X. Meng, C. X. Liu, X. D. Zhang, W. Dong and W. Y. Chen, *Appl. Phys. Lett.*, 2009, **94**, 043311.
252. J. Kruger, U. Bach and M. Gratzel, *Adv. Mater.*, 2000, **12**, 447.
253. C. Goh, S. R. Scully and M. D. McGehee, *J. Appl. Phys.*, 2007, **101**, 114503.
254. S. K. Hau, H. L. Yip, O. Acton, N. S. Baek, H. Ma and A. K. Y. Jen, *J. Mater. Chem.*, 2008, **18**, 5113.
255. S. K. Hau, H. L. Yip, N. S. Baek, J. Y. Zou, K. O'Malley and A. K. Y. Jen, *Appl. Phys. Lett.*, 2008, **92**, 253301.
256. S. K. Hau, H. L. Yip, H. Ma and A. K. Y. Jen, *Appl. Phys. Lett.*, 2008, **93**, 233304.
257. Y. E. Ha, M. Y. Jo, J. Park, Y.-C. Kang, S. I. Yoo and J. H. Kim, *J. Phys. Chem. C*, 2013, **117**, 2646.
258. S. K. Hau, Y.-J. Cheng, H.-L. Yip, Y. Zhang, H. Ma and A. K.-Y. Jen, *ACS Applied Materials & Interfaces*, 2010, **2**, 1892.
259. T. Stubhan, M. Salinas, A. Ebel, F. C. Krebs, A. Hirsch, M. Halik and C. J. Brabec, *Adv. Energ. Mater.*, 2012, **2**, 532.
260. C. W. Tang and S. A. VanSlyke, *Appl. Phys. Lett.*, 1987, **51**, 913.
261. J. H. Burroughes, D. D. C. Bradley, A. R. Brown, R. N. Marks, K. Mackay, R. H. Friend, P. L. Burns and A. B. Holmes, *Nature*, 1990, **347**, 539.
262. R. H. Friend, R. W. Gymer, A. B. Holmes, J. H. Burroughes, R. N. Marks, C. Taliani, D. D. C. Bradley, D. A. dos Santos, J.-L. Bredas, M. Logdlund and W. R. Salaneck, *Nature*, 1999, **397**, 121.
263. B. W. D'Andrade and S. R. Forrest, *Adv. Mater.*, 2004, **16**, 1585.
264. L. Akcelrud, *Prog. Polym.Sci.*, 2003, **28**, 975.
265. J. G. C. Veinot and T. J. Marks, *Acc. Chem. Res.*, 2005, **38**, 632.
266. G. Hughes and M. R. Bryce, *J. Mater. Chem.*, 2005, **15**, 94.
267. A. P. Kulkarni, C. J. Tonzola, A. Babel and S. A. Jenekhe, *Chem. Mater.*, 2004, **16**, 4556.
268. F. Huang, Y. J. Cheng, Y. Zhang, M. S. Liu and A. K.-Y. Jen, *J. Mater. Chem.*, 2008, **18**, 4495.
269. J. G. C. Veinot and T. J. Marks, *Acc. Chem. Res.*, 2005, **38**, 632.
270. G. Hughes and M. R. Bryce, *J. Mater. Chem.*, 2005, **15**, 94.

271. A. P. Kulkarni, C. J. Tonzola, A. Babel and S. A. Jenekhe, *Chem. Mater.*, 2004, **16**, 4556.
272. F. Huang, Y. J. Cheng, Y. Zhang, M. S. Liu and A. K.-Y. Jen, *J. Mater. Chem.*, 2008, **18**, 4495.
273. Q. L. Huang, J. F. Li, G. A. Evmenenko, P. Dutta and T. J. Marks, *Chem. Mater.*, 2006, **18**, 2431.
274. Q. L. Huang, G. A. Evmenenko, P. Dutta, P. Lee, N. R. Armstrong and T. J. Marks, *J. Am. Chem. Soc.*, 2005, **127**, 10227.
275. Q. L. Huang, G. Evmenenko, P. Dutta and T. J. Marks, *J. Am. Chem. Soc.*, 2003, **125**, 14704.
276. I. L. Liakos, R. C. Newman, E. McAlpine and M. R. Alexander, *Surf. Interface Anal.*, 2004, **36**, 347.
277. A. Vioux, J. Le Bideau, P. H. Mutin and D. Leclercq, *Top. Curr. Chem.*, 2004, **232**, 145.
278. V. M. Bermudez, A. D. Berry, H. Kim and A. Pique, *Langmuir*, 2006, **22**, 11113.
279. A. Vioux, J. Le Bideau, P. H. Mutin and D. Leclercq, *Top. Curr. Chem.*, 2004, **232**, 145.
280. J. A. Bardecker, H. Ma, T. D. Kim, F. Huang, M. S. Liu, Y. J. Cheng, G. Ting and A. K.-Y. Jen, *Adv. Funct. Mater.*, 2008, **18**, 3964.
281. S.-Y. Yu, D.-C. Huang, Y.-L. Chen, K.-Y. Wu and Y.-T. Tao, *Langmuir*, 2012, **28**, 424.
282. Y.-T. Tao, K.-Y. Wu, K.-H. Huang and T.-P. Perng, *Org. Electron.*, 2011, **12**, 602.
283. C.-Y. Chen, K.-Y. Wu, Y.-C. Chao, H.-W. Zan, H.-F. Meng and Y.-T. Tao, *Org. Electron.*, 2011, **12**, 148.
284. A. K. Havare, M. Can, S. Demic, S. Okur, M. Kus, H. Aydin, N. Yagmurcukardes and S. Tari, *Synth. Met.*, 2011, **161**, 2397.
285. L. R. Dalton, A. W. Harper, B. Wu, R. Ghosn, J. Laquindanum, Z. Liang, A. Hubbel and X. Chengzeng, *Adv. Mater.*, 1995, **7**, 519.
286. L. R. Dalton, W. H. Steier, B. H. Robinson, C. Zhang, A. Ren, S. Garner, A. T. Chen, T. Londergan, L. Irwin, B. Carlson, L. Fifield, G. Phelan, C. Kincaid, J. Amend and A. Jen, *J. Mater. Chem.*, 1999, **9**, 1905.
287. P. N. Prasad and D. J. Williams, *Introduction to Nonlinear Optical Effects in Molecules and Polymers*, John Wiley & Sons, Inc., New York, 1991.
288. (a) I. Ledoux and J. Zys, in *Novel Optical Materials and Applications*, I. C. Khoo, F. Simoni and C. Umeton, eds., John Wiley & Sons, New York 1997, p. 1; (b) W. H. Steier, A. Chen, S.-S. Lee, S. Garner, H. Zhang, V. Chuyanov, L. R. Dalton, F. Wang, A. S. Ren, C. Zhang, G. Todorova, A. Harper, H. R. Fetterman, D. Chen, A. Udupa, D. Bhattacharya and B. Tsap, *Chem. Phys.*, 1999, **245**, 487; (c) D. M. Burland, *Chem. Rev. special issue on Optical Nonlinearities in Chemistry*, 1994, **94**, 1.
289. (a) T. J. Marks and M. A. Ratner, *Angew. Chem., Int. Ed. Engl.*, 1995, **34**, 155–173; (b) S. Yitzchaik and T. J. Marks, *Acc. Chem. Res.*, 1996, **29**, 197; (c) B. J. Coe, *Chem. Eur. J.*, 1999, **5**, 2464; (d) M. J. Roberts,

G. A. Lindsay, W. N. Herman and K. J. Wynne, *J. Am. Chem. Soc.*, 1998, **120**, 11202; (e) W. M. K. P. Wijekoon, S. K. Wijayu, J. D. Bhawalkar, P. N. Prasad, T. L. Penner, N. J. Armstrong, M. C. Ezenyilimba and D. J. Williams, *J. Am. Chem. Soc.*, 1996, **118**, 4480; (f) H. E. Katz, W. L. Wilson and G. Scheller, *J. Am. Chem. Soc.*, 1994, **116**, 6636; (g) S. D. Bella, I. Fragalá, I. Ledoux, M. A. D. Garcia and T. J. Marks, *J. Am. Chem. Soc.*, 1997, **119**, 9550.

290. A. Facchetti, A. Abbotto, L. Beverina, S. Bradamante, M. E. van der Boom, G. Evmenenko, P. Dutta, T. J. Marks and G. A. Pagani, *Chem. Mater.*, 2002, **14**, 4996–5005.
291. (a) A. Facchetti, L. Beverina, M. E. van der Boom, P. Dutta, A. Shukla, C. E. Stern, G. Evmenenko, G. A. Pagani and T. J. Marks, *J. Am. Chem. Soc.*, 2006, **128**, 2142–2153; (b) A. Facchetti, A. Abbotto, L. Beverina, S. Bradamante, M. E. van der Boom, G. Evmenenko, P. Dutta, T. J. Marks and G. A. Pagani, *Chem. Mater.*, 2003, **15**, 1064.
292. H. E. Katz, W. L. Wilson and G. Scheller, *J. Am. Chem. Soc.*, 1994, **116**, 6636.
293. H. E. Katz, *Chem. Mater.*, 1994, **6**, 2227.
294. (a) D. Li, M. A. Ratner, T. J. Marks, C. Zhang, J. Yang and G. K. Wong, *J. Am. Chem. Soc.*, 1990, **112**, 7389; (b) W. Lin, S. Yitzchaik, W. P. Lin, A. Malik, M. K. Durbin, A. G. Richter, G. K. Wong, P. Dutta and T. J. Marks, *Angew. Chem. Int. Ed.*, 1995, **34**, 1497; (c) S. B. Roscoe, S. Yitzchaik, A. K. Kakkar, T. J. Marks, Z. Y. Xu, T. G. Zhang, W. P. Lin and G. K. Wong, *Langmuir*, 1996, **12**, 5338.
295. T. J. Marks and R. A. Ratner, *Angew. Chem. Int. Ed.*, 1995, **34**, 155.
296. D. Li, M. A. Ratner, T. J. Marks, C. Zhang, J. Yang and G. K. Wong, *J. Am. Chem. Soc.*, 1990, **112**, 7389.
297. P. Zhu, M. E. van der Boom, H. Kang, G. Evmenenko, P. Dutta and T. J. Marks, *Chem. Mater.*, 2002, **14**, 4982.
298. Y.-G. Zhao, A. Wu, H.-L. Lu, S. Chang, W.-K. Lu, S. T. Ho, M. E. van der Boom and T. J. Marks, *Applied Physics Letters*, 2001, **79**, 587.
299. Y.-G. Zhao, S. Chang, A. Wu, H.-L. Lu, S. T. Ho, M. E. van der Boom and T. J. Marks, *Optical Engineering*, 2003, **42**, 298.

CHAPTER 5

Amphiphilic Design for Supramolecular Materials with Opto-Electronic Functions

SUBI J. GEORGE,* ANKIT JAIN AND K. VENKATA RAO

Supramolecular Chemistry Laboratory, New Chemistry Unit, Jawaharlal Nehru Centre for Advanced Scientific Research (JNCASR), Jakkur, Bangalore 560064, India
*Email: george@jncasr.ac.in

5.1 Introduction

Amphiphiles are a class of molecules that are classified based on their dual affinity for solvating both polar and nonpolar solvents. Traditionally, the molecules are designed such that they contain definite domains of hydrophilic and hydrophobic parts. Owing to this unique solvating configuration amphiphiles have been parents to various kinds of nanostructured aggregates, all of them following the principle of energy minimization when encountering a solvent that preferentially solvates one end.[1] Quite naturally, control over the morphology can be attained if we vary the parameters such as the ratio between the volume fraction of hydrophobic to hydrophilic parts, and induction of secondary aggregation forces such as hydrogen bonding or π–π interaction. There is an enormous amount of literature exemplifying the above facts.[2]

Amphiphilic design has been put to the test for various functional molecules. One such class of molecules is the π-conjugated molecules. Most π-conjugated molecules that are known to be semiconducting are promising

RSC Smart Materials No. 12
Supramolecular Materials for Opto-Electronics
Edited by Norbert Koch

Published by the Royal Society of Chemistry, www.rsc.org

when considering opportunities for novel optoelectronic functions. They not only provide a cost-effective alternative, they also pave the way for flexible plastic electronic devices.[3] If one considers performance characteristics of these devices two important things need to be considered, firstly the chemical structure of π-systems and secondly, but all the more importantly, their hierarchical supramolecular organization. Self-assembly, without a doubt, offers an attractive way to get a handle on the hierarchical organization of these π-conjugated systems while maintaining thermodynamic control.[4] An enormous amount of effort has been made in the last decade to replicate the proposed theory into action, *i.e.* to obtain ordered nanostructures of π-conjugated chromophores so as to observe anisotropic electronic coupling and to have an authority over their performance in devices.[5] The bigger goal, however, has been to use these self-assembled nanostructures as electrical components in nanosized (5–100 nm) electronic devices.[6] Supramolecular self-assembly of π-conjugated molecules has progressed significantly considering their application in nanosized electronics.[7] There are some challenges, though, for using conjugated polymers in devices. Major among them is poor charge transport. This could be due to various probable reasons. Firstly, due to less π–π ordering between polymer chains on devices, a major controlling factor to nano phases seems to be the chain dynamics, and secondly because of the structural defects due to the polydispersity typically associated with polymeric synthesis. These issues can be taken into consideration by self-assembly based approaches of monodisperse π-conjugated oligomers. This would also be advantageous as ease of solution processability is not being sacrificed. However, even though supramolecular systems were ordained with advantages, their efficiencies on a device did not seem appreciable. One of the reasons for low efficiencies in supramolecular chromophoric systems could be the molecular design with solubilizing side chains, which on the one hand negates crystallization and promotes solution phase self-assembly but, on the other hand, hampers the molecular order and disrupts the extended π–π stacking in the assemblies. Thus, in organic opto-electronics, wherein one deals with various kinds of chromophores, morphology control, and better packing of π-conjugated chromophores, is greatly desired.

In this context, an amphiphilic design for self-assembly of chromophores can be of particular interest to attain diverse nanostructures. Additionally, it has been shown that solvophobic interactions between various parts of the amphiphilic systems can result in non-dynamic assemblies with higher association constants compared to their lipophilic counterparts.[8] Thus, a combination of amphiphilic design with the electro-active chromophore can be highly potent in giving rise to highly anisotropic assemblies with stronger π–π interactions and hence resulting in better electronic mobilities. This non-dynamic trait is critical in providing stability to the nanostructure. Needless to add that this attained immunity to external forces can go a long way in improving the life time and efficiency of devices based on amphiphilic supramolecular structures. This non-dynamic nature also

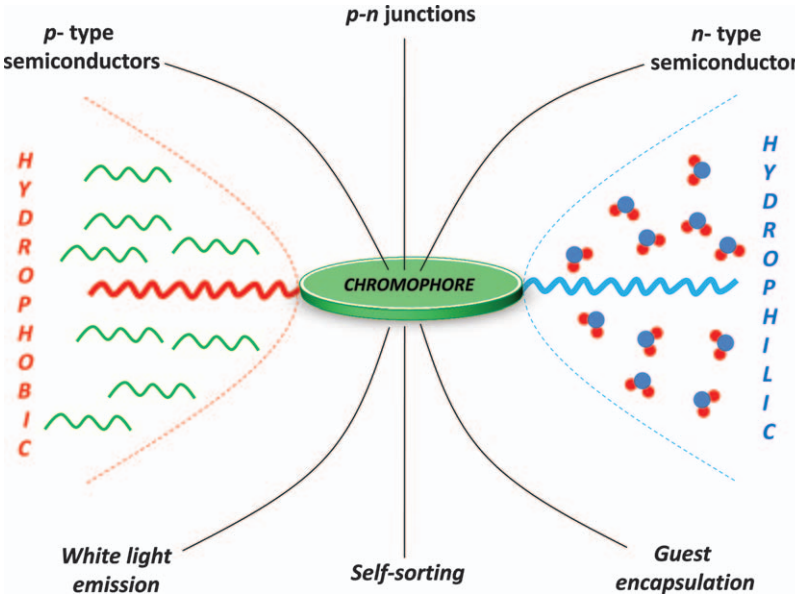

Scheme 5.1 Schematic showing the functional versatility chromophoric amphiphiles.

enables us to stabilize a conformation of transition dipoles and thus can hold a co-assembly together far more strongly. These properties can be used in studying distance and conformation dependent phenomenon like energy transfer. Furthermore, concepts such as compartmentalization, which have long been in the realm of biological sciences, can be applied to varied applications simply by taking advantage of the high propensity of amphiphiles to segregate in different phases depending on their interaction energy (Scheme 5.1).

In this chapter, we highlight the self-assembly of various π-conjugated amphiphiles that have been synthesized for various opto-electronic applications. However, for clarity, we have divided the chapter into two major sections: The first is based on electronic functions and the second on optical functions. The section on electronic functionality follows a sequential account starting with p-type semiconducting chromophores, followed by the n-type semiconductors. Further ahead, after the discussion on unconventional chromophores, we go on to elaborate the multi-chromophoric donor (D)–acceptor (A) amphiphilic systems, which combine p- and n-type semiconducting moieties, that mark an attempt towards synthesis of supramolecular p-n junctions. We end this section with a discussion on a much more exotic type of amphiphiles, *i.e.* supramolecular amphiphiles; recent attempts from our group to contribute in this particular field are also discussed. The second section on optical functionality starts with a discussion on amphiphiles that were employed in studying energy transfer. These systems include oligo(*p*-phenylenevinylene) (OPV) and naphthalene

diimide based amphiphiles. Later we elaborate the exhaustive study that exists on fluorene-based systems and how energy transfer has been used as a tool to understand supramolecular dynamics and conformation. An offshoot of the above work resulted in the synthesis of white-light-emitting amphiphilic aggregates; these systems have been duly reviewed. We conclude the section with a note on amphiphilic systems in which guest compartmentalization and hence induced energy transfer has been used to give further insight into the supramolecular assembly.

5.2 Electronic Functionality

5.2.1 p-Type Semiconducting Amphiphiles

5.2.1.1 Oligo(p-phenylenevinylene)s (OPVs)

Poly(*p*-phenylenevinylene)s (PPVs) have been proven to be exciting materials for photovoltaics, and electroluminescent devices owing to their excellent luminescence properties,[9] hence the study of their oligomeric counterparts, oligo(*p*-phenylenevinylene)s (OPVs), is all the more important. Various attempts and elegant designs have been investigated to achieve better packing of π-rings and hence better electronic mobilities.[10] One of the strategies employed has been the amphiphilic design in OPV chromophores to improve their supramolecular ordering as it plays a crucial role in their device performance.

Amphiphilic design in OPVs was first demonstrated by Wong *et al*. but instead of majoring on the packing their focus lay on the high solubility of the bolaamphiphilic species and hence a higher concentration to study third order nonlinearity.[11] Wang *et al*., however, in 2004 studied the assembly of rod coil amphiphiles with OPV units as rods (**1–3**) (Figure 5.1). These amphiphiles self-assemble into cylindrical micelles in solution. A detailed

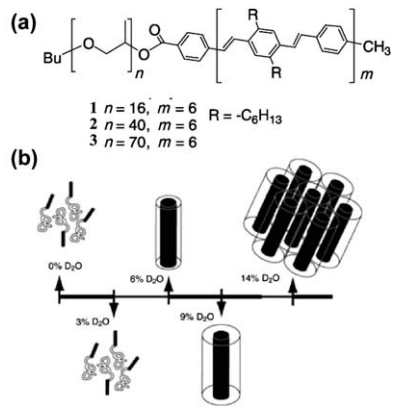

Figure 5.1 (a) Molecular structure of OPV block copolymers. (b) Schematic representation of the self-assembly of copolymer **3** in solution.
Reproduced from ref. 12 with permission from Wiley-VCH Verlag GmbH.

study of the morphological transformation from dimers into higher hexagonally packed micelles has been proved using SANS.[12]

Self-assembly of amphiphilic OPV derivatives substituted with PEG (poly(ethylene glycol)) on one end and hydrophobic alkyl chains on the other (**4**) (Figure 5.2a–c) was studied by Stupp *et al*.[13] These molecules inherently act as thermotropic liquid crystalline materials. They, however, also self-assemble in water and in other polar solvents like acetonitrile by forming lyotropic liquid crystalline mesophases, which at higher concentrations give rise to luminescent gels.

Very recently, George *et al*. reported OPV amphiphiles (**5**) end functionalized with alkyl and tetra(ethylene glycol) (TEG) chains, which self-assemble in THF–water mixture (Figure 5.2d).[14] These amphiphilic OPVs self-assemble into 2D sheets through a combination of π–π and solvophobic interactions with well-defined supramolecular ordering between the chromophores

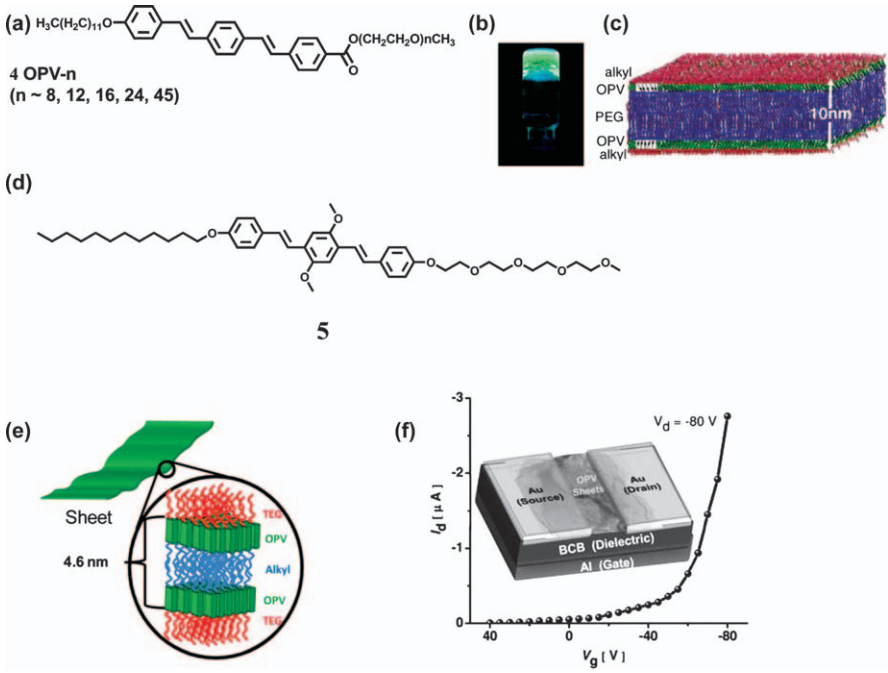

Figure 5.2 (a) Molecular structures of OPV amphiphiles functionalized with PEGs having different chain lengths. (b) and (c) OPV amphiphile (**4**, $n = 24$) derived hydrogel irradiated under 365 nm UV light and its bilayer packing respectively. (d) Molecular structure of OPV amphiphile (**5**) and (e) schematic representation of its molecular organization in the sheets. (f) Transconductance curves for sheets made from **5** in top contact bottom gate FET; inset: schematics of the device structure with these sheets as active layer.
(b) and (c) Reproduced from ref. 13 with permission from The American Chemical Society. (e)–(f) Reproduced from ref. 14 with permission from Wiley-VCH Verlag GmbH.

(Figure 5.2e). The fact that amphiphilic assembly cannot only be used for controlling the arrangement of chromophores but also has constructive influences on the hole mobilities, hence achieving high mobilities from solution processable self-assembly of this class of chromophores, was thus exemplified (Figure 5.2f). OPV 2D sheets showed FET mobility values as high as 8×10^{-3} cm^2 V^{-1} s^{-1}, which in fact is among some highest reported values for self-assembled chromophoric structures. An additional point to be noted here is that these values are even comparable to those obtained by FET studies on OPV crystals. This particular turnaround can be assumed to be due to the amphiphilic design, which upon self-assembly in water brings about stronger π-stacking and hence improved mobility features.

Self-assembly of OPV chromophores can also promoted by functionalizing them with peptides. Here additional advantages can be reaped in terms of the H-bonding along with the amphiphilicity that the peptides bring about; a wise choice of peptide sequence is needed. In this context, β-sheet forming peptides have come to be of particular significance. Bilayers with antiparallel orientation of OPVs in a β-sheet conformation at the solid–liquid interface have been reported by Meijer *et al*. using scanning tunnelling microscopy (STM) studies on OPV-peptide conjugates (**6**, **7**). Solution phase self-assembly studies were carried out in water and the formation of various 1D nanostructures such as nanofibers and nanotubes (Figure 5.3a–d) was revealed.[15] Additionally Tovar *et al*. have reported a class of OPV–peptide conjugates (**8**) that form hydrogels and result in highly aligned nanowires when extruded from a syringe.[16] The alignment was further supported by the fact that these substrates showed optical birefringence. This strategy was further extended to more electron rich chromophores such as oligothiophenes (**9**) to achieve macroscopically aligned nanowires with high anisotropic mobility ($\sim$0.03 cm^2 V^{-1} s^{-1}) (Figure 5.3e–i).

5.2.1.2 *Hexa-benzocoronenes (HBCs)*

Hexa-peri-benzocoronenes (HBCs) are a well-studied class of organic semiconductors. They are characterized by their efficient hole transporting behaviour and large π ring which inculcates in this particular system a strong tendency to self-organize. Müllen *et al*. have studied in detail the self-assembly behaviour of hydrophobic HBCs along with their charge carrier mobilities in the liquid crystalline state.[17] Aida *et al*. on the other hand have been particularly engrossed in studying assembly characteristics of amphiphilic HBCs (**10, 11**). Owing to this they elaborated a bottom-up synthesis strategy to attain supramolecular graphitic nanotubes.[18] These nanotubes are formed in solution by self-assembly of HBC chromophores driven by their characteristic π–π stacking. Amphiphilicity ordains additional solvophobic effects that result in bilayer formation through interdigitation of alkyl chains (Figure 5.4a–c). The resultant nanotubes retain the electro-active nature of constituent chromophores as exhibited from their redox active nature. A single nanotube exhibits resistivity of 2.5 MΩ at 285 K after

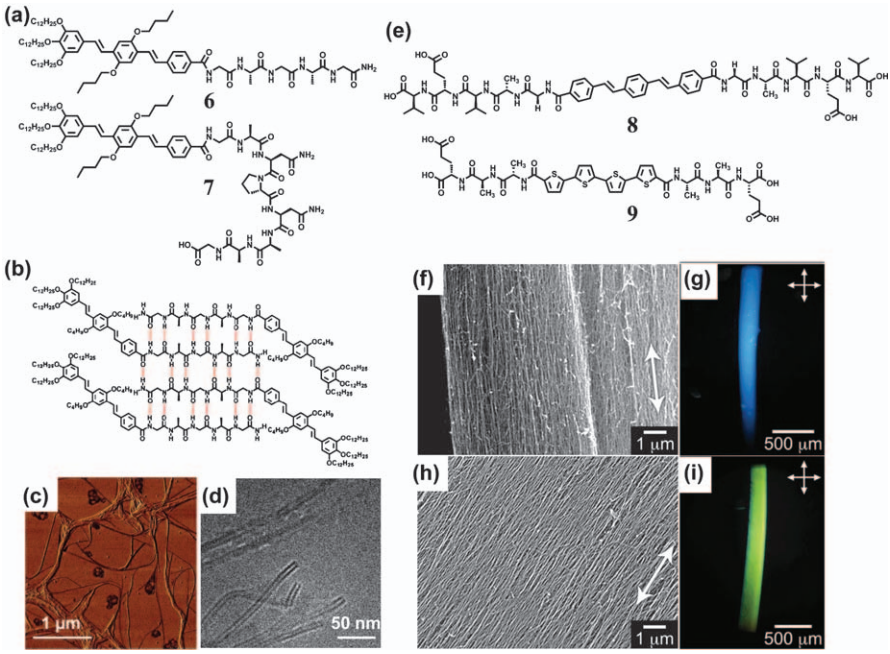

Figure 5.3 (a) Molecular structures of OPV peptide amphiphiles (**6** and **7**). (b) Molecular structure of an antiparallel β-sheet conformation of a monolayer of **6**. (c) AFM image of nanofibers of **6** formed in water. (d) Cryo-TEM image of **7** in water. (e) Molecular structures of OPV and oligothiophene peptide amphiphiles that form hydrogels. Representative SEM images of aligned structures composed of (f) **8** and (h) **9**. Optical birefringence of macroscale peptide fibres composed of (g) **8** and (i) **9** as seen under crossed polarizers.
(b)–(d) Reproduced from ref. 15 with permission from The American Chemical Society. (e)–(i) Reproduced from ref. 16 with permission from Wiley-VCH Verlag GmbH.

treatment with $NOBF_4$, which acts as an oxidising agent. Interestingly, the resulting nanotubes from **11** appear to be aligned along the fibre long axis. The ease with which these fibres can be processed was shown by the fact that these bundles could be literally ''fished'' from the aggregated solution with a glass hook. This unidirectional alignment and long-range ordering in amphiphilic nanostructures resulted in high anisotropic conductivity upon iodine doping (Figure 5.4d–f).[19] Similar conductivity studies were also carried out for other chiral HBC nanostructures.[20] The chirality aspect is particularly important as that can result in coiled π-electronic pathways thus finally resulting in novel device applications. One challenge, however, that remained was the stability of these nanostructures under oxidative I_2 doping. The above challenge was overcome by an ingenious methodology to covalently polymerize the molecules upon aggregation. Methodologies such as photodimerization[21] and ring-opening metathesis polymerization

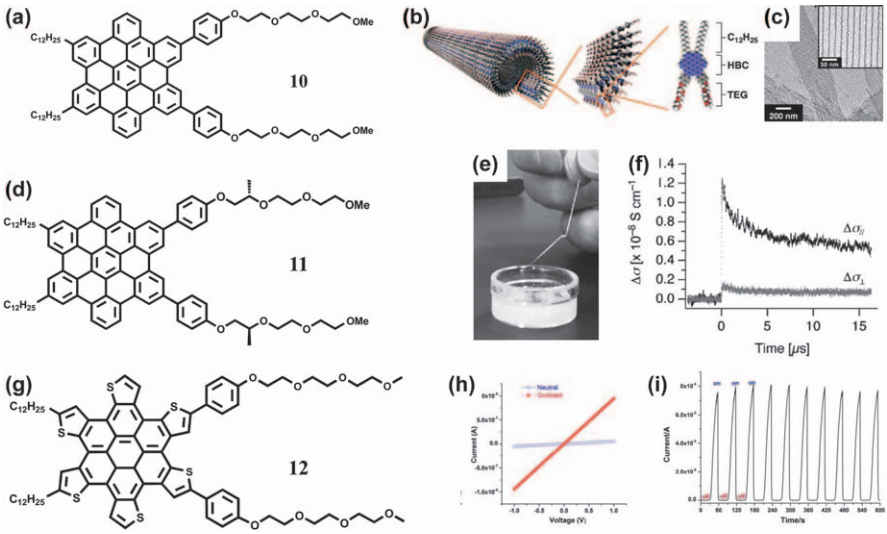

Figure 5.4 (a) Molecular structures of HBC amphiphile **10**. (b) Schematic illustrations of the hierarchical structures of a nanotube formed from **10** and (c) TEM images of amphiphilic HBC (alkyl chain is $C_{13}H_{27}$) nanotubes at different magnifications. (d) Molecular structures of chiral HBC amphiphile (**11**). (e) A macroscopic fiber consisting of bundled nanotubes of **11** processed by using a glass hook. (f) Transient conductivities ($\Delta\sigma$) at 298 K of a macroscopic fiber consisting of bundled nanotubes of **11** observed for the parallel ($\Delta\sigma_{||}$) and perpendicular ($\Delta\sigma_{\perp}$) directions to the electric-field vector of the microwave. (g) Molecular structure and (h) *I–V* curve of a device fabricated from the nanofibers of **12** before and after oxidation with $NOBF_4$ at 298 K. (i) Photocurrent on/off switch plot of **12**-PCBM bled when the light is turned on or off in an interval of 30 s at 2 V bias voltage. (b) and (c) Reproduced from ref. 18*b* with permission from The American Chemical Society. (e) and (f) Reproduced from ref. 19 with permission from Wiley-VCH Verlag GmbH. (h) and (i) Reproduced from ref. 23 with permission from The American Chemical Society.

(ROMP)[22] were employed by Aida *et al*. to finally gain access to stable nanostructures upon I_2 doping. This strategy also provided a route for stabilizing the metastable nanostructures, which were previously only formed as intermediates to the final nanotube structure.

Inspired by these results, amphiphilic thieno derivative of HBCs (**12**) (Figure 5.4g) were recently synthesized by Müllen *et al*.[23] These are more soluble than conventional HBC amphiphiles and hence can be called soft-HBCs. Hexathienocoronene amphiphiles showed varied morphology with change in solvents in which aggregation was induced, for example helices in dioxane and nanotubes in acetone. Their self-assemblies on a bulk scale and as well as on a solid–liquid interface were also established. Nanofibres formed from **12** were redox active and showed a resistivity of 1.1 MΩ at 295 K after oxidation with $NOBF_4$. This value is lower than the values obtained by Aida *et al*. for **11** and the difference has been attributed to the electron rich

centre of **12** (Figure 5.4h). A device was fabricated with a blend of hexathienocoronene amphiphiles and PCBM in the molar ratio of 1 : 2 and was tested for generation of photocurrent; 8 nA of photocurrent generation with an on/off ratio of 6×10^4 exemplifies the potential in these molecules (Figure 5.4i).

5.2.2 n-Type Semiconducting Amphiphiles

5.2.2.1 Perylene Bis-imides (PBIs)

Perylene bis-imides (PBIs), also known as perylene diimides (PDIs), are well-studied *n*-type organic semiconductors. These chromophores owe their characteristics to wide spectral overlap with the solar spectrum, high photostability, and a sufficiently large π ring that induces better electronic coupling and facilitates nanostructure formation.[24] Considering their efficient electron transporting nature, PBI dyes are prime alternatives for fullerene acceptors as n-type semiconducting materials in organic photovoltaics.[25,26] In this particular context various non-covalent strategies have been employed to study and further improve the supramolecular ordering of PBIs, which would consequently result in efficient opto-electronic functions.[27] Würthner *et al*. have been particularly active in elucidating the self-assembly of PBI dyes in water[28] and organic solvents.[29] They have employed various non-covalent interactions such as H-bonding and solvophobic interactions in addition to strong π–π interactions between PBI chromophores. Consequently, they have observed that π–π stacking of PBIs in water is very strong with an association constant K of over 10^8 M^{-1}. As can be envisaged from this result, self-assembly of PBIs in water would be a potent approach for creation of novel n-type semiconducting materials, with enhanced opto-electronic functions.

Self-assembly of water soluble cationic PBI amphiphiles (**13**, **14**) (Figure 5.5a) was first studied by Chang *et al*.[30] At appropriate concentrations these molecules result in lyotropic phases in water, forming highly aligned assemblies on substrates. Consequently, the dichroic ratios are comparable with that of commercial polarizers. Alternatively, Zang *et al*. have studied uncharged bolaamphiphiles of PBI (**15**). A molecularly dissolved solution of propoxyethyl PBI (**15**) was injected into methanol resulting in formation of nanobelts.[31] When these structures are exposed to hydrazine vapours, which are used as electron donors, PBI radical anions are formed and owing to which these nanobelts display a high conductivity of 10^{-3} S cm^{-1} at room temperature (Figure 5.5b,c).[32] Furthermore, they have also produced long nanobelts (few mm) by the self-organization of PBI amphiphile (**16**) in ethanol–water mixtures. π-Stacking in these PBIs is proposed to be oriented along the length of the nanobelt.[33] Single nanobelts were used for two-probe device measurements and showed thrice as higher current after electron injection by hydrazine vapours as compared to untreated nanobelts.

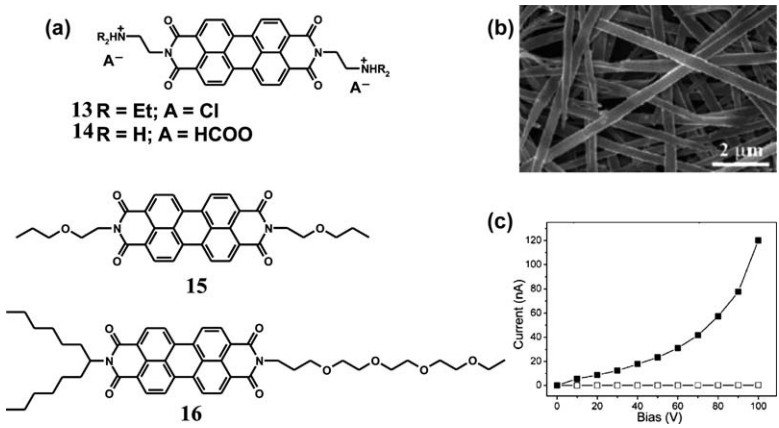

Figure 5.5 (a) Molecular structures of amphiphilic PBIs. (b) SEM image of nanobelts of **15**. (c) *I–V* curves measured on a nanobelt of **15** in air (open rectangle) and in saturated hydrazine vapour (closed rectangle).
(b) and (c) Reproduced from refs. 31 and 32, respectively, with permission from The American Chemical Society.

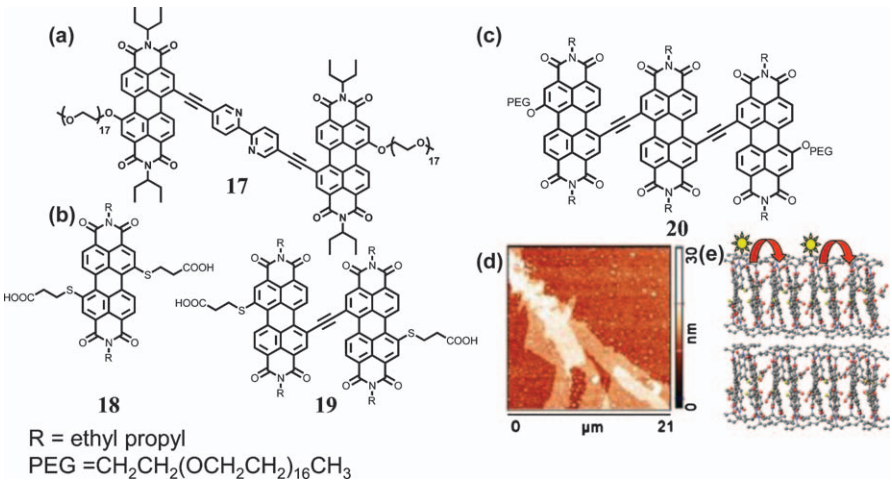

Figure 5.6 (a)–(c) Molecular structures of oligo PBI amphiphiles (**17–20**). (d) Self-assembled nanosheets of **20** formed in water and (e) schematic representation of exciton migration in these nanosheets.
(d) and (e) Reproduced from ref. 36 with permission from The American Chemical Society.

Rybtchinski *et al.* have investigated the self-assembly characteristics of oligo PBI amphiphiles in water. [34] Interestingly, self-assembled networks of poly(ethylene glycol) (PEG) functionalized oligo PBI amphiphile (**17**, Figure 5.6) were demonstrated as systems for nano-filtration membranes for nanoparticles.[35] This result reiterates the non-dynamic nature and rigidity of

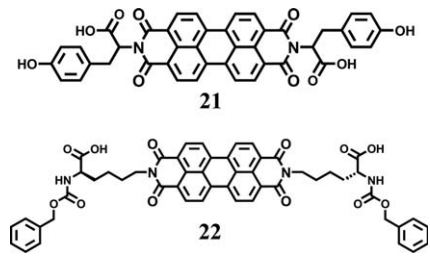

Figure 5.7 Molecular structure of (a) L-tyrosine functionalized PBI (**21**) and (b) L-lysine functionalized PBI (**22**).

the amphiphilic design. Additionally, Rybtchinski *et al*. have shown that other PBIs amphiphiles (**18–20**) self-assemble in water to give crystalline 2D structures. These nanostructures showed efficient exciton migration up to 120 nm (Figure 5.6d,e).[36] Moreover, exciton diffusion coefficients obtained from these 2D structures are better than previously benchmarked PTCDA (perylene tetracarboxylic dianhydride)[37] crystalline films. Clearly, such a rigid 2D morphology of this class of amphiphiles, which also possess wide spectral coverage owing to the chromophore, would go a long way towards the fabrication of efficient light-harvesting systems.

As in the case of p-type semiconducting chromophores, PBIs can also be functionalized with peptides to enable interesting morphologies. Banerjee *et al*. have exemplified this by using L-tyrosine functionalized PBI amphiphiles (**21**, Figure 5.7). These molecules self-assemble in water through H-bonding and π–π stacking and additionally are responsive to external stimuli such as pH. Luminescent hydrogels could be thus attained, and these gel networks exhibit photo-switchable conductivity when irradiated by white light with high on/off ratios.[38] Furthermore, Li *et al*. have reported the modulation of L-lysine-functionalized PBI (**22**) nanostructures by changing the ratio between acetone and water during the self-assembly process. Structures could be modulated from fibres to sheets to nanotubes with respective conductivities of 10^{-3}, 10^{-2}, and 10^{-6} S cm^{-1}.[38]

5.2.3 Miscellaneous π-Conjugated Amphiphiles

Apart from PDIs amphiphilic design has been adopted in the assembly of various other chromophores. For instance, Pei *et al*. have synthesized and studied the self-assembly of ''butterfly shaped'' benzodithiophene amphiphiles (**23**, Figure 5.8).[39] In chloroform–methanol mixtures these molecules self-assemble into self-standing bilayered sheets due to π–π and solvophobic interactions. The ordered and tight packing in these structures results in mobilities up to 0.02 $cm^2\ V^{-1}\ s^{-1}$.

Kajitani *et al*. exploited the amphiphilic design to achieve frustrated assembly of dipoles in dibenzo[*a,c*]phenazine dipoles (**24**) (Figure 5.9a). The amphiphilic molecules in liquid crystalline state were found to align

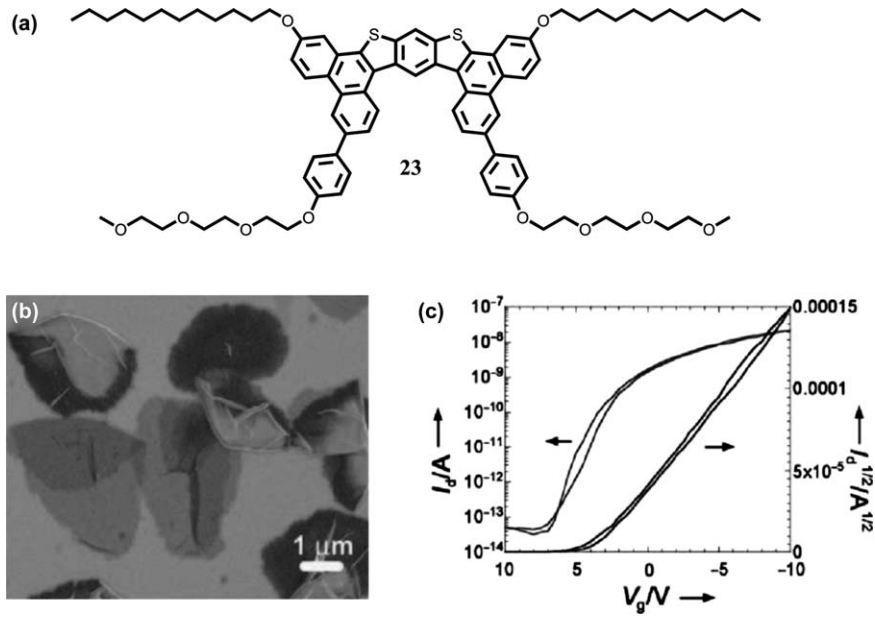

Figure 5.8 (a) Molecular structure of butterfly shaped amphiphile (**23**). (b) SEM image of 2D nano sheets of **23**. (c) Charge transfer characteristics of a 2D film transistor made of **23** nanosheets.
(b) and (c) Reproduced from ref. 39 with permission from Wiley-VCH Verlag GmbH.

homeotropically on a glass substrate over a large area. Instead of aligning in conventional head-to-tail configuration, which is an energy minimised format for dipolar interactions, the governing factor is the microphase separation between polar ethylene glycol chains and nonpolar alkyl chains, which forces these molecules to align in head to head fashion (Figure 5.9b,c). DSC studies show that this molecule displays LC mesophase between the range 69–80 °C and 76–57 °C on heating and cooling cycles, respectively. XRD analysis of this LC state showed diffractions that were indexed for (100), (110), (200), and (210) planes and further analysis showed that they in fact correspond to a 2D hexagonal superlattice. A more interesting fact, however, is that model compounds, which consist of hydrophobic derivatives, amphiphilic derivatives with shorter ethylene glycol chains, and benzo triphenylene amphiphiles, which do not possess a dipole moment, do not assemble into a super lattice structure. The above observation puts the spot light on amphiphilic design as well as the dipolar chromophore as responsible for a superlattice LC structure. This can be visualized under a polarizing optical microscope, where large dark areas could be seen that are actually dendritic structures as seen through an optical microscope. Mobilities were calculated in perpendicular and parallel using FP-TRMC. The degree of anisotropy was calculated for the amphiphilic as well as the blank lipophile; the latter came out to be four-times higher (Figure 5.9d,e).[40] A word of caution, however, has

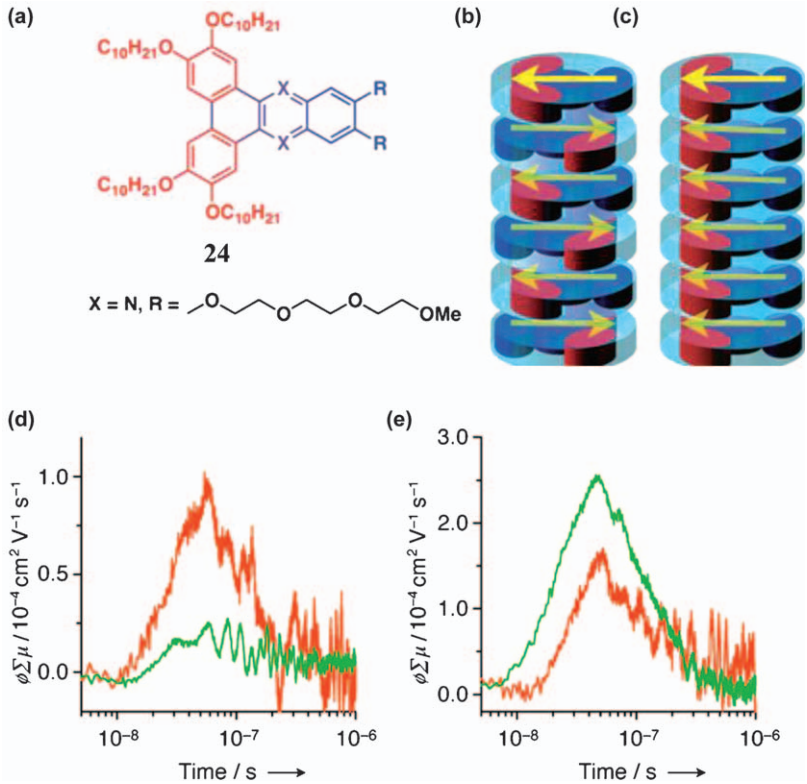

Figure 5.9 (a) Molecular structure of dibenzo[*a,c*]phenazine derivative (**24**). (b) and (c) Schematic illustrations of 1D columnar assemblies with head-to-tail (b) and head-to-head arrangements (c) of the aromatic mesogen. Yellow arrows indicate the dipole moment of the dibenzo[*a,c*]phenazine core. (d) and (e) FP-TRMC profiles at 70 °C of LC films of **24** (d) and its lipophilic derivative (e) as measured perpendicular (orange) and parallel (green) to the microwave electric-field vector.
(a)–(e) Reproduced from ref. 40 with permission from Wiley-VCH Verlag GmbH & Co.

been issued by the authors, which entertains the possibility of interaction between the hydrophilic part of the molecule and the polar functional groups such as hydroxyl on the glass substrate. This interaction could also contribute to the homeotropic assembly on glass. A major contribution for the amphiphilic design, however, cannot be excluded.

Jeong *et al.* showed the macroscopically orientation of amphiphilic TTF (**25**) (Figure 5.10) derivative using a similar amphiphilic concept. [41]

George *et al.* have synthesized coronene bis-imide (CBI) amphiphiles (**26**) (Figure 5.10) that self-assemble in THF–water.[42] The morphology of these CBI amphiphiles was fine-tuned by varying the ratio between THF and water. These molecules could be alternative n-type semiconducting chromophores with the advantage of a morphology that can be easily modulated and a high planar π-surface.

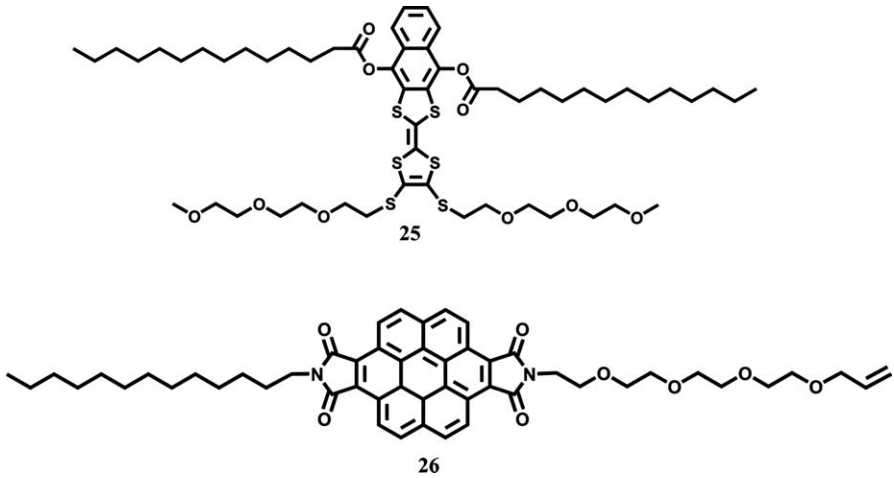

Figure 5.10 Molecular structures of amphiphilic TTF (**25**) and CBI derivatives (**26**).

Naphthalene diimides (NDIs) are another class of *n*-type semiconducting amphiphilic chromophores the self-assembly of which has been extensively reported. The various forms that the self-assembled structures take are tubes, coiled ribbons, twisted tapes, and helices.[43] Electronic investigation of these amphiphiles though has not been carried out; they, however, are materials with immense potential.

5.2.4 Multi-chromophoric p-n Amphiphiles

While attempting a co-assembly of p-type and n-type semiconducting chromophores one can end up in either segregated or co-stacked conformations. Though both of these conformations have their respective applications, establishment of strict control over both of them is of prime importance. As discussed in previous sections, amphiphilic molecules have a high propensity to phase separate depending on their interaction energies – such a feature could be made use of while attempting a chromophoric segregation. Care, however, must be taken that, though p- and n-type semiconducting moieties should be phase separated, the distance between the phases should be optimum so as to facilitate electron transfer. As it turns out, such a binding condition can be achieved with relative ease in an amphiphilic design. Thus, as an interesting extension of their established study on HBC amphiphiles Aida *et al.* opted for the amphiphilic approach for creating segregated donor and acceptor stacks or, in other words, p/n junctions at nanoscale. Though there have been attempts to use the structural dissimilarity between chromophoric amphiphiles like OPV and PDI to induce segregated stacks, the key feature in Aida *et al.*'s design is in using the donor and acceptor in the same molecule and on the opposite ends of amphiphiles. Not only does this concept ensure almost quantitative yield of segregation, it also provides parallel channels for the electron- and

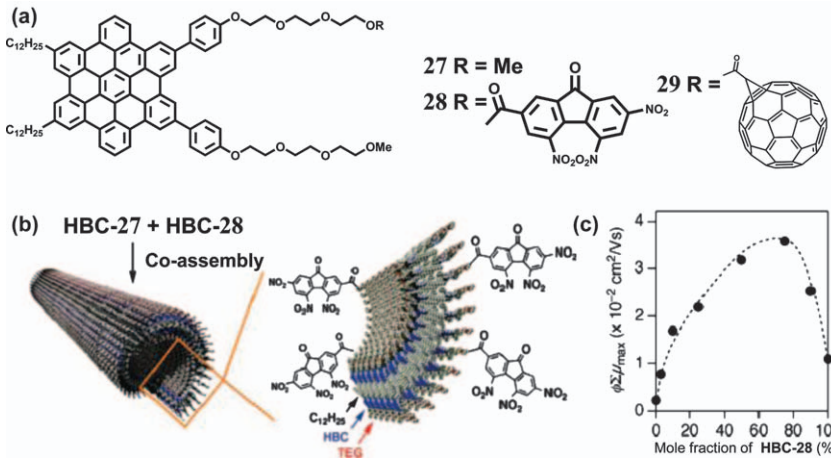

Figure 5.11 (a) Molecular structures of D-A HBC amphiphiles (**27**–**29**). (b) Schematic illustration of the formation of a co-assembled graphitic nanotube from **27** and **28**. TEG is triethylene glycol. (c) Plot of transient photoconductivity maximum values *versus* mole fractions of **28** in **27** nanotubes. (b) and (c) Reproduced from ref. 45*b* with permission from The American Chemical Society.

hole-transport as well. The basic design of the system builds on the bilayered nanotubes of hexabenzocoronenes amphiphiles (**27**–**29**) (Figure 5.11a) that has been standardized by Aida *et al*. The proposed molecular packing of such a nanotube in water sees HBC units encapsulated within the hydrophobic bilayer with both interior and exterior part exposed to water and hence aligned with water-soluble TEG motifs (Figure 5.11b). Taking advantage of these segregated hydrophobic and hydrophilic phases they functionalized the TEG part with acceptors such as TNF (**28**) and fullerene (**29**) and hence achieved ambipolar transport of electrons and holes in the parallel channels thus created. Interestingly, a plot of maximum photoconductivity with varying mole fraction of **28** in **27** showed a nonlinear trend, such that photoconductivity peaked at around 70% of **28** and decreased from then on.[44] Such a trend hints towards a variable internal morphology within the supramolecular structure with changing equivalents of participating components (Figure 5.11c).[45] In subsequent studies the authors could functionalize the acceptor TNF non-covalently on the nanotubes using a salt bridge interaction.[46]

Moreover, the technique has also been generalized to molecules forming not only nanotubes but simple morphologies like tapes and fibres as well, all taking the advantage of segregated nanophases generated by amphiphilic design. This generalization has allowed the use of various other systems apart from HBCs. Various groups have used a combination of D-A amphiphiles such as PDIs-oligothiophene (**34**), PCBM-porphyrin (**30**–**33**, **35**), PCBM-oligothiophene (**32**), NDI-naphthol (**36**–**38**), and NDI-porphyrin (**39**) to obtain favourable results (Figure 5.12).[47]

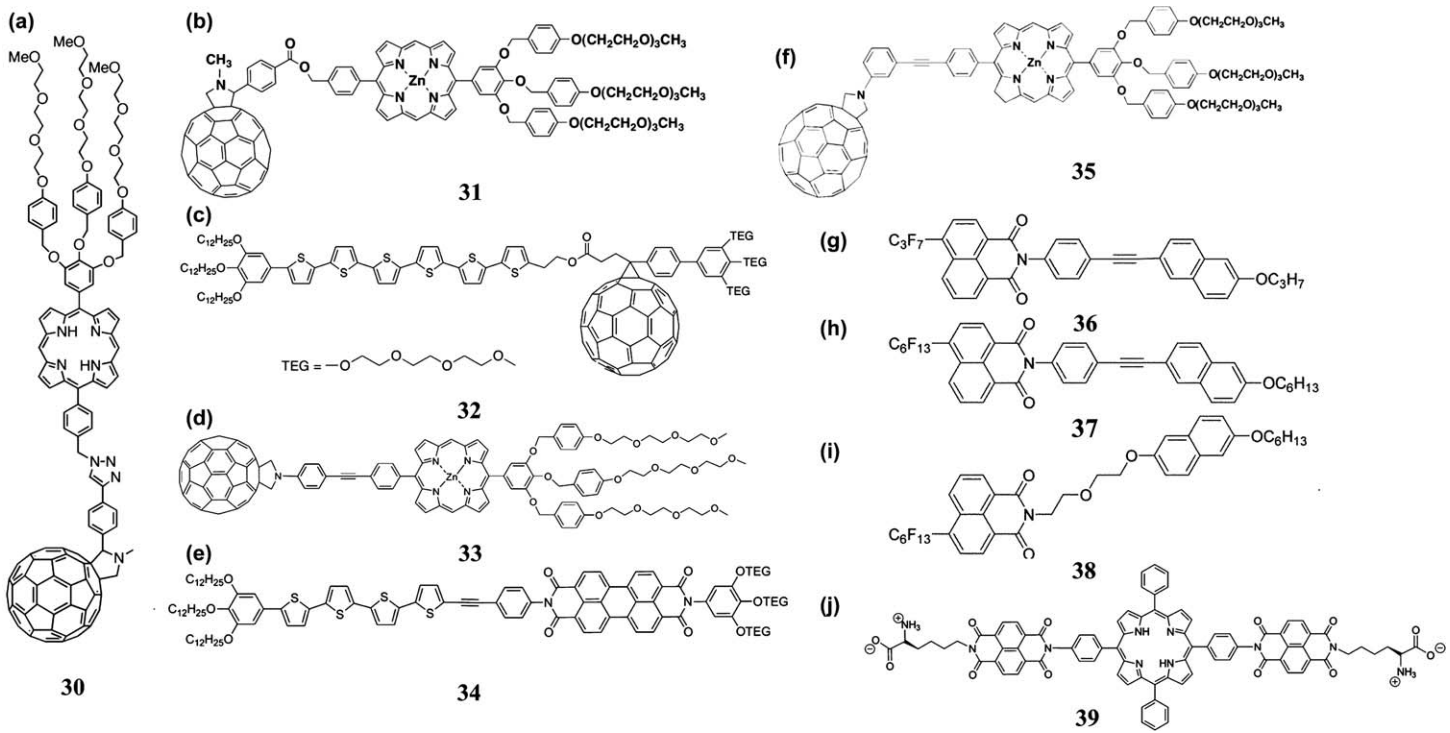

Figure 5.12 Molecular structures of various D-A amphiphiles. (a) Reproduced from ref. 47*g* with permission from The American Chemical Society. (b) and (f) Reproduced from ref. 47*f* with permission from The American Chemical Society. (c) Reproduced from ref. 47*a* with permission from The American Chemical Society. (d) Reproduced from ref. 47*c*. (e) Reproduced from ref. 47*b* with permission from Wiley-VCH Verlag GmbH. (g)–(i) Reproduced from ref. 47*d*. (j) Reproduced from ref. 47*e* with permission from The American Chemical Society.

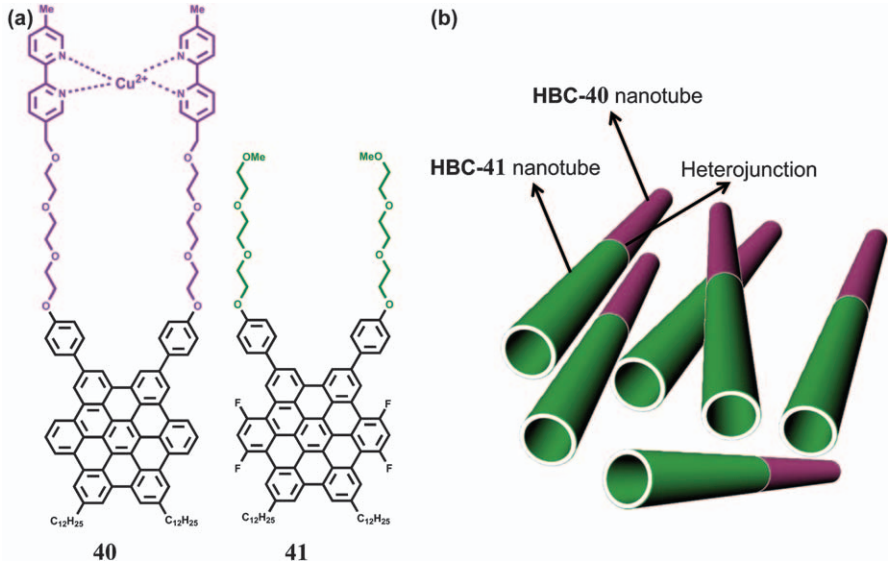

Figure 5.13 (a) Molecular structures of amphiphilic D (**40**) and A (**41**) HBCs and (b) schematic illustration for the preparation of non-covalently connected linear heterojunction nanotubes.

Ultimately, Aida *et al*. were also successful in making segregated linear heterojunction arrays of donor–acceptor chromophores (**40**, **41**) (Figure 5.13a).[48] Though this was a highly sought after design it was very difficult to achieve in self-assembled structures due to the dynamic nature of the molecules. This was finally realized by Aida *et al.* after taking into consideration and distilling various supramolecular design principles into one. In first step, the HBC amphiphile with 2-2′ bipyridine at the hydrophilic end is assembled into nanotubes. This part acts as the p-type semiconducting part of the resultant structure. To these nanotubes zinc triflate is added, which binds to the bipyridine ends, acting as a contrast agent in EDX imaging and also strengthening the nanotubes for further processing. An additional advantage of using Zn^{2+} is to avoid bundling of nanotubes as they would be forced away by the resulting electrostatic repulsion. In the next and most crucial step these nanotubes were dispersed in a solution of fluorine substituted HBS amphiphiles. The fluorine substitution not only made the HBC core and n-type semiconductor but also kept it structurally very similar to the p-type semiconducting counterpart. Hence, finally, these n-type semiconducting chromophores assemble as nanotubes on these p-type semiconductor seeds, resulting in a nano-scale heterojunction (Figure 5.13b). Transient microwave conductivity study showed that indeed in this arrangement the charge separated lifetime is much higher than in blank experiments with values as high as 8.8 μs.

5.2.5 Supramolecular Amphiphiles

Instead of molecules inherently being amphiphilic another approach is the so-called supramolecular amphiphilic approach[49], which takes advantage of ground state CT interaction between two molecules, resulting in an amphiphilic dimer that further self-assembles into aggregated morphologies. Recent advances in self-assembly resulted in the non-covalent synthesis of 1D nanowires having mixed stack-CT (MS-CT) D-A organization. Along similar lines, Zhang *et al*. have investigated, quite extensively, the self-assembly and morphological characteristics of various D-A molecules that form supramolecular amphiphiles in water. Zhang *et al*. observed that when an electron-rich amphiphilic pyrene derivative is mixed with electron-deficient nitro derivatives it forms a CT complex with morphological features that are in complete contrast to the parent components.[50] A micellar assembly was observed and hence the concept of supramolecular amphiphiles was hypothesized. This design was further extended to various derivatives, one such example is that of anionic pyrene molecules (**42**), which act as electron donor, and viologen (**43**), which is the electron-deficient counterpart. Characteristic surfactant like behaviour was observed from the resultant CT complexes in water as they formed wormlike like micelles, the stiffness of which could be tuned with external stimuli such as pH (Figure 5.14).[51] Another extension of this successful strategy has been the use of an alkoxynaphthol and naphthalene diimide CT pair. The dimensionality of morphologies could be controlled from 2D nanosheets to 1D nanofibers of these CT amphiphiles. This task was carried out by modulating two factors: (i) the size and shape of D-A molecules and (ii) the introduction of competitive CT interactions with pyrene donor molecules.[52] The performances of these CT nanostructures have not been tested on devices.

Though quite a few systems containing supramolecular amphiphiles are now known, there have been very few studies of their electronic properties for further application. Our group has been actively involved in exploring CT as self-assembly driving force, with special impetus for supramolecular amphiphiles.[53] Adding to the continuing research we have been able synthesise and study CT structures with high mobilities.[54] We have taken advantage of the ground state CT interactions between a dodecyl functionalized methyl viologen derivative (**45**) and coronene tetracarboxylate salt (**44**) (Figure 5.15a). The two components upon self-assembly form a bimolecular amphiphile that further self-assembles into a cylindrical micelle of 6 nm diameter (Figure 5.15b, c). As the concentration of these micelles increases, they start to form bundles that give the impression of a nanofibre.

The hole mobility calculated for these nano-structures as conducting components in FET devices was as high as 4.4 $cm^2\ V^{-1}\ s^{-1}$ (Figure 5.15d, e). We have tried to extend a similar approach to a different set of D-A molecules having OPV (**46**) and PBI cores (**47**). Though these D and A molecules are structurally different, efficient co-assembly was achieved *via* ground state

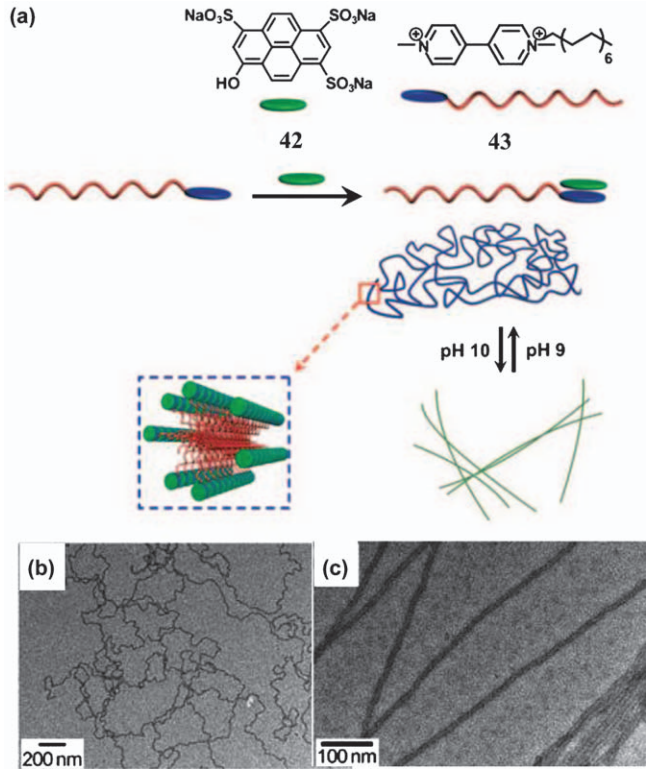

Figure 5.14 (a) Molecular structures of anionic D (**42**) and cationic A (**43**) and schematic representation of the preparation of the pH-responsive nanofibers through self-assembly of a **42**–**43** supramolecular amphiphile. TEM images of **42**–**43** amphiphile in (b) pH 9 buffer and (c) pH 10 buffer solution.
Reproduced from ref. 51 with permission from Wiley-VCH Verlag GmbH.

CT, which highlights the importance of non-covalent amphiphilic design (Figure 5.16b). In this case the shape of the D-A amphiphile resembles a wedge shaped surfactant, which further self-assembles into bilayer nanotubes (Figure 5.16c, d). Conductive AFM measurements on these CT-nanotubes showed high conductivity on the order of 0.02 S cm^{-1} (Figure 5.16e).

5.3 Optical Functionality

Flora and fauna across the world absorb energy from the solar spectrum and convert it into meaningful work by harvesting light by the help of chromophore assemblies present inside. In an attempt to understand how this process works, the knowledge gathered has made it possible for us to design and synthesize systems artificially for light harvesting. One of the many

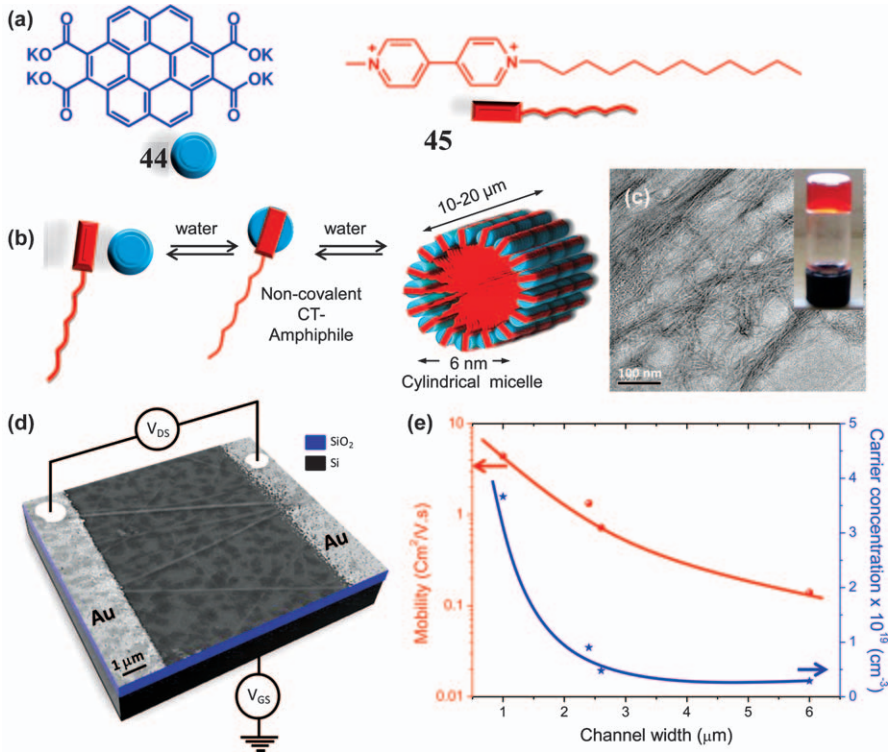

Figure 5.15 (a) Molecular structures of polycyclic aromatic donor (**44**) and viologen acceptor (**45**). (b) Schematic representation of the non-covalent amphiphile and its self-assembly into high aspect ratio cylindrical micelles. (c) A SEM image of CT-nanofibers between gold electrodes adapted in the schematic of the FET. (d) Variation in the field effect mobility and the carrier concentration with the channel width.
(a)–(c) and (d)–(e) Reproduced from refs. 53*b* and 54*a*, respectively, with permission from Wiley-VCH Verlag GmbH.

prerequisites for energy transfer to occur is the relative non-dynamic nature of orientation between the chromophoric transition dipoles. Among numerous strategies employed to achieve the above, the amphiphilic strategy stands out due to its relatively non-dynamic nature.

Energy transfer in amphiphilic assemblies was employed as early as 1989 by Kunitake *et al*.[55] Although the studies were on an air–liquid interface, the potential of such an approach was evident. Meijer *et al*. were among the first to study energy transfer in aggregates of amphiphilic systems. A set of OPV amphiphiles (**48**, **49**) (Figure 5.17a), which self-assemble in water to form vesicles, were synthesized and their self-assembly was studied. The dynamics and energy transfer was studied with the aid of a confocal microscope, which helped in direct visualization of this event on the length scale of nanoparticles (Figure 5.17b). Emission spectra at a single vesicle level were recorded in both co-assembled nanoparticle systems and a mixture of D

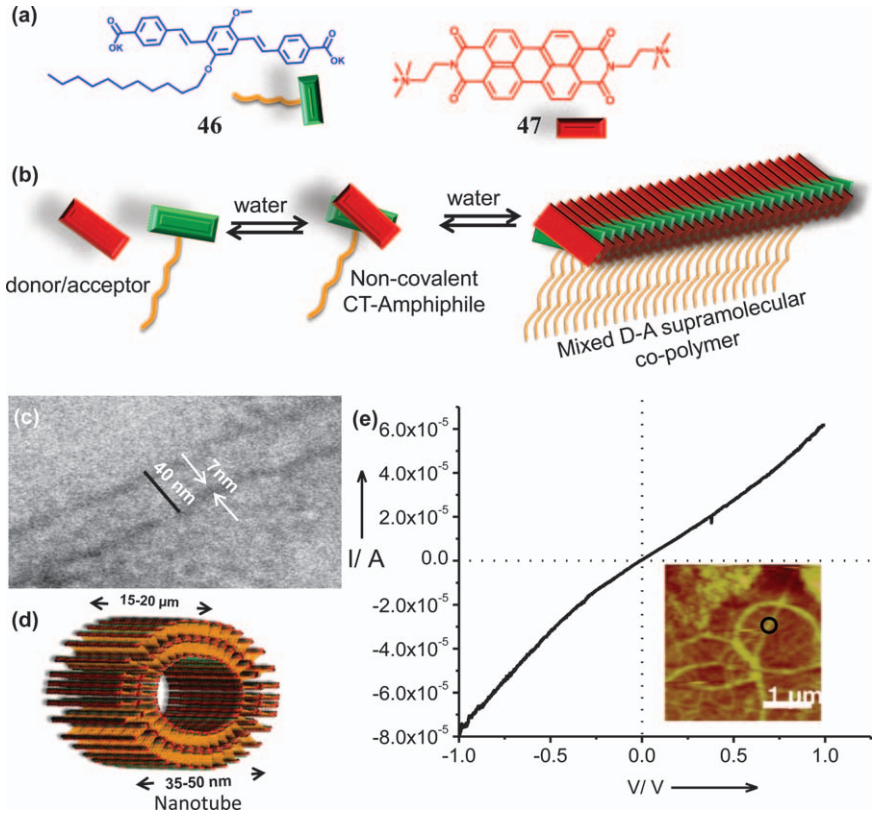

Figure 5.16 (a) Molecular structures of OPV donor (**46**) and PBI acceptor (**47**). (b) Schematic representation of MS-CT supramolecular formation *via* self-assembly of non-covalent amphiphile. (c) TEM image and (d) schematic representation of double walled nanotube formed from the **46–47** non-covalent amphiphile. (e) C-AFM *I–V* curves of nanotubes drop-casted onto the gold-coated glass substrate. The black circle in the inset image shows the nanotube on which the *I–V* measurements were performed. Reproduced from ref. 54*b* with permission from Wiley-VCH Verlag GmbH.

and A vesicles (Figure 5.17c). In the initial stages of the mixed nanoparticle system, independent D and A NPs could be identified. However, as the system was annealed at 45 °C, over time only the acceptor emission form of the vesicles could be seen, hence reiterating the direct visualization of the exchange process.[56]

Schenning *et al.* have taken advantage of this non-dynamicity and designed an array of amphiphilic fluorene derivatives (**50–53**) (Figure 5.18a) to study effects such as FRET and have commented on the internal distribution morphology of mixed amphiphilic structures.[57] In preliminary reports, formation of nanoparticles from these amphiphiles was established. These nanoparticles were found to be stable up to 70 °C in THF–water. The design

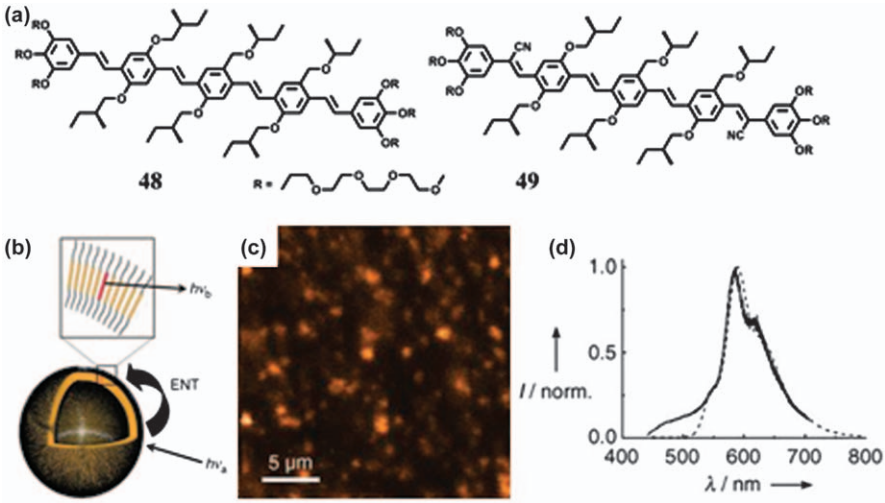

Figure 5.17 (a) Molecular structures of OPV amphiphiles having oligo(ethylene glycol) functionalized gallic wedges. (b) Schematic representation of energy transfer process from **48** to **49** in single co-assembled vesicles. (c) Scanning confocal microscopy images and (d) resulting fluorescence spectra ($\lambda_{exc} = 411$ nm) of mixtures of **48** and **49** (2 mol.% of **49**). The fluorescence of these single vesicles (solid lines) is compared to the corresponding solution spectra (dashed lines).
Reproduced from ref. 56 with permission from Wiley-VCH Verlag GmbH.

principles in the synthesis of these molecules have been to largely keep the backbone constant, so as not to change the self-assembly characteristic, and yet through chemical functionalization to change the bandgap of these molecules. This attempt resulted in the synthesis of four molecules, **50–53**, emitting in the blue, green, yellow and red region respectively (Figure 5.18b). After establishing that all of the molecules assemble into nanoparticles, advantage can be taken of the spectral overlap between these set of molecules and thus they can be used as an energy donor–acceptor pair. Further studies prove the fact that when molecular mixtures were taken in THF and injected in water they showed a significant amount of energy transfer. However, the mixture of particles, when taken together, does not show any FRET, thus reinstating the non-dynamic nature of these amphiphilic structures. Subsequently, appropriate mixing of chromophores was shown to give white-light-emitting nanoparticles (Figure 5.18 c). This study paved the way for further studies on narcissistic and social self-sorting in this class of molecules.

In a further detailed study Schenning *et al*. tried to get a handle on both the dynamicity of the particle as well as the morphology of donors and acceptors in a single particle. For control of dynamicity a set of various fluorene derivatives in which the length and philicity of the side chains were systematically changed was synthesised.[58] Energy transfer within the

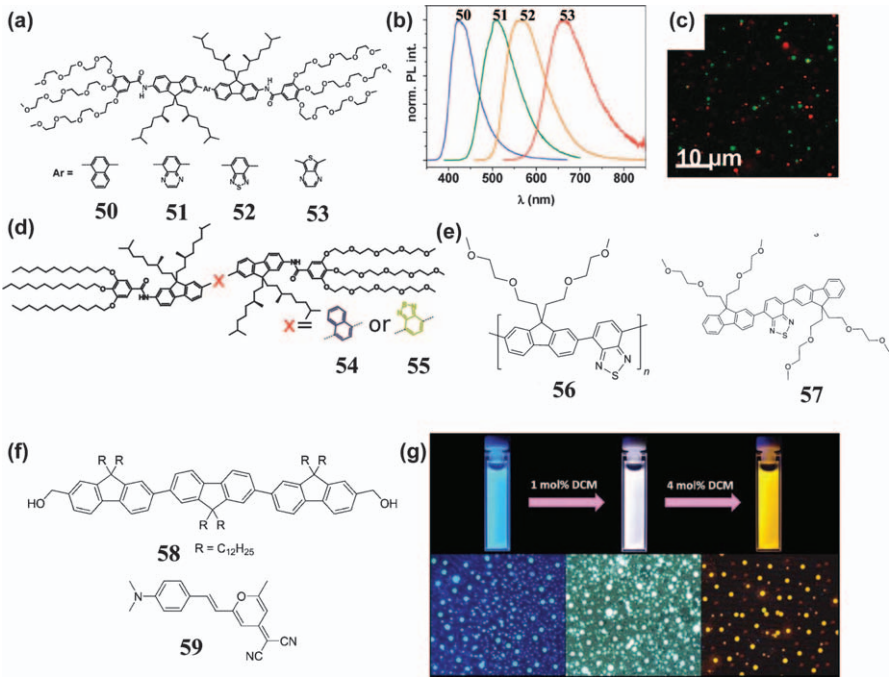

Figure 5.18 (a) Chemical structures of the fluorene based bolaamphiphiles **52–55**. (b) Normalised photoluminescence spectra of **50–53** in aqueous solution. (c) Fluorescence microscopy image of a mixture of aggregates of pure **52** and **53** in a water–gelatine mixture. (d) and (e) Molecular structures of fluorene-based amphiphiles (**54–57**). (f) Molecular structures of fluorene bis-alcohol (**58**) and acceptor dye (**59**). (g) (Top) Photographs of the nanoparticle dispersion in aqueous medium with different concentrations of DCM and (bottom) the corresponding fluorescence microscopic images.
(a)–(c) and (f)–(g) Reproduced from refs. 57 and 61, respectively. (d) Reproduced from ref. 59 with permission from The American Chemical Society. (e) Reproduced from ref. 60 with permission from Wiley-VCH Verlag GmbH.

chromophores has been used as a major tool to study the dynamics of nanoparticles in solution. Furthermore, the percentage of acceptor with respect to the donor (**54**, **55**) (Figure 5.18d) was varied and with the attained energy transfer induced quenching of donor conclusions were drawn on the morphology of the acceptors in the donor matrix.[59] The Stern–Volmer plot results indicate that the quenching mechanism is not a trivial one and cannot simply be classified into dynamic or static regime. Calculation of the interaction volumes and exciton diffusion length clarified the picture, revealing that at lower concentrations of acceptor there is efficient energy transfer as acceptors are uniformly dispersed in the donor matrix. However, as the equivalents of acceptor starts increasing, domains of acceptors start forming and hence decrease the interfacial area between the D-A pair, thus

decreasing the efficiency of energy transfer. Recently, in an interesting study Schenning *et al* compared the properties of a polymeric (**56**) and supramolecular nanoparticle (**57**) such that the chromophoric backbone remained the same (Figure 5.18e). Apart from various conclusions such as enhanced stability of polymeric species, energy transfer was used as a tool to determine the capability of hydrophobic guest encapsulation. With enhanced acceptor emission, polymeric particles were proven to have better encapsulation capability.[60] However, supramolecular particles are good for release of guest molecules.

Another offshoot from the previous works of Schenning *et al*. has been the synthesis of white-light-emitting nanoparticles. They achieved it, however, in a four-component system. Takeuchi *et al*. simplified this to a great extent and produced the same in a simple guest induced bi-component energy transfer (**58**).[61] DCM (**59**) dye has been chosen as an acceptor and an appropriate mixture results in white emissive particles (Figure 5.18f,g). PBI amphiphiles (**60**, **61**) (Figure 5.19a) have been reported by Würthner *et al*. that self-assemble into vesicles.[62] A supramolecular pH sensing mechanism has been demonstrated in which the acceptor molecule, *i.e.* the dipyrene moiety (**62**) (Figure 5.19b), changes conformation with the pH. At high pH

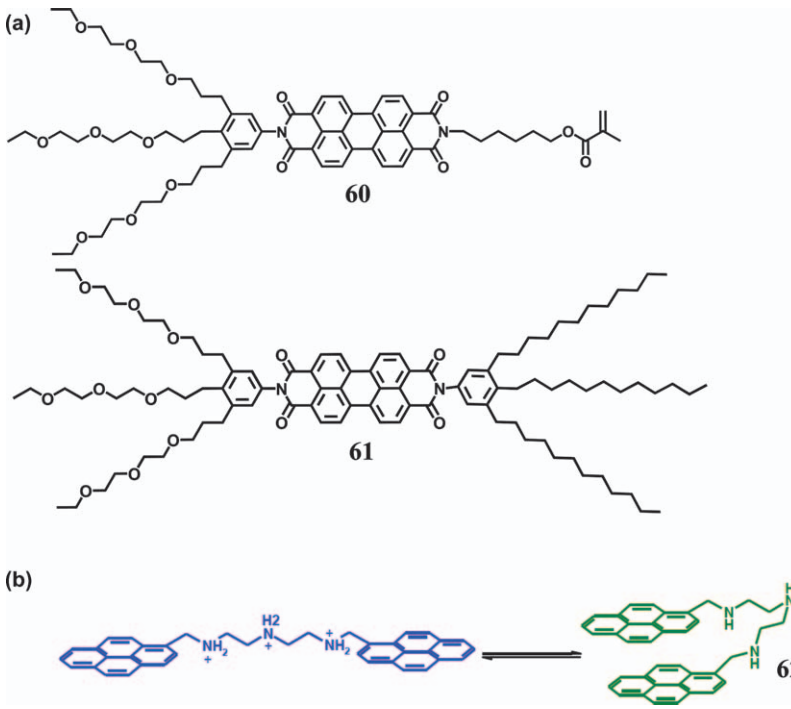

Figure 5.19 (a) Molecular structures of wedge shaped amphiphilic PBIs (**60** and **61**). (b) Molecular structure of donor (**62**) and pH induced conformation change

values the molecules form an intramolecular dimer that emits as an excimer (Figure 5.19b). On decreasing the pH, however, the molecule changes conformation due to repulsion from the ammonium backbone and thus emits in the molecularly dissolved region. As the donor molecules are encapsulated inside the acceptor vesicles, on changing the external pH emission of these vesicles can be tuned from blue to red. This is because of the varying amount of spectral overlap between donor and acceptor molecules as the pH is varied, thus resulting in variable extent of energy transfer. At an optimum pH (pH 9) white-light-emitting vesicles were achieved with CIE co-ordinates of (0.32, 0.31).

Guest encapsulation in amphiphilic systems,[63] as mentioned before, can be used to prove interesting arguments. For example, Numata *et al*. have used it to great effect for proving whether their assemblies have open ends.[64] They have synthesized porphyrin amphiphiles (**63**) (Figure 5.20a), which initially assemble into vesicles in dichloroethane (DCE)/water mixture, but as DCE is evaporated they transform into nanotubes (Figure 5.20b). The size of the nanotubes can be changed depending on the concentration of the dye used. Since the interior of these tubes would be hydrophobic they can

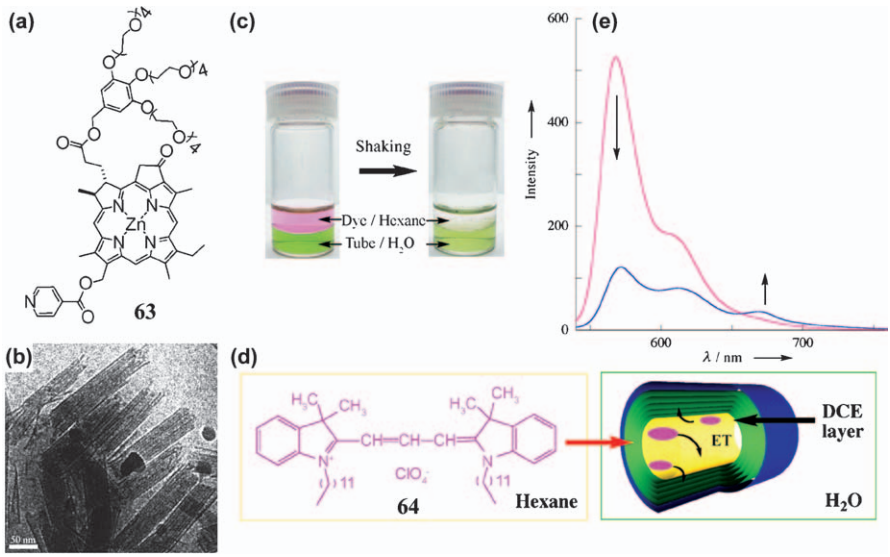

Figure 5.20 (a) Molecular structure of Zn–chlorophyll based amphiphile (**63**). (b) Cryo-TEM images of the tubular structures of **63** obtained from DCE solutions. (c) Photographs of two immiscible solutions (**64** in hexane and **63** in water). (d) Schematic illustration of encapsulation of the cyanine dye (**64**) into nanotubes. (e) Fluorescence spectra of the cyanine dye after extraction into the tubular structure(blue line) and the sample containing the same concentration of the cyanine dye dissolved in DCE/hexane (99 : 1, v/v; red line).
Reproduced from ref. 64 with permission from Wiley-VCH Verlag GmbH.

selectively take up hydrophobic dyes (**64**) inside and moreover if this dye is a FRET pair an effect can be seen by quenching of donor emission. The above postulated process was realized when liquid extraction of the dye solution in hexane with the nanotubes in water resulted in transfer of dye from the hexane phase to the water phase (Figure 5.20c–e), thus implying that the tubes have open ends.

5.4 Conclusion

We have summarized in this chapter various chromophoric amphiphiles and their application in studying either charge transport or optical functionalities. The underlining theme that emerges is that there are multiple dimensions to an amphiphile, such as the non-dynamicity, the propensity to form ordered phases based on their energy of interaction, the feature of inducing molecular anisotropy over large scales, the feature of easily attainable nanostructures or may it be the compartmentalization that they provide. These features can either be used separately or in tandem to yield materials with interesting properties. Thus, even though amphiphiles have been a topic of study for more than half a century, the insights and applications that they have to share is far from over.

References

1. (a) T. Shimizu, M. Masuda and H. Minamikawa, *Chem. Soc. Rev.*, 2005, **105**, 1401; (b) N. Kimizuka, *Self-Assembled Nanomaterials I*, ed. T. Shimizu, Springer, Berlin-Heidelberg, 2008, 219(1), 1–26.
2. A. Sorrenti, O. Illa and R. M. Ortuno, *Chem. Soc. Rev.*, 2013, **41**, 8200.
3. (a) C. D. Dimitrakopolous and P. R. L. Malenfant, *Adv. Mater.*, 2002, **14**, 99; (b) D. Braun, *Mater. Today*, 2002, **5**, 32; (c) R. H. Friend, R. W. Gymer, A. B. Holmes, J. H. Burroughes, R. N. Marks, C. Taliani, D. D. C. Bradley, D. A. dos Santos, J.-L. Brédas, M. Löglund and W. R. Salaneck, *Nature*, 1999, **397**, 121; (d) A. O. Patil, A. J. Heeger and F. Wudl, *Chem. Rev.*, 1988, **88**, 183; (e) A. Kraft, A. C. Grimsdale and A. B. Holmes, *Angew. Chem. Int. Ed.*, 1998, **37**, 402; (f) A. C. Grimsdale, K. L. Chan, R. E. Martin, P. G. Jokisz and A. B. Holmes, *Chem. Rev.*, 2009, **109**, 897; (g) R. H. Kim, H. J. Kim, I. Bae, S. K. Hwang, D. B. Velusamy, S. M. Cho, K. Takaishi, T. Muto, D. Hashizume, M. Uchiyama, P. André, F. Mathevet, B. Heinrich, T. Aoyama, D.-E. Kim, H. Lee, J.-C. Ribierre and C. Park, *Nat. Commun.*, 2014, **5**, DOI: 10.1038/ncomms4583; (h) J. Zhang, Z. Li, H. Xing, W. Zhang, L. Guo, Y. Liu, M. S. Wong and G. Yu, *Org. Chem. Front.*, 2014, **1**, 333; (i) K. Takimiya, I. Osaka, T. Mori and M. Nakano, *Acc. Chem. Res.*, 2014, **47**, 1493.
4. F. J. M. Hoeben, P. Jonkheijm, E. W. Meijer and A. P. H. J. Schenning, *Chem. Rev.*, 2005, **105**, 1491.
5. (a) E. W. Meijer and A. P. H. J. Schenning, *Nature*, 2002, **419**, 353; (b) J.-M. Lehn, *Science*, 2002, **295**, 2400; (c) G. M. Whitesides and

B. Grzybowski, *Science*, 2002, **295**, 2418; (d) T. Aida, E. W. Meijer and S. I. Stupp, *Science*, 2012, **335**, 813; (e) E. Moulin, G. Cormos and N. Giuseppone, *Chem. Soc. Rev.*, 2012, **41**, 1031.

6. A. P. H. J. Schenning and E. W. Meijer, *Chem. Commun.*, 2005, 3245.
7. (a) E. Moulin, F. Niess, M. Maaloum, E. Buhler, I. Nyrkova and N. Giuseppone, *Angew. Chem. Int. Ed.*, 2010, **49**, 6974; (b) V. Faramarzi, F. Niess, E. Moulin, M. Maaloum, J.-F. Dayen, J.-B. Beaufrand, S. Zanettini, B. Doudin and N. Giuseppone, *Nat. Chem.*, 2012, **4**, 485; (c) Y.-Y. Noh, J.-J. Kim, Y. Yoshida and K. Yase, *Adv. Mater.*, 2003, **15**, 699; (d) X. L. Chen, A. J. Lovinger, Z. Bao and J. Sapjeta, *Chem. Mater.*, 2001, **13**, 1341.
8. W. Zhang, W. Jin, T. Fukushima, N. Ishii and T. Aida, *J. Am. Chem. Soc.*, 2013, **135**, 114.
9. (a) M. R. Robinson, S. J. Wang, A. J. Heeger and G. C. Bazan, *Adv. Funct. Mater.*, 2001, **11**, 413; (b) T. Goodson III, W. Li, A. Gharavi and L. Yu, *Adv. Mater.*, 1997, **9**, 639; (c) V. Gebhardt, A. Bacher, M. Thelakkat, U. Stalmach, H. Meier, H.-W. Schmidt and D. Haarer, *Synth. Met.*, 1997, **90**, 123; (d) J. H. Burroughes, D. D. C. Bradley, A. R. Brown, R. N. Marks, K. Mackay, R. H. Friend, P. L. Burns and A. B. Holmes, *Nature*, 1990, **347**, 539.
10. (a) M. Durkut, M.-M. Torrent, P. Hadley, P. Jonkheijm, A. P. H. J. Schenning, E. W. Meijer, S. J. George and A. Ajayaghosh, *J. Chem. Phys.*, 2006, **124**, 154704; (b) A. Ajayaghosh and V. K. Praveen, *Acc. Chem. Res.*, 2007, **40**, 644.
11. (a) M. S. Wong, M. Samoc, A. Samoc, B. Luther-Daviesa and M. G. Humphrey, *J. Mater. Chem.*, 1998, **8**, 2005; (b) Y. Tao, A. Donat-Bouillud, M. D'Iorio, J. Lam, T. C. Gorjanc, C. Py, M. S. Wong and Z. H. Li, *Thin Solid Films*, 2000, **363**, 298; (c) Y. Tao, A. Donat-Bouillud, M. D'Iorio, J. Lam, T. C. Gorjanc, C. Py and M. S. Wong, *Synthetic Metals*, 2000, **111–112**, 417.
12. H. Wang, W. You, P. Jiang, L. Yu and H. Hau Wang, *Chem. Eur. J.*, 2004, **10**, 986.
13. J. F. Hulvat, M. Sofos, K. Tajima and S. I. Stupp, *J. Am. Chem. Soc.*, 2005, **127**, 366.
14. B. Narayan, S. P. Senanayak, A. Jain, K. S. Narayan and S. J. George, *Adv. Funct. Mater.*, 2013, **23**, 3053.
15. R. Matmour, I. De Cat, S. J. George, W. Adriaens, P. Leclère, P. H. H. Bomans, N. A. J. M. Sommerdijk, J. C. Gielen, P. C. M. Christianen, J. T. Heldens, J. C. M. van Hest, D. W. P. M. Löwik, S. De Feyter, E. W. Meijer and A. P. H. J. Schenning, *J. Am. Chem. Soc.*, 2008, **130**, 14576.
16. B. D. Wall, S. R. Diegelmann, S. Zhang, T. J. Dawidczyk, W. L. Wilson, H. E. Katz, H.-Q. Mao and J. D. Tovar, *Adv. Mater.*, 2011, **23**, 5009.
17. M. D. Watson, A. Fechtenkötter and K. Müllen, *Chem. Rev.*, 2001, **101**, 1267.
18. (a) J. P. Hill, W. Jin, A. Kosaka, T. Fukushima, H. Ichihara, T. Shimomura, K. Ito, T. Hashizume, N. Ishii and T. Aida, *Science*, 2004,

304, 1481; (b) W. Jin, Y. Yamamoto, T. Fukushima, N. Ishii, J. Kim, K. Kato, M. Takata and T. Aida, *J. Am. Chem. Soc.*, 2008, **130**, 9434.
19. Y. Yamamoto, T. Fukushima, W. Jin, A. Kosaka, T. Hara, T. Nakamura, A. Saeki, S. Seki, S. Tagawa and T. Aida, *Adv. Mater.*, 2006, **18**, 1297.
20. T. Yamamoto, T. Fukushima, A. Kosaka, W. Jin, Y. Yamamoto, N. Ishii and T. Aida, *Angew. Chem. Int. Ed.*, 2008, **47**, 1672.
21. J. Motoyanagi, T. Fukushima, N. Ishii and T. Aida, *J. Am. Chem. Soc.*, 2006, **128**, 4220.
22. T. Yamamoto, T. Fukushima, Y. Yamamoto, A. Kosaka, W. Jin, N. Ishii and T. Aida, *J. Am. Chem. Soc.*, 2006, **128**, 14337.
23. L. Chen, K. S. Mali, S. R. Puniredd, M. Baumgarten, K. Parvez, W. Pisula, S. De Feyter and K. Müllen, *J. Am. Chem. Soc.*, 2013, **135**, 13531.
24. (a) F. Würthner, *Chem. Commun.*, 2004, 1564; (b) M. R. Wasielewski, *Acc. Chem. Res.*, 2009, **42**, 1910.
25. (a) H. Usta, A. Facchetti and T. J. Marks, *Acc. Chem. Res.*, 2011, **44**, 501; (b) R. R. Reghu, H. K. Bisoyi, J. V. Grazulevicius, P. Anjukandi, V. Gaidelis and V. Jankauskas, *J. Mater. Chem.*, 2011, **21**, 7811.
26. S. Rajaram, R. Shivanna, S. K. Kandappa and K. S. Narayan, *J. Phys. Chem. Lett.*, 2012, **3**, 2405.
27. (a) T. Seki, X. Lin and S. Yagai, *Asian J. Org. Chem.*, 2013, **2**, 708; (b) Z. Chen, A. Lohr, C. R. Saha-Möller and F. Würthner, *Chem. Soc. Rev.*, 2009, **38**, 564.
28. D. Görl, X. Zhang and F. Würthner, *Angew. Chem. Int. Ed.*, 2012, **51**, 6328.
29. (a) T. E. Kaiser, H. Wang, V. Stepanenko and F. Würthner, *Angew. Chem. Int. Ed.*, 2007, **46**, 5541; (b) X.-Q. Li, V. Stepanenko, Z. Chen, P. Prins, L. D. A. Siebbeles and F. Würthner, *Chem. Commun.*, 2006, 3871; (c) F. Würthner, C. Bauer, V. Stepanenko and S. Yagai, *Adv. Mater.*, 2008, **20**, 1695.
30. I. K. Iverson and S.-W. Tam-Chang, *J. Am. Chem. Soc.*, 1999, **121**, 5801.
31. K. Balakrishnan, A. Datar, R. Oitker, H. Chen, J. Zuo and L. Zang, *J. Am. Chem. Soc.*, 2005, **127**, 10496.
32. Y. Che, A. Datar, X. Yang, T. Naddo, J. Zhao and L. Zang, *J. Am. Chem. Soc.*, 2007, **129**, 6354.
33. Y. Che, A. Datar, K. Balakrishnan and L. Zang, *J. Am. Chem. Soc.*, 2007, **129**, 7234.
34. E. Krieg and B. Rybtchinski, *Chem. Eur. J.*, 2011, **17**, 9016.
35. E. Krieg, H. Weissman, E. Shirman, E. Shimoni and B. Rybtchinski, *Nat. Nanotechnol.*, 2011, **6**, 141.
36. C. Shahar, J. Baram, Y. Tidhar, H. Weissman, S. R. Cohen, I. Pinkas and B. Rybtchinski, *ACS Nano*, 2013, **7**, 3547.
37. E. Engel, K. Leo and M. Hoffmann, *Chem. Phys.*, 2006, **325**, 170.
38. (a) S. Roy, D. K. Maiti, S. Panigrahi, D. Basak and A. Banerjee, *RSC Adv.*, 2012, **2**, 11053; (b) Y. Sun, C. He, K. Sun, Y. Li, H. Dong, Z. Wang and Z. Li, *Langmuir*, 2011, **27**, 11364.
39. J. Yin, Y. Zhou, T. Lei and J. Pei, *Angew. Chem. Int. Ed.*, 2011, **50**, 6320.

40. M.-C. Yeh, Y.-L. Su, M.-C. Tzeng, C. W. Ong, T. Kajitani, H. Enozawa, M. Takata, Y. Koizumi, A. Saeki, S. Seki and T. Fukushima, *Angew. Chem. Int. Ed.*, 2012, **51**, 1.
41. N. Kim, L. Wang, D.-Y. Kim, S.-Ho Hwang, S.-Wei Kuo, M.-H. Lee and K.-U. Jeong, *Soft Matter*, 2012, **8**, 9183.
42. K. V. Rao and S. J. George, *Org. Lett.*, 2010, **12**, 2656.
43. (a) H. Shao, M. Gao, S. H. Kim, C. P. Jaroniec and J. R. Parquette, *Chem. Eur. J.*, 2011, **17**, 12882; (b) H. Shao, J. Seifert, N. C. Romano, M. Gao, J. J. Helmus, C. P. Jaroniec, D. A. Modarelli and J. R. Parquette, *Angew. Chem. Int. Ed.*, 2010, **49**, 7688; (c) H. Shao, T. Nguyen, N. C. Romano, D. A. Modarelli and J. R. Parquette, *J. Am. Chem. Soc.*, 2009, **131**, 16374; (d) M. Kumar and S. J. George, *Chem. Eur. J.*, 2011, **17**, 11102.
44. A. Saeki, Y. Koizumi, T. Aida and S. Seki, *Acc. Chem. Res.*, 2012, **45**, 1193.
45. (a) Y. Yamamoto, T. Fukushima, Y. Suna, N. Ishii, A. Saeki, S. Seki, S. Tagawa, M. Taniguchi, T. Kawai and T. Aida, *Science*, 2006, **314**, 1761; (b) Y. Yamamoto, T. Fukushima, A. Saeki, S. Seki, S. Tagawa, N. Ishii and T. Aida, *J. Am. Chem. Soc.*, 2007, **129**, 9276; (c) Y. Yamamoto, G. Zhang, W. Jin, T. Fukushima, N. Ishii, A. Saeki, S. Seki, S. Tagawa, T. Minari, K. Tsukagoshi and T. Aida, *Proc. Nat. Acad. Sci. USA*, 2009, **106**, 21051; (d) Y. He, Y. Yamamoto, W. Jin, T. Fukushima, A. Saeki, S. Seki, N. Ishii and T. Aida, *Adv. Mater.*, 2010, **22**, 829.
46. G. Zhang, W. Jin, T. Fukushima, A. Kosaka, N. Ishii and T. Aida, *J. Am. Chem. Soc.*, 2007, **129**, 719.
47. (a) W.-S. Li, Y. Yamamoto, T. Fukushima, A. Saeki, S. Seki, S. Tagawa, H. Masunaga, S. Sasaki, M. Takata and T. Aida, *J. Am. Chem. Soc.*, 2008, **130**, 8886; (b) W.-S. Li, A. Saeki, Y. Yamamoto, T. Fukushima, S. Seki, N. Ishii, K. Kato, M. Takata and T. Aida, *Chem. Asian J.*, 2010, **5**, 1566; (c) R. Charvet, K. Ariga, J. P. Hill, Q. Ji, A. H. Khan and S. Acharya, *Chem. Commun.*, 2011, 6825; (d) T. L. Benanti, P. Saejueng and D. Venkataraman, *Chem. Commun.*, 2007, 692; (e) S. Tu, S. H. Kim, J. Joseph, D. A. Modarelli and J. R. Parquette, *J. Am. Chem. Soc.*, 2011, **133**, 19125; (f) R. Charvet, Y. Yamamoto, T. Sasaki, J. Kim, K. Kato, M. Takata, A. Saeki, S. Seki and Takuzo Aida, *J. Am. Chem. Soc.*, 2012, **134**, 2524; (g) Y. Hizume, K. Tashiro, R. Charvet, Y. Yamamoto, A. Saeki, S. Seki and T. Aida, *J. Am. Chem. Soc.*, 2010, **132**, 6628.
48. W. Zhang, W. Jin, T. Fukushima, A. Saeki, S. Seki and T. Aida, *Science*, 2011, **334**, 340.
49. X. Zhang and C. Wang, *Chem. Soc. Rev.*, 2011, **40**, 94.
50. C. Wang, S. C. Yin, H. P. Xu, Z. Q. Wang and X. Zhang, *Angew. Chem., Int. Ed.*, 2008, **47**, 9049.
51. C. Wang, Y. S. Guo, Y. P. Wang, H. P. Xu, Z. Q. Wang and X. Zhang, *Angew. Chem., Int. Ed.*, 2009, **48**, 8962.
52. K. Liu, Y. Yao, Y. Liu, C. Wang, Z. Li and X. Zhang, *Langmuir*, 2012, **28**, 10697.
53. (a) A. Jain, K. V. Rao, U. Mogera, A. A. Sagade and S. J. George, *Chem. Eur. J.*, 2011, **17**, 12355; (b) K. V. Rao, K. Jayaramulu, T. K. Maji and

S. J. George, *Angew. Chem. Int. Ed.*, 2010, **49**, 4218; (c) K. Jalani, M. Kumar and S. J. George, *Chem. Commun.*, 2013, 5174.
54. (a) A. A. Sagade, K. V. Rao, U. Mogera, S. J. George, A. Datta and G. U. Kulkarni, *Adv. Mater.*, 2013, **25**, 559; (b) K. V. Rao and S. J. George, *Chem. Eur. J.*, 2012, **18**, 14286.
55. N. Kimizuka and T. Kunitake, *J. Am. Chem. Soc.*, 1989, **111**, 3758.
56. F. J. M. Hoeben, I. O. Shklyarevskiy, M. J. Pouderoijen, H. Engelkamp, A. P. H. J. Schenning, P. C. M. Christianen, J. C. Maan and E. W. Meijer, *Angew. Chem. Int. Ed.*, 2006, **45**, 1232.
57. R. Abbel, R. van der Weegen, E. W. Meijer and A. P. H. J. Schenning, *Chem. Commun.*, 2009, 1697.
58. A. Kaeser, I. Fischer, R. Abbel, P. Besenius, D. Dasgupta, M. A. J. Gillisen, G. Portale, A. L. Stevens, L. M. Herz and A. P. H. J. Schenning, *ACS Nano*, 2013, **7**, 408.
59. A. L. Stevens, A. Kaeser, A. P. H. J. Schenning and L. M. Herz, *ACS Nano*, 2012, **6**, 4777.
60. I. Fischer, A. Kaeser, M. A. M. Peters-Gumbs and A. P. H. J. Schenning, *Chem. Eur. J.*, 2013, **19**, 10928.
61. C. Vijayakumar, K. Sugiyasu and M. Takeuchi, *Chem. Sci.*, 2011, **2**, 291.
62. X. Zhang, S. Rehm, M. M. Safont-Sempere and F. Würthner, *Nat. Chem.*, 2009, **1**, 623.
63. N. Kameta, K. Ishikawa, M. Masuda, M. Asakawa and T. Shimizu, *Chem. Mater.*, 2012, **24**, 209.
64. M. Numata, D. Kinoshita, N. Taniguchi, H. Tamiaki and A. Ohta, *Angew. Chem. Int. Ed.*, 2012, **51**, 1844.

CHAPTER 6

Chiral Supramolecular Structures as Spin Filters

RON NAAMAN*[a] AND DAVID H. WALDECK[b]

[a] Department of Chemical Physics, Weizmann Institute, Rehovot 76100, Israel; [b] Department of Chemistry, University of Pittsburgh, Pittsburgh PA 15260, USA
*Email: ron.naaman@weizmann.ac.il

6.1 Introduction

Spin-based devices are already serving as the reader heads in hard disks, and spintronics is widely viewed as a way to advance electronics and to reduce energy consumption.[1–3] Beyond such immediate goals, spintronics is a promising approach to realizing the more futuristic goal of quantum computing.[4] A basic building block in every spin-based device is the spin valve, which allows the transfer of information about one preferred spin direction (spin polarization) over the other. The development and use of spin valves followed shortly after the discovery of the giant magneto-resistance (GMR) effect.[5,6] A GMR-based spin valve consists of a permanent ferromagnetic layer that is separated from a second 'free' ferromagnetic layer by a thin nonmagnetic film, so that the free ferromagnetic layer can have its magnetization switched by a relatively low magnetic field. The relative orientation of the magnetization direction in the two ferromagnetic layers defines the resistance of the device. Such GMR-based devices are used for reading the magnetic moment of domains in hard disk memory.

Typically spintronics devices are made from inorganic materials and device production is complicated by the need to match the required

RSC Smart Materials No. 12
Supramolecular Materials for Opto-Electronics
Edited by Norbert Koch

Published by the Royal Society of Chemistry, www.rsc.org

magnetic properties with the structural properties of the inorganic films. This challenge, and others, is the reason for the interest in using organic materials for spintronics. Indeed, spintronic devices that include organic molecules have been studied extensively in recent years.[7–11] Typically, the organic molecules in such devices do not serve as electron spin polarizers; rather, they act as a medium through which the electrons/spins are transferred.[8] Magnetic organic molecules, which are being considered as electronic device analogs, are not yet at a stage where they can be used as spin filters at room temperature.[12,13]

A newly discovered effect, termed chiral induced spin selectivity (CISS), offers promise for the use of organic materials to manipulate electron spins (Figure 6.1). CISS has been reported for electron transmission and conduction through organic molecules.[14] In particular, the electron transport through chiral molecules is spin selective, and the consequent spin polarization can be very large as compared to inorganic spin filters. This phenomenon is unanticipated, as organic molecules are known for their small spin–orbit coupling (SOC) and the molecules used are not magnetic. These observations provide a challenge, as the conventional approach to spin–orbit coupling in chemical physics is unable to explain the magnitude of the SOC that is required to describe the experimental effects.

Because many biomolecules are chiral and many biochemical reactions involve chiral molecules, much effort has been placed on understanding enantioselectivity in chemical transformations[15–17] and the physicochemical properties of chiral molecules.[18] Although chiral molecules do not possess parity symmetry, they do have time reversal symmetry. It is necessary to have a charge flowing through them in order to break time-reversal symmetry and thus meet the symmetry requirements for generating a magnetic field.[19] The magnetic field thus created may interact with the magnetic dipole of the electrons' spin. In short, this mechanism provides a model for understanding how the spin selective electron transmission through chiral systems arises.

In what follows we overview the theoretical work related to the CISS effect and the experiments that demonstrate the effect. This discussion will be followed with a description of some applications.

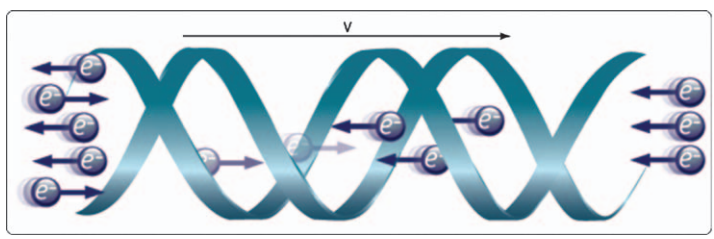

Figure 6.1 Schematic representation of the CISS effect. When electrons are moving within a left-handed or right-handed chiral potential, their spin is aligned parallel or anti-parallel to their velocity, respectively. Taken from ref. 14.

6.2 Theory

The CISS effect has been investigated quite extensively in several theoretical works.[20–27] Despite this effort no dominant theory has yet emerged to explain the phenomenon; however, the theoretical models do capture many of the features that are observed in experiment. Several approaches to treating the CISS effect have been attempted; among them are the scattering of electrons in a chiral potential, tight binding calculations that include the spin–orbit coupling resulting from the motion of the electron in a chiral potential, angular momentum selection, and the properties of a spin moving in a curved path. Although differences exist between these mechanisms and their conclusions, in most cases the CISS effect originates from an effective magnetic field acting on the electron as it passes through a chiral electric potential. This magnetic field stabilizes one orientation of the spin's magnetic dipole *versus* the other.

Formally, this interaction may be written as a ''Rashba'' type of interaction.[28] The common Rashba term in the Hamiltonian is given by:

$$H_{\mathrm{R}} = \alpha(\vec{\sigma} \times \vec{p}) \cdot \vec{\mathrm{z}} \tag{6.1}$$

in which α is the Rashba coefficient, $\vec{\sigma}$ is the Pauli spin matrix, $\vec{p}$ is the electron's momentum, and $\vec{z}$ is the propagation direction. This term results from the fact that as an electron moves within a chiral potential it experiences a magnetic field $\vec{B}$, which may be approximated as:

$$\vec{B} = \frac{\vec{\mathrm{v}}}{c^2} \times \vec{E}_{\mathrm{chiral}} \tag{6.2}$$

in which $\vec{\mathrm{v}}$ is the electron velocity, $\vec{E}$ is the electric field, and c is the speed of light. The spin–orbit coupling can be written as:

$$H_{\mathrm{SOC}} = \frac{g\mu_{\mathrm{B}}}{2c^2}\left(\vec{\mathrm{v}} \times \vec{E}\right) \cdot \vec{\sigma} \tag{6.3}$$

in which μ_{B} is the Bohr magneton and g is the g-factor for an electron. Note that Eqn (6.3) has a negative sign for the stabilized spin orientation and a positive sign for the destabilized spin orientation. The sign of the SOC energy is determined by the sign of the electron velocity and the sign of the electric field. The sign of the velocity is determined by the electron propagation direction, and the sign of the electric field depends on both the handedness of the molecule and on the field applied on the molecule (and/or its dipole moment direction).

In helical systems, it is useful to distinguish between the velocity and the net direction of propagation. As Eqn (6.2) shows, the magnetic field generated by the electron transit is perpendicular to the instantaneous velocity of the electron, which has a significant component oriented perpendicular to the net displacement. This component gives rise to a magnetic field that acts either parallel or antiparallel to the direction of propagation,

depending on the handedness of the molecule and the sign of the electric field. This feature is well known from the study of classical coils.

If electrons are passing through a right-handed helical molecule and the electric field across the molecule is parallel to the helix axis, then the preferred spin orientation is antiparallel to the velocity of the electrons emerging from the molecule. Correspondingly, the destabilized spin orientation is parallel to the electrons' velocity. If either the handedness or the field direction changes, the preferred spin direction will be flipped. If both quantities change then the preferred spin direction will be the same. This behavior is clearly demonstrated by the data shown in Figure 6.2 for the spin

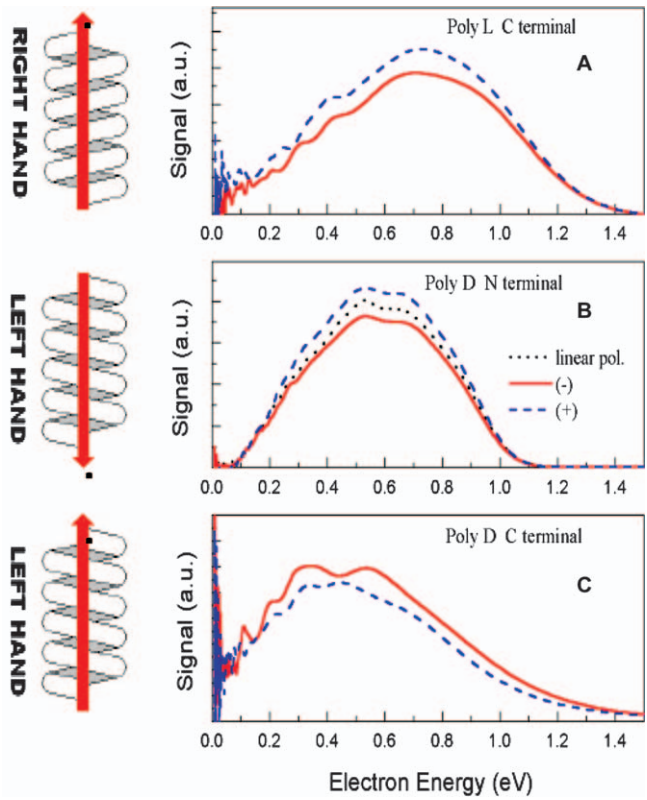

Figure 6.2 Energy distribution for photoelectrons ejected with a left (negative spin polarization; red, solid) or right circularly polarized laser (positive spin polarization; blue, dashed) pulse. The signal obtained with a linearly polarized laser pulse is shown as a dotted black line in (B). The electrons were transmitted through monolayers of polyalanine molecules attached to gold substrate *via* cysteine. The monolayer is made either from polyalanine made of L-enantiomer and attached to a gold substrate through the carboxylic end (LC, (A)) or from D-enantiomers bound to the surface through the carboxylic or amide groups (DC (B) and DN (C)). The red arrows indicate the direction of the dipole moment when the bottom is the direction of the substrate.
Adapted with modifications from ref. 29.

dependent electron transmission through monolayers of self-assembled polyalanine molecules.[29] The polyalanine molecules have a large dipole moment and they can be adsorbed either with their dipole moment pointed toward the surface or with it pointed away from the surface.

A comparison of the photoemission yields in Figure 6.2(A) and (C) shows that the preferred spin orientation flips if the chirality of the polyalanine is changed and the direction of the dipole moment is the same (C-terminus down); in contrast, a comparison of the data in Figure 6.2(B) and (C) shows that the preferred spin orientation flips if the direction of the molecule's dipole moment orientation is changed for a fixed chirality (D-polyalanine forms left-handed helix).

6.2.1 Spin–Orbit Coupling Magnitude

It is commonly believed that to rationalize the observed experimental effects, the Rashba term (Eqn. 6.1) must have a magnitude on the order of hundreds of meV. This value is larger by one to two orders of magnitude than the SOC in carbon atoms and by many orders of magnitude as compared to the spin–orbit coupling (SOC) calculated for hydrocarbon molecules. Although the existing models only account for the large SOC in an *ad hoc* way, two conceptual approaches towards a better understanding of the high value of the SOC are emerging. One approach considers that the core electrons contribute to the magnitude of the electric field acting on the electron. In fact, attempts to calculate the ''Rashba'' term in semiconductors has revealed that one needs to include the core electrons to get SOC values that are in reasonable agreement with experiment.[30] Hence the Rashba term is not simply related to the SOC of the valence electrons of the constituent atoms, but has additional contributions from the atomic core. A second approach considers the large SOC to arise from the curvature of mesoscopic systems. For example, this explanation has been used to explain the 4 meV SOC value measured for carbon nanotubes, which is several orders of magnitude larger than the value one finds for the SOC in hydrocarbon molecules.[31] The subject of calculating SOC in mesoscopic systems from first principles is still an open issue and it requires more theoretical effort.

6.2.2 Resonances

Several works predict that the CISS effect will be enhanced for narrow resonances.[22,27] The size of the enhancement, according to these models, is inversely proportional to the width of the resonance through which the electrons are transferred. This effect can be appreciated from a simplified model that considers the molecule through which the electron is transmitted to act as a resonator. In this approximation the magnitude of the observed effect is not given simply by the SOC term, but this term has to be multiplied by the quality factor (Q) of the resonator. Namely, the SOC term has to be multiplied by $\omega/\Delta\omega$, in which ω is the energy of the resonance and $\Delta\omega$ is its width. Just as the width of the resonance in an optical resonator is

related to the characteristic photon lifetime in the resonator, the width here is inversely proportional to the time the electron resides on the molecule.

The coupling between the linear momentum and the spin in chiral systems gives rise to interesting outcomes. For building intuition about these outcomes it is helpful to draw analogies to other cases where similar phenomena exist, namely, the quantum Hall effect and topological insulators.[32–34] We will relate here to the second case, which has more apparent similarities with CISS in chiral molecules. For example, one can infer that elastic back scattering is forbidden in a simplified limit. Upon backscattering of an electron by a scattering center, the spin, which is coupled to the linear momentum, must accumulate a phase of π or $-\pi$. Other things being equal, this means that two equivalent paths must exist with a spin phase difference of 2π. Because the spin function for $S=\frac{1}{2}$ flips sign upon accumulating a phase of 2π, these two paths destructively interfere and the amplitude of the reflected wavefunction is zero. Thus, the coupling between spin and linear momentum has no amplitude for the backscattering channel. Clearly, if the coupling between the spin and the momentum is not very strong, then only in some cases will the phase difference be precisely 2π and as a result some elastic backscattering will take place.

6.3 Experimental Results

6.3.1 Spin-Dependent Photoelectron Transmission

Figure 6.2 shows the photoelectron signal obtained when a gold substrate is coated with a self-assembled monolayer of polyalanine and the photoemission is induced by circular polarized light. The difference in the signal for one polarization *versus* the other indicates the spin selectivity. The polyalanine molecule has a very large dipole moment, and it can be bound to the gold either through the carboxylic acid end or the amine end; namely, one can control whether the dipole moment is pointing away from the surface or towards the surface. The spin selectivity flips when the handedness changes from L to D. However, the spin selectivity also flips when molecules with the same handedness are attached to the substrate so that the orientation of the dipole moment relative to the electrons' velocity is inverted. Besides demonstrating that spin selectivity (or spin filtering) occurs, these observations demonstrate that a Rashba-type of mechanism operates. Namely, the spin selectivity depends on the electric field direction within the molecule, as reflected by the direction of the molecule's dipole moment.

In other experiments the spin selectivity in photoelectron transmission through a monolayer of double stranded DNA was confirmed by measuring the spin polarization of the electrons directly.[35] The electron spin polarization may be defined as:

$$P=\frac{I_{+}-I_{-}}{I_{+}+I_{-}}$$

where I_+ and I_- are the signals for electrons with their spin aligned parallel and antiparallel to their velocity vector, respectively. Experiments of this type were performed on purple membranes that contain the protein bacteriorhodopsin (see Figure 6.3).[36]

The results for the transmission of electrons through a purple membrane, which contains bacteriorhodopsin molecules, are shown in Figure 6.3 for a sub-monolayer (patches) of the membrane (left) and for the case where the membrane (right) completely covers the gold substrate. In the case of submonolayer coverage, a spin polarization of $P = 5 \pm 3\%$ was observed, whereas for complete coverage the polarization increased to $P = 14 \pm 5\%$. More than ten different samples were measured, for which the method of preparation varied somewhat. Careful inspection of the data in Figure 6.3 (left-hand panels) indicates that the polarization of the laser light, which is

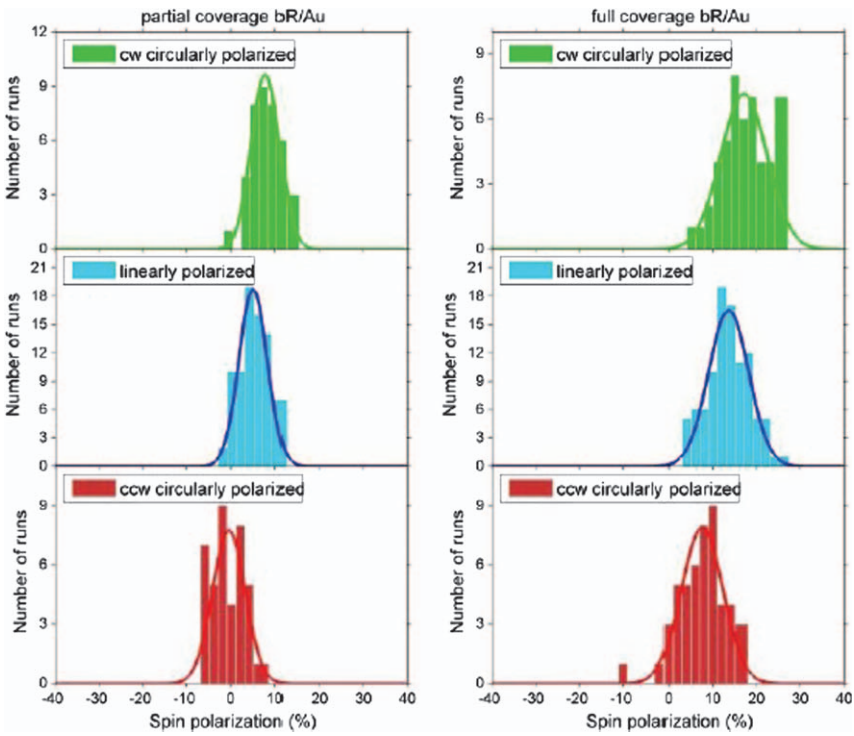

Figure 6.3 Spin polarization measured for photoelectrons, which are ejected by clockwise (cw, green), counter clockwise (ccw, red) and linear (blue) polarized laser radiation, after having traversed a purple membrane containing bacteriorhodopsin (10% in volume) adsorbed on gold. When the photoelectrons are ejected from gold substrates an average spin polarization of about $P = 5\%$ and $P = 14\%$ is measured for partial (left-hand panels) and completely covered surfaces (right-hand panels), respectively.
Taken from ref. 35.

applied to photoeject the electrons from the gold and into the membrane, has a small effect on the spin-polarization measured. This observation reflects a dependence of the Au photoelectrons' spin on the laser polarization. It is important to appreciate that circularly polarized light excites spin-polarized electrons from clean gold and that the sign of the polarization depends on the helicity of the light, whereas linearly polarized light generates a photoelectron distribution with no spin-polarization [*e.g.* ref. 35]. In contrast, when the gold substrate is covered with bR, the sign of the electron spin-polarization is always positive, independent of the polarization of the exciting radiation (Figure 6.3, right-hand panels); however, the light polarization influences the magnitude of the spin-polarization.

The dependence of the measured P on the light polarization can be rationalized if the bR is considered to be an imperfect spin filter. Assuming that the electrons excited by linearly polarized light are initially unpolarized when excited from a clean substrate (*i.e.*, the same number of parallel and anti-parallel spin orientations), the measured spin-polarization of $P = 14 \pm 5\%$ after the membrane indicates that for every four electrons with parallel spin that pass through the bR only three electrons with anti-parallel spin are allowed to pass, on average. In the case of clockwise (cw) circularly polarized light one finds $P = 17 \pm 5\%$, which is higher than the linearly polarized case because the electrons already have a positive spin polarization when excited from the bare polycrystalline Au substrate. In fact, the increase over the case for the linear polarization corresponds to a polarization of 3.1% in the initial photoelectron population. For the case of counter-clockwise (ccw) circularly polarized light one measures $P = 8 \pm 5\%$. This decrease occurs because the photoelectrons excited from bare polycrystalline gold by ccw circularly polarized light are negatively spin-polarized, with a polarization of -2.5%. After transmission of the electrons through bR, a predominant alignment of electron spin orientation parallel to their direction of propagation (positive spin-polarization) is observed. Therefore, one can conclude that the protein within the membrane filters the transmitted electrons by their spin (acts as a spin polarizer) and that its effect prevails. The initial polarization of the electrons before entering the membrane has only a minor effect on the final spin polarization, but a significant effect on the magnitude.

Figure 6.4 displays results obtained with an aluminium substrate. Here the spin polarization observed for the completely covered surface is $P = 15 \pm 4\%$. As expected, no effect of the laser polarization can be detected, because the spin polarization of photoelectrons ejected from the aluminium does not vary with the laser light polarization. Owing to weak spin–orbit coupling in Al (0.12 eV as compared with 4.54 eV for gold) circularly polarized light does not excite spin-polarized electrons.

The photoelectron distribution for transmission through bR has a positive electron spin polarization, whereas the photoelectron distribution for transmission through double-stranded DNA has a negative electron spin polarization. This difference occurs even though the helices are right handed

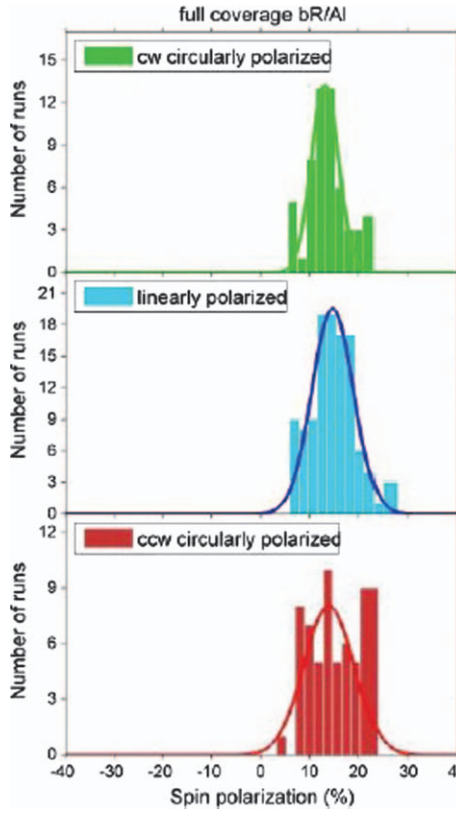

Figure 6.4 Spin polarization measured for photoelectrons that are ejected from aluminium by clockwise (*cw*, green) circular, counter clockwise (ccw, red) circular and linearly (blue) polarized laser radiation, after having traversed a purple membrane containing bacteriorhodopsin, 10% in volume. When the electrons were ejected from aluminium substrates, a spin polarization of about $P = 15\%$ was measured.
Reproduced from ref. 35.

in the two cases and may result from the difference in the direction of the electric field within the two systems.

6.3.2 Spin-Dependent Conductivity

Experiments that demonstrate the spin-dependent conductance of molecules have been performed using conducting-probe AFM measurements of conduction through double stranded DNA molecules adsorbed on magnetized nickel substrates,[37] by monitoring the magnetoresistance and the spin-filtering efficiency of DNA sandwiched in ferromagnetic nanostructures[38] and by studying electron transfer through chiral assemblies of porphyrins.[39] In addition to these studies, more recent work on spin-dependent electron conduction through the purple membrane has been probed by recording

cyclic voltammetry (CV) curves as a function of the magnetization of a Ni substrate supporting the purple membrane.[36]

Figure 6.5 shows the results reported for the voltammetry study. Figure 6.5(a) shows cyclic voltammograms (CVs) recorded on the bare Ni, with roughly 2 nm of thermal oxide NiO on the surface, for the $Fe(CN)_6^{4-}$/$Fe(CN)_6^{3-}$ redox couple. The forward (anodic) potential scan from -0.05 to $+0.35$ V involves Fe^{2+} oxidation, whereas the backward (cathodic) scan involves Fe^{3+} reduction. The oxidation and reduction current peaks in Figure 6.5(a) are separated by 90 mV at a scan rate of 50 mV s^{-1}, lie within the Ni potential window,[40] and do not show a magnetic field dependence.

Figure 6.5(b) shows CV curves for two different magnetic field directions that were recorded for a Ni substrate covered with the purple membrane containing the bR. In contrast to the voltammograms in Figure 6.5(a), those in Figure 6.5(b) are characterized by a ''quasi-reversible'' behavior. In particular, the voltammograms in panel (b) have a factor of ten lower faradaic current and display broad oxidation and reduction shoulders including a larger separation in the potential values. Shoulders are roughly found at $+0.250$ V in the forward oxidation curve and at $+0.075$ V in the backward reduction curve. This behavior is commonly observed when charge transfer through adsorbed molecular films takes place, as is found in the case of CV performed with surfaces coated with self-assembled monolayers of α-helical peptides and alkanethiols.[41] The change in the CV curves, from a reversible (Figure 6.5a) to a quasi-reversible (Figure 6.5b) behavior, is consistent with a higher resistance of the purple membrane.

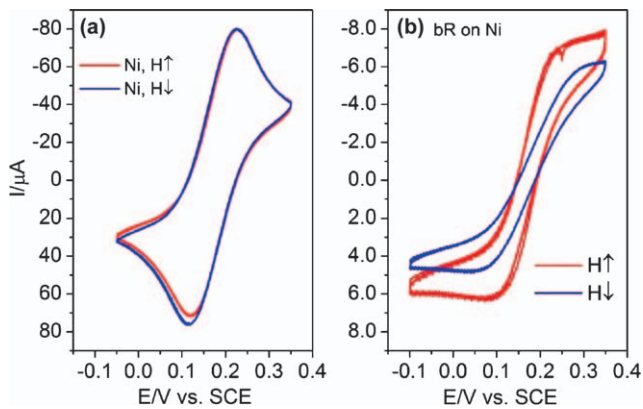

Figure 6.5 Cyclic voltammograms (scan rate of 50 mV s^{-1}) are shown for an Ni working electrode in contact with $[Fe(CN)_6]^{2-}$/$[Fe(CN)_6]^{3-}$ redox couple in an aqueous electrolyte at pH 7. (a) The case of a Ni bare surface (with a few nanometer thick oxide) and (b) for the bR thin film physisorbed on the Ni working electrode. Note the current scale change between (a) and (b). In each case the magnetic field direction was varied with respect to the electrode surface's normal (conventionally UP and DOWN); $H = 0.35$ T.
Adapted from ref. 36.

The dependence of the current on the magnetic field direction in Figure 6.5(b) suggests that the electron transfer through bR (electronic conduction) depends on the electron spin orientation. Moreover, the difference between the current, recorded in the magnet UP (red curve Figure 6.5b) and magnet DOWN (blue curve Figure 6.5b), displays a small dependence on the potential.[†] An average difference of $18 \pm 3\%$ was observed between the currents for the magnet UP and magnet DOWN configurations, determined at the starting (−0.10 V) and ending (+0.35 V) potentials for the anodic scan. A control experiment in which the bR was denatured but retained in the membrane on the Ni electrode shows a strong reduction in current and no magnetic field dependence; see ref. 36 for details.[42,43]

These data provide robust evidence that the charge transport through the membrane is facilitated by the protein and its helical structure. Even though pinholes and other defects may be present in the bR film, they are not expected to change with magnetic field direction, and the flipping of the magnetic field direction should not change the structural properties nickel/bR-membrane/solution interface. Thus any leakage current, resulting from direct contact between the redox molecules in solution and the electrode surface, should not change with the magnetic field direction. Although the quantitative value of the current anisotropy (i_{UP}-i_{DOWN}/i_{AVG}) may change because of pinholes, the qualitative observation of an anisotropy in the current is not affected.

6.3.2.1 *Spin Selective Electron Transfer Studied by a Capacitance Device*

Recently, a device capable of monitoring photo-induced spin transfer through organic molecules was reported.[44] The device (see Figure 6.6) was made using standard nanofabrication techniques and allows one to directly establish the relative efficiency of the charge transfer, the type of the charge being transferred (holes or electrons), and the existence of spin polarization. In this study photoexcitation was used to produce an electron–hole pair in a dye molecule attached to the DNA and the spin selectivity was observed in the hole transfer[45,46] from the excited dye to the silver substrate on which the DNA molecules were self-assembled. The capabilities of this device were demonstrated by showing that photoinduced charge transfer through double stranded DNA oligomers is spin selective and that the selectivity increases with the length of the DNA.

The device (see Figure 6.6) is fabricated by photolithography. First, a 1 μm-wide band of Ni is evaporated onto oxidized silicon and then a thin-layer of aluminium oxide (0.5 nm thick) is deposited on top of it. After the alumina deposition, a 1 μm-wide, and 50 or 35 nm-thick, band

[†]The difference in the current, ΔI, for the two directions of the magnet is $\Delta I = 1.3$ μA at -0.05 V, corresponding to a difference of about 21% and $\Delta I = 1.5$ μA at $+0.35$ V, namely, a difference of 18.8%.

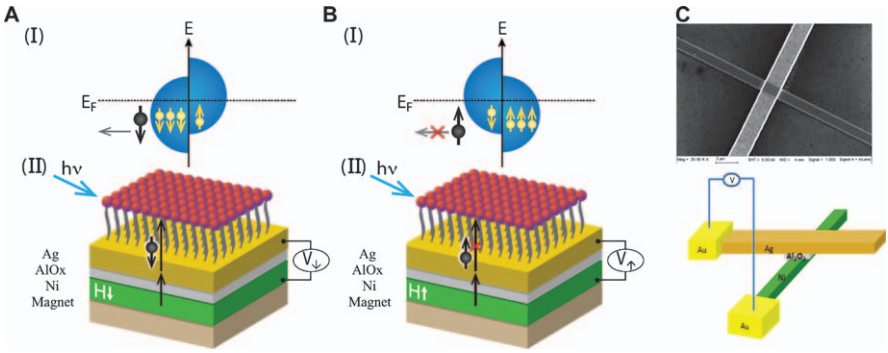

Figure 6.6 A chiral spintronics device. A(I) and B(I) show the energy level alignment, and A(II) and B(II) show schemes for the device in the two modes of operation. The device consists of a Ni metal layer, a dielectric layer of AlO_x, and a layer of Ag. An electromagnet is used to define the external magnetic field and to magnetize the nickel layer (white arrow). On top of the Ag film, DNA molecules are self-assembled with a dye molecule (red circles) attached to their tail. Upon application of a magnetic field, the density of states of the spin sub-bands in the Ni are split so that the majority spin states, which are aligned parallel to the applied magnetic field, are stabilized and the density of the minority spin states, which are aligned antiparallel to the applied magnetic field, are destabilized. Thus the electrons with a spin oriented parallel to the applied field are the majority carriers. Upon excitation of the dye, electrons are transferred from the silver to fill the hole in the HOMO of the dye. Because the helical DNA is a spin filter, this electron transfer forms a spin-specific hole in the silver that can be filled by electrons with the right spin orientation ejected from the Ni. When Ni is polarized so that it does not eject this specific spin orientation (B), the voltage measured is more positive than if the preferred spin orientation is ejected (A). (C) Scanning electron microscope image of the device and a scheme describing the electrical connection. Adapted from ref. 44.

of silver is evaporated and oriented at 90° relative to the Ni trace (Figure 6.6C). DNA molecules are self-assembled on the silver through a thiol group (see ref. 47). The other end of the DNA has a dye molecule, Cy3 or Cy5, which can be excited at 530 or 650 nm, respectively.

Upon photoexcitation of the dye molecules, a photovoltage is generated across the device and it depends on the direction of the applied magnetic field (Figure 6.7A and B). Excitation of the dye molecule leads to hole transfer through the DNA.[46] Hole transfer means that electrons from the silver substrate are transferred to the HOMO orbital of the photoexcited dye, creating a hole on the Ag film. This picture is substantiated by the positive voltage that is observed between the silver film and the grounded nickel film (Figure 6.7A). Further confirmation of this picture was made by measuring photoinduced charge transfer between CdSe nanoparticles (NPs) and the silver substrate, when the NPs are attached *via* dialkylthiols. In this latter case it is known that electron transfer[48] is more efficient than hole transfer

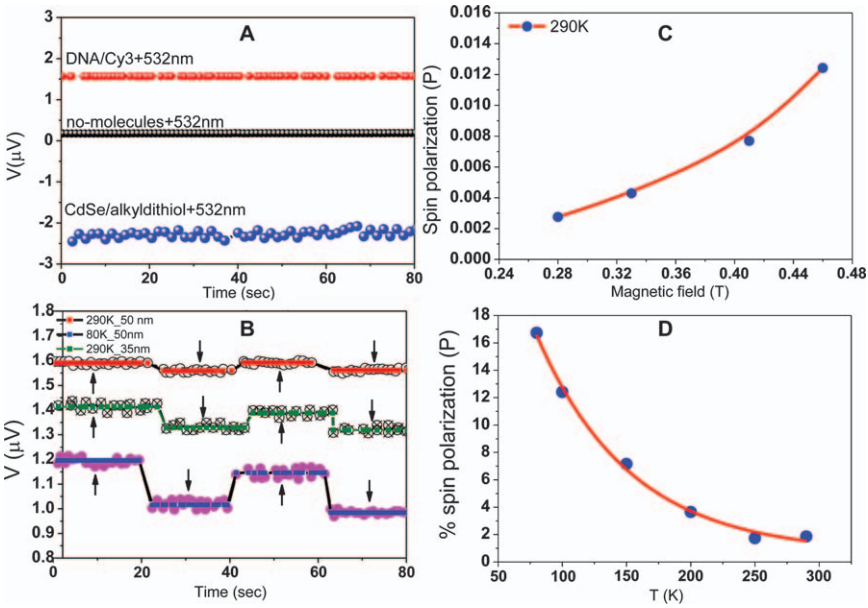

Figure 6.7 (A) Graph of the steady-state photovoltage (532 nm irradiation) that is measured between the nickel and the silver layers ($T = 290$ K) for the case of a monolayer of DNA with a Cy3 dye (red), for the case of no molecules (black) and for the case of CdSe nanoparticles that are attached by alkylthiols (blue). (B) Time profile of the photovoltage with the applied magnetic field direction; for 50 nm thick silver at 290 K (red) and 80 K (blue) and for 35 nm thick silver at 290 K (green). The black arrows indicate the direction of the magnetic field. (C) Spin polarization plotted as a function of the magnetic field strength at 290 K. (D) The temperature dependence of the spin polarization is shown for the case of a 50 nm thick silver layer. Taken from ref. 44.

and indeed the potential measured is negative (Figure 6.7A). Note that no effect of the magnetic field direction was observed in this latter case, as the molecules are not chiral. Figure 6.7(A) also shows that when the bare device is illuminated (no molecules adsorbed) with 532 nm light, a very small photovoltage signal is measured, which is magnetic field independent.

Because of the CISS effect, electrons with spin orientation antiparallel to the electron propagation direction are transferred more efficiently through the DNA than are those with their spin oriented parallel to the propagation direction; thus the silver film becomes electron spin polarized because of the creation of spin-specific holes. For the arrangement in Figure 6.6(A), the magnetic moment of the Ni layer (the white arrow) is aligned *anti-parallel* to the direction of the spin transferred from the silver to the dye through the chiral molecules. Hence, electrons from just underneath the Fermi energy in the Ni are injected into the silver and neutralize it. For the arrangement in Figure 6.6(B), the Ni is polarized in the opposite direction so that not as many electrons with spin oriented in the appropriate direction are available

to fill the spin-specific holes in the silver. Therefore, it is expected that a lower voltage will be measured when the system is in the configuration of Figure 6.6(A), as compared to that shown in Figure 6.6(B).

Although the measurements are steady-state it is instructive to consider the current fluxes that are observed. Subsequent to the hole transfer from the dye to the Ag, an electron is transferred from the radical anion to the Ag within some characteristic time (typically less than a nanosecond[49]), so that the dye is neutralized and returns to its ground state. Because the electron transfer rate from the silver to the dye (or the hole transfer rate from the dye to the silver) is faster than the back transfer rate, a photovoltage is created because of an excess of average positive charge on the silver. The amount of excess positive charge that is transferred can be estimated based on the photovoltage and the resistance of the AlO_x layer, which is typically around 1 kΩ when no magnetic field is applied. A typical photovoltage value is about 1 μV, when the laser power is 3.5 μW, which indicates that an excess of about 6.3×10^9 electrons s^{-1} are transferred from the silver to the dye molecules. Because the density of the DNA on the surface is about ~10^{13} molecules cm^{-2} and the surface area of the device is 10^{-8} cm^2, each dye molecule on the surface obtains an electron at a rate of $>6.3\times10^4$ s^{-1}, on average.

If a magnetic field is applied in order to polarize the Ni layer, the magnitude of the photovoltage changes and it depends on the direction of the applied magnetic field. If the Ni's magnetic moment points toward the organic layer, the voltage $V_+ > V_-$ where V_+ (V_-) is the voltage generated with the Ni layer's magnetization pointing into (out of) the plane, as indicated in Figure 6.7. The higher voltage measured for a magnetic field aligned parallel to the electrons' propagation direction indicates that the spin polarization of the electrons transferred through the molecules from the silver is aligned antiparallel to their velocity.

The spin polarization, P, for the device is defined as $P=(V_+ - V_-)/V_0$, where V_0 is the voltage with no magnetic field applied; it represents the voltage at which the Ni has equal populations of *both* spins at the Fermi level, *i.e.*, the Ni layer is not magnetized. The polarization values given here are not corrected for the fact that the spin selectivity of Ni is not 100%; hence, the actual polarization of the spin transferred through the DNA is higher. Although the values of $(V_+ - V_-)$ vary significantly from one device to another because of variations in the resistance of the AlO_x layer and in the contacts, as seen in Figure 6.7(B), the variations in P between the devices is very small.

Figure 6.7(C) shows the dependence of P on the magnetic field H for a 50 nm thick film. Clearly, the signal increases as the magnetic field strength increases. This magnetic field dependence arises from the change in the ratio between the majority spin and the minority spin populations near the Fermi level. As the magnetic field increases, this ratio also increases. Thus the polarization of the hole population in the Ag layer is greater than or equal to the anisotropy found here for the photovoltage. All the measurements in Figure 6.7(B) were performed at a field of 0.46 Tesla, for which the polarization of the Ni is saturated (see ref. 44).

The data in Figure 6.7(B) show that the spin polarization is affected by the thickness of the silver film. The polarization measured at room temperature, for 50 and 35 nm-thick silver layers, is 1.6% and 5.7%, respectively. The difference in these values probably results from the decay in spin orientation of the holes in the silver by electron–phonon coupling and spin–orbit coupling and because the polarized electrons injected from the Ni must traverse the Ni/AlO_x interface, the AlO_x/Ag interface, and the silver layer. The origin of the spin depolarization was explored by studying the temperature dependence of the polarization anisotropy (Figure 6.7D). The temperature dependence data in Figure 6.7(D) can be accounted for by considering the scattering of polarized spins with lattice phonons, namely, the Elliot–Yafet mechanism.[50,51] The fitting of these data to an exponential dependence on temperature gives an activation barrier, or characteristic temperature, of approximately 81 ± 5 K, which is much smaller than the Debye temperature for bulk silver, 200 K.[52] The smaller characteristic temperature may result from several factors, including the Ag film being polycrystalline, scattering at the interfaces between phases, and scattering within the AlO_x. Hence, the characteristic temperature obtained from this fit is an effective depolarization parameter for the system.

Figure 6.8(A) shows that $\Delta V = (V_+ - V_-)$ has a linear dependence on light intensity. These data indicate that the spin polarization does not depend on the number of electrons transferred, and therefore that electron–electron interactions among the transferred electrons are not important for the electron current densities studied here. The dependence of P on the length of the DNA is shown in Figure 6.8(B) for three different lengths of DNA: 30, 40, and 50 base-pairs long. The ratio between the polarizations measured for different lengths resembles that obtained in other work for photoelectrons transmitted through DNA.[35]

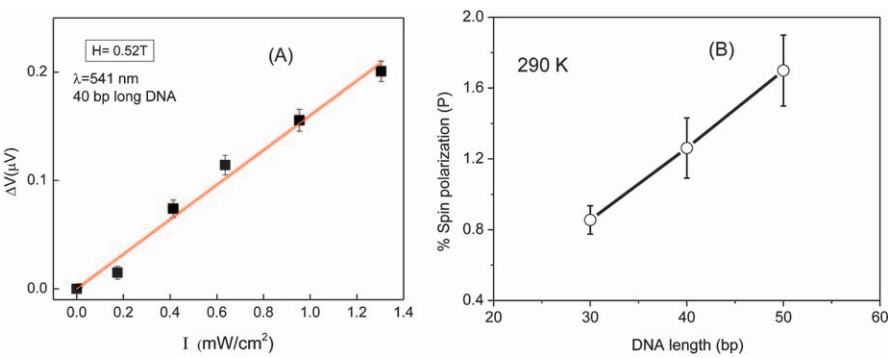

Figure 6.8 (A) The difference in voltage measured when the magnetic field is pointing towards or away from the organic layer, $\Delta V = (V_+ - V_-)$, as a function of the laser intensity for a 50 nm-thick silver layer; the DNA contains the Cy3 dye and is illuminated at 532 nm. (B) Spin polarization measured for DNA of different lengths: 30, 40, and 50 base-pairs long.

The device described by Figure 6.6 can serve as a spin valve and as an optical-based readout for magnetic memory, as well as other spintronics-related functions. More recently this device has been used to monitor spin specific electron transfer in the protein azurin and in photosystem 1.[53]

6.4 Applications and Implications

While much fundamental development remains before the CISS effect is fully understood, several applications and implications can be identified already. Long range electron transfer is an essential aspect of redox reactions that underlie many biochemical events and the CISS effect is expected to be important in several such systems that possess chiral subunits, such as α-helices and β-sheets. In fact, recent studies of peptides, proteins (bR and azurin), and preliminary results on Photosystem 1 all indicate that the CISS effect operates in their redox chemistry. Whether or not the CISS effect can explain magnetic field effects in biology and shed new light on the mechanism for magnetic field assisted navigation of birds and fish[54] will require detailed studies on spin selectivity and temperature effects in those systems. On a separate front, it is becoming clear that the CISS mechanism may be used to create a new generation of memory storage devices, which are discussed more below.

6.4.1 Memory Device

The need for smaller (denser), high speed, and low power universal memory continues to be an important driver for the improvement in computation speed, and the CISS effect may prove useful to apply in new generation devices. New generation technologies for serving as universal memories are magnetic memory (MRAM)[55] and spin-transfer torque memory (STT-RAM).[56–59] Both MRAM and STT-RAM are based on the spin filter concept with a permanent magnet and a free layer. If the free layer and the permanent magnet are aligned in parallel, the resistivity of the device is lower than when they are aligned antiparallel to each other.

A magnetic-based Si-compatible universal memory device without a permanent magnet was recently developed.[60] This magnet-free spin memory technology (MSM) uses organic molecules as spin filters rather than the common ferromagnetic-based spin filters. In this device, spin-selective charge is transferred through a self-assembled monolayer of polyalanine and magnetizes a thin Ni layer. Although this new design principle should allow miniaturization of the memory bit to a single magnetic nanoparticle size, the devices are micron scale and use self-assembled monolayers (SAMs) of α helix L-polyalanine (AHPA-L) adsorbed on gold.

The schematic diagram in Figure 6.9 illustrates the concept for the device operation. As electrons are ejected from the gold substrate, they are transferred through the right-handed chiral AHPA-L into the Ni layer, and finally to the collector gold electrode. Because the transmission through the

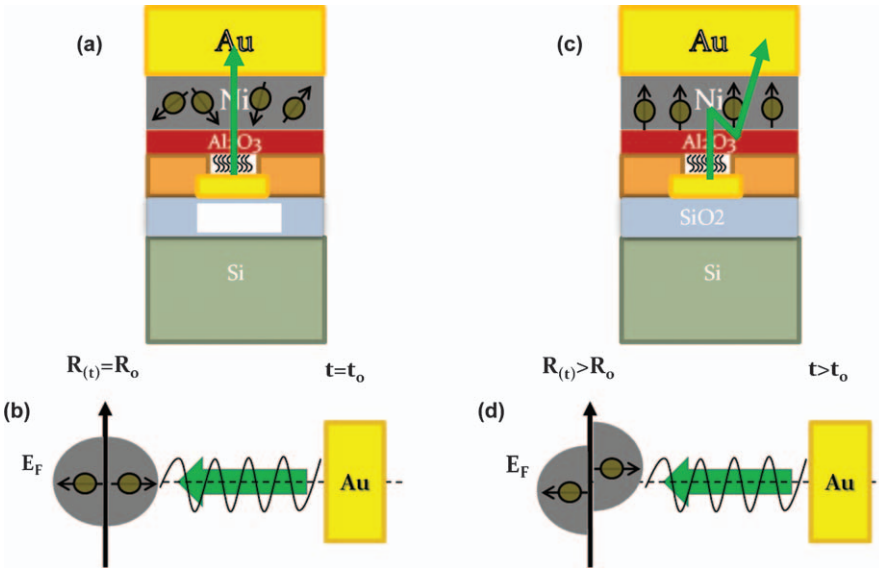

Figure 6.9 Schematic drawing of the experimental concept: (a) Initially, a low resistance is measured as spins parallel to the electron's velocity (green arrow) are transferred through the chiral layer into the non-magnetized Ni. (b) The polarized electrons are injected into Ni near E_F, in this state of low resistance. (c) Further injection of spin-polarized electrons increases the Ni magnetization, and after some time the Ni magnetization is aligned parallel to the injected spins. (d) After having been magnetized, the majority and minority spin density of states are split near E_F and the majority spin states inside the Ni are almost completely filled; therefore, the resistivity increases as the injection of majority spins continues.
Taken from ref. 60.

AHPA-L is spin selective, the electrons entering the nickel have one dominant spin orientation, which is controlled by the molecules' chirality and the propagation direction of the electrons; in this specific case, the spin is oriented mainly parallel to the electrons' velocity (*vide infra*). As the electrons pass through the nickel layer they transfer spin torque to it and create a magnetization. When magnetized, the nickel's resistivity increases for electrons having spins aligned parallel to the magnetic dipole of the nickel.[61] Because the easy axis of a thin Ni layer lies in the plane[62] and the Ni film is magnetized perpendicular to its surface, the magnetic moment rotates to the in-plane direction on a timescale that is temperature-dependent. This magnetization is not stable, however, and demagnetization occurs depending on the thickness of the layer.[63]

Figure 6.10 shows the perpendicular magnetization as a function of the applied field at various fixed temperatures, and the inset shows the time dependence of the device resistance at two different temperatures and a constant voltage of −2.5 V. The resistance change, under a constant voltage,

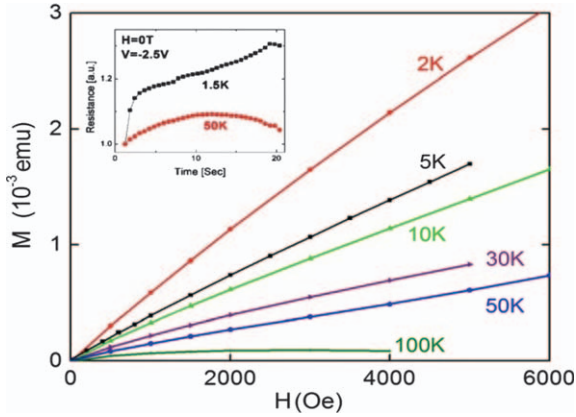

Figure 6.10 The perpendicular magnetization of the device with a thin Ni layer is plotted as a function of the external magnetic field up to 0.5 T, at different temperatures. The magnetization is stronger at 2 K than at 50 K. Inset: resistance change with time in the sample under a constant voltage of −2.5 V and 0 T external magnetic field at 1.5 K and at 50 K. Adapted from ref. 60.

is strong at 1.5 K and weak at 50 K. The *M–H* isotherms were measured up to 0.5 T at various temperatures. The data indicate that the saturation point is considerably delayed for the lower temperatures. Presumably, this occurs because the in-plane anisotropy makes it difficult for the field to lift the domain magnetization out of the sample plane. Considering that the thickness of the nickel film is 30 nm, the perpendicular magnetization measured at $H = 0.5$ T and at $T = 2$ K is significantly larger than expected, especially considering that out-of-plane is usually the hard direction of magnetization for the Ni films.

Because of the strong in-plane anisotropy, the domain's magnetization lies within the sample plane in the absence of a magnetic field and at temperatures above 50 K. Hence, it is expected that a magnetization arising from spin-torque transfer will be observed only at low temperatures for this device. As the Ni becomes magnetized, the current decreases and de-magnetization competes with the magnetization process and consequently reduces the resistivity, as indicated in the insert of Figure 6.10 for 50 K. For longer periods, oscillatory behavior is measured under constant voltage. When the resistance decreases and the current increases, the magnetization is enhanced. For a magnetized sample, the resistance increases again and the current decreases.

Figure 6.11 shows how the resistance changes with time for a device at a temperature of 2 K and an applied voltage of −2.5 V, for three different field strengths. The black curve (no external field) shows that the resistance rises with time until it reaches a maximum value. This maximum value represents a steady state between the competing processes of magnetization, which results from the spin-torque transfer, and the demagnetization, which arises

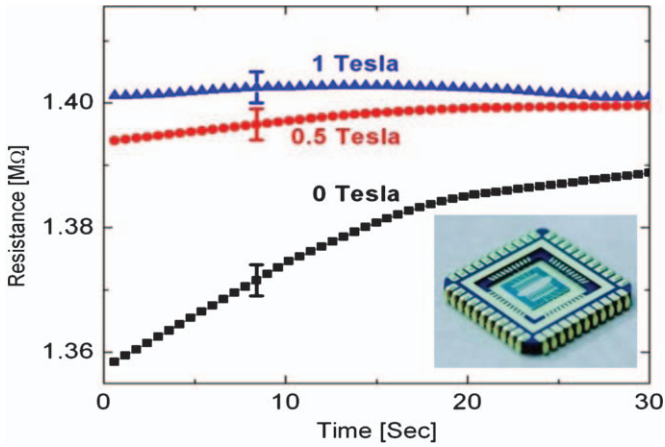

Figure 6.11 Black squares represent the resistance increase as current is driven through the chiral layer at a constant voltage of −2.5 V. Red circles (blue triangles) show data for the same measurement under a 0.5 T (1 T) magnetic field parallel to the current direction. Inset: optical microscopy picture of the measured device. Error bars indicate the maximum fluctuation of the measuring device.
Reproduced from ref. 60.

from the in-plane anisotropy and other effects such as direct tunneling or loss of the spin alignment in the barrier. Applying a magnetic field (0.5 T red curve) parallel to the current direction magnetizes the Ni and therefore the resistance starts at a higher value. For 1 T, the Ni is fully magnetized, the resistance is the highest, and little change in resistance is measured with time.

For this device the magnetization of the thin nickel film does not depend on the direction that the current flows. For the CISS effect the spin polarization is related to the electrons' velocity; hence, when the electrons' velocity reverses direction so does the spin of the transferred electrons. Therefore, while in one direction of current (electrons transported through the chiral molecules to the Ni) the majority spins are injected, reversing the current (electrons transported from the Ni through the chiral molecules' filter) removes the minority spins from the Ni layer, so that it is magnetized in the direction of the majority spins. Consequently, the writing can be done using both voltage directions, and the reading must be performed by driving a small current and monitoring the resistivity. To erase the memory one can apply a high voltage (higher than the barriers for the transport of both spin orientations through the layer) so that both types of spins are injected at similar rates to the Ni layer, and therefore demagnetize the Ni.[37]

The memory effect is demonstrated in Figure 6.12. First the Ni was magnetized at −15 V and read by using lower voltages of −2 or 2 V. For 2 V the minority-spin carriers' transfer and a low resistance is observed that increases with time; for −2 V one starts at a high resistance by injecting

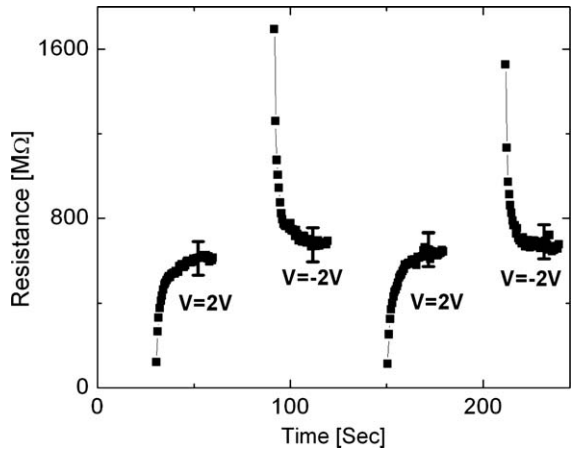

Figure 6.12 Resistance for the device as a function of time and applied voltage. The magnetization (information) is written at a bias voltage of −15 V for 30 s (empty spaces between +2 V and −2 V measurements), and it is read at lower voltages of +2 V and −2 V. The initial resistance is high for one direction of current and low for the opposite direction of current. Measurements were performed at 1.5 K and under a 0 T external magnetic field. Error bars indicate the maximum fluctuation of the measuring device.
Adapted from ref. 61.

majority spins. Owing to strong demagnetization of the Ni, the memory survives for only a few seconds; however, this writing and reading is repeatable and there is more than an order of magnitude difference between the resistivity measured for −2 V and +2 V during the first few seconds.

The technology presented here is Si compatible, and a device could be miniaturized to the limit achieved by Si technology (22 nm today). The permanent magnetic layers in the memory device can be miniaturized only to a size of about 100 nm, however, because of material limitations.[64] Recent progress on selective adsorption techniques may be able to address this challenge.[65] In fact, it should be possible to fabricate a memory device with many ports of chiral molecules that inject spins into the paramagnetic layer. By choosing several of the ports to inject the spin up and several ports to inject the spin down, a memory operating at a high base that can perform XOR logic may be realized. Development needs to be performed to find a better ferromagnetic material or improve the Ni layer so that longer memory times can be achieved.

6.5 Conclusions

The CISS effect is a relatively newly discovered phenomenon and much fundamental work remains to be done to fully understand and appreciate its implications. Despite the extensive theoretical work on the subject to date,

its mechanism is not yet fully understood. Experiment indicates that CISS may operate in biological redox reactions and thus be of importance in biology. Studies on chiral organic molecules have been shown to hold considerable promise for spintronics applications and this was illustrated by the description of a spin-torque memory device.

Acknowledgements

R.N. acknowledges partial support from the Minerva Foundation and from the Minerva Schmidt Center as well as support from the Israel Science Foundation and the German-Israel Science Foundation. D.H.W. acknowledges support from the US-NSF (CHE1059037 and DMR1412030).

References

1. *International Technology Roadmap for Semiconductors*, Executive Summary for 2009. http://www.itrs.net/links/2009ITRS/2009Chapters_2009Tables/2009_ExecSum.pdf.
2. F. Pulizzi, *Nat. Mat.*, 2012, **11**, 367.
3. J. Sinova and I. Zutic, *Nat. Mat.*, 2012, **11**, 368.
4. D. P. Divincenzo, *Science*, 1995, **270**, 255.
5. M. N. Baibich, J. M. Broto, A. Fert, F. Nguyen Van Dau, F. Petroff, P. Etienne, G. Creuzet, A. Friederich and J. Chazelas, *Phys. Rev. Lett.*, 1988, **61**, 2472.
6. G. Binash, P. Grünberg, F. Saurenbach and W. Zinn, *Phys. Rev. B*, 1989, **39**, 4828.
7. V. Dediu, M. Murgia, F. C. Matacotta, C. Taliani and S. Barbanera, *Solid State Commun.*, 2002, **122**, 181.
8. Z. H. Xiong, D. Wu, Z. V. Vardeny and J. Shi, *Nature*, 2004, **427**, 821.
9. T. L. Francis, O. Mermer, G. Veeraraghavan and M. Wohlgenannt, *New J. Phys.*, 2004, **6**, 185.
10. G. Szulczewski, S. Sanvito and M. Coey, *Nat. Mat.*, 2009, **8**, 693.
11. Koopmans, W. Wagemans, F. L. Bloom, P. A. Bobbert, M. Kemerink and M. Wohlgenannt, *Philos Transact A Math Phys Eng Sci.*, 2011, **369**, 3602.
12. M. Urdampilleta, S. Klyatskaya, J-P. Cleuziou, M. Ruben and W. Wernsdorfer, *Nat. Mat.*, 2011, **10**, 502.
13. S. Sanvito, *Nat. Mat.*, 2011, **10**, 484.
14. R. Naaman and D. H. Waldeck, *J. Phys Chem. Lett.*, 2012, **3**, 2178.
15. *Comprehensive Asymmetric Catalysis* (Eds.: E. N. Jacobsen, A. Pfaltz, H. Yamamoto), Springer, Berlin, 1999.
16. *Catalytic Asymmetric Synthesis*, 2nd ed. (Eds.: I. Ojima), Wiley, New York, 2000.
17. See also: T. P. Yoon and E. N. Jacobsen, *Science*, 2003, **299**, 1691.
18. L. D. Barron, *Nature*, 2000, **405**, 895.
19. *Molecular Light Scattering and Optical Activity.* Second edition. L. D. Barron, Cambridge University Press, Cambridge, 2004.

20. S. Yeganeh *et al.*, *J. Chem. Phys.*, 2009, **131**, 124128.
21. E. Medina, F. Lopez, M. Ratner and V. Mujica, *EPL (Eur. Phys. Lett.)*, 2012, **99**, 17006.
22. R. Gutierrez, E. Diaz, R. Naaman and G. Cuniberti, *Phys. Rev. B*, 2012, **85**, 081404.
23. R. Gutierrez, E. Diaz, C. Gaul, T. Brumme, F. Dominguez-Adame and G. Cuniberti, *J. Phys. Chem. C*, 2013, **117**, 22276.
24. (a) A.-M. Guo and Q.-f. Sun, *Phys. Rev. Lett.*, 2012, **108**, 218102; (b) A. M. Guo and Q. F. Sun, *Phys. Rev. B*, 2012, **86**, 115441.
25. D. Rai and M. Galperin, *J. Phys. Chem. C*, 2013, **117**, 13730.
26. J. Gersten, K. Kaasbjerg and A. Nitzan, *J. Chem. Phys.*, 2013, **139**, 114110.
27. D. Vager and Z. Vager, *Phys. Lett. A*, 2012, **376** 1895.
28. E. I. Rashba, *Fiz. Tverd. Tela*, 1960, **2**, 1224[*Sov. Phys. Solid State* 1960, **2**, 1109]; Yu. A. Bychkov and E. I Rashba, *Pis'ma Zh. Eksp. Teor. Fiz.*, 1984, **39**, 66[*JETP Lett.* 1984, **39**, 78].
29. I. Carmeli, V. Skakalova, R. Naaman and Z. Vager, *Angew. Chem. Int. Edition*, 2002, **41**, 761.
30. R. Winkler, *Spin–Orbit Coupling Effects in Two-Dimensional Electron and Hole Systems*, Springer Tracts in Modern Physics, vol. 191, Springer-Verlag, Berlin, Heidelberg, 2003, pp. 70–71.
31. F. Kuemmeth, S. Ilani, D. C. Ralph and P. L. McEuen, *Nature*, 2008, **452**, 448.
32. M. Buttiker, *Phys Rev. B*, 1988, **38**, 9375.
33. T. Martin and S. Feng, *Phys. Rev. Lett.*, 1990, **64**, 1971.
34. X.-L. Qi and S.-C. Zhang, *Physics Today, January*, 2010, **63**, 33.
35. B. Göhler, V. Hamelbeck, T. Z. Markus, M. Kettner, G. F. Hanne, Z. Vager, R. Naaman and H. Zacharias, *Science*, 2011, **331**, 894.
36. D. Mishra, T. Z. Markus, R. Naaman, M. Kettner, B. Göhler, H. Zacharias, N. Friedman, M. Sheves and C. Fontanesi, *Proc. Natl. Acad. Sci. U.S.A.*, 2013, **110**, 14872.
37. Z. Xie, T. Z. Markus, S. R. Cohen, Z. Vager, R. Gutierrez and R. Naaman, *Nano Lett.*, 2011, **11**, 4652.
38. S. Ravi, P. Sowmiya and A. Karthikeyan, *SPIN*, 2013, **3**, 1350003.
39. J. J. Wei, C. Schafmeister, G. Bird, A. Paul, R. Naaman and D. H. Waldeck, *J. Phys. Chem. B*, 2006, **110**, 1301.
40. M. R. Barbosa, S. G. Real, J. R. Vilche and A. J. Arvia, *J. Electrochem. Soc.*, 1988, **135**, 1077; Z. Mekhalif, J. Riga, J. J. Pireaux and J. Delhalle, *Langmuir*, 1997, **13**, 2285; Z. Mekhalif, F. Laffineur, N. Couturier and J. Delhalle, *Langmuir*, 2003, **19**, 637.
41. (a) P. A. Brooksby, K. H. Anderson, A. J. Downard and A. D. Abel, *Langmuir*, 2010, **26**, 1334; (b) D. E. Khoshtariya, T. D. Dolidze, L. D. Zusman and D. H. Waldeck, *J. Phys. Chem.*, 2001, **105**, 1818.
42. W. Chen, *Ann N Y Acad. Sci.*, 2006, **1066**, 92.
43. K. J. Freedman, S. R. Haq, J. B. Edel, P. Jemth and M. J. Kim, *Scientific Reports*, **20133**, 163, DOI: 10.1038/srep01638 1.
44. K. S. Kumar, N. Kantor-Uriel, S. P. Mathew, R. Guliamov and R. Naaman, *Phys. Chem. Chem. Phys.*, 2013, **15**, 18357.

45. C. R. Treadway, M. G. Hill and J. K. Barton, *Chem. Phys*, 2002, **281**, 409.
46. B. Giese, J. Amaudrut, A. K. Kohler, M. Spormann and S. Wessely, *Nature*, 2001, **412**, 318.
47. K. S. Kumar and R. Naaman, *Langmuir*, 2012, **28**, 14514.
48. E. P. A. M. Bakkers, A. W. Marsman, L. W. Jenneskens and D. Vanmaekelbergh, *Angew. Chem. Int. Ed.*, 2000, **39**, 2297.
49. (a) P. Kaden, E. Mayer-Enthart, A. Trifonov, T. Fiebig and H. A. Wagenknecht, *Angew. Chem. Int. Ed.*, 2005, **44**, 1636; (b) S. O. Kelley, R. E. Holmlin, E. D. A. Stemp and J. K. Barton, *J. Am. Chem. Soc.*, 1997, **119**, 9861.
50. (a) R. J. Elliott, *Phys. Rev.*, 1954, **96**, 266; (b) Y. Yafet in *Solid State Physics, Vol. 14* (Eds.: S. Frederick, T. David), Academic Press, 1963, pp. 1–98.
51. H. Idzuchi, Y. Fukuma, L. Wang and Y. Otani, *App. Phys. Lett.*, 2012, **101**, 022415.
52. A. Bid, A. Bora and A. K. Raychaudhuri, *Phys. Rev. B*, 2006, **74**, 035426.
53. I. Carmeli, K. S. Kumar, O. Hieflero, C. Carmeli and R. Naaman, *Angew. Chemie*, 2014, **53**, 8953.
54. K. Maeda, A. J. Robinson, K. B. Henbest, H. J. Hogben, T. Biskup, M. Ahmad, E. Schleicher, S. Weber, C. R. Timmel and P. J. Hore, *Proc. Natl. Acad. Sci. USA*, 2012, **109**, 4774.
55. W. J. Gallagher and S. S. P. Parkin, *IBM Journal of Research and Development*, 2006, **50**, 5.
56. Y. Huai, *AAPPS Bulletin*, 2008, **18**, 33.
57. J. A. Katine and E. E. Fullerton, *J. Magnetism Magnetic Materials*, 2008, **320**, 1217.
58. D. C. Ralph and M. D. Stiles, *J. Magnetism and Magnetic Materials*, 2008, **320**, 1190.
59. C. Wang, Y.-T. Cui, J. A. Katine, R. A. Buhrman and D. C. Ralph, *Nat Phys.*, 2011, **7**, 496.
60. O. Ben Dor, S. Yochelis, S. P. Mathew, R. Naaman and Y. Paltiel, *Nat. Commun.*, 2013, http://dx.doi.org/10.1038/ncomms3256.
61. C. Chappert, A. Fert and F. N. Van Dau, *Nat Mater.*, 2007, **6**, 813.
62. G. Kartopu *et al.*, *J. App. Phys.*, 2011, **109**, 033909.
63. G. Bochi *et al.*, *Phys. Rev. B*, 1995, **52**, 7311.
64. S. S. P. Parkin, M. Hayashi and L. Thomas, *Science*, 2008, **320**, 190.
65. O. Koslovsky, S. Yochelis, N. Livneh, M. G. Harats, R. Rapaport and Y. Paltiel, *J. Nanomaterials*, 2012, **2012**, Article ID 938495.

CHAPTER 7

Solution Processed Multilayer Organic Light Emitting Diodes

MANUEL AUER,[a,c] LEONID PEVZNER,[b] STEFAN SAX[c] AND EMIL J. W. LIST-KRATOCHVIL*[c,d]

[a] Institute of Physics, Humboldt Universität zu Berlin, Berlin, Germany; [b] Max Plank Institute of Polymer Research, Mainz, Germany; [c] Nanotec Center Weiz GmbH, Weiz, Austria; [d] Institute of Solid State Physics, Graz University of Technology, Graz, Austria
*Email: emil.list@ntc-weiz.at

7.1 Introduction

Since the first demonstration of an efficient organic light-emitting diode (OLED) by Tang *et al.*[1], several developments in the field of organic semiconductors led to the establishment of organic light emitting diodes (OLEDs) as a competitive technology for lighting and display applications. Nowadays, OLEDs are already integrated in the displays of many consumer products like smartphones as well as tablets and companies like Osram and Phillips are readying white OLED panels for mass-market lighting applications at the time of writing. Using the example of lighting technologies, OLEDs are already superior in terms of efficiency, while the manufacturing costs are still higher than for incandescent lighting (Figure 7.1).

In general, the fabrication of an OLED involves the deposition of at least one organic layer on top of a transparent conductive oxide (TCO) which serves as the anode. The cathode is usually deposited under vacuum and consists of a low work function metal. To date the existing procedures for the deposition of the organic layers are either based on vacuum sublimation of

RSC Smart Materials No. 12
Supramolecular Materials for Opto-Electronics
Edited by Norbert Koch

Published by the Royal Society of Chemistry, www.rsc.org

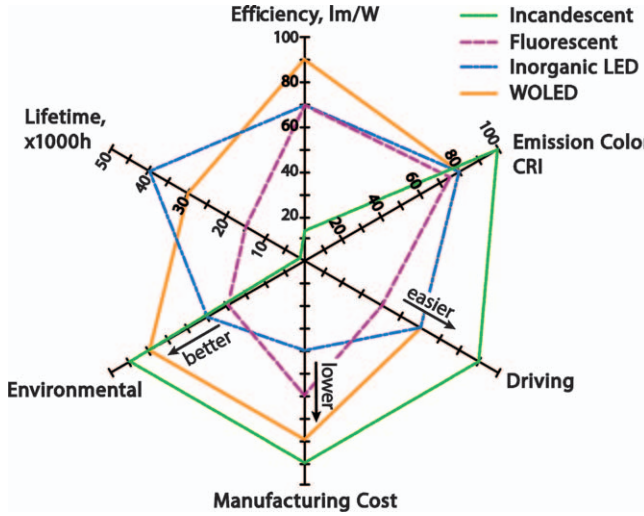

Figure 7.1 Semiquantitative comparison of the key performance parameters of white organic light emitting diodes (WOLED) relative to incandescent lamps, fluorescent tubes, and inorganic white LEDs. Taken and modified from ref. 2.

small molecules or on the deposition of conjugated polymers from a solution (wet-chemical process). Contemporary OLED devices are built using vacuum sublimation techniques that, compared to wet chemical processes like spin- or dip-coating, roll-to-roll processing and inkjet printing, suffer from the need for sophisticated instruments, substantial material waste and low throughput.[3] Additionally, in the case of OLED displays, pixilation *via* shadow masks limits the scalability and resolution of vacuum sublimation.[4] Even though wet chemical processes present a significant advantage in terms of lower manufacturing costs, the performance of devices built this way still trail vacuum sublimated OLED devices. A further obstacle is presented by the fact that most organic semiconductor materials suitable for wet-chemical processing are soluble in the same solvents. Compared to vacuum sublimation techniques where one layer is evaporated on top of the previously deposited ones, the similar solubility of the employed organic semiconductor materials complicates the fabrication of well-defined multilayer structures in a wet chemical process.

To understand the need for multilayer geometries, a short explanation is given for inorganic light emitting diodes (LED)s. Omitting the detailed physics behind an inorganic LED (for details the reader is referred to Kittel[5]), the fundamental working principle is presented in Figure 7.2(a). Electrons are injected into the n-doped region, while holes enter the device from the p-doped side. Both charge carriers drift towards the p-n junction and, assuming ideal circumstances, upon recombination of both charge carriers light corresponding to the energy of the band gap of the semiconductor is

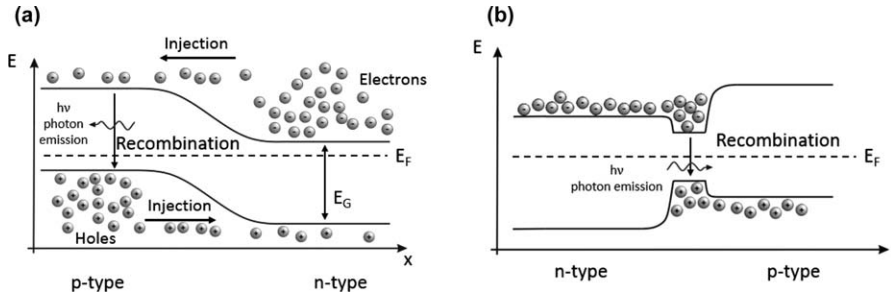

Figure 7.2 (a) Light generation in a p-n junction of a light emitting diode (LED). (b) Double heterojunction of a laser diode. Electrons are prevented from escaping by the wide energy gap of the p-doped side, while holes are confined by the n-doped wide bandgap side

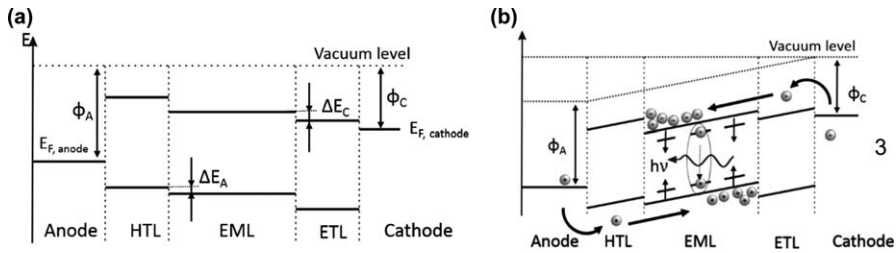

Figure 7.3 Assembly of a typical multilayer OLED presented under (a) the flat-band condition and (b) applied external bias.

emitted. In reality, however, the quantum efficiency of this recombination process is going to be lower than unity and a fraction of charge carriers are going to exit the device before they can generate a photon. One way to confine the charge carriers into a small region and thereby increase the charge carrier density is represented by a double heterojunction (Figure 7.2b). Here a small bandgap semiconductor is sandwiched between two either p- or n-doped wide bandgap semiconductors. Holes enter the device from the p-doped wide bandgap semiconductor, while electrons enter from the n-doped side. Under the influence of an applied external field, the charge carriers drift towards the center of the device, where the conduction and valence bands of the small bandgap semiconductor are energetically located below and above the wide bandgap semiconductor, respectively. This way, the charge carriers are confined within the small bandgap semiconductor and the charge carrier density is effectively increased, leading to increased quantum efficiency.

In a traditional multilayer OLED the emissive layer (EML) is sandwiched between a hole- and an electron-transporting layer (HTL and ETL, respectively). From the flat-band condition in Figure 7.3(a) (no external bias) the resulting energy barriers between the HTL and ETL into the EML (ΔE_C for electrons from the ETL and ΔE_A for holes from the HTL) can be identified.

Upon applying an external field (Figure 7.3b), the injection of charge carriers can take place and ultimately photons can be generated by the recombination of the injected charge carriers (since details are beyond the scope of this chapter, the reader is referred to excellent reviews by Koch[6] and Brütting[7] as well as to the book on OLEDs by Müllen and Scherf[8]).

Besides the confinement function described above, depending on the choice of the employed organic semiconductors, the injection of holes and electrons is facilitated. Additionally, any quenching processes[9–11] occurring at the electrodes are avoided as well.

As already established, the issue of dissolution of already applied layers aggravates the fabrication of well-defined multilayer structures in a wet-chemical process.

Therefore, several mechanisms and methods were devised to enable the fabrication of efficient multilayer structures. These fabrication strategies, some of which are presented below, can be mainly divided into three categories:

1. Methods that allow the solution-based formation of multilayer devices from similar solvents without any modification of the organic semiconductor (Section 7.2).
2. A modification of the organic semiconductor that allows the processed layer to be rendered insoluble also enables the fabrication from similar solvents (Section 7.3).
3. The use of orthogonal solvent systems where one solvent is unable to dissolve the other layer/s is possible with specifically designed materials (Section 7.4).

Finally, we provide a short conclusion and outlook where we summarize the current status in the field of solution-processed multilayer OLEDs (Section 7.5).

7.2 Multilayer Structures from the same Solvent by Diverse Fabrication Strategies

As already mentioned, most organic semiconductors are soluble in similar organic solvents. Often, this problem is addressed by a modification of the organic semiconductors to render them soluble in different solvents (Section 7.4) or by the introduction of cross-linking functionalities (Section 7.3). However, both approaches require a modification of the organic semiconductor and are therefore not universally applicable.

For this reason quite a few fabrication strategies that allow the fabrication from the same solvent have been developed. The more successful approaches to achieve solution-processed multilayer OLEDs from the same solvent are presented in this section. For each concept the basic idea is described and the viability is demonstrated by means of selected reports from the literature.

7.2.1 Blade Coating

The blade coating process is schematically presented in Figure 7.4. A small quantity of the solution containing the organic semiconductor is applied to the surface. Then the solution is homogeneously distributed across the surface by the movement of a blade at a fixed distance from the surface. The suitability as a multilayer solution-based process is given by the addition of a hot plate on which the substrate to be coated rests and the application of a hot wind to the surface. Therefore, rapid evaporation of the solvent occurs and possible damage to the preceding layer is avoided or at least minimized. The thickness of the resulting films is determined by the gap between the blade and the surface and the concentration of the applied solution.

The first blade-coating multilayer OLED was reported in 2008 by the group of Horng.[12] In this work the group proved the applicability of blade-coating for manufacturing multilayer polymer light emitting diodes (PLED) by using a poly(*para*-phenylene-vinylene) copolymer Super-Yellow (S-Y) in the first and poly(9,9-dioctylfluorene) (PFO, Figure 7.5) in the second layer. Both polymers were applied from a toluene solution with the hot plate set to 70 °C. Examination of the lateral profile of the fabricated substrate by scanning electron microscope revealed that a sharply defined interface exists. Additional bilayer devices incorporating either poly[(9,9-di-octylfluorenyl-2,7-diyl)-*co*-(4,4′-(*N*-(4-*sec*-butylphenyl))di-phenylamine)] (TFB, Figure 7.5) or 2-(4-*tert*-butylphenyl)-5-(4-biphenylyl)-1,3,4-oxadiazole (PBD, Figure 7.5) as hole transport layer (HTL) or electron transport layer (ETL) respectively in conjunction with PFO yielded efficiencies of up to 2.9 cd A^{-1}, emphasizing the suitability of blade-coating in a solution-based process.

In a next step, the group of Horng[13] successfully demonstrated the applicability of blade-coating for multilayer solution processed small molecule organic light emitting diodes (SMOLED). However, the attained efficiencies

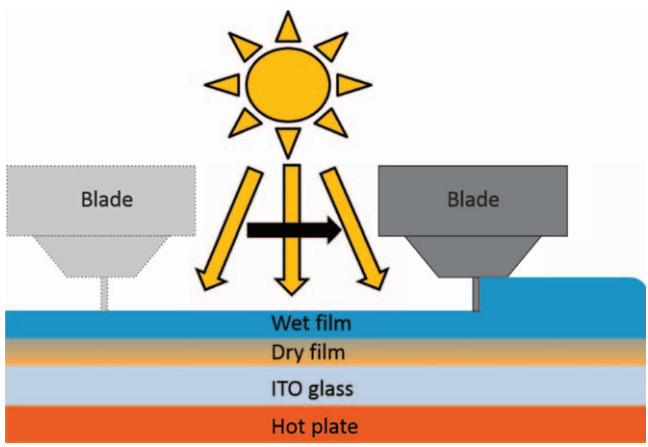

Figure 7.4 Visualization of the blade-coating process.

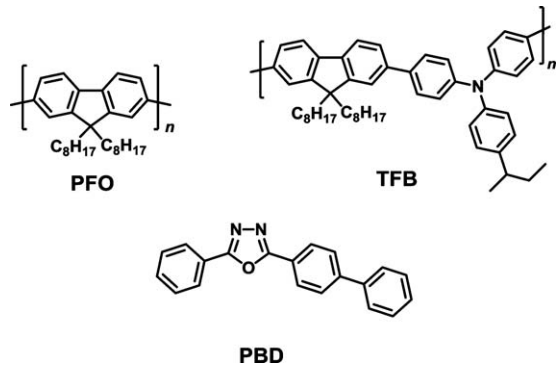

Figure 7.5 Chemical structures of the compounds used by Horng *et al*. to fabricate solution-processed bilayer devices.

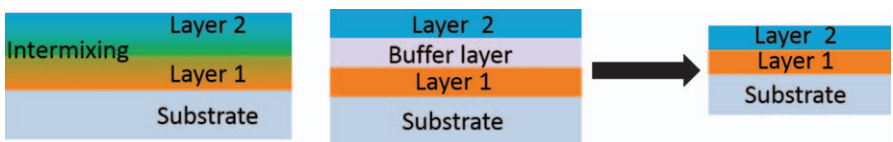

Figure 7.6 Fabrication of a bilayer substrate by using a liquid buffer layer.

were well below the control devices fabricated by vacuum sublimation. Crystallization of the applied small molecular layers caused by high annealing temperatures was identified as the probable cause. Further work extended towards blade-coating diverse small molecular ETLs[14] and general process optimization for the fabrication of SMOLEDs was performed.[15,16]

7.2.2 Liquid Buffer Layer

First presented by Tseng *et al*., this method prevents the dissolution of already applied organic layers by incorporating a protective liquid buffer layer (BL).[17] The protection from dissolution provided by the BL is directly related to its viscosity. Additionally, the liquid comprising the BL should exhibit a low boiling point. The fabrication steps are summarized schematically in Figure 7.6. After the deposition of the first organic layer, the BL is first deposited on top of this organic layer. The next organic layer is then coated on top of the previously applied BL. As a consequence of the high viscosity of the BL, the solvent of the next organic layer does not mix with the BL, resulting in the protection of the previously applied organic layer from dissolution. During the spin coating step of the second layer, most of the solvent and BL evaporate, leaving only some residue of BL in between the two layers. Given that the BL has a sufficiently low boiling point and small molecular weight it can be removed by an annealing step.

In the aforementioned report by Tseng *et al.*,[17] glycerol, propylene glycol and *n*-octane were investigated as possible BL. The protection capabilities were verified by applying the different liquids on top of 200 nm of LUMATION BP105 (BP) followed by a cooling step to 0 °C to increase the viscosity of the BL. Afterwards the substrates were spin-rinsed with toluene, chloroform and xylene. Of the three BLs, glycerol and propylene glycol provided perfect protection of the organic layer from dissolution with no detectable decrease in thickness.

Later Tseng *et al.*[18–20] demonstrated the fabrication of bilayer devices using different polymers and exploiting propylene glycol as a BL. An interesting approach by Lee *et al.* inserted PEDOT : PSS as a liquid buffer layer to produce bilayer polymeric WOLED.[21]

7.2.3 Electrospray Deposition

Electrospray deposition (ESD) was first introduced as a fabrication method for thin film radioactive sources in nuclear research and found broad application in several areas, such as polymer coatings, sample preparation in mass spectrometry and so on. In ESD, a high voltage is applied to a liquid that usually resides in a glass or metal capillary. The liquid ideally forms a Taylor cone at the tip of the capillary, which driven by the applied voltage emits a liquid jet (the schematics of an ESD apparatus are depicted in Figure 7.7). Small and highly charged liquid droplets are formed and radially dispersed due to Coulomb repulsion. The size of the droplet is influenced by the flow rate of the solution and the effective electric field. Depending on the parameters, droplet sizes of several hundred nanometers are attainable.[22–24]

The successful application of ESD for the fabrication of solution processed multilayer PLEDs has been demonstrated by the fabrication of bilayer

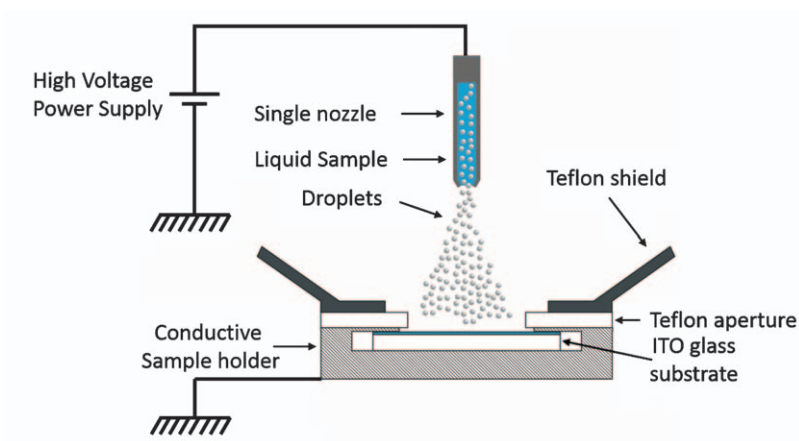

Figure 7.7 ESD apparatus configuration used for the fabrication of OLED thin films. Taken and modified from ref. 25.

devices consisting of a blue-emitting polymer and a green-emitting polymer, without any detectable dissolution of the blue-emitting layer.[26,27] Furthermore, a multilayer OLED consisting of small molecular weight materials from ESD was reported.[28]

While ESD holds great promise for the efficient fabrication of large-scale multilayer devices, great care has to be taken with regard to the quality of the obtained films.

7.2.4 Transfer Printing

Another strategy for the fabrication of solution-processed multi-layer devices is represented by the so-called transfer-printing process. While transfer printing of metals and semiconductors has been studied in rigorous detail,[29] successful transfer-printing of layers of organic semiconductors was reported only quite lately, in 2008 by Yim *et al.*[30]. Details of the manufacturing procedure are depicted in Figure 7.8. As can be seen, the organic layer is processed on top of a sacrificial layer (in this case poly(sodium 4-styrene sulfonate) (PSSNa)) on a Si wafer. The organic and the sacrificial layer are then transferred to a poly(dimethylsiloxane) (PDMS) stamp by placing the Si wafer in a water bath, which dissolves the PSSNa layer. Subsequently, the

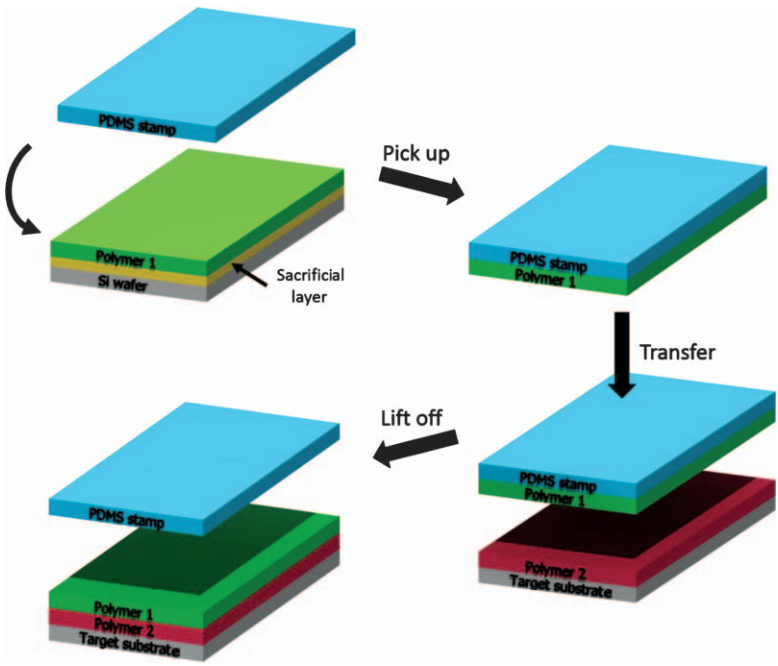

Figure 7.8 Schematic representation of a transfer printing process for multi-layer OLEDs.

PDMS stamp was placed on the accepting substrate and due to the lower adhesion strength of PDMS compared to the already deposited organic layer on the receiving substrate the organic layer on the PDMS stamp was transferred to the receiving substrate.

Benchmarking the manufacturing process against cross-linking and 1 : 1 blending of TFB (Figure 7.5)/poly(9,9-di-*n*-octylfluorene-*alt*-benzo-thiadiazole) (F8BT, Figure 7.9) bilayer OLEDs confirmed that transfer-printing is superior or at least competitive compared to the other manufacturing processes in terms of device performance.

A similar fabrication process was reported by Kim *et al.*[31] where PDMS was exchanged with poly(urethane acrylate) (PUA) as the stamp material. In terms of competitiveness they were able to demonstrate device performance values in the range 50–90% of evaporated control devices.

7.2.5 Lamination

Following a similar approach to transfer printing, lamination, which is sometimes referred to as template activated surface process (TAS),[32] not only involves the transfer of a single layer but also the remaining layers required to complete the OLED (Figure 7.10).

Guo *et al.*[32] reported on the successful fabrication of bilayer devices using TAS. In detail the fabrication of the device is divided into an anode and a cathode part. The anode part included a structured ITO electrode with PEDOT : PSS and a hole-transporting or emissive layer cast on top of it, while the cathode part entailed a cathode consisting of LiF and aluminium (Al) as well as the emissive layer. Finishing the fabrication process, the two parts

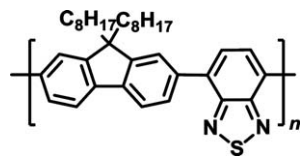

Figure 7.9 Chemical structure of F8BT.

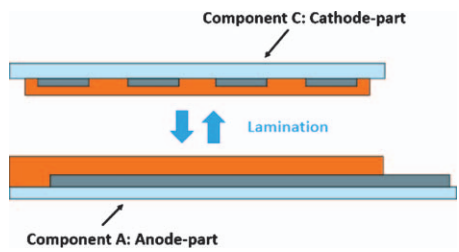

Figure 7.10 Schematic representation of the TAS process. Taken and modified from ref. 32.

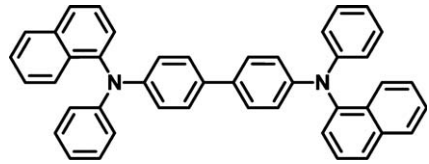

Figure 7.11 Chemical structure of α-NPD.

of the device are put together on a pre-heated hot plate at 60 °C with a minor pressure applied for a few minutes. Bilayer devices consisting of *N*,*N*′-diphenyl-*N*,*N*′-bis(l-naphthyl)-1-1′-biphenyl-4,4′′-di-amine (α-NPD, Figure 7.11) as a hole-transporting material and PFO (Figure 7.5) as a blue-emissive material were able to attain brightness values of 700 cd m^{-2} and maximum efficiencies of 0.26 cd A^{-1}, which was respectable at the time. A follow-up report from the authors determined the formation of good contacts between the organic layers, refuting suspicion of the contacts.[33]

7.3 Multilayer Structures from the same Solvent by Chemical Reaction

In general, any process or reaction that causes the individual conjugated molecules (either small molecules or also polymers) to form insoluble films by linking together is called cross-linking. Once a film is cross-linked the next layer can be processed on top of it without any dissolution (Figure 7.12). Most of the time this is achieved by the incorporation of reactive substituents that are activated either by thermal, light or chemical treatment.

Importantly, cross-linkable materials have to fulfill certain conditions to be valuable for the fabrication of multi-layer OLEDs:

- The curing procedure should not negatively affect electrical and optical properties as well as device lifetimes.
- Unavoidable byproducts of the cross-linking reaction should also leave the device performance unimpaired.
- Often, volume shrinkage is observable due to the cross-linking reaction. The resulting mechanical stress in the film has frequently been speculated to lead to reduced device lifetimes. Logically, the possible volume shrinkage has to be as low as possible.
- Obviously, the reactive substituents need to be stable during the synthesis of the precursors and only become active by the application of the initiator.

Within this section we provide an overview of successful fabrication schemes that render individual films insoluble and give some examples reported in the literature.

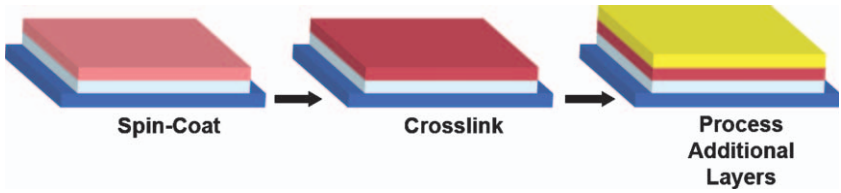

Figure 7.12 Schematic representation of the steps involved in a cross-linking process for solution processed OLEDs.
Modified from ref. 34.

7.3.1 Cross-Linking by the Addition of Reactive Groups

Among the most popular approaches for the solution-based fabrication of multilayer OLEDs is represented by the addition of cross-linking functionalities to a conjugated polymer/small molecule. This section gives examples of successful reactive groups. Furthermore, the reaction mechanisms behind these cross-linking chemistries are described and exemplary reports from the literature are provided.

7.3.1.1 Siloxanes

The cross-linking mechanism of siloxanes is pictured in Scheme 7.1. The reaction is initiated by hydrolysis, which is then followed by condensation of the resulting silanols. As a result, very stable Si–O–Si linkages are formed. However, remaining water, alcohols or hydrogen halides of the hydrolysis or condensation steps are potential contaminants in the cross-linked siloxane films that might have adverse effects on the resulting device performance.

Among the earliest examples of the utilization of siloxanes to achieve cross-linked films was a report by Li *et al.* in 1999.[35] They published a tris(trichlorosilyl)-functionalized triarylamine hole-transport material Si-TPA (Figure 7.13), which could be spin-coated and subsequently cross-linked. Cross-linking was achieved by a hydrolysis step accomplished by exposure to moisture followed by a curing step at 120 °C, yielding hard, stable and adherent films. Successful cross-linking was attested by differential scanning calorimetry (DSC) and thermogravimetric analysis (TGA). An additional ''scotch tape'' test verified the resistance towards delamination.

The surface topology of the cross-linked films was investigated by AFM and confirmed the presence of smooth and defect free films.[35]

Yan *et al.*[36] utilized a bis(diarylamino)biphenyl (TPD) group with attached trichlorosilyl functionalities to fully solution process an OLED. This was achieved by depositing a blend $TPDSi_2$ (Figure 7.14) and TFB (Figure 7.5) (1 : 1 weight) onto PEDOT : PSS from a toluene solution. Cross-linking was achieved spontaneously *via* exposure to air resulting in smooth and insoluble films. As an electron transporting material F8BT (Figure 7.9) was deposited on top of the now insoluble film to yield an ITO/PEDOT : PSS/$TPDSi_2$: TFB/F8BT/Ca/Al device geometry.

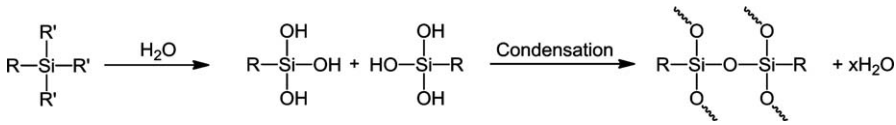

Scheme 7.1 Siloxane-based cross-linking.

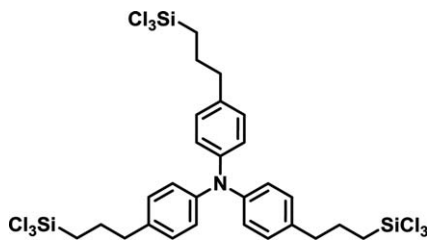

Figure 7.13 Chemical structure of Si-TPA.

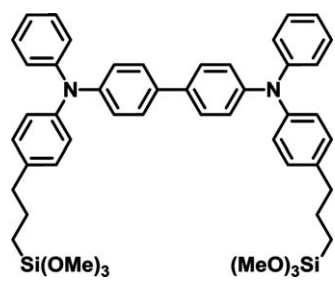

Figure 7.14 Chemical structure of $TPDSi_2$.

Compared to an ITO/PEDOT : PSS/F8BT/Ca/Al device, the current efficiency was an order of magnitude higher.

An interesting application of chlorosilyl groups was reported by Huang *et al.*[37] where the chlorosilyl moieties were utilized to react with the hydroxyl groups on the surface of ITO leading to strong self-assembled mono- and multilayers that can change the charge injection properties at this interface within an OLED. The SAMs were assembled by immersing the substrates in toluene solution of compounds TPDSi-1, TPDSi-2 and TPDSi-3 (Figure 7.15). Excessive material was removed by a rinsing step after a thermal treatment at 80 °C for an hour. Cross-linking was then promoted by another thermal treatment at 120 °C for another hour. Distinguishing these compounds from other cross-linkable materials is the ability to form a covalent bonding with the ITO and thereby yield better contact and stability of the so-formed HTL. The usefulness of this approach was established by the 100-times better EQE (external quantum efficiency) of devices with an ITO/TPDSi-3/PFO/Ca/Al compared to devices without TPDSi-3 as a SAM.

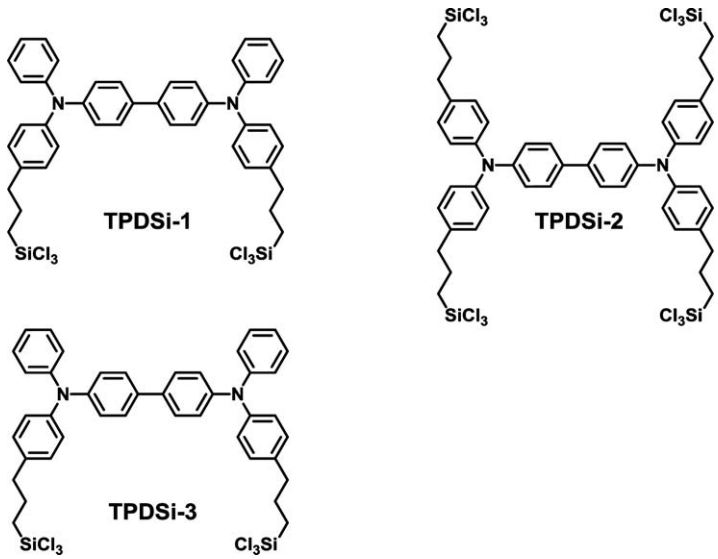

Figure 7.15 Chemical structures of TPDs functionalized with chlorosilyl groups.

7.3.1.2 Styrenes

Cross-linking of styrene functionalized organic semiconductors can be initiated thermally *via* the well-known radical mechanism. To initiate the polymerization no additional reagents are required and therefore no additional side products are formed. Therefore, as long as the organic semiconductor remains thermally stable at the required temperatures and unreactive towards the cross-linking groups, the styrene chemistry represents a highly attractive choice for the implementation of a cross-linking functionality. To date, styrenes have been attached to small-molecules as well as polymers (Scheme 7.2). A significant amount of work focused on the implementation of styrenes in order to control the morphology and solubility of the emissive layer.

For example, a styrene end-capped PPV (PPV-Cl, Figure 7.16) derivative was studied by Wang *et al.*[38] Even though insoluble layers of PPV have been prepared using a precursor method (also see Section 7.3.3), the risk of performance degradation caused by potential byproducts can be avoided by using cross-linkable styryl end groups. UV–Vis spectra of cross-linked thin films (baked at 175 °C for 1 h) before and after a solvent treatment as well as additional AFM investigations demonstrated that smooth and insoluble films were formed. Furthermore, the properties of this compound with regards to performance and multilayer capability were investigated in a single and bilayer device assembly. The single layer featured an ITO/PEDOT : PSS/PPV-Cl/Ca/Al assembly, while the bilayer also incorporated an ETL in the shape of PBD (Figure 7.5) blended in poly(methyl methacrylate) (PMMA).

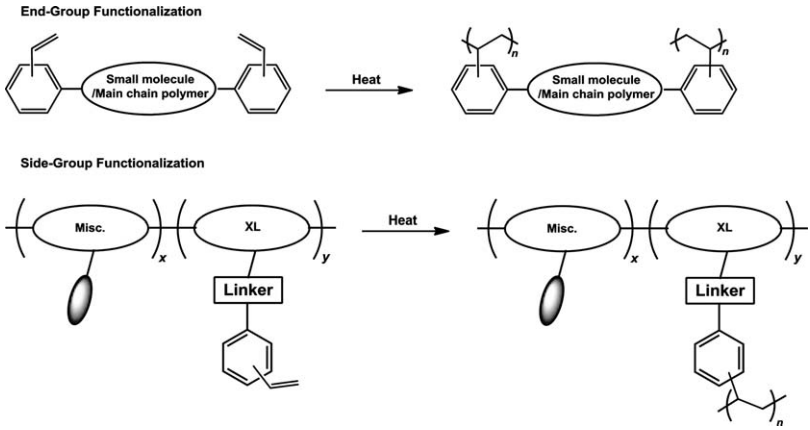

Scheme 7.2 Thermally initiated cross-linking of styrene-functionalized molecules and polymers.
Modified from ref. 34.

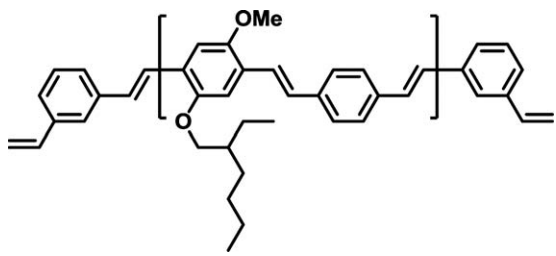

Figure 7.16 Chemical structure of PPV-Cl.

The single layer attained only a low luminance efficiency of 0.054 cd A^{-1} emitting in the yellow–green part of the spectrum, while the bilayer device saw a respectable increase in luminance efficiency to 0.7 cd A^{-1}.

On top of the functionalization of EMLs, styrenes have also been incorporated into hole-transporting materials.[39]

7.3.1.3 Acrylates

Cross-linking of compounds bearing acrylate groups is achieved *via* a radical mechanism, where the radical initiator is activated either thermally or photochemically. Insoluble films can subsequently be formed when a molecule is functionalized with at least two acrylate groups. So far, there have been few reports about acrylate-functionalized organic semiconductors. A notable report from 2006 successfully demonstrated the inhibition of the crystallization of evaporated tris(8-hydroxyquinolinato)aluminium (Alq_3) layers.[40] According to Scheme 7.3 the cross-linking process of the acrylate groups was initiated photochemically by irradiating a photoinitiator with UV

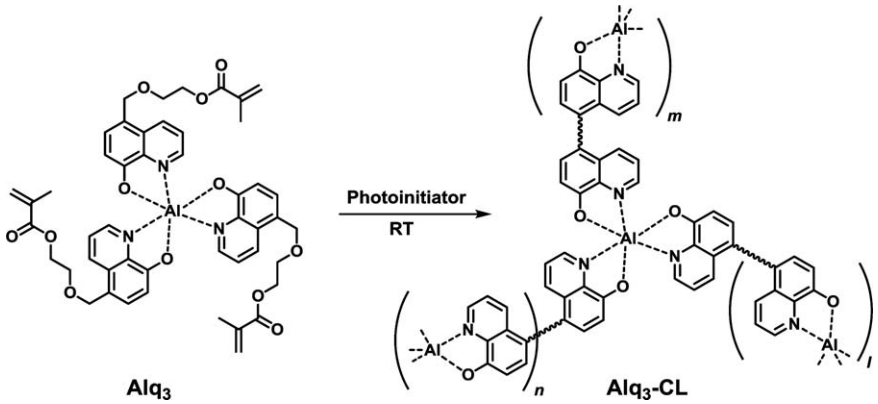

Scheme 7.3 Cross-linkable tris(8-hydroxyquinolinato)aluminium derivative and its homopolymerization.

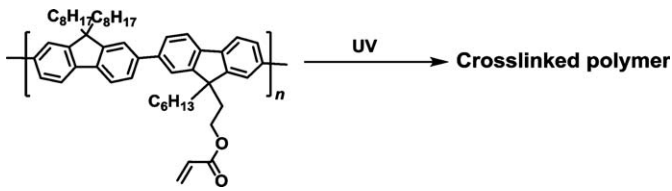

Scheme 7.4 Cross-linking process of PF-Acr.

radiation as well as by a thermal activation at 150 °C for 15 min. Cross-linking of the resulting homo- and copolymer (with *N*-vinylcarbazole) was verified by DSG and TGA. Compared to standard Alq_3, the well-known glass transition temperature of 120 °C could not be observed. Coupled with the increased thermal stability evidenced by TGA *versus* standard Alq_3 the successful formation of a cross-linked film was assumed.

Acrylates were also demonstrated to efficiently form cross-linked films when incorporated into the side-chains of a polyfluorene to yield PF-Acr (Scheme 7.4).[41] The polymer was rendered insoluble by subjecting the film to UV light (365 nm) for 15 min. Cross-linking was confirmed *via* IR spectra as well as UV–Vis absorption spectra.

While the UV treatment successfully rendered the PF-film insoluble in common organic solvents, an emission at 517 nm appeared in the PL and EL spectra, which was ascribed to the formation of keto defects[42–44] as a result of the photo-crosslinking.

7.3.1.4 Trifluorovinylethers

As an exception of the Woodward–Hoffman rules trifluorovinylether (TFVE) groups undergo thermally activated [2 + 2] cycloadditions that form hexafluorocyclobutane moieties at temperatures of about 200 °C (Scheme 7.5).

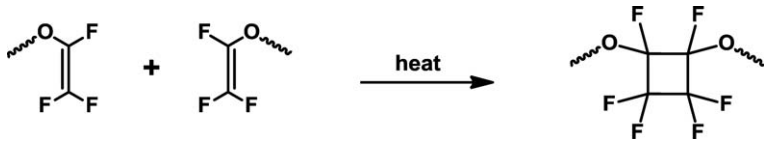

Scheme 7.5 Thermal [2 + 2] cycloaddition of trifluorovinyl ether.

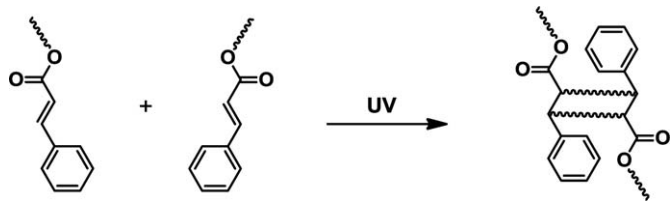

Scheme 7.6 [2 + 2] Cycloaddition of cinnamates.

The process involves a minimum amount of side reactions and as a result can occur in the presence of many of the common functional groups. Therefore, TFVE groups represent attractive cross-linking groups with the only drawback remaining in the possible thermal instability of the active material at the required high reaction temperature. For the design of cross-linkable organic semiconductors, the fact that the TFVE groups undergo a dimerization compared to a polymerization is important since at least three TFVE groups are necessary to assure cross-linked films.

In 2006, Lim *et al.*[45] reported on a TFVE-functionalized hole transport small molecule intended to replace PEDOT : PSS as a hole-transport/hole injection layer. Films of this novel compound evidenced good thermal stability with respect to weight loss, whereas DSC exhibited a large exothermic peak at 230 °C. Full insolubilization in chlorobenzene was achieved after 2 h of heating at 230 °C, yielding films with a root mean square (RMS) of 0.47 nm compared to 1.15 nm for PEDOT : PSS as determined by AFM measurements. Increased efficiencies clearly corroborated the usefulness of TVFE cross-linking groups, whereas the drawback of extended high temperature heating required for full cross-linking remains.

7.3.1.5 Cinnamates

Cinnamates have been successfully utilized as a cross-linking moiety for polymers.[46,47] Since cross-linking is facilitated by UV activated [2 + 2] cycloaddition, at least a moderate transparency of the active groups at approximately 290 and 345 nm is required to achieve insoluble films. Additionally, at least three cinnamate groups are required per molecule, since the type of reaction represents a dimerization (Scheme 7.6).

One of the first reports involving cross-linking reactions for the fabrication of insoluble and robust films came from Li *et al.*[48] They reported on the

synthesis of a poly(methacrylate) ter-polymer with distyrylbenzene-, oxadiazole-, and cinnamate-containing side chains. Deposited films were cross-linkable *via* UV irradiation for 10 min. Successful cross-linking was corroborated by DSC where an increased glass-transition temperature was recorded (increase from 107 to 154 °C). However, absorption spectra recorded of the cross-linked films exhibited decreased absorption of the distyrylbenzene and cinnamate absorption, which might be the result of undesirable photodamage from the UV-initiated cross-linking process.

Possible photodamage of the active groups by UV-initiated cross-linking was investigated by Zhang *et al.*[49] who studied a copolymer of methacrylate monomers with TPD and cinnamate or chalcone groups containing side chains. UV–Vis spectra were recorded after different UV exposure times and showed a decrease in the overall near-UV absorption for the copolymers. However, possible photodegradation was ruled out as the cause by determining the absorbance of a homopolymer containing only the hole-transport TPD monomer, which exhibited no change after UV irradiation. Insolubilization of the copolymers was investigated by UV–Vis spectra before and after a tetrahydrofuran (THF) washing treatment. Lastly, the performance of the cross-linked hole-transport copolymers in an OLED was tested in an ITO/copolymer/Alq3/Mg device where the copolymer was both cross-linked and not cross-linked. Surprisingly, the cross-linked films exhibited decreased performance compared to the not cross-linked films even though the hole-transport moieties were found to be unaffected by the UV treatment.

7.3.1.6 Oxetanes

Oxetane groups are strained four-membered cyclic ethers that can form linear polyethers *via* a cationic ring-opening polymerization (CROP).[50] Given that a suitable initiator of the polymerization process is added, molecules functionalized with two or more oxetanes can be cross-linked (Scheme 7.7).

The initiators of the CROP are often UV photoacid-generators like diaryliodonium or triarylsulfonium salts. Excitation of these photoacid generators leads to bond cleavage and consequently a strong acid is generated. Unfortunately, the destructive generation of protons in the presence of a low-bandgap dye such as the active material was observed.[51,52]

Given that the utilized active materials are not susceptible to strong Brønsted acids, cross-linking *via* oxetane groups has the potential advantage of a rather low shrinkage during polymerization and with general relatively high polymerization rates.[53–55] Polymerization rates can even be improved

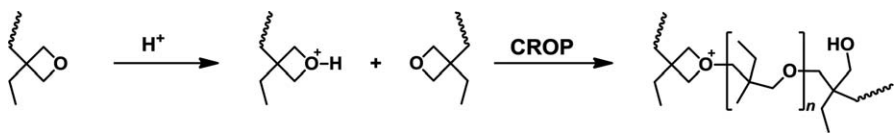

Scheme 7.7 Cationic polymerization of oxetanes.

by a thermal treatment following the photoinitiation step. When oxetane groups are employed as a cross-linking chemistry, the presence of protons or oxonium species following the CROP has to be kept in mind. Nonetheless, to date several groups have reported on high efficiency OLEDs based on oxetane groups for cross-linking capabilities.

One of the first reports on oxetane-based cross-linking came from Bayerl *et al.* in 1999.[53] The performance of TPD functionalized with short or extended oxetane groups (TPDOx1 and TPDOx2, Figure 7.17) with respect to a successful cross-linking was investigated. Cross-linking was verified by the deposition of the synthesized compounds on ITO along with 1 wt% of a photoacid followed by UV exposure (1 min at 302 nm). The glass-transition events observable for the monomers in DSC completely vanished for the UV-treated films and indicated a successful cross-link. To assess the impact of cross-linking on the device performance two devices were built with an ITO/TPDOx1 and TPDOx2/Al architecture where only one device received a cross-linking treatment. Remarkably, the cross-linked device boasted an approximately 15 times higher current maximum compared to the non-cross-linked reference device.

In 2003, Müller *et al.* demonstrated a series of conjugated polymers patternable by photomasking due to incorporated oxetane moieties.[56] Using this approach and different feed ratios of arylene units in the backbone, copolymers with different emission colors were synthesized (MH1–MH4, Scheme 7.8). The ability to employ photo-patterning allowed for the successful fabrication of a fully solution processed multi-color display. In detail, the different copolymers were processed consecutively and the individual pixels were formed by subjecting the polymers to UV radiation (3 s at 302 nm) in the presence of a photoacid generator. Successful cross-linking was verified by IR measurements, which indicated the disappearance of the oxetane groups. As a side effect of the cross-linking process, oxonium cations were formed that required neutralization by treatment with several bases. The impact of cross-linking on the device performance was investigated by using cross-linked and pristine films in an ITO/PEDOT : PSS/MH1–MH4/Ca/Al assembly. The performance of all polymers was found to suffer only marginally from cross-linking, while they exhibited increased resistance to breakdown at higher current densities.

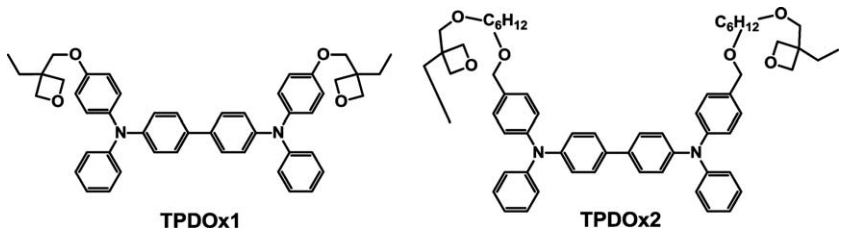

Figure 7.17 Chemical structures of TPDs functionalized with short or extended oxetane groups.

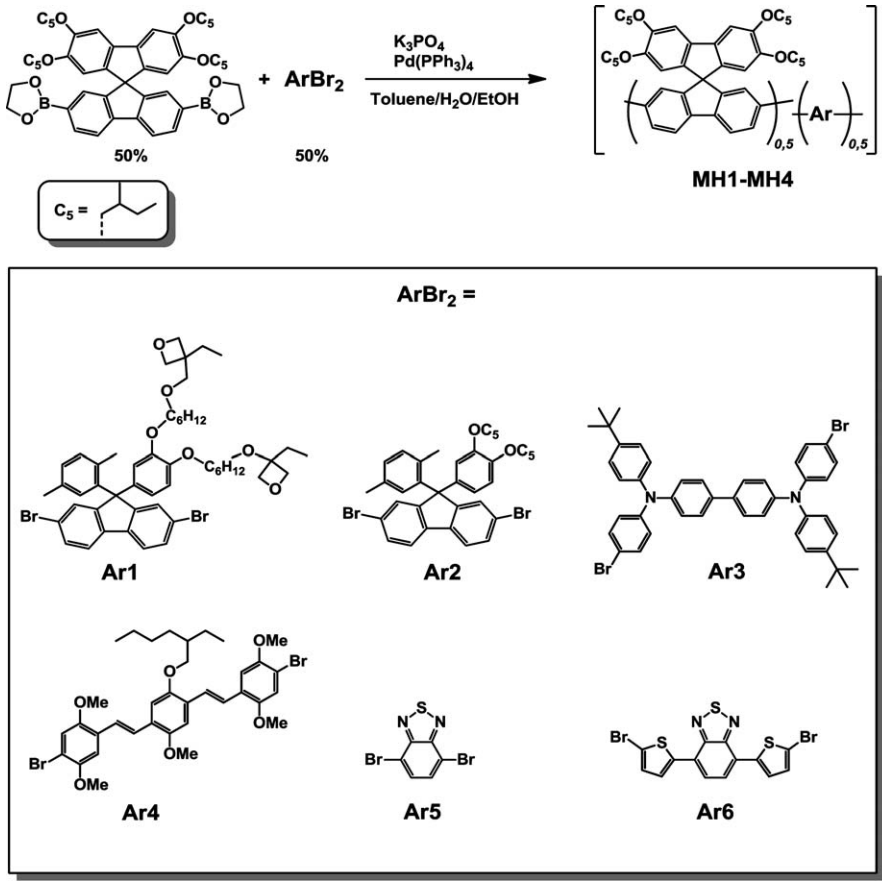

Scheme 7.8 Cross-linkable copolymers containing bis(oxetane)-functionalized moieties and building blocks **Ar1–6** in varying feed ratios. Taken and modified from ref. 56.

The group of Meerholz studied a series of cross-linkable hole-transport molecules TPDOx3–TPDOx5 based on TPD containing oxetane functionalities (Figure 7.18). All films were cross-linked with UV (365 nm for 10 s) and subsequently cured at 120 °C to further promote cross-linking. Successful cross-linking was verified by absorbance measurements before and after rinsing treatments in common organic solvents. Devices with single- and dual-HTLs, onto which an emissive layer consisting of poly(*N*-vinylcarbazole) (PVK, Figure 7.19) as well as different iridium (Ir) phosphors and ETL with oxadiazole-derivatives, were solution processed. At the time of publication, some of the reported devices exhibited remarkable performance characteristics especially for solution-processed OLEDs. Among the best results was a green-emitting device that attained a maximum external quantum efficiency (EQE) of 18.8% with a calculated power efficiency of 50 lm W^{-1} at 100 cd m^{-2}.

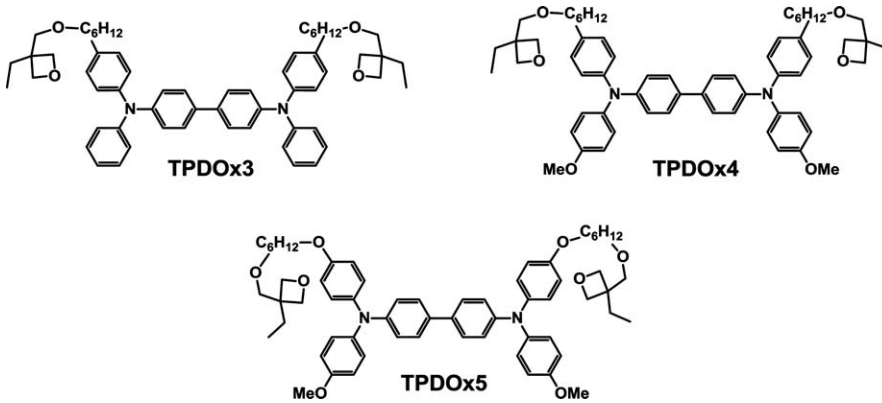

Figure 7.18 Chemical structure of TPD molecules with incorporated oxetane moieties.

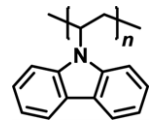

Figure 7.19 Chemical structure of PVK.

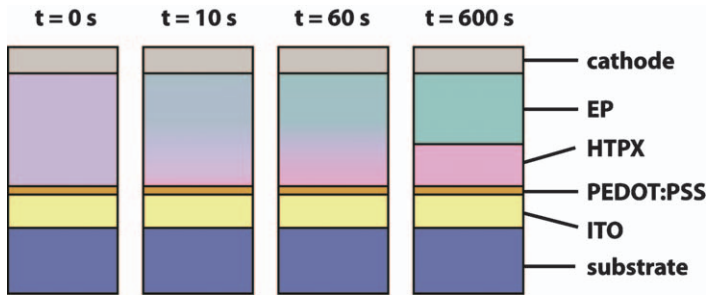

Figure 7.20 Procedure for SIPS. A blend of the hole-transport material and a non-cross-linkable electroluminescent polymer is spin-coated on top of a PEDOT : PSS layer. The acidic cross-linking of the hole-transport material is from the PEDOT : PSS surface and is started by thermal treatment of the substrate leading to a phase-separation from the non-cross-linkable polymer.
Modified from ref. 57.

Another interesting approach was reported by Köhnen *et al*. in 2011, where oxetane groups where used to manufacture two layers by a solution process at the same time.[57] This procedure, termed surface-initiated phase separation (SIPS, Figure 7.20), was investigated using a cross-linkable triarylamine-based hole conductor (HTLX) and a non-cross-linkable blue-emitting fluorine-based copolymer (BP), as well as a white-emitting co-polymer (WP) with red- and green-emitting units copolymerized with a blue-emitting host.

SIPS was carried out by thermal treatment of the substrate at 200 °C for time spans from 1 to 10 min. The successful cross-linking was verified by DSC measurements, which indicated a dramatic rise in the T_g near the PEDOT interface. The resulting double layer ITO/PEDOT : PSS/HTLX : BP/Ba/Ag devices were able to reach current efficiencies of up to 2.6 cd A^{-1} depending on the duration of the thermal annealing step, which is quite close to the attained 3 cd A^{-1} for a reference device with discrete layers.

7.3.2 Thermal Stabilization

A comparatively simple method for the realization of multilayer structures was reported by Kim *et al.*[58] where they rendered parts of a TFB (Figure 7.5) layer insoluble by a thermal annealing step at 180 °C (above the T_g of TFB) for 1 h in a glove-box. The still soluble parts were removed by an additional spin-rinsing step with a solvent leaving only a thin (~10 nm) and uniform (<0.1 nm rms roughness) layer of TFB on the substrate. A device with a TFB hole-transporting interlayer and F8BT (Figure 7.9) as an EML yielded peak efficiencies of 7.1 cd A^{-1} or an EQE of 2.1%, which is six times higher than the performance recorded for a control device without the interlayer.

To date, several polymers have been found to be suitable for the formation of insoluble interlayers[59] and the thermal stabilization of more than one layer[60] was reported as well.

Recently, Nau *et al.*[61] reported a highly efficient deep-blue-emitting bilayer structure consisting of the hole transporting CP-AE and emissive CP-ABCD copolymers specified in Figure 7.21.

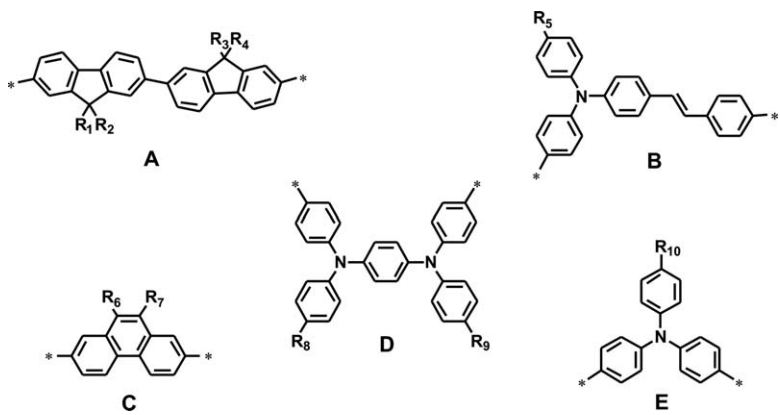

Figure 7.21 Chemical structures of the individual copolymer building blocks: (A) 9,9,9′,9′-tetraorganyl-2,2′-bifluorenyl; (B) (*E*)-4-organyl-*N*-phenyl-*N*-(4-styrylphenyl)aniline; (C) 9,10-diorganyl-phenanthrene; (D) N^1,N^4-bis(4-organylphenyl)-N^1,N^4-diphenylbenzene-1,4-diamine; and (E) 4-organyl-*N*,*N*-diphenylaniline; R_n where *n* is 1–10 represents organyl groups. CP-AE consists of component A and E at a ratio of 50 : 50; CP-ABCD consists of component A, B, C, and D at an A : B : C : D ratio of 46 : 2 : 50 : 2.

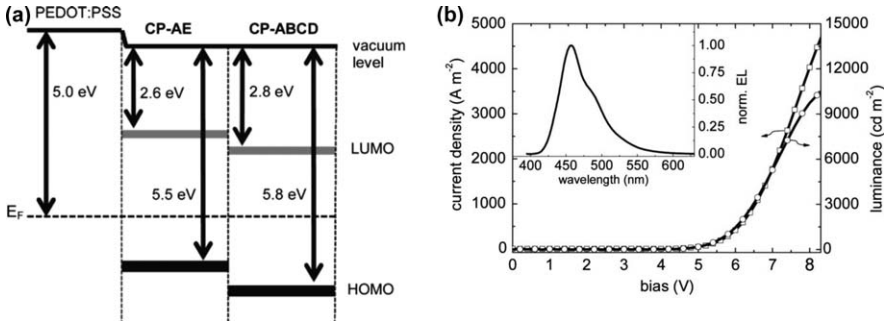

Figure 7.22 (a) Schematic energy level diagram of the PEDOT : PSS/CP-AE/CP-ABCD multilayer structure obtained by UPS and (b) current density (open squares) and luminance (open circles) as a function of the bias voltage in an ITO/PEDOT : PSS (60 nm)/CP-AE (20 nm)/CP-ABCD (60 nm)/Cs_2CO_3 (0.15 nm)/Al (100 nm) device.
Taken from ref. 61.

In detail, the bilayer devices were assembled by exploiting thermal stabilization to render the hole-transporting compound CP-AE completely insoluble after an annealing step at 200 °C for 1 h. On top of that a layer of CP-ABCD was spin-cast followed by a vacuum deposited caesium carbonate (Cs_2CO_3)/Al cathode layer.

Ultraviolet photoelectron spectroscopy (UPS) measurements revealed a favorable staggered energetic structure (Figure 7.22a) resulting in a shift of the recombination zone away from the exciton quenching PEDOT : PSS interface. As a consequence very high current efficiencies of 9.7 cd A^{-1} at CIE1931 color space coordinates of $x = 0.144$, $y = 0.129$ are achieved that at the time of writing are among the highest for fluorescent deep-blue-emitting OLEDs.

7.3.3 The Precursor Route

Another option to implement solution processed multilayer devices is *via* the precursor route where a soluble non-conjugated polymer is deposited as film and transformed into the fully conjugated emissive layer upon thermal treatment.[62] Although rarely mentioned in the context of manufacturing processes for multilayer assemblies the precursor route provides a promising option for the application of a few mainly poly(*para*-phenylenevinylene) (PPV) based materials[63] and is mentioned for the sake of completeness.

Morgado *et al.*[64] reported on a bilayer device fabricated using PPV processed *via* the established precursor route[65] (Scheme 7.9) where the precursor is converted into PPV thermally at 170 °C for 10 h under vacuum (10^{-5} mbar). This PPV layer is insoluble in common organic solvents allowing for a solution-based deposition of the next organic layer. Bilayer devices consisting of emissive layers of PFO : F8BT (5 wt%) were able to attain a current efficiency of 4.1 cd A^{-1}, which is considerably higher than

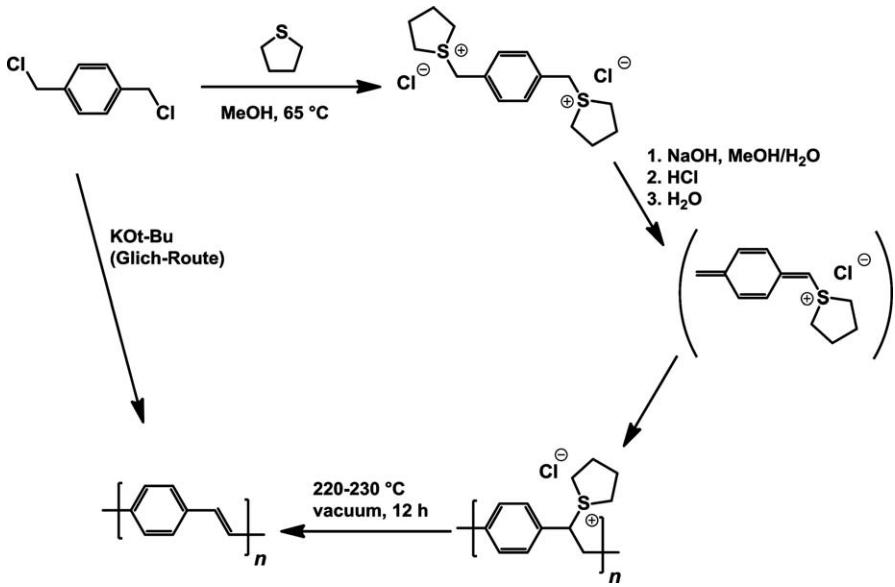

Scheme 7.9 Reaction scheme for the preparation of PPV *via* a precursor route.

2.1 cd A^{-1} achieved for the single-layer device, thereby demonstrating the effectiveness of this particular approach.

7.3.4 Universal Cross-Linking

Contrary to the cross-linking approaches discussed in Section 7.3.1, where the organic semiconductors are chemically modified, the approaches introduced in this section work by initiating a photo-crosslinking reaction between two organic semiconductors *via* diverse insertion reactions. So far, many studies have used bis(fluorophenyl azide) (FPA)[66–69] which enables a photo-crosslink after exposure to deep-UV light (approximately 254 nm). Following up on their report on ionic bisFPAs as cross-linkers for polyelectrolyte films,[70] Png *et al.* improved upon their original FPA design to ensure an efficient photo-crosslinking of conjugated polymers.[71] Necessitated by the occurrence of unwanted arene–perfluoroarene interaction, a steric hindrance was implemented into FPA yielding ethylene bis(4-azido-2,3,5-trifluoro-6-isopropylbenzoate) (sFPA, Figure 7.23) thereby eliminating the quenching of excitons as well as the formation of electron traps. The universal cross-linking mechanism arises by the photolysis of azides, which generates long-lived singlet nitrene species that participate in a plethora of reactions.[72–74]

Fortunately, in a polymeric organic semiconductor the major reaction pathway is the insertion of the singlet nitrenes into alkyl C–H bonds of the side-chains (Figure 7.23). Nonetheless, other reaction types like triplet reactions or ring-expanded ketenimine reactions are possible (Figure 7.24), but

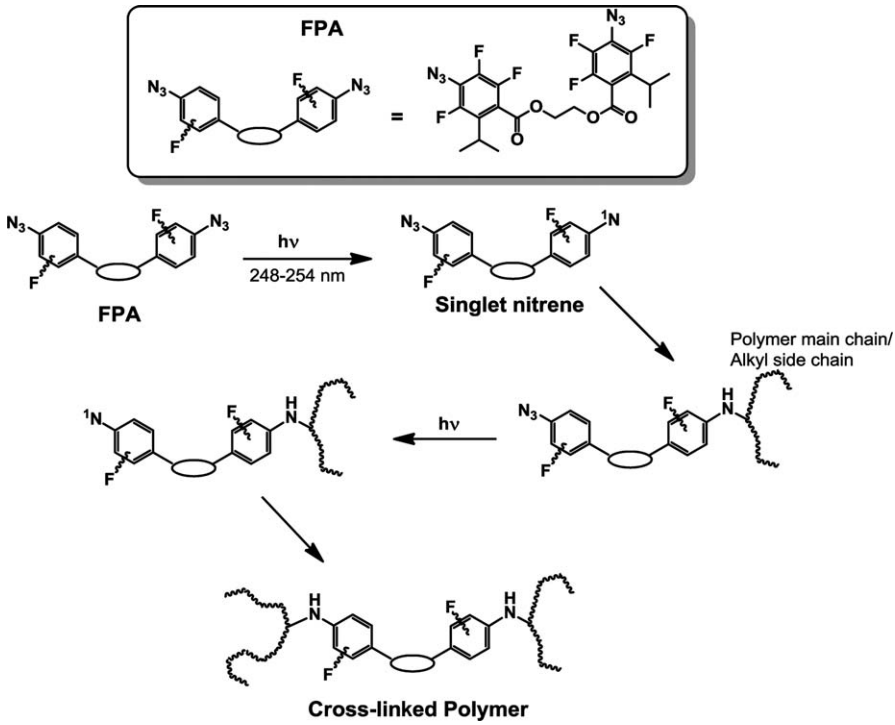

Figure 7.23 Schematic of the desired FPA photocross-linking process (inset depicts the chemical structure of a sFPA).

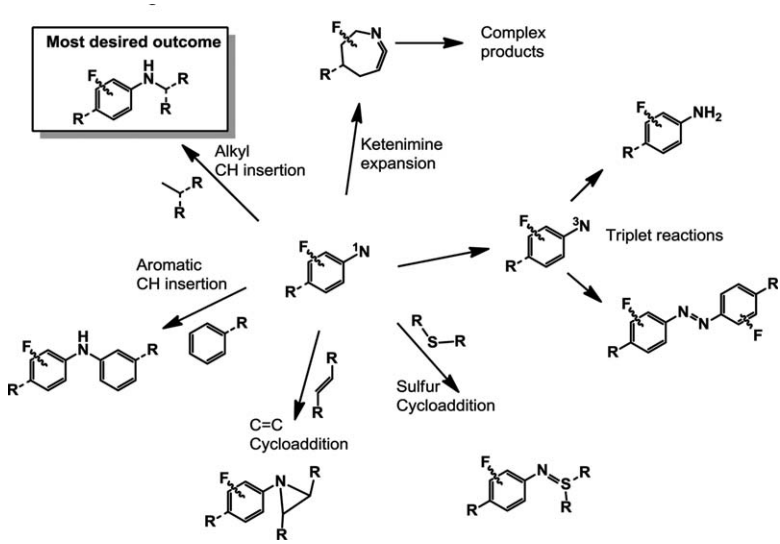

Figure 7.24 Overview of possible reactions of photogenerated singlet nitrenes in polymer OSCs.
Taken from ref. 71.

the yields of these reactions were found to be lower than 0.02 in the solid state. Most importantly, the attacks of the singlet nitrogen on the π-conjugated core are prevented by the already mentioned steric substitution.

In general, extremely high cross-linking efficiencies are attained by the nonspecific cross-linking mechanism of sFPA. Therefore, only very low concentrations (below 1 mol.%) are required, resulting in a negligible amount of stranded reactive groups that negatively impact device performance. The effectiveness of this cross-linking approach was investigated in a solar cell as well as in an OLED with a TFB (Figure 7.5) hole transport layer as well as F8BT (Figure 7.9) as the emissive layer. Optimum device efficiencies (18 cd A^{-1}) were achieved at a TFB thickness of 15 nm, constituting a more than twofold improvement compared to the device fabricated *via* thermal stabilization of the TFB layer (Section 7.3.2).

7.4 Multilayer Structures from Orthogonal Solvents

To understand the concept of orthogonal solvents it is first necessary to understand why an organic semiconductor becomes dissolved by one solvent but remains unaffected by the other. The physical quantity that describes the probability of dissolution is the energy of free mixing:[75]

$$\Delta G_m = \Delta H_m - T\Delta S_m \tag{7.1}$$

Here, ΔG_m is the Gibbs free energy of mixing, ΔH_m denotes the enthalpy of mixing, while T is the temperature and ΔS_m the entropy of mixing. Positive values for ΔG_m imply that the organic semiconductor will not dissolve in the solvent, for negative values dissolution is possible. Since dilute solutions of organic semiconductors often do not behave as ideal solutions, an accurate determination of ΔS_m is not a trivial task. In the case of polymers the observation can be made that the entropy ΔS_m decreases with increasing chain length, leading to better solubility of small molecular weight polymers. Generally, however, it is reasonable to assume that the major contributions to ΔG_m stem from the enthalpy of free mixing.

An estimation for the enthalpy of mixing is given by:

$$\Delta H_m = V(\delta_1 - \delta_2)^2 \Phi_1 \Phi_2 \tag{7.2}$$

where V is the volume of the mixture, Φ_i defines the volume fraction of molecule i and the Hildebrand solubility parameter of molecule i is given by δ_i and defined as:

$$\delta = \sqrt{\frac{E}{V}} \tag{7.3}$$

Here E is defined as the sum of all intermolecular forces and termed as the cohesive energy. Evidently, a smaller difference in the solubility parameters between the solvent and the organic semiconductor leads to an increased likelihood of solvation. In the case of organic semiconductors, the cohesive

energy can be broken down into contributions from polar (P), dispersive (D) and hydrogen bonding (H) forces:

$$E = E_D + E_P + E_H \tag{7.4}$$

The respective contributions of these forces are determined by the organic semiconductor and the solvent. However, due to the multitude of possible interactions, the solubility of an organic semiconductor in a solvent is very hard to predict.

While the Hildebrand solubility parameter is often useful for predicting the solubility of non-polar or slightly polar materials without hydrogen bonding, it is not particularly well suited to predict an intermixing of different solvents. However, some solvent combinations are characterized by quite dramatic differences in the polar, dispersive and hydrogen bonding forces, which is enough to qualitatively explain the lack of intermixing. These combinations are the so-called orthogonal solvents.

The three possible classes of orthogonal solvents are polar (usually hydroxylic), non-polar organic and fluorous solvents. Figure 7.25 shows a schematic representation of the three orthogonal solvent classes as well as a picture of phase separated solutions of the three classes.

Conjugated polymer materials for solution processed OLEDs are typically processed from either chlorinated organic solvents (*e.g.* chloroform) or aromatic organic solvents (*e.g.* toluene), which are both non-polar organic solvents. Such materials are usually insoluble in polar and perfluorinated solvents and can therefore be coated from solutions in these orthogonal solvents. Among the first solution-processed multi-layer OLEDs was a report presented in 1995 by Pommerehne *et al.*[77] Tri(stilbene)amine, a hole transport material, was spin-coated in polysulfone matrix from

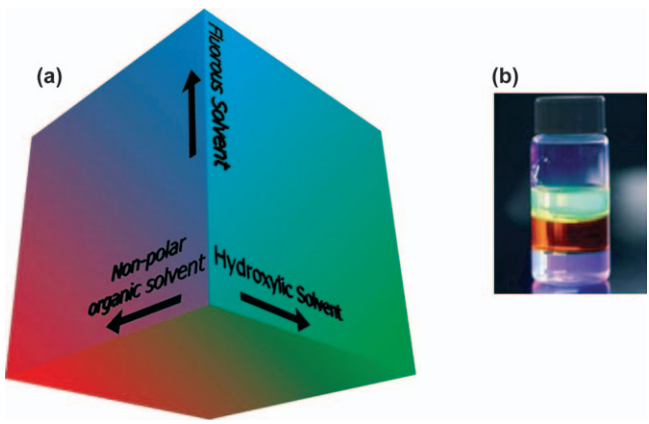

Figure 7.25 (a) Schematic representation of three classes of mutually orthogonal materials. (b) Photograph of three phase-separated solutions, which represent each class.
Taken from ref. 76 and modified.

chloroform. This polysulfone layer remained unharmed during the subsequent deposition of a non-polar aromatic emitting material mixed with polystyrene from cyclohexane.

7.4.1 Polar Solvents

Typical polar solvents for orthogonal processing are alcohols and water. Besides their orthogonality, polar solvents have the advantages of being cheap and environmentally benign. An obvious way to achieve solubility of electronic materials in polar solvents is their functionalization with charged moieties. Hence, conjugated polymers with ionic side chains have been developed. In 2004 Huang *et al*. presented several water-soluble fluorene based polymers with cationic side chains as efficient blue (FH_+-b) and green (FH_+-g) emitters (Figure 7.26).[78,79] One year later Ma *et al*. used similar polymers containing 1,3,4-oxadiazole units in the main chain (WM_+-EML, Figure 7.26) as an electron transport layer in double-layer devices.[77]

In 2008 S.-H. Oh *et al*. presented similar polyfluorenes functionalized with additional diethylene glycol groups in the side-chains capable of reversibly binding metal ions (SHO_+-M-EML, Figure 7.26).[80] Benchmarks were carried out with AIPF11, as a HIL, and a green-emitting polyfluorene derivative (LUMATION 1100 series, Dow Chemical Company) as the EML. SHO_+-M-EML was, although water soluble, spin-coated from methanol on top of a green-emitting EML to form the EIL. The fabricated devices were of an ITO/AIPF11/LUMATION 1100/SHO_+-M-EML/Al structure while the control device of course had an ITO/AIPF11/LUMATION 1100/Al assembly. The control device attained a maximum luminance of 267 cd m^{-2} at 13.5 V while the best

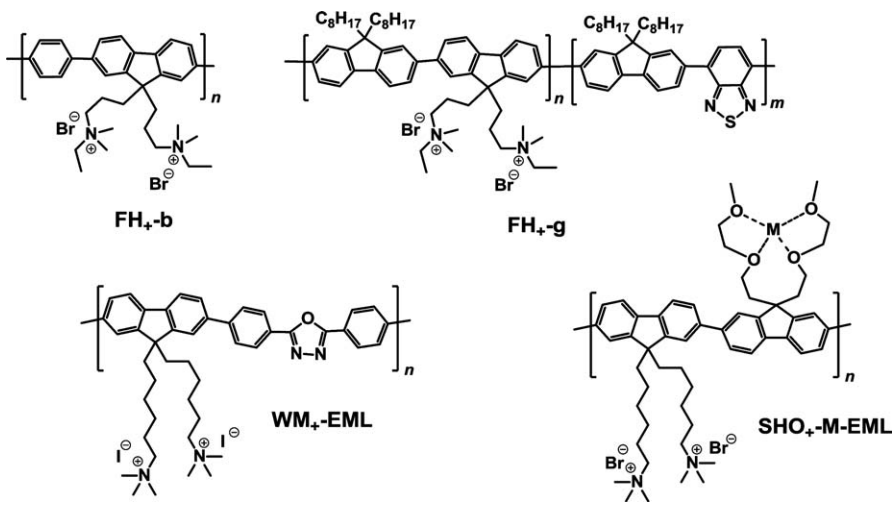

Figure 7.26 Chemical structures of water-soluble fluorene based homo- and copolymers.

SHO_+-M-EML with a Ca atom bound to it experienced a dramatically decreased onset and much higher maximum luminance values of about 20 000 cd m^{-2}. With respect to current efficiency, the increases were even more dramatic with only 0.02 cd A^{-1} recorded for the Al-only control device and 15.4 cd A^{-1} for SHO_+-M-EML with a Ca atom. Migration of the metal ions loosely bound to the ethylene oxide side chain units was identified as the mechanism for the dramatically better electron injection.

Conjugated polymers with anionic side-chains were also orthogonally processed to form HTLs. W. Shi *et al*. reported on a solution processed double-layer PLED with the anionic fluorene triphenylamine copolymer PFT-CF3 (Figure 7.27) as the HTL and different fluorene-based blue, green and red emitting polymers as the EML.[81]

PFT-CF3 was soluble exclusively in polar solvents (methanol, dimethyl sulfoxide (DMSO), dimethylformamide (DMF)) and showed outstanding film forming properties and a very high stability to non-polar organic solvents. If PFT-CF3 was used as a HTL instead of PEDOT/PSS, the EQE of the green and red emitting devices improved by more than 60%.

The use of ionic side-chains leads to intrinsic electrochemical doping at the polymer/electrode interface.[82] Although in some cases desirable, there is some concern that mobile ions during device operation can have detrimental effects on the LED lifetime. Therefore, F. Huang presented polar but neutral, electron-rich polymers (WM_+-ETL, Figure 7.28) as ETL for PLEDs.[83]

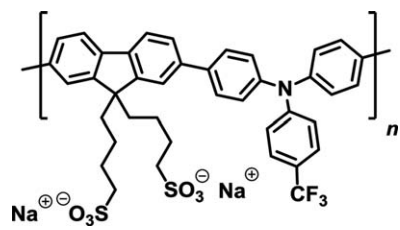

Figure 7.27 Chemical structure of PFT-CF3.

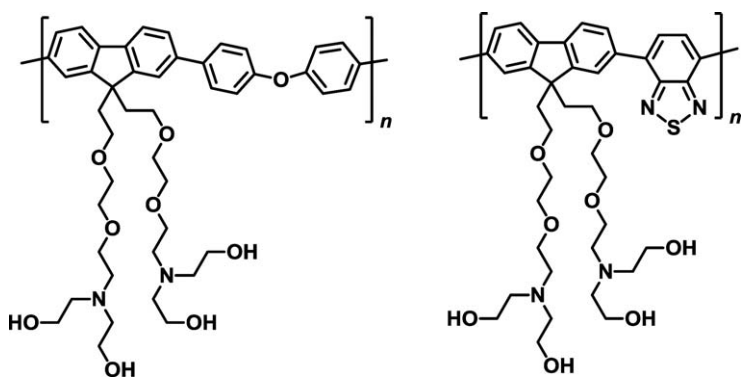

Figure 7.28 Chemical structures of WM_+-ETLs.

Devices with fluorescent and phosphorescent EMLs were built and the performance of the WM_+-ETLs was investigated by control devices without the ETL. In detail, the devices featured an emissive layer consisting of a blend of 2,2′-(1,3-phenylene)bis[5-(4-*tert*-butylphenyl)-1,3,4-oxadiazole] (OXD-7, Figure 7.29), bis(2,4-difluorophenylpyridinato FIr6 (Figure 7.29) and PVK (Figure 7.19) in an ITO/PEDOT : PSS/PVK or PVK : OXD-7(30 wt%) : FIr6(5 wt%)/WM_+-ETL/Al configuration. In the case of the fluorescent device, the current efficiency increased from 0.04 cd A^{-1} for the control device to 2.89 cd A^{-1} when WM_+-ETL was added as an ETL. For fabrication of the ETLs for phosphorescent devices small amounts of water were added to avoid interface erosion of OXD-7 by methanol. Thereby, the current efficiency EQE of 0.48% could be increased to up to 12.2% for the devices with the ETL.

In 2010 Sax *et al.*[84] reported on a bilayer OLED manufactured using the combination non-polar poly(tetraarylindenofluorene) (PIF, Figure 7.30) and poly[9,9-bis(methoxytetra(ethylene glycolyl)-2,7-fluorene)-*alt*-(9,9-bis(methoxy-poly(ethylene glycolyl)-2,7-fluorene))] (PF_{polar}, Figure 7.30). PF_{polar} was synthesized by copolymerizing two comparably simple polar fluorene monomers functionalized at the 9-position with PEG750 and tetra(ethylene glycol) side chains, respectively. However, the resulting polymers showed limited reproducibility of the molecular weight. This was because the PEGylated monomer was polydisperse and hygroscopic.

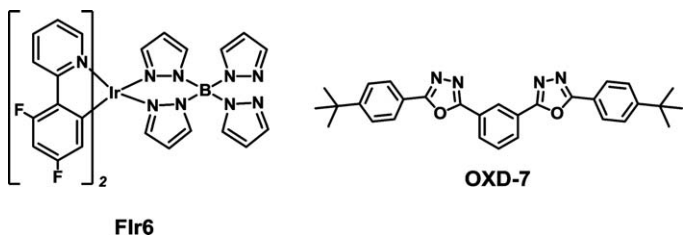

Figure 7.29 Chemical structures of the compounds used by Huang *et al.* for the fabrication of devices with WM_+-ETL.

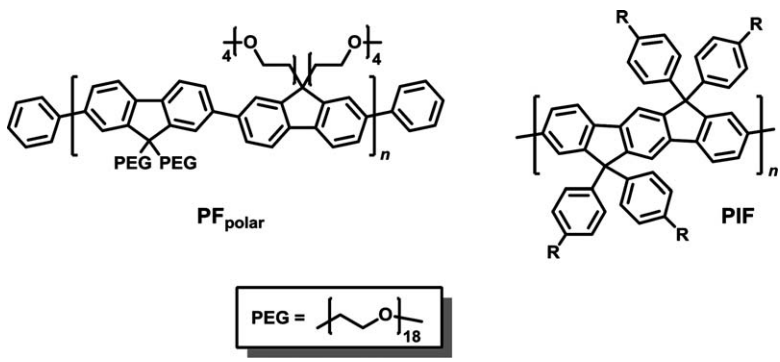

Figure 7.30 Chemical structures of a novel polar-soluble PF_{polar} and PIF.

To investigate the suitability in an orthogonal solvent process a possible resolvation of the PIF-layer by the polar PF_{polar} solution was ruled out by treating a PIF film with pure ethanol followed by AFM microscopy. Electro-optical characterization of devices with an ITO/PEDOT : PSS/PIF/CsF/Al, ITO/PEDOT : PSS/PF_{polar}/CsF/Al and ITO/PEDOT : PSS/PIF/PF_{polar}/CsF/Al configuration revealed a dramatic increase in performance for the bilayer device when compared to the single layer PIF device (Figure 7.31). Quantum mechanical calculations revealed the emergence of a hole-blocking barrier in the range of 0.1 eV (Figure 7.32). This barrier induced an increased formation of excitons in the PIF layer, thereby explaining the five-fold increase in device efficiency compared to a PIF-only device.

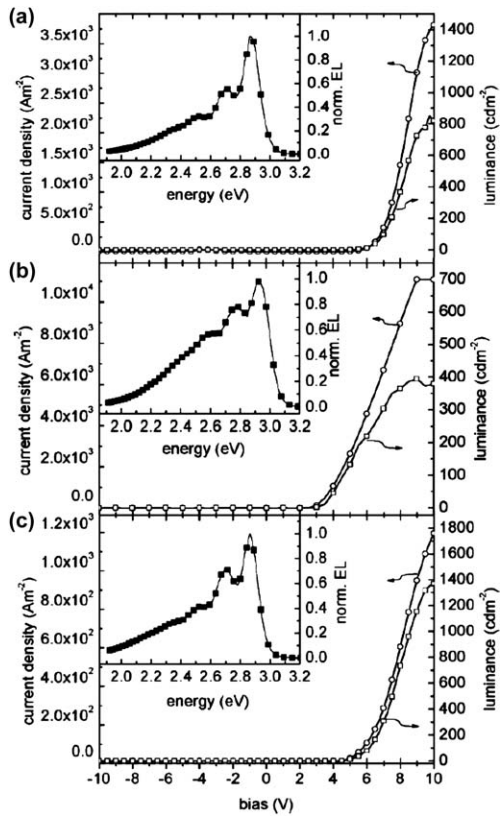

Figure 7.31 Current density and luminance as a function of the applied bias voltage in an ITO/PEDOT : PSS/PIF/CsF/Al (a), ITO/PEDOT : PSS/PF_{polar}/CsF/Al (b) and ITO/PEDOT : PSS/PIF/PF_{polar}/CsF/Al (c) device. Inset: the normalized EL spectrum of the respective device configuration. A peak efficiency of 0.25, 0.06 and 1.23 cd A^{-1} was attained for the devices a, b and c, respectively.
Taken from ref. 84.

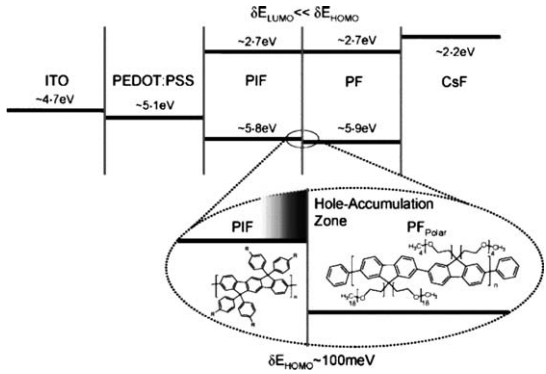

Figure 7.32 Schematic diagram of the energy levels of the multi-layer device structure and the chemical structure of the utilized polymers. The asymmetric shift of the HOMO levels obtained by quantum-chemical calculations is magnified.
Taken from ref. 84.

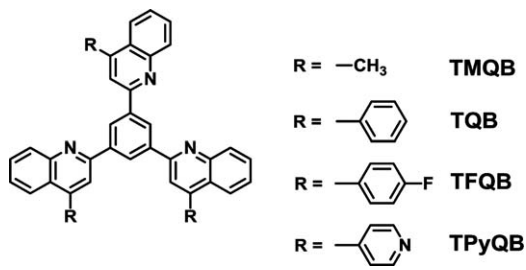

Figure 7.33 Chemical structure of the polar soluble oligoquinolines synthesized by Ahmed *et al*.

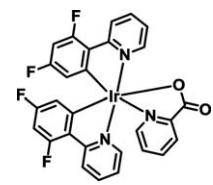

Figure 7.34 Chemical structure of FIrpic.

In 2011 E. Ahmed *et al*. reported the use of dendritic oligoquinolines (Figure 7.33), a new type of polar soluble, small molecule electron transport material in blue phosphorescent organic light emitting diodes (PhOLEDs).[85] The devices showed exceedingly high performances, the best having a luminous efficiency of 30.5 cd A^{-1} at a brightness of 4130 cd m^{-2} with an EQE of 16%. The emission layer consisted of a blend of 60 : 40 PVK (Figure 7.19) and OXD-7 (Figure 7.29) doped with 10 wt% Ir-based triplet emitter FIrpic (Figure 7.34) and was deposited as 70 nm films from chlorobenzene.

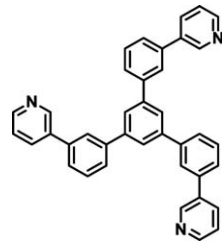

Figure 7.35 Chemical structure of TmPyPB.

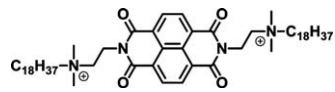

Figure 7.36 Structure of DC18.

Films (20 nm) of the oligoquinolines were spin-cast from a 3 : 1 mixture of formic acid and water, a polar solvent mixture orthogonal to the non-polar emissive layer.

One year after Ahmed's publication his coworker T. Earmme presented even further improved devices with the same EML but new oligoquinolines doped with Li_2CO_3 and Cs_2CO_3 as the ETL.[86] The highest device performance was achieved for the oligoquinoline TmPyPB (Figure 7.35) doped with Cs_2CO_3, having a luminous efficiency of 37.7 cd A^{-1} with an EQE of 19%.

Recently, L. J. Rozanski *et al*. reported on the successful application of the naphthalene diimide derivative DC18 (Figure 7.36), again a small polar molecule, as an ETL.[87] The best performance was achieved in combination with F8BT as the active layer, having a luminous efficiency of 6.9 cd A^{-1} with an EQE of 19% and a maximum luminance of 3395 cd m^{-2}. While the active layers were cast from the non-polar solvents chlorobenzene or chloroform, DC18 was deposited from the orthogonal, polar solvent ethanol.

7.4.2 Fluorinated Solvents

One of the first reports focusing on the orthogonal solubility aspect of fluorinated polymers (earlier work on fluorinated polymers concentrated on the electron-withdrawing effects of fluor[88–90]) came from H. H. Fong *et al*. where conjugated polymers with fluorinated side-chains were used for designing patterned multi-layer assemblies of light emitting materials.[91] Prior to that Fong's coworker J.-K. Lee found that even though polyfluorenes with fluorinated side-chains give poor results in PLEDs due to charge trapping, they can be successfully employed if small quantities of acceptor monomers like benzotriazoles are copolymerized with the fluorene monomers.[92] The structures of the copolymers and the polyfluorene homopolymer R_F-PF are depicted in Figure 7.37.

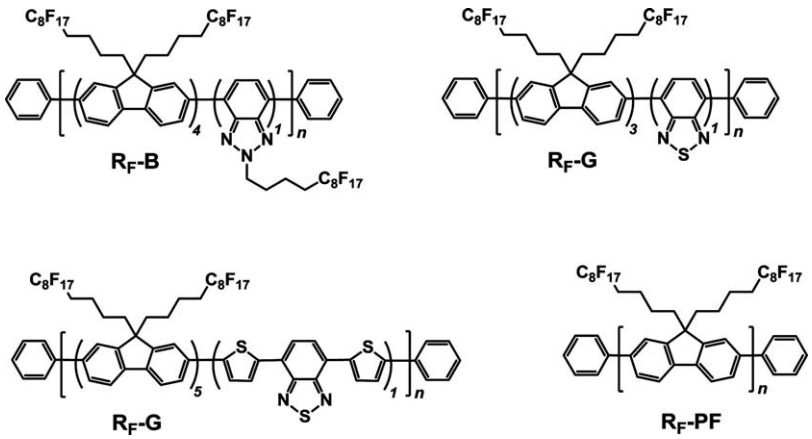

Figure 7.37 Chemical structure of polyfluorene homo- and copolymers soluble in fluorinated solvents.

The polymers were soluble and processable from benzotrifluoride (BTF), bis(trifluoromethyl)benzene (BTMB) and additionally in the non-toxic and environmentally benign hydrofluoro-ethers, which are also orthogonal to many common organic solvent and electronic materials.

While these compounds would be suitable for use in a non-polar/fluorinated orthogonal solvent approach, the orthogonal processability of the green- and red-emitting compounds was demonstrated. This was possible by processing the green-emitting material from a BTF solution while the red-emitting layer was fabricated using the less aggressive solvent BTMB. The thereby formed ITO/PEDOT : PSS/F8/R_F-G/R_F-R/Ca/Al device exhibited a red emission with an EL peak at 620 nm and a peak current efficiency of 0.3 cd A^{-1}.

Quite recently L. Pevzner *et al.*[97] reported on the synthesis of several polyfluorene compounds with branched semi-perfluorinated short side chains and compared them to a polymer with long linear perfluorinated side-chains. Branched, short perfluoroalkyl chains have the potential to induce fluorophilicity while avoiding the disadvantages of long perfluoroalkyl chains, like accumulation in biological systems and degradation to persistent, toxic products. The polymers fPF1–fPF5, depicted in Figure 7.38, exhibited very similar properties in terms of solubility, photophysics and wetting behavior.

These polyfluorenes with perfluoroalkyl side-chains were soluble in hexafluorobenzene (C_6F_6), Freons and benzotrifluoride but insoluble in common organic solvents (chloroform, toluene, THF). They could, however, be solubilized in these solvents by adding ≥10% of a suitable fluorous solvent. fPF1–fPF5 are potentially suitable materials for multi-layer PLEDs since they are processable from hexafluorobenzene, which is non-toxic and orthogonal to common organic solvents.

fPF4 was investigated in more detail with respect to suitability in an orthogonal solvent process with PEGPF (Section 7.4.3) and non-polar PF by contact angle measurements (Table 7.1) as well as AFM investigations. The contact

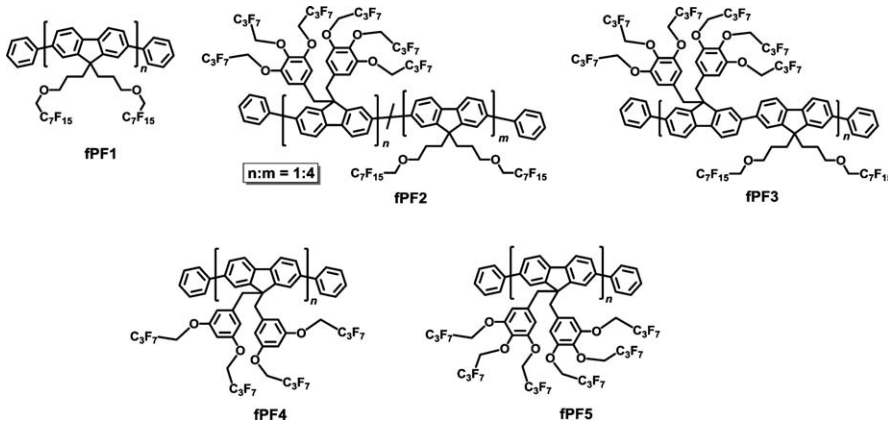

Figure 7.38 Chemical structure of polyfluorene homo- and copolymers with fluorinated side-chains.

angle measurements suggested that any combination of PEGPF, PF and fPF4 should be possible when the combination of toluene, ethanol and C_6F_6 is used.

As can be seen by the AFM topography images in Figure 7.39, the only defect-free bilayer configuration is represented by the combination of fPF4 with PEGPF coated on top of it. fPF4 on PF was characterized by the formation of inhomogeneities quite possibly caused by the formation of micellar structures of fPF4 driven by the incompatibility of the perfluorinated side chains with the hydrophobic fPF4 surface.

Still, it was clearly demonstrated that fPF is suitable for application in a non-polar/fluorinated orthogonal solvent approach, when care is taken with regards to the coating ability of the respective material combinations.

7.4.3 Hybrid Approaches

This last section details a multitude of solution-based multi-layer manufacturing techniques that either involved a change of the design of the active organic material or a careful processing strategy. Of course, attempts have been made to combine these approaches to achieve even more layers than would have been possible by using only one strategy or to compensate for a drawback in the chosen fabrication mechanism.

Recently, Zheng *et al*. reported on the fabrication of an all-solution processed PLED display.[94] Here only the fabrication strategy for a single green-emitting all-solution processed PLED is detailed. The device was fabricated by implementing a non-polar/polar orthogonal solvent system. In detail, a layer consisting of poly[2-(4-(30,70-dimethyloctyloxy)-phenyl)-*p*-phenylene-vinylene] (P-PPV, Figure 7.40) was spin-coated from a non-polar solvent. On top of that, a blend of polyfluorene polyelectrolyte poly[(9,9-bis(3-(*N*,*N*-dimethylamino)propyl)-2,7-fluorene)-*alt*-2,7-(9,9-dioctylfluorene)] ($PFNR_2$, Figure 7.40) and an UV-curable epoxy adhesive (ELC 2500CL, Electro-Lite Corp.) was applied from a methanol solution forming a buffer layer. In a next

Table 7.1 Contact angles of various solvents on a regular PF derivative, PEGPF and on fPF as well as the corresponding surface energies of the materials. Reproduced from ref. 97 with permission from Wiley-VCH Verlag GmbH & Co. KGaA, Weinheim.

	Contact angle (°)					Surface energy (mN m^{-1})[a]		
	Water	CH_2I_2	Toluene	Ethanol	C_6F_6	Total	Dispersive part	Polar part
PEGPF	56.3 ± 4.6	25.7 ± 2.0	12.1 ± 1.8	17.6 ± 0.8	9.3 ± 1.2	58.1 ± 4.6	45.9 ± 3.4	12.2 ± 1.2
PF	89.3 ± 2.0	49.0 ± 3.6	16.4 ± 3.2	35.6 ± 1.6	10.4 ± 0.9	36.6 ± 1.8	34.9 ± 1.7	1.1 ± 0.1
fPF4	92.4 ± 0.4	83.2 ± 3.4	24.9 ± 0.6	37.7 ± 0.7	6.2 ± 0.9	21.1 ± 0.5	15.9 ± 0.3	5.2 ± 0.2

[a]Evaluated by the method of Owens and Wendt.[93]

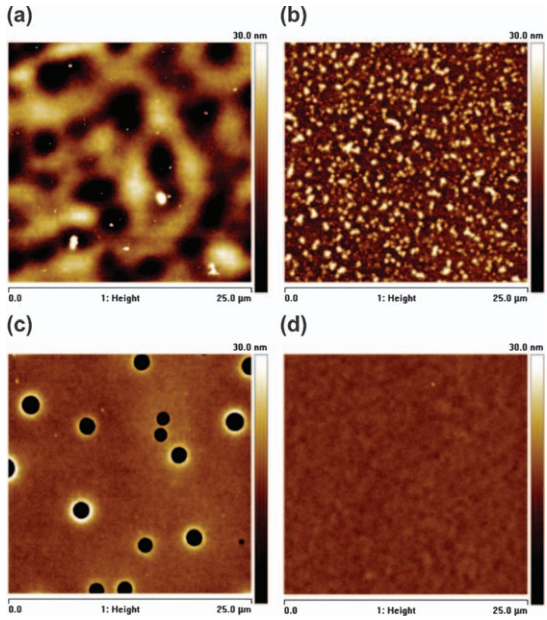

Figure 7.39 AFM surface topography images of bilayer structures (25×25 μm^2) of fPF4/PF (a), fPF4/PEGPF (b), PF/fPF4 (c) as well as of fPF4/PEGPF (d). The surface roughness R_q is 7.3, 4.7, 8.7 and 0.7 nm, respectively. Reproduced from ref. 97 with permission from Wiley-VCH Verlag GmbH & Co. KGaA, Weinheim.

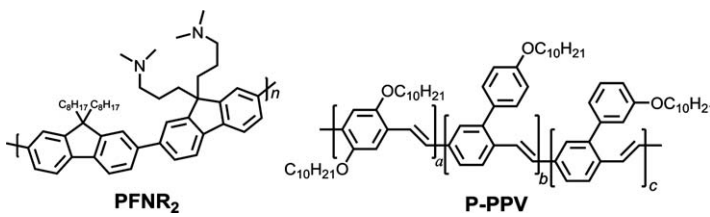

Figure 7.40 Molecular structure of the water/alcohol-soluble $PFNR_2$ electron-injection compound and the green-emitting P-PPV.

step the buffer layer was UV-cured for 2 min followed by a thermal annealing at 65 °C for 30 min. Cross-linking of the buffer layer prevented dissolution by the silver-cathode formed by ink-jet printing a polar solvent (triethylene glycol monoethyl ether) dispersion on top of the buffer layer.

The merits of this particular approach were tested with various device configurations. A device with an ITO/PEDOT : PSS/P-PPV/$PFNR_2$/Ag(ink-jet printed) attained 2.926 cd m^{-2} with a peak current efficiency of 0.67 cd A^{-1} while an ITO/PEDOT : PSS/P-PPV/$PFNR_2$/Ag(evaporated) device was able to produce luminance values of 10 816 cd m^{-2} at a current efficiency of 9.34 cd A^{-1}. The huge discrepancy in device performance is a clear indicator that the interaction of the solvent of the silver-ink with the $PFNR_2$ EIL layer is

detrimental for the device performance. This is confirmed by the dramatically increased performance of a device with a cross-linked buffer layer (ITO/PEDOT : PSS/P-PPV/PFNR2:ELC 2500CL)/Ag(ink-jet printed) where luminance values of 11 451 cd m^{-2} and a peak current efficiency of 7.87 cd A^{-1} were observed.

One notable combination of clever fabrication and material modification was reported by Trattnig *et al.*[95] They reported on the combination of the previously described thermal stabilization of TFB (Figure 7.5) as a HTL and an orthogonal solvent approach using the polar-soluble PEGPF as an ETL (chemical structures of the emissive copolymer PPyrTPA[96] and PEGPF are detailed in Figure 7.41). Compared to the already presented PF_{polar} (Figure 7.30), the synthetic procedure of PEGPF eliminated that issue of monomer polydispersity as encountered in the synthesis of PF_{polar} by introducing the PEG750 side chains in the last step into a well-defined, high molecular weight polymer. Additionally, the reaction time of the Suzuki polymerization was lowered from 6 to 1 day.

Using these compounds, devices featuring an ITO/PEDOT : PSS/TFB/PPyrTPA/PEGPF/Ca/Al assembly were manufactured. Following the previously described thermal stabilization of TFB (Section 7.3.2), a thin and insoluble layer was obtained. Consecutively, the emissive and the electron transporting PPyrTPA and PEGPF layers were spin-coated on top of TFB without dissolving each other by an orthogonal non-polar/polar solvent approach. Finally, the device was finished by vacuum deposition of a multilayer Ca/Al cathode.

AFM and XPS measurements of the individual layers after each processing step confirm the formation of smooth and homogeneous layers (Figure 7.42).

In addition to the excellent quality of the obtained films, the clever combination of these manufacturing processes yielded an energetic structure (Figure 7.43) that increases the exciton generation rate by means of an elevated charge carrier density in the EML.

The effectiveness of this hybrid approach in terms of device performance enhancements was verified by the fabrication of devices consisting of only

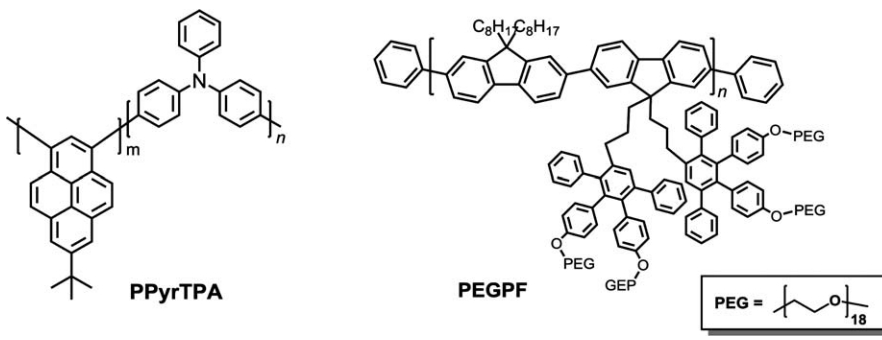

Figure 7.41 Chemical structures of the emissive PPyrTPA and electron-transporting PEGPF.

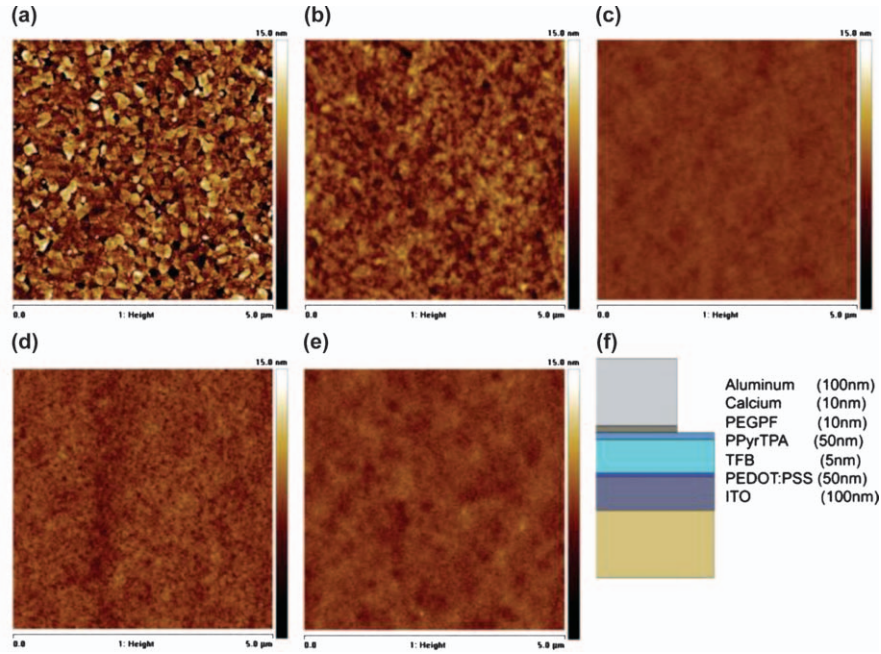

Figure 7.42 AFM topography images (5 μm×5 μm) of (a) ITO, (b) PEDOT : PSS, (c) TFB, (d) PPyrTPA and (e) PEGPF acquired in tapping mode. The thickness of the individual layers is presented in (f).
Taken from ref. 95.

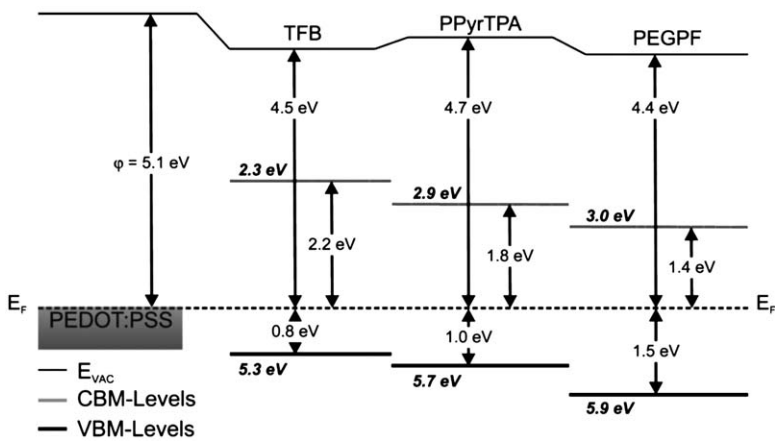

Figure 7.43 Energy level diagram of a PEDOT : PSS/TFB/PPyrTPA/PEGPF stack detailing the VBM and CBM energy levels, IE and EA (estimated from the optical absorption), as well as the workfunction ϕ of the individual layers. The offset between the CBMs of PPyrTPA and PEGPF amounts to 0.4 eV, while the offset of the VBMs of TFB and PPyrTPA is 0.2 eV.
Taken from ref. 95.

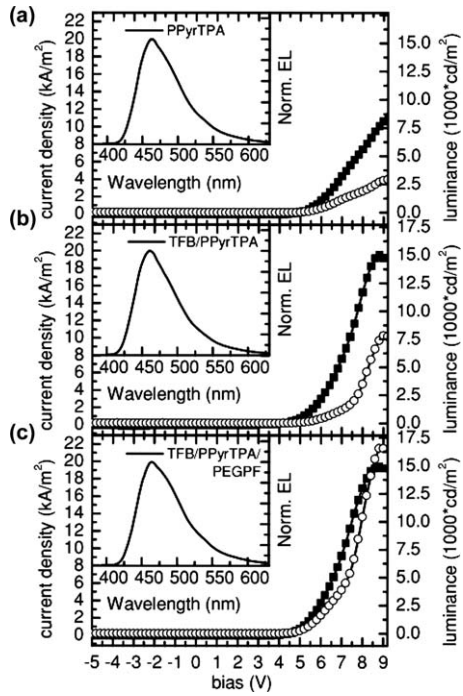

Figure 7.44 Current density (line with squares)–luminance (line with circles) as a function of the applied bias voltage of (a) single (PPyrTPA)-, (b) double (TFB/PPyrTPA)- and (c) triple (TFB/PPyrTPA/PEGPF)-layer devices. Inset: electroluminescence emission spectra acquired at a current density of 1.11 kA m^{-2}.
Taken from ref. 95.

Table 7.2 Electroluminescent characteristics of investigated single- and bilayer and triple-layer devices (taken from ref. 95).

Organic layer geometry	Onset voltage (V)[a]	η(cd A^{-1})[b]	Max. luminance (cd m^{-2})	EL peak (nm)[c]	CIE 1931 coordinates[c]
PPyrTPA	4.4	0.27	2924	462	$x = 0.159$, $y = 0.197$
TFB/PPyrTPA	4.0	0.43	7817	460	$x = 0.157$, $y = 0.174$
TFB/PPyrTPA/ PEGPF	3.9	1.42	16540	465	$x = 0.163$, $y = 0.216$

[a]Voltage at a luminance of 1 cd m^{-2}.
[b]Value of maximum efficiency.
[c]At a current density of 1.11 kA m^{-2}.

the emissive PPyrTPA-layer, the HTL TFB and emissive PPyrTPA layer as well as the full triple-layer TFB/PPyrTPA/PEGPF stack. The results of the *J–V–L* measurement are depicted in Figure 7.44 with corresponding performance values detailed in Table 7.2. Evidently, the addition of the TFB interlayer as

well as the PEGPF layer yielded a respectable increase in luminance from 2924 to 16540 cd m^{-2} and more importantly a 5.3-fold increase in effciency (from 0.27 to 1.42 cd A^{-1}).

7.5 Conclusion and Outlook

As detailed in the introduction, many contemporary commercially available display and lighting appliances based on OLEDs are fabricated by thermal vacuum sublimation. Restrained by low throughput and considerable material waste, the migration from thermal vacuum sublimation to solution-based processes, such as roll-to-roll, inkjet printing or slot-dye coating, is necessary. However, the fact that most organic semiconductors are soluble in similar organic solvents prevents a straightforward assembly of efficient charge-carrier confining and accordingly functionalized (in the sense of transport and injection functionalities) multilayer structures such as is possible by thermal vacuum sublimation.

Since the realization of well-defined interfaces is of utmost importance, a considerable amount of research has focused on the development of a broad range of fabrication schemes for solution-processed multilayer devices. In principle these processes can be distinguished by the combination of solvents used for the different layers as well as by any chemical reaction taking place that renders the fabricated layer insoluble. As presented within this chapter, it is nowadays possible to fabricate multilayer geometries from the same solvent without any damage to the already applied layers. While this approach potentially allows the use of a great variety of commercially available organic semiconductors for the fabrication of multilayer OLEDs, perfecting the fabrication process can be quite time consuming and in some instances simply be impossible. Processing from an equal solvent is also possible when the fabricated layers are rendered insoluble. Many approaches towards insolubilization require the introduction of cross-linking chemistry, which is not universally possible for organic semiconductors. Then there is the option to process the individual layers from orthogonal solvents. However, to date most of the reported orthogonal solvent systems also require a redesign of the organic semiconductor and thus the same restrictions as for the cross-linking approach apply.

It is apparent that for each approach drawbacks in the form of available organic compounds, quality of the fabricated layers, *etc*. apply. For this reason, hybrid approaches that combine different fabrication schemes are becoming increasingly popular.

It can be concluded that with the great variety of reported solution-based fabrication schemes, industry finally has enough choice to implement specifically tailored solution-based processes for the large-scale fabrication of OLED display and lighting products.

Acknowledgements

The authors would like to extend their gratitude to Martin Baumgarten from the Max Planck Institute of Polymer Research for his valuable input. Furthermore we would also like to thank the team at Nanotec Center Weiz for the fruitful discussions as well as Claudia Berger for her help with some of the figures.

References

1. C. W. Tang and S. A. Van Slyke, Organic electroluminescent diodes, *Appl Phys Lett*, 1987, **51**, 913.
2. M. C. Gather, A. Köhnen and K. Meerholz, White organic light-emitting diodes, *Adv Mater*, 2011, **23**, 233–48.
3. David K. Flattery, Curtis R. Fincher DLL, B. O'Regan Marie and JSR, Clearing the Road to Mass Production of OLED Television, *Inf Disp*, 2011, **1975**, 8–13.
4. T. Sonoyama, M. Ito, S. Seki, S. Miyashita, S. Xia and J. Brooks, Ink-jet-printable phosphorescent organic light-emitting-diode devices, *J Soc Inf Disp*, 2008, **16**, 1229.
5. Kittel Charles, *Introduction to Solid State Physics*. ed 8, Johnson S (ed), John Wiley & Sons, 2005, p 704.
6. N. Koch, Organic electronic devices and their functional interfaces, *ChemPhysChem*, 2007, **8**, 1438–55.
7. W. Brütting, S. Berleb and A. G. Mückl, Device physics of organic light-emitting diodes based on molecular materials, *Org Electron*, 2001, **2**, 1–36.
8. K. Müllen, U. Scherf, *Organic Light Emitting Devices*. Müllen K, Scherf U (eds), Weinheim, FRG: Wiley-VCH Verlag GmbH, 2006, p 426.
9. A. Van Dijken, A. Perro, E. Meulenkamp and K. Brunner, The influence of a PEDOT:PSS layer on the efficiency of a polymer light-emitting diode, *Org Electron*, 2003, **4**, 131–141.
10. S. A. Choulis, V.-E. Choong, A. Patwardhan, M. K. Mathai and F. So, Interface Modification to Improve Hole-Injection Properties in Organic Electronic Devices, *Adv Funct Mater*, 2006, **16**, 1075–1080.
11. Y. Z. Wang and A. J. Epstein, Interface Control of Light-Emitting Devices Based on Pyridine-Containing Conjugated Polymers, *Acc Chem Res*, 1999, **32**, 217–224.
12. S.-R. Tseng, H.-F. Meng, K.-C. Lee and S.-F. Horng, Multilayer polymer light-emitting diodes by blade coating method, *Appl Phys Lett*, 2008, **93**, 153308.
13. J.-D. You, S.-R. Tseng, H.-F. Meng, F.-W. Yen, I.-F. Lin and S.-F. Horng, All-solution-processed blue small molecular organic light-emitting diodes with multilayer device structure, *Org Electron*, 2009, **10**, 1610–1614.
14. Z.-Y. Liu, S.-R. Tseng, Y.-C. Chao, C.-Y. Chen, H.-F. Meng and S.-F. Horng, Solution-processed small molecular electron transport layer

for multilayer polymer light-emitting diodes, *Synth Met*, 2011, **161**, 426–430.
15. Y.-F. Chang, Y.-C. Chiu, H.-C. Yeh, H.-W. Chang, C.-Y. Chen and H.-F. Meng, Unmodified small-molecule organic light-emitting diodes by blade coating, *Org Electron*, 2012, **13**, 2149–2155.
16. Y.-F. Chang, Y.-C. Chiu, H.-W. Chang, Y.-S. Wang, Y.-L. Shih and C.-H. Wu, Interface and thickness tuning for blade coated small-molecule organic light-emitting diodes with high power efficiency, *J Appl Phys*, 2013, **114**, 123101.
17. S.-R. Tseng, S.-C. Lin, H.-F. Meng, H.-H. Liao, C.-H. Yeh and H.-C. Lai, General method to solution-process multilayer polymer light-emitting diodes, *Appl Phys Lett*, 2006, **88**, 163501.
18. S.-R. Tseng, S.-Y. Li, H.-F. Meng, Y.-H. Yu, C.-M. Yang and H.-H. Liao, High-efficiency blue multilayer polymer light-emitting diode based on poly(9,9-dioctylfluorene), *J Appl Phys*, 2007, **101**, 084510.
19. S.-R. Tseng, H.-F. Meng, C.-H. Yeh, H.-C. Lai, S.-F. Horng and H.-H. Liao, High-efficiency blue multilayer polymer light-emitting diode fabricated by a general liquid buffer method, *Synth Met*, 2008, **158**, 130–134.
20. H.-M. Shih, C.-J. Lin, S.-R. Tseng, C.-H. Lin and C.-S. Hsu, Synthesis of New Blue Anthracene-based Conjugated Polymers and Their Applications in Polymer Light-Emitting Diodes, *Macromol Chem Phys*, 2011, **212**, 1100–1108.
21. S. Lee, Y. Im, K. K. Lee and E. Lim, Polymeric White Organic Light-Emitting Diodes with Two Emission Layers, *J Nanosci Nanotechnol*, 2012, **12**, 3688–3691.
22. A. Jaworek and A. T. Sobczyk, Electrospraying route to nanotechnology: An overview, *J Electrostat*, 2008, **66**, 197–219.
23. I. B. Rietveld, K. Kobayashi, H. Yamada and K. Matsushige, Electrospray deposition, model, and experiment: toward general control of film morphology, *J Phys Chem B*, 2006, **110**, 23351–64.
24. O. Wilhelm, L. Mädler and S. E. Pratsinis, Electrospray evaporation and deposition, *J Aerosol Sci*, 2003, **34**, 815–836.
25. J. Ju, Y. Yamagata and T. Higuchi, Thin-Film Fabrication Method for Organic Light-Emitting Diodes Using Electrospray Deposition, *Adv Mater*, 2009, **21**, 4343–4347.
26. T. Ishikawa, K. Fujita and T. Tsutsui, Small-Area Deposition of Light Emission Polymer by Evaporative Spray Deposition from Ultradilute Solution Technique, *Jpn J Appl Phys*, 2005, **44**, 6292–6294.
27. Y. Aoki, M. Shakutsui and K. Fujita, Stacking layered structure of polymer light emitting diodes prepared by evaporative spray deposition using ultradilute solution for improving carrier balance, *Thin Solid Films*, 2009, **518**, 493–496.
28. Y. Koishikawa, H. Miyazaki, M. Yahiro and C. Adachi, Multi-layered organic light-emitting diode fabrication using low molecular weight materials by electrospray method, *Thin Solid Films*, 2013, **545**, 527–532.

29. M. A. Meitl, Z-T. Zhu, V. Kumar, K. J. Lee, X. Feng and Y. Y. Huang, Transfer printing by kinetic control of adhesion to an elastomeric stamp, *Nat Mater*, 2005, **5**, 33–38.
30. K.-H. Yim, Z. Zheng, Z. Liang, R. H. Friend, W. T. S. Huck and J.-S. Kim, Efficient Conjugated-Polymer Optoelectronic Devices Fabricated by Thin-Film Transfer-Printing Technique, *Adv Funct Mater*, 2008, **18**, 1012–1019.
31. K.-H. Kim, S.-Y. Huh, S. Seo and H. H. Lee, Solution-based formation of multilayers of small molecules for organic light emitting diodes, *Appl Phys Lett*, 2008, **92**, 093307.
32. T.-F. Guo, S. Pyo, S.-C. Chang and Y. Yang, High Performance Polymer Light-Emitting Diodes Fabricated by a Low Temperature Lamination Process, *Adv Funct Mater*, 2001, **11**, 339–343.
33. T.-F. Guo, G. He, S. Pyo and Y. Yang, Investigation of the interfacial properties of laminated polymer diodes, *Appl Phys Lett*, 2002, **80**, 4042.
34. C. A. Zuniga, S. Barlow and S. R. Marder, Approaches to Solution-Processed Multilayer Organic Light-Emitting Diodes Based on Cross-Linking, *Chem Mater*, 2011, **23**, 658–681.
35. W. Li, Q. Wang, J. Cui, H. Chou, S. E. Shaheen and G. E. Jabbour, Covalently Interlinked Organic LED Transport Layers via Spin-Coating/Siloxane Condensation, *Adv Mater*, 1999, **11**, 730–734.
36. H. Yan, B. J. Scott, Q. Huang and T. J. Marks, Enhanced Polymer Light-Emitting Diode Performance Using a Crosslinked-Network Electron-Blocking Interlayer, *Adv Mater*, 2004, **16**, 1948–1953.
37. Q. Huang, G. A. Evmenenko, P. Dutta, P. Lee, N. R. Armstrong and T. J. Marks, Covalently bound hole-injecting nanostructures. Systematics of molecular architecture, thickness, saturation, and electron-blocking characteristics on organic light-emitting diode luminance, turn-on voltage, and quantum efficiency, *J Am Chem Soc*, 2005, **127**, 10227–42.
38. H. Sun, Z. Liu, Y. Hu, L. Wang, D. Ma and X. Jing, Crosslinkable poly(p-phenylenevinylene) derivative, *J Polym Sci Part A Polym Chem*, 2004, **42**, 2124–2129.
39. Y.-H. Niu, M. S. Liu, J.-W. Ka, J. Bardeker, M. T. Zin and R. Schofield, Crosslinkable Hole-Transport Layer on Conducting Polymer for High-Efficiency White Polymer Light-Emitting Diodes, *Adv Mater*, 2007, **19**, 300–304.
40. N. Du, R. Tian, J. Peng, Q. Mei and M. Lu, Cross-Linked Alq3-Containing Polymers with Improved Electroluminescence Efficiency Used for OLEDs, *Macromol Rapid Commun*, 2006, **27**, 412–417.
41. G. Wu, C. Yang, B. Fan, B. Zhang, X. Chen and Y. Li, Synthesis and characterization of photo-crosslinkable polyfluorene with acrylate side-chains, *J Appl Polym Sci*, 2006, **100**, 2336–2342.
42. E. J. W. List, R. Guentner, P. Scanducci de Freitas and U. Scherf, The Effect of Keto Defect Sites on the Emission Properties of Polyfluorene-Type Materials, *Adv Mater*, 2002, **14**, 374.

43. H. Scheiber, M. Graf, H. Plank, E. Zojer, C. Slugovc and S. Kappaun, The Influence of UV Irradiation on Ketonic Defect Emission in Fluorene-Based Copolymers, *Adv Funct Mater*, 2008, **18**, 2480–2488.
44. U. Scherf and E. J. W. List, Semiconducting Polyfluorenes—Towards Reliable Structure-Property Relationships, *Adv Mater*, 2002, **14**, 477–487.
45. B. Lim, J. Hwang, J. Y. Kim, J. Ghim, D. Vak and Y. Noh, Synthesis of a new cross-linkable perfluorocyclobutane-based hole-transport material, *Org Lett*, 2006, **8**, 4703–6.
46. A. Rehab and N. Salahuddin, Photocrosslinked polymers based on pendant extended chalcone as photoreactive moieties, *Polymer (Guildf)*, 1999, **40**, 2197–2207.
47. Y. Nakayama and T. Matsuda, Preparation and characteristics of photocrosslinkable hydrophilic polymer having cinnamate moiety, *J Polym Sci Part A Polym Chem*, 1992, **30**, 2451–2457.
48. X. Li, T. Yong, J. Grüner, A. B. Holmes, S. C. Moratti and F. Cacialli, A blue light emitting copolymer with charge transporting and photocrosslinkable functional units, *Synth Met*, 1997, **84**, 437–438.
49. Y.-D. Zhang, R. D. Hreha, G. E. Jabbour, B. Kippelen, N. Peyghambarian and S. R. Marder, Photo-crosslinkable polymers as hole-transport materials for organic light-emitting diodes, *J Mater Chem*, 2002, **12**, 1703–1708.
50. J. V. Crivello, B. Falk and M. R. Zonca, Photoinduced cationic ring-opening frontal polymerizations of oxetanes and oxiranes, *J Polym Sci Part A Polym Chem*, 2004, **42**, 1630–1646.
51. J. L. Dektar and N. P. Hacker, Novel photoinduced electron transfer reactions between naphthalene and triphenylsulphonium salts, *J Photochem Photobiol A Chem*, 1989, **46**, 233–238.
52. J. V. Crivello and U. Bulut, Curcumin: A naturally occurring long-wavelength photosensitizer for diaryliodonium salts, *J Polym Sci Part A Polym Chem*, 2005, **43**, 5217–5231.
53. M. S. Bayerl, T. Braig, O. Nuyken, D. C. Müller, M. Großig; and K. Meerholz, Crosslinkable hole-transport materials for preparation of multilayer organic light emitting devices by spin-coating, *Macromol Rapid Commun*, 1999, **20**, 224–228.
54. O. Nuyken, R. Böhner and C. Erdmann, Oxetane photopolymerization-A system with low volume shrinkage, *Macromol Symp*, 1996, **107**, 125–138.
55. M. Sangermano, S. Giannelli, R. A. Ortiz, M. L. B. Duarte, A. K. R. Gonzalez and A. E. G. Valdez, Synthesis of an oxetane-functionalized hemispiroorthocarbonate used as a low-shrinkage additive in the cationic ultraviolet curing of oxetane monomers, *J Appl Polym Sci*, 2009, **112**, 1780–1787.
56. C. D. Müller, A. Falcou, N. Reckefuss, M. Rojahn, V. Wiederhirn and P. Rudati, Multi-colour organic light-emitting displays by solution processing, *Nature*, 2003, **421**, 829–33.

57. A. Köhnen, N. Riegel, D. C. Müller and K. Meerholz, Surface-Initiated Phase Separation-Fabrication of Two-Layer Organic Light-Emitting Devices in a Single Processing Step, *Adv Mater*, 2011, **23**, 4301–4305.
58. J.-S. Kim, R. H. Friend, I. Grizzi and J. H. Burroughes, Spin-cast thin semiconducting polymer interlayer for improving device efficiency of polymer light-emitting diodes, *Appl Phys Lett*, 2005, **87**, 023506.
59. S. A. Choulis, V.-E. Choong, M. K. Mathai and F. So, The effect of interfacial layer on the performance of organic light-emitting diodes, *Appl Phys Lett*, 2005, **87**, 113503.
60. L. Duan, B. D. Chin, N. C. Yang, M.-H. Kim, H. D. Kim and S. T. Lee, Multilayer blue polymer light-emitting devices with spin-coated interlayers, *Synth Met*, 2007, **157**, 343–346.
61. S. Nau, N. Schulte, S. Winkler, J. Frisch, A. Vollmer and N. Koch, Highly Efficient Color-Stable Deep-Blue Multilayer PLEDs: Preventing PEDOT:PSS-Induced Interface Degradation, *Adv Mater*, 2013, **25**, 4420–4.
62. R. A. Wessling, The polymerization of xylylene bisdialkyl sulfonium salts, *J Polym Sci Polym Symp*, 2007, **72**, 55–66.
63. T. Junkers, J. Vandenbergh, P. Adriaensens, L. Lutsen and D. Vanderzande, Synthesis of poly(p-phenylene vinylene) materials via the precursor routes, *Polym Chem*, 2012, **3**, 275.
64. J. Morgado, R. H. Friend and F. Cacialli, Improved efficiency of light-emitting diodes based on polyfluorene blends upon insertion of a poly(p-phenylene vinylene) electron-confinement layer, *Appl Phys Lett*, 2002, **80**, 2436.
65. J. H. Burroughes, D. D. C. Bradley, A. R. Brown, R. N. Marks, K. Mackay and R. H. Friend, Light-emitting diodes based on conjugated polymers, *Nature*, 1990, **347**, 539–541.
66. S. X. Cai, D. J. Glenn, M. Kanskar, M. N. Wybourne and J. F. W. Keana, Development of Highly Efficient Deep-UV and Electron Beam Mediated Cross-Linkers: Synthesis and Photolysis of Bis(perfluorophenyl) Azides, *Chem Mater*, 1994, **6**, 1822–1829.
67. K. A. Schnapp, R. Poe, E. Leyva, N. Soundararajan and M. S. Platz, Exploratory photochemistry of fluorinated aryl azides. Implications for the design of photoaffinity labeling reagents, *Bioconjug Chem*, 1993, **4**, 172–177.
68. J. F. W. Keana and S. X. Cai, New reagents for photoaffinity labeling: synthesis and photolysis of functionalized perfluorophenyl azides, *J Org Chem*, 1990, **55**, 3640–3647.
69. S. X. Cai, J. F. W. Keana, J. C. Nabity and M. N. Wybourne, Conducting polymers as deep-UV and electron beam resists. Direct production of micrometer scale conducting structures from poly(3-octylthiophene), *J Mol Electron*, 1991, **7**, 63–68.
70. S.-H. Khong, S. Sivaramakrishnan, R.-Q. Png, L.-Y. Wong, P.-J. Chia and L.-L. Chua, General Photo-Patterning of Polyelectrolyte Thin Films via Efficient Ionic Bis(Fluorinated Phenyl Azide) Photo-Crosslinkers and their Post-Deposition Modification, *Adv Funct Mater*, 2007, **17**, 2490–2499.

71. R.-Q. Png, P.-J. Chia, J.-C. Tang, B. Liu, S. Sivaramakrishnan and M. Zhou, High-performance polymer semiconducting heterostructure devices by nitrene-mediated photocrosslinking of alkyl side chains, *Nat Mater*, 2010, **9**, 152–8.
72. S. Bräse, C. Gil, K. Knepper and V. Zimmermann, Organic azides: an exploding diversity of a unique class of compounds, *Angew Chem Int Ed Engl*, 2005, **44**, 5188–240.
73. A. Marcinek, M. S. Platz, S. Y. Chan, R. Floresca, K. Rajagopalan and M. Golinski, Unusually long lifetimes of the singlet nitrenes derived from 4-azido-2,3,5,6-tetrafluorobenzamides, *J Phys Chem*, 1994, **98**, 412–419.
74. R. Poe, K. Schnapp, M. J. T. Young, J. Grayzar and M. S. Platz, Chemistry and kinetics of singlet (pentafluorophenyl)nitrene, *J Am Chem Soc*, 1992, **114**, 5054–5067.
75. R. J. Young, P. A. Lovell, *Introduction to Polymers*. Third Edit., CRC Press, Boca Raton, FL, 2011, p 688.
76. A. A. Zakhidov, J.-K. Lee, J. A. DeFranco, H. H. Fong, P. G. Taylor and M. Chatzichristidi, Orthogonal processing: A new strategy for organic electronics, *Chem Sci*, 2011, **2**, 1178.
77. J. Pommerehne, H. Vestweber, W. Guss, R. F. Mahrt, H. Bässler and M. Porsch, Efficient two layer leds on a polymer blend basis, *Adv Mater*, 1995, **7**, 551–554.
78. W. Ma, P. K. Iyer, X. Gong, B. Liu, D. Moses and G. C. Bazan, Water/Methanol-Soluble Conjugated Copolymer as an Electron-Transport Layer in Polymer Light-Emitting Diodes, *Adv Mater*, 2005, **17**, 274–277.
79. F. Huang, L. Hou, H. Wu, X. Wang, H. Shen and W. Cao, High-efficiency, environment-friendly electroluminescent polymers with stable high work function metal as a cathode: green- and yellow-emitting conjugated polyfluorene polyelectrolytes and their neutral precursors, *J Am Chem Soc*, 2004, **126**, 9845–53.
80. S.-H. Oh, D. Vak, S.-I. Na, T.-W. Lee and D.-Y. Kim, Water-Soluble Polyfluorenes as an Electron Injecting Layer in PLEDs for Extremely High Quantum Efficiency, *Adv Mater*, 2008, **20**, 1624–1629.
81. W. Shi, L. Wang, F. Huang, R. Liu, W. Yang and Y. Cao, Anionic triphenylamine- and fluorene-based conjugated polyelectrolyte as a hole-transporting material for polymer light-emitting diodes, *Polym Int*, 2009, **58**, 373–379.
82. S. Sax, G. Mauthner, T. Piok, S. Pradhan, U. Scherf and E. J. W. List, Intrinsic electrochemical doping in blue light emitting polymer devices utilizing a water soluble anionic conjugated polymer, *Org Electron*, 2007, **8**, 791–795.
83. F. Huang, Y. Zhang, M. S. Liu and A. K.-Y. Jen, Electron-Rich Alcohol-Soluble Neutral Conjugated Polymers as Highly Efficient Electron-Injecting Materials for Polymer Light-Emitting Diodes, *Adv Funct Mater*, 2009, **19**, 2457–2466.
84. S. Sax, N. Rugen-Penkalla, A. Neuhold, S. Schuh, E. Zojer and E. J. W. List, Efficient blue-light-emitting polymer heterostructure

devices: the fabrication of multilayer structures from orthogonal solvents, *Adv Mater*, 2010, **22**, 2087–91.
85. E. Ahmed, T. Earmme and S. A. Jenekhe, New Solution-Processable Electron Transport Materials for Highly Efficient Blue Phosphorescent OLEDs, *Adv Funct Mater*, 2011, **21**, 3889–3899.
86. T. Earmme and S. A. Jenekhe, Solution-Processed, Alkali Metal-Salt-Doped, Electron-Transport Layers for High-Performance Phosphorescent Organic Light-Emitting Diodes, *Adv Funct Mater*, 2012, **22**, 5126–5136.
87. L. J. Rozanski, E. Castaldelli, F. L. M. Sam, C. A. Mills, G. Jean-François Demets and S. R. P. Silva, Solution processed naphthalene diimide derivative as electron transport layers for enhanced brightness and efficient polymer light emitting diodes, *J Mater Chem C*, 2013, **1**, 3347.
88. H. Kameshima, N. Nemoto and T. Endo, Synthesis and properties of fluorene-based fluorinated polymers, *J Polym Sci Part A Polym Chem*, 2001, **39**, 3143–3150.
89. W. Lu, J. Kuwabara, T. Iijima, H. Higashimura, H. Hayashi and T. Kanbara, Synthesis of π-Conjugated Polymers Containing Fluorinated Arylene Units via Direct Arylation: Efficient Synthetic Method of Materials for OLEDs, *Macromolecules*, 2012, **45**, 4128–4133.
90. T. Zhang, L. Deng, R. Wang, W. Zhou and J. Li, Novel fluorene/trifluoromethylphenylene copolymers: Synthesis, spectra stability and electroluminescence, *Dye Pigment*, 2012, **94**, 380–385.
91. H. H. Fong, J.-K. Lee, Y.-F. Lim, A. A. Zakhidov, W. W. H. Wong and A. B. Holmes, Orthogonal processing and patterning enabled by highly fluorinated light-emitting polymers, *Adv Mater*, 2011, **23**, 735–9.
92. J.-K. Lee, H. H. Fong, A. A. Zakhidov, G. E. McCluskey, P. G. Taylor and M. Santiago-Berrios, Semiperfluoroalkyl Polyfluorenes for Orthogonal Processing in Fluorous Solvents, *Macromolecules*, 2010, **43**, 1195–1198.
93. D. K. Owens and R. C. Wendt, Estimation of the surface free energy of polymers, *J Appl Polym Sci*, 1969, **13**, 1741–1747.
94. H. Zheng, Y. Zheng, N. Liu, N. Ai, Q. Wang and S. Wu, All-solution processed polymer light-emitting diode displays, *Nat Commun*, 2013, **4**, 1–7.
95. R. Trattnig, L. Pevzner, M. Jäger, R. Schlesinger, M. V. Nardi and G. Ligorio, Bright Blue Solution Processed Triple-Layer Polymer Light-Emitting Diodes Realized by Thermal Layer Stabilization and Orthogonal Solvents, *Adv Funct Mater*, 2013, **23**, 4897–4905.
96. R. Trattnig, T. M. Figueira-Duarte, D. Lorbach, W. Wiedemair, S. Sax and S. Winkler, Deep blue polymer light emitting diodes based on easy to synthesize, non-aggregating polypyrene, *Opt Express*, 2011, **19**, A1281–93.
97. L. Pevzner, M. Auer, R. Trattnig, M. Klapper, E. J. W. List-Kratochvil and K. Müllen, *Isr. J. Chem.*, 2014, **54**, 736–747.

CHAPTER 8

Concepts and Modeling for Charge Transport in Organic Electronic Materials

K. SEBASTIAN RADKE,[a,b,c] F. ORTMANN*[a,b] AND G. CUNIBERTI[a,b,c]

[a] Institute for Materials Science and Max-Bergmann Center of Biomaterials, Technische Universität Dresden, 01062 Dresden, Germany; [b] Dresden Center for Computational Materials Science (DCCMS), Technische Universität Dresden, 01062 Dresden, Germany; [c] Center for Advancing Electronics (cfaed), Technische Universität Dresden, 01062 Dresden, Germany
*Email: frank.ortmann@tu-dresden.de

8.1 Introduction

In the past few years, the physical properties of organic semiconductors have been studied in considerable detail. Despite the fact that there is still a limited understanding of the relevant microscopic charge transport scenarios in such systems, various organic electronic devices such as organic light-emitting diodes (OLEDs),[1–4] organic memory cells,[5,6] organic field-effect transistors,[7–9] organic photovoltaic cells (OPVCs),[10–13] vertical triodes,[14,15] and high-frequency diodes[16,17] have been successfully demonstrated. To realize further improvements towards next generation devices present limitations in terms of materials have to be assessed to avoid efficiency losses, for which a reliable theoretical description and a microscopic

RSC Smart Materials No. 12
Supramolecular Materials for Opto-Electronics
Edited by Norbert Koch

Published by the Royal Society of Chemistry, www.rsc.org

understanding of the underlying processes are required. Correspondingly, modeling should enter the level of predictability for both device operation and material properties enabling one to establish an *in silico* material design whose scope encompasses molecular properties, supramolecular morphology and charge transport characteristics.

In most cases, charge transport in organic molecular materials is bound to the frontier molecular orbitals (MO), *i.e.* for electron transport the lowest unoccupied molecular orbitals (LUMO) and for hole transport the highest occupied molecular orbitals (HOMO), which is somewhat analogous to conventional inorganic semiconductors (Si, GaAs, *etc*.) involving valence and conduction bands. However, the conduction processes differ strongly and carrier mobilities are typically a few orders of magnitude lower even for ultrapure organic crystals. In addition, electron mobilities are often much below hole mobilities. Neither of these observations can be explained by the small electronic coupling between molecular building blocks alone although, undoubtedly, it is an important difference to inorganic compounds. The stronger susceptibility to structural disorder of organic semiconductors, and mainly the stronger coupling of the electronic degrees of freedom to the dynamical (atomic) degrees of freedom, have to be considered as these materials arrange mostly in weakly-bonded assemblies dominated by van der Waals and π–π interactions. As a consequence, not only are charge transport characteristics different, also the theoretical description requires taking all such effects into account.

One starting point for theoretical approaches is to consider the degree of charge carrier localization. Indeed, this is a highly relevant concept that leads in the limiting cases of delocalized (localized) charges to well characterized concepts of band transport (hopping transport) of carriers. As a general trend with increasing temperature, the carriers should become more localized such that these materials usually do not display (at room temperature) band transport through delocalized states over long distances (compared with the average intermolecular separation), but rather exhibit hopping motion of carriers between spatially localized states.[18–20] The degree of localization, however, is still a matter of strong debate and depends sensitively on the specific molecular structure and material morphology, which is often not fully clear. In comparison to conventional inorganic materials, an entirely different temperature dependence can be observed (larger mobility with increasing temperature) due to the increase of thermally activated processes similarly to dirty metals, opening up one possibility for an improved performance of organic devices.

Besides their technological relevance, organic semiconductors can also be regarded as a test bed to study fascinating physics of electron–phonon coupled systems, *e.g.* when the interaction between electrons and vibrations (phonons) significantly influences the macroscopic behavior of the material. The tunability of the electron–phonon coupling by chemical means appears as an intriguing perspective in this regard.

Depending on the localization of the charge carriers and the assumed dominant charge transport mechanism in the considered material, three different classes of transport simulations are commonly applied. For sufficiently low temperature, charge transport may occur coherently *via* tunneling processes. An analysis of such transport characteristics can be carried out using either a band transport model or a non-equilibrium Green function technique.[21] Especially, the latter approach can be extended, when weak energetic disorder is also present. However, stronger dynamic disorder, as present at higher temperatures, may invalidate such methods.[22,23] On the opposite side, in the limit of incoherent hopping transport, kinetic Monte Carlo simulations on the basis of hopping rates (*e.g.* derived from semiclassical Marcus theory) provide a reasonable description of the charge carrier transport.[24–27] Here, several rate-equation approaches, which also partly take coherent transport effects into account, aim at extending the applicability of kinetic Monte Carlo simulations towards lower temperatures.[28] In-between both limits, however, in the medium temperature regime from 250 to 350 K, into which falls the operating temperatures of organic electronic devices, the transport in organic semiconductors depends sensitively upon an interplay of band-like and hopping transport calling for the application of methods that work without any assumptions on the underlying charge transport mechanism. Although approximation-free theories do not exist for the intermediate regime, polaron transport approaches can give deep insight into the prevailing physics and can be extended towards the description including the presence of static disorder within numerical propagation techniques.[4]

Correspondingly, this chapter is structured as follows. In Section 8.2, the Kubo formalism is introduced as a basic and very general approach to determine the electrical conductivity and the charge carrier mobility. In Section 8.3, the Holstein–Peierls Hamiltonian describing a system with strong electron–phonon interactions and numerical methods to determine the material parameters in this Hamiltonian are discussed and disorder models are briefly introduced. Sections 8.4 and 8.5 are dedicated to charge transport simulation techniques, *i.e.* polaron transport approaches and quantum dynamic propagation techniques, respectively, used for an evaluation of the charge carrier mobility according to the Kubo formula. The chapter closes with a résumé in Section 8.6.

8.2 Kubo Formalism

A central physical quantity describing charge transport properties of a material is the carrier conductivity, which can be described within the Kubo transport framework,[29] where the Kubo formula relates the conductivity to the current–current correlation function. This formula is a result of an expansion of the current response J_x of a system (the x direction is assumed to be the transport direction) to the applied electric field (in general in the y direction), for which the term linear response theory has been

introduced.[30] The resulting value for J_x is then given by the expectation value of the current operator $\hat{J}_x$:

$$J_x = \langle \hat{J}_x \rangle = \mathrm{Tr}\left[\hat{\rho}(t)\hat{J}_x\right] \tag{8.1}$$

where $\hat{\rho}(t)$ is the density matrix of the system including the electric field at time t and Tr[...] means the usual trace operation over a complete basis. As a result of the expansion, one can finally write for the dc conductivity at temperature T:

$$\sigma_{xy} = \frac{1}{\Omega}\int_0^{\infty} \mathrm{d}t \int_0^{1/k_\mathrm{B}T} \mathrm{d}\lambda \mathrm{Tr}\left[\hat{\rho}(0)\hat{J}_y\hat{J}_x(t + i\hbar\lambda)\right] \tag{8.2}$$

where Ω is the system volume. The indices x,y in Eq. (8.2) denote the Cartesian components of the tensor σ_{xy} and k_B is the Boltzmann constant. For the specific cases considered here, we can further assume a simplified form for the diagonal conductivity ($x = y$):

$$\sigma = \sigma_{xx} = \frac{1}{2k_\mathrm{B}T\Omega}\int_{-\infty}^{\infty} \mathrm{d}t\, \mathrm{Tr}\left[\hat{\rho}(0)\hat{J}_x\hat{J}_x(t)\right] \tag{8.3}$$

By introducing the position operator $\hat{x}$ with its time dependence given by:

$$\hat{x}(t) = \widehat{U}^{\dagger}(t)\hat{x}\widehat{U}(t)$$

where $\widehat{U}(t)$ is the time evolution operator, the conductivity σ can be explicitly related to the dynamics of charge carrier wave functions and its spreading in space. The operator $\Delta\hat{X}(t) = [\hat{x}(t) - \hat{x}(0)]$ characterizes the time dependence of the wave function spread, and we can write:

$$\sigma = \frac{e_0^2}{2k_\mathrm{B}T\Omega}\lim_{t\to\infty}\frac{\mathrm{d}}{\mathrm{d}t}\mathrm{Tr}\left[\hat{\rho}(0)\,\Delta\hat{X}^2(t)\right] \tag{8.4}$$

At $T = 0$ K this corresponds to the standard result of the Kubo–Greenwood approach:

$$\sigma(E) = \frac{e_0^2}{2}\lim_{t\to\infty}\frac{\mathrm{d}}{\mathrm{d}t}\Delta X^2(E,t) \tag{8.5}$$

where the energy resolved wave function spread:

$$\Delta X^2(E,t) = \mathrm{Tr}\left[\delta\left(E - \widehat{H}\right)\Delta\hat{X}^2(t)\right]$$

with $\delta\left(E - \widehat{H}\right)$ the Dirac delta distribution is used. Finally, the charge carrier mobility μ can be easily accessed by using the definition $\mu = (\sigma/e_0N_\mathrm{c})$ where N_c is the number of charge carriers. The above formula holds quite generally. To come to the more specific cases of interest here, we will specify the Hamiltonian used for organic semiconductors in the next section.

We will see that the evaluation of expressions (8.3) and (8.4) that are derived in the framework of the Kubo formalism is particularly difficult since

no clear small parameter can be identified in the system Hamiltonian $\hat{H}$ which could justify perturbative approaches. Instead, different crossovers of various energies occur and only limiting cases are easily accessible such as the high temperature limit for example.

8.3 *Ab Initio* Material Parameters and Disorder Models

In Section 8.3.1, we derive the Holstein–Peierls Hamiltonian as a possible model to describe systems with strong electron–phonon interactions. In Section 8.3.2, we describe different *ab initio* methods to determine the material parameters present in the Holstein–Peierls Hamiltonian which are also indicative in guiding further modeling or approximations involved in the calculation of charge transport characteristics. In Section 8.3.3, different models for static disorder (which is present in realistic materials) are briefly discussed.

8.3.1 Hamiltonian for Coupled Electrons and Phonons

An important feature of organic semiconductors that is relevant for charge transport is that some vibrational frequencies in organic materials are relatively low. Weak intermolecular forces, which are of the van der Waals type or due to weak hydrogen bonds, and large molecular masses lead to intermolecular modes with wavenumbers below 300 cm^{-1}. This corresponds to an energy scale that is easily accessible at room temperature. These low-frequency modes have a strong impact on the electronic structure of the molecular system as they trigger dynamical changes in the orbital coupling due to changes in the mutual orientation and distance of molecular orbitals sensitively affecting the charge transport characteristics. In other words, the softness of organic materials leads to a continuously fluctuating potential landscape for the travelling electrons (or electron holes), an effect that can be captured conceptually by interaction terms between electrons and phonons. On the other hand, although high-frequency modes can couple strongly to the charges as well, only zero-point vibrational contributions may be of significant influence on electronic transport as the thermal energy is too small to trigger an influence on the temperature dependence of transport.

A common model for electron–phonon interaction goes back to Holstein[18,31] and is described in the following. For a given Hamiltonian that describes a completely frozen lattice $\{\mathbf{R}_{\mathbf{ks}^{(0)}}\}$, one writes in second-quantization notation for the electronic part:

$$\hat{H} = \sum_{MN} \varepsilon^{(0)}_{MN} \hat{a}^{\dagger}_{M} \hat{a}_{N} \tag{8.6}$$

where the indices M and N run over the molecules of the system, $\hat{a}^{\dagger}_{M}$ and $\hat{a}_{N}$ denote the electron creation and annihilation operators, respectively, and

$\varepsilon_{MN}^{(0)}$ are the electronic parameters, *i.e.* the orbital energies (on-site energies) for $M=N$ and the transfer integrals for $M \neq N$. If only the electronic coupling as in Eq. (8.6) was present and disorder was weak, delocalized states and a band-like transport behavior would result from the electronic structure. Owing to the softness of the material, however, possible geometric changes in the ground state geometry $\mathbf{R}_{\mathbf{k}s}^{(0)} \rightarrow \mathbf{R}_{\mathbf{k}s} = \mathbf{R}_{\mathbf{k}s}^{(0)} + \mathbf{u}_{\mathbf{k}s}$ ($\mathbf{k}$ labels the unit cell and s the atom from the atomic basis) have to be considered, which may induce changes in the on-site energies and transfer integrals. These fluctuations are captured by a Taylor series expansion:

$$\widehat{H} = \sum_{MN} \left(\varepsilon_{MN}^{(0)} + \varepsilon_{MN}^{(1)} \right) \hat{a}_M^\dagger \hat{a}_N \tag{8.7}$$

where first-order changes $\varepsilon_{MN}^{(1)}$ are given as follows:

$$\varepsilon_{MN}^{(1)} = \sum_{\mathbf{k}s} \mathbf{u}_{\mathbf{k}s} \cdot \nabla_{\mathbf{R}_{\mathbf{k}s}} \varepsilon_{MN}(\{\mathbf{R}_{\mathbf{k}s}\})\big|_{\mathbf{R}_{\mathbf{k}s}=\mathbf{R}_{\mathbf{k}s}^{(0)}} \tag{8.8}$$

After quantization of the vibrational degrees of freedom in the harmonic approximation, Eq. (8.7) leads to the Holstein–Peierls Hamiltonian (including the phonon energy as the last term):[32]

$$\widehat{H} = \sum_{MN} \left(\varepsilon_{MN}^{(0)} + \sum_{\mathbf{Q}} \hbar\omega_{\mathbf{Q}} g_{MN}^{\mathbf{Q}} \left(\hat{b}_{\mathbf{Q}}^\dagger + \hat{b}_{-\mathbf{Q}} \right) \right) \hat{a}_M^\dagger \hat{a}_N + \sum_{\mathbf{Q}} \hbar\omega_{\mathbf{Q}} \left(\hat{b}_{\mathbf{Q}}^\dagger \hat{b}_{\mathbf{Q}} + \frac{1}{2} \right) \tag{8.9}$$

where $g_{MN}^{\mathbf{Q}}$ is the electron–phonon coupling matrix associated to the mode $\mathbf{Q}$ and to the electronic parameter ε_{MN}. The term $\omega_{\mathbf{Q}}$ denotes the phonon frequency and $\hat{b}_{\mathbf{Q}}^\dagger$ and $\hat{b}_{\mathbf{Q}}$ are the phonon creation and annihilation operators, respectively. The index $\mathbf{Q}$ represents both the wave vector $\mathbf{q}$ and the phonon branch j. The last term in Eq. (8.9) characterizes the phonon degrees of freedom with the phonon frequencies $\omega_{\mathbf{Q}}$ and the second term is the coupling term, which represents changes in the ground state geometry due to phonons and their impact on the electronic structure. It accounts for transfer processes from site N to site M mediated by the emisson ($\hat{b}_{\mathbf{Q}}^\dagger$) or absorption ($\hat{b}_{-\mathbf{Q}}$) of phonons even in the absence of transfer integrals ($\varepsilon_{MN}=0$).

To derive a more practical expression for evaluating the electron–phonon coupling matrix, we rewrite expression (8.8) as:

$$\varepsilon_{MN}^{(1)} = \sum_{j,\mathbf{q}} \left(\frac{\hbar}{2\omega_j(\mathbf{q}) N_\Omega} \right)^{1/2} \frac{\partial \varepsilon_{MN}}{\partial X_j(\mathbf{q})} \left[\hat{b}_j^\dagger(\mathbf{q}) + \hat{b}_j(-\mathbf{q}) \right] \tag{8.10}$$

where N_Ω is the number of unit cells. By comparison with the coupling term of the Holstein–Peierls Hamiltonian in Eq. (8.9), we find:

$$g_{MN}^{j}(\mathbf{q}) = \frac{1}{\hbar\omega_j(\mathbf{q})} \left(\frac{\hbar}{2\omega_j(\mathbf{q}) N_\Omega} \right)^{1/2} \frac{\partial \varepsilon_{MN}}{\partial X_j(\mathbf{q})} \tag{8.11}$$

In a primitive unit cell, this expression reduces for Γ point modes to:

$$g^{j}_{MN} = \frac{1}{\left(\hbar\omega_j\right)^{3/2}} \frac{\hbar}{\sqrt{2}} \frac{\partial \varepsilon_{MN}}{\partial X_j} \tag{8.12}$$

which is the basis for the first-principles calculation of the local and non-local electron–phonon coupling elements discussed below in Section 8.3.2.2.

8.3.2 *Ab Initio* Material Parameters

In this section, we first focus on how to determine the material parameters of the Holstein–Peierls Hamiltonian. Clearly, the necessary specificity and accuracy can only be provided by appropriate *ab initio* methods. Thus, in the following, we present two density functional theory (DFT) based approaches, *i.e.* one in real space which is based on the orbitals of individual molecules and one in *k*-space which is based on the analysis of the DFT band structure. The real-space method has the advantage that it enables one to evaluate the electronic structure in systems, where static and dynamic disorder are present. However, dimer calculations, although being straightforward and fast, neglect mostly the influence of the molecular environment (or crystal field) on the material parameters. Attempts to correct these effects in the framework of semi-empirical approaches such as the Thole model have been published (see also Chapter 9 in this book).[33]

In the reciprocal-space methods, in contrast, the effects of surrounding molecules are included when calculating the parameters from the band structure of the molecular crystal. The disadvantage here is that this approach is not suitable for the analysis of disordered structures. Notwithstanding this, the influence of such structural disorder on the macroscopic transport properties of a material can be analyzed by including additional disorder models in the simulations as discussed in Section 8.3.3.

8.3.2.1 Electronic Material Parameters

First, we analyze the electronic part of the Hamiltonian in Eq. (8.9). For hole (electron) transport only the states derived from the molecular HOMOs (LUMOs) are necessary to consider when all other states are energetically well separated from these. It is then convenient to focus exclusively on the HOMO (LUMO)-derived states in the transport description.

In the real-space approach, the orbital energies ε_{MM} are defined by:

$$\varepsilon_{MM} = \langle \psi_M | \widehat{H}_{\text{eff}} | \psi_M \rangle \tag{8.13}$$

where $|\psi_M\rangle$ is a frontier molecular orbital of molecule M in the gas phase. Accordingly, the orbital energies can be obtained for isolated molecules by calculating the MOs and approximating the electronic Hamiltonian $\widehat{H}_{\text{eff}}$

by the Kohn–Sham Hamiltonian (in dependence on the exchange-correlation functional used). The transfer integrals ε_{MN} are defined as follows:

$$\varepsilon_{MN} = \langle \psi_M | \widehat{H}_{\text{eff}} | \psi_N \rangle \tag{8.14}$$

Together with the orbital energies this defines a complete tight-binding description of the electronic Hamiltonian. We note, however, that the used basis, consisting of MOs, is not orthogonal in the condensed structure. It would be desirable to use an orthogonal basis instead. A solution to this problem is given by Löwdin's symmetric transformation that corrects the non-orthogonality while maintaining as much as possible the initial local character of the monomer orbitals.[34] In the limit of small values for the elements of the overlap matrix given by $S_{MN} = \langle \psi_M | \psi_N \rangle$, the corrected transfer integrals are given by:

$$(\varepsilon')_{MN} \approx \varepsilon_{MN} - \frac{1}{2} S_{MN}(\varepsilon_{MM} + \varepsilon_{NN}) \tag{8.15}$$

In this expression, ε_{MM} and ε_{NN} are calculated for the Kohn–Sham matrix of the isolated molecular dimer. If the elements of the overlap matrix S_{MN} are not small, the transfer integrals can be determined iteratively.

The reciprocal-space method for the evaluation of the electronic system parameters is based on an analysis of the *ab initio* band structure. Firstly, the average orbital energy can be obtained from the average band energy. While this average is not of physical relevance, the difference in the orbital energies (if present) is. Secondly, the difference in the orbital energies and the transfer integrals $(\varepsilon')_{MN}$ is obtained by means of a fit procedure in the Brillouin zone with a tight binding expression that contains the important nearest neighbor terms.[35] In this way, the *ab initio* band structure is mapped onto a set of parameters with effective transfer integrals and orthogonalization is not necessary. For a unit cell including two molecules, the corresponding expression reads $(\varepsilon')_{\mathbf{k}} = \pi_{\mathbf{k}} \pm \sqrt{\sigma_{\mathbf{k}}}$, where the two different combinations of signs lead to the two bands derived from the two molecules. The mean energy of the two branches is given by $\pi_{\mathbf{k}} = \sum_{\mathbf{R}} \varepsilon_{MM}^{\mathbf{R}} e^{i\mathbf{kR}}$, where $\varepsilon_{MM}^{\mathbf{R}}$ connects equivalent molecules in neighboring unit cells (with $\mathbf{R}$ being a lattice vector). The transfer integrals between inequivalent molecules of neighboring cells are calculated by fitting the difference $\varepsilon_{\mathbf{k}} - \pi_{\mathbf{k}}$. Without any interactions between molecules of the same cell or inequivalent molecules of neighboring unit cells, the two branches can be degenerate, which would give one mean value $\pi_{\mathbf{k}}$. However, this is usually not the case and the bands can be represented by the resulting Davydov splitting for each value of $\mathbf{k}$. An example of such fits, which is performed on a regular k-point grid, is given in ref. 36.

We note that it is also possible to extend this procedure to larger unit cells, *e.g.* containing four molecules such as in the case of guanine where four bands have to be fitted at the same time.[37] Convergence of this procedure can be achieved by including transfer integrals between more distant orbitals.

8.3.2.2 Electron–Phonon Coupling

In the subsection above, we discussed a purely electronic Hamiltonian of the system in absence of vibrations. If the latter are taken into account, modulations of the orbital energies ε_{MM} are given by the local electron–phonon couplings g^{Q}_{MM} arising from both intramolecular vibrations and vibrations involving molecules in its vicinity, *i.e.* intermolecular vibrations. The Hamiltonian with exclusively local interactions is also referred to as the Holstein molecular crystal model. In the full Holstein–Peierls model, also the variation of the transfer integrals ε_{MM} by vibrations, resulting in a fluctuation of the spacing between molecules and/or the relative orientations of adjacent molecules, is considered through the non-local coupling constants g^{Q}_{MN}. In the following, we focus on the determination of coupling parameters based on *ab initio* calculations using Eq. (8.12).

In the case of local electron–phonon coupling, the molecular geometry is distorted from the ground state according to the vibrational patterns of the normal modes, and the values g^{j}_{MM} are determined from linear fits of resulting changes in the electronic energies with the phonon amplitude X_j. For the real-space method this can be approximated by monomer calculations. However, especially low energy modes are significantly influenced or driven by the presence of adjacent molecules. This makes it necessary to perform such analysis for larger assemblies of molecules in a supercell that is larger than the unit cell by displacing the positions of the atoms according to the obtained eigenvectors of the normal modes. In the reciprocal-space approach, the lattice is distorted according to the phonon eigenvector and the modulation of the band structure encodes the local electron–phonon couplings which again can be extracted from linear fits of resulting changes in the ε_{MM}. Here also the average onsite energy change may be of relevance.

The fluctuations of the transfer integrals ε_{MN} are mostly caused by low energetic intramolecular modes like bending or torsional vibrations as well as intermolecular vibrations or librations resulting in relatively large non-local electron–phonon coupling elements g^{Q}_{MN} for these modes. Calculation of the couplings for the intramolecular modes as well as the optical intermolecular modes can be performed analogously to the determination of the local electron–phonon couplings by analyzing the variation in the transfer integrals $(\varepsilon')_{MN}$ with respect to the phonon amplitude. This can be realized either based on dimer calculations neglecting the impact of the surrounding molecules or by evaluating the band structure with respect to a certain normal mode (frozen phonon approach).

In recent years, the non-local electron–phonon couplings for acoustic modes have also attracted more and more interest and have been shown to be as essential as the couplings to optical and intramolecular modes for pentacene and related molecular systems.[38,39] Here, the dimer approach is expanded beyond the Γ-point approximation by evaluating the non-local electron–phonon coupling for supercells several times larger than the unit cell taking into account phonon dispersion effects.

Finally, as an alternative approach we mention that the deformation of the molecular structure upon charging the neutral molecule toward the relaxed cationic and anionic state can be determined followed by a projection of these cationic and anionic deformation patterns onto the complete set of vibrational eigenvectors of the neutral molecule. This gives also access to the local coupling parameters.

8.3.3 Disorder Models

Already, the above-discussed Hamiltonians (for purely local coupling or both local and nonlocal coupling) are formidable challenges for the evaluation of transport quantities such as the dc conductivity σ in Eq. (8.4). Even more challenging, additional terms mimicking static disorder have to be considered for the description of common systems. A simple and generic model for this is the Anderson model, which introduces uncorrelated on-site energies, which are chosen at random from an interval $\left[-\frac{W}{2};\frac{W}{2}\right]$ according to a box-distribution. The width W of this uniform distribution represents the disorder strength. When such disorder is turned on, states at the band edge become first localized while states are most robust to disorder in the band center. Beyond such uncorrelated disorder, correlations in the onsite energy profile are likely to exist due to electrostatic effects and should be properly taken into account.

An alternative to the Anderson model are Gaussian[40] or exponential disorder models (or combinations) which are widely used to describe specific trap state distributions. A comprehensive comparison between these, however, is beyond the scope of the present chapter.

8.4 Polaron Transport Approaches

In Section 8.2, the Kubo formula to describe the charge carrier mobility was introduced. The involved current–current correlation function, however, is complicated to evaluate because particles and phonons are strongly coupled in the Hamiltonian as discussed in Section 8.3. Different methods to approach the correlation function exist in the literature.[20,41–44] As an alternative, numerical integration approaches decoupling electronic and atomic degrees of freedom and studying the evolution of wave packets have been presented.[45,46] Since such approaches seem restricted computationally to one-dimensional systems so far and the predictability of the carrier mobility is debated,[46,47] we focus in the following on analytical (though approximate) solutions within the framework of the Kubo formalism. In Section 8.4.1, an analytical representation of the full three-dimensional mobility will be derived, which allows us to describe the direction dependence of transport. Such an approach also allows us to explore the effect of finite electronic bandwidth (finite carrier localization) on the charge transport characteristics, which are often assumed to be vanishing although nearest neighbor transfer integrals

can exceed 100 meV,[48] as well as to derive certain limiting cases. In general, finite bandwidth effects have been discussed by Kenkre,[49] and a theoretical derivation has been carried out with an analytical evaluation of the Kubo formula in ref. 20. To focus on the basic physics, the nonlocal Peierls-type electron–phonon coupling is dropped for clarity in the following.

8.4.1 Three-Dimensional Anisotropic Mobility

It is insightful to start with some considerations about numbers. The charge carrier mobilities of organic molecular materials rarely exceed 10 $cm^2\ V^{-1}\ s^{-1}$ and, thus, the average velocity (for electric fields of 1 kV cm^{-1}) amounts to about 1 Å ps^{-1}. For systems where larger fields have to be applied, the mobilities are usually lower by orders of magnitude. So for a typical nearest neighbor distance of 1 nm, an average transfer time between molecular sites of $\tau \approx 10$ ps is required and marks a lower limit. A corresponding energy value can be calculated to $\hbar/\tau = 0.2$ meV. This transfer energy is almost three orders of magnitude smaller than the bare electronic transfer integrals. Not surprisingly, one can conclude that the charges do not move on the time scale of the electronic transfer integrals, which would correspond to a ballistic transport situation. In contrast, motion of carriers is strongly correlated with their polarization cloud, *i.e.* polarons can form and move on the above-derived smaller time scale. Consequently, it may be assumed that the charge carriers are almost fully dressed by phonons, which is at the heart of the polaron concept, which turns out to be highly successful in describing transport.

Taking this into account, one can use this polaron concept by introducing polaronic states instead of electronic ones in order to evaluate the Kubo formula (8.3). In fact an exact expression can be obtained by a polaron transformation for all operators $\hat{O}$ by means of the unitary replacement $\hat{O} \rightarrow \hat{\tilde{O}} = \hat{S}\hat{O}\hat{S}^{\dagger}$ as:

$$\mathrm{Tr}\left[\hat{\rho}(0)\hat{j}\hat{j}(t)\right] = \mathrm{Tr}\left[\hat{\tilde{\rho}}(0)\hat{\tilde{j}}\hat{\tilde{j}}(t)\right] \tag{8.16}$$

This further suggests the definition of an effectively reduced polaron transfer integral $\tilde{\varepsilon}_{MN}$. Note that this quantity is smaller than ε_{MM} but not zero. Moreover, it depends on temperature through the numbers of phonons determined by the Bose function.

In contrast to the fully localized polaron limit, which neglects the bandwidth effect completely ($\varepsilon \rightarrow 0$), one can describe the phonon averaged polaron Hamiltonian in $\mathbf{k}$ space still with finite bandwidth according to:

$$\hat{\tilde{H}} = \sum_{\mathbf{k}} \tilde{\varepsilon}(\mathbf{k})\hat{a}^{\dagger}_{\mathbf{k}}\hat{a}_{\mathbf{k}} + \sum_{\mathbf{Q}} \hbar\omega_{\mathbf{Q}}\left(\hat{b}^{\dagger}_{\mathbf{Q}}\hat{b}_{\mathbf{Q}} + \frac{1}{2}\right) \tag{8.17}$$

which is used to evaluate the quantum statistics through $\hat{\tilde{\rho}}$, *i.e.* the thermal averaging in the Kubo formula (8.16).

At this point it is important to mention that the particular form of Eq. (8.17) is derived from its equivalent form in real space through a simple Fourier transform and does not imply that polarons show solely band transport. It will become clear that hopping contributions are equally included.

Introducing the short-hand notation $\tilde{\varepsilon}_{0N} \equiv \tilde{\varepsilon}_N$, one finally obtains for the mobility in its full tensorial form:[20]

$$\mu_{\alpha\beta} = -\frac{e_0}{2N_C N_\Omega \hbar^2 k_B T} \sum_{LMN} R_{L\alpha} R_{N\beta} \tilde{\varepsilon}_L \tilde{\varepsilon}_N \sum_{\mathbf{k}_1\mathbf{k}_2} \mathrm{e}^{-i\mathbf{k}_1(\mathbf{R}_M+\mathbf{R}_N)} \mathrm{e}^{i\mathbf{k}_2(\mathbf{R}_M-\mathbf{R}_L)} n_{\mathbf{k}_1}(1-n_{\mathbf{k}_2})$$
$$\int_{-\infty}^{+\infty} \mathrm{d}t \mathrm{e}^{\frac{it}{\hbar}[\tilde{\varepsilon}(\mathbf{k}_1)-\tilde{\varepsilon}(\mathbf{k}_2)]} \exp\left\{ -\sum_{\mathbf{Q}} \left[N_{\mathbf{Q}} \mathrm{e}^{\mathrm{i}\omega_{\mathbf{Q}}\mathrm{t}} + (1+N_{\mathbf{Q}}) \mathrm{e}^{-i\omega_{\mathbf{Q}}t} \right] G^{\mathbf{Q}}_{0L0N} \mathrm{e}^{-i\mathbf{Q}\mathbf{R}_M} \right\} \tag{8.18}$$

This generalized mobility expression includes the effect of finite polaron bands and is discussed below. It should be highlighted that the band energies $\tilde{\varepsilon}(\mathbf{k})$ of the polaron states $\mathbf{k}_i$ directly enter expression (8.18) and $n_{\mathbf{k}_1} \equiv n_{\tilde{\varepsilon}(\mathbf{k}_1)}$ is the Fermi function for polarons. $N_{\mathbf{Q}}$ is the phonon occupation number and the quantity $G^{\mathbf{Q}}_{0L0N}$ an effective electron–phonon coupling constant. Owing to the extension to finite bandwidth, the polaron densities $n_{\mathbf{k}_i}$ are no longer constant but describe a temperature-dependent band occupation. This will be important for the generalization to systems with static disorder that is discussed later in this chapter.

Equation (8.18) contains coherent and incoherent (hopping) transport contributions, which may be separated according to $\mu = \mu^{(\mathrm{coh})} + \mu^{(\mathrm{inc})}$. The coherent contribution can be inferred from Eq. (8.18) by setting the effective electron–phonon coupling $G^{\mathbf{Q}}_{0L0N}$ to 0, which yields:

$$\mu_{\alpha\beta} = -\frac{e_0}{2N_C N_\Omega \hbar^2 k_B T} \sum_{LMN} R_{L\alpha} R_{N\beta} \tilde{\varepsilon}_L \tilde{\varepsilon}_N \sum_{\mathbf{k}_1\mathbf{k}_2} \mathrm{e}^{-i\mathbf{k}_1(\mathbf{R}_M+\mathbf{R}_N)} \mathrm{e}^{i\mathbf{k}_2(\mathbf{R}_M-\mathbf{R}_L)} n_{\mathbf{k}_1}(1-n_{\mathbf{k}_2})$$
$$\int_{-\infty}^{+\infty} \mathrm{d}t \mathrm{e}^{\frac{it}{\hbar}[\tilde{\varepsilon}(\mathbf{k}_1)-\tilde{\varepsilon}(\mathbf{k}_2)]} \tag{8.19}$$

After introducing a finite polaron lifetime τ from static disorder (as in the small-polaron theory), one finds for the coherent contribution:[20]

$$\mu^{(\mathrm{coh})}_{\alpha\beta} = \frac{\sqrt{\pi} e_0}{2N_C k_B T} \sum_{\mathbf{k}} n_{\mathbf{k}}(1-n_{\mathbf{k}}) \tilde{\nu}_\alpha(\mathbf{k}) \tilde{\nu}_\beta(\mathbf{k}) \tau(\mathbf{k}) \tag{8.20}$$

Hereby, the polaron band velocity is given as:

$$\tilde{\nu}_\alpha = \frac{1}{\hbar} \frac{\partial \tilde{\varepsilon}(\mathbf{k})}{\partial k_\alpha}.$$

The appearance of the band velocity in the expression is caused by the inclusion of finite electronic bandwidth in the theory. The coherent

contribution to the mobility may also be regarded as the low-temperature limit of the total mobility since phonon-induced incoherent contributions vanish. In this low-T limit the coherent contribution is similar to the well-known expression obtained from band theory and Boltzmann equation treatment for constant relaxation time (τ). Without polaron effects, expression (8.20) describes the mobility in the framework of the relaxation time approximation.[50,51] Here, τ can for instance be calculated with the Fermi golden rule. For disordered systems discussed below, finite τ naturally arises from the presence of scatterers and can be captured in a time propagation scheme (Section 8.5.2) such that it does not have to be used as empirical parameter there. The essential improvement of the polaronic approach with respect to classical band theory can be characterized by the replacement of electronic bands by temperature-dependent polaronic bands ($\varepsilon \rightarrow \tilde{\varepsilon}$). We finally note that the above-discussed band-transport term (8.20) does not appear in the limit of strictly localized charge carriers in Holstein's small-polaron theory where the band picture breaks down (zero bandwidths).

A simplified expression for the remaining incoherent mobility contribution $\mu^{(\mathrm{inc})}$ can be found elsewhere[20] and will not be discussed here. However, it should be mentioned that this incoherent contribution vanishes completely for zero electron–phonon interaction. On the other hand, for finite electron–phonon coupling it is the dominating part for high temperatures for which all phonon modes are increasingly occupied. This high-T limit of Eq. (8.18) is analyzed further below.

Here we focus on an illustration of the approach and plot in Figure 8.1 the hole mobilities of naphthalene in comparison to the experimental data.

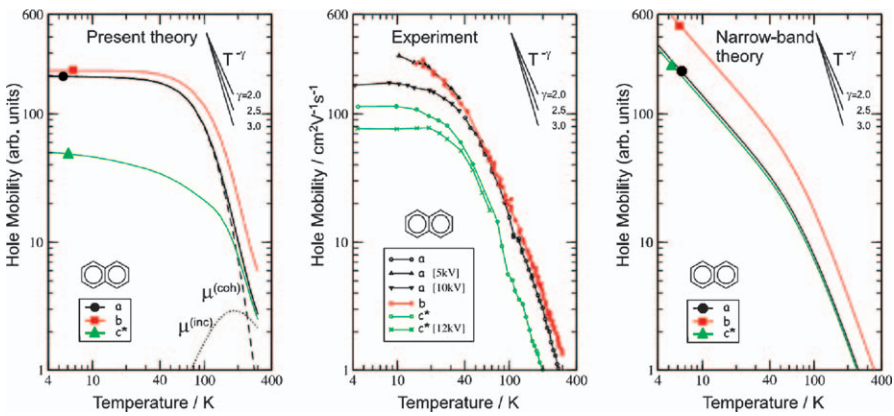

Figure 8.1 Anisotropy and temperature dependence of hole mobilities in naphthalene crystals. (left) Theory as presented in the text (ref. 52). (middle) Experimental data taken from ref. 53. (right) Theory with narrow-band approximation (ref. 54).
Reproduced after ref. 52 with permission. Copyright 2009 American Physical Society.

The contributions $\mu^{(\mathrm{coh})}$ and $\mu^{(\mathrm{inc})}$ are separated in the left-hand panel of this figure. Results within the narrow-band approximation are plotted in the right-hand panel. It is seen from the comparison to experiment that all qualitative features of the measured mobility can indeed be described by Eq. (8.18). This includes the mobility anisotropy, which is weak in the $a-b$ plane (herring-bone plane of the crystal) but shows strongly reduced values in the perpendicular c^* direction (green curves in Figure 8.1), and it also includes the temperature dependence, which can be described reliably in contrast to the narrow-band theory.

8.4.2 Limiting Cases

The carrier mobility obtained above will be discussed here in limiting cases. Equation (8.18) is a generalization of Holstein's small-polaron model because the narrow-band approximation was avoided and, instead, the full bandwidth was taken into account by means of a mixed real-space and reciprocal-space representation. We further illustrate the relation of both approaches by considering the limit of zero bandwidth in Section 8.4.2.1. In Sections 8.4.2.2 and 8.4.2.3, the charge carrier mobility is discussed in the limit of high and low temperatures, respectively.

8.4.2.1 Narrow-Band Limit

An important limiting case of the polaron model is when the transfer integrals in the Hamiltonian are very small. While this might not be the case for some high mobility organic semiconductors like rubrene or durene,[55,56] it is instructive to study this limit because the above results become exact. The so-called narrow-band limit is approached by setting $\tilde{\varepsilon}(\mathbf{k}_1) = \tilde{\varepsilon}(\mathbf{k}_2)$ for all wave vectors in Eq. (8.18), which implies that the Fermi distribution can be replaced by a constant carrier density c with $n_{\mathbf{k}} \to c \equiv N_c/N_\Omega$. Consequently, Eq. (8.18) reduces to:

$$\mu_{\alpha\beta}^{(\mathrm{NBA})} = \frac{e_0(1-c)}{2k_\mathrm{B}T}\tilde{V}_{\alpha\beta}^{\mathrm{pol}}\int_{-\infty}^{+\infty}\mathrm{d}t\mathrm{e}^{2\Sigma_j\Phi_j(t)g_j^2}\mathrm{e}^{-\left(\frac{t}{\tau}\right)^2} \tag{8.21}$$

This result is the narrow-band result as derived previously for the case of local electron–phonon coupling.[30,43] In ref. 43, the generalization to nonlocal electron–phonon interaction has also been successfully derived in the narrow band limit, which will not be discussed here. Discussion of the mobility concentrates here on the case of local electron–phonon coupling only. Equation (8.21) may also be split into a coherent and incoherent part using the separation:[18]

$$\mathrm{e}^{2\Sigma_j\Phi_j(t)g_j^2} = 1 + \left(\mathrm{e}^{2\Sigma_j\Phi_j(t)g_j^2} - 1\right)$$

In general, there are two main differences between the general theory and the narrow-band approximation. First, in the general case, there are

additional scattering channels (for inelastic scattering, *i.e.*, $\tilde{\varepsilon}(\mathbf{k}_1) \neq \tilde{\varepsilon}(\mathbf{k}_2)$) compared to the narrow-band theory, which only take elastic scattering into account, where the energy difference for initial and final polaron states is always zero, $\tilde{\varepsilon}(\mathbf{k}_1) = \tilde{\varepsilon}(\mathbf{k}_2)$. Second, the transport channels that were already included in the narrow-band theory are much better described in Eq. (8.18) since the state energy ε is incorporated properly and influences significantly the transport properties, while the narrow-band approximation partially neglects the energy dispersion, which immediately leads to an incorrect matching of initial and final state energies for elementary scattering processes.

Clearly, for high enough temperatures the above replacements, which have been introduced to arrive at the narrow-band result, become exact, and the full theory coincides with the narrow-band theory. In contrast, for low and medium temperatures one observes strong improvements over the narrow-band approximation by using Eq. (8.18). This will be further discussed below.

8.4.2.2 High Temperatures

With rising temperature, the effective polaron mass increases, which is a direct consequence of the band narrowing. As a result, in the $T \to \infty$ limit, the coherent mobility behaves like $\mu^{(\mathrm{coh})} \to 0$. For the remaining incoherent contribution, the distribution function $n_{\mathbf{k}}$ for polarons becomes constant ($n_{\mathbf{k}} \to c$) if the temperature is high enough that the bandwidth becomes smaller than $k_{\mathrm{B}}T$. If the bandwidth is also smaller than all relevant phonon energies, the narrow-band limit applies and one can set $\tilde{\varepsilon}(\mathbf{k}_1) = \tilde{\varepsilon}(\mathbf{k}_2)$ in Eq. (8.18) and obtain:

$$\mu_{\alpha\beta}^{(\mathrm{inc})} \to \frac{e_0(1-c)}{2k_{\mathrm{B}}T} \tilde{V}_{\alpha\beta}^{\mathrm{pol}} \int_{-\infty}^{+\infty} \mathrm{d}t \left(\mathrm{e}^{2\Sigma_j \Phi_j(t) g_j^2} - 1 \right) \mathrm{e}^{-\left(\frac{t}{\tau}\right)^2} \tag{8.22}$$

For sufficiently large temperatures ($2N_j g_j^2 > 1$), the -1 term in the parenthesis is negligibly small and the left-hand side of Eq. (8.22) equals the narrow-band result from Eq. (8.21). In fact, Eq. (8.22) corresponds to the hopping term in Holstein's original narrow-band theory. The high-T limit of Eq. (8.22) reads:

$$\mu^{(\mathrm{inc})} \propto T^{-\frac{3}{2}} \mathrm{e}^{-\frac{E_{\mathrm{p}}}{k_{\mathrm{B}}T}} \tag{8.23}$$

where $E_{\mathrm{p}} = \frac{1}{2} g_j^2 \hbar \omega_j$ is the polaron binding energy in case of a single effective mode j.[43] Since the coherent contribution $\mu^{(\mathrm{coh})}$ vanishes for high temperatures, $\mu^{(\mathrm{inc})}$ dominates and it follows that this activation law holds for the total mobility μ in Eq. (8.18).

Additionally, it should be highlighted that the temperature dependence found in Eq. (8.23) is the same as in the classical Marcus theory for electron transfer.[57,58] In the Marcus theory, the polaron binding energy E_{p} is regarded as a barrier for the charge carrier between two states of localization on

different sites (initial and final states for the charge transfer process). Note that beyond the maximum of $\mu(T)$ in Eq. (8.23) ($k_BT > \frac{2}{3}E_p$), the mobility is a decreasing function of T, while for lower temperatures ($k_BT < \frac{2}{3}E_p$), one finds an activation behavior giving larger μ for larger T.

8.4.2.3 *Low Temperatures*

To calculate the $T \to 0$ limit of the coherent contribution (8.20) in the full theory, we make use of the low-temperature limit of the product $n_{\mathbf{k}}(1 - n_{\mathbf{k}})$ which can be expressed as the energy derivative of the Fermi–Dirac distribution according to:

$$n_{\mathbf{k}}(1 - n_{\mathbf{k}}) = k_BT\frac{\partial n_{\tilde{\varepsilon}(\mathbf{k})}}{\partial \tilde{\varepsilon}(\mathbf{k})}$$

The energy derivative at zero temperature (step function) leads to the limit:

$$\lim_{T\to 0}\frac{\partial n_{\tilde{\varepsilon}(\mathbf{k})}}{\partial \tilde{\varepsilon}(\mathbf{k})} = \delta[\tilde{\varepsilon}(\mathbf{k}) - \zeta]$$

From a physical point of view, this means that only the polarons from within a thermal layer of width $\propto k_BT$ at the chemical potential ζ contribute to transport. As a consequence, this k_BT term exactly cancels the prefactor $1/k_BT$ in Eq. (8.20) resulting in a finite carrier mobility for $T = 0$ K, which only depends on τ. Importantly, this is a major improvement over the narrow-band theory, which involves a replacement $n_{\mathbf{k}}(1 - n_{\mathbf{k}}) \to c(1 - c)$ and results in a $1/k_BT$ divergence. Therefore, the correct inclusion of the Fermi–Dirac statistics in the present theory is essential for removal of this unphysical singularity. Figure 8.1 illustrates this by comparing both cases with a low-T saturation of the mobility (left-hand panel) and a $1/T$ divergence for the narrow-band theory (right-hand panel).

In the special case of an isotropic system with a parabolic band structure, one obtains the low-T limit as:

$$\mu^{(\mathrm{coh})} = \frac{\sqrt{\pi}e_0\tau}{2m^*_{\mathrm{pol}}} \tag{8.24}$$

which resembles the Drude expression for the mobility but generalized to polarons as charge carriers. The polaron effective mass is given by:

$$m^*_{\mathrm{pol}} = m^*_{\mathrm{el/hole}}\mathrm{e}^{\Sigma_j g_j^2} \tag{8.25}$$

This mass is increased compared to the bare electron/hole mass due to the coupling to the phonons, *i.e.* the polarization cloud adds some extra mass. Note that the expression (8.24) including the scattering time τ, although compact, is certainly an oversimplified form for the general case as such a

scattering time must include the description of all the physical processes including momentum and energy conservation of the underlying scattering processes in a single parameter.

The low-T regime of the incoherent mobility $\mu^{(\mathrm{inc})} = \mu - \mu^{(\mathrm{coh})}$ is analyzed for a single scatterer j of frequency ω_j in the limit of a small phonon occupation number ($N_j \ll 1$). Assuming ultrapure crystals where static disorder is much smaller than phonon induced dynamic disorder, *i.e.* $1/\tau \ll \omega_j$, one finds the largest term:

$$\mu^{(\mathrm{inc})} \propto g_j^2 \frac{N_j}{T} \approx \frac{g_j^2}{T} \mathrm{e}^{-\frac{\hbar\omega_j}{k_\mathrm{B}T}} \tag{8.26}$$

Basically, this result describes an activation law with the phonon energy as a relevant energy barrier. The process behind this leading term is a phonon absorption process, which elevates the polaron above the Fermi energy. The frequency of occurrence of such an event is proportional to N_j, the number of available phonons. Additionally, the activation law should rather be regarded as a probability than a real barrier. Finally, the $T \to 0$ limit of Eq. (8.26) is obtained as $\mu^{(\mathrm{inc})} \to 0$, *i.e.* the incoherent mobility vanishes.

We also note that, although the reciprocal space has been used above to derive a convenient expression for the coherent mobility, it is not necessary to restrict to translation symmetric (*i.e.* periodic) systems. By transforming to a real-space representation it becomes clear how to generalize this approach to disordered systems. In such systems, analytical approaches become inconvenient and numerical schemes are preferred. In the next section we will demonstrate the working principles of time-propagation methods that can be employed in systems with disorder.

8.5 Quantum Dynamic Charge Propagation Techniques

8.5.1 Introduction

Until now, we explained the analysis of charge transport based on the Kubo formalism by evaluating Eq. (8.3) using the polaron model. However, it is also possible to determine the conductivity σ according to Eq. (8.5) by calculating explicitly the spatiotemporal behavior of the wave function spreading ΔX. Accordingly it is necessary to simulate the propagation of the wave function analogous to solving the time-dependent Schrödinger equation. Here, several approaches have been developed and applied successfully in recent years. On the one hand, the dynamic behavior of the molecular system and its effect on the electronic structure can be represented within the framework of the polaron model by investigating the spatiotemporal evolution of the polaron state.[59] Consequently, these methods consider the full quantum nature and dynamics of electrons and phonons. On the other hand, the thermal fluctuations of the electronic parameters can be treated

explicitly by performing a propagation of the charge carrier wave function on a vibrating lattice.[60] Here, only the electrons are treated quantum mechanically, while the phonons are described classically within the framework of molecular dynamics (MD) simulations.

In the following, we will present one example for each approach. First, let us derive a basic method to solve the time-dependent Schrödinger equation numerically, which is essential to propagate the wave function of the charge carrier Ψ in real time and real space. The corresponding equation of motion to be solved leads to the formal solution:

$$\left|\Psi(t_j)\right\rangle = \widehat{U}(t_j, t_i)\left|\Psi(t_i)\right\rangle = \mathrm{e}^{-i\widehat{H}(t_j - t_i)}\left|\Psi(t_i)\right\rangle \tag{8.27}$$

where $\widehat{U}(t, t_0)$ is the propagator of the time-independent Hamiltonian $\widehat{H}$ (for time dependent $\widehat{H}$ this is valid for a sufficiently small time interval $\Delta t = t_j - t_j$) and $\hbar$ is set to 1 in this subsection for simplicity. Here, the wave function $|\Psi\rangle$ can either be represented in the eigenstate basis $\{|\Psi_n\}$ with the corresponding eigenenergies E_n being the diagonal elements of the Hamiltonian matrix $\mathbf{H}$ or can be formulated by a grid-based method, *e.g.* in the discrete variable representation.[61] The necessary diagonalization can be prohibitive for the former and thus, in the following, we will use a grid-based method representing the wave function by a n-dimensional vector $\mathbf{c}(t)$. Its complex, time-dependent elements $c_n(t)$ are defined by the projection:

$$c_n(t_j) = \langle\Psi_n|\Psi(t_j)\rangle \tag{8.28}$$

Its temporal evolution in the eigenstate representation then reads:

$$\mathbf{c}(t_j) = \mathbf{U}(t_j, t_i)\mathbf{c}(t_i) = \mathrm{e}^{-i\mathbf{H}(t_j - t_i)}\mathbf{c}(t_i) \tag{8.29}$$

There exist several numerical approaches to evaluate the propagation steps described by this expression. One efficient technique is given by the Chebychev polynomial expansion following the idea to approach the propagator $\mathbf{U}(t_j, t_i)$ by a Chebychev series taking the form:

$$\mathbf{U}(t_j, t_i) = \sum_{k=0}^{N} a_k(t_j - t_i)\Phi_k(\mathbf{H}) \tag{8.30}$$

where the complex Chebychev polynomials depend on the Hamiltonian and obey the recursion relation:

$$\Phi_{k+1}(\mathbf{H}) = -2i\mathbf{H}\Phi_k(\mathbf{H}) + \Phi_{k-1}(\mathbf{H}) \tag{8.31}$$

Correspondingly, for the numerical implementation, the argument of Φ_k has to be mapped onto the interval $[-i; i]$. Consequently, the spectrum of $\mathbf{H}$ is shifted and scaled to the range $[-1; 1]$. Then, the propagation is performed with the normalized Hamiltonian, and a shift parameter is introduced to compensate for the normalization. The time-dependent

expansion coefficients $a_k(t_j - t_i)$ in Eq. (8.30) are related to the Bessel functions $J_k(t_j - t_i)$ as follows:

$$a_0(t_j - t_i) = J_0(t_j - t_i) \text{ and } a_k(t_j - t_i) = 2J_k(t_j - t_i) \tag{8.32}$$

The order of the Chebychev expansion N has to be chosen large enough to ensure the convergence of the series, which usually is easy to achieve due to the properties of the Bessel functions.

8.5.2 Polaron Theory Based Charge Propagation

Here we combine the analytical expression of Eq. (8.20) with the above-described propagation methods using the polaron Hamiltonian (8.17) in the evolution operator. In fact, one observes that Eq. (8.20) is the diffusion coefficient for polarons $\tilde{\nu}^2\tau = \frac{1}{2}D$, which can be equally defined in ordered and disordered systems and is related to the mean square spreading of polaronic wave packets analogous to Eq. (8.5), with which one can write:

$$\mu_\alpha^{(\mathrm{coh})} = \frac{\Omega}{e_0 c k_B T}\int \mathrm{d}E\sigma(E,t)n_E(1-n_E) \tag{8.33}$$

Hereby the relation $\sigma(E,t) = \frac{e_0^2}{2}D(E)\rho(E)$ with $\rho(E)$ the density of states for disordered systems has been used. The finite temperature in this approach enters through the prefactor $(1/k_BT)$ and the term $n_E(1 - n_E)$.

The behavior of the coherent mobility is analyzed for a model organic crystal as defined in Figure 8.2(a) which consists of a three-dimensional (orthorhombic) crystal of anisotropic aspect ratio and with different transfer integrals in different directions. Orthorhombic symmetry is used for simplicity and implies vanishing off-diagonal tensor components for the mobility. The model for electron–phonon coupling is restricted to a single dispersion-less phonon

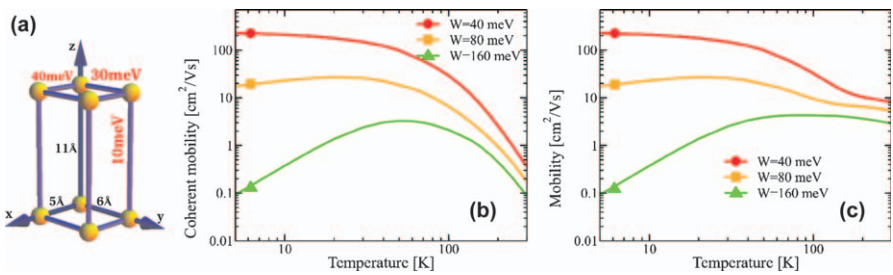

Figure 8.2 (a) Crystal geometry and transfer integrals for the model used for transport simulations. (b) Mobility $\mu_x^{(\mathrm{coh})}$ (Eq. 8.33) and (c) mobility $\mu_x^{(\mathrm{coh})} + \mu_x^{(\mathrm{inc})}$ (Eq. 8.34) for the model crystal in (a) with a single coupling phonon mode ($\hbar\omega = 12$ meV) and effective electron–phonon coupling ($g_\lambda = 0.7$). Disorder strength W in the Anderson model is used as indicated.
Adapted after ref. 59, with permission. Copyright 2011 American Physical Society.

mode for simplicity (for specific values, see figure caption), while the full phonon-spectrum can be included in principle as is clear from Eqs. (8.33) and (8.34). Disorder is introduced through an Anderson model with varying disorder strength W and the carrier concentration is fixed to $c = 10^{-3}$.

For this model, Figure 8.2(b) shows the influence of the disorder on transport and in particular on its temperature dependence. Disorder tends to localize the charge carriers most at low temperatures. A mobility drop by three orders of magnitude is obtained when increasing W by a factor of 4. The effect is much weaker at high temperatures. In addition, at high temperatures the second (incoherent) part has to be taken into account. It can be written for elevated temperatures as:

$$\mu_{\alpha}^{(\mathrm{inc})} = \frac{e_0 \Omega^2}{2c\hbar^2 k_{\mathrm{B}} T} \sum_{M} R_M^2 \tilde{\varepsilon}_M^2 \int \mathrm{d}E_1 dE_2 \rho(E_1)\rho(E_2) n_{E_1}[1 - n_{E_2}] \int \mathrm{d}t e^{it(E_1 - E_2)/\hbar} \left\{ \exp\left[2\Phi_{\lambda}(t) g_{\lambda}^2\right] - 1 \right\} \tag{8.34}$$

Figure 8.2(c) shows the total mobility by summing Eqs. (8.34) and (8.33). A notable difference to the curves in (b) is visible at high temperatures where such phonon-assisted transport is the dominating contribution. In this regime, band-narrowing effects and phonon activation are in competition and, for the chosen model, yield a mobility decay with increasing T. The influence of disorder is clearly much weaker at high T although it is still present. As a result of increasing disorder the overall temperature dependence changes from a band-like behavior to dominating activation-like behavior.

8.5.3 Mixed Quantum–Classical Propagation

In recent years, much effort has been made to calculate the electronic parameters, *i.e.* the orbital energies and the transfer integrals, for various systems at different levels of theory. As presented in the previous sections, most of the calculations performed so far rely on the implicit assumption that the presence of moving charge carriers does not strongly modify the values of electronic coupling and molecular orbital energies; however, this assumption seems to break down in some situations. For example, one can expect that in the case of hole transport the coupling between two neutral organic molecules may differ from the coupling between cationic and neutral molecular species. Additionally, it is observed experimentally that the charge carrier mobility is significantly influenced by the charge carrier density in the material, indicating that the presence of charge carriers should be taken into account explicitly in improved charge transport simulations.

In this section, we present a computational methodology that is free from adjustable parameters and allows us to include in a consistent way the influence of a propagating charge onto the dynamics as well as the electronic parameters of the system through which it is moving. Using this approach, we demonstrate that the explicit inclusion of a moving charge can have a strong effect on the values of these parameters and hence on the qualitative

behavior of the transport characteristics of the system. The section is structured as follows: In Section 8.5.3.1 the self-consistent propagation scheme used is described, in Section 8.5.3.2 the impact of the charge carrier on the electronic structure is discussed, and in Section 8.5.3.3 the charge transport characteristics in coronene and pentacene are analyzed.

8.5.3.1 Self-Consistent Propagation Scheme

The structure of the propagation scheme follows the descriptions given in refs 60 and 62, which is also depicted schematically in Figure 8.3. Based on an equilibrated geometry, which serves as initial structure, the migration of a charge carrier, which is initially localized on a single molecular site, is simulated in real time and real space under joint consideration of electronic and atomic dynamics. Each cycle of the propagation scheme consists of an electronic system-parameterization step with respect to charge effects followed by determination of the dynamics of the charge carrier, and a simulation of the atomic dynamics with included additional electrostatic potentials for the simulation of the charge carrier. In the following, the particular steps are explained in detail.

Initialization. The first step is to pick a structural initial guess consisting of the preparation of the model system. This includes the equilibration of the neutral molecular system with periodic boundary conditions by using a suitable level of theory for the MD simulation. Here, *ab initio* approaches provide a realistic representation of the electronic structure and the molecular dynamics, but reduce strongly the possible system sizes due to the high computational effort (typical supercells can be seen in Figure 8.4 for coronene and pentacene). After the equilibration, the charge

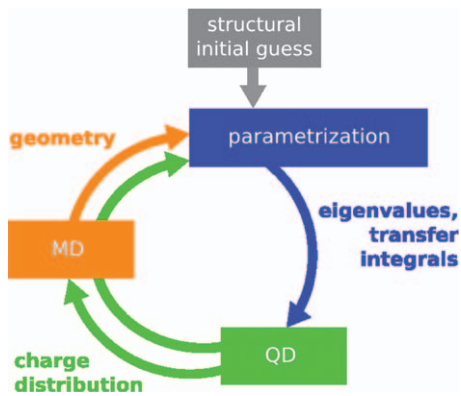

Figure 8.3 Schematic representation of the *ab initio* real space and time propagation scheme for charge carriers through organic molecular systems consisting of three parts: The calculation of the eigenvalues and transfer integrals (parameterization), the quantum dynamical propagation of the charge carrier wave function (QD), and a molecular dynamics step (MD). Adapted from ref. 60 with permission. Copyright 2012 Wiley-VCH Verlag GmbH, Weinheim.

carrier (in this section a hole) is assumed to be completely localized on a certain molecule, *i.e.* molecule 1 displayed in Figure 8.4. According to the shape of the charged orbital of the molecule, the charge can be replaced by a distribution of point charges over the molecule to represent its electrostatic potential as shown in Figure 8.4 for coronene and pentacene. To extract the charge carrier after crossing the system, traps are attached on the opposite side of the molecular system (molecule 10 for coronene and molecules 15 and 16 for pentacene) because of the limited system size. They absorb the charge carrier when reaching the end of the system.

Parameterization. For the initial structure as well as after each MD step, the ADF package[63–65] is used to determine the orbital energies ε_{MM} and the nearest neighbor transfer integrals ε_{MN} since this code allows for the analysis of fractionally charged molecules. As charge affects on the electronic structure of the molecular system shall be taken into account, according to a coarse-grained representation of the system in the MO basis, a fractional charge $n_M e_0$ is assigned to each molecular site M based on the calculated wave function of the charge carrier obtained from the QD step. Here n_M is a number between zero and one and e_0 is the elementary charge. Initially, molecule 1 is charged with e_0 ($n_1 = 1$), whereas all other molecules are neutral ($n_l = 0$). However, cycle after cycle, the wave function is more and more delocalized over the molecular stack represented by the fractional

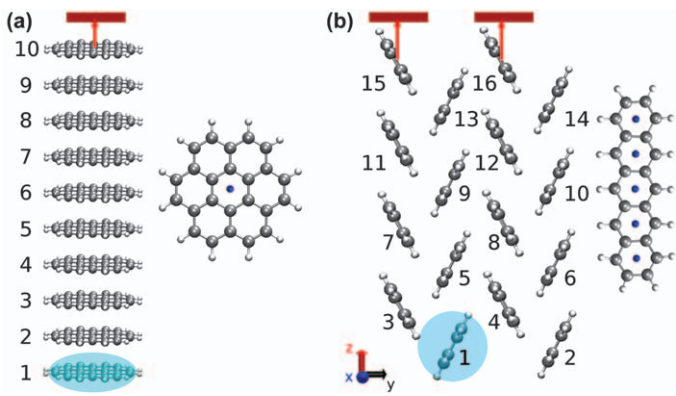

Figure 8.4 Preparation of a coronene and a pentacene system for the propagation scheme. (a) The simulated one-dimensional coronene model system with numbered molecules. Initially, the point charge is completely localized on molecule 1, which is marked by the blue spot. On the opposite side of the molecular stack, a trap, symbolized by the red bars, is connected *via* the Lindblad formula to the molecular system at molecule 10. (b) The simulated two-dimensional pentacene model system with numbered molecules. Initially, the point charge is completely localized on molecule 1, which is marked by the blue spot. On the opposite side of the molecular stack, two traps, symbolized by the red bars, are connected to the molecular system at molecules 15 and 16.

occupation in the HOMO that is reduced to n_M. In addition to the effect of the fractional charge $n_M e_0$ on the electronic structure of this molecule M, also the fractional charges (distributed over molecules in a point-charge approach as displayed in Figure 8.4) of the neighboring molecules defining an electric field are taken into account for the calculation of the orbital energies. Analogously, the transfer integrals ε_{MN} are directly obtained from the interactions of the fragments M and N by using the fragment orbital approach implemented in ADF.[66] Correspondingly, the dimer of the two neighboring molecular sites M and N exhibits the fractional net charge $n_{MN}e_0 = (n_M + n_N)e_0$. Also here, the electric field defined by the surrounding fractionally charged molecules is taken into account. Owing to the changes in the electronic structure affected by the presence of the charge carrier, the MOs from the HOMO down to the HOMO-5 as well as the corresponding transfer integrals between all combinations of these orbitals have to be included in the calculations. The sets of system parameters, orbital energies and transfer integrals, are calculated for every molecule and every combination including the actual charge distribution for time steps of 1 fs, which proved to be sufficient to describe the time evolution accurately.

Quantum Dynamics. Based on the determined system parameters $\mathbf{H}(t)$ of the actual time step, the time evolution of the hole wave function is calculated by a quantum dynamical propagation scheme. The basic structure of the propagation scheme used is similar to the one presented in the previous section. However, the consideration of lower lying MOs with respect to the HOMO demands the implementation of transitions of the fractional hole population from the HOMO-x levels to the HOMO that is expected to occur on short time scales. Additionally, the trap steps catching irreversibly the charge carrier wave function when reaching the end of the molecular stack have to be included. As such quantum systems cannot be represented by isolated ones, dissipative effects have to be included in the simulation. Therefore, the wave function description is transferred to the density matrix representation $\hat{\rho}(t) = |\Psi(t)\rangle\langle\Psi(t)|$, which allows us to incorporate effects such as energy relaxation in the quantum dynamical calculation. Then, the temporal evolution of the density matrix can be represented by the Liouville–von Neumann equation:

$$\dot{\boldsymbol{\rho}}(t) = \mathscr{L}\boldsymbol{\rho}(t) = \left(\mathscr{L}_{\text{sys}} + \mathscr{L}_{\text{D}}\right)\boldsymbol{\rho}(t) = -i[\mathbf{H}, \boldsymbol{\rho}] + \mathscr{L}_{\text{D}}\boldsymbol{\rho}(t) \tag{8.35}$$

Here, $\mathscr{L}$ is the Liouvillian superoperator of the whole system consisting of a non-dissipative term $\mathscr{L}_{\text{sys}}$ and a dissipative term $\mathscr{L}_{\text{D}}$. A reliable ansatz to describe L_{D} is given by the Lindblad approach[67–69] treating the relaxation in the framework of the system only. Although it is a semi-phenomenological mathematical approach, the Lindblad equation gives the correct mathematical and physical properties to the dynamics of the system by preserving complete positivity of the density matrix during the non-unitary time

evolution. It enables one to include information on the system-bath coupling in this model. $\mathscr{L}_{\mathrm{D}}$ can be written as follows:

$$\mathscr{L}_{\mathrm{D}}\hat{\rho}(t) = \sum_{a}\left(\hat{C}_a\hat{\rho}\hat{C}_a^{\dagger} - \frac{1}{2}\left[\hat{C}_a^{\dagger}\hat{C}_a, \hat{\rho}\right]_{+}\right) \tag{8.36}$$

where $\hat{C}_a$ are the Lindblad operators corresponding to raising and lowering operators of the a-th two-level system $|b_1\rangle, |b_2\rangle$:

$$\hat{C}_a = \sqrt{\gamma}|b_1\rangle\langle b_2| \text{ and } \hat{C}_a^{\dagger} = \sqrt{\gamma}|b_2\rangle\langle b_1| \tag{8.37}$$

In the simulations, a characteristic transition rate of $\gamma = 0.1$ fs^{-1} is used, which is a reliable time scale for the charge transitions from lower MOs to the HOMO as well as from the molecules to the traps. The Liouville–von Neumann equation (Eq. (8.35)) is then solved to determine the migration of the hole in the density matrix approach according to:

$$\boldsymbol{\rho}(t_j) = \mathrm{e}^{\mathscr{L}(t_j - t_i)}\boldsymbol{\rho}(t_i) \tag{8.38}$$

Numerically, this equation of motion can be solved by applying the Faber polynomial method.[70] The Faber polynomials are similar to the Chebychev polynomials but work not only for matrices with real eigenvalues but also if the eigenvalues occur in the complex plane. Basically, the family of Faber polynomials $\{F_k\}_{k\in N}$ associated with a conformal mapping $\zeta(\omega)$ can be defined *via* the recursion relation:

$$F_{k+1} = zF_k(z) - \sum_{j=0}^{k} c_j F_{k-j}(z) - kc_k \tag{8.39}$$

where $\{c_k\}$ are the coefficients of the conformal mapping $\zeta(z)$. It can be shown that an adequate conformal mapping $\zeta(\omega)$ to integrate the dissipative Liouville–von Neumann equation is given by:

$$\zeta(\omega) = \omega + m + \frac{d}{\omega} \tag{8.40}$$

where the complex parameters d and m depend on the relative strength of the Hamiltonian and the dissipative contributions. The associated Faber polynomials in matrix representation now read:

$$F_{k+1}(\mathscr{L})\boldsymbol{\rho}(t_i) = (\mathscr{L} - m\mathbf{I})F_k(\mathscr{L})\boldsymbol{\rho}(t_i) - dF_{k-1}(\mathscr{L})\boldsymbol{\rho}(t_i) \tag{8.41}$$

with $k \geq 2$ and the initial values:

$$F_0(\mathscr{L})\boldsymbol{\rho}(t_i) = \boldsymbol{\rho}(t_i) \tag{8.42}$$

$$F_1(\mathscr{L})\boldsymbol{\rho}(t_i) = (\mathscr{L} - m\mathbf{I})\boldsymbol{\rho}(t_i) \tag{8.43}$$

$$F_2(\mathscr{L})\boldsymbol{\rho}(t_i) = (\mathscr{L} - m\mathbf{I})F_1(\mathscr{L})\boldsymbol{\rho}(t_i) - 2d\boldsymbol{\rho}(t_i) \tag{8.44}$$

The exponential function $e^{\mathscr{L}(t_j-t_i)}$ in Eq. (8.38) is analytic inside the domain $G(\mathscr{L} \in G)$ and can be expanded in terms of the Faber polynomials associated with ζ. This yields:

$$e^{\mathscr{L}(t_j-t_i)} = \sum_{k=0}^{\infty} \frac{1}{2\pi i} \int_{|\omega|=1} d\omega \frac{e^{\zeta(\omega)(t_j-t_i)}}{\omega^{k+1}} F_k(\mathscr{L}) = \sum_{k=0}^{\infty} \alpha_k(t_j, t_i) F_k(\mathscr{L}) \tag{8.45}$$

Finally, the density matrix $\boldsymbol{\rho}$ can be determined by:

$$\boldsymbol{\rho}(t_j) \approx P_n^{t_j,t_i}(\mathscr{L})\boldsymbol{\rho}(t_i) = \sum_{k=0}^{\infty} \alpha_k(t_j, t_i) F_k(\mathscr{L})\boldsymbol{\rho}(t_i) \tag{8.46}$$

where one can calculate analytically the coefficients $\alpha_k(t_j, t_i)$ by using the Bessel functions of first kind J_k:

$$\alpha_k(t_j, t_i) = \left(-\frac{i}{\sqrt{-d}}\right)^k e^{m(t_j-t_i)} J_k\left(2\sqrt{-d}(t_j - t_i)\right) \tag{8.47}$$

Application of this method to model charge transfer in molecular systems is based on a successive calculation of the time evolution of the charge carrier wave function in the case where nuclear and electronic degrees of freedom are coupled. As discussed above, small transfer integrals together with a coupling to the dynamical degrees of freedom lead to relatively long average transfer times between sites in organic materials, which allows for a propagation step of 0.1 fs. As the parameterization is done every fs to construct the electronic system Hamiltonian, a linear interpolation is performed to obtain the electronic parameters for every 0.1 fs.

Molecular Dynamics. After having obtained a new charge distribution from the precedent quantum dynamical step, the MD simulation of the molecular system is performed for 1 fs containing the information of the hole density matrix represented by point charges defining an electric field. Consequently, the presence of the fractional charges distributed over the molecules does not only change the system parameters as explained for the parameterization step but can also affect the structural dynamics. Each MD step is based on the geometry and velocities from the previous MD simulation and the new distribution of the fractional charges from the previous QD step. The calculations are performed in the canonical ensemble. It has to be mentioned that the initial localization of the charge carrier on a single molecule can generate problems in the simulation since due to the additional forces the velocities and correspondingly the kinetic energy of the system of the atoms increase.

8.5.3.2 Influence of the Charge Carrier on the Electronic Structure and the Molecular Dynamics. In this subsection we discuss how explicit treatment of the charge carrier wave function influences the system dynamics as well as the electronic system parameters and accordingly the transport

properties for pentacene. The parameterization is performed using a semi-local GGA-type PBE exchange-correlation functional[71,72] and the DZP basis set.[73] For the MD simulation, the GTH-PADE functional[74–76] and the TZV2P-GTH basis set[77] are combined with the CHARMM force field.[78] First, we discuss the time series of the orbital energies in dependence of the moving charge. The dynamic behavior of the orbital energies from HOMO to HOMO-5 for molecule 1, which is the initially charged molecule, and molecule 16, being connected to a trap and hosting a negligible charge, is presented in Figure 8.5(a). Owing to the presence of the charge carrier, the whole orbital energy spectrum of molecule 1 is drastically lowered in comparison to the energy spectrum of molecule 16, on which hardly any charge is localized during the simulation time due to the neighboring trap state. It has to be highlighted that charge effects can shift the orbital energies by more than 1 eV, which strongly exceeds the effect of thermal fluctuations (0.1 eV). The orbital energies of molecule 1 quickly rise with decreasing population numbers (Figure 8.5c) moving towards to the neutral values. The dynamic behavior of the orbital energies displays weakly oscillatory characteristics in the presence of a small charge population as well as for the neutral molecule and a discontinuous time dependence otherwise, coinciding with the rapid charge redistribution (Figure 8.5c) in the first 100 fs. This could, however, also be an effect of convergence problems of ADF. In Figure 8.5(b), the time series of the orbital energies from HOMO to HOMO-2 of the molecules 1, 3 and 4

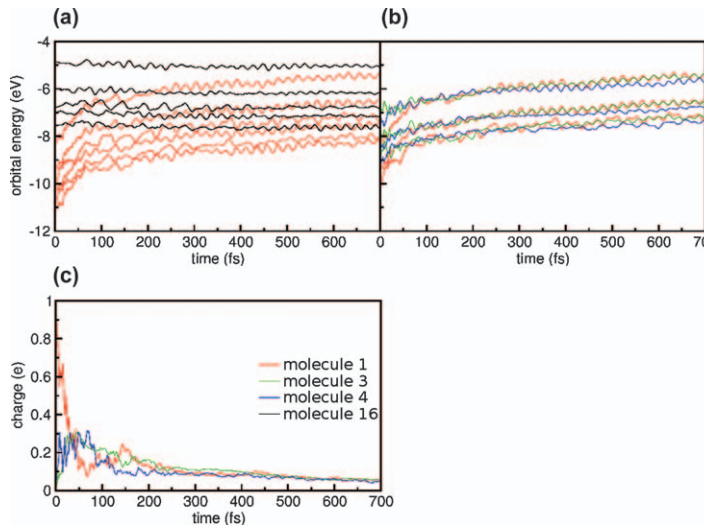

Figure 8.5 Charge effects on the orbital energies. (a) Time series of the MOs from HOMO to HOMO-5 for molecules 1 and 16. (b) Time series of the MOs from HOMO to HOMO-2 for molecules 1, 3, and 4. (c) Time series of the charge population of molecules 1, 3, and 4. The numbering of the molecules is according to Figure 8.4(b).

are presented, which are not only influenced by the additional fractional occupation but also by polarization effects due to the excess charges of neighboring molecules. For the first 50 fs, when the charge carrier wave function is relatively strongly localized on these three molecules, the HOMO energy of molecule 1 is closer to the HOMO-1 levels of the molecules 3 and 4 than to the HOMO levels of these sites, enlarging the probability for a charge transfer from the HOMO of molecule 1 to the HOMO-1 of the neighboring molecules. More MOs than the HOMO levels can be involved in the conduction process because of the lowering of the orbital energies due to the presence of the charge carrier. Consequently, the propagation scheme should also consider these intermolecular charge transitions from the HOMO to HOMO-x, requiring the determination of the corresponding transfer integrals.

For an analysis of the explicit influence of the charge carrier on the transfer integrals, we compare two structurally equivalent HOMO–HOMO transfer integrals, *e.g.* the clearly charge influenced transfer integral between molecule 1 and the neighboring molecule 3 as well as the relatively charge-unaffected one between the molecules 14 and 16. The time series of both considered combinations is depicted in Figure 8.6(a) over 700 fs, the respective histograms in Figure 8.6(b), and for the corresponding populations see Figure 8.6(c). Although the time series are relatively short and not fully statistically representative, first trends can be traced

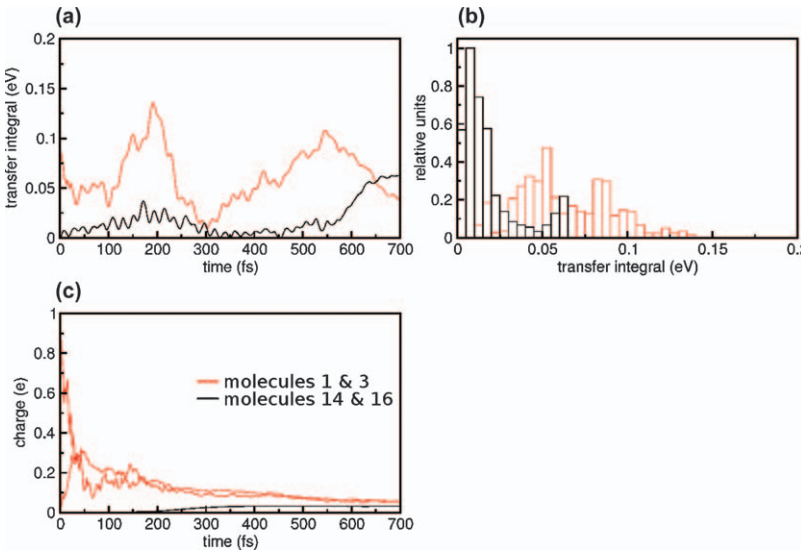

Figure 8.6 Charge effects on the transfer integrals. (a) Time series of the HOMO–HOMO transfers integrals between molecules 1 and 3 (red), and between molecules 14 and 16 (blue). (b) Corresponding statistics of the time series. (c) Charge populations of molecules 1 and 3 (both red), and molecule 14 (black). The charge of molecule 16 is negligible because of the connection to the trap.

that for the analyzed time series the transfer integral is considerably higher in the presence of a charge, especially if both molecules possess a similar fractional charge, than the transfer integral between nearly neutral molecules, which is also indicated by the average values of the absolute transfer integrals deduced from the corresponding statistics presented in Figure 8.6(b). However, a difference in the fluctuations of the transfer integrals of both dimers cannot be found for the data. It seems that the dynamic behavior is dominated by thermal effects instead of a charge effect. The broad histogram of the charge-influenced transfer integral displayed in Figure 8.6(b) follows from the strong decay of the charge population on both molecules 1 and 3.

8.5.3.3 *Charge Transport Characteristics under Consideration of Charge Effects*

The potential of the *ab initio* quantum dynamical charge propagation scheme described in the previous subsection is demonstrated by applying this scheme to the calculation of the mobility of a hole along a one-dimensional stack of coronene molecules analogous to those studied experimentally by Feng *et al.*[79] and a two-dimensional herringbone stacked pentacene system according to the theoretical studies by Shuai *et al.*[80]

One-Dimensional Coronene System. As displayed in Figure 8.4(a), the chosen one-dimensional model system involves ten coronene molecules, which prove to be sufficient to obtain a reliable insight into the charge transport characteristics. The parameterization is again performed at the PBE/DZP level, and the SCC-DFTB method[81,82] is applied for the MD simulation. The propagation of the charge carrier wave function for temperatures ranging from 300 to 500 K is depicted in Figure 8.7. In general, we see that the wave packet can propagate more rapidly across the stack at higher temperatures, which is accompanied by a rapid broadening of the charge distribution. However, the charge carrier is relatively localized over five molecules after 600 fs at room temperature, which indicates that the dynamical disorder is not strong enough to overcome the

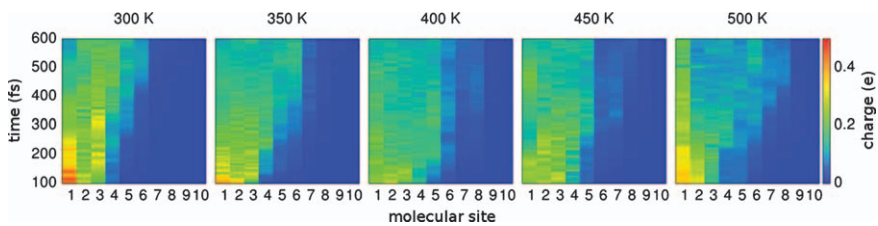

Figure 8.7 Hole dynamics in a one-dimensional coronene stack at different temperatures. The wave function is visualized as a function of time and of the populated molecular sites. Adapted from ref. 60.

collective stabilization of the wave function caused by the interaction with nearest-neighboring and next-to-nearest-neighboring sites. Up to around 400 K, the situation changes since dynamical disorder increases, which leads to a rapid broadening of the charge distribution. At even higher temperatures (500 K), the charge carrier is nearly delocalized over the whole stack after 600 fs.

Next, let us analyze the time-dependent diffusion coefficient D, which can be obtained from the time series of the propagating wave packet using:

$$D_i(t) = \sum_M \frac{n_M(t) x_{iM}^2}{2t} \tag{8.48}$$

where the molecular site M is charged by $n_M e_0$ and has a distance of x_{iM} in x_i direction with respect to molecule 1. In Figure 8.8(a), the time-dependent diffusion coefficient $D(t)$ is depicted for a temperature of 300 K based on two different simulations, *i.e.* one taking charge effects explicitly into account (grey solid line) and one performed without including charge effects in the calculations of the dynamics as well as the electronic parameters (black dashed line). Basically, by comparing both time series, it has to be pointed out that the presence of the charge carrier does not only influence the charge propagation in a quantitative way, but it also affects significantly the charge transport process. While, for the simulation without charge effects, only a quasi-ballistic transport regime is observed within the time scale investigated, which would cause a considerable overestimation of the charge carrier mobility μ, the explicit inclusion of charge effects in a self-consistent fashion leads to the appearance of different transport regimes. After an initial quasi-ballistic delocalization during the first few femtoseconds

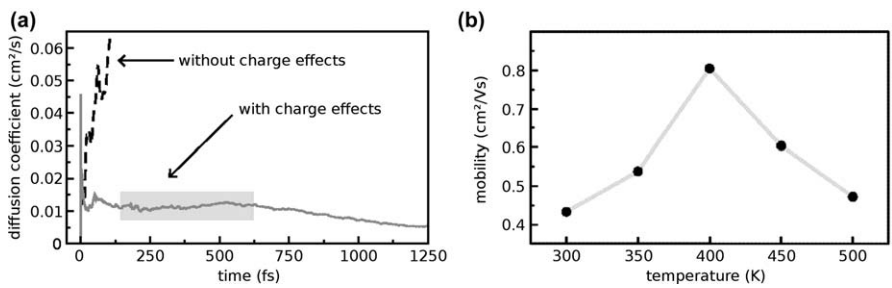

Figure 8.8 Hole transport characteristics in a one-dimensional coronene stack. (a) Time-dependent diffusion coefficient calculated for the coronene stack at a temperature of 300 K. The grey line corresponds to a simulation, where explicit effects of the charge carrier wave function on the molecular dynamics and the electronic structure are included giving a diffusive-like transport regime (shaded box from 170 to 600 fs). In contrast, a simulation without these charge effects leads to a ballistic-like behavior of the diffusion coefficient as shown by the black dashed line. (b) Temperature-dependent hole mobility calculated from the nearly time-independent diffusion coefficient.
Adapted from ref. 60.

giving a steep linear increase of the diffusion coefficient, the motion of the charge carrier becomes diffusive, which enables one to determine a nearly time-independent diffusion coefficient between 170 and 600 fs (see shaded region in Figure 8.8a). The following slight decrease of the diffusion constant can be associated with the irreversible trapping process at molecule 10.

Based on the nearly time-independent diffusion coefficient the charge carrier mobility $\mu(T)$ can also be determined for different temperatures by using the Einstein relation:

$$\mu(T) = \frac{D}{k_B T} \tag{8.49}$$

The corresponding results are shown in Figure 8.8(b). Basically, we find a maximum of the mobility for temperatures around 400 K, which is in agreement with experiments reporting a similar temperature dependence of the mobility for similar systems.[83] The increase of mobility for temperatures from 300 to 400 K can be explained by a more effective coupling along the stack caused by thermal fluctuations. For even higher temperatures, the further increased dynamical disorder weakens the π–π coupling and, thus, results in a reduction of the mobility, which is consistent with the experimentally observed sublimation region.[84]

Two-Dimensional Pentacene System. Now, we focus on the characterization of the diffusive motion of the charge carriers in the pentacene system depicted in Figure 8.4(b). The simulations are performed at the same level of theory as used for coronene. The time series of the populations of each molecular site is displayed in Figure 8.9 for a temperature of 300 K. Initially, the hole is completely localized on molecule 1 but becomes

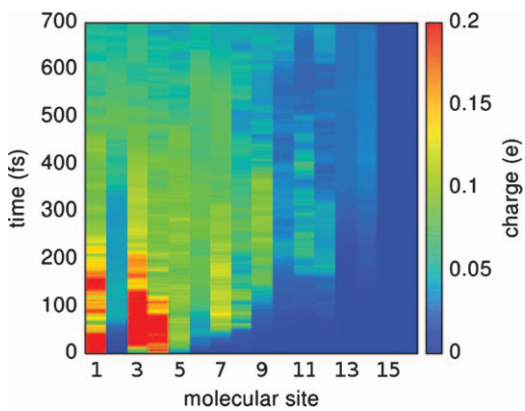

Figure 8.9 Hole dynamics in a two-dimensional pentacene system at 300 K. The wave function is visualized as a function of time and of the populated molecular sites.

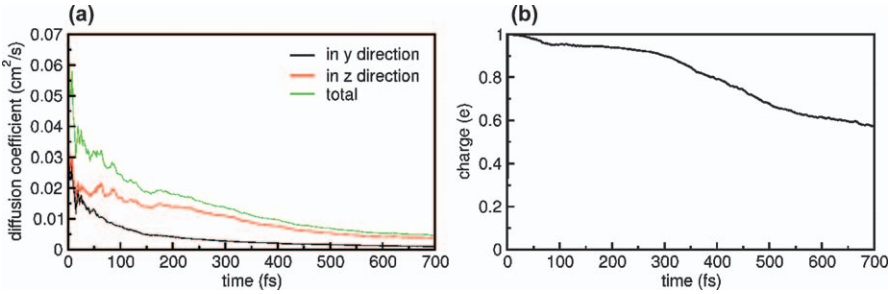

Figure 8.10 Analysis of the diffusion constant for a two-dimensional pentacene system at 300 K. (a) Time series of the total diffusion constant as well as the diffusion constants in the y and z direction. (b) Total charge population of the system with respect to time.

rapidly delocalized. Already after 50 fs, the charge carrier wave function is considerably distributed over nine molecular sites and has already reached the traps indicated by a decreasing total population of the system (Figure 8.10b), and after 150 fs the hole is completely delocalized over the whole model system. This strong delocalization is in clear contrast to the observations made for the one-dimensional coronene stack and can be assigned to the higher dimensionality of the system.

The time-dependent diffusion coefficient $D_i(t)$ in x_i direction is calculated with Eq. (8.48). The time series of the diffusion coefficients in the y and z directions (for the definition of the axes see Figure 8.4b) as well as the total diffusion coefficient are presented in Figure 8.10a). The diffusion coefficient in the z direction is higher than in y direction because of a clearly limited model system in the y direction and a higher number of conduction channels in the z direction. One can divide the displayed data into three intervals showing a different time behavior. Corresponding to the highly localized starting conditions, the diffusion coefficient is initially high according to a pseudo-ballistic transport leading to a fast delocalization process. Afterwards, the diffusion coefficient decays rapidly with an increasing delocalization of the charge carrier wave function. Owing to the very fast motion in the first 100 fs, the first fractions of the charge carrier wave function are trapped as shown in Figure 8.10(b). Between 100 fs and 200 fs, the charge carrier experiences a short diffusion process mostly in the z direction with a relatively constant diffusion constant D_z enabling one to determine the related charge carrier mobility μ_z. By averaging over the time period $t \in [100\text{ fs}; 200\text{ fs}]$, one obtains $D_z = 0.016\text{ cm}^2\text{ s}^{-1}$ and $\mu_z = 0.6\text{ cm}^2\text{ V}^{-1}\text{ s}^{-1}$, which is a realistic, but small, value compared to experimentally observed total mobilities between 1 and 10 $\text{cm}^2\text{ V}^{-1}\text{ s}^{-1}$ for ultrapure pentacene-based field-effect transistors.[85] This discrepancy might be caused by static effects because we performed our investigations on a slightly disordered supercell. The subsequent decay of the time series of the diffusion coefficient is affected by an increasing population of the traps. Basically, by choosing a larger model

system, the results for the charge mobility could be improved. Additionally, determination of the mobility in the y direction and accordingly an analysis of the transport anisotropy would become possible, but the application of the propagation scheme is limited by the required computational effort to the investigated system size. Nevertheless, we could successfully show that this charge transport model is indeed applicable for higher-dimensional charge transport materials and it is able to reproduce experimental values for the charge carrier mobility.

8.6 Résumé

In this chapter we have tried to give an overview of various frameworks to simulate charge transport in organic semiconductors. The literature is full of different transport approaches and often it is difficult to make a comparison as different assumptions in these approaches are made that are not closely related to one another, or the methods are targeting different situations and regimes.

Here we focused on techniques that are based on a full quantum description or on mixed classical–quantum propagation schemes. Unfortunately, space is not sufficient here to deepen these further or to include more approaches. Fortunately, in the accompanying Chapter 9 presents complementary techniques based on kinetic Monte Carlo simulations. We also had to leave out approaches based on different kinds of disorder models. In addition, we would have liked to show the performance of the presented approaches in more detail than was possible above but have chosen to focus more on the fundamentals and basic concepts which should be of high value to the reader. Therefore, we have discussed only a few illustrative examples which are directly related to experimental systems and have compared them to available transport measurements. A comparative study would be desirable to get an idea of the possible relative performances of the various approaches and their computational costs, which is left for future research.

On the other hand, we believe that future research might not converge to a silver-bullet type of approach for all possible situations but that the coexistence of different methodologies can be useful to target different questions in such complex materials (which are the subject of this volume) on various levels such that effort and insight is in reasonable balance.

Very important goals towards understanding molecular materials are high specificity of the modeling and predictability of the theoretical description. Concerning specificity it is commonly accepted that *ab initio* simulations are necessary to obtain reliable material parameters for electronic properties and electron–phonon couplings. We have shown in this chapter different routes to obtain these. Concerning predictability, we believe that there is still some way to go as today the simulation of quantitative values for carrier mobilities has still not been demonstrated convincingly. This remains therefore a general objective for future research.

Acknowledgements

We gratefully acknowledge support from the German Excellence Initiative *via* the Cluster of Excellence EXC 1056 ''Center for Advancing Electronics Dresden'' (cfAED). Additionally, this work was partially supported by the Heinrich Böll Stiftung e.V. Computational resources were provided by the Center for Information Services and High Performance Computing (ZIH) of Dresden University of Technology.

References

1. C. W. Tang and S. A. Van Slyke, *Appl. Phys. Lett.*, 1987, **51**, 913.
2. J. H. Burroughes, D. D. C. Bradley, A. R. Brown, R. N. Marks, K. Mackay, R. H. Friend, P. L. Burns and A. B. Holmes, *Nature*, 1990, **347**, 539.
3. C. Murawski, K. Leo and M. C. Gather, *Adv. Mater.*, 2013, **25**, 6801.
4. S. Reineke, M. Thomschke, B. Lüssem and K. Leo, *Rev. Mod. Phys.*, 2013, **85**, 1245.
5. J. Ouyang, C. Chu, C. R. Szmanda, L. Ma and Y. Yang, *Nature*, 2004, **3**, 918.
6. Q.-D. Ling, D.-J. Liaw, C. Zhu, D. S.-H. Chan, E.-T. Kang and K.-G. Neoh, *Prog. Polym. Sci.*, 2008, **33**, 917.
7. G. Horowitz, *Adv. Mat.*, 1998, **10**, 365.
8. M. E. Gershenson, V. Podzorov and A. F. Morpurgo, *Rev. Mod. Phys.*, 2006, **78**, 973.
9. H. Sirringhaus, *Adv. Mater.*, 2005, **17**, 2411.
10. C. Lungenschmied, G. Dennler, H. Neugebauer, S. N. Sariciftci, M. Glatthaar, T. Meyer and A. Meyer, *Sol. Energy Mater. Sol. Cells*, 2007, **91**, 379.
11. M. Riede, B. Lussem, K. Leo, *Comprehensive Semiconductor Science and Technology*, ed. P. Bhattacharya, R. Fornari, and H. Kamimura, Elsevier, Amsterdam, 2011, pp. 448–507.
12. J.-L. Brédas, J. E. Norton, J. Cornil and V. Coropceanu, *Acc. Chem. Res.*, 2009, **42**, 1691.
13. M. Riede, C. Uhrich, J. Widmer, R. Timmreck, D. Wynands, G. Schwartz, W.-M. Gnehr, D. Hildebrandt, A. Weiss, J. Hwang, S. Sundarraj, P. Erk, M. Pfeiffer and K. Leo, *Adv. Funct. Mater.*, 2011, **21**, 3019.
14. Y. Yang and A. J. Heeger, *Nature*, 1994, **372**, 344.
15. H. Kleemann, A. A. Günther, K. Leo and B. Lüssem, *Small*, 2013, **9**, 3670.
16. S. Steudel, V. A. K. Myny, C. Deibel, S. de Vusser, J. Genoe and P. Heremans, *Nat. Mat.*, 2005, **4**, 597.
17. H. Kleemann, S. Schumann, U. Jörges, F. Ellinger, K. Leo and B. Lüssem, *Org. Electron.*, 2012, **13**, 1114.
18. T. Holstein, *Ann. Phys.*, 1959, **8**, 343.
19. V. Coropceanu, J. Cornil, D. A. da Silva Filho, Y. Olivier, R. Silbey and J.-L. Brédas, *Chem. Rev.*, 2007, **107**, 926.

20. F. Ortmann, F. Bechstedt and K. Hannewald, *Phys. Rev. B*, 2009, **79**, 235206.
21. D. Ryndyk, R. Gutiérrez, B. Song, G. Cuniberti, *Energy Transfer Dynamics in Biomaterial Systems, Springer Series in Chemical Physics*, vol. 93, ed. I. Burghardt, V. May, D. A. Micha, and E. R. Bittner, Springer, Berlin Heidelberg, 2009, pp. 213–335.
22. L. Wang, Q. Li, Z. Shuai, L. Chen and Q. Shi, *Phys. Chem. Chem. Phys.*, 2010, **12**, 3309.
23. G. Nan, L. Wang, X. Yang, Z. Shuai and Y. Zhao, *J. Chem. Phys.*, 2009, **130**, 024704.
24. R. A. Marcus, *Rev. Mod. Phys.*, 1993, **65**, 599.
25. G. R. Hutchison, M. A. Ratner and T. J. Marks, *J. Am. Chem. Soc.*, 2005, **127**, 2339.
26. M. Schrader, R. Fitzner, M. Hein, C. Elschner, B. Baumeier, K. Leo, M. Riede, P. Bäuerle and D. Andrienko, *J. Am. Chem. Soc.*, 2012, **134**, 6052.
27. W. F. Pasveer, J. Cottaar, C. Tanase, R. Coehoorn, P. A. Bobbert, P. W. M. Blom, D. M. de Leeuw and M. A. J. Michels, *Phys. Rev. Lett.*, 2005, **94**, 206601.
28. S. H. Lin, C. H. Chang, K. K. Liang, R. Chang, Y. J. Shiu, J. M. Zhang, T.-S. Yang, M. Hayashi, F. C. Hsu, *Advances in Chemical Physics*, John Wiley & Sons Inc., Hoboken, 2002, pp. 1–88.
29. R. Kubo, *J. Phys. Soc. Jap.*, 1957, **12**, 570.
30. G. D. Mahan, *Many-Particle Physics*, Kluwer Academic Publishers, New York, 2000.
31. T. Holstein, *Ann. Phys.*, 1959, **8**, 325.
32. K. Hannewald, V. M. Stojanovic, J. M. T. Schellekens, P. A. Bobbert, G. Kresse and J. Hafner, *Phys. Rev. B*, 2004, **69**, 075211.
33. B. Thole, *Chem. Phys.*, 1981, **59**, 341.
34. P. Löwdin, *J. Chem. Phys.*, 1950, **18**, 365.
35. F. Ortmann, K. Hannewald and F. Bechstedt, *Appl. Phys. Lett.*, 2008, **93**, 222105.
36. F. Ortmann, F. Bechstedt and K. Hannewald, *Phys. Stat. Sol.*, 2011, **248**, 511.
37. F. Ortmann, K. Hannewald and F. Bechstedt, *J. Phys. Chem. B*, 2009, **113**, 7367.
38. Y. Li, Y. Yi, V. Coropceanu and J.-L. Brédas, *Phys. Rev. B*, 2012, **85**, 245201.
39. Y. Yi, V. Coropceanu and J.-L. Brédas, *J. Chem. Phys.*, 2012, **137**, 164303.
40. H. Bässler, *Phys. Stat. Sol. (b)*, 1993, **175**, 15.
41. S. Fratini and S. Ciuchi, *Phys. Rev. Lett.*, 2003, **91**, 256403.
42. V. M. Kenkre, J. D. Andersen, D. H. Dunlap and C. B. Duke, *Phys. Rev. Lett.*, 1989, **62**, 1165.
43. K. Hannewald and P. A. Bobbert, *Phys. Rev. B*, 2004, **69**, 075212.
44. Y. C. Cheng and R. J. Silbey, *J. Chem. Phys.*, 2008, **128**, 114713.
45. M. Hultell and S. Stafström, *Chem. Phys. Lett.*, 2006, **428**, 446.

46. A. Troisi and G. Orlandi, *Phys. Rev. Lett.*, 2006, **96**, 086601.
47. S. Ciuchi, S. Fratini and D. Mayou, *Phys. Rev. B*, 2011, **83**, 081202.
48. K. S. Radke, R. Scholz, F. Ortmann, K. Leo and G. Cuniberti, *J. Phys. Chem. C*, 2014, **118**, 6537.
49. V. M. Kenkre, *Phys. Lett. A*, 2002, **305**, 443.
50. J. M. Ziman, *Electrons and Phonons*, Clarendon Press, Oxford, 2001.
51. D. K. Ferry, *Semiconductor Transport*, Taylor & Francis, London, 2000.
52. F. Ortmann, F. Bechstedt and K. Hannewald, *New J. Phys.*, 2010, **12**, 023011.
53. N. Karl, *Organic Semiconductors*, Springer, Berlin, 1985, pp. 106–218.
54. K. Hannewald and P. A. Bobbert, *Appl. Phys. Lett.*, 2004, **85**, 1535.
55. D. A. da Silva Filho, E.-G. Kim and J.-L. Brédas, *Adv. Mater.*, 2005, **17**, 1072.
56. F. Ortmann, K. Hannewald and F. Bechstedt, *Phys. Rev. B*, 2007, **75**, 195219.
57. R. A. Marcus and N. Sutin, *Biochim. Biophys. Acta*, 1985, **811**, 265.
58. R. A. Marcus, *Rev. Mod. Phys.*, 1993, **65**, 599.
59. F. Ortmann and S. Roche, *Phys. Rev. B*, 2011, **84**, 180302(R).
60. C. Gollub, S. Avdoshenko, R. Gutierrez, Y. Berlin and G. Cuniberti, *Isr. J. Chem.*, 2012, **52**, 452.
61. D. Tannor, *Introduction to Quantum Mechanics: A Time-dependent Perspective*, University Science Books, 2007.
62. K. S. Radke, *Diploma Thesis*, TU Dresden, 2011.
63. G. te Velde, F. M. Bickelhaupt, E. J. Baerends, C. Fonseca Guerra, S. J. A. van Gisbergen, J. G. Snijders and T. Ziegler, *J. Comput. Chem.*, 2001, **22**, 931.
64. C. Fonseca Guerra, J. G. Snijders, G. te Velde and E. J. Baerends, *Theor. Chem. Acc.*, 1998, **99**, 391.
65. E. J. Baerends, T. Ziegler, J. Autschbach, D. Bashford, A. Berces, F. M. Bickelhaupt, C. Bo, P. M. Boerrigter, L. Cavallo, D. P. Chong, L. Deng, R. M. Dickson, D. E. Ellis, M. van Faassen, L. Fan, T. H. Fischer, C. Fonseca Guerra, A. Ghysels, A. Giammona, S. J. A. van Gisbergen, A. W. Götz, J. A. Groeneveld, O. V. Gritsenko, M. Grüning, S. Gusarov, F. E. Harris, P. van den Hoek, C. R. Jacob, H. Jacobsen, L. Jensen, J. W. Kaminski, G. van Kessel, F. Kootstra, A. Kovalenko, M. V. Krykunov, E. van Lenthe, D. A. McCormack, A. Michalak, M. Mitoraj, J. Neugebauer, V. P. Nicu, L. Noodleman, V. P. Osinga, S. Patchkovskii, P. H. T. Philipsen, D. Post, C. C. Pye, W. Ravenek, J. I. Rodríguez, P. Ros, P. R. T. Schipper, G. Schreckenbach, J. S. Seldenthuis, M. Seth, J. G. Snijders, M. Sola, M. Swart, D. Swerhone, G. te Velde, P. Vernooijs, L. Versluis, L. Visscher, O. Visser, F. Wang, T. A. Wesolowski, E. M. van Wezenbeek, G. Wiesenekker, S. K. Wolff, T. K. Woo, A. L. Yakovlev, *SCM*, Theoretical Chemistry, Vrije Universiteit Amsterdam, 2010.
66. F. C. Grozema, S. Tonzani, Y. A. Berlin, G. C. Schatz, L. D. A. Siebbeles and M. A. Ratner, *J. Am. Chem. Soc.*, 2008, **130**, 5157.
67. G. Lindblad, *Commun. Math. Phys.*, 1973, **33**, 305.

68. G. Lindblad, *Commun. Math. Phys.*, 1974, **39**, 111.
69. G. Lindblad, *Commun. Math. Phys.*, 1976, **48**, 119.
70. L. Pesce, *PhD Thesis, Freie Universität Berlin*, 1998.
71. J. P. Perdew, K. Burke and Y. Wang, *Phys. Rev. B*, 1996, **54**, 16533.
72. J. P. Perdew, K. Burke and M. Ernzerhof, *Phys. Rev. Lett.*, 1996, **77**, 3865.
73. T. H. Dunning, *J. Chem. Phys.*, 1989, **90**, 1007.
74. S. Goedecker, M. Teter and J. Hutter, *Phys. Rev. B*, 1996, **54**, 1703.
75. J. H. C. Hartwigsen, S. Goedecker and J. Hutter, *Phys. Rev. B*, 1998, **58**, 3641.
76. M. Krack, *Theor. Chem. Acc.*, 2005, **114**, 145.
77. J. VandeVondele and J. Hutter, *J. Chem. Phys.*, 2007, **127**, 114105.
78. C. M. Baker, V. M. Anisimov and A. D. MacKerell, *J. Phys. Chem. B*, 2011, **115**, 580.
79. X. Feng, V. Marcon, W. Pisula, M. R. Hansen, J. Kirkpatrick, F. Grozema, D. Andrienko, K. Kremer and K. Müllen, *Nat. Mater.*, 2009, **8**, 421.
80. L. Wang, Q. Li, Z. Shuai, L. Chen and Q. Shi, *Phys. Chem. Chem. Phys.*, 2010, **12**, 3309.
81. B. Aradi, B. Hourahine and T. Frauenheim, *J. Phys. Chem. A*, 2007, **111**, 5678.
82. M. Elstner, D. Porezag, G. Jungnickel, J. Elsner, M. Haugk, T. Frauenheim, S. Suhai and G. Seifert, *Phys. Rev. B*, 1998, **58**, 7260.
83. A. M. v. d. Craats, J. M. Warman, A. Fechtenkötter, J. D. Brand, M. A. Harbison and K. Müllen, *Adv. Mater.*, 1999, **11**, 1469.
84. R. M. Stephenson and S. Malanowski, *Handbook of the Thermodynamics of Organic Compounds*, Springer, The Netherlands, 1987, pp. 1–471.
85. B. Stadlober, M. Zirkl, M. Beutl, G. Leising, S. Bauer-Gogonea and S. Bauer, *Appl. Phys. Lett.*, 2005, **86**, 242902.

CHAPTER 9

Simulations of Morphology and Charge Transport in Supramolecular Organic Materials

DENIS ANDRIENKO

Max Planck Institute for Polymer Research, Ackermannweg 10,
55128 Mainz, Germany
Email: denis.andrienko@mpip-mainz.mpg.de

9.1 Introduction

Conjugated polymers and cyclic π-systems have been studied for almost a decade in order to develop various optoelectronic devices, such as light-emitting diodes, field effect transistors, optically pumped lasers, and organic solar cells. Progress in the field has been remarkable, with the recently announced 12% efficient organic solar cells and light emitting diodes (OLEDs), having already entered the market of flat panel displays and lighting applications. Despite these advancements, there is still a lack of understanding of the fundamental processes taking place in the active layers of such devices, hindering further development. This is, however, hardly surprising considering the complexity of the processes involved, where one needs to have a thorough understanding of a system's behavior on multiple time- and length-scales.

RSC Smart Materials No. 12
Supramolecular Materials for Opto-Electronics
Edited by Norbert Koch

Published by the Royal Society of Chemistry, www.rsc.org

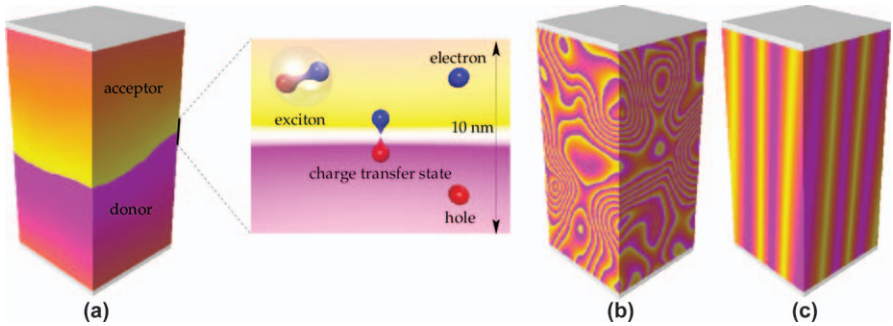

Figure 9.1 (a) Basic mechanisms of a solar cell function: exciton creation, diffusion, dissociation at the donor–acceptor interface; charge separation and diffusion towards the electrodes. (b) Morphology with a large surface/volume ratio and efficient charge separation. (c) Morphology with efficient charge transport towards electrodes in addition to efficient charge separation.

In an organic solar cell, for example, light absorption leads to the generation of excited, strongly-bound electron–hole pairs (excitons) (Figure 9.1a). To achieve substantial energy conversion efficiencies, these need to be dissociated into free charge carriers with a high yield. Free charge carriers, in turn, should be able to diffuse towards the electrodes such that they can be injected into an external circuit. Hence, to increase the efficiency of a solar cell, one should reduce the bandgap of the absorbing molecule (*e.g.* by using the donor–acceptor molecular architecture), engineer the level alignment at the heterojunction to have efficient splitting of Frenkel excitons into charge transfer states, and increase the charge mobility in the mesophases to reduce the non-geminate recombination. All of these processes are sensitive to the morphology of the blend (examples shown in Figure 9.1b,c).

Similarly, in a phosphorescent OLED, electrons and holes are injected into the transport layers *via* the electrodes, which ensures their balanced delivery to the emission layer (EML). To allow for triplet-harvesting, the EML consists of an organic semiconductor (host) doped by an organo-metallic emitter (guest). Excitation of the emitter can be achieved either by an energy transfer process, *i.e.* by the formation of an exciton on a host molecule and a subsequent energy transfer to the dopant, or by a direct charge transfer process. In the latter case, one of the charge carriers is trapped on the emitter and attracts a charge of the opposite sign, forming a neutral exciton on-site. This is argued to lead to more efficient OLEDs as compared to cases where excitation occurs by energy transfer. The goal is therefore to achieve a sufficiently fast charge/energy transport dynamics within the EML, while taking into account the interplay between the molecular electronic structure, the morphological order, and the relative alignment of the transport/excited state energy levels of the host and the guest.

Thus, it seems that a roadmap for the computer-based optimization of organic semiconductors is well-defined: One needs to predict the material's

morphology, calculate the energetic landscape for elementary excitations (*i.e.* charges and excitons), evaluate rates of various processes (*i.e.* charge/exciton transfer, geminate/non-geminate recombination), solve the time-dependent master equation, and analyze distributions of currents and occupation probabilities to extract/optimize measurable properties such as open-circuit voltage, short circuit current for solar cells, and color, efficiency, and lifetime for OLEDs. This would comprise a solution to the so-called ''forward'' (structure to property) problem. Repeating this procedure for a set of computer-generated compounds, these could then be pre-screened prior to their actual synthesis. One might even imagine the possibility of inverting the structure–property relationships by using machine-learning techniques and appropriate molecular descriptors.

In reality, however, the computer design of organic semiconductors has yet to reach this level of competence. In most cases, direct synthesis and characterization of a particular compound is still faster, easier and in most cases more reliable than computer-based predictions of its properties. The question is – Why? There are, in fact, several reasons for this. First of all, solving the forward problem is a non-trivial, interdisciplinary task (Figure 9.2), which requires the combined knowledge of quantum chemistry (molecular electronic structure, couplings, rates), statistical physics (self-assembly, drift-diffusion dynamics, optics), and engineering (device geometry, light in- and out-coupling).

Second, it is also a multiscale problem: On a molecular scale, every molecule has its own unique environment created by its neighbors with local

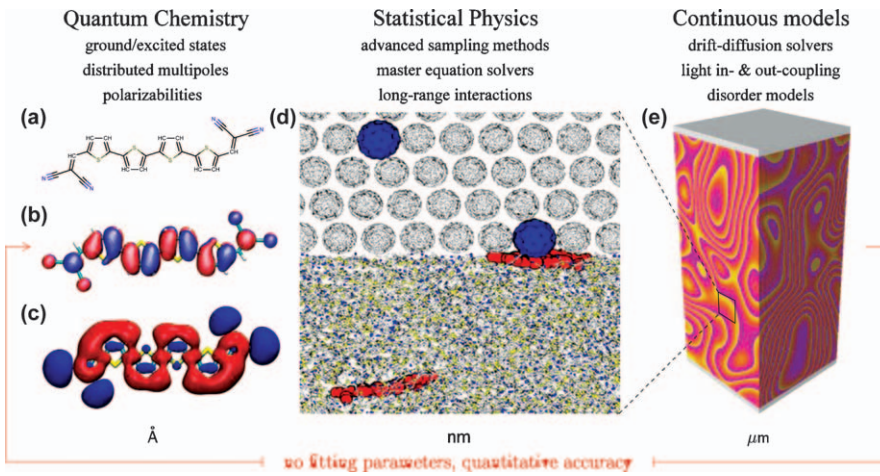

Figure 9.2 Multiscale nature of processes in organic materials. (a)–(c) Properties of isolated molecules used for accurate descriptions of electrostatic and polarization effects. (d) Simulations of large-scale atomistic morphologies using coarse-grained and force-field based models. Efficient solvers for the master equation with configuration-dependent rates. (e) Accurate parameterization of macroscopic descriptions.

electric fields leading to level shifts, broadening, and spatial correlations of charge/exciton energies. On a mesoscopic scale, the size of phase-separated domains of the donor and acceptor governs the efficiency of exciton splitting and charge percolation in a solar cell; the connectivity of the guest molecules in a host matrix determines the efficiency with which charges are delivered to the phosphorescent guest. In addition, on a macroscopic scale, light in–out-coupling needs to be accounted for to maximize absorption and emission. Likewise, the typical time scales of dynamic processes such as charge and energy transfer span several orders of magnitude. Hence, charge/exciton kinetics cannot be treated *via* numerical methods with a fixed time step, but rate-based descriptions must be employed instead.

Finally, to be predictive, the methods need to be quantitative. That is, not only each particular method is required to provide accurate values for the quantities of interest but the entire procedure of ''bottom-up scaling'' from the micro- to the macroscopic world should be robust. To illustrate this, let us focus on exciton and charge transport in a solar cell. Here, the energetic landscape is crucial for the excitation mobility. The main contributions to this landscape are from the (long-range) electrostatic interactions between the charged molecule and its environment, as well as excitation stabilization due to the polarization of its surroundings. To describe long-range interactions, cutoffs as large as 5–10 nm are required to accurately predict site energies. Systems of these sizes simply cannot be treated using first principles and an adequate classical representation needs to be employed. For excited states (*e.g.* Frenkel excitons), classical treatments alone are infeasible and QM/MM techniques are required. With the site energies at hand, one can evaluate the rates, which in general exponentially depend on site energy differences. This implies that all errors made when evaluating the energetic landscape will propagate into, for example, the charge mobility, exponentially. Therefore, an error propagation assessment at every level of parameter transfer is essential.

To this end, three distinct directions of modeling organic semiconductors have been pursued. At the most coarse level, *continuum* drift-diffusion equations have been employed to interpret experimental data, *e.g.* current–voltage characteristics.[1–3] This type of modeling is based on generic physical principles: only a few material-specific parameters, such as dielectric constants, charge carrier and exciton mobilities, diffusion constants, and creation/recombination rates, enter the equations. The continuum approach helps to analyze and optimize complex multilayered devices, but it by no means is limited to the device-engineering tasks. It can also be used to establish universal relationships between device parameters, for example the relation between the open-circuit voltage of a solar cell, the difference between the electron affinity and ionization potential of the acceptor and the donor materials, and the value of the short circuit current.[4,5]

The use of the continuum approach would not be possible without prior knowledge of charge/exciton diffusion constants, mobilities, injection barriers, *etc.* In organic semiconductors, these quantities have a non-trivial

dependence on the external field, the charge density, as well as the material's parameters. The generic expressions of these dependencies are often obtained by employing *mesoscale*-level descriptions. At the mesoscale, the electronic properties of single molecules and molecular pairs are coarse-grained into a few essential parameters, such as the hop attempt frequency, the hopping range, and the distributions and spatial correlations of the site energies. The morphological details are also ignored and regular lattices, potentially with a positional disorder, are used. The Gaussian-disorder family of models[6–12] has been particularly successful in providing analytical forms of these dependencies, helping to unveil the role of spatial correlations of the site energies on the field dependence of the charge mobility, as well as providing a unified description for mobility *versus* charge-carrier density for high and medium charge densities, achieved either in a field-effect transistor or a diode measurement.[13]

By construction, mesoscale models do not provide a direct link to the underlying chemical structure or material morphology. Moreover, model parameters must be extracted from experimental data, making material design and compound pre-screening virtually impossible. To remedy the situation, *microscopic* descriptions attempt to incorporate the molecular electronic structure and material's morphology into the charge/exciton transport models. A missing link between the micro- and mesoscales is normally introduced by employing more realistic charge/exciton transfer theories and by parameterizing the corresponding rates using first-principles calculations. This parametrization has to combine atomistic-level details of the material morphology with the information about the molecular electronic structure, and include accurate predictions of electrostatic and induction energies. Last but not least, efficient off-lattice master equation solvers with explicit Coulomb interactions must be used to study transport dynamics.

The aforementioned tasks are both computationally and methodologically challenging but definitely worth pursuing, as they help to establish the missing links between chemical structure, processing conditions, and the relevant macroscopic quantities of a device, *e.g.* open-circuit voltage in a solar cell or charge carrier distribution in an organic light emitting diode. Such links, or structure–property-processing relationships, help us to design new chemicals, optimize their processing, and enable compound pre-screening prior to their actual synthesis.

In what follows, we review the latest developments in microscale modeling of organic materials. This includes predictions of morphologies at an atomic level of detail (Section 9.2), charge/exciton transfer theories (Section 9.3.2), evaluation of electronic coupling elements (Section 9.3.3), site energies (Section 9.3.5), as well as methods required to solve the off-lattice master equation. Since the computational cost of microscopic approaches sets limits to accessible system sizes, special attention is paid to artifacts arising due to finite-size effects (Section 9.4), the truncation of long-range interactions (Section 9.6), and stochastic models which bridge the gap between the microscopic and mesoscopic worlds (Section 9.5).

9.2 Morphology Simulations

Let us first address the subject of the morphology. Molecular ordering in an organic semiconducting film can vary from completely amorphous to highly crystalline. The degree of ordering is often tunable by varying the chemical structure or processing conditions. In organic light emitting diodes, for example, where well-controlled homogeneous morphologies are required and high charge carrier mobilities are not essential, amorphous solids are used. As high charge carrier mobilities are needed in field effect transistors, single crystals or highly ordered polycrystalline films are employed. Similarly, in solar cells, high charge carrier mobilities in the donor and acceptor are required for efficient charge extraction. Excessive crystallinity can, however, be detrimental for the formation of a phase-separated morphology in a bulk heterojunction cell. In many cases, even ''highly crystalline'' organic semiconductors are only partially ordered in the active layer of a device. The morphological disorder can occur on different length scales, from local defects and grain boundaries to mixed amorphous/crystalline islands. Such morphological disorder can lead to energetic disorder (energetic traps) and large variations of electronic couplings (topological traps), hampering the transport of mobile charge carriers. To account for such effects, realistic models of molecular ordering must be capable of predicting the degree of molecular ordering, including the trap concentration. This is certainly one of the main challenges when it comes to modeling of morphologies at an atomistic level of detail. Another challenge is the supramolecular assembly of organic semiconductors: local molecular ordering coexists with large-scale heterogeneities, both equally important for efficient functionality. Thus, multiscale simulation techniques should be developed, capable of covering both length-scales, from ångströms to micrometers, as well as time-scales from femtoseconds to hours.

The theoretical and computational toolbox currently used to study self-assembling properties of organic materials is very versatile: On the highest level of resolution, it includes accurate quantum chemical calculations capable of predicting properties of isolated molecules. Less computationally demanding density functional methods can deal with much larger molecules and oligomers, including side chains, and are often used to compare ground state energies of experimentally proposed arrangements of atoms in a unit cell. To assess crystalline packing modes at ambient conditions and during annealing, as well as to study amorphous melts and longer chain lengths, classical force-fields are parametrized. To access even longer length- and time-scales (*i.e.* micrometers and microseconds) coarse-grained models are developed. The ultimate goal of these simulations is to self-assemble the compound *in silico*, *i.e.* to predict its polymorphs as well as the degree of disorder in the kinetically trapped molecular arrangements. The honest assessment, however, is that we are fairly far from achieving this goal. The main obstacles are the insufficient accuracy of the methods employed at a specific level of resolution, the long simulation times required to study

self-assembly, and the uncontrolled error propagation from one level to another, *e.g.* when parameterizing force-fields based on quantum chemical calculations or when developing coarse-grained models using force-field-generated reference data. In what follows, we summarize the available simulation techniques and point out which properties of single molecules and of molecular arrangements they are capable of providing.

9.2.1 First-Principles Calculations

Computationally demanding first principles calculations are mostly used to gain insight into the electronic structure, the ground state geometry of isolated molecules, and the properties of neutral periodic crystalline molecular arrangements. These calculations can, to some extent, serve as a guide for a qualitative understanding of properties of molecular assemblies. In the general case, however, processes in organic materials are extremely sensitive to the local molecular environment, the degree of long-range ordering, and the presence of defects and disorder. The results of first principles calculations should therefore be complemented by the environmental contributions. For computational efficiency, the latter are normally accounted for perturbatively, using classical force-fields. The parameters of these force-fields, *e.g.* distributed multipoles and polarizabilities, bonded and non-bonded interaction potentials, can also be obtained from first principles.[14–18]

However, first principles methods cannot be routinely applied in all cases, even for isolated organic molecules. A typical example here is the conjugated polymers (oligomers),[19–25] where the extended π-conjugation flattens the backbone, whereas the non-bonded interactions between consecutive repeat units (steric repulsions, Coulomb, and van der Waals interactions) often tend to distort the planarity. Typical energy differences between planar and non-planar conformations are of the order of 10 meV, which is the accuracy threshold of density functional methods. Hence, one is forced to use more accurate but computationally demanding quantum-chemical methods,[19] especially when parametrizing bonded interactions. At the same time, in conjugated polymers, the ground-state torsional angle between repeat units depends on the oligomer length and torsional potentials can be correlated up to a few nearest-neighbors.[25,26] This makes geometry predictions a formidable task, even for the case of isolated oligomers.

Another niche of research where first principles methods are employed is in studies of crystalline molecular arrangements. Here, density functional theory has been used to establish whether experimentally reported crystal structures correspond to well-defined energy minima.[23,27–29] Since the van der Waals interaction provides one of the major contributions to the cohesive energy of a crystal, density-functional approaches have to be complemented by either *ad hoc* terms[30,31] or using semi-classical approaches.[16,32,33] Similar to the situation with a single isolated chain, typical energy differences between diverse packing motives are of the order of

10 meV per unit cell and, hence, theoretical methods are at their accuracy limits, making it difficult to rank the different molecular arrangements. Note, that unit-cell optimizations and free energy estimates are often performed at 0 K, and so entropic effects are ignored.

Apart from force-field parameterizations, formation energies, and densities of states of crystalline arrangements, first principles methods can also be used to evaluate some of the ingredients of charge and exciton transfer rates and, in general, to study chemical reactions occurring upon the oxidation, reduction, and excitation of organic molecules. Representative examples are evaluations of electronic coupling elements between diabatic states (discussed in more detail in Section 9.3.3), reorganization energies (Section 9.3.4), and electron affinities and ionization potentials of isolated molecules. They are also imperative for identifying localized states in polymeric systems, where both strong and weak electronic couplings coexist in the same molecule and simple criteria for conjugation segments cannot be identified (Section 9.3.1). Finally, first principles methods can be used to parametrize model Hamiltonians, which are solved when charge transfer and nuclear dynamics occur on a similar timescale, or when nuclear dynamics are not harmonic and the analytical expression for the transfer rate is not available.[34–39] These approaches are discussed in more detail in the contribution of Ortmann, Radke, and Cuniberti in this book (Chapter 8).

9.2.2 Atomistic Models

To study larger systems and longer time-scales, various types of force fields are developed. These integrate out electronic degrees of freedom and operate with the (many-body) interaction potential between nuclei. The potential is used to propagate classical equations of motion, sample the phase space of the system in a specified ensemble, and evaluate averages of macroscopic observables. The basis functions used to represent the potential energy surface are often chosen according to chemical intuition and split into bonded (bonds, angles, torsions) and non-bonded (van der Waals, Coulomb) contributions, for which simple analytical expressions or tabulated functions can be used. A detailed overview of this classical approach can be found in several original works as well as textbooks.[16,40–42]

For the sake of computational efficiency, induction effects (molecular polarizabilities) are implicitly incorporated by adjusting partial charges and van der Waals interactions. Parametrizations of effective charges and Lennard-Jones parameters require experimental input such as transition temperatures, density, and other thermodynamic properties, and are often performed for a specific state point and a mesophase. Transferability to other compounds (*e.g.* from biological systems to organic semiconductors) is not guaranteed. The most common re-parametrization includes the adjustment of the equilibrium values for bond lengths and angles, the fitting torsional potentials to *ab initio* calculations, and the reparametrization of partial charges using the electrostatic potential fits of an isolated molecule.

A representative example is the gradual refinement of the P3HT force-field, where parameters of an existing force-field have first been refined in order to reproduce the torsional potential between thiophene units and electrostatic potential around an isolated oligomer[43,44] and, subsequently, to account for the change in the backbone potential with increasing oligomer length.[20,22,24,44–46]

A more computationally demanding, *polarizable* force-field incorporates induction effects *via* distributed polarizabilities and includes higher multipoles in the description of electrostatics. As such, it rigorously accounts (in a perturbative way) for electrostatic, induction,[14] and van der Waals[16] interactions on the same footing. Since all parameterizations can be performed from first principles, it is the only method that can be used for systematic pre-screening of new compounds. In large systems, however, the evaluation of induced dipoles requires a self-consistent solution of coupled non-linear equations, which is computationally demanding. Thus, in practice, such large-scale morphologies are simulated using standard (or adjusted) force-fields while site energies required for the evaluation of rates are computed using polarizable force-fields.[47–49]

Three typical examples of employing classical force-field simulations to analyze or even predict molecular alignment of organic semiconductors are shown in Figure 9.3: Figure 9.3(a) depicts lamellar arrangement of the conjugated polymer, regioregular P3HT,[44,50] obtained by equilibrating the experimentally known crystal structure of the P3HT polymorph I. Notably, even with these, classical descriptions, only highly crystalline morphologies and high-temperature amorphous melts can be studied. Figure 9.3(b) shows the vacuum-deposited layer of a small-molecule organic dye (DCV5T) on top of crystalline C_{60}, which assembles into a glassy phase with nematic ordering. Finally, Figure 9.3(c) shows an amorphous host/guest system generated by thermal annealing of a binary mixture of two organic compounds used in the active layer of an OLED.[51,52]

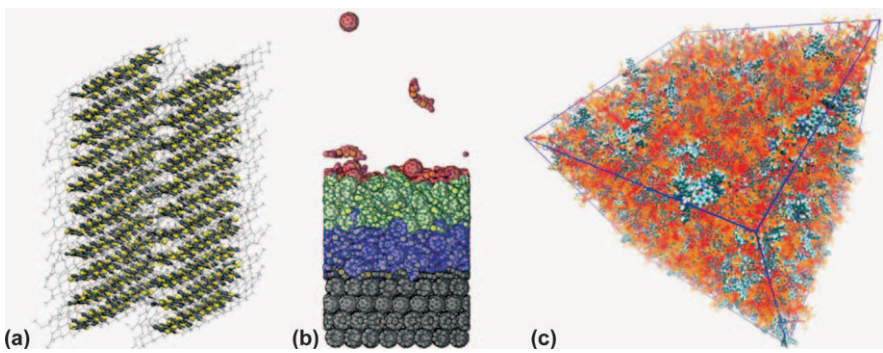

Figure 9.3 (a) Lamellar molecular arrangement of regioregular P3HT; (b) bulk heterojunction solar cell (C_{60} : DCV5T) simulated by depositing single molecules of C_{60} and DCV5T on top of a C_{60} crystal; (c) amorphous host–guest system of an active layer of an OLED.

9.2.3 Coarse-Grained Models

In many cases, not only local but also large-scale material ordering is essential for a functional device. Single grains in field-effect transistors or domain sizes of the donor and acceptor materials in a solar cell can, for example, be as large as several hundreds of nanometers. At the same time, the time-scales involved in some of the stages of material processing (solvent evaporation, annealing) can range anywhere from seconds up to hours. Such length- and time-scales cannot feasibly be reached by atomistic molecular dynamics simulations. One can, however, explore the fact that certain parts of the system evolve on much slower times and larger length-scales (*e.g.* a thiophene ring rotation in a polythiophene occurs on a much slower time-scale than a characteristic bond vibration). One can therefore combine several coherently moving atoms, connected *via* fast degrees of freedom (*e.g.* bonds), into a single interaction site. By doing this, we reduce the number of degrees of freedom to be propagated and, more importantly, obtain a much smoother potential energy landscape in terms of the coarse-grained degrees of freedom (softer interaction potentials, less friction), allowing one to simulate ten to hundred longer times and system sizes.

The coarse-graining procedure in itself involves three steps: choice of the coarse-grained degrees of freedom, identification of a merit function (norm), which quantifies the difference between the fine- and coarse-grained representations, and determination of the coarse-grained potential energy surface (PES). The entire procedure can be thought of as a projection of the fine- onto the coarse-grained PES and is therefore sensitive to the number and types of basis-functions employed in the CG representation. In practice, these are limited by the functional forms included in the coarse-grained force field, which usually exclude many-body contributions. To perform correct statistical sampling of the coarse-grained degrees of freedom, the potential of mean force should be used as their interaction potential,[54] which is inherently a many-body potential. The accuracy of the coarse-grained model thus becomes sensitive to the way the projection is performed as well as the number of basis functions that are used to represent the coarse-grained force-field.[55] Existing projection schemes either try reproducing various pair distribution functions (structure-based coarse-graining[56–59]), matching the forces,[54,60,61] minimizing the information loss in terms of relative entropy,[62] or using liquid state theory.[63] An extensive overview of such coarse-graining techniques is provided in ref. 64.

In the field of organic semiconductors, one of the most challenging tasks is to quantify the self-organizing abilities of a material solely based on its chemical structure. Relevant self-assembled structures in this field are lamellar arrangements of conjugated polymers, partially crystalline phases of a small-molecule donor/acceptor material, or molecular alignments at the interface between the organic layers. Since these require systems on the order of (hundreds of) thousands of molecules, various coarse-grained models have been developed.[65–69]

A typical example of a coarse-grained model is the three-site model developed for P3HT. Here, the P3HT monomers are coarse-grained into three interaction sites placed at the center-of-mass of each of the thiophene rings and on every three methyl groups of the hexyl side-chain. This model is capable of reproducing the lamellar molecular arrangements of P3HT, as well as the phase separation observed in P3HT/PCBM blends.[68,70]

Often, the accuracy of the coarse-grained model can be improved by explicitly incorporating information about macroscopic properties of the system, *i.e.* its equation of state or the symmetry of its mesophase.[71,72] Moreover, one can further reduce the number of degrees of freedom by introducing anisotropic interaction potentials. An example of such a model with soft interaction potentials is shown in Figure 9.4. Here, all of the non-bonded interactions are chosen such that the system has a desired phase behavior (biaxial nematic to nematic to isotropic phase transition) while all of the torsion and dihedral angle distributions reproduce those of the underlying isolated atomistic chain in θ-solvent conditions.[53] Using this model, one can equilibrate systems as large as $50\times50\times50$ nm^3, containing 5×10^5 chains with 32 monomers per chain. The model predicts reasonable values for the persistence length and Frank elastic constants and also provides some insight into how the collective orientation of backbones affects the energetic landscape for drift-diffusion of charges, which turns out to be spatially correlated even without taking long-range Coulomb interactions into account.

Finally, the most coarse models for morphology simulations employ field-theoretical descriptions, *e.g.* the self-consistent field theory method with the Flory–Huggins Cahn–Hillard functional. The bulk heterojunction morphologies,[73–77] generated by this method, can be used as input for either a self-consistent solution of the continuity-transport equations for electrons, holes, and excitons in conjunction with Poisson's equation[73,76–79] or they can be coupled to a suitable kinetic Monte Carlo algorithm.[74,75,80] These approaches help us to study the effect of boundary conditions on

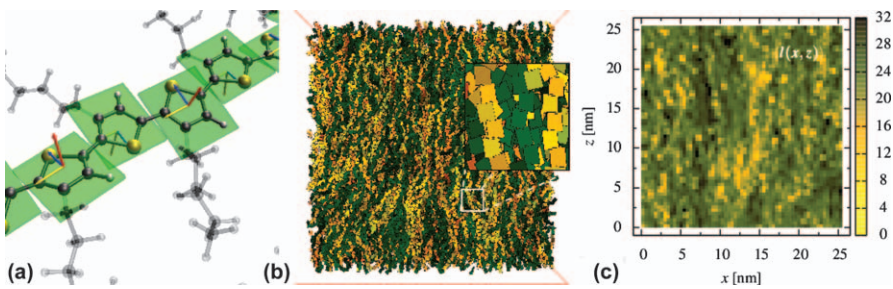

Figure 9.4 (a) Atomistic and coarse-grained representation of a P3HT side chain. (b) Biaxial nematic alignment in a melt of P3HT chains. (c) Spatially-correlated distribution of conjugation segments, leading to a correlated energetic landscape.
Adapted with permission from ref. 53. Copyright (2013) American Chemical Society.

self-assembly and orientation of lamellar phases, as well as the influence of the degree of phase separation and ordering on the photovoltaic device characteristics.

9.3 Charge Transport

We will now discuss the simulation techniques used to assess semiconducting properties of organic materials, in particular the charge carrier mobility. Since a first-principles-based analysis of non-equilibrium electron transport in these materials is computationally infeasible, one has to decide upon an appropriate model for charge transport, or a model Hamiltonian. For perfectly ordered crystalline organic semiconductors, the Drude model based on band theory is often used, where the charge mobility is determined from the mean relaxation time of the band states and the effective mass of the charge carrier.[81–83] Such band-based models can be further extended to account for electron–phonon coupling.[34,39,84] At ambient conditions, however, the thermal fluctuations of the non-local electron–phonon coupling or the transfer integral can become of the same order of magnitude as its average value, such that charge transport becomes diffusion-limited by thermal disorder. The corresponding description (semiclassical dynamics) can be achieved by using a Hamiltonian with interacting electronic and nuclear degrees of freedom.[38] If the nuclear dynamics are much slower than the dynamics of the charge carrier while the electronic coupling is weak, a Hamiltonian with a static disorder is assumed with an electronic density of localized states and hopping rates between them. The latter approach is often used to study amorphous and partially ordered small-molecule-based organic semiconductors. Hopping rates can be postulated empirically as in the Gaussian disorder models[8] or evaluated from quantum-chemical calculations and combined with various charge transfer theories as discussed in Section 9.3.2.

The appropriate description for a particular material model is often predetermined by experiment. For example, an increase in the mobility with rising temperature is often interpreted as a sign of *temperature-activated hopping* transport, with localized charges (charged states) and thermally activated (sometimes tunneling-assisted) charge transfer reactions. Charge localization allows one to cast charge transport as a series of charge transfer reactions. If the charge transfer rates of these reactions are known, the resulting master equation for the occupation probabilities of localized states can be used to study charge dynamics in the system. The solution to the master equation provides information about the charge distribution and currents, and eventually the mobility, all as a function of temperature, the external field, the charge density, and, importantly, the underlying morphology. In what follows, we first introduce the quantities necessary for describing charge transfer reactions, then discuss the simulation techniques required for their evaluation, and finally illustrate how to solve the master equation to obtain the charge carrier mobility.

9.3.1 Diabatic States

The first-principles description of a charge transfer, or an oxidation–reduction reaction, of type $A^{-}B \rightarrow AB^{-}$ can be obtained by analyzing solutions to the Schrödinger equation with a dimer Hamiltonian:

$$\hat{H} = \frac{\hbar^2}{2m_e}\sum_i \nabla_i^2 - \sum_{i,I}\frac{Z_I e^2}{|\vec{r}_i - \vec{R}_I|} + \frac{1}{2}\sum_{i\neq j}\frac{e^2}{|\vec{r}_i - \vec{r}_j|} - \sum_I \frac{\hbar^2}{2M_I}\nabla_I^2 + \frac{1}{2}\sum_{I\neq J}\frac{Z_I Z_J e^2}{|\vec{R}_I - \vec{R}_J|}, \tag{9.1}$$

where the nuclei of a dimer AB with charges $Z_I e$ and masses M_I are located at positions $\vec{R}_I$ and electronic coordinates are denoted as $\vec{r}_i$. A practical way of solving this equation is to introduce the Born–Oppenheimer approximation, which assumes that electronic motion in a specific state of a system occurs on significantly faster time-scales than the motion of the nuclei. This allows one to separate the electronic and nuclear degrees of freedom and to solve the electronic Hamiltonian, assuming a parametric dependence on the nuclear degrees of freedom. The solution of the electronic Hamiltonian, that is, a set of orthogonal *adiabatic* states $\phi_\nu(\vec{r};\vec{R})$, can be used to expand the molecular wavefunction:

$$\psi(\vec{r};\vec{R}) = \sum_\nu \chi_\nu(\vec{R})\varphi_\nu(\vec{r};\vec{R}) \tag{9.2}$$

After substituting this expansion into the Schrödinger equation, we obtain a set of coupled equations for $\chi_\nu(\vec{R})$. The (non-adiabatic) coupling between the adiabatic states, which is mediated by the nuclear kinetic energy operator, is referred to as *dynamic coupling*. Its calculation requires knowledge of the first and second derivatives of the electronic wavefunction. In addition, the electronic wavefunction can change rapidly during the charge transfer reaction, implying that this coupling can be singular within a narrow range of nuclear configuration space, leading to numerical complications. To summarize, adiabatic functions are useful as long as non-adiabatic couplings can be neglected, *i.e.* when charge transfer occurs within a single electronic state driven by a slow nuclear reaction coordinate.

In practice, it is, however, convenient to use *diabatic* basis functions φ_ν, which are eigenstates of the electronic Hamiltonian, evaluated at some fixed nuclear configuration $\vec{R}_0$. Expanding the wavefunction in this basis, we again obtain a set of coupled linear equations but now the couplings are not mediated by the non-adiabaticity operator. This is because diabatic basis functions do not depend on $\vec{R}$ but are shifted from the kinetic to the potential energy operator. In general, any complete basis set that solves the stationary Schrödinger equation and yields negligible small matrix elements of the nonadibaticity operator can be used. An example of this is a so-called "frozen-core" approximation, where the diabatic states of a dimer are

constructed from the frontier orbitals of (neutral) isolated monomers[85–88] and it is assumed that the reduction/oxidation of a monomer does not alter the rest of the orbitals. Another option is to use the constrained density-functional theory, where a density constraint is applied, forcing the charge to localize on the individual monomers of the dimer.[89] Note that more computationally demanding approaches have also been proposed.[90–101]

Determining the diabatic states in polymeric systems is another important area of computational studies that deserves special attention. Indeed, in the case of small molecules or relatively short oligomers, one can often assume that the charge is localized on the entire molecule. In polymers, however, it has been proposed that the charge localizes on molecular (conjugated) segments or regions between conjugation breaking, where strong deviation from planarity occurs.[47,102] This idea has been used to interpret spectroscopic data, but is difficult to justify when wanting to rigorously define a sharp threshold that separates complete conjugation breaking from full conjugation between oligomers. Moreover, many polymers form crystalline domains that are so extended that no conjugation breaks occur for nanometers[103] but the charge is certainly more localized than that, either due to the disorder present in the semicrystalline phase or the electron–phonon coupling.[104,105]

Hence, to determine the charge localization, there is no other alternative than computing the electronic wavefunction of a large model system that is generated by classical simulations. The excited state of the charged simulation box cannot be computed with modern computational methods and therefore it becomes impossible to even evaluate the nuclear relaxation (reorganization energy) for the hopping between two states. For these reasons, all attempts to evaluate the wavefunction of a large model of polymers have focused on neutral systems and have so far interpreted only the one-electron states (molecular orbitals) as possible sites where the excess charge can be localized.[36,106] Results are normally presented in terms of the density of states (DOS) and localization length, although it should be noted that the two quantities should only be used for systems with orbitals fully filled and empty above and below the band gap. Such descriptions are also not directly comparable with the models in Section 9.3.2, which take into account electron and nuclear polarization, but have to make assumptions for the localization length.

For the one-electron states to be representative of the actual localization of the charge carrier, a further condition needs to be satisfied. The charge needs to be localized predominantly by the conformational disorder of the polymer and not by the electron–phonon coupling. If the electron coupling is particularly strong, the frontier orbitals may be delocalized over many monomers. However, when an excess charge is added, the nuclear polarization will localize the charge, completely modifying the electronic wavefunction with respect to the neutral calculation. Calculations for, *e.g.* P3HT, support this approximation[36,107] but it should be noted that polaron sizes are heavily dependent on the DFT methodology[108] and that the same assumption might not hold for new families of semiconducting polymers[109]

in which large conjugated units are more weakly coupled by smaller conjugated linkers. In general, if the polaron size of a perfectly ordered system is much larger than the orbital in the disordered model, it is acceptable to determine the charge localization from calculations that neglect the electron–phonon coupling as a first approximation. Again, for P3HT, there is a consensus that the localization of the wavefunction largely originates from the disorder and not the electron–phonon coupling, since there is a correlation between the increased order of P3HT and increased mobility.[110–112]

Assuming that the calculation of a ground state wavefunction of a polymer model yields information about the charge localization for the carrier states, it is still not trivial to carry out such calculations. It is not obvious to know in advance how large should a model of bulk polymer be to reproduce the DOS and localization length without the results being affected by finite size effects. The experience of available calculations with P3HT and PPV suggests that a model containing several chains of 20 to 40 monomers displays electronic properties that do not depend appreciably on the chain length[113] (it should not be forgotten though that the morphology depends on the chain length until much larger molecular weight.[114]) Such models will contain tens of thousands of atoms, a number still one order of magnitude larger than what is normally achievable by the current software specialized in linear scaling *ab initio* calculations.

However, many ideas of linear scaling methodology can be used to develop *ad hoc* methods that are able to compute in more approximate fashion the wavefunction for large systems by using a very localized basis set that reduces the number of matrix elements to be evaluated.[115–117] Different schemes have been proposed to evaluate the diagonal and off-diagonal elements of such reduced Hamiltonian, including a fragment molecular orbital approach[118] and a charge patching method.[106,119,120] General formalism for such methods have been developed by the quantum chemistry community.[115,121–123]

The various partitioning schemes proposed for polymer systems are very often complemented by further approximations that take into account the chemical structure of the investigated system. As the frontier orbitals are invariably localized on the conjugated fragment of the monomer, while a large fraction of the molecular weight is taken up by the polymer side chains that do not contribute to the charge transport states, it is customary to remove the side chains in the calculation, sometimes substituting them with effective point charges that simulate the missing electrostatic effects.[113] For lamellar systems (such as P3HT and PBTTT) it is a good approximation to neglect the electronic coupling between lamellae, thereby describing a system that is essentially two-dimensional.[36,124] An alternative approach to full or *ad hoc* linear scaling DFT methods is the calculation through approximate DFT methods such as the tight binding DFT.[125] This family of methods has been developed over the years and the most convenient version of the methodology is the self-consistent charge-density functional tight binding.[126] One–two order of magnitudes acceleration of the electronic

structure calculation can be achieved by an approximate evaluation of the Kohn–Sham–Fock matrix elements in the atomic orbital basis. A very broad range of applications apart from organic semiconductors have been proposed[123] but relatively few have been reported for semiconducting polymers.[127] Finally, an obvious choice for the calculation of electronic structure on large scale systems would be by semi-empirical methods. These have been the method of choice for many years to explore charge- and exciton-dynamics[128,129] in single chain polymers containing carbon atoms but there are very few systematic studies on their reliability for polymers containing heteroatoms.

Once the one-electron states of a large system have been evaluated, it is still challenging to derive a master equation (Section 9.3.6) that describes the transitions between these states. Vukmirović and Wang have proposed a perturbative expression assuming that these states are coupled by non-adiabatic coupling terms that can be evaluated explicitly[106] or approximated using the overlap between the absolute value of the wavefunction.[130] The proposed expression does not contain the effect of nuclear reorganization in the presence of an additional charge and is valid only in the limit of vanishing reorganization energies, like in the Miller–Abrahams rates.[131] Using this approach, it has been highlighted that the DOS does not contain all of the information needed to evaluate the mobility and that it is possible to have reduced broadening of the DOS due to increased order but still have low mobility because of the coupling between the states is reduced.[132] Alternative methods to combine nuclear polarization and disorder effects have been proposed, but these could so far only be applied to simple model systems.[133,134] An extended discussion of charge delocalization in polymeric systems is provided in ref. 135.

9.3.2 Charge Transfer Rates

The simplest rate expression for a charge transfer reaction can be derived for a system with classical harmonic vibrational degrees of freedom or the high-temperature limit.[136,137] The diabatic and adiabatic potential energy surfaces of a dimer are shown in Figure 9.5. The corresponding rate expression reads:

$$k_{A\to B} = \frac{2\pi}{\hbar}\frac{J_{AB}^2}{\sqrt{4\pi\lambda kT}}\exp\left[-\frac{(\Delta U_{AB}-\lambda)^2}{4\lambda kT}\right] \tag{9.3}$$

This so-called Marcus-rate depends only on three microscopic parameters, namely, the reorganization energy λ, the electronic coupling J_{AB}, and the driving force $\Delta U_{AB} = U_A - U_B$, all of which can be evaluated using quantum-chemical methods, classical polarizable force-fields, or quantum-classical hybrid methods, as discussed in the following sections.

Note that both classical and semi-classical expressions for charge transfer rates are often criticized as being not applicable for studying charge

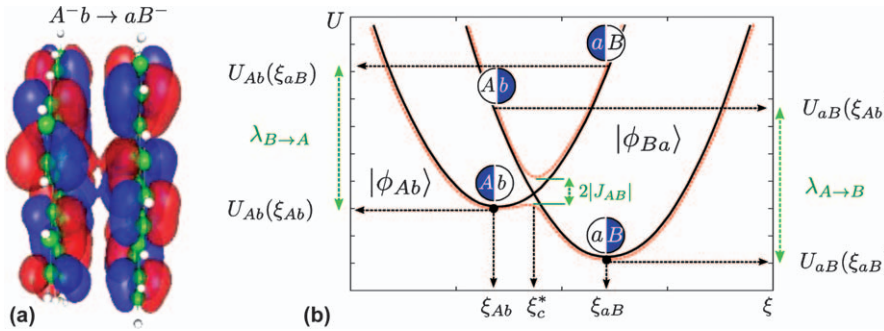

Figure 9.5 (a) Diabatic states constructed using the molecular orbitals participating in a charge transfer reaction (frozen core approximation). (b) Diabatic (solid black line) and adiabatic (dashed red line) potential energy surfaces of two electronic dimer states $|\varphi_{AB}\rangle$ and $|\varphi_{aB}\rangle$, participating in the charge transfer reaction $A^{-}B \rightarrow AB^{-}$ along the reaction coordinate ξ.

transport in well ordered organic semiconductors. Having said this, one has to also acknowledge that, so far, it is the only way of linking a large-scale morphology to the charge dynamics in partially disordered materials. Of course, this should not serve as an excuse for not validating the Marcus expression (or its quantum equivalent) for the charge transfer rates. In fact, various generalizations of this expression to quantum-mechanical modes have been derived.[138–140] Moreover, indications that these expressions are better suited for describing charge transport, especially at low temperatures and high fields, have recently been reported.[141]

9.3.3 Electronic Coupling Elements

Electronic coupling elements, or transfer integrals, between molecules i and j are given by the off-diagonal matrix elements[99,137]:

$$J_{ij} = \left\langle \phi_i | \hat{H} | \phi_j \right\rangle \tag{9.4}$$

where $\phi_{i,j}$ are the diabatic states often approximated by the frontier orbitals of the molecules, and $\hat{H}$ is the dimer Hamiltonian. These quantities are normally evaluated using electronic structure theory. Expanding the adiabatic states of the dimer into monomer states produces the following secular equation:

$$(\mathbf{H} - E\mathbf{S})\mathrm{C} = 0 \tag{9.5}$$

where **H** and **S** are the Hamiltonian and overlap matrices of the system:

$$\mathbf{H} = \begin{pmatrix} e_i & H_{ij} \\ H_{ij}^{*} & e_j \end{pmatrix}, \mathbf{S} = \begin{pmatrix} 1 & S_{ij} \\ S_{ij}^{*} & 1 \end{pmatrix} \tag{9.6}$$

and the eigenfunctions:

$$e_i = \left\langle \phi_i \mid \hat{H} \mid \phi_j \right\rangle,\ e_j = \left\langle \phi_j \mid \hat{H} \mid \phi_i \right\rangle,\ H_{ij} = \left\langle \phi_i \mid \hat{H} \mid \phi_j \right\rangle,\ S_{ij} = \left\langle \phi_i \mid \phi_j \right\rangle$$

In the basis of its eigenfunctions, the Hamiltonian operator is diagonal, $\langle \varphi_n^D | \hat{H} | \varphi_m^D \rangle = E_n \delta_{nm}$. Hence, eq. (9.5) can be rewritten as:

$$H_{ij} = \sum_n \left\langle \phi_i | \phi_j^D \right\rangle E_n \left\langle \phi_{n_i}^D | \phi_j \right\rangle \tag{9.7}$$

Expanding the monomer and dimer functions into a basis set of atom-centered orbitals:

$$|\phi_k\rangle = \sum_\alpha M_\alpha^{(k)} |\varphi_\alpha\rangle,\ |\phi_n^D\rangle = \sum_\alpha D_\alpha^{(n)} |\varphi_\alpha\rangle$$

the projections read as:

$$\langle \varphi_i | \varphi_n^D \rangle = \sum_n M_\alpha^{(k)} \left\langle \alpha | \sum_\beta D_\beta^{(n)} | \beta \right\rangle = \overline{\boldsymbol{M}}_{(k)}^\dagger \mathscr{S} \overline{\boldsymbol{D}}_{(n)} \tag{9.8}$$

where $\mathscr{S}$ is the overlap matrix of the atomic basis functions. The Hamiltonian and overlap then take the form:

$$H_{ij} = \overline{\boldsymbol{M}}_{(i)}^\dagger \mathscr{S} \mathbf{D} \mathbf{E} \mathbf{D}^\dagger \mathscr{S}^\dagger \overline{\boldsymbol{M}}_{(j)} \tag{9.9}$$

$$S_{ij} = \overline{\boldsymbol{M}}_{(i)}^\dagger \mathscr{S} \mathbf{D} \mathbf{D}^\dagger \mathscr{S}^\dagger \overline{\boldsymbol{M}}_{(j)} \tag{9.10}$$

The final required transformation is the diagonalization of the diabatic states imposed by the charge-transfer Hamiltonian.[142] An orthonormal basis set that retains the local character of the monomer orbitals can be obtained by using the Lödwin transformation, $\mathbf{H}^{\text{eff}} = \mathbf{S}^{-1/2}\mathbf{H}\mathbf{S}^{-1/2}$, yielding an effective Hamiltonian with its entries directly related to the site energies ε_i and transfer integrals J_{ij}:

$$\mathbf{H}^{\text{eff}} = \begin{pmatrix} \varepsilon_i & J_{ij} \\ J_{ij}^\star & \varepsilon_j \end{pmatrix}. \tag{9.11}$$

The projection method can be significantly simplified if semiempirical methods are employed for the dimer Hamiltonian[85–87] as well as made computationally more efficient by avoiding self-consistent dimer calculations.[88] Notably, the density functional and semiempirical methods can introduce a systematic error when used to evaluate electronic couplings.[140,142]

As the electronic coupling and, correspondingly, charge carrier mobility is intimately related to molecular overlap, it is very sensitive to relative positions and orientations of neighboring molecules. To illustrate this, Figure 9.6 (left-hand side) shows the absolute value of the electronic coupling element as a function of the azimuthal rotation angle for several

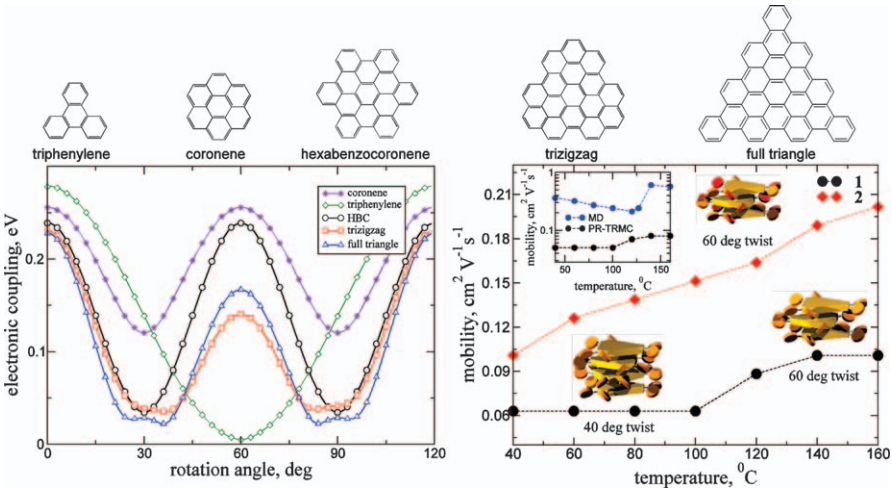

Figure 9.6 (Left-hand side) Absolute values of the electronic coupling element as a function of the azimuthal rotation angle for several symmetric polyaromatic hydrocarbon cores. The separation was fixed to 0.36 nm. (Right-hand side) Charge mobilities as a function of temperature as measured by the PR-TRMC technique. Inset: direct comparison to simulation. Adapted with permission from ref. 143. Copyright (2009) Macmillan Publishers Limited.

polyaromatic hydrocarbons. Here, the most favorable molecular arrangement is either co-facial or twisted by 60° (except triphenylene). For efficient charge transport, it is therefore preferable to lock the relative molecular orientations at the positions of the maxima of the transfer integral, which can be achieved by adjusting the density and type of side chains.[143]

This example shows that it is in principle possible to predict the optimal molecular arrangement for charge transport. This description, however, relies on a static picture, whereas in reality electronic couplings are time-dependent. To understand whether a static picture can be employed, one has to compare the distributions of the relaxation times of the electronic coupling elements and site energies to the distributions of the escape times of a charge carrier. For instance, for P3HT, even the slowest escape times for holes do not extend into the decorrelation regime of the electronic couplings. Charge-carrier dynamics are therefore limited by the static disorder of the electronic couplings, since their relaxation times exceed typical timescales of hopping transport. Hence, it is possible to resort to a single charge-transfer rate without time-averaging of electronic couplings of a pair of molecules.[44] The reason for the slow relaxation times of electronic couplings is the chemical structure of P3HT: every thiophene unit is linked to an alkyl side-chain with slow dynamics, both in the crystalline and amorphous phases. This overdamps the backbone dynamics, in particular the torsional motions of the thiophene units, and results in slow variations of the electronic couplings. Interestingly, in a very similar conjugated polymer PBTTT,

where the thienothiophene units are not linked to the side-chains (implying a lower side-chain density and higher crystallinity), electronic couplings have significantly faster dynamics, which is beneficial for charge transport.[44,144,145]

9.3.4 Reorganization Energies

The internal reorganization energy is a measure for how much the geometry of the charge transfer complex adapts while the charge is transferred. The reorganization energy can be estimated based on four points on the diabatic potential energy surfaces (PES) (Figure 9.5):

$$\begin{aligned}\lambda_{A\to B} &= U_a(\xi_A) - U_a(\xi_a) + U_B(\xi_b) - U_B(\xi_B),\\ \lambda_{B\to A} &= U_b(\xi_B) - U_b(\xi_b) + U_A(\xi_a) - U_A(\xi_A)\end{aligned} \tag{9.12}$$

Here, $U_{a,b}$ and $U_{A,B}$ refer to the diabatic states of molecule A,B in their neutral and charged state, respectively. Treatments that do not approximate the PES in terms of a single shared normal mode are also available,[47,137,146]

An additional contribution to the overall λ results from the reorganization of the environment in which the charge transfer takes place, giving rise to λ^{out}. In a classical case, this outer-sphere reorganization energy contributes to the exponent in the rate expression in the same way as its internal counterpart. Assuming that charge transfer is significantly slower than electronic polarization but much faster than nuclear the rearrangement of the environment, λ^{out}, can be evaluated from the electric displacement fields created by the charge transfer complex,[137] provided that the Pekar factor is known. It also turns out that the classical Marcus expression for the outer-sphere reorganization energy (inversely proportional to the molecular separation) can predict negative values of λ^{out} for small intramolecular separations, which is unphysical and hence shall be used with care.[140]

For a P3HT chain of 20 monomers, the reorganization energy of 0.1 eV is relatively small compared to the 0.2–0.4 eV observed in many small-molecule based organic semiconductors due to the better delocalization of the charge. Additionally, steric hindrance prevents conformational changes of the polymer chain upon charging if embedded in a π-stacked crystal, since the resulting constraint on the backbone planarity lowers the reorganization energy.[147]

9.3.5 Driving Forces

The energetic landscape, that is, the change in the system's energy when a charge or exciton is drift-diffusing in an organic material, is one of the most crucial quantities affecting a device's functionality. In solar cells, for example, it assists the splitting of the Frenkel excitons into charge transfer states (and consequently into free charges), as well as influences the charge and exciton mobility and diffusion constants. In OLEDs, it is possible to

force charge carriers to form an exciton on a specific molecule (phosphorescent guest) by adjusting the energetic landscape.

For every molecular pair, the free energy difference (or *driving force* ΔU_{AB}) is given by the difference in *site energies* $U_A - U_B$, that is, the energy separation between the diabatic PES minima as shown in Figure 9.5. The latter include an internal contribution U^{int}, namely, the electron affinities for electrons and ionization potentials for holes of isolated molecules. U^{int} can vary from one molecular pair to another because of different energy levels for different types of molecules, or different conformers of the same molecule. The external contribution is due to the electrostatic, U^{est}, and the induction, U^{ind}, interactions of a charged/excited state with the environment:

$$\begin{aligned} U_A &= U_{Ab}(\xi_{Ab}) - U_{ab}(\xi_{ab}) = \left(U_{Ab}^{\text{int}} - U_{ab}^{\text{int}}\right) + \left(U_{Ab}^{\text{est}} - U_{ab}^{\text{est}}\right) + \left(U_{Ab}^{\text{ind}} - U_{ab}^{\text{ind}}\right) \\ U_B &= U_{aB}(\xi_{aB}) - U_{ab}(\xi_{ab}) = \left(U_{aB}^{\text{int}} - U_{ab}^{\text{int}}\right) + \left(U_{aB}^{\text{est}} - U_{ab}^{\text{est}}\right) + \left(U_{aB}^{\text{ind}} - U_{ab}^{\text{ind}}\right) \end{aligned} \tag{9.13}$$

Here, the subscript *ab* denotes the reference (neutral) state of the system, with all molecules being in their ground states.

It is the interaction with the environment that is the most difficult to evaluate: since the underlying interactions are long-ranged, large system sizes are needed to converge the values of site energies. To self-consistently account for both the electrostatic and the polarization effects, classical models are normally employed such as the polarizable force-fields. These models are computationally demanding (despite being classical) and are often not accurate enough when used "out of the box". For example, the Thole model, which performs extremely well for biomolecular systems, can easily underestimate the anisotropy of a molecular polarizability tensor for an extended π-conjugated system.

9.3.5.1 *Electrostatic Contribution*

The electrostatic interaction energy in the site-energy calculation can be evaluated as the first-order energy correction term, which stems from treating an external field as a perturbing term in the molecular Hamiltonian. This term is normally evaluated using atomic distributed multipoles, where the interaction energy U_{AB} of two molecules A and B, located at positions $\vec{X}$ and $\vec{Y}$, reads:

$$U_{AB} = \frac{1}{4\pi\varepsilon_0} \int\int \mathrm{d}^3x \mathrm{d}^3y \frac{\rho_A(\vec{x})\rho_B(\vec{y})}{|\vec{Y} + \vec{y} - \vec{X} - \vec{x}|} \tag{9.14}$$

Here ρ_A and ρ_B are charge densities of molecules A and B, respectively.

Using the spherical-harmonic addition theorem,[14] this energy can be re-written in terms of the molecular multipole moments, defined with respect to the molecule's local frame:

$$U_{AB} = \frac{1}{4\pi\varepsilon_0}\sum_{l_1,l_2}\sum_{k_1,k_2}\begin{pmatrix} l_1+l_2 \\ l_1 \end{pmatrix}\hat{Q}^A_{l_1k_1}\hat{Q}^B_{l_2k_2} \times S^{k_1k_2}_{l_1l_2l_1+l_2}|\vec{X}-\vec{Y}|^{-l_1-l_2-1} \tag{9.15}$$

These moments, $\hat{Q}^A_{lm} = \int \mathrm{d}^3x\rho_A(\vec{x})R_{lm}(\vec{x})$, interact with each other *via* a tensor that contains the distance and orientation dependence. Note that here we have used the fact that $|\vec{x}-\vec{y}| < |\vec{X}-\vec{Y}|$, namely, that the molecular charge densities must not interpenetrate. $R_{l,m}$, $I_{l,m}$ are the regular and irregular spherical harmonics, respectively.[148]

The molecular multipole moments can be converted between two co-ordinate frames, Σ_1 and Σ_2, according to:

$$Q^{(\Sigma_1)}_{lk} = \sum\nolimits_m Q^{(\Sigma_2)}_{lm}D^l_{mk}(\varphi,\theta,\psi)$$

Here, ϕ, θ, ψ are the Euler angles, and $[D^l_{mk}]$ is a Wigner rotation matrix. This allows one to perform the electrostatic parametrization of a molecule in a conveniently chosen local frame as well as include the transformation from the local to the global interaction frame in a tensor that takes care of both the distance and orientation dependence:

$$T^{A,B}_{l_1k_1l_2k_2} = \frac{1}{4\pi\varepsilon_0}\begin{pmatrix} l_1+l_2 \\ l_1 \end{pmatrix}S^{k_1k_2}_{l_1l_2l_1+l_2}|\vec{X}-\vec{Y}|^{-l_1-l_2-1} \tag{9.16}$$

The interaction energy thus reduces to an expression consisting of only molecular multipole moments defined with respect to the molecular local frame and the generic interaction tensors $T^{A,B}_{l_1k_1l_2k_2}$ (tabulated up to $l_1+l_3=5$ in ref. 149):

$$U_{AB} = \hat{Q}^A_{l_1k_1}T^{A,B}_{l_1k_1l_2k_2}\hat{Q}^B_{l_2k_2} \tag{9.17}$$

where we have used the Einstein sum convention for the multipole-moment components l_ik_i. The electrostatic part of the site-energy, which enters exponentially in the Marcus rate expression for a charge localized on molecule A, then reads:

$$\Delta U^{cn}_A = \sum_{B\neq A}(\hat{Q}^{A,c}_{l_1k_1} - \hat{Q}^{A,n}_{l_1k_1})T^{A,B}_{l_1k_1l_2k_2}\hat{Q}^{B,n}_{l_2k_2} \tag{9.18}$$

where the superscripts c and n denote the molecular multipole moments in the neutral and charged state, respectively, and the sum extends over all external molecules B.

9.3.5.2 *Distributed Multipoles*

In eq. (9.17), we have provided an expression for the electrostatic interaction energy in terms of *molecule-centered* multipole moments. To arrive at this

expression, the separation between the molecular centers, $|\vec{X}-\vec{Y}|$, was assumed to be larger than that of any of the respective charge-carrying volume elements of the two molecules, $|\vec{x}-\vec{y}|$. In a molecular solid, this demand can hardly be satisfied, considering the dense packing and strongly anisotropic charge density. This inevitably leads to the breakdown of the single-point expansion at small separations. It is possible to avoid this breakdown by choosing multiple expansion sites per molecule in such a way as to accurately represent the molecular electrostatic potential, with a set of suitably chosen multipole moments $\{Q^a_{lk}\}$ allocated to each site. We then simply extend the expression for the interaction energy between two molecules A and B in the single-point expansion, eq. (9.17), and include the sum over all expansion sites $a \in A$ and $b \in B$:

$$U_{AB} = \sum_{a\in A}\sum_{b\in B} \hat{Q}^a_{l_1k_1} T^{a,b}_{l_1k_1l_2k_2} \hat{Q}^b_{l_2k_2} \equiv \hat{Q}^a_{l_1k_1} T^{a,b}_{l_1k_1l_2k_2} \hat{Q}^b_{l_2k_2} \tag{9.19}$$

Here, we have used the Einstein sum convention for the site indices a and b on the right-hand side of the equation, in addition to the same sum convention which is already in place for the multipole-moment components.

There are several strategies on how to arrive at such a collection of *distributed multipoles*,[14,15,150–153] which can be classified according to whether the multipoles are derived from the electrostatic potential, generated by the SCF charge density, or from a decomposition of the wavefunction itself. The CHELPG (CHarges from ELectrostatic Potentials, Grid-based) method, for example, relies on performing a least-squares fit of atom-placed charges to reproduce the electrostatic potential, as evaluated from the SCF density on a regularly spaced grid,[151,154] while the distributed multipole analysis (DMA)[152,153] operates directly on the quantum-mechanical density matrix, expanded in terms of atom- and bond-centered Gaussian functions.

9.3.5.3 *Induction Interaction*

Similar to the distributed multipole expansion of molecular electrostatic fields, one can derive a distributed polarizability expansion of the molecular field response by including the multipole-expansion in the perturbing Hamiltonian term $\hat{W} = \hat{Q}^a_t \phi^a_t$, where the Einstein sum convention is used for both superscripts a (referencing an expansion site) and subscripts t (summarizing the multipole components (l, k) in a single index). Thus, the second-order energy correction reads[14]:

$$W^{(2)} = -\sum_{n\neq 0} \frac{|\langle 0|\hat{Q}^a_t \varphi^a_t|n\rangle|^2}{W_n - W_0} \tag{9.20}$$

We then absorb the quantum-mechanical response into a set of intramolecular site-site polarizabilites, where $-\alpha^{aa'}_{tt'}\phi^{a'}_{t'}$ yields the induced

multipole moment Q_t^a at site a, which results from a field component $\phi_{t'}^{a'}$ at site a'[14]:

$$\alpha_{tt'}^{aa'} = \sum_{n\neq 0} \frac{\langle 0|\hat{Q}_t^a|n\rangle\langle n|\hat{Q}_{t'}^{a'}|0\rangle}{W_n - W_0} + h.c. \tag{9.21}$$

With this set of higher-order polarizabilities at hand, we obtain the induction stabilization in a distributed formulation as $W^{(2)} = -\frac{1}{2}\varphi_t^a \alpha_{tt'}^{aa'} \varphi_{t'}^{a'}$. The derivatives of $W^{(2)}$ with respect to the components of the field ϕ_t^a at a polar site a then yield the correction to the permanent multipole moment Q_t^a at that site, $\Delta Q_t^a = \partial W^{(2)}/\partial \phi_t^a = -\alpha_{tt'}^{aa'} \phi_{t'}^{a'}$.

Using the multipole corrections ΔQ_t^a, we can now extend the electrostatic interaction energy (eq. 9.19) to include the induction contribution to the field energy U_{ext}, while accounting for the induction work U_{int}:

$$U_{\text{ext}} = \frac{1}{2}\sum_A \sum_{B\neq A} (Q_t^a + \Delta Q_t^a) T_{tu}^{ab} (Q_u^b + \Delta Q_u^b) \tag{9.22}$$

$$U_{\text{int}} = \frac{1}{2}\sum_A \Delta Q_t^a \eta_{tt'}^{aa'} \Delta Q_{t'}^{a'} \tag{9.23}$$

Here, the inverse of the positive-definite tensor $\eta_{tt'}^{aa'}$ is simply given by the distributed polarizabilities tensor $\alpha_{tt'}^{aa'}$, where we have included explicit sums over all molecules A and B.

We then use a variational approach to calculate the multipole corrections ΔQ_t^a:

$$\delta(U_{\text{ext}} + U_{\text{int}}) = \delta Q_t^a \left[\sum_{B\neq A} T_{tu}^{ab} (Q_u^b + \Delta Q_u^b) + \eta_{tt'}^{aa'} \Delta Q_{t'}^{a'} \right] \tag{9.24}$$

which leads to a set of self-consistent equations for the induced moments, which for large systems are solved iteratively:

$$\Delta Q_t^a = -\sum_{B\neq A} \alpha_{tt'}^{aa'} T_{t'u}^{a'b} (Q_u^b + \Delta Q_u^b) \tag{9.25}$$

The total energy can now be decomposed into two energy terms:

$$\begin{aligned} U_{pp} &= \sum_A \sum_{B>A} Q_t^a T_{tu}^{ab} Q_u^b \\ U_{pu} &= \frac{1}{2}\sum_A \sum_{B>A} \left[\Delta Q_t^a T_{tu}^{ab} Q_u^b + \Delta Q_t^b T_{tu}^{ab} Q_u^a \right] \end{aligned} \tag{9.26}$$

Here, $U_{pp} \leftrightarrow W^{(1)}$ is the electrostatic interaction energy, that is, the first-order correction due to the interaction of the permanent multipole moments. $U_{pu} \leftrightarrow W^{(2)}$ is the induction energy associated with the interaction of the

induced moments on a single molecule with the permanent moments induced on surrounding molecules.

9.3.5.4 *Thole's Model*

Equations (9.25) and (9.26) allow us to compute the electrostatic and induction energy contributions to the site energies in a self-consistent manner based on a set of molecular distributed multipoles $\{Q_t^a\}$ and polarizabilities $\{\alpha_{tt'}^{aa'}\}$, which can be obtained from wavefunction decomposition or fitting schemes, as discussed in Section 9.3.5.2. The $\{\alpha_{tt'}^{aa'}\}$ are formally given by eq. (9.21). This expression is somewhat impractical, though possible to evaluate (see ref. 152), such that various empirical methods have been developed. The Thole model,[155,156] for example, treats polarizabilities α^a in the local dipole approximation. It is based on a modified dipole–dipole interaction, which can be reformulated in terms of the interactions of smeared charge densities. This eliminates the divergence of the head-to-tail dipole–dipole interaction at small separations (Å scale).[155–157] Smearing out the charge distribution mimics the nature of the QM wavefunction, which effectively prevents the polarization catastrophe.

The smearing of the nuclei-centered multipole moments is obtained *via* a fractional charge density $\rho_f(\vec{u})$, which should be normalized to unity and fall off rapidly as of a certain radius $\vec{u} = \vec{u}(\vec{R})$. The latter is related to the physical distance vector $\vec{R}$, connecting two interacting sites *via* a linear scaling factor that takes into account the magnitude of the isotropic site polarizabilities α^a. This isotropic fractional charge density gives rise to a modified potential:

$$\varphi(u) = -\frac{1}{4\pi\varepsilon_0}\int_0^u 4\pi u'\rho(u')\mathrm{d}u' \tag{9.27}$$

The multipole interaction tensor $T_{ij\ldots}$ (this time in Cartesian coordinates) can be related to the fractional charge density in two steps: First, it is rewritten in terms of the scaled distance vector $\vec{u}$:

$$T_{ij\ldots}(\vec{R}) = f(\alpha^a\alpha^b)\, t_{ij\ldots}\left[\vec{u}(\vec{R}, \alpha^a\alpha^b)\right] \tag{9.28}$$

where the specific form of $f(\alpha^a\alpha^b)$ results from the choice of $u(\vec{R},\alpha^a\alpha^b)$. Second, the smeared interaction tensor $t_{ij\ldots}$ is given by the appropriate derivative of the potential in eq. (9.27):

$$t_{ij\ldots}(\vec{u}) = -\partial_{u_i}\partial_{u_j}\ldots\varphi(\vec{u}) \tag{9.29}$$

It turns out that for a suitable choice of $\rho_f(\vec{u})$, the modified interaction tensors can be rewritten in such a way that powers n of the distance $R = |\vec{R}|$ are damped *via* a damping function $\lambda_n\left[\vec{u}(\vec{R})\right]$.[158]

Several fractional charge densities $\rho_f(\vec{u})$ have been tested for the purpose of yielding best results for the molecular polarizability as well as the interaction energies. For most organic molecules, a fixed set of atomic polarizabilities

($\alpha_C = 1.334$, $\alpha_H = 0.496$, $\alpha_N = 1.073$, $\alpha_O = 0.873$, $\alpha_S = 2.926$ Å^3) based on atomic elements gives satisfactory results,[156] though reparametrizations are advised for ions and molecules with extended conjugated π-systems.

One of the common approaches, *e.g.*, in the AMOEBA force-field,[158] uses an exponentially-decaying fractional charge density:

$$\rho(u) = \frac{3a}{4\pi}\exp(-au^3) \tag{9.30}$$

where $\vec{u}(\vec{R}, \alpha^a\alpha^b) = \vec{R}/(\alpha^a\alpha^b)^{1/6}$ and $a = 0.39$ is the smearing exponent. The distance at which the charge–dipole interaction is reduced by a factor γ is then given by:

$$R_\gamma = \left[\frac{1}{a}\ln\left(\frac{1}{1-\gamma}\right)\right]^{1/3}(\alpha_i\alpha_j)^{1/6} \tag{9.31}$$

The interaction damping radius, associated with $\gamma = \frac{1}{2}$, revolves around an interaction distance of 2 Å. A half-interaction distance on this range indicates how damping is primarily important for the intramolecular field interaction of induced dipoles.

9.3.5.5 *Case Studies*

The expansion of the molecular field and field response in terms of distributed multipoles and polarizabilities is an efficient approach to solve for the first- and second-order corrections to the molecular Hamiltonian, which result from a perturbation by the molecular environment. This approach has been used to evaluate energetic landscapes in amorphous organic semiconductors,[47,51,52,159] where the width of the site energy distribution is often very large and can be attributed to randomly oriented molecular dipoles.[160,161] Owing to long-range electrostatic interactions, the resulting energetic disorder is always spatially correlated (Figure 9.7a). Spatial correlations lead to current filaments, as shown in Figure 9.7(a,b), and a Poole–Frenkel dependence of the charge carrier mobility on the externally applied electric field.[162]

Using this perturbative approach, it has also been shown that thermal fluctuations can lead to large variations in local electric fields and, hence, large energetic disorder (even in crystalline systems).[44,144,147] Finally, the method has also been employed to study energetics at organic interfaces.[49,163–169] Additional complications associated with the dimensionality reduction at interfaces and long-ranginess of Coulomb interactions are discussed in Section 9.6.

For crystalline polymers, it has been shown that the width of the distribution of the site energies (energetic disorder) depends on the side-chain packing and polymer regioregularity: 100% regioregular P3HT always has narrower site energy distributions than the 90% P3HT,[44,144] The magnitude of the disorder compares well with the width of the DOS, as extracted from

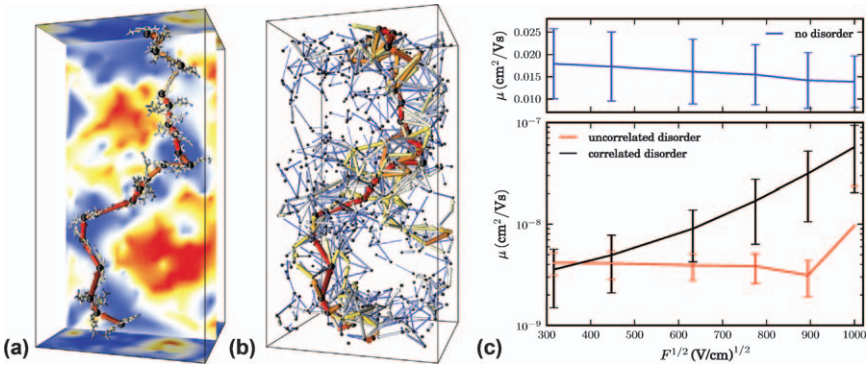

Figure 9.7 (a) Current filament and energetic landscape visualized in a slice of a disordered (amorphous) morphology of DCV4T. (b) Local currents contributing to 90% of the total current in the system. The dots are the molecular centers of mass, while the arrows depict the local currents (their thickness and color are proportional to the logarithm of the current's amplitude). Adapted with permission from ref. 159. Copyright (2012) The Royal Society of Chemistry. (c) Poole–Frenkel plots for a system of 4096 Alq_3 molecules. To illustrate the role of disorder and correlations, we show the field dependence for a system without energetic disorder (top panel) and without spatial correlations, that is after randomly shuffling site energies.
Adapted with permission from ref. 140. Copyright (2011) The American Chemical Society.

time-of-flight experiments,[170,171] where values for σ of 56 and 71 meV, respectively, have been proposed from a fit of the field-dependence of the mobility as obtained within the Gaussian disorder model.[8] On the level of chain ordering, the increase in energetic disorder can also be related to the increase in paracrystallinity along the π-stacking direction,[44] with the energetic disorder being linearly related to the amplitude of backbone–backbone distance fluctuations.

9.3.6 Charge Mobility

With the site energies and electronic couplings at hand, one is now able to calculate charge transfer rates (Section 9.3.2) for the set of electronically coupled pairs of conjugated segments. The directed graph which describes charge transport in the system is then fully parametrized and charge dynamics can be described *via* a master equation of the form:

$$\frac{\partial P_\alpha}{\partial t} = \sum_\beta \left[P_\beta K_{\beta\to\alpha} - P_\alpha K_{\alpha\to\beta} \right] \tag{9.32}$$

where P_α is the probability to find the systems in state α. The rates $K_{\alpha\to\beta}$ are the transition rates from state α to state β. For single-carrier dynamics, the number of available states α is the number of conjugated segments in the

system, with each state associated with molecule A being singly occupied. Using the single-site occupation probability P_A and transfer rates $K_{A\to B}$, eq. (9.32) simplifies to:

$$\frac{\partial p_A}{\partial t} = \sum_B [p_B k_{B\to A} - p_A k_{A\to B}] \tag{9.33}$$

This equation, valid in the limit of low charge densities, has the form $\partial_t \vec{p} = \tilde{k}\vec{p}$ and can be solved using linear solvers. In the more general cases (*i.e.* more than one carrier), expressing eq. (9.32) in terms of site occupation probabilities can be done using a mean-field approximation.[172] For this, the analogue of eq. (9.33) becomes, however, nonlinear and requires special solvers. If, in addition, several different types of carriers (holes, electrons, excitons) are present in the system, with their creation/annihilation processes taking place, it is practically impossible to link state and site occupation probabilities to the corresponding rates.

Instead, the solution of eq. (9.32) can be obtained by means of kinetic Monte Carlo (KMC) methods. KMC explicitly simulates the dynamics of charge carriers by constructing a Markov chain in state space and is suitable for both transient and stationary solutions of the master equation. A variable time-step size implementation of KMC is often employed due to the broad distribution of rates $K_{A\to B}$, which easily spans many orders of magnitude.

The stationary solution of eq. (9.33) can be used to evaluate several macroscopic observables.[47] For comparison with TOF, impedance spectroscopy, or similar measurements, the charge-carrier mobility tensor $\tilde{\mu}$ in the electric field $\vec{E}$ can be calculated as:

$$\tilde{\mu}\vec{E} = \sum_{A,B} p_A k_{A\to B}(\vec{R}_A - \vec{R}_B) \tag{9.34}$$

Alternatively, the charge-carrier mobility along the direction of the external field $\vec{E}$ can be obtained from a trajectory:

$$\mu = < \frac{\Delta\vec{R}\cdot\vec{E}}{\Delta t|\vec{E}|^2} > \tag{9.35}$$

where $<\ldots>$ denotes averaging over all trajectories, Δt is the total run time of a trajectory and $\Delta\vec{R}$ denotes the net displacement of the charge.

Charge dynamics are therefore guided by an interplay of topological connectivity of the directed graph, determined by the electronic coupling elements, and the ratios of forward to backward rates, prescribed by the energetic landscape. In discotic liquid crystals, for example, the graph is practically one-dimensional, *i.e.* even a few defects can block charge transport along π-conjugated columns.[143,173,174] In crystalline organic semiconductors, the presence of a strong well-defined π-stacking direction can turn out to be disadvantageous for efficient charge transport, since it might inhibit other transport directions and is prone to charge trapping if energetic disorder is present in the system.[147,159] In amorphous

semiconductors, the directed graph is always three-dimensional and the transport is mostly determined by energetic disorder and correlations, as illustrated in Figure 9.7(c) for a system of 4096 Alq_3 molecules. Here, the energetic disorder reduces the value of mobility by six orders of magnitude. The Poole–Frenkel behavior for small fields can only be observed if correlated disorder is taken into account. Note that for systems with large energetic disorder, simulations systematically overestimate the absolute values of non-dispersive mobilities due to significant finite size effects (see also Section 9.4).

Transport studies on different levels of complexity have been performed to investigate hole transport along the π-stacking direction of conjugated polymers.[36,44,144,175] Since the transport has a one-dimensional character, it can already be anticipated that a broad distribution of electronic couplings limits the charge mobility along the lamellae.[147,159,173,174,176–179] Indeed, mobility values are typically broadly distributed (from lamellae to lamelae), with small mobilities as low as 10^{-7} cm^2 V^{-1} s^{-1} for P3HT.[44] It has also been observed that the regioregularity effect occurs exclusively due to increased energetic disorder and that the higher mobility in the more regioregular material is entirely attributable to the narrowing of the density of states that arises from an increased order in hole–quadrupole interaction distances. This reduction can be traced back to the amplified fluctuations in backbone–backbone distances, *i.e.* the material's paracrystallinity.

9.4 Finite-Size Effects

Microscopic charge transport simulations are computationally demanding: First, electronic coupling elements need to be evaluated for all neighboring molecules. Second, evaluation of the electrostatic and induction contributions to the site energy requires large cutoffs or even special summation techniques (Section 9.6). This sets the limit on system sizes, which currently is on the order of hundreds of thousands of molecules. It is thus important to make sure that there are no finite size effects present when evaluating macroscopic properties of the system.

In fact, these effects are observed even experimentally in systems with large energetic disorder. Indeed, time-of-flight measurements of mobility can become unreliable: in thin organic films charge transport is dispersive and transients do not have a characteristic plateau used to determine the transient time.[6,180–182] Using thicker samples normally remedies the situation. It might seem that one can perform the same trick in computer simulations and replicate the (periodic) simulation box in the direction of the applied field. It turns out that the straightforward increase in the system size will still give incorrect (higher) values of charge carrier mobility. The reason for this is that all duplicated boxes have exactly the same (and small) number of independent site energies. Hence, statistical averages will always be performed over this small set of site energies, and charge carriers will traverse the sample at a different (higher) temperature than in an infinitely

large system. An additional averaging over different (statistically uncorrelated) repeated snapshots is required, since the origin of the problem is in the limited number of sites available for every distinct Monte Carlo simulation.

This type of finite size effects becomes much smaller at higher temperatures, since the relevant dimensionless parameter (at least in the Gaussian disorder model) is the width of the site energy distribution σ divided by k_BT. In fact, an empirical expression:

$$(\sigma/k_BT_{ND})^2 = -5.7 + 1.05 \ln N$$

can be used to estimate at what temperature the ''transition'' between the dispersive and non-dispersive transport occurs, where N is the number of the hopping sites (molecules) in the system. This observation has been used to perform an *ad hoc* correction of finite-size effects[183]: Nondispersive mobilities were calculated for a set of temperatures above T_{ND}. Then, an explicit temperature dependence was used to extrapolate the value of mobility to room temperature.

A clear drawback of this method is that is relies on an explicit knowledge of the temperature-dependence of mobility. While the exact analytical expression of this dependence is available only for one-dimensional systems[184,185]:

$$\mu(T) = \frac{\mu_0}{T^{3/2}} \exp\left[-\left(\frac{a}{T}\right)^2 - \left(\frac{b}{T}\right)\right] \tag{9.36}$$

it can still be used in a three-dimensional case in a rather broad temperature range (this has been verified by performing simulations for systems of different sizes and at different temperatures).

To illustrate the relevance of such extrapolation, charge transport in the amorphous mesophase of Alq_3 has been simulated in systems of different sizes.[183] In a system of 512 molecules simulated mobility was of the order of 10^{-6} cm^2 V^{-1} s^{-1}, while in a box of 4096 molecules an order of magnitude lower value has been measured. An extrapolation procedure resulted in a mobility of 10^{-9} cm^2 V^{-1} s^{-1}, which is three orders of magnitude lower than the one simulated in a small system. Note that the magnitude of the correction is very sensitive to the value of energetic disorder σ. While in Alq_3 $\sigma = 0.14$ eV, in an amorphous DCV4T $\sigma = 0.25$ eV and one can overestimate the value of mobility by seven(!) orders of magnitude.[186]

9.5 Stochastic Models

A separate issue of organic materials is their stability. This is especially important for OLEDs, where the efficiency roll-off and life-time of a device are intimately connected. Device degradation modeling poses, however, statistical challenges, since we are dealing with rare events that require large

simulation boxes, in particular in the lateral dimension (which in OLED is of the order of square mm). A pragmatic solution to this problem is to parametrize a mesoscopic lattice model (*e.g.* Gaussian disorder model, GDM) on the results of microscopic simulations and use this model to study charge/exciton distributions and dynamics in larger systems.[186]

The convenience of GDM originates from their simplicity: material morphology is represented by a regular lattice, while charge transfer rates decay exponentially with the intermolecular separation and energy differences are incorporated *via* the Boltzmann prefactor. This approach, initiated by Bässler, has been successfully used by several groups to understand the role of traps, finite charge carrier density, energetic disorder, and other mesoscopic parameters on charge mobility.[8,13,161,187–190]

At the same time, the necessity of extending the existing discrete mesoscopic models has also become clear: first, the parametrization based on microscopic simulations is not straightforward.[186] Second, either stationary or transient quantities are quantitatively reproduced, while for the description of transient (degradation) processes both should agree with experimental data. A potential solution to this problem is to introduce an off-lattice model, which can be directly linked to the microscopic model and would thus offer a much closer description of physical processes in the system.

One of the ways to achieve this is to provide a stochastic way of generating the material morphology and charge transfer rates.[191–193] For morphologies, for example, a stochastic process should reproduce given correlation functions, densities, and coordination numbers. For the charge transfer rates, a simple procedure can be developed by analyzing the distributions of parameters entering the charge transfer rate. In an amorphous mesophase of Alq_3, for example, the distribution of electronic couplings at every particular intermolecular separation is Gaussian. The dependence of the width and the mean of this Gaussian on intermolecular separation can be determined from microscopic simulations. Regarding the site energies, spatial correlations can be introduced by using a moving-average procedure, where site energies of the neighbors within a certain cutoff are mixed into initially independent Gaussian site-energy distribution.

Stochastic models developed for amorphous mesophases of Alq_3 and DCV4T could reproduce the mobility-field and mobility-density dependencies.[186,191,193] This indicates that they indeed can serve as an intermediate step between the completely microscopic descriptions and macroscopic, drift-diffusion-equations based models. The current challenge is to extend such models to anisotropic and heterogeneous systems.

9.6 Interfaces and Long-Range Interactions

As discussed in Section 9.3.5, the contribution of the environment to the energy of a localized charged state is taken into account in a perturbative

way, by evaluating the corresponding electrostatic and induction terms. Van der Waals interactions are normally ignored, since only the site energy differences enter the charge transfer rate, *i.e.* if the molecular polarization tensor does not change upon charging a molecule, this contribution is negligible. Evaluation of the electrostatic contribution includes, among others, Coulomb interactions of partial charges or higher distributed multipoles. These interactions are inherently long-range and require special summation techniques, *e.g.* Ewald summation, which is widely used in atomistic molecular dynamics simulations.[194] In this approach, the Coulomb interaction potential is split into two terms, one of which is converging rapidly in real and the other in reciprocal space. Induction contribution can also be incorporated in such a scheme.[158] While this method is well developed, it is designed for neutral systems, whereas for charge transport we would be interested in energies of a localized charge interacting with the neutral environment. The presence of a charged excitation (and its polarization cloud) violates periodicity of the system, which is essential for calculations in the reciprocal space.

A solution to this problem has been proposed by Poelking *et al.*[195]: the non-periodic (foreground) part of the system, which incorporates the charged excitation and its induction cloud, is superimposed onto a periodic, neutral background, which is computed using the Ewald summation method. The real-space interaction between these two regions is mediated by fields created by the background charge distribution, including induced moments. A modified shape term[196] is added to account for the net charge and quadrupole of the simulations cell. This term takes into account surface effects and depends on the summation geometry.

By applying this technique to organic/organic interfaces it has been shown that a cutoff of 4–8 nm is sufficient to converge the energy of a periodic three-dimensional system. For heterogeneous ordered systems (*e.g.* interfaces) the convergence turns out to be significantly slower, for example for a 12 nm thick slab the energy is far from converged even for the cutoff of 22 nm (see ref. 195 and Figure 9.8). Hence, this method is imperative to use in two-dimensional periodic systems or, in general, heterogeneous systems with a long-range molecular ordering. The differences between using simulations with a cutoff and without it are remarkable: the additional electrostatic/induction contribution can change from 0.5 eV (10 nm cutoff) to –0.7 eV (infinite system). The correct treatment of electrostatic contribution can therefore *reverse* the role of donor and acceptor as conditioned by gas-phase energy levels and energy levels calculated with a seemingly ample cutoff. It also predicts that the energy profiles for electrons and holes are flat at the organic–organic interfaces, while cutoff based calculations lead to a significant level bending. Finally, it allows to establish a relationship between structural coherence and state energetics: the structural coherence is probed up to a μm scale, hence emphasizing the role of extended crystallites (and their alignment) at interfaces.

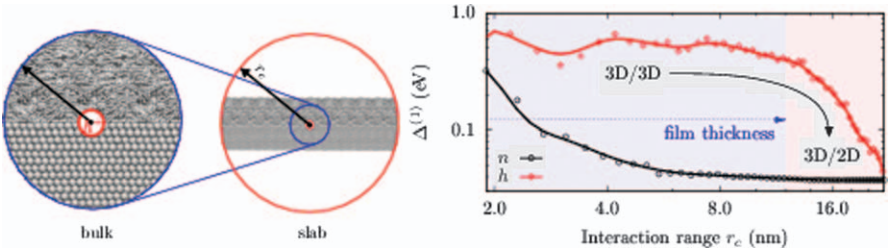

Figure 9.8 Variation of the electrostatic interaction energy with interaction range (r_c) for a positively charged (h) and neutral (n) DCV4T molecule in a nematically ordered thin film of thickness 12 nm. The crossover from a bulk-like to a slab-like convergence occurs as r_c exceeds film thickness. The converged value for a positively charge molecule is –0.7 eV (not shown on the graph).

9.7 Excited States

Excited and charge transfer states are at the heart of the functionality of solar cells and OLEDs. Through them, photons dissociate into free charges and free charges recombine radiatively. In both situations, however, processes related to these excitations are still poorly understood. Efficient exciton dissociation, for example, has been attributed to the assistance of charge separation by a gradient in the free-energy landscape,[197,198] structural heterogeneity as a function of distance to the interface,[199] doping and charged defects,[200] increase in entropy as the electron and hole move away from the interface,[201] formation of hot charge transfer states,[202] or long-range tunneling.[203] To gain more microscopic insight into the role of excited and charge transfer states is not only of fundamental interest, but is also directly relevant for a better understanding of, for example, the shape of the current–voltage curves of photovoltaic devices. For solar cells, in particular, this should help to understand the origin of the fill factor, which largely determines the device efficiency and can vary dramatically between different blends.

We therefore must aim at quantitative descriptions of excited states, their rates of geminate and non-geminate recombination, mobilities and diffusion coefficients. Such quantitative studies, however, require an accurate description of nonlocal electron–hole interactions. To this end, there is no optimal method for taking them into account and the scientific community has attempted various approaches. Among the available methods, the use of time-dependent density-functional theory (TDDFT)[204] is appealing because of its moderate computational demands. TDDFT calculations based on local exchange-correlation kernels yield reasonable excitation energies for small- and medium-sized molecules, provided that the excited states are formed from local transitions, are mainly composed of a single transition, and no extended π-systems are involved.[205,206]

Such assumptions are, however, problematic for charge-transfer excitons,[207,208] for which the interactions of spatially separated electrons (on acceptor) and holes (on donor) are not correctly described. Range-separated exchange-correlation kernels[209,210] can be used to overcome this deficiency but often need compound-specific adjustments.[211,212] Quantum-chemical approaches, such as coupled-cluster methods, on the other hand, allow for an accurate treatment of electron–electron and electron–hole interactions, but are computationally too demanding.[213–215]

Recently, it has been shown that the limitations of these methods can be overcome by using many-body Green's functions theory within the GW approximation and the Bethe–Salpeter equation (GW-BSE).[216–218] It has been successfully applied to determine optical excitations in crystals,[219–221] polymers,[222,223] and small inorganic[224,225] and organic[223,226] molecules.

To this end, the many-body Green's functions theory within the GW approximation and the Bethe–Salpeter equation have been benchmarked for a series of prototypical small-molecule based pairs.[227–229] This method has predicted energies of local Frenkel and intermolecular charge-transfer excitations with an accuracy of tens of meV.[230] Analysis of energy levels and binding energies of excitons in dimers of dicyanovinyl-substituted quaterthiophene and fullerene[231] as well as zinc-tetraphenylporphyrin and C_{70}-fullerene[232] has shown that the transition from Frenkel to charge transfer excitons is endothermic and the binding energy of charge transfer excitons is still of the order of 1.5–2 eV. Hence, even such an accurate dimer-in-vacuum-based description does not yield internal energetics favorable for the generation of free charges either by thermal energy or by an external electric field. These results indicate that accounting for the explicit molecular environment is as important as an accurate knowledge of internal dimer energies and should clearly be the focus of research aiming at quantitative descriptions of excitations in organic materials.

9.8 Software

An extensive list of standard simulations packages can be found elsewhere.[48,233] Here, we only provide a brief overview of the package that was especially designed for coarse-grained simulations of morphologies and microscopic calculations of charge mobility, the Versatile Object-oriented Toolkit for Coarse-graining and Charge Transport Applications (VOTCA, www.votca.org). Most of the aforementioned methods are implemented in this package (Figure 9.9).

VOTCA consists of several modules: systematic coarse-graining (VOTCA-CSG), charge/exciton transport (VOTCA-CTP, VOTCA-MOO), and the kinetic Monte Carlo (VOTCA-KMC). The coarse-graining (VOTCA-CSG) package[55] implements several coarse-graining techniques, among them force-matching, inverse Monte Carlo, and iterative Boltzmann inversion. It is a platform for method development of new approaches for obtaining well-defined coarse-grained models. The purpose of the charge transport (VOTCA-CTP)

package[140] is to simplify the work-flow for charge and energy transport simulations, provide a uniform error control for these methods, a flexible platform for their development, and to eventually also allow for *in silico* pre-screening of organic semiconductors for specific applications.

A typical work-flow of charge transport simulations is depicted in Figure 9.9. The first step is the simulation of the atomistic morphology (VOTCA-CSG), which is then partitioned into hopping sites. Subsequently, the coordinates of the hopping sites are used to construct a list of pairs of molecules, known as the neighbor list. For each pair, an electronic coupling element (VOTCA-MOO), the reorganization energy, the driving force, and eventually the hopping rate are evaluated. The neighbor list, combined with the hopping rates, defines a directed graph. The corresponding master equation can then be solved using the kinetic Monte Carlo method (VOTCA-KMC), which allows one to explicitly monitor the charge dynamics in a system, as well as calculate time- or ensemble-averages of occupation probabilities, charge fluxes, correlation functions, and field-dependent mobilities.

The package is written in modular C++ while the workflow is implemented using scripting languages and controlled by several extensible

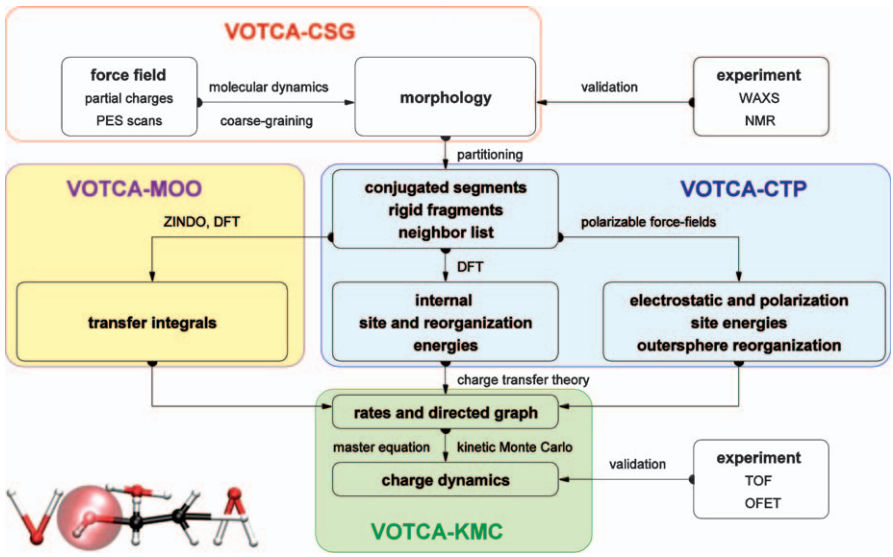

Figure 9.9 Modules of the VOTCA package, www.votca.org: Ground-state geometries, partial charges, refined force-fields, and coarse-grained models are used to simulate atomistically-resolved morphologies. After partitioning on conjugated segments and rigid fragments, a list of pairs of molecules (neighbor list) can be constructed. Transfer integrals, reorganization and site energies, and eventually hopping rates are then calculated for all pairs from this list. From this, a directed graph is generated and the corresponding master equation is solved using the kinetic Monte Carlo method.

markup language (XML) input files, which make it a robust yet easily modifiable toolkit for new developers. The code is available as a complete package in various Linux distributions and is partitioned into five libraries (tools, csg, ctp, kmc, moo), with each library providing a distinct functionality. Data transfer between individual programs is implemented *via* a relational (SQLite) database. CMake is used to build, test, and package the toolkit.

9.9 Outlook

To conclude, substantial method development is still necessary to achieve parameter-free modeling of organic semiconductors. Although the list is far from complete, several methodological issues to resolve are:

- Prediction of partially-ordered, non-equilibrium morphologies influenced by the material's processing, especially for polymeric semiconductors. This includes force-field parametrization from first-principles and the development of accurate coarse-grained models, as well as advanced sampling techniques.
- Definition of diabatic states, in particular if they are delocalized over parts of the molecule or over several molecules.
- Development of more accurate and efficient methods for the evaluation of electrostatic and induction effects when evaluating site energy differences, especially for charged systems with aperiodic charge distributions in a periodic neutral environment.
- Embedding of (computationally demanding) treatment of explicit long-range Coulomb interactions (including induction) when solving the master equation, *i.e.* re-evaluation of state-dependent rates at every Monte Carlo step.
- Developing computationally efficient off-lattice models for morphologies and rates, as well as the parametrization techniques for specific compounds.
- Quantitative treatment of excited states embedded in a heterogeneous polarizable molecular environment.

Note, that advancements in all of the above-mentioned directions are absolutely vital before one can even start to think about devising accurate structure–property relationships for organic semiconductors.

Acknowledgements

This work was partly supported by the DFG program IRTG 1404, DFG grant SPP 1355, and BMBF grants MEDOS (FKZ 03EK3503B) and MESOMERIE (FKZ 13N10723). We are grateful to Carl Poelking, Pascal Kordt, Anton Melnyk, Jens Wehner, Kurt Kremer, and Mara Jochum for critical reading of this manuscript.

References

1. Wolfgang Tress, Karl Leo and Moritz Riede, Influence of hole-transport layers and donor materials on open-circuit voltage and shape of i-v curves of organic solar cells, *Adv. Funct. Mater.*, 2011, **21**(11), 2140–2149.
2. Thomas Kirchartz and Jenny Nelson, Device modelling of organic bulk heterojunction solar cells, *Top. Curr. Chem.*, 2013, 1–46.
3. P. de Bruyn, A. H. P. van Rest, G. a. H. Wetzelaer, D. M. de Leeuw and P. W. M. Blom, Diffusion-limited current in organic metal-insulator-metal diodes, *Phys. Rev. Lett.*, 2013, **111**(18), 186801.
4. L. J. A. Koster, V. D. Mihailetchi, R. Ramaker and P. W. M. Blom, Light intensity dependence of open-circuit voltage of polymer:fullerene solar cells, *Appl. Phys. Lett.*, 2005, **86**(12), 123509.
5. Ilja Lange, Juliane Kniepert, Patrick Pingel, Ines Dumsch, Sybille Allard, Silvia Janietz, Ullrich Scherf and Dieter Neher, Correlation between the open circuit voltage and the energetics of organic bulk heterojunction solar cells, *J. Phys. Chem. Lett.*, 2013, **4**(22), 3865–3871.
6. Harvey Scher and Elliott Montroll, Anomalous transit-time dispersion in amorphous solids, *Phys. Rev. B*, 1975, **12**(6), 2455–2477.
7. B. Movaghar, B. Pohlmann and W. Schirmacher, Theory of electronic hopping transport in disordered materials, *Philosophical Magazine Part B*, 1980, **41**(1), 49–63.
8. H. Baessler, Charge transport in disordered organic photoconductors a Monte Carlo simulation study, *Phys. Status Solidi B*, 1993, **175**(1), 15–56.
9. Sergei Baranovski and Oleg Rubel, Description of charge transport in amorphous semiconductors. In Sergei Baranovski, editor, *Charge Transport in Disordered Solids with Applications in Electronics*, pages 49–96. John Wiley & Sons, Ltd, 2006.
10. M. Bouhassoune, S. L. M. van Mensfoort, P. A. Bobbert and R. Coehoorn, Carrier-density and field-dependent charge-carrier mobility in organic semiconductors with correlated gaussian disorder, *Organic Electronics*, 2009, **10**(3), 437–445.
11. J. O. Oelerich, D. Huemmer, M. Weseloh and S. D. Baranovskii, Concentration dependence of the transport energy level for charge carriers in organic semiconductors, *Appl. Phys. Lett.*, 2010, **97**(14), 143302.
12. S. D. Baranovskii, Theoretical description of charge transport in disordered organic semiconductors, *Physica Status Solidi (b)*, 2014, **251**(3), 487–525.
13. W. F. Pasveer, J. Cottaar, C. Tanase, R. Coehoorn, P. A. Bobbert, P. W. M. Blom, D. M. de Leeuw and M. A. J. Michels, Unified description of charge-carrier mobilities in disordered semiconducting polymers, *Phys. Rev. Lett.*, 2005, **94**(20), 206601.
14. A. J Stone. *The Theory of Intermolecular Forces*. Clarendon Press, Oxford, 1997.

15. Christian Kramer, Tristan Bereau, Alexander Spinn, Klaus R. Liedl, Peter Gedeck and Markus Meuwly, Deriving static atomic multipoles from the electrostatic potential, *Journal of Chemical Information and Modeling*, 2013, **53**(12), 3410–3417.
16. Alexandre Tkatchenko, Robert A. DiStasio, Roberto Car and Matthias Scheffler, Accurate and efficient method for many-body van der Waals interactions, *Phys. Rev. Lett.*, 2012, **108**(23), 236402.
17. Pedro E. M. Lopes, Benoit Roux and Alexander D. MacKerell Jr, Molecular modeling and dynamics studies with explicit inclusion of electronic polarizability: theory and applications, *Theoretical Chemistry Accounts*, 2009, **124**(1–2), 11–28.
18. Piotr Cieplak, François-Yves Dupradeau, Yong Duan and Junmei Wang, Polarization effects in molecular mechanical force fields, *J. Phys-Condens. Mat.*, 2009, **21**(33), 333102.
19. Seiji Tsuzuki, Kazumasa Honda and Reiko Azumi, Model chemistry calculations of thiophene dimer interactions: Origin of -stacking, *J. Am. Chem. Soc.*, 2002, **124**(41), 12200–12209.
20. Seth B. Darling and Michael Sternberg, Importance of side chains and backbone length in defect modeling of poly(3-alkylthiophenes), *J. Phys. Chem. B*, 2009, **113**(18), 6215–6218.
21. C. F. N. Marchiori and M. Koehler, Dipole assisted exciton dissociation at conjugated polymer/fullerene photovoltaic interfaces: A molecular study using density functional theory calculations, *Synthetic Metals*, 2010, **160**(7–8), 643–650.
22. Ram S. Bhatta, Yeneneh Y. Yimer, Mesfin Tsige and David S. Perry, Conformations and torsional potentials of poly(3-hexylthiophene) oligomers: Density functional calculations up to the dodecamer, *Computational and Theoretical Chemistry*, 2012, **995**, 36–42.
23. Antonino Famulari, Guido Raos, Alberto Baggioli, Mosè Casalegno, Riccardo Po and Stefano V. Meille, A solid state density functional study of crystalline thiophene-based oligomers and polymers, *J. Phys. Chem. B*, 2012, **116**(49), 14504–14509.
24. Ram S. Bhatta, Yeneneh Y. Yimer, David S. Perry and Mesfin Tsige, Improved force field for molecular modeling of poly(3-hexylthiophene), *J. Phys. Chem. B*, 2013, **117**(34), 10035–10045.
25. Ram S. Bhatta and David S. Perry, Correlated backbone torsional potentials in poly(3-methylthiophene), *Computational and Theoretical Chemistry*, 2013, **1008**, 90–95.
26. Alberto Baggioli and Antonino Famulari, On the inter-ring torsion potential of regioregular p3ht: a first principles reexamination with explicit side chains, *Phys. Chem. Chem. Phys.*, 2014, **16**(9), 3983–3994.
27. Arnaud Maillard and Alain Rochefort, Structural and electronic properties of poly(3-hexylthiophene) π-stacked crystals, *Phys. Rev. B*, 2009, **79**(11).
28. Renato Colle, Giuseppe Grosso, Alberto Ronzani and Claudio M. Zicovich-Wilson, Structure and x-ray spectrum of crystalline poly(3-hexylthiophene)

from DFT-van der Waals calculations, *physica status solidi (b)*, 2011, **248**(6), 1360–1368.
29. Weiyu Xie, Y. Y. Sun, S. B. Zhang and John E. Northrup, Structure and sources of disorder in poly(3-hexylthiophene) crystals investigated by density functional calculations with van der Waals interactions, *Phys. Rev. B*, 2011, **83**(18), 184117.
30. Stefan Grimme, Semiempirical GGA-type density functional constructed with a long-range dispersion correction, *J. Comput. Chem.*, 2006, **27**(15), 1787–1799.
31. O. Anatole von Lilienfeld, Ivano Tavernelli, Ursula Rothlisberger and Daniel Sebastiani, Optimization of effective atom centered potentials for london dispersion forces in density functional theory, *Phys. Rev. Lett.*, 2004, **93**(15), 153004.
32. D. C. Langreth, B. I. Lundqvist, S. D. Chakarova-Käck, V. R. Cooper, M. Dion, P. Hyldgaard, A. Kelkkanen, J. Kleis, Lingzhu Kong, Shen Li, P. G. Moses, E. Murray, A. Puzder, H. Rydberg, E. Schröder and T. Thonhauser, A density functional for sparse matter, *J. Phys-Condens. Mat.*, 2009, **21**(8), 084203.
33. Oleg A. Vydrov and Troy Van Voorhis, Nonlocal van der Waals density functional made simple, *Phys. Rev. Lett.*, 2009, **103**(6), 063004.
34. K. Hannewald and P. A. Bobbert, Ab initio theory of charge-carrier conduction in ultrapure organic crystals, *Appl. Phys. Lett.*, 2004, **85**(9), 1535.
35. David L. Cheung and Alessandro Troisi, Modelling charge transport in organic semiconductors: from quantum dynamics to soft matter, *Phys. Chem. Chem. Phys.*, 2008, **10**(39), 5941.
36. David P. McMahon, David L. Cheung, Ludwig Goris, Javier Dacuna, Alberto Salleo and Alessandro Troisi, Relation between microstructure and charge transport in polymers of different regioregularity, *J. Phys. Chem. C*, 2011, **115**(39), 19386–19393.
37. Thorsten Vehoff, Yeon Sook Chung, Karen Johnston, Alessandro Troisi, Do Y. Yoon and Denis Andrienko, Charge transport in self-assembled semiconducting organic layers: Role of dynamic and static disorder, *J. Phys. Chem. C*, 2010, **114**(23), 10592–10597.
38. A. Troisi and G. Orlandi, Charge-transport regime of crystalline organic semiconductors: Diffusion limited by thermal off-diagonal electronic disorder, *Phys. Rev. Lett.*, 2006, **96**(8).
39. Frank Ortmann, Friedhelm Bechstedt and Karsten Hannewald, Charge transport in organic crystals: Theory and modelling, *Physica Status Solidi (b)*, 2011, **248**(3), 511–525.
40. A. D. MacKerell, D. Bashford, M. Bellott, R. L. Dunbrack, J. D. Evanseck, M. J. Field, S. Fischer, J. Gao, H. Guo, S. Ha, D. Joseph-McCarthy, L. Kuchnir, K. Kuczera, F. T. K. Lau, C. Mattos, S. Michnick, T. Ngo, D. T. Nguyen, B. Prodhom, W. E. Reiher, B. Roux, M. Schlenkrich, J. C. Smith, R. Stote, J. Straub, M. Watanabe, J. Wiórkiewicz-Kuczera, D. Yin and M. Karplus, All-atom empirical potential for molecular

modeling and dynamics studies of proteins, *J. Phys. Chem. B*, 1998, **102**(18), 3586–3616.

41. William L. Jorgensen, David S. Maxwell and Julian Tirado-Rives, Development and testing of the OPLS all-atom force field on conformational energetics and properties of organic liquids, *J. Am. Chem. Soc.*, 1996, **118**(45), 11225–11236.
42. Wendy D. Cornell, Piotr Cieplak, Christopher I. Bayly, Ian R. Gould, Kenneth M. Merz, David M. Ferguson, David C. Spellmeyer, Thomas Fox, James W. Caldwell and Peter A. Kollman, A second generation force field for the simulation of proteins, nucleic acids, and organic molecules, *J. Am. Chem. Soc.*, 1995, **117**(19), 5179–5197.
43. Valentina Marcon and Guido Raos, Molecular modeling of crystalline oligothiophenes: Testing and development of improved force fields, *J. Phys. Chem. B*, 2004, **108**(46), 18053–18064.
44. Carl Poelking and Denis Andrienko, Effect of polymorphism, regioregularity and paracrystallinity on charge transport in poly(3-hexylthiophene) p3ht. nanofibers, *Macromolecules*, 2013, **46**(22), 8941–8956.
45. Margherita Moreno, Mosè Casalegno, Guido Raos, Stefano V. Meille and Riccardo Po, Molecular modeling of crystalline alkylthiophene oligomers and polymers, *J. Phys. Chem. B*, 2010, **114**(4), 1591–1602.
46. Tran Thinh To and Stefan Adams, Accurate poly(3-hexylthiophene) forcefield from first-principle modeling, *Nanoscience and Nanotechnology Letters*, 2012, **4**(7), 703–711.
47. Victor Rühle, James Kirkpatrick and Denis Andrienko, A multiscale description of charge transport in conjugated oligomers, *J. Chem. Phys.*, 2010, **132**(13), 134103–134103–9.
48. Luca Muccioli, Gabriele D'Avino, Roberto Berardi, Silvia Orlandi, Antonio Pizzirusso, Matteo Ricci, Otello Maria Roscioni and Claudio Zannoni, Supramolecular organization of functional organic materials in the bulk and at organic/organic interfaces: A modeling and computer simulation approach, *Top. Curr. Chem.*, 2013, 1–63.
49. Gabriele D'Avino, Sébastien Mothy, Luca Muccioli, Claudio Zannoni, Linjun Wang, Jérôme Cornil, David Beljonne and Frédéric Castet, Energetics of electron–hole separation at p3ht/PCBM heterojunctions, *J. Phys. Chem. C*, 2013, **117**(25), 12981–12990.
50. Orestis Alexiadis and Vlasis G. Mavrantzas, All-atom molecular dynamics simulation of temperature effects on the structural, thermodynamic, and packing properties of the pure amorphous and pure crystalline phases of regioregular p3ht, *Macromolecules*, 2013, **46**(6), 2450–2467.
51. Falk May, Mustapha Al-Helwi, Björn Baumeier, Wolfgang Kowalsky, Evelyn Fuchs, Christian Lennartz and Denis Andrienko, Design rules for charge-transport efficient host materials for phosphorescent organic light-emitting diodes, *J. Am. Chem. Soc.*, 2012, **134**(33), 13818–13822.

52. Falk May, Björn Baumeier, Christian Lennartz and Denis Andrienko, Can lattice models predict the density of states of amorphous organic semiconductors?, *Phys. Rev. Lett.*, 2012, **109**(13), 136401.
53. Patrick Gemünden, Carl Poelking, Kurt Kremer, Denis Andrienko and Kostas Ch, Daoulas. Nematic ordering, conjugation, and density of states of soluble polymeric semiconductors, *Macromolecules*, 2013, **46**(14), 5762–5774.
54. W. G. Noid, J. Chu, G. S. Ayton, V. Krishna, S. Izvekov, G. A. Voth, A. Das and H. C. Andersen, The multiscale coarse graining method. 1. a rigorous bridge between atomistic and coarse-grained models, *J. Chem. Phys.*, 2008, **128**, 244114.
55. Victor Rühle, Christoph Junghans, Alexander Lukyanov, Kurt Kremer and Denis Andrienko, Versatile object-oriented toolkit for coarse-graining applications, *J. Chem. Theory. Comput.*, 2009, **5**(12), 3211–3223.
56. A. K. Soper, Empirical potential Monte Carlo simulation of fluid structure, *Chem. Phys.*, 1996, **202**, 295–306.
57. Alexander P. Lyubartsev and Aatto Laaksonen, Calculation of effective interaction potentials from radial distribution functions: A reverse Monte Carlo approach, *Phys. Rev. E*, 1995, **52**(4), 3730–3737.
58. D. Reith, M. Pütz and F. Müller-Plathe, Deriving effective mesoscale potentials from atomistic simulations, *J. Comp. Chem.*, 2003, **24**(13), 1624–1636.
59. Mara Jochum, Denis Andrienko, Kurt Kremer and Christine Peter, Structure-based coarse-graining in liquid slabs, *J. Chem. Phys.*, 2012, **137**(6), 064102.
60. F. Ercolessi and J. B. Adams, Interatomic potentials from 1st-principles calculations - the force-matching method, *Europhys. Lett.*, 1994, **26**(8), 583–588.
61. S. Izvekov, M. Parrinello, C. J. Burnham and G. A. Voth, Effective force fields for condensed phase systems from ab initio molecular dynamics simulation: A new method for force-matching, *J. Chem. Phys.*, 2004, **120**(23), 10896–10913.
62. M. Scott Shell, The relative entropy is fundamental to multiscale and inverse thermodynamic problems, *J. Chem. Phys.*, 2008, **129**(14), 144108.
63. W. G. Noid, J. W. Chu, G. S. Ayton and G. A. Voth, Multiscale coarse-graining and structural correlations: Connections to liquid-state theory, *J. Phys. Chem. B*, 2007, **111**(16), 4116–4127.
64. W. G. Noid, Perspective: Coarse-grained models for biomolecular systems, *J. Chem. Phys.*, 2013, **139**(9), 090901.
65. Khanh Do, David M. Huang, Roland Faller and Adam J. Moulé, A comparative MD study of the local structure of polymer semiconductors p3ht and PBTTT, *Phys. Chem. Chem. Phys.*, 2010, **12**(44), 14735.

66. David M. Huang, Roland Faller, Khanh Do and Adam J. Moulé, Coarse-grained computer simulations of polymer/fullerene bulk heterojunctions for organic photovoltaic applications, *J. Chem. Theory. Comput.*, 2010, **6**(2), 526–537.
67. Cheng-Kuang Lee, Chun-Wei Pao and Chih-Wei Chu, Multiscale molecular simulations of the nanoscale morphologies of p3ht:PCBM blends for bulk heterojunction organic photovoltaic cells, *Energy & Environmental Science*, 2011, **4**(10), 4124–4132.
68. Eric Jankowski, Hilary S. Marsh and Arthi Jayaraman, Computationally linking molecular features of conjugated polymers and fullerene derivatives to bulk heterojunction morphology, *Macromolecules*, 2013, **46**(14), 5775–5785.
69. V. Rühle, J. Kirkpatrick, K. Kremer and D. Andrienko, Coarse-grained modelling of polypyrrole morphologies, *Phys. Stat. Solidi B*, 2008, **245**, 844.
70. Kyra N. Schwarz, Tak W. Kee and David M. Huang, Coarse-grained simulations of the solution-phase self-assembly of poly(3-hexylthiophene) nanostructures, *Nanoscale*, 2013, **5**(5), 2017–2027.
71. Kostas Ch Daoulas and Marcus Müller, Comparison of simulations of lipid membranes with membranes of block copolymers. In Wolfgang Peter Meier and Wolfgang Knoll, editors, *Polymer Membranes/Biomembranes, number 224 in Advances in Polymer Science*, pages 43–85. Springer, Berlin, Heidelberg, 2010.
72. Marcus Müller, Studying amphiphilic self-assembly with soft coarse-grained models, *J. Stat. Phys.*, 2011, **145**(4), 967–1016.
73. Gavin A. Buxton and Nigel Clarke, Predicting structure and property relations in polymeric photovoltaic devices, *Phys. Rev. B*, 2006, **74**(8), 085207.
74. Anton Pershin, Sergii Donets and Stephan A. Baeurle, A new multiscale modeling method for simulating the loss processes in polymer solar cell nanodevices, *J. Chem. Phys.*, 2012, **136**(19), 194102.
75. Sergii Donets, Anton Pershin, Martin J. A. Christlmaier and Stephan A. Baeurle, A multiscale modeling study of loss processes in block-copolymer-based solar cell nanodevices, *J. Chem. Phys.*, 2013, **138**(9), 094901.
76. Manas Shah and Venkat Ganesan, Correlations between morphologies and photovoltaic properties of rod-coil block copolymers, *Macromolecules*, 2010, **43**(1), 543–552.
77. Hari K. Kodali and Baskar Ganapathysubramanian, A computational framework to investigate charge transport in heterogeneous organic photovoltaic devices, *Comput. Methods Appl. Mech. Eng.*, 2012, **247–248**, 113–129.
78. J. A. Barker, C. M. Ramsdale and N. C. Greenham, Modeling the current–voltage characteristics of bilayer polymer photovoltaic devices, *Phys. Rev. B*, 2003, **67**(7), 075205.

79. C. M. Martin, V. M. Burlakov, H. E. Assender and D. A. R. Barkhouse, A numerical model for explaining the role of the interface morphology in composite solar cells, *J. Appl. Phys.*, 2007, **102**(10), 104506.
80. Robin G. E. Kimber, Edward N. Wright, Simon E. J. O'Kane, Alison B. Walker and James C. Blakesley, Mesoscopic kinetic Monte Carlo modeling of organic photovoltaic device characteristics, *Phys. Rev. B*, 2012, **86**(23), 235206.
81. Y. C. Cheng, R. J. Silbey, D. A. da Silva Filho, J. P. Calbert, J. Cornil and J. L. Brédas, Three-dimensional band structure and bandlike mobility in oligoacene single crystals: A theoretical investigation, *J. Chem. Phys.*, 2003, **118**(8), 3764–3774.
82. Yanting Yang, Yanming Yang, Fugen Wu and Zhigang Wei, First-principles electronic structure of copper phthalocyanine (CuPc), *Solid State Communications*, 2008, **148**(11–12), 559–562.
83. Edgar A. Silinsh and Vladislav Capek. *Organic Molecular Crystals: Interacton Localization, and Transport Phenomena*. American Institute of Physics, 1 edition, 1997.
84. Yuan-Chung Cheng and Robert J. Silbey, A unified theory for charge-carrier transport in organic crystals, *J. Chem. Phys.*, 2008, **128**(11), 114713.
85. J. L. Brédas, J. P. Calbert, D. A. da Silva Filho and J. Cornil, Organic semiconductors: A theoretical characterization of the basic parameters governing charge transport, *Proc. Natl. Acad. Sci. USA*, 2002, **99**(9), 5804–5809.
86. Veaceslav Coropceanu, Jérôme Cornil, Demetrio A. da Silva Filho, Yoann Olivier, Robert Silbey and Jean-Luc Brédas, Charge transport in organic semiconductors, *Chem. Rev.*, 2007, **107**(4), 926–952.
87. James Kirkpatrick, An approximate method for calculating transfer integrals based on the ZINDO hamiltonian, *Int. J. Quantum Chem.*, 2008, **108**(1), 51–56.
88. Björn Baumeier, James Kirkpatrick and Denis Andrienko, Density-functional based determination of intermolecular charge transfer properties for large-scale morphologies, *Phys. Chem. Chem. Phys.*, 2010, **12**(36), 11103.
89. Troy Van Voorhis, Tim Kowalczyk, Benjamin Kaduk, Lee-Ping Wang, Chiao-Lun Cheng and Qin Wu, The diabatic picture of electron transfer, reaction barriers, and molecular dynamics, *Annual Review of Physical Chemistry*, 2010, **61**(1), 149–170.
90. S. F. Boys, Construction of some molecular orbitals to be approximately invariant for changes from one molecule to another, *Rev. Mod. Phys.*, 1960, **32**(2), 296–299.
91. Michael Baer, Adiabatic and diabatic representations for atom-molecule collisions: Treatment of the collinear arrangement, *Chem. Phys. Lett.*, 1975, **35**(1), 112–118.

92. Robert J. Cave and Marshall D. Newton, Generalization of the Mulliken-Hush treatment for the calculation of electron transfer matrix elements, *Chem. Phys. Lett.*, 1996, **249**(1–2), 15–19.
93. Gregory J. Atchity and Klaus Ruedenberg, Determination of diabatic states through enforcement of configurational uniformity, *Theoretical Chemistry Accounts*, 1997, **97**(1–4), 47–58.
94. C. Alden Mead and Donald G. Truhlar, Conditions for the definition of a strictly diabatic electronic basis for molecular systems, *J. Chem. Phys.*, 1982, 77(12), 6090–6098.
95. T. Pacher, L. S. Cederbaum and H. Köppel, Approximately diabatic states from block diagonalization of the electronic hamiltonian, *J. Chem. Phys.*, 1988, **89**(12), 7367–7381.
96. Eugene S. Kryachko, On generalized Mulliken–Hush approach of electronic transfer: Inclusion of non-zero off-diagonal diabatic dipole moment, *J. Phys. Chem. A*, 1999, **103**(22), 4368–4370.
97. Hisao Nakamura and Donald G. Truhlar, The direct calculation of diabatic states based on configurational uniformity, *J. Chem. Phys.*, 2001, **115**(22), 10353–10372.
98. Joseph E. Subotnik, Sina Yeganeh, Robert J. Cave and Mark A. Ratner, Constructing diabatic states from adiabatic states: Extending generalized Mulliken–Hush to multiple charge centers with Boys localization, *J. Chem. Phys.*, 2008, **129**(24), 244101.
99. Chao-Ping Hsu, The electronic couplings in electron transfer and excitation energy transfer, *Accounts Chem. Res.*, 2009, **42**(4), 509–518.
100. Xiaolei Zhu and David R. Yarkony, Toward eliminating the electronic structure bottleneck in nonadiabatic dynamics on the fly: An algorithm to fit nonlocal, quasidiabatic, coupled electronic state hamiltonians based on ab initio electronic structure data, *J. Chem. Phys.*, 2010, **132**(10), 104101.
101. Michele Pavanello and Johannes Neugebauer, Linking the historical and chemical definitions of diabatic states for charge and excitation energy transfer reactions in condensed phase, *J. Chem. Phys.*, 2011, **135**(13), 134113.
102. Elisabetta Collini and Gregory D. Scholes, Coherent intrachain energy migration in a conjugated polymer at room temperature, *Science*, 2009, **323**(5912), 369–373.
103. Alberto Salleo, R. Joseph Kline, Dean M. DeLongchamp and Michael L. Chabinyc, Microstructural characterization and charge transport in thin films of conjugated polymers, *Adv. Mater.*, 2010, **22**(34), 3812–3838.
104. D. Beljonne, J. Cornil, H. Sirringhaus, P. J. Brown, M. Shkunov, R. H. Friend and J.-L. Brédas, Optical signature of delocalized polarons in conjugated polymers, *Adv. Funct. Mater.*, 2001, **11**(3), 229–234.
105. Peter J. Brown, Henning Sirringhaus, Mark Harrison, Maxim Shkunov and Richard H. Friend, Optical spectroscopy of field-induced charge in

self-organized high mobility poly(3-hexylthiophene), *Phys. Rev. B*, 2001, **63**(12), 125204.
106. Nenad Vukmirović and Lin-Wang Wang, Density of states and wave function localization in disordered conjugated polymers: A large scale computational study, *J. Phys. Chem. B*, 2011, **115**(8), 1792–1797.
107. Sanjio S. Zade, Natalia Zamoshchik and Michael Bendikov, From short conjugated oligomers to conjugated polymers. lessons from studies on long conjugated oligomers, *Accounts Chem. Res.*, 2011, **44**(1), 14–24.
108. Iffat H. Nayyar, Enrique R. Batista, Sergei Tretiak, Avadh Saxena, Darryl L. Smith and Richard L. Martin, Role of geometric distortion and polarization in localizing electronic excitations in conjugated polymers, *J. Chem. Theory. Comput.*, 2013, **9**(2), 1144–1154.
109. Hugo Bronstein, Zhuoying Chen, Raja Shahid Ashraf, Weimin Zhang, Junping Du, James R. Durrant, Pabitra Shakya Tuladhar, Kigook Song, Scott E. Watkins, Yves Geerts, Martijn M. Wienk, Rene A. J. Janssen, Thomas Anthopoulos, Henning Sirringhaus, Martin Heeney and Iain McCulloch, Thieno[3,2-b]thiophene-diketopyrrolopyrrole-containing polymers for high-performance organic field-effect transistors and organic photovoltaic devices, *J. Am. Chem. Soc.*, 2011, **133**(10), 3272–3275.
110. Edward H. Magin and Paul M. Borsenberger, Electron transport in n,n'-bis(2-phenethyl)-perylene-3,4: 9,10-bis(dicarboximide), *J. Appl. Phys.*, 1993, **73**(2), 787–791.
111. Mark Van der Auweraer, Frans C. De Schryver, Paul M. Borsenberger and Heinz Bässler, Disorder in charge transport in doped polymers, *Adv. Mater.*, 1994, **6**(3), 199–213.
112. Jui-Fen Chang, Jenny Clark, Ni Zhao, Henning Sirringhaus, Dag W. Breiby, Jens W. Andreasen, Martin M. Nielsen, Mark Giles, Martin Heeney and Iain McCulloch, Molecular-weight dependence of interchain polaron delocalization and exciton bandwidth in high-mobility conjugated polymers, *Phys. Rev. B*, 2006, **74**(11), 115318.
113. Ting Qin and Alessandro Troisi, Relation between structure and electronic properties of amorphous MEH-PPV polymers, *J. Am. Chem. Soc.*, 2013, **135**(30), 11247–11256.
114. S. Shaked, S. Tal, Y. Roichman, A. Razin, S. Xiao, Y. Eichen and N. Tessler, Charge density and film morphology dependence of charge mobility in polymer field-effect transistors, *Adv. Mater.*, 2003, **15**(11), 913–916.
115. Mark S. Gordon, Jonathan M. Mullin, Spencer R. Pruitt, Luke B. Roskop, Lyudmila V. Slipchenko and Jerry A. Boatz, Accurate methods for large molecular systems, *J. Phys. Chem. B*, 2009, **113**(29), 9646–9663.
116. Chris-Kriton Skylaris, Peter D. Haynes, Arash A. Mostofi and Mike C. Payne, Introducing ONETEP: Linear-scaling density functional simulations on parallel computers, *J. Chem. Phys.*, 2005, **122**(8), 084119.

117. José M. Soler, Emilio Artacho, Julian D. Gale, Alberto García, Javier Junquera, Pablo Ordejón and Daniel Sánchez-Portal, The SIESTA method for ab initio order-n materials simulation, *J. Phys-Condens. Mat.*, 2002, **14**(11), 2745.
118. David P. McMahon and Alessandro Troisi, An ad hoc tight binding method to study the electronic structure of semiconducting polymers, *Chem. Phys. Lett.*, 2009, **480**(4–6), 210–214.
119. Nenad Vukmirović and Lin-Wang Wang, Electronic structure of disordered conjugated polymers: Polythiophenes, *J. Phys. Chem. B*, 2009, **113**(2), 409–415.
120. Nenad Vukmirović and Lin-Wang Wang, Charge carrier motion in disordered conjugated polymers: A multiscale ab initio study, *Nano Letters*, 2009, **9**(12), 3996–4000.
121. Dmitri G. Fedorov and Kazuo Kitaura, Extending the power of quantum chemistry to large systems with the fragment molecular orbital method, *J. Phys. Chem. A*, 2007, **111**(30), 6904–6914.
122. Kazuo Kitaura, Eiji Ikeo, Toshio Asada, Tatsuya Nakano and Masami Uebayasi, Fragment molecular orbital method: an approximate computational method for large molecules, *Chem. Phys. Lett.*, 1999, **313**(3–4), 701–706.
123. Tomáš Kubař and Marcus Elstner, A hybrid approach to simulation of electron transfer in complex molecular systems, *Journal of The Royal Society Interface*, 2013, **10**(87), 20130415.
124. Jiangang Liu, Yue Sun, Xiang Gao, Rubo Xing, Lidong Zheng, Shupeng Wu, Yanhou Geng and Yanchun Han, Oriented poly(3-hexylthiophene) nanofibril with the π–π stacking growth direction by solvent directional evaporation, *Langmuir*, 2011, **27**(7), 4212–4219.
125. D. Porezag, Th. Frauenheim, Th. Köhler, G. Seifert and R. Kaschner, Construction of tight-binding-like potentials on the basis of density-functional theory: Application to carbon, *Phys. Rev. B*, 1995, **51**(19), 12947–12957.
126. M. Elstner, D. Porezag, G. Jungnickel, J. Elsner, M. Haugk, Th. Frauenheim, S. Suhai and G. Seifert, Self-consistent-charge density-functional tight-binding method for simulations of complex materials properties, *Phys. Rev. B*, 1998, **58**(11), 7260–7268.
127. Tao Liu and Alessandro Troisi, Understanding the microscopic origin of the very high charge mobility in PBTTT: Tolerance of thermal disorder, *Adv. Funct. Mater.*, 2014, **24**(7), 925–933.
128. Åsa Johansson and Sven Stafström, Polaron dynamics in a system of coupled conjugated polymer chains, *Phys. Rev. Lett.*, 2001, **86**(16), 3602–3605.
129. William Barford and David Trembath, Exciton localization in polymers with static disorder, *Phys. Rev. B*, 2009, **80**(16), 165418.
130. Nenad Vukmirović and Lin-Wang Wang, Carrier hopping in disordered semiconducting polymers: How accurate is the Miller–Abrahams model?, *Appl. Phys. Lett.*, 2010, **97**(4), 043305.

131. Allen Miller and Elihu Abrahams, Impurity conduction at low concentrations, *Phys. Rev.*, 1960, **120**(3), 745–755.
132. Nenad Vukmirović, A comparative study of electronic properties of disordered conjugated polymers, *Phys. Chem. Chem. Phys.*, 2013, **15**(10), 3543–3551.
133. Franz X. Bronold, Andreas Alvermann and Holger Fehske, Anderson localization in strongly coupled disordered electron–phonon systems, *Philosophical Magazine*, 2004, **84**(7), 673–704.
134. R. Fornari and Alessandro Troisi, Theory of charge hopping along a disordered polymer chain, *Phys. Chem. Chem. Phys.*, 2014, **16**, 9997–10007.
135. Carl Poelking, Kostas Daoulas, Alessandro Troisi and Denis Andrienko, Morphology and charge transport in p3ht: A theorist's perspective, *Adv. Polym. Sci.*, 2014.
136. Rudolph Marcus, Electron transfer reactions in chemistry. Theory and experiment, *Rev. Mod. Phys.*, 1993, **65**(3), 599–610.
137. Volkhard May and Oliver Kühn. *Charge and Energy Transfer Dynamics in Molecular Systems*. Wiley-VCH, 3rd, revised and enlarged edition, 2011.
138. Hermann Grabert and Ulrich Weiss, Quantum tunneling rates for asymmetric double-well systems with ohmic dissipation, *Phys. Rev. Lett.*, 1985, **54**(15), 1605–1608.
139. Matthew P. A. Fisher and Alan T. Dorsey, Dissipative quantum tunneling in a biased double-well system at finite temperatures, *Phys. Rev. Lett.*, 1985, **54**(15), 1609–1612.
140. Victor Rühle, Alexander Lukyanov, Falk May, Manuel Schrader, Thorsten Vehoff, James Kirkpatrick, Björn Baumeier and Denis Andrienko, Microscopic simulations of charge transport in disordered organic semiconductors, *J. Chem. Theory. Comput.*, 2011, **7**(10), 3335–3345.
141. Kamal Asadi, Auke J. Kronemeijer, Tobias Cramer, L. Jan Anton Koster, Paul W. M. Blom and Dago M. de Leeuw, Polaron hopping mediated by nuclear tunnelling in semiconducting polymers at high carrier density, *Nature Communications*, 2013, **4**, 1710.
142. E. F. Valeev, V. Coropceanu, D. A. da Silva Filho, S. Salman and J.-L. Bredas, Effect of electronic polarization on charge-transport parameters in molecular organic semiconductors, *J. Am. Chem. Soc.*, 2006, **128**(30), 9882.
143. Xinliang Feng, Valentina Marcon, Wojciech Pisula, Michael Ryan Hansen, James Kirkpatrick, Ferdinand Grozema, Denis Andrienko, Kurt Kremer and Klaus Müllen, Towards high charge-carrier mobilities by rational design of the shape and periphery of discotics, *Nat. Mater.*, 2009, **8**(5), 421–426.
144. Carl Poelking, Eunkyung Cho, Alexander Malafeev, Viktor Ivanov, Kurt Kremer, Chad Risko, Jean-Luc Brédas and Denis Andrienko, Characterization of charge-carrier transport in semicrystalline polymers: Electronic couplings, site energies, and charge-carrier dynamics

in poly(bithiophene-alt-thienothiophene) PBTTT, *J. Phys. Chem. C*, 2013, **117**(4), 1633–1640.
145. Y. Olivier, L. Muccioli, V. Lemaur, Y. H. Geerts, C. Zannoni and J. Cornil, Theoretical characterization of the structural and hole transport dynamics in liquid-crystalline phthalocyanine stacks, *J. Phys. Chem. B*, 2009, **113**(43), 14102.
146. J. R. Reimers, A practical method for the use of curvilinear coordinates in calculations of normal-mode-projected displacements and Duschinsky rotation matrices for large molecules, *J. Chem. Phys.*, 9103, **115**(20), 2001.
147. Manuel Schrader, Roland Fitzner, Moritz Hein, Chris Elschner, Björn Baumeier, Karl Leo, Moritz Riede, Peter Bäuerle and Denis Andrienko, Comparative study of microscopic charge dynamics in crystalline acceptor-substituted oligothiophenes, *J. Am. Chem. Soc.*, 2012, **134**(13), 6052–6056.
148. Christof Hättig, Recurrence relations for the direct calculation of spherical multipole interaction tensors and coulomb-type interaction energies, *Chem. Phys. Lett.*, 1996, **260**(3–4), 341–351.
149. Christof Hättig and Bernd Artur Heß, Calculation of orientation-dependent double-tensor moments for coulomb-type intermolecular interactions, *Molecular Physics*, 1994, **81**(4), 813–824.
150. Toon Verstraelen, Ewald Pauwels, Frank De Proft, Veronique Van Speybroeck, Paul Geerlings and Michel Waroquier, Assessment of atomic charge models for gas-phase computations on polypeptides, *J. Chem. Theory. Comput.*, 2012, **8**(2), 661–676.
151. Curt M. Breneman and Kenneth B. Wiberg, Determining atom-centered monopoles from molecular electrostatic potentials. the need for high sampling density in formamide conformational analysis, *J. Comput. Chem.*, 1990, **11**(3), 361–373.
152. A. J. Stone and M. Alderton, Distributed multipole analysis, *Molecular Physics*, 1985, **56**(5), 1047–1064.
153. Anthony J. Stone, Distributed multipole analysis: stability for large basis sets, *J. Chem. Theory Comput.*, 2005, **1**(6), 1128–1132.
154. Lisa Emily Chirlian and Michelle Miller Francl, Atomic charges derived from electrostatic potentials: a detailed study, *J. Comput. Chem.*, 1987, **8**(6), 894–905.
155. B. T. Thole, Molecular polarizabilities calculated with a modified dipole interaction, *Chem. Phys.*, 1981, **59**(3), 341–350.
156. Piet Th. van Duijnen and Marcel Swart, Molecular and atomic polarizabilities: Thole's model revisited, *J. Phys. Chem. A*, 1998, **102**(14), 2399–2407.
157. Jon Applequist, James R. Carl and Kwok-Kueng Fung, Atom dipole interaction model for molecular polarizability. Application to polyatomic molecules and determination of atom polarizabilities, *J. Am. Chem. Soc.*, 1972, **94**(9), 2952–2960.

158. Pengyu Ren and Jay W. Ponder, Polarizable atomic multipole water model for molecular mechanics simulation, *J. Phys. Chem. B*, 2003, **107**(24), 5933–5947.
159. Manuel Schrader, Christian Körner, Chris Elschner and Denis Andrienko, Charge transport in amorphous and smectic mesophases of dicyanovinyl-substituted oligothiophenes, *J. Mater. Chem.*, 2012, **22**(41), 22258–22264.
160. Sergey V. Novikov and Anatoly V. Vannikov, Cluster structure in the distribution of the electrostatic potential in a lattice of randomly oriented dipoles, *J. Phys. Chem.*, 1995, **99**(40), 14573–14576.
161. S. Novikov, D. Dunlap, V. Kenkre, P. Parris and A. Vannikov, Essential role of correlations in governing charge transport in disordered organic materials, *Phys. Rev. Lett.*, 1998, **81**(20), 4472–4475.
162. D. Dunlap, P. Parris and V. Kenkre, Charge–dipole model for the universal field dependence of mobilities in molecularly doped polymers, *Phys. Rev. Lett.*, 1996, **77**(3), 542–545.
163. Mathieu Linares, David Beljonne, Jerome Cornil, Kelly Lancaster, J.-L. Brédas, Stijn Verlaak, Alexander Mityashin, Paul Heremans, Andreas Fuchs, Christian Lennartz, Julien Idé, Raphael Méreau, Philippe Aurel, Laurent Ducasse and Frederic Castet, On the interface dipole at the pentacene-fullerene heterojunction: a theoretical study, *J. Phys. Chem. C*, 2010, **114**(7), 3215–3224.
164. Stijn Verlaak, David Beljonne, David Cheyns, Cedric Rolin, Mathieu Linares, Frédéric Castet, Jérôme Cornil and Paul Heremans, Electronic structure and geminate pair energetics at organic-organic interfaces: The case of pentacene/c60 heterojunctions, *Adv. Funct. Mater.*, 2009, **19**(23), 3809–3814.
165. Stijn Verlaak and Paul Heremans, Molecular microelectrostatic view on electronic states near pentacene grain boundaries, *Phys. Rev. B*, 2007, **75**(11), 115127.
166. Shane R. Yost, Lee-Ping Wang and Troy Van Voorhis, Molecular insight into the energy levels at the organic donor/acceptor interface: a quantum mechanics/molecular mechanics study, *J. Phys. Chem. C*, 2011, **115**(29), 14431–14436.
167. Shane R. Yost and Troy Van Voorhis, Electrostatic effects at organic semiconductor interfaces: A mechanism for ''cold'' exciton breakup, *J. Phys. Chem. C*, 2013, **117**(11), 5617–5625.
168. Sébastien Mothy, Maxime Guillaume, Julien Idé, Frédéric Castet, Laurent Ducasse, Jérôme Cornil and David Beljonne, Tuning the interfacial electronic structure at organic heterojunctions by chemical design, *J. Phys. Chem. Lett.*, 2012, **3**(17), 2374–2378.
169. Julien Idé, Sébastien Mothy, Adrien Savoyant, Alain Fritsch, Philippe Aurel, Raphaël Méreau, Laurent Ducasse, Jérôme Cornil, David Beljonne and Frédéric Castet, Interfacial dipole and band

bending in model pentacene/c60 heterojunctions, *Int. J. Quantum Chem.*, 2013, **113**(4), 580–584.

170. Ralf Mauer, Marcel Kastler and Frédéric Laquai, The impact of polymer regioregularity on charge transport and efficiency of p3ht:PCBM photovoltaic devices, *Adv. Funct. Mater.*, 2010, **20**(13), 2085–2092.
171. Amy M. Ballantyne, Lichun Chen, Justin Dane, Thomas Hammant, Felix M. Braun, Martin Heeney, Warren Duffy, Iain McCulloch, Donal D. C. Bradley and Jenny Nelson, The effect of poly(3-hexylthiophene) molecular weight on charge transport and the performance of polymer:fullerene solar cells, *Adv. Funct. Mater.*, 2008, **18**(16), 2373–2380.
172. J. Cottaar and P. A. Bobbert, Calculating charge-carrier mobilities in disordered semiconducting polymers: Mean field and beyond, *Phys. Rev. B*, 2006, **74**(11), 115204.
173. J. Kirkpatrick, V. Marcon, J. Nelson, K. Kremer and D. Andrienko, Charge mobility of discotic mesophases: a multiscale quantum and classical study, *Phys. Rev. Lett.*, 2007, **98**(22), 227402.
174. Falk May, Valentina Marcon, Michael Ryan Hansen, Ferdinand Grozema and Denis Andrienko, Relationship between supramolecular assembly and charge-carrier mobility in perylenediimide derivatives: the impact of side chains, *J. Mater. Chem.*, 2011, **21**(26), 9538.
175. Yi-Kang Lan, Cheng Han Yang and Hsiao-Ching Yang, Theoretical investigations of electronic structure and charge transport properties in polythiophene-based organic field-effect transistors, *Polymer International*, 2010, **59**(1), 16–21.
176. H. Scher, S. Alexander and E. W. Montroll, Field-induced trapping as a probe of dimensionality in molecular crystals, *Proc. Natl. Acad. Sci. USA*, 1980, **77**(7), 3758–3762.
177. V. Marcon, J. Kirkpatrick, W. Pisula and D. Andrienko, Supramolecular structure of perylene tetracarboxdiimides, *Phys. Status Solidi B*, 2008, **245**(5), 820–824.
178. Denis Andrienko, James Kirkpatrick, Valentina Marcon, Jenny Nelson and Kurt Kremer, Structure–charge mobility relation for hexabenzocoronene derivatives, *Phys. Status Solidi B*, 2008, **245**(5), 830–834.
179. Jenny Nelson, Joe J. Kwiatkowski, James Kirkpatrick and Jarvist M. Frost, Modeling charge transport in organic photovoltaic materials, *Accounts Chem. Res.*, 2009, **42**(11), 1768–1778.
180. P. M. Borsenberger, L. Pautmeier and H. Bässler, Charge transport in disordered molecular solids, *J. Chem. Phys.*, 1991, **94**(8), 5447.
181. P. Borsenberger, L. Pautmeier and H. Bässler, Nondispersive-to-dispersive charge-transport transition in disordered molecular solids, *Phys. Rev. B*, 1992, **46**(19), 12145–12153.
182. P. M. Borsenberger, E. H. Magin, M. Der VanAuweraer and F. C. De Schryver, The role of disorder on charge transport in molecularly doped

polymers and related materials, *Physica Status Solidi (a)*, 1993, **140**(1), 9–47.
183. Alexander Lukyanov and Denis Andrienko, Extracting nondispersive charge carrier mobilities of organic semiconductors from simulations of small systems, *Phys. Rev. B*, 2010, **82**(19), 193202.
184. Bernard Derrida, Velocity and diffusion constant of a periodic one-dimensional hopping model, *J. Stat. Phys.*, 1983, **31**(3), 433–450.
185. Kazuhiko Seki and M. Tachiya, Electric field dependence of charge mobility in energetically disordered materials: Polaron aspects, *Phys. Rev. B*, 2001, **65**(1), 014305.
186. Pascal Kordt, Ole Stenzel, Björn Baumeier, Volker Schmidt and Denis Andrienko, Parametrization of extended gaussian disorder models from microscopic charge transport simulations, *J. Chem. Theory. Comput.*, 2014, **10**(6), 2508–2513.
187. J. Cottaar, L. J. A. Koster, R. Coehoorn and P. A. Bobbert, Scaling theory for percolative charge transport in disordered molecular semiconductors, *Phys. Rev. Lett.*, 2011, **107**(13), 136601.
188. Y. Yimer, P. Bobbert and R. Coehoorn, Charge transport in disordered organic host's guest systems: Effects of carrier density and electric field, *Synthetic Metals*, 2399, **159**(21–22), 2009.
189. J. A. Freire and C. Tonezer, Density of states and energetic correlation in disordered molecular systems due to induced dipoles, *J. Chem. Phys.*, 2009, **130**(13), 134901.
190. J. J. M. van der Holst, F. W. A. van Oost, R. Coehoorn and P. A. Bobbert, Monte Carlo study of charge transport in organic sandwich-type single-carrier devices: Effects of Coulomb interactions, *Phys. Rev. B*, 2011, **83**(8), 085206.
191. B. Baumeier, O. Stenzel, C. Poelking, D. Andrienko and V. Schmidt, Stochastic modeling of molecular charge transport networks, *Phys. Rev. B*, 2012, **86**(18), 184202.
192. T. Brereton, O. Stenzel, B. Baumeier, D. Andrienko, V. Schmidt and D. Kroese, Efficient Simulation of Markov chains using segmentation, *Methodology Comput. Appl. Probability*, 2014, **16**(2), 465.
193. O. Stenzel, C. Hirsch, T. Brereton, B. Baumeier, D. Andrienko, D. P. Kroese, V. Schmidt, A generalized toolkit for studying the charge transport properties of materials via random walks in random environments, submitted.
194. P. P. Ewald, Die berechnung optischer und elektrostatischer gitterpotentiale, *Annalen der Physik*, 1921, **369**(3), 253–287.
195. Carl Poelking, Max Tietze, Chris Elschner, Karl Leo, Björn Baumeier, Denis Andrienko, Decisive role of long-range interactions and mesoscopic order at organic interfaces, submitted, 2014.
196. E. R. Smith, Electrostatic energy in ionic crystals, *Proceedings of the Royal Society of London. A. Mathematical and Physical Sciences*, 1981, **375**(1763), 475–505.

197. A. Wilke, P. Amsalem, J. Frisch, B. Bröker, A. Vollmer and N. Koch, Electric fields induced by energy level pinning at organic heterojunctions, *Appl. Phys. Lett.*, 2011, **98**(12), 123304.
198. David Beljonne, Jérôme Cornil, Luca Muccioli, Claudio Zannoni, Jean-Luc Brédas and Frédéric Castet, Electronic processes at organic-organic interfaces: insight from modeling and implications for opto-electronic devices, *Chem. Mater.*, 2011, **23**(3), 591–609.
199. David P. McMahon, David L. Cheung and Alessandro Troisi, Why holes and electrons separate so well in polymer/fullerene photovoltaic cells, *J. Phys. Chem. Lett.*, 2011, **2**(21), 2737–2741.
200. A. Liu, S. Zhao, S.-B. Rim, J. Wu, M. Könemann, P. Erk and P. Peumans, Control of electric field strength and orientation at the donor–acceptor interface in organic solar cells, *Adv. Mater.*, 2008, **20**(5), 1065–1070.
201. Brian A. Gregg, Entropy of charge separation in organic photovoltaic cells: The benefit of higher dimensionality, *J. Phys. Chem. Lett.*, 2011, **2**(24), 3013–3015.
202. Askat E. Jailaubekov, Adam P. Willard, John R. Tritsch, Wai-Lun Chan, Na Sai, Raluca Gearba, Loren G. Kaake, Kenrick J. Williams, Kevin Leung, Peter J. Rossky and X.-Y. Zhu, Hot charge-transfer excitons set the time limit for charge separation at donor/acceptor interfaces in organic photovoltaics, *Nat. Mater.*, 2013, **12**(1), 66–73.
203. Domenico Caruso and Alessandro Troisi, Long-range exciton dissociation in organic solar cells, *Proc. Natl. Acad. Sci. USA*, 2012, **109**(34), 13498–13502.
204. Erich Runge and E. K. U. Gross, Density-functional theory for time-dependent systems, *Phys. Rev. Lett.*, 1984, **52**(12), 997–1000.
205. Zheng-Li Cai, Karina Sendt and Jeffrey R. Reimers, Failure of density-functional theory and time-dependent density-functional theory for large extended π systems, *J. Chem. Phys.*, 2002, **117**, 5543.
206. Eneritz Muguruza González, Leonardo Guidoni and Carla Molteni, Chemical and protein shifts in the spectrum of the photoactive yellow protein: a time-dependent density functional theory/molecular mechanics study, *Phys. Chem. Chem. Phys.*, 2009, **11**, 4556.
207. David J Tozer, Relationship between long-range charge-transfer excitation energy error and integer discontinuity in Kohn–Sham theory, *J. Chem. Phys.*, 2003, **119**(24), 12697–12699.
208. Andreas Dreuw and Martin Head-Gordon, Failure of time-dependent density functional theory for long-range charge-transfer excited states: The zincbacteriochlorin-bacteriochlorin and bacteriochlorophyll-spheroidene complexes, *J. Am. Chem. Soc.*, 2004, **126**(12), 4007–4016.
209. Roberto Peverati and Donald G. Truhlar, Improving the accuracy of hybrid meta-GGA density functionals by range separation, *J. Phys. Chem. Lett.*, 2011, **2**(21), 2810–2817.
210. A. Karolewski, T. Stein, R. Baer and S. Kümmel, Communication: Tailoring the optical gap in light-harvesting molecules, *J. Chem. Phys.*, 2011, **134**(15), 151101–151101–4.

211. Tamar Stein, Leeor Kronik and Roi Baer, Reliable prediction of charge transfer excitations in molecular complexes using time-dependent density functional theory, *J. Am. Chem. Soc.*, 2009, **131**(8), 2818–2820.
212. John S. Sears, Thomas Koerzdoerfer, Cai-Rong Zhang and Jean-Luc Brédas, Communication: Orbital instabilities and triplet states from time-dependent density functional theory and long-range corrected functionals, *J. Chem. Phys.*, 2011, **135**(15), 151103–151103–4.
213. Mathias Pabst, Dage Sundholm and Andreas Köhn, Ab initio studies of triplet-state properties for organic semiconductor molecules, *J. Phys. Chem. C*, 2012, **116**(29), 15203–15217.
214. Itamar Borges, Adélia J. A. Aquino, Andreas Köhn, Reed Nieman, William L. Hase, Lin X. Chen and Hans Lischka, Ab initio modeling of excitonic and charge-transfer states in organic semiconductors: The PTB1/PCBM low band gap system, *J. Am. Chem. Soc.*, 2013, **135**(49), 18252–18255.
215. Bernd Lunkenheimer and Andreas Köhn, Solvent effects on electronically excited states using the conductor-like screening model and the second-order correlated method ADC(2), *J. Chem. Theory. Comput.*, 2013, **9**(2), 977–994.
216. L. Hedin and S. Lundqvist, Effects of electron-electron and electron–phonon interactions on the one-electron states of solids. In *Solid State Physics: Advances in Research and Application*, volume 23, pages 1–181. Academix Press, New York, 1969.
217. Michael Rohlfing and Steven G. Louie, Electron-hole excitations and optical spectra from first principles, *Phys. Rev. B*, 2000, **62**(8), 4927.
218. Giovanni Onida, Lucia Reining and Angel Rubio, Electronic excitations: density-functional versus many-body Green's-function approaches, *Rev. Mod. Phys.*, 2002, **74**(2), 601.
219. Stefan Albrecht, Lucia Reining, Rodolfo Del Sole and Giovanni Onida, Ab initio calculation of excitonic effects in the optical spectra of semiconductors, *Phys. Rev. Lett.*, 1998, **80**(20), 4510.
220. Yuchen Ma and Michael Rohlfing, Optical excitation of deep defect levels in insulators within many-body perturbation theory: The f center in calcium fluoride, *Phys. Rev. B*, 2008, 77(11), 115118.
221. Eric L. Shirley, Ab initio inclusion of electron–hole attraction: Application to x-ray absorption and resonant inelastic x-ray scattering, *Phys. Rev. Lett.*, 1998, **80**(4), 794.
222. Michael Rohlfing and Steven G. Louie, Optical excitations in conjugated polymers, *Phys. Rev. Lett.*, 1999, **82**(9), 1959.
223. Emilio Artacho, M. Rohlfing, M. Côté, P. D. Haynes, R. J. Needs and C. Molteni, Structural relaxations in electronically excited poly(paraphenylene), *Phys. Rev. Lett.*, 2004, **93**(11), 116401.
224. Michael Rohlfing and Steven G. Louie, Excitonic effects and the optical absorption spectrum of hydrogenated Si clusters, *Phys. Rev. Lett.*, 1998, **80**(15), 3320.

225. Sohrab Ismail-Beigi and Steven G. Louie, Excited-state forces within a first-principles Green's function formalism, *Phys. Rev. Lett.*, 2003, **90**(7), 076401.
226. Murilo L. Tiago and James R. Chelikowsky, Optical excitations in organic molecules, clusters, and defects studied by first-principles Green's function methods, *Phys. Rev. B*, 2006, **73**(20), 205334.
227. X. Blase and C. Attaccalite, Charge-transfer excitations in molecular donor–acceptor complexes within the many-body Bethe-Salpeter approach, *Appl. Phys. Lett.*, 2011, **99**(17), 171909.
228. X. Blase, C. Attaccalite and V. Olevano, First-principles GW calculations for fullerenes, porphyrins, phtalocyanine, and other molecules of interest for organic photovoltaic applications, *Phys. Rev. B*, 2011, **83**(11), 115103.
229. Carina Faber, Ivan Duchemin, Thierry Deutsch, Claudio Attaccalite, Valerio Olevano and Xavier Blase, Electron–phonon coupling and charge-transfer excitations in organic systems from many-body perturbation theory, *Journal of Materials Science*, 2012, **47**(21), 7472–7481.
230. Björn Baumeier, Denis Andrienko, Yuchen Ma and Michael Rohlfing, Excited states of dicyanovinyl-substituted oligothiophenes from many-body Green's functions theory, *J. Chem. Theory Comput.*, 2012, **8**(3), 997–1002.
231. Björn Baumeier, Denis Andrienko and Michael Rohlfing, Frenkel and charge-transfer excitations in donor–acceptor complexes from many-body Green's functions theory, *J. Chem. Theory. Comput.*, 2012, **8**(8), 2790–2795.
232. Ivan Duchemin and Xavier Blase, Resonant hot charge-transfer excitations in fullerene-porphyrin complexes: many-body Bethe–Salpeter study, *Phys. Rev. B*, 2013, **87**(24), 245412.
233. Denis Andrienko and Kurt Kremer, Simulations. In Krzysztofty-jaszewski, Yves Gnanou, and Ludwik Leibler, editors, *Macromolecular Engineering*, pages 1431–1469. Wiley-VCH Verlag GmbH, 2007.

Subject Index

Ab initio material parameters, 277–282
  electronic material parameters, 279–280
  electron–phonon coupling, 281–282
Acrylates, 239–240
Ad hoc methods, 323
Adiabatic states, 321
Adsorption energy, 58–59
Adsorption potential, 64
Amphiphiles, 173–176
Amphiphilic systems
  electronic functionality, 176–191
  optical functionality, 191–198
Atomistic models, 316–317
Azimuthal anisotropy, 61
Azimuthal rotation angle, 326–327

BDATB. *See* 1,4-Bis(2,4-diamino-1,3,5-triazine)benzene
Bethe–Salpeter equation, 342
BHJ solar cells. *See* Bulk heterojunction (BHJ) solar cells
Binary molecular networks, 109–112
  metal–organic coordination networks (MOCNs), 110–112
  on-surface covalent-bonded molecular networks, 112–115
  tunable 2D molecular arrays on graphite, 110
1,4-Bis(2,4-diamino-1,3,5-triazine)benzene (BDATB), 63, 101
Bismelamine BM12 derivatives, 4, 5
Blade coating process, 230–231
Bulk heterojunction (BHJ) solar cells, 32–34, 36, 39, 144–152

Cationic ring-opening polymerization (CROP), 242, 243
Charge mobility, 335–337
Charge transfer rates, 324–325
Charge transport, 300–304, 320
  charge transfer rates, 324–325
  diabatic states, 321–324
  driving forces, 328–335
  electronic coupling elements, 325–328
  one-dimensional coronene system, 300–302
  organic electronic materials, 273–304
  reorganization energies, 328
  two-dimensional pentacene system, 302–304
Charge transport package, 342–343
Chiral induced spin selectivity (CISS), 204, 205, 208, 215, 218
Chiral supramolecular structures
  applications and implications, 218–222
  experimental results, 208–218
  memory device, 218–222
  resonances, 207–208
  spin-dependent conductivity, 211–218

Chiral supramolecular structures (*continued*)
spin-dependent photoelectron transmission, 208–211
spin–orbit coupling (SOC), 207
theory, 205–208
Chloro[subphthalocyaninato]-boron(III) (SubPc), 77
Cinnamates, 241–242
CISS. *See* Chiral induced spin selectivity
CMake, 344
Coarse-grained models, 318–320
Coarse-graining package, 342
COF. *See* Covalent organic frameworks
Continuum drift-diffusion, 312
Copper phthalocyanine (CuPc), 61–62, 84–85
Copper tetraphenyl-porphine (CuTTP), 61–62
Corannulene, trifluoromethylated, 11
Coronene bis-imide (CBI) amphiphiles, 185
Coulomb interactions, 313
Covalent bonding, 69–74
Covalent organic frameworks (COF), 8, 9, 17
CROP. *See* Cationic ring-opening polymerization
Cushion-effect charge redistribution, 81

Degrees of freedom, 321
Density of states (DOS), 322, 324
Diabatic states, 321–324, 325
Dibenzotetrathienocoronene (6-DBTTC), 39
Diketopyrrolopyrrole (DPP) derivatives
organic photovoltaic devices, 37–38
Dipole-dipole interactions, 76
Discotic quaterrylene tetracarboxylic diimide, 24
Disorder models, 277, 282
Distributed multipoles, 330–331
DOS. *See* Density of states
Driving forces, 328–335
case studies, 334–335
distributed multipoles, 330–331
electrostatic interaction energy, 329–330
induction interaction, 331–333
Thole's model, 333–334
DSCs. *See* Dye-sensitized solar cells
Dye-sensitized solar cells (DSCs), 32
Dynamic coupling, 321

EA. *See* Electron affinity
EIB. *See* Electron injection barrier
Electron affinity (EA), 80, 83
Electronic coupling elements, 325–328
Electronic functionality, 176–191
miscellaneous π-conjugated amphiphiles, 183–186
multi-chromophoric p-n amphiphiles, 186–189
n-type semiconducting amphiphiles, 181–183
p-type semiconducting amphiphiles, 176–181
supramolecular amphiphiles, 190–191
Electronic material parameters, 279–280
Electron injection barrier (EIB), 81
Electron–phonon coupling, 281–282
Electrons, 277–279
Electro-optic devices, 154–158
Electrospray deposition (ESD) fabrication method, 232–233
Electrostatic interaction energy, 329–330, 332, 341
Ewald summation method, 340
Excited states, 341–342

Finite-size effects, 337–338
First-principles calculations, 315–316
Fluorene derivatives, organic light emitting diodes, 27
Fluoroaluminium phthalocyanines, 8

Fluoroaluminium phthalocyanines (PcAlF), 8
Frenkel excitons, 312, 328
Friedel oscillations, 78
Frozen-core approximation, 321

Glaser coupling, 73
Green's functions theory, 342

HBCs. *See* Hexa-peri-benzocoronenes
Hexabenzocoronene derivatives, organic photovoltaic devices, 38–39
Hexa-peri-benzocoronenes (HBCs), 178–181
Hexathienocoronenes (HTCs), 11
HIB. *See* Hole injection barrier
Hole injection barrier (HIB), 81
Holstein–Peierls Hamiltonian, 275, 277, 278
HTCs. *See* Hexathienocoronenes
Hydrogen bonding, 65–68

IDIS. *See* Induced density of interface states
IE. *See* Ionization energy
Induced density of interface states (IDIS), 83–84
Intermolecular interactions, 63–80
  covalent bonding, 69–74
  dipole-dipole interactions, 76
  hydrogen bonding, 65–68
  metal-coordination, 68–69
  substrate-mediated interactions, 78–80
  Van der Waals interactions, 74–76
1,8-Iodooctane, 34
Ionization energy (IE), 80, 83

J-aggregates dyes, 41

Kinetic Monte Carlo (KMC) methods, 336, 343
Kohn–Sham–Fock matrix elements, 324
Kubo formalism, 275–277

Lamellar fibers, 3
Lamination process, 234–235
Liquid buffer layer, 231–232
Long-range interactions, 339–341
Low-dimensional supramolecular assemblies, 98–116
  1D molecular chains, 99–106
  2D molecular networks, 106–115

Marcus rate, 324–325, 330
Memory device, 218–222
Metal-coordination, 68–69
Metal-organic coordination networks (MOCNs), 110–112
Miscellaneous π-conjugated amphiphiles, 183–186
Mixed quantum–classical propagation, 292–304
  charge carrier influence, electronic structure and molecular dynamics, 297–300
  charge transport characteristics, 300–304
  self-consistent propagation scheme, 293–297
MOCNs. *See* Metal-organic coordination networks
Molecular self-assembly concepts, 120–125
Molecule-centered multipole moments, 330
Morphology simulations, 314–320
  atomistic models, 316–317
  coarse-grained models, 318–320
  first-principles calculations, 315–316
Multi-chromophoric p-n amphiphiles, 186–189
Multicomponent self-assembly strategies
  electronic considerations in, 80–88
  intermolecular interactions, 63–80

Multicomponent self-assembly strategies (*continued*)
molecule-substrate interactions, 57–63
standard interfacial models, 80–84
supramolecular environment-dependent electronic properties, 84–88
for supramolecular systems, 53–89
taming the driving forces, 55–57
Multi walled carbon nanotubes (MWCNTs), 10
MWCNTs. *See* Multi walled carbon nanotubes

Naphthalene diimides (NDIs), 186
NDIs. *See* Naphthalene diimides
N,N′-diphenyl-N,N′-bis(l-naphthyl)-1-1′-biphenyl-4,4′′-di-amine (α-NPD), 235
N-pyridyl-perylene-imide, 40
N-type semiconducting amphiphiles, 181–183

Octachloro zinc phthalocyanines (ZnPcCl8), 60–61
OFETs. *See* Organic field-effect transistors
OLEDs. *See* Organic light emitting diodes
Oligo(*p*-phenylenevinylene) (OPPV) derivatives, OLED, 26–27
Oligo(p-phenylenevinylene)s (OPVs), 176–178
Oligothiophene–barbituric acid, 4, 5
Oligothiophene nanofibers, 34–35
OMARGs. *See* Oriented multicolored antiparallel redox gradients
OMBD. *See* Organic molecular beam deposition
One dimensional (1D) molecular chains, 99–106
assembled through hydrogen bonding, 101–102
metal–organic coordination bonds assisted assembly of, 103–104
on-surface synthesis through covalent bonding of, 104–106
substrate template directed self-assembly of, 100–101
One-dimensional coronene system, 300–302
On-surface covalent-bonded molecular networks, 112–115
Optical functionality, 191–198
OPVs. *See* Oligo-(p-phenylenevinylene)s
Organic field-effect transistors (OFETs), 18–25, 128–144
aromatic molecules, 24–25
perylene derivatives, 21–24
phthalocyanine derivatives, 21
tetrathiafulvalene derivatives, 20
thiophene derivatives, 19–20
Organic light emitting diodes (OLEDs), 152–154
acrylates, 239–240
blade coating process, 230–231
cinnamates, 241–242
cross-linking, reactive groups addition, 236–246
electrospray deposition (ESD) fabrication method, 232–233
fluorene derivatives, 27
fluorinated solvents, 257–259
H-bond and metallo-supramolecular polymers, 30–31
hybrid approaches, 259–265
lamination process, 234–235
liquid buffer layer, 231–232
metallic and inclusion complexes, 29–30
oligo(*p*-phenylenevinylene) (OPPV) derivatives, 26–27
orthogonal solvents, concept of, 250–252
oxetanes, 242–246
polar solvents, 252–257

polyaromatic molecules, 27–29
precursor route, 247–248
siloxanes, 236–238
solution processed multilayer, 226–265
styrenes, 238–239
thermal stabilization, 246–247
transfer printing process, 234
trifluorovinylethers, 240–241
universal cross-linking approach, 248–250
Organic molecular beam deposition (OMBD), 53–54
Organic opto-electronic devices
bulk-heterojunction solar cells, 144–152
electro-optic devices, 154–158
organic field-effect transistors, 128–144
organic light emitting diodes, 152–154
SAM and SAMT applications, 125–128
Organic/organic interfaces, 340
Organic photovoltaic devices
aromatic molecules, 40–41
diketopyrrolopyrrole (DPP) derivatives, 37–38
hexabenzocoronene derivatives, 38–39
porphyrin and phthalocyanine derivatives, 36–37
rylene derivatives, 39–40
thiophene derivatives, 32–35
triarylamines molecules, 40
Organic solar cell, 310
Organogels, 24–25, 27–28, 34–35
Oriented multicolored antiparallel redox gradients (OMARGs), 39
Oxetanes, 242–246
Oxetanes, cationic polymerization of, 242

PBIs. *See* Perylene bis-imides
Perfluoropentacene (PFP), 58–59, 84–85
Perylene bis-imide nanofibers, 34–35
Perylene bis-imides (PBIs), 181–183
Perylene derivatives
organic field-effect transistors (OFETs), 21–24
supramolecular materials, 11–14
Perylene diimides (PDIs). *See* Perylene bis-imides (PBIs)
3,4,9,10-Perylenetetracarboxylic diimide (PTCDI), 63, 64, 65, 66
Perylene-tetracarboxylic diimides (PTCDIs), 11–14
PFP. *See* Perfluoropentacene
[6,6]-Phenyl-C_{61}-butyric acid methyl ester (PCBM), 32
Phonons, 277–279
Phthalocyanine derivatives
organic field-effect transistors, 21
organic photovoltaic devices, 36–37
Phthalocyanines, 7
Polaron theory based charge propagation, 291–292
Polaron transport approaches, 282–283
high temperatures, 287–288
limiting cases, 286–289
low temperatures, 288–289
narrow-band limit, 286–287
three-dimensional anisotropic mobility, 283–286
Polar solvents, 252–257
Poly(3-hexylthiophene) (P3HT), 32
Poly(didodecylquaterthiophene-*alt*-didodecylbithiazole), 19
Polyaromatic derivatives, supramolecular material, 10–11
Polyfluorene, 27
Polypyrrole, 9
Porphyrin derivatives
organic photovoltaic devices, 36–37
supramolecular materials, 7–10
Porphyrin-fullerene dyads, 36
Porphyrin synthon, 36

Precursor route, 247–248
Propoxyethyl-PTCDI, 4, 5
Pseudo-crystalline electroactive domains, 2
PTCDIs. *See* Perylene-tetracarboxylic diimides
P-type semiconducting amphiphiles, 176–181
  hexa-peri-benzocoronenes (HBCs), 178–181
  oligo(p-phenylenevinylene)s (OPVs), 176–178
Pyrrole derivatives, supramolecular material, 7–10

Quantum dynamic charge propagation techniques, 289–304
  mixed quantum–classical propagation, 292–304
  polaron theory based, 291–292

Rashba term, 205, 207
Receptor modules, 9
Resonances, 207–208
Rylene derivatives, organic photovoltaic device, 39–40

Schottky–Mott model, 81, 83
Self-consistent propagation scheme, 293–297
  initialization, 293–294
  molecular dynamics, 297
  parameterization, 294–295
  quantum dynamics, 295–297
SHJ. *See* Supramolecular n/p-heterojunction (SHJ) approach
Siloxanes, 236–238
Single-component supramolecular structures, 107–109
Single-walled carbon nanotubes (SWCNTs), 10
Site energies, 329
SOC. *See* Spin-orbit coupling
Spin-dependent conductivity, 211–218
Spin-dependent photoelectron transmission, 208–211
Spin-orbit coupling (SOC), 204, 205, 207
Spin selective electron transfer, 213–218
Standard interfacial models, 80–84
STANWs. *See* Supramolecular triarylamine nanowires
Stern–Volmer plot, 195
Stimuli-responsive gels, 17
Stochastic models, 338–339
Styrenes, 238–239
Substrate-mediated intermolecular interactions, 78–80
Sumanene, 11
Supramolecular amphiphiles, 190–191
Supramolecular environment-dependent electronic properties, 84–88
Supramolecular materials
  aromatic molecules, 15–18
  conjugated polymers, 15–16
  perylene derivatives, 11–14
  polyaromatic derivatives, 10–11
  porphyrin derivatives, 7–10
  pyrrole derivatives, 7–10
  tetrathiafulvalene derivatives, 6–7
  thiophene derivatives, 2–6
  triarylamine derivatives, 14–15
Supramolecular n/p-heterojunction (SHJ) approach, 39
Supramolecular pH sensing mechanism, 196
Supramolecular polymerization, 30
Supramolecular triarylamine nanowires (STANWs), 14–15
SWCNTs. *See* Single-walled carbon nanotubes

TDDFT. *See* Time-dependent density-functional theory
Temperature-activated hopping transport, 320
Template activated surface process (TAS). *See* Lamination process

2,3,5,6-Tetrafluoro-7,7′,8,8′-tetracyano-*p*-quinodimethane (F_4TCNQ), 6–7
Tetrathiafulvalene, 6
Tetrathiafulvalene derivatives
  organic field-effect transistors, 20
  supramolecular materials, 6–7
Thermal stabilization, 246–247
Thiophene derivatives
  organic field-effect transistors (OFETs), 19–20
  organic photovoltaic devices, 32–35
  supramolecular materials, 2–6
Time-dependent density-functional theory (TDDFT), 341
Time-dependent diffusion coefficient, 303
Time-of-flight methods, 16
Transfer printing process, 234
Triarylamine derivatives, supramolecular material, 14–15
Trifluorovinylethers, 240–241
Two dimensional (2D) molecular networks, 106–115
  binary molecular networks, 109–112
  single-component supramolecular structures, 107–109
Two-dimensional pentacene system, 302–304

Ullmann coupling, 71, 74, 104, 105
Universal cross-linking approach, 248–250

Van der Waals interactions, 74–76
Versatile Object-oriented Toolkit for Coarse-graining and Charge Transport Applications (VOTCA), 342–343
  charge transport package, 342–343
  coarse-graining package, 342
  kinetic Monte Carlo method, 343
  modules of, 343
VOTCA. *See* Versatile Object-oriented Toolkit for Coarse-graining and Charge Transport Applications

White organic light emitting diodes (WOLED), 227
WOLED. *See* White organic light emitting diodes
Work function, 82–83, 86

Zinc chlorins, 7–8
Zinc meso-tetra(4-pyridyl)porphyrin, 37